

Springer Series in MATERIAL SCIENCE

Editors: R. Hull R. M. Osgood, Jr. J. Parisi H. Warlimont

The Springer Series in Materials Science covers the complete spectrum of materials physics, including fundamental principles, physical properties, materials theory and design. Recognizing the increasing importance of materials science in future device technologies, the book titles in this series reflect the state-of-the-art in understanding and controlling the structure and properties of all important classes of materials.

- | | |
|--|---|
| <p>71 Dissipative Phenomena in Condensed Matter
Some Applications
By S. Datta Gupta and S. Puri</p> <p>72 Predictive Simulation of Semiconductor Processing
Status and Challenges
Editors: J. Dabrowski and E.R. Weber</p> <p>73 SiC Power Materials
Devices and Applications
Editor: Z.C. Feng</p> <p>74 Plastic Deformation in Nanocrystalline Materials
By M.Yu. Gutkin and I.A. Ovid'ko</p> <p>75 Wafer Bonding
Applications and Technology
Editors: M. Alexe and U. Gösele</p> <p>76 Spirally Anisotropic Composites
By G.E. Freger, V.N. Kestelman, and D.G. Freger</p> <p>77 Impurities Confined in Quantum Structures
By P.O. Holtz and Q.X. Zhao</p> <p>78 Macromolecular Nanostructured Materials
Editors: N. Ueyama and A. Harada</p> | <p>79 Magnetism and Structure in Functional Materials
Editors: A. Planes, L. Manosa, and A. Saxena</p> <p>80 Ion Implantation and Synthesis of Materials
By M. Nastasi and J.W. Mayer</p> <p>81 Metallopolymer Nanocomposites
By A.D. Pomogailo and V.N. Kestelman</p> <p>82 Plastics for Corrosion Inhibition
By V.A. Goldade, L.S. Pinchuk, A.V. Makarevich and V.N. Kestelman</p> <p>83 Spectroscopic Properties of Rare Earths in Optical Materials
Editors: G. Liu and B. Jacquier</p> <p>84 Hartree–Fock–Slater Method for Materials Science
The DV-X Alpha Method for Design and Characterization of Materials
Editors: H. Adachi, T. Mukoyama, and J. Kawai</p> <p>85 Lifetime Spectroscopy
A Method of Defect Characterization in Silicon for Photovoltaic Applications
By S. Rein</p> <p>86 Wide-Gap Chalcopyrites
Editors: S. Siebentritt and U. Rau</p> |
|--|---|

Volumes 20–70 are listed at the end of the book.

S. Rein

Lifetime Spectroscopy

A Method of Defect Characterization
in Silicon for Photovoltaic Applications

With 153 Figures and 29 Tables



Springer

Dr. Stefan Rein

Fraunhofer Institute for Solar Energy Systems
Department Solar Cells, Materials and Technology
Heidenhofstr. 2, 79110 Freiburg, Germany
E-mail: stefan.rein@ise.fraunhofer.de

Series Editors:

Professor Robert Hull

University of Virginia
Dept. of Materials Science and Engineering
Thornton Hall
Charlottesville, VA 22903-2442, USA

Professor R. M. Osgood, Jr.

Microelectronics Science Laboratory
Department of Electrical Engineering
Columbia University
Seeley W. Mudd Building
New York, NY 10027, USA

Professor Jürgen Parisi

Universität Oldenburg, Fachbereich Physik
Abt. Energie- und Halbleiterforschung
Carl-von-Ossietzky-Strasse 9-11
26129 Oldenburg, Germany

Professor Hans Warlimont

Institut für Festkörper-
und Werkstoffforschung,
Helmholtzstrasse 20
01069 Dresden, Germany

ISSN 0933-033X

ISBN-10 3-540-25303-3 Springer Berlin Heidelberg New York

ISBN-13 978-3-540-25303-7 Springer Berlin Heidelberg New York

Library of Congress Cataloging-in-Publication Data

This work is subject to copyright. All rights are reserved, whether the whole or part of the material is concerned, specifically the rights of translation, reprinting, reuse of illustrations, recitation, broadcasting, reproduction on microfilm or in any other way, and storage in data banks. Duplication of this publication or parts thereof is permitted only under the provisions of the German Copyright Law of September 9, 1965, in its current version, and permission for use must always be obtained from Springer. Violations are liable to prosecution under the German Copyright Law.

Springer is a part of Springer Science+Business Media.
springeronline.com

© Springer-Verlag Berlin Heidelberg 2005
Printed in Germany

The use of general descriptive names, registered names, trademarks, etc. in this publication does not imply, even in the absence of a specific statement, that such names are exempt from the relevant protective laws and regulations and therefore free for general use.

Typesetting by the editors

Production: LE-T_EX Jelonek, Schmidt & Vöckler GbR, Leipzig

Cover concept: eStudio Calamar Steinen

Cover production: *design & production* GmbH, Heidelberg

Printed on acid-free paper

SPIN: 11320067

57/3141/YL

5 4 3 2 1 0

*To my parents, my wife and my children,
with my love.*

Preface

The monograph deals with lifetime spectroscopy, a group of new spectroscopic techniques to characterize defects in semiconductor materials. Electrically active defects may limit the performance of many semiconductor devices even if they are present in concentrations below the detection limit of conventional techniques. An important example concerns the energy conversion efficiency of solar cells. The development of strategies to reduce or avoid such harmful defects must start with their identification, which becomes increasingly difficult as the electronic quality of the semiconductor material improves. Because of its high sensitivity to all electrically active – and thus relevant – defects, lifetime spectroscopy is ideally suited for such an identification. This is reflected in the rapidly growing interest in lifetime spectroscopy which can be observed in the photovoltaic field.

Although the first publications on lifetime spectroscopy date back to the early 1990s, the potential of lifetime spectroscopy had not yet been analyzed systematically, which led to incorrect estimates even among specialists. In the present monograph, the possibilities and limitations of the different lifetime spectroscopic techniques are investigated in depth within a detailed theoretical evaluation, which allows the spectroscopic potential of the various techniques to be accurately assessed for the first time. Verification of the theoretical predictions within a comprehensive experimental study on different, technologically relevant metal impurities is another priority and demonstrates the usefulness of the different lifetime spectroscopic techniques as diagnostic tools. Finally, the successful characterization of the metastable defect in Czochralski silicon, which is well known due to its harmful impact on solar cell efficiency but could not previously be detected by any conventional technique, demonstrates the applicability of lifetime spectroscopy in practice.

Since the monograph thus covers the relevant topics of theoretical evaluation, experimental verification and application in practice, it represents a complete course on lifetime spectroscopy which may be interesting for different groups of readers. On the one hand, it is intended as an introduction to this field, with a uniform presentation of the techniques, a detailed physical explanation of all observed effects and a comprehensive

development of the theoretical results. The illustration of these results is based on a newly developed type of diagram – the defect parameter solution surface (DPSS) – which represents one of the key concepts of the work as it clearly visualizes the spectroscopic potential of the different techniques and thereby enables immediate understanding. Basic knowledge in the field of carrier lifetime and lifetime measurement techniques is helpful but not essential, as the basics are summarized in the first two chapters. Since lifetime measurements already represent a standard tool for process control in the photovoltaics industry, the monograph aims to deepen the reader's understanding of the complex quantity, carrier lifetime, and to stimulate its spectroscopic analysis.

On the other hand, the monograph is intended as a reference book for scientists and engineers who are actively involved in semiconductor material characterization and defect engineering in research institutes and industrial laboratories. Chapter and section summaries as well as detailed tabular overviews of the theoretical, methodological and experimental results allow both quick access to the major results and simple location of detailed information in the text. As the data evaluation technique proposed here not only gives deeper insight into the analytical potential of the different techniques but also allows the precision and consistency of lifetime spectroscopic results to be estimated quantitatively, it represents a very versatile tool which may set a new standard. Since there is a growing demand for increasingly sensitive techniques to trace ever-diminishing quantities of impurities due to the increasingly stringent requirements of electronic devices, it appears certain that lifetime spectroscopy will become widespread not only in photovoltaics but also in other branches of the semiconductor industry. Furthermore, as the methodological results of the monograph are completely detached from the technique used for the lifetime measurements, they form a general basis for a spectroscopic evaluation of lifetime data and are thus expected to stimulate new developments in different fields of material characterization.

I am obliged to Professor Wolfram Wettling and Dr Gerhard Willeke for their guidance and unfailing encouragement, for allowing me great freedom in this research and for giving me the opportunity to write this monograph. My sincere thanks go also to Dr Stefan Glunz for his valuable advice, for contributing many good ideas and for critically reading the manuscript.

I would also like to thank Dr Wilhelm Warta for many useful discussions and Tobias Rehrl, Patrick Lichtner and Stephan Diez for their cooperation and exchange of ideas. I am also very grateful to Eddy Tavaszi and Stefan Kaufmann for their tireless and reliable lifetime measurements,

and to Elisabeth Schäffer for many measurements of solar cells and never-failing assistance with complicated graphic programs. As for technical assistance, I want to thank the entire clean-room team at Fraunhofer ISE for solar cell processing and especially Antonio Leimenstoll for his close cooperation and help with the preparation of countless Cz samples, Harald Lautenschlager, Mira Kwiatkowska and Christian Schetter for etching and sintering samples, Gernot Emanuel and his plasma-processing staff for the silicon-nitride passivation of wafers and Henner Kampwerth for grinding wafers. I would like to thank all my PhD colleagues and the other members of the Solar Cell Department at Fraunhofer ISE for providing a friendly and enjoyable environment to work in.

My gratitude also extends to Professor Andres Cuevas and Dr Daniel Macdonald of the Australian National University for their cooperation in the field of lifetime spectroscopy and the productive exchange of knowledge and ideas, Dr Ron Sinton of Sinton Consulting for his valuable advice on the QSSPC technique, Professor Tadashi Saitho of Tokyo National University for organizing international joint research on the Cz defect, and the members of the VOCSI project for many interesting and highly stimulating scientific meetings on the Cz defect. In addition, I would like to thank Dr Takao Abe from the Shin-Etsu company and Dr Bob Falster from MEMC for interesting Cz-Si samples and Dr Ulrich Lambert from the Wacker Siltronic company for providing most of the metal-contaminated samples which led to decisive results in this work.

Concerning manuscript preparation, I am grateful to Brigitte Rein for her indefatigable and reliable proof-reading, Dr Helen Rose Wilson for excellent language polishing and Thomas Rein for his valuable formatting assistance. Finally, I would like to express my deepest thanks to my wife Nicole for her unfailing support and to my children Janis, Sophie and Simon for their understanding that compiling a monograph requires much time and patience.

Freiburg
December 2004

Stefan Rein

Contents

Abbreviations, acronyms and symbols	XVII
Abbreviations and acronyms	XVII
Arabic symbols	XVIII
Greek symbols.....	XXIV
Introduction	1
Motivation	1
Aims and outline	3
References	4
1. Theory of carrier lifetime in silicon	5
1.1 Introduction	5
1.2 Fundamentals 1: basic and advanced models for the fundamental semiconductor quantities.....	6
1.2.1 Intrinsic carrier concentration and doping: the basic model	6
1.2.2 Temperature dependence of the majority carrier concentration: the standard model	12
1.2.3 Impact of advanced temperature models for $N_{C,V}(T)$ and $E_{gap}(T)$: the advanced model.....	21
1.2.4 Tabular overview of the T -models	30
1.3 Fundamentals 2: generation, recombination and carrier lifetime	31
1.4 Carrier recombination mechanisms	32
1.4.1 Radiative recombination	33
1.4.2 Auger recombination.....	35
1.4.3 Bulk recombination through defects (Shockley-Read-Hall)	41
1.4.4 Surface recombination through defects.....	49
1.5 Effective lifetime and the separation of bulk lifetime	51
1.6 Chapter summary	55
References	56

2. Lifetime measurement techniques	59
2.1 Introduction	59
2.2 Quasi-steady-state photoconductance technique (QSSPC)	61
2.3 Microwave-detected photoconductance decay technique (MW-PCD)	63
2.3.1 Microwave reflection and associated restrictions	63
2.3.2 MW-PCD measurement setup.....	64
2.3.3 The cryostat.....	66
References	68
3. Theory of lifetime spectroscopy	69
3.1 Introduction	69
3.2 General analysis of possibilities and restrictions.....	71
3.2.1 The Shockley-Read-Hall equation	72
3.2.2 Influence of the defect parameters on the SRH lifetime under LLI conditions.....	76
3.2.3 Injection-dependent SRH lifetime – IDLS	80
3.2.4 Temperature-dependent LLI-SRH lifetime – TDLS	84
3.2.5 Section summary	89
3.3 Injection-dependent lifetime spectroscopy (IDLS): advanced analysis	91
3.3.1 Superposed effects: measurability of the injection-dependent shape of the SRH lifetime	93
3.3.2 The defect parameter solution surface (DPSS)	102
3.3.3 Theoretical analysis I: features of the DPSS curves.....	107
3.3.4 Theoretical analysis II: defect characterization by analyzing a set of IDLS curves with different doping concentrations....	135
3.3.5 Section summary	144
3.4 Temperature-dependent lifetime spectroscopy (TDLS): improved standard analysis and its limitations.....	147
3.4.1 Basic problem of data evaluation and data linearization.....	148
3.4.2 Improved techniques of data linearization	152
3.4.3 Resolution capability of TDLS	162
3.5 Temperature-dependent lifetime spectroscopy (TDLS): superposed effects and advanced analysis.....	177
3.5.1 Temperature-dependent capture cross-sections: origin, impact and relevance	178
3.5.2 Impact of superposed external carrier trapping	186
3.5.3 Impact of the temperature dependence of the majority carrier concentration.....	188

3.5.4 Impact of the optimum advanced model for the temperature dependence of $N_C(T)$, $N_V(T)$, $E_{gap}(T)$ on the TDLS curve	192
3.5.5 Experiment: accurate TDLS simulation on the basis of the advanced T -model	200
3.5.6 Determination of additional defect parameters by modeling the whole TDLS curve	203
3.5.7 Defect parameter solution surface of TDLS curves (DPSS) ..	210
3.5.8 Applicability of TDLS: onset temperature and width of the linear Arrhenius increase	216
3.5.9 Discussion of the fundamental assumptions of TDLS theory ..	220
3.5.10 Section summary	223
3.6 Combination of the results from TDLS and IDLS: combined DPSS analysis	228
3.7 Temperature- and injection-dependent lifetime spectroscopy (T -IDLS)	231
3.7.1 Defect characterization by analyzing a set of IDLS curves measured at various temperatures	232
3.7.2 Possibilities and restrictions of the simultaneous T -IDLS analysis	236
3.7.3 Section summary	247
3.8 Chapter summary and conclusion	248
References	253

4. Defect characterization on intentionally metal-contaminated silicon samples	257
4.1 Introduction	257
4.2 Experimental details	259
4.2.1 Sample preparation I: intentional metal contamination	259
4.2.2 Sample preparation II: surface passivation and its quality	263
4.2.3 Determination of the doping concentration	271
4.2.4 IDLS – measurement and modeling procedure	273
4.2.5 TDLS – measurement and modeling procedure	276
4.3 Molybdenum	285
4.3.1 Advanced TDLS analysis	285
4.3.2 Advanced IDLS analysis	295
4.3.3 Combined DPSS analysis of TDLS and IDLS	299
4.3.4 Comparison with results in the literature and discussion	301
4.3.5 Conclusion	302
4.4 Titanium	303
4.4.1 Advanced N_{dop} -IDLS analysis	304
4.4.2 Advanced TDLS analysis	310

4.4.3 Combined DPSS analysis of TDLS and IDLS	318
4.4.4 Comparison of results and discussion	321
4.4.5 Conclusion	325
4.5 Nickel	326
4.5.1 TDLS analysis of a <i>p</i> -type sample	327
4.5.2 TDLS analysis of an <i>n</i> -type sample	333
4.5.3 Conclusion	335
4.6 Iron	336
4.6.1 Previous work and special physical properties	338
4.6.2 Defect transformation and its effect on carrier lifetime	341
4.6.3 Defect configuration of interstitial iron (Fe_i^+)	350
4.6.4 Defect configuration of iron-boron pairs (FeB)	362
4.6.5 Additional information from a combined analysis of the FeB- and Fe_i -dominated IDLS curves.....	369
4.6.6 Conclusion	378
4.7 Detailed comparison of results	380
4.7.1 Comparison of experimental results: defect parameters	380
4.7.2 Comparison of methodological results: verification of theoretical predictions	386
4.8 Chapter summary	391
References	392
5. The metastable defect in boron-doped Czochralski silicon	397
5.1 Introduction	397
5.2 Analysis I: major components	399
5.2.1 Intentionally oxygen-contaminated float zone silicon	399
5.2.2 Modified Czochralski silicon	400
5.2.3 Normalized defect concentration	401
5.3 Analysis II: quantitative correlation with different impurities	403
5.3.1 Experimental procedure	403
5.3.2 Quantitative correlation with boron	405
5.3.3 Quantitative correlation with oxygen	405
5.3.4 Impact of thermal pretreatments	408
5.3.5 Quantitative correlation with carbon	410
5.3.6 Discussion and preliminary defect model	411
5.3.7 Impact of intrinsic point defects	413
5.3.8 Conclusion	415
5.4 Analysis III: mechanism of defect transformation	415
5.4.1 Kinetics of defect annihilation	415
5.4.2 Kinetics of defect formation	418

5.5 Analysis IV: electronic structure of the Cz defect.....	425
5.5.1 TDLS analysis.....	426
5.5.2 IDLS analysis	431
5.5.3 Combined DPSS analysis of IDLS and TDLS	433
5.5.4 Conclusion and discussion	434
5.6 Reduction of the Cz-specific defect concentration.....	436
5.6.1 Permanent improvement of the material quality by an optimized high-temperature process.....	436
5.6.2 Impact of the process parameters	440
5.6.3 Discussion	445
5.6.4 Conclusion	446
5.7 Material quality and realistic prediction of solar cell performance ..	446
5.7.1 Carrier lifetime investigation	447
5.7.2 Performance of solar cells on standard boron-doped Cz-Si: specific limitations and realistic prediction.....	449
5.7.3 Conclusion	455
5.8 Chapter summary	455
References	457
Summary and further work	461
Theory of lifetime spectroscopy: physical understanding and implementation	462
Experiment: lifetime spectroscopic study of intentionally metal-contaminated samples.....	464
Experiment: study of the metastable defect in Czochralski silicon.....	467
Relevance of the results and outlook	469
References	470
Zusammenfassung und Ausblick	471
Theorie der Lebensdauerspektroskopie:	
Physikalisches Verständnis und technische Umsetzung	472
Experiment: Lebensdauerspektroskopische Untersuchungen an gezielt metallisch verunreinigten Proben	475
Experiment: Untersuchung des metastabilen Defektes in Czochralski-Silizium.....	478
Relevanz der Ergebnisse und Ausblick.....	481
Literatur.....	482
Index	483

Abbreviations, acronyms and symbols

Abbreviations and acronyms

Acronym	Description
AM	air mass
arb.	arbitrary
Av	average
B, B _i , B _s	boron, interstitial boron, substitutional boron
BGN	band gap narrowing
BGH, BH	band gap half
B _i O ₁	defect complex of boron and oxygen
B _s O ₂	defect complex of boron and an oxygen dimer
BSF	back surface field
B _s X	defect complex of boron and an unknown component X
C _s	substitutional carbon
CB	conduction band
CE	Coulomb enhancement
CP133	damage etch
CV	capacitance voltage
Cz	Czochralski (silicon)
DLTS	deep-level transient spectroscopy
DPSS	defect parameter solution surface
DPSS-DG	DPSS definition gap
DPSS-IP	DPSS intersection point
DPSS-PL	DPSS plateau value
DPSS-VR	DPSS validity range
DPSS-ZP	DPSS zero point
EM	effective mass
Fe, Fe _i	iron, interstitial iron
FeB	iron-boron pair
FTIR	Fourier transform infrared spectroscopy
FZ	float zone (silicon)
Ga	gallium
HLI	high-level injection
HT	high temperature
IC	intrinsic conduction

IDLS	injection-dependent lifetime spectroscopy
ISE	Fraunhofer Institute for Solar Energy Systems
LLI	low-level injection
LS	lifetime spectroscopy
LSF	least squares fit
LT	low temperature
MajBH	band gap half close to the majority band
mc	multicrystalline (silicon)
MCz	magnetic Czochralski (silicon)
MinBH	band gap half close to the minority band
MLI	mid-level injection
Mo	molybdenum
MW-PCD	microwave-detected photoconductance decay
N_{dop} -IDLS	injection-dependent lifetime spectroscopy at various doping conc.
Ni	nickel
O _i	interstitial oxygen
O _{2i}	oxygen dimer
PC1D	semiconductor device simulation software
PECVD	plasma-enhanced chemical vapor deposition
PT100	platinum temperature sensor
QSSPC	quasi-steady-state photoconductance
RCA	cleaning procedure for the silicon surface
REDR	recombination-enhanced defect reaction
RP-PERC	random pyramid passivated emitter and rear cell
RT	room temperature
Si	silicon
SRH	Shockley-Read-Hall
SRV	surface recombination velocity
TDLS	temperature-dependent lifetime spectroscopy
Ti	titanium
T -IDLS	injection-dependent lifetime spectroscopy at various temperatures
V	vacancies
VB	valence band
X	unknown defect component

Arabic symbols

Symbol	Description	Unit
$a, b, c \dots i$	numerical constants in the effective mass model	—
B	coefficient of radiative band-to-band recombination	$\text{cm}^3 \text{s}^{-1}$
C	pre-factor to determine $[\text{Fe}]_{\text{total}}$ from lifetime data	cm^{-3}s
C_1	numerical constant in the FeB equilibrium fraction	cm^3

C_2	numerical constant in the FeB pair association time	$\text{cm}^{-3}\text{K}^{-1}\text{s}$
C_a	ambipolar Auger coefficient	cm^6s^{-1}
C_n, C_p	Auger coefficients	cm^6s^{-1}
C_n^*, C_p^*	Auger coefficients including Coulomb interaction	cm^6s^{-1}
c_n, c_p	capture coefficients for electrons and holes	cm^3s^{-1}
c_n^*, c_p^*	capture rates for electrons and holes	s^{-1}
Chi^2	error of a least squares fit	—
$(\text{Chi}^2)^{\text{DPSS}}$	error of a least squares fit (fitted DPSS parameter: DPSS- Chi^2 curve)	—
D	diffusivity	cm^2s^{-1}
D_a, D_n, D_p	ambipolar, electron, hole diffusion constant	cm^2s^{-1}
D_{it}	interface trap density	$\text{cm}^{-2}\text{eV}^{-1}$
D_C, D_V	density of allowed states in the CB and VB	$\text{cm}^{-3}\text{eV}^{-1}$
E	energy	eV
E_A, E_D	energy level of the dopant, acceptors and donors	eV
E_{ann}	activation energy, defect annihilation process in Cz-Si	eV
E_C	conduction band edge	eV
E_C-E_t	defect energy depth from the CB (true defect parameter)	eV
$(E_C-E_t)^{\text{BEST}}$	defect energy depth	eV
$(E_C-E_t)^{\text{DPSS}}$	(optimum TDLS fit result for varied N_{dop})	eV
$(E_C-E_t)^{\text{DPSS}}$	defect energy depth	eV
$(E_C-E_t)^{\text{DPSS-DG}}$	(varied DPSS parameter: DPSS energy) definition gap of the DPSS- k curve related to IDLS (DPSS characteristic)	eV
$(E_C-E_t)^{\text{DPSS-ZP}}$	zero point of the DPSS- k curve related to IDLS (DPSS characteristic)	eV
$(E_C-E_t)^{\text{DG/DPSS-ZP}}$	definition gap of the DPSS zero-point function (DPSS characteristic)	eV
$(E_C-E_t)^{\text{DPSS-IP 1,2}}$	energy positions of the 1 st /2 nd DPSS-IP in a superposed DPSS- k diagram associated with a set of IDLS curves	eV
E^{corr}	energy correction term at the 2 nd DPSS-IP in a superposed DPSS- k diagram associated with a set of IDLS curves	eV
E_{diss}	activation energy for the dissociation of iron-boron pairs	eV
E_F	Fermi energy	eV
E_F^{Adv}	Fermi energy, on the basis of the advanced T -model	eV
E_F^{Stand}	Fermi energy, on the basis of the standard T -model	eV
$E_{gap}, E_{gap}^{300\text{K}}$	energy band gap, at 300 K	eV
E_{gap}^{Green}	energy band gap, T -dependent according to Green	eV
E_{gap}^{Sze}	energy band gap, T -dependent according to Sze	eV
E_{gen}	activation energy, defect generation process in Cz-Si	eV
E_i	intrinsic Fermi energy	eV

E_{mig}	diffusion barrier of interstitial iron	eV
E_t	defect energy level (true defect parameter)	eV
E_V	valence band edge	eV
e_n, e_p	emission rates for electrons and holes	s ⁻¹
E_∞	activation energy, multiphonon emission capture process	eV
f	Fermi-Dirac distribution function	—
f, g, h	functional interrelations	—
f_A	ionization degree, fraction of ionized acceptor atoms	—
FF	fill factor	—
f_{abs}	absorption fraction	—
f_i	intrinsic excitation degree, $p_0(T)/N_A$	—
f_t	probability of occupation of a defect level by an electron (Fermi-Dirac distribution function)	—
g_{eeh}, g_{ehh}	enhancement factors of the eeh - and ehh -Auger process	—
G	generation rate	cm ⁻³ s ⁻¹
G_0	generation rate in thermal equilibrium	cm ⁻³ s ⁻¹
G_{bulk}	bulk generation rate	cm ⁻³ s ⁻¹
h	Planck's constant	J s
I_{av}	illumination intensity	mW/cm ²
I_{bias}	intensity of the bias light	mW/cm ²
I_{deg}	intensity of the degradation light	mW/cm ²
J_n	electron current density	mA/cm ²
J_{SC}	short-circuit current density	mA/cm ²
$J_{SC,0}$	short-circuit current density, initial value in Cz-Si	mA/cm ²
$J_{SC,d}$	short-circuit current density, stable degraded value in Cz-Si	mA/cm ²
k	defect symmetry factor $k := \sigma_n/\sigma_p$ (true defect parameter)	—
k_B	Boltzmann's constant	eV/K
k^{BEST}	defect symmetry factor (optimum TDLS fit result for varied N_{dop})	—
k^{DPSS}	defect symmetry factor (fitted DPSS parameter: DPSS- k curve)	—
$k^{DPSS-IP}$	defect symmetry factor at the 1 st /2 nd DPSS-IPs in a superposed DPSS- k diagram associated with a set of IDLS curves	—
$k^{DPSS-PL}$	symmetry factor of the DPSS plateau region (DPSS characteristic)	—
m_e^*, m_h^*	effective mass of electrons and holes	—
m_l	numerical constant in the effective mass model	—
m_0	electron rest mass in the effective mass model	—
N	electron density in non-equilibrium	cm ⁻³
n_0	electron density in thermal equilibrium	cm ⁻³

n_1	electron SRH density	cm ⁻³
n_1^{DPSS}	electron SRH density (varied DPSS parameter)	cm ⁻³
$n_1^{DPSS-DG}$	electron SRH density related to the DPSS-DG energy	cm ⁻³
$n_1^{DPSS-ZP}$	electron SRH density related to the DPSS-ZP energy	cm ⁻³
$n_1^{DG/DPSS-ZP}$	electron SRH density related to the definition-gap energy of the DPSS-ZP function	cm ⁻³
$n_{1,trap}$	SRH density associated with a trapping center	cm ⁻³
n_i, n_i^{300K}	intrinsic carrier concentration, T -dependent and at 300 K	cm ⁻³
N_s	electron density at the surface	cm ⁻³
n_{s0}	electron density at the surface in thermal equilibrium	cm ⁻³
N	numerical factor of the effective density of states	cm ⁻³
N_A, N_D	concentration of dopant atoms, acceptors and donors	cm ⁻³
N_A^-, N_D^+	concentration of dopant atoms, ionized	cm ⁻³
N_A^0, N_D^0	concentration of dopant atoms, non-ionized	cm ⁻³
N_C, N_V	eff. density of states, in the CB and VB	cm ⁻³
N_C^{300K}, N_V^{300K}	eff. density of states, at 300 K	cm ⁻³
N_C^{PCID}, N_V^{PCID}	eff. density of states, with $T^{3/2}$ -dependence	cm ⁻³
N_C^{EM}, N_V^{EM}	eff. density of states, based on the effective mass model	cm ⁻³
N_{crit}	critical recombination center density, validity limit of standard SRH theory due to internal trapping	cm ⁻³
N_{crit}^{LLI}	critical recombination center density, lower bound of N_{crit}	cm ⁻³
N_{dop}	doping concentration	cm ⁻³
N_{onset}	doping reference point (empirical bulk lifetime model)	cm ⁻³
N_{ph}^{1sun}	density of photons in solar light with 1 sun irradiance	cm ⁻² s ⁻¹ sun ⁻¹
N_T	density of trapped excess electrons	cm ⁻³
N_t	defect concentration (conc. of recombination centers)	cm ⁻³
N_t^*	normalized defect concentration	cm ⁻³
N_{tA}, N_{tP}	concentration of the Cz defect, in the active state (A) and in the passive state (P)	cm ⁻³
$N_{t,norm}$	[B _s]-normalized defect concentration	cm ⁻³
$N_{t,norm}^{LT}, N_{t,norm}^{HT}$	[B _s]-normalized defect concentration, in the starting material (LT) and in high-temperature-treated material (HT)	cm ⁻³
N_{trap}	density of trapping centers	cm ⁻³
p	hole density in non-equilibrium	cm ⁻³
p_0	hole density in thermal equilibrium	cm ⁻³
p_1	hole SRH density	cm ⁻³
p_1^{DPSS}	hole SRH density (varied DPSS parameter)	cm ⁻³
$p_1^{DPSS-DG}$	hole SRH density related to the DPSS-DG energy	cm ⁻³
$p_1^{DPSS-ZP}$	hole SRH density related to the DPSS-ZP energy	cm ⁻³
$p_1^{DG/DPSS-ZP}$	hole SRH density related to the definition-gap energy of the DPSS-ZP function	cm ⁻³

p_s	hole density at the surface	cm^{-3}
p_{s0}	hole density at the surface in thermal equilibrium	cm^{-3}
q	elementary charge	C
r	ratio N_C/N_V of the effective density of states at 300 K	—
R	recombination rate	$\text{cm}^{-3}\text{s}^{-1}$
R_0	recombination rate in thermal equilibrium	$\text{cm}^{-3}\text{s}^{-1}$
R_{ann}	defect annihilation rate in Cz-Si	s^{-1}
R_{gen}	defect generation rate in Cz-Si	s^{-1}
R_n	recombination activity of the Cz defect (passive state)	s^{-1}
R_P	recombination rate via the Cz defect (passive state)	$\text{cm}^{-3}\text{s}^{-1}$
S	surface recombination velocity	cm/s
S	solubility	cm^{-3}
t	time	s
T	temperature	K
T_0	transition temperature where the T -IDLS curves turn over	K
$T_<, T_>$	T range where the defect-dependent contribution to LLI-SRH lifetime is negligible (<) and dominant (>)	K
$T_{\text{Arrh-Onset}}$	onset temperature of the Arrhenius increase (TDLS)	K
$T_{\text{Advanced Arrh-Onset}}$	onset temperature of the Arrhenius increase (TDLS), on the basis of the advanced T -model	K
T_{fit}	T range underlying the SRH modeling of a TDLS curve	K
T_{FO}	freeze-out temperature	K
T_H	selected temperature in the $T_>$ region	K
$T_{\text{IC}}, T_{\text{IC-Onset}}$	onset temperature of intrinsic conduction	K
$T_{\text{IC}}^{\text{Adv}}, T_{\text{IC-Onset}}^{\text{Advanced}}$	onset temperature of intrinsic conduction, on the basis of the advanced T -model	K
$T_{\text{IC}}^{\text{Stand}}, T_{\text{IC-Onset}}^{\text{Standard}}$	onset temperature of intrinsic conduction, on the basis of the standard T -model	K
T_{iso}	temperature of an isothermal annealing experiment	K
T_L	selected temperature in the $T_<$ region	K
T_{trans}	T range in-between $T_<$ and $T_>$	K
U	net recombination rate	$\text{cm}^{-3}\text{s}^{-1}$
U_{Auger}	net Auger recombination rate	$\text{cm}^{-3}\text{s}^{-1}$
U_{bulk}	net bulk recombination rate	$\text{cm}^{-3}\text{s}^{-1}$
U_{eff}	effective net recombination rate	$\text{cm}^{-3}\text{s}^{-1}$
U_{rad}	net radiative recombination rate	$\text{cm}^{-3}\text{s}^{-1}$
U_S	net surface recombination rate	$\text{cm}^{-2}\text{s}^{-1}$
U_{SRH}	net SRH recombination rate via defects	$\text{cm}^{-3}\text{s}^{-1}$
U_v	net recombination rates of the individual mechanisms	$\text{cm}^{-3}\text{s}^{-1}$
U_1	activation energy, FeB equilibrium fraction	eV
U_2	activation energy, FeB pair association time	eV

V	ratio of the recombination activities of two defect levels	—
V/I	resistance	Ω
V_{OC}	open-circuit voltage	V
$V_{OC,0}$	open-circuit voltage, initial value in Cz-Si	V
$V_{OC,d}$	open-circuit voltage, stable degraded value in Cz-Si	V
v_{th}, v_{th}^{300K}	thermal velocity, T -dependent and at 300 K	cm/s
W	wafer thickness	cm
x, y	space coordinates	cm
X	systematic error in an identification of τ_{eff} with τ_{bulk}	%
$x^{A,B}, x^{D1,D2}$	pairs of indexes to distinguish the parameters of two different defects in a two-defect SRH fit	—
$x^{S1,S2}$	pair of indexes to distinguish the parameters of two solutions	—
X	lifetime weighting factor (two-defect fit)	—
X	[B _s] correlation exponent	—
X^{LT}, X^{HT}	[B _s] correlation exponent, in the starting material (LT) and in high-temperature-treated material (HT)	—
Y	[O _i] correlation exponent	—
Y_C, Y_R	[O _i] correlation exponent, determined on the complete data set (C) and on a reduced data set (R)	—
$Y_{MCz}, Y_{Cz,MCz}$	[O _i] correlation exponent, determined on a set of MCz samples and a set of Cz and MCz samples	—
Y^{LT}, Y^{HT}	[O _i] correlation exponent, in the starting material (LT) and in high-temperature-treated material (HT)	—
Z	[C _s] correlation exponent	—
[B _s]	concentration of substitutional boron	cm ⁻³
[B _s] _{norm}	concentration of substitutional boron, reference point for N_i , normalization	cm ⁻³
[C _s]	concentration of substitutional carbon	cm ⁻³
[Fe] _{total}	total iron concentration	cm ⁻³
[Fe] _{Av}	total iron conc., average value over a Δn range	cm ⁻³
Δ [Fe] _{Av}	total iron conc., standard deviation over a Δn range	cm ⁻³
[FeB]	concentration of iron-boron pairs	cm ⁻³
[Fe _i]	concentration of interstitial iron	cm ⁻³
[Ga]	concentration of gallium	cm ⁻³
[Mo]	concentration of molybdenum	cm ⁻³
[Ni]	concentration of nickel	cm ⁻³
[O _i]	concentration of interstitial oxygen	cm ⁻³ , ppma
[O _i] ^{LT} , [O _i] ^{HT}	concentration of interstitial oxygen, in the starting ma- terial (LT) and in high-temperature-treated material (HT)	cm ⁻³ , ppma
[Ti]	concentration of titanium	cm ⁻³
[V]	concentration of vacancies	cm ⁻³

Greek symbols

Symbol	Description	Unit
α	correlation exponent of $R_{gen}(N_A)$, $\tau_{Cz}(N_A)$ and $\sigma(T)$	—
α	temperature coefficient of $E_{gap}(T)$	eV/K
β	correlation exponent of $R_{gen}(I_{deg})$	—
β	temperature offset of $E_{gap}(T)$	K
δG	photogeneration relative to bias point, trapping correction	$\text{cm}^{-3}\text{s}^{-1}$
$\delta(\Delta n)$	excess electron density relative to bias point, trapping corr.	cm^{-3}
ΔE_{active} , $\Delta E_{passive}$	defect energy depth of the Cz defect (active/passive state)	eV
ΔE_t , ΔE_t^{true}	defect energy depth relative to the closer band edge (true defect parameter)	eV
ΔE_t^{fit}	defect energy depth extracted from a linear TDLS fit	eV
ΔE_t^{IP-2}	defect energy depth extracted from the 2 nd DPSS-IP	eV
ΔE_t^{max}	maximum overestimate of the true energy depth by the DPSS-ZP energy	eV
ΔG_{av}	generation rate, averaged over wafer thickness	$\text{cm}^{-3}\text{s}^{-1}$
$\Delta\eta$	efficiency difference before/after degradation in Cz-Si	%
ΔJ_{SC}	J_{SC} difference before/after degradation in Cz-Si	mA/cm^2
$\Delta_{rel}[k]$	relative standard deviation of the DPSS- k curves associated with a set of IDLS curves	%
Δn , Δp	excess electron density, excess hole density	cm^{-3}
Δn_{av} , Δp_{av}	excess electron/hole density, averaged over wafer thickness	cm^{-3}
Δn_{bias}	excess electron density at the bias point, trapping corr.	cm^{-3}
$\Delta n_{crossover}$	position of the crossover of the Fe _i - and FeB-dominated IDLS curves	cm^{-3}
Δn_{fit}	Δn range underlying the SRH modeling of an IDLS curve	cm^{-3}
Δn_{min}	minority carrier density proportional to the base-line photoconductance, trapping correction	cm^{-3}
Δn_s , Δp_s	excess electron/hole density at the surface	cm^{-3}
$\Delta\sigma$	excess photoconductance	Ω^{-1}
$\Delta\tau_{SRH}$	SRH lifetime difference under HLI and LLI (general)	s
$\Delta\tau_{SRH}^p$	SRH lifetime difference, in <i>p</i> -type	s
$\Delta\tau_{SRH}^{p,MajBH}$	SRH lifetime difference, in <i>p</i> -type for a MajBH defect	s
$\Delta\tau_{SRH}^{p,MinBH}$	SRH lifetime difference, in <i>p</i> -type for a MinBH defect	s
$\Delta T_{Arrh-Onset}$	width of the <i>T</i> range exhibiting the Arrhenius increase	K
ΔV_{OC}	V_{OC} difference before/after degradation in Cz-Si	mV
η	injection level	—
η	conversion efficiency	%
η_0	conversion efficiency, initial value in Cz-Si	%

η_d	conversion efficiency, stable degraded value in Cz-Si	%
η_{max}	conversion efficiency, theoretical limit	%
μ_n, μ_p	mobility of electrons and holes	$\text{cm}^2\text{V}^{-1}\text{s}^{-1}$
Π	probability of defect transformation	—
ρ, ρ_{base}	specific base resistivity	Ωcm
σ	photoconductance	Ω^{-1}
σ	capture cross-section, uniform T -dependence of σ_n and σ_p	cm^2
σ_0, σ_∞	capture cross-section, T -independent pre-factors	cm^2
σ_n, σ_p	capture cross-section of electrons and holes	cm^2
σ_{trap}	excess photoconductance due to traps	Ω^{-1}
τ	carrier recombination lifetime (lifetime)	s
τ_0	upper lifetime limit (empirical bulk lifetime model)	s
τ_0	initial lifetime in Cz-Si, after an annealing step	s
τ_0^{LLI}	lifetime under low-level injection, before dissociation of FeB pairs	s
τ_1^{LLI}	lifetime under low-level injection, after dissociation of FeB pairs	s
τ_A, τ_B	stable degraded lifetime in HT-treated Cz-Si, processes A and B	s
τ_a	asymptotic lifetime in a two-level system with one trapping and one recombination center	s
τ_{app}	trapping-affected apparent lifetime	s
τ_{assoc}	defect association time of FeB pairs	s
τ_{Auger}	Auger lifetime (Auger recombination lifetime)	s
τ_{Auger}^{HLL}	Auger lifetime under high-level injection	s
$\tau_{Auger}^{LLI,n}, \tau_{Auger}^{LLI,p}$	Auger lifetime under low-level injection, in n/p -type	s
τ_{bulk}	bulk lifetime (bulk recombination lifetime)	s
τ_{bulk}^{LLI}	bulk lifetime under low-level injection	s
$\tau_{bulk,max}^{LLI}$	bulk lifetime under low-level injection, theoretical limit	s
$\tau_{CE-Auger}$	Coulomb-enhanced Auger lifetime	s
$\tau_{CE Auger}^{LLI,n}, \tau_{CE Auger}^{LLI,p}$	Coulomb-enhanced Auger lifetime under low-level injection, in n/p -type	s
τ_{corr}	carrier lifetime after bias correction	s
τ_{Cz}	bulk lifetime due to recombination via the Cz defect	s
τ_d	stable degraded lifetime in Cz-Si, after illumination	s
$\tau_{d,fit}$	empirical fit of doping-dependent τ_d data	s
τ_{eff}	effective lifetime (effective recombination lifetime)	s
$\tau_{eff}^{LLI}, \tau_{eff}^{HLL}$	effective lifetime under low-/high-level injection	s
$\tau_{eff,diff}$	effective lifetime, differential	s
$\tau_{ExpTerm}$	defect-dependent contribution to LLI-SRH lifetime (Arrhenius term)	s

τ_i	stable degraded lifetime in as-grown Cz-Si	s
τ_{gen}	time constant of defect generation in Cz-Si	s
$\tau_{n0}, \tau_{n0}^{300K}$	electron capture time constant, T -dependent and at 300 K	s
$\tau_{p0}, \tau_{p0}^{300K}$	hole capture time constant, T -dependent and at 300 K	s
τ_{n0}^{DPSS}	electron capture time constant (fitted DPSS parameter: DPSS- τ_{n0} curve)	s
$\tau_{n0}^{DPSS}(T)$	DPSS- τ_{n0} curves of a T -IDLS experiment	s
$\tau_{n0}^{DPSS}(300K)$	DPSS- τ_{n0} curves of a T -IDLS experiment, normalized to 300 K	s
$\tau_{n0}^{DPSS-IP}$	values of the DPSS- τ_{n0} curve at the energy position of the DPSS- k intersection points	s
τ_{p0}^{DPSS}	hole capture time constant (fitted DPSS parameter: DPSS- τ_{p0} curve)	s
τ_{rad}	radiative lifetime (radiative recombination lifetime)	s
$\tau_{rad}^{LLI}, \tau_{rad}^{HLI}$	radiative lifetime under low-/high-level injection	s
τ_{res}	lifetime due to recombination via all residual recomb. channels except for SRH recomb. via the Cz defect	s
τ_{SRH}	SRH lifetime (Shockley-Read-Hall recomb. lifetime)	s
$\tau_{SRH}^{deep}, \tau_{SRH}^{shallow}$	SRH lifetime for a deep and a shallow energy level	s
$\tau_{SRH}^{LLI}, \tau_{SRH}^{HLI}$	SRH lifetime under low-/high-level injection (exact expression)	s
$\tau_{SRH,n}^{LLI,p}, \tau_{SRH,p}^{LLI,n}$	LLI-SRH lifetime, in n -/ p -type	s
$\tau_{SRH}^{LLI,p,MajBH}$	LLI-SRH lifetime, in p -type for a MajBH defect	s
$\tau_{SRH}^{LLI,p,MinBH}$	LLI-SRH lifetime, in p -type for a MinBH defect	s
$\tau_{SRH,<}^{LLI}$	LLI-SRH lifetime, in the $T_<$ region	s
$\tau_{SRH,>}^{LLI}$	LLI-SRH lifetime, in the $T_>$ region (Arrhenius increase)	s
$\tau_{SRH,IC}^{LLI}$	LLI-SRH lifetime, in the T range of intrinsic conduction	s
$\tau_{surface}$	surface recombination lifetime	s
τ_{total}	total SRH lifetime (several defect centers)	s
τ_v	lifetime of the individual recombination channels	s
τ^*	LLI-SRH lifetime, linearized T -dependence (simple procedure)	s
τ_{n0}^*	electron capture time, simulated T -dependence	s
τ^{**}	electron capture time, measured T -dependence	s
τ^{***}	LLI-SRH lifetime, linearized T -dependence (advanced procedure)	s

Introduction

Motivation

At present, 90 % of the solar cells fabricated worldwide are made of crystalline silicon. An important approach to reduce the costs of these cells is to increase their energy conversion efficiency. As efficiency is strongly related to material quality, the analysis of electrically active defects, which may be introduced during crystal growth or during the solar cell manufacturing process, is of special importance, since these defects in general limit the material quality.

The most important microscopic parameter to characterize material quality is carrier recombination lifetime. Although deep-level transient spectroscopy (DLTS) is accepted to be one of the most sensitive techniques to detect and analyze small concentrations of electrically active defects [1], defect concentrations below the detection limit of DLTS can still significantly affect carrier recombination lifetime. A prominent example of such a recombination-active defect is the metastable defect in industrially-used monocrystalline Czochralski silicon [2, 3]. Although this defect could not be detected up to now by means of DLTS, carrier lifetime decreases by 90 % of its initial value when the defect is activated, which leads directly to a relative efficiency loss of 10 % in high-efficiency solar cells. This example shows the high sensitivity of carrier lifetime to electrically active defects, and also the important impact bulk defects may have on solar cell efficiency. Another semiconductor device with a similar sensitivity to bulk defects is the dynamic random access memory chip (RAM), where material quality and thus carrier lifetime determine the refresh time [4].

An improvement of device performance requires the reduction or avoidance of such recombination-active defects, which in turn requires their identification in order to identify critical process steps and to provide a reasonable starting-point for process optimization. Apart from detecting the presence of recombination-active defects, lifetime measurements allow direct identification of impurities if the injection and temperature dependence of carrier lifetime is analyzed. The different approaches, which all

rely on standard Shockley-Read-Hall theory (SRH theory) [5, 6], are referred to as *lifetime spectroscopy* (LS). Beyond its extraordinary sensitivity, the principle advantage of lifetime spectroscopy over traditional defect-characterization techniques is that it uses the recombination process to analyze defect centers and thus provides insight into precisely those defects which are actually relevant to semiconductor devices such as solar cells and random-access memories.

Although lifetime spectroscopy has the potential to be one of the most sensitive diagnostic tools for the identification of impurities in semiconductors and although some LS techniques have already been reported in the literature, lifetime spectroscopy is not yet established as a standard technique for defect characterization, the analytical potential of most LS techniques being unclear so far.

However, interest in lifetime spectroscopy is growing fast. First, this is due to the improved boundary conditions for lifetime measurements achieved during the past years. On the one hand, several new contactless lifetime measurement techniques have been developed. Of these, the quasi-steady-state photoconductance technique, recently developed by Sinton and Cuevas [7] and already well established, is ideally suited to measure carrier lifetime over a broad injection range, thus facilitating the use of techniques based on injection-dependent lifetime spectroscopy. On the other hand, high-quality surface passivation has been developed, and this now allows reliable measurements of bulk recombination properties [8]. An important advantage of these passivation techniques, which are mostly based on silicon nitride, is the use of low-temperature processes, which ensures that there are no changes in the bulk properties during sample preparation.

Second, lifetime spectroscopy is gaining in importance as there is a growing demand for increasingly sensitive techniques to track ever diminishing quantities of impurities, which affect electronic devices due to the more and more stringent requirements on them. In integrated-circuit technology, for example, the tolerable levels of contamination are decreasing due to the decreasing dimensions. Rapidly diffusing metals, such as iron and copper, can limit device production yield by increasing the junction leakage current and degrading the dielectric properties of gate oxides, thus leading to breakdown [9]. In photovoltaics, as demonstrated in the initial example, an unknown intrinsic defect in Czochralski silicon and low concentrations of undetermined metal impurities in multicrystalline silicon limit the energy conversion efficiency.

Moreover, a closer examination of the defect properties known for the metal impurities reveals that, in spite of the intensive investigations, performed especially in the early 1980s, knowledge of most metal impurities is insufficient if one wants to assess their impact on recombination and solar cell performance. One problem is that most impurities exhibit different energy levels, which have been reported without giving any information about their effective recombination activity, as this information is not available if conventional techniques are used. Since lifetime spectroscopy uses the recombination process itself to identify the defects, it is expected to fill this gap.

Aims and outline

Covering the whole field of lifetime spectroscopy, the theoretical part of this monograph aims at the development and assessment of a variety of different lifetime spectroscopic techniques focusing on two issues: on the one hand, on a detailed theoretical evaluation of the spectroscopic potential of the different LS techniques and on the other hand, on the development of transparent data evaluation procedures to make the different LS techniques applicable as a diagnostic tool.

Experimental LS investigations on samples intentionally contaminated with known metal impurities aim to confirm the analytical potential predicted for the different LS techniques in order to demonstrate the general applicability of lifetime spectroscopy as a diagnostic tool. Moreover, these investigations aim to complete our knowledge of the defects related to the different metal impurities and in particular, to identify the recombination-active defect level, which is highly relevant for photovoltaics.

Experimental LS investigations performed on the undetermined metastable defect in Czochralski silicon aim at a determination of its electronic structure, which represents the ultimate test for the practical use of lifetime spectroscopy. Moreover, additional lifetime investigations should determine the major components of the defect as well as the physical mechanism of defect transformation.

Following these aims, the book is divided into five chapters:

Chapter 1 introduces some key concepts related to carrier lifetime and discusses different models for the temperature dependence of the fundamental semiconductor quantities, which will be used throughout the work.

Chapter 2 briefly describes the two photoconductance-based measurement techniques used in this work for lifetime measurements.

Chapter 3 presents the detailed theoretical investigations into the spectroscopic potential of lifetime spectroscopy and thus represents the core of the work. The different LS techniques are developed and analyzed in separate sections and finally compared in the chapter summary.

Chapter 4 applies lifetime spectroscopy to intentionally metal-contaminated silicon samples. A concise overview of the experimental and methodological results achieved by investigations into the individual metal impurities is given.

Chapter 5 focuses on the metastable defect in Cz silicon with special emphasis on the application of lifetime spectroscopy.

References

- [1] D.V. Lang, *Deep-level transient spectroscopy: a new method to characterize traps in semiconductors*, J. Appl. Phys. **45** (7), 3023–32 (1974).
- [2] H. Fischer and W. Pschunder, *Investigation of photon and thermal induced changes in silicon solar cells*, Proc. 10th IEEE PVSC (Palo Alto, California, USA, 1973), pp. 404–11.
- [3] S.W. Glunz, S. Rein, J.Y. Lee, and W. Warta, *Minority carrier lifetime degradation in boron-doped Czochralski silicon*, J. Appl. Phys. **90** (5), 2397–404 (2001).
- [4] F. Shimura, T. Okui, and T. Kusama, *Noncontact minority-carrier lifetime measurement at elevated temperatures for metal-doped Czochralski silicon crystals*, J. Appl. Phys. **67** (11), 7168–71 (1990).
- [5] W. Shockley and W.T.J. Read, *Statistics of the recombinations of holes and electrons*, Phys. Rev. **87** (5), 835–42 (1952).
- [6] R.N. Hall, *Electron-hole recombination in germanium*, Phys. Rev. **87**, 387 (1952).
- [7] R.A. Sinton and A. Cuevas, *Contactless determination of current-voltage characteristics and minority-carrier lifetimes in semiconductors from quasi-steady-state photoconductance data*, Appl. Phys. Lett. **69** (17), 2510–2 (1996).
- [8] J. Schmidt, *Untersuchungen zur Ladungsträgerrekombination an den Oberflächen und im Volumen von kristallinen Silicium-Solarzellen*, Dissertation, Universität Hannover (1998).
- [9] S. Johnston and R.K. Ahrenkiel, *Measurement of the temperature dependence of silicon recombination lifetimes*, Defect and Impurity Engineered Semiconductors II (Symposium) (Warrendale, PA, USA, 1998), pp. 607–12.

1. Theory of carrier lifetime in silicon

1.1 Introduction

As the name indicates, lifetime spectroscopy uses the recombination lifetime for defect characterization. Since this lifetime is a complex quantity, its accurate measurement and interpretation are mandatory for a successful application of lifetime spectroscopy. Thus, the present chapter introduces some key concepts related to recombination lifetime that will be used throughout the work.

Section 1.2 first introduces the fundamental semiconductor quantities and presents a detailed discussion of the temperature dependence of the carrier densities which has a decisive impact on the temperature-dependent carrier lifetime, as will be shown theoretically and experimentally in Chaps. 3 and 4, respectively. The essential terms of *recombination* and *carrier lifetime* are then introduced in Sect. 1.3. Following that, Sect. 1.4 introduces the different recombination mechanisms in semiconductors and discusses their relative importance in crystalline silicon. Basically, they may be divided into intrinsic processes, which occur even in the ideal non-disturbed semiconductor, and into extrinsic processes, which are related to impurities or lattice defects. With the radiative and the Auger band-band recombination the two intrinsic processes of bulk recombination are presented in Sects. 1.4.1 and 1.4.2, respectively. The extrinsic recombination via defects in the bulk is discussed in Sect. 1.4.3 on the basis of the statistics developed by Shockley, Read and Hall [1, 2]. As this theory forms the basis of lifetime spectroscopy, the concept of its derivation is briefly delineated, leading to the general expression for SRH lifetime which represents the starting point for the detailed theoretical investigations in Chap. 3. Discussing the fundamental prerequisites of standard SRH theory, a useful criterion recently developed to control its validity is introduced [3]. Its application successfully proves the validity of standard SRH theory for the investigations of the present work. The fundamentals of recombination via defects at the wafer surface are then discussed in Sect. 1.4.4, including the basic mechanisms for reducing the surface recombination rate. The effective lifetime arising from the superposition of these recombination processes is discussed in Sect. 1.5. As the main topic

of the monograph is the characterization of bulk defects, the impact of surface recombination on the effective carrier lifetime is investigated quantitatively, to estimate the required surface passivation quality which allows the measured effective lifetime to be directly identified with bulk lifetime.

1.2 Fundamentals 1: basic and advanced models for the fundamental semiconductor quantities

Since the modeling of the temperature-dependent carrier lifetime turns out to be sensitive to the accurate number of electrons and holes per unit volume, the present section is dedicated to a detailed derivation of their exact temperature dependence, the description being performed on three levels of accuracy. To introduce the fundamental concepts, we first discuss the *basic model* which corresponds to the model generally applied in solar cell physics, based on a temperature-independent majority carrier density. The temperature dependence of the majority carrier density is incorporated in the *standard model*, which takes into account the effects of freeze-out at low temperatures and intrinsic conduction at high temperatures. Finally, the *advanced model* considers the effect of an advanced temperature model for the effective densities of states and takes into account the temperature dependence of the energy band gap. The impact of these models on the temperature dependence of carrier lifetime will be shown in Sects. 3.5 and 3.6. In Chap. 4 we will finally demonstrate that accurate modeling of the measured temperature dependence of carrier lifetime actually requires the advanced temperature model.

1.2.1 Intrinsic carrier concentration and doping: the basic model

The energy band structure of a semiconductor is characterized by a narrow forbidden band gap which separates the valence and the conduction band. The width of this energy gap is given by $E_{gap} := E_C - E_V$, with E_C and E_V being the bottom and top of the conduction and the valence band, respectively. The densities of allowed states in the conduction and the valence band show a characteristic energy distribution which is given by $D_C(E) \propto (m_e^*)^{3/2} \times (E - E_C)^{1/2}$ and $D_V(E) \propto (m_h^*)^{3/2} \times (E_V - E)^{1/2}$, respectively. Note, that m_e^* and m_h^* are the effective masses of electrons and holes, respectively, which incorporate the effect of a periodic lattice potential and typically differ from each other.

At $T=0$, the allowed states in the valence band are completely occupied while those in the conduction band are empty. As temperature increases,

an increasing number of electrons is thermally excited across the energy gap into the conduction band. If the Pauli exclusion principle¹ is taken into account, the Fermi-Dirac distribution function

$$f(E) = \left[1 + \exp\left(\frac{E - E_F}{k_B T}\right) \right]^{-1} \quad (1.1)$$

is found to describe the occupation probability of the allowed electron states of any given energy E in thermal equilibrium. In Eq. (1.1) T is the absolute temperature, k_B Boltzmann's constant and E_F the Fermi energy. Using the density of allowed states in both bands $D_C(E)$ and $D_V(E)$ and the probability $f(E)$ of their occupation, the absolute electron and hole density in the conduction and the valence band can be calculated from

$$n = \int_{E_C}^{\infty} D_C(E) f(E) dE \quad \text{and} \quad p = \int_{-\infty}^{E_V} D_V(E) f(E) dE \quad (1.2)$$

respectively. The integration of these expressions is greatly simplified as long as the Fermi energy is several $k_B T$ distant from the band edges, i.e., $E_C - E_F \gg k_B T$ and $E_F - E_V \gg k_B T$, since the Fermi-Dirac distribution (1.1) may then be reduced to the Boltzmann distribution $f(E) = \exp[-(E - E_F)/k_B T]$. This prerequisite, which is characteristic of a *non-degenerate* semiconductor, will be assumed throughout the work and verified in retrospect.²

In thermal equilibrium the following expressions are thus gained from Eq. (1.2) for the electron concentration n_0 in the conduction band and the hole concentration p_0 in the valence band [4, p.18]:

$$n_0 = N_C \exp\left(-\frac{E_C - E_F}{k_B T}\right) \quad (1.3a)$$

$$p_0 = N_V \exp\left(-\frac{E_F - E_V}{k_B T}\right) \quad (1.3b)$$

¹ The Pauli exclusion principle implies that each allowed state can be occupied by, at most, two electrons of opposite spin.

² The critical parameters for a validation of this assumption are the doping concentration N_{dop} and the temperature T . In the present work carrier lifetime is measured on samples with doping concentrations from 10^{14} – 10^{16} cm⁻³ in a temperature range from 100 to 600 K. In spite of the temperature-related increase of $k_B T$ from 9 to 52 meV, the assumption of *non-degeneracy* is valid in the whole parameter range of interest since the Fermi level is shifted towards mid-gap with increasing temperature (see Fig. 1.4).

As expected, n_0 and p_0 strongly depend on the Fermi level E_F and the temperature T . N_C and N_V are the effective densities of states in the conduction and the valence band, respectively. They depend on the effective masses of electrons and holes, respectively, and contain an additional weaker temperature dependence, which results directly from the integration of Eq. (1.2) and is given by [4, p.17]:

$$N_{C/V}(T; m_{e/h}^*) = N_{C/V}^{300K}(m_{e/h}^*) \times \left(\frac{T}{300K} \right)^{3/2} \quad (1.4)$$

If the product of the equilibrium carrier concentrations n_0 and p_0 is formed, a fundamental feature of carriers in a semiconductor is revealed, the so-called *law of mass action* of carriers [4, p.18]:

$$n_0 p_0 = N_C N_V \exp\left(-\frac{E_{gap}}{k_B T}\right) =: n_i^2 \quad (1.5)$$

In contrast to the equilibrium carrier concentrations themselves, their product $n_0 p_0$ no longer depends on the Fermi level E_F , but only on the temperature and doping-independent material parameters, which implies the introduction of a new material parameter n_i . Thus, irrespective of the doping level of a sample, the product of electron and hole density is constant ($n_0 p_0 = n_i^2$), provided that the semiconductor is in thermal equilibrium and non-degenerate.

A Intrinsic semiconductor

In the ideal case of an undoped (intrinsic) semiconductor, the thermal excitation of electrons into the conduction band can only occur from the valence band. As a consequence, the electron density in the conduction band equals the hole density in the valence band. Their common value corresponds to the material parameter n_i which is thus known as the intrinsic carrier concentration:

$$n_0 = p_0 = n_i \quad (1.6)$$

At 300 K a value of 10^{10} carriers per cm^3 has been determined for n_i [5]. If n_0 and p_0 in Eq. (1.6) are substituted by the expressions from Eqs. (1.3b) and (1.3a), we find an expression for the Fermi level E_F :

$$E_F - E_V \equiv E_i - E_V = \frac{E_{gap}}{2} - \frac{k_B T}{2} \ln\left(\frac{N_V}{N_C}\right) \quad (1.7)$$

Except for a small temperature-dependent correction term, which results from the numerical difference of the effective densities of states in the valence and the conduction band, the Fermi level in an intrinsic semiconductor, which is also known as *intrinsic energy* E_i , lies approximately in the middle of the forbidden band.

B Extrinsic semiconductor

However, in the case of a doped (extrinsic) semiconductor the position of the Fermi level and thus the equilibrium concentrations n_0 and p_0 of electrons and holes decisively depend on the type and the concentration of the dopant used.

For doping, the semiconductor is intentionally contaminated with special impurities which are incorporated substitutionally on lattice sites and form shallow energy levels in the band gap. Silicon as a group IV semiconductor can be doped with group III and group V elements. Since group V elements, such as phosphorus, form energy levels close to the conduction band edge, they easily donate their extra electron to the conduction band. They are thus known as donors and induce an n -doping. Analogous, group III elements, such as boron, are known as acceptors, since they form energy levels close to the valence band edge and thus easily accept an electron from this band. This increases the hole density in the valence band and thus induces a p -doping. In their ionized state, donors have a net positive and acceptors a net negative charge. In the following, N_A and N_D denote the total acceptor and donor densities while N_A^- and N_D^+ refer to their ionized fraction.

Typical doping concentrations N_{dop} range from 10^{13} – 10^{20} dopant atoms per cm^3 . Since N_{dop} is thus several orders of magnitude higher than the intrinsic carrier concentration n_i , the law of mass action (1.5) implies a separation of electrons and holes into majority and minority carriers. An approximate and simple calculation of the actual electron and hole densities in a doped semiconductor is based on two assumptions: (i) impurity depletion, i.e., the complete ionization of all dopant atoms, which implies $N_A^- \approx N_A$ and $N_D^+ \approx N_D$, respectively, and (ii) a negligible contribution of the intrinsic carrier concentration to the majority carrier concentration, i.e., $n_i \ll N_A$ and $n_i \ll N_D$, respectively. Since both assumptions are well fulfilled in a broad temperature range around room temperature, the approximation gives results of more than adequate accuracy in this temperature range. While the majority carrier concentration can thus be equated with the doping concentration, the corresponding minority carrier concentration has to be calculated from Eq. (1.5). This leads to

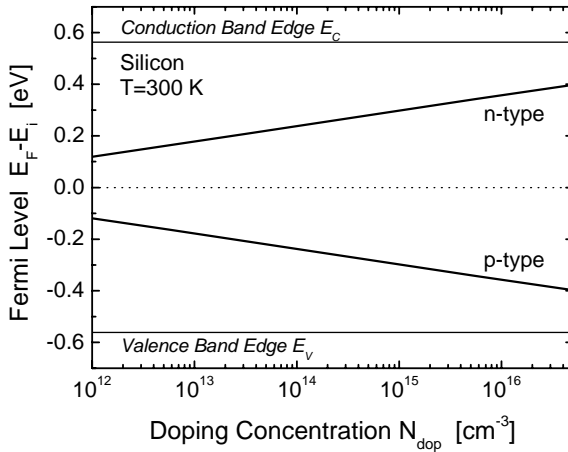


Fig. 1.1. Fermi level E_F as a function of doping concentration in *n*- and *p*-type silicon at 300 K according to Eq. (1.10). The dopant is assumed to be completely ionized (impurity depletion). As will be shown in Sect. 1.2.2A, this assumption is only valid at 300 K for $N_{dop} < 2.5 \times 10^{16} \text{ cm}^{-3}$.

$$p_0 = N_A \quad \text{and} \quad n_0 = \frac{n_i^2}{N_A} \ll p_0 \quad \text{for a } p\text{-type semiconductor,} \quad (1.8a)$$

$$n_0 = N_D \quad \text{and} \quad p_0 = \frac{n_i^2}{N_D} \ll n_0 \quad \text{for an } n\text{-type semiconductor.} \quad (1.8b)$$

Since Eqs. (1.3a) and (1.3b) for the equilibrium carrier concentrations n_0 and p_0 also apply for the more general case of a doped semiconductor, an expression for the position of the Fermi level can easily be derived:

$$E_F - E_V = k_B T \ln \left(\frac{N_V}{N_A} \right) \quad \text{for a } p\text{-type semiconductor,} \quad (1.9a)$$

$$E_C - E_F = k_B T \ln \left(\frac{N_C}{N_D} \right) \quad \text{for an } n\text{-type semiconductor.} \quad (1.9b)$$

Thus, in a doped semiconductor the position of the Fermi level is directly determined by the doping concentration. As displayed in Fig. 1.1, the Fermi level is shifted with increasing doping concentration towards the valence band edge in the case of a *p*-doped semiconductor and towards the conduction band edge in the case of an *n*-doped semiconductor. For symmetry reasons between *n*- and *p*-type, the Fermi levels in Fig. 1.1 are not calculated with respect to one of the band edges but with respect to the

intrinsic energy E_i , given in Eq. (1.7). The underlying expression can be directly derived if the Eqs. (1.9) are combined with Eq. (1.7). Note that the upper and the lower signs in Eq. (1.10) hold for a *p*-type and an *n*-type semiconductor, respectively:

$$E_F - E_i = \mp \frac{E_{gap}}{2} \pm k_B T \ln \left[\frac{(N_V N_C)^{1/2}}{N_{dop}} \right] \quad (1.10)$$

C Definition of the basic model

Based on these fundamental concepts, we now define the *basic model* for the temperature dependence of the semiconductor quantities as it will be used in Chaps. 3 and 4 for the calculation and modeling of carrier lifetime.

Concerning the equilibrium carrier concentrations, the fundamental assumption of the basic model is – as for the above derivation – a temperature-independent majority carrier concentration, which equals the doping concentration, e.g. in *p*-type: $p_0 = N_A$. In spite of the actual strong temperature dependence of the minority carrier concentration via $n_i(T)$ as described by Eq. (1.8), the minority carrier concentration is also considered as independent of the temperature in the basic model. It is calculated from Eq. (1.8) using the intrinsic carrier concentration at 300 K, e.g. in *p*-type: $n_0 = n_i^{300K}/N_A$. This additional simplification is introduced for the sake of consistency, since the temperature dependence of the minority carrier density only becomes important for the calculation of the carrier lifetime at temperatures where the majority carrier concentration changes as well. This will be shown in Sects. 1.2.2 and 1.2.3. The basic model is expected to give accurate results in a broad temperature range around room temperature where the above assumption is valid.

Although neglected in the calculation of p_0 and n_0 , the simple $T^{3/2}$ -dependence of the effective densities of states in the conduction and the valence band, which is displayed in Eq. (1.4), is considered whenever N_C and N_V appear in other quantities.

D Set of parameters used for simulations with the basic model

The set of material parameters used for theoretical calculations with the basic model is taken from the semiconductor-device-simulation program PC1D(version 5.8)[6]. A complete determination of the system is achieved if the following three material parameters are specified at 300 K:

$$\begin{aligned}
 E_{gap} &= 1.124 \text{ eV} && \text{energy band gap in silicon,} \\
 n_i^{300\text{K}} &= 1.0 \times 10^{10} \text{ cm}^{-3} && \text{intrinsic carrier concentration [5],} \\
 r := \frac{N_C^{300\text{K}}}{N_V^{300\text{K}}} &= 1.06 && \text{ratio of the effective densities of states.}
 \end{aligned}$$

Making use of Eq. (1.5), the effective densities of states in the valence and the conduction band can be directly calculated at 300 K:

$$\begin{aligned}
 N_C^{300\text{K}} &= \left[r \left(n_i^{300\text{K}} \right)^2 \exp\left(\frac{E_{gap}}{k_B 300\text{K}}\right) \right]^{1/2} = 2.84 \times 10^{19} \text{ cm}^{-3}, \\
 N_V^{300\text{K}} &= \left[\frac{1}{r} \left(n_i^{300\text{K}} \right)^2 \exp\left(\frac{E_{gap}}{k_B 300\text{K}}\right) \right]^{1/2} = 2.68 \times 10^{19} \text{ cm}^{-3},
 \end{aligned}$$

with Boltzmann's constant given by $k_B = 8.62 \times 10^{-5}$ eV/K.

1.2.2 Temperature dependence of the majority carrier concentration: the standard model

Up to now, the majority carrier concentration in a doped semiconductor has been regarded as temperature-independent, which allows the semiconductor to be accurately described around room temperature. Nevertheless, the underlying assumptions of (i) *impurity depletion* and (ii) a negligible contribution of *intrinsic conduction* become invalid at temperatures much lower and higher than 300 K, respectively.

In fact, at sufficiently low temperatures the fraction of ionized doping atoms is reduced due to the reduced energy available for thermal excitation, and impurity depletion is no longer given. As a result of this so-called *freeze-out* of the doping atoms the majority carrier concentration decreases with decreasing temperature. At sufficiently high temperatures on the other hand, the concentration of intrinsic carriers, which are thermally excited across the band gap, exceeds the doping concentration. As then even the doped semiconductor becomes dominated by intrinsic conduction, the majority carrier concentration is no longer constant but increases with increasing temperature. Concerning the temperature dependence of the majority carrier concentration, the temperature range thus displays a tripartition (for *p*-type) [4, p.26]:

$$\begin{aligned}
 T = 0\text{--}150 \text{ K} &\quad \text{region of } \textit{freeze-out} && p_0(T) < N_A, \\
 T = 150\text{--}500 \text{ K} &\quad \text{region of } \textit{impurity depletion} && p_0(T) = N_A, \\
 T > 500 \text{ K} &\quad \text{region of } \textit{intrinsic conduction} && p_0(T) > N_A.
 \end{aligned}$$

Note that the transition temperatures strongly depend on the doping concentration, the given temperatures being valid for a doping level of approximately 10^{15} cm^{-3} .

Since the lifetime spectroscopic investigations in Chap. 4 are performed in a temperature range from 100 to 600 K, the temperature dependence of the majority carrier concentration is expected to affect the temperature-dependent lifetime curves. Although the temperature region of impurity depletion is most important for temperature-dependent lifetime spectroscopy, it will be shown in Sect. 3.5 and Chap. 4 that an accurate modeling of the lifetime curve over the whole temperature range increases the accessible spectroscopic information and significantly improves the accuracy of the spectroscopic result. Thus, an accurate calculation of the complete temperature dependence of the equilibrium carrier concentrations is indispensable. Here, we do not only focus on the derivation of the temperature dependence itself, but also on the exact determination of the transition temperatures between the three regions and their dependence on the doping concentration. The latter should demonstrate the relevance of improved temperature models in the investigated temperature range and allow an individual a priori identification of the critical temperature regions.

The general approach to determine the precise values for the electron and hole concentrations starts from the fundamental condition of charge neutrality. For example, for *p*-type material it takes the form

$$n_0(T) + N_A^-(T) = p_0(T) \quad (1.11)$$

which considers both the densities p_0 and n_0 of free carriers and the concentration N_A^- of negatively charged ionized acceptor atoms. Making use of the law of mass action (1.5), which is the second important equation, the minority carrier concentration n_0 can be written as function of p_0 . As a result Eq. (1.11) becomes a quadratic equation in p_0 which provides the general solution for the majority carrier concentration $p_0(T)$:

$$p_0(T) = 1/2 \left[N_A^-(T) + \sqrt{N_A^-(T)^2 + 4 n_i(T)^2} \right] \quad (1.12)$$

The majority carrier concentration thus depends on its intrinsic value $n_i(T)$ and on the unknown density N_A^- of ionized doping atoms. To arrive at an explicit expression for $p_0(T)$, Eq. (1.12) is analyzed in the following in the temperature regions of freeze-out and intrinsic conduction. The obtained partial solutions are then combined to a composite function which represents the general solution for $p_0(T)$.

A Freeze-out

At low temperatures, $N_A^-(T)$ strongly depends on temperature due to the above mentioned freeze-out of doping atoms. To allow the magnitude of the freeze-out effect to be assessed directly, the ionization degree f_A is introduced, which equals the fraction of ionized acceptor atoms and thus ranges below 1:

$$f_A(T) := N_A^-(T) / N_A \quad (1.13)$$

Since $f_A(T)$ and $N_A^-(T)$ strongly depend on the Fermi level and the energy level of the acceptor atoms, respectively, the determination of their temperature dependence requires a physical model for the population of impurity levels in thermal equilibrium. As shown in the literature [7, p.581], the population statistics of impurity levels differ slightly from the common Fermi-Dirac statistics (1.1), since the population of localized states has to consider electron-electron interactions, which essentially prohibit the double occupation of donor levels by electrons and acceptor levels by holes.³ The complete statistics provide the following expressions for the densities $N_D^0(T)$ and $N_A^0(T)$ of non-ionized donors and acceptors, respectively:⁴

$$N_D^0(T) = \frac{N_D}{1 + \frac{1}{2} \exp\left(\frac{E_D - E_F}{k_B T}\right)}, \quad N_A^0(T) = \frac{N_A}{1 + \frac{1}{2} \exp\left(\frac{E_F - E_A}{k_B T}\right)} \quad (1.14)$$

with E_D and E_A denoting the energy level of the donors and acceptors, respectively. The combination of Eqs. (1.13) and (1.14) yields the functional dependence of f_A :

³ Donor levels for example can either be empty or occupied by one electron of either spin whereas a double occupation by electrons of opposite spin is essentially prohibited due to the mutual Coulomb repulsion. Acceptor levels on the other hand can either be singly or doubly occupied by electrons, but not empty, which can be explained as above from the hole point of view [7, p.581].

⁴ Actually, the population statistics yield expressions for the mean densities n_D and p_A of electrons in the donor levels and holes in the acceptor levels, respectively. But due to the maximum single-occupation of both types of levels, n_D and p_A can be directly identified with the densities N_D^0 of non-ionized donors (singly occupied by an electron) and N_A^0 of non-ionized acceptors (singly occupied by a hole), respectively. The difference in the maximum occupancy of localized (impurity) and delocalized (band) states is reflected in the factor of 1/2 in the denominators of Eq. (1.14).

$$f_A(T) := \frac{N_A^-(T)}{N_A} = \frac{N_A - p_A(T)}{N_A} = \left[1 + 2 \exp\left(-\frac{E_F - E_A}{k_B T}\right) \right]^{-1} \quad (1.15)$$

Since $f_A(T) \equiv f_A(T; E_F, E_A)$, the Fermi level E_F can be expressed as a function of the ionization degree f_A :

$$E_F(T; f_A, E_A) = E_A + k_B T \ln \left[\frac{2f_A(T)}{1 - f_A(T)} \right] \quad (1.16)$$

Nevertheless, since both quantities, f_A and E_F , are undetermined a priori, Eqs. (1.16) and (1.15) are of no direct use with regard to the explicit calculation of $p_0(T)$ for given material parameters. To overcome this problem, $E_F(T)$ has to be expressed in general terms as a function of the doping concentration N_A .

Such an expression follows directly from Eq. (1.12) which can be solved for E_F if $p_0(T)$ is given by Eq. (1.3a). In the temperature region of freeze-out, Eq. (1.12) simplifies and gives $p_0(T) \approx N_A^-(T) = f_A(T) \times N_A$ since the intrinsic carrier concentration n_i there can be neglected, provided that there is an extrinsic semiconductor: $n_i(T) \ll N_A, N_A^-$. Although it is not required for the derivation of E_F from a theoretical point of view, the use of the simplified Eq. (1.12) has the appeal that it simplifies the expression gained for E_F without loss of accuracy:

$$E_F(T; f_A, N_A) = E_V + k_B T \ln \left[\frac{N_V(T)}{f_A(T) N_A} \right] \quad (1.17)$$

If either the two expressions (1.16) and (1.17) for the Fermi level are equated or the N_A -dependent expression (1.17) for the Fermi level is inserted in Eq. (1.15), an expression for the ionization degree $f_A(T)$ is gained after some rearranging, which only depends on temperature and known material parameters and thus allows a numerical calculation of $f_A(T)$ and $p_0(T)$, respectively:

$$f_A(T; N_A, E_A) = \frac{-1 + \sqrt{1 + 2 C(T; N_A, E_A)}}{C(T; N_A, E_A)}$$

with $C(T; N_A, E_A) := \frac{4N_A}{N_V(T)} \exp\left(\frac{E_A - E_V}{k_B T}\right)$ (1.18)

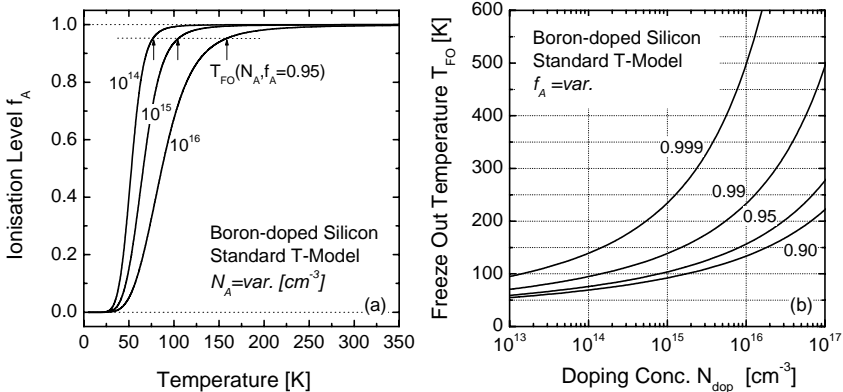


Fig. 1.2. (a) Ionization degree f_A of boron atoms in silicon as a function of temperature for different doping concentrations. Arrows indicate the T_{FO} positions for an f_A threshold of 0.95. (b) Freeze-out temperature T_{FO} in boron-doped silicon as a function of the doping concentration for different threshold limits of the ionization degree.

The ionization degree f_A of boron atoms in silicon, which form an energy level at $E_A-E_V=0.045 \text{ eV}$ [4, p.21], is plotted in Fig. 1.2a as a function of temperature for different doping concentrations. As indicated by the arrows, the onset of freeze-out can be characterized by a transition temperature T_{FO} which strongly depends on the doping concentration N_A and the specified threshold value for the ionization level f_A (in Fig. 1.2a given by the dotted line at $f_A=0.95$). Unfortunately, the derivation of an analytical expression for $T_{FO}(N_A; f_A)$ fails since Eq. (1.18) is unsolvable for temperature. Nevertheless, a graphical solution can be deduced insofar as an analytical expression for the inverse function $N_A(T_{FO}; f_A)$ is derived from Eq. (1.18) which is then plotted in an $x(y)$ - instead of a $y(x)$ -plot. After some rearranging of Eq. (1.18) the result is:

$$N_A(T_{FO}; f_A) \equiv N_A(T_{FO}, f_A, E_A) = \frac{1-f_A}{2f_A^2} N_V(T_{FO}) \exp\left(-\frac{E_A - E_V}{k_B T_{FO}}\right)$$

Figure 1.2b displays the inverse function $T_{FO}(N_A; f_A)$ as a function of the doping concentration N_A for various ionization degrees f_A , again calculated for boron-doped silicon. As can be seen, the transition temperature T_{FO} increases with increasing doping concentration N_A . The fact that the freeze-out of doping atoms already occurs at higher temperatures in more highly doped material, originates from the reduced distance between Fermi and doping level, which results in a reduced ionization of the doping atoms. In addition Fig. 1.2b shows the strong dependence of transition temperature

T_{FO} on the ionization level f_A which is predefined as the threshold value for the transition from impurity depletion to freeze-out. If an ionization degree of 99 % is regarded as a sufficient criterion for impurity depletion, at a temperature of 300 K, samples up to a doping concentration of $2.5 \times 10^{16} \text{ cm}^{-3}$ can be treated in the limit of impurity depletion, which demonstrates that the freeze-out effect can be neglected at room temperature. In contrast, at 100 K, which corresponds to the lowest temperature worked at in the present study, the freeze-out effect has to be considered for samples doped as low as 10^{14} cm^{-3} , since for a medium doping concentration of, e.g., 10^{15} cm^{-3} , almost 10 % of the doping atoms are already frozen out at 100 K.

B Intrinsic conduction

At sufficiently high temperatures, the effect of thermally induced intrinsic conduction starts to dominate the majority carrier concentration $p_0(T)$. Since $n_i(300 \text{ K}) = 10^{10} \text{ cm}^{-3}$ is several orders of magnitude smaller than the doping concentration, the transition from extrinsic to intrinsic conduction appears at temperatures much higher than 300 K, i.e., at temperatures for which impurity depletion can be assumed and thus $N_A^-(T) = N_A$. This assumption simplifies Eq. (1.12), which then allows the temperature-dependent majority carrier concentration $p_0(T)$ to be calculated directly if $n_i(T)$ is replaced by its defining expression (1.5). Figure 1.3a displays the majority carrier concentration $p_0(T)$ as a function of inverse temperature for various doping concentrations, showing the exponential increase due to intrinsic conduction at high temperatures.

Analogous to the freeze-out effect, the onset of intrinsic conduction can be characterized by a transition temperature T_{IC} , which is defined as the temperature at which the majority carrier concentration $p_0(T)$ exceeds the doping concentration N_A by a predefined factor $f_i > 1$. This factor can be interpreted as an intrinsic excitation degree:

$$p_0(T_{IC}) =: f_i \times N_A \quad (1.20)$$

The arrows in Fig. 1.3a indicate the T_{IC} positions for $f_i = 2$. As can be seen, the onset of intrinsic conduction is shifted to higher temperatures T_{IC} when doping concentration increases, which is reflected for more highly doped samples by a broadening of the temperature region, in which majority carrier concentration is dominated by extrinsic conduction and thus independent of temperature. An analytical expression for $T_{IC}(N_A; f_i)$ should follow from Eq. (1.12) for $N_A^-(T) = N_A$ and upon substitution of $p_0(T)$ from Eq. (1.20). But since Eq. (1.12) is again unsolvable for temperature, only an expression for the inverse function $N_A(T_{IC}; f_i)$ can be deduced:

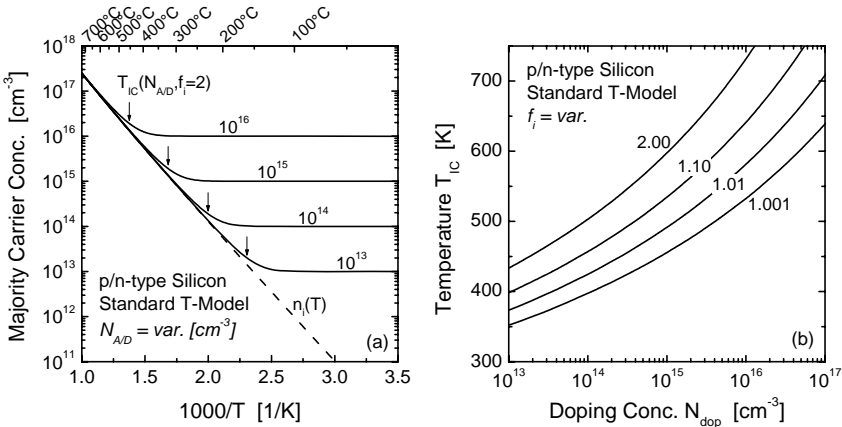


Fig. 1.3. (a) Majority carrier concentration as a function of inverse temperature for different doping concentrations, considering the effect of thermally induced intrinsic conduction according to Eq. (1.12) for $N_A^- = N_A$. The intrinsic carrier concentration $n_i(T)$ (dashed line) is calculated on the basis of the basic T-model according to Eq. (1.5). The temperature at which the majority carrier concentration $p_0(T)$ exceeds N_{dop} by a predefined factor $f_i > 1$ is defined as the onset temperature T_{IC} of intrinsic conduction. Arrows indicate the T_{IC} positions for $f_i = 2$. (b) Onset temperature of intrinsic conduction T_{IC} as a function of doping concentration for different transition factors f_i .

$$N_A(T_{IC}; f_i) = \frac{n_i(T_{IC})}{\sqrt{f_i^2 - f_i}} \quad (1.21)$$

Equation (1.21) being plotted in an $x(y)$ - instead of a $y(x)$ -plot, Fig. 1.3b displays the onset temperature $T_{IC}(N_A; f_i)$ of intrinsic conduction as a function of the doping concentration N_A for different values for the factor f_i , again calculated for boron-doped silicon. As expected, the transition temperature T_{IC} is the lower the lower the doping concentration N_A and the lower the factor f_i , which is assumed as a threshold for the transition from extrinsic to intrinsic conduction. The significance of the doping dependence of T_{IC} becomes evident with a numerical example. If $f_i = 1.10$ is defined as the threshold for the transition to intrinsic conduction, a decrease in the doping concentration by only two orders of magnitude from 10^{16} to 10^{14} cm⁻³ results in a T_{IC} decrease by 180 K from 640 to 460 K. Thus at 600 K, which is the highest temperature worked at in the present study, the effect of intrinsic conduction has to be considered for samples up to a doping concentration of 5×10^{15} cm⁻³, since for a lower doping concentration of, e.g., 10^{15} cm⁻³, the intrinsic carrier density already exceeds the extrinsic carrier density by 100 % ($f_i = 2$).

C Fermi level in the standard model

Combining the results obtained in the region of freeze-out and intrinsic conduction, we are now able to define the *standard model* for the temperature dependence of the equilibrium carrier concentrations as it will be used in Chaps. 3 and 4 for the calculation and modeling of carrier lifetime.

Since, for the derivation of $p_0(T)$, we simplified the general Eq. (1.12) by neglecting the intrinsic carrier concentration $n_i(T)$ at low temperatures and by assuming $N_A^-(T)=N_A$ at high temperatures,⁵ the general solution for the majority carrier concentration $p_0(T)$ has to be defined as a composite function of both partial solutions, which requires a suitable division of the temperature range. According to Figs. 1.2b and 1.3b, $T=350\text{ K}$ represents a suitable division temperature since there neither freeze-out nor intrinsic conduction affect semiconductors doped in a broad range from 1×10^{13} to $5\times 10^{16}\text{ cm}^{-3}$. Thus, the general temperature dependence of the majority carrier concentration $p_0(T)$ (in *p*-type material) may be written as

$$p_0(T) = \begin{cases} f_A(T) N_A & \text{for } T < 350^\circ\text{C}, \\ 1/2 \times \left[N_A + \sqrt{N_A^2 + 4n_i(T)^2} \right] & \text{for } T \geq 350^\circ\text{C}, \end{cases} \quad (1.22)$$

with the ionization degree $f_A(T)$ and the intrinsic carrier concentration $n_i(T)$ given by Eqs. (1.18) and (1.5), respectively. Both equations depend on the effective densities of states $N_C(T)$ and $N_V(T)$, whose temperature dependence is described by the simple $T^{3/2}$ -dependence given in Eq. (1.4), which is used in the basic model as well. In contrast to the basic model, the standard model also considers the complete temperature dependence of the minority carrier concentration $n_0(T)$. Making use of the law of mass action (1.5), it directly results from $p_0(T)$ and $n_i(T)$:

$$n_0(T) = n_i(T)^2 / p_0(T) \quad (1.23)$$

Finally, we are now able to present a generalized expression for the Fermi level E_F , which considers both freeze-out and intrinsic conduction and thus allows its temperature dependence to be described completely. If the derivation given in Sect. 1.2.1B is followed, the resultant E_F expression for a *p*-type doping takes the form:⁶

⁵ Note that neither simplification has been required from a theoretical point of view, but they led to a significant simplification of the resulting expressions without loss of accuracy in the temperature range of definition.

⁶ In the case of an *n*-type doping, the general expression for the Fermi level simply follows from Eq. (1.24) if the whole expression is multiplied by the factor (1) and $p_0(T)$ is replaced by the majority carrier concentration $n_0(T)$, whose temperature dependence has to be derived analogously to Eq. (1.22).

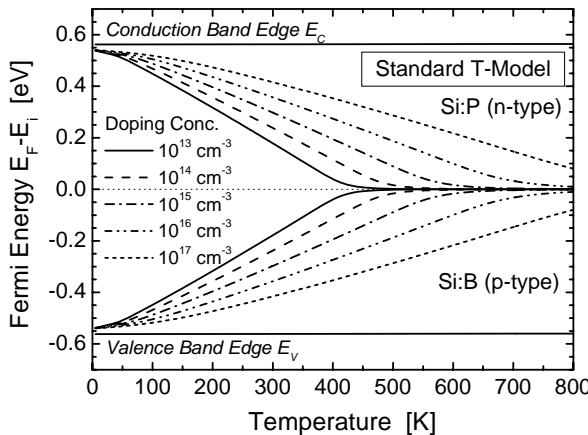


Fig. 1.4. Fermi level $E_F(T)$ as a function of temperature for *p*- and *n*-type silicon with different doping concentrations. For symmetry reasons the intrinsic Fermi level E_i (approximately mid-gap) is chosen as zero energy. The calculations are based on Eq. (1.24) considering both freeze-out and intrinsic conduction as described in the standard *T*-model.

$$E_F - E_i = - \frac{E_{gap}}{2} + k_B T \ln \left[\frac{(N_V N_C)^{1/2}}{p_0(T)} \right] \quad (1.24)$$

For symmetry reasons between *n*- and *p*-type, the Fermi level E_F is again calculated with respect to the intrinsic energy E_i . Note that the general E_F expression (1.24) only differs from the simple E_F expression (1.10) in that the direct doping dependence is replaced by a dependence on the temperature-dependent majority carrier concentration $p_0(T)$ given by Eq. (1.22).

Figure 1.4 displays the Fermi level calculated from Eq. (1.24) as a function of temperature for *n*- and *p*-type silicon with different doping concentrations. The discussed effects of freeze-out and intrinsic conduction are directly reflected in the observed temperature dependence of E_F . Irrespective of the doping concentration, the Fermi level is shifted with decreasing temperature towards the corresponding band edge which causes the freeze-out of doping atoms. With increasing temperature on the contrary, the Fermi level moves towards mid-gap. As soon as E_F reaches mid-gap, the doped semiconductor is completely dominated by intrinsic conduction and differences due to doping type and concentration disappear. Apart from that, the trends observed in Fig. 1.1 for the doping dependence of E_F are confirmed for arbitrary temperatures: the Fermi level E_F is located closer to the valence (in *p*-type) and the conduction band edge (in *n*-type) the higher the doping concentration.

1.2.3 Impact of advanced temperature models for $N_{C,V}(T)$ and $E_{gap}(T)$: the advanced model

As will be shown in Sect. 3.4 and Chap. 4, even the standard model does not allow the temperature-dependent lifetime curves to be modeled accurately. Since the intrinsic carrier concentration $n_i(T)$ and thus the equilibrium carrier concentrations $p_0(T)$ and $n_0(T)$ strongly depend on the values of E_{gap} , $N_C(T)$ and $N_V(T)$ as manifested in Eqs. (1.5), (1.22) and (1.23), further extensions of the temperature model for the fundamental semiconductor quantities arise from (i) a consideration of the temperature- and doping-induced narrowing of the silicon band gap and (ii) the use of advanced temperature models for the effective densities of states, which take into account an additional temperature dependence of the effective masses. In the following we briefly introduce these models, which are discussed in detail in [8], focussing (i) on their deviation from the more common simpler models and (ii) on their impact on the semiconductor quantities derived in the previous sections.

A Characteristics of the models

The band gap in silicon is known to decrease with increasing temperature. Its temperature dependence has been determined from the absorption edge of silicon and is accurately described in a T range from 0–1000 K by the following empirical equation published by Sze [4, p.15]:

$$E_{gap}(T) = E_{gap}(0) - \frac{\alpha T^2}{T + \beta} \quad (1.25)$$

with a zero-point energy gap $E_{gap}(0) = 1.170 \text{ eV}$, a temperature coefficient $\alpha = 4.73 \times 10^{-4} \text{ eV/K}$ and a temperature offset $\beta = 636 \text{ K}$.

Figure 1.5a displays the temperature dependence of the energy band gap $E_{gap}(T)$ for the Sze model, calculated from Eq. (1.25) (solid line), as well as for a slightly modified model published by Green [9, p.60] (dash-dotted line). Although older, the Sze model⁷ is preferred to the Green model since it provides the well determined value of 1.124 eV for the silicon band gap at 300 K. The deviation of the excluded E_{gap} -models, $E_{gap} = \text{const.}$ and E_{gap}^{Green} , from the Sze model, which is chosen as optimum, is displayed in Fig. 1.5b (lower half) in percentages. The deviation between $E_{gap} = \text{const.}$ and E_{gap}^{Sze} (dashed line) demonstrates the relevance of considering the temperature dependence of E_{gap} which becomes evident by an E_{gap} shrinkage

⁷ Note that in the semiconductor-device-simulation program PC1D (version 5.8) [6] the Sze model is also used to describe $E_{gap}(T)$.

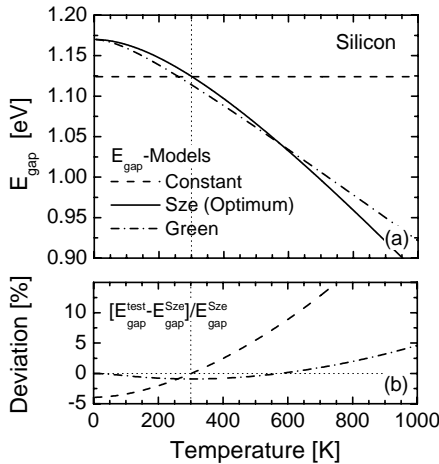


Fig. 1.5. (a) Temperature dependence of the energy band gap $E_{gap}(T)$ for different models. (b) Deviation in percentages of the excluded E_{gap} -models from the Sze model, which is chosen as optimum. While the deviation between $E_{gap} = \text{const.}$ and E_{gap}^{Sze} (dashed line) demonstrates the relevance of considering the temperature dependence of E_{gap} , the deviation between E_{gap}^{Green} and E_{gap}^{Sze} (dash-dotted line) is a measure of the uncertainty of the model used.

of 10 % at 600 K compared to the value at 300 K. The deviation between E_{gap}^{Green} and E_{gap}^{Sze} (dash-dotted), on the contrary, is a measure for the uncertainty of the model used. In the relevant temperature range up to 650 K this uncertainty is below 1 % and can thus be neglected.

In addition, the band gap may be reduced due to the effect of doping-induced band gap narrowing (BGN), which is superimposed onto the pure temperature effect discussed above. Using the BGN model implemented in the semiconductor-device-simulation software DESSIS [10], we calculated the band gap narrowing as a function of temperature for different doping concentrations. The result is displayed in Fig. 1.6a in units of meV. As expected, the BGN increases with increasing doping concentration and decreasing temperature. To assess the relevance of BGN, Fig. 1.6b (lower half) shows the ratio of BGN and total band gap width in percentages. Since the ratio remains below 0.5 % in the relevant doping ($< 10^{16} \text{ cm}^{-3}$) and temperature (100–650 K) range and thus below the uncertainty of the $E_{gap}(T)$ -model, the impact of BGN on the total band gap width can be neglected in the present study.

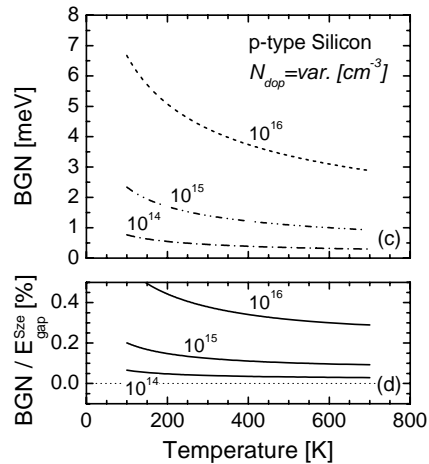


Fig. 1.6. (a) Absolute values of superposed doping-induced band gap narrowing (BGN) as a function of temperature for different doping concentrations in meV units. (b) Ratio of BGN and total band gap width in percentages. Since the ratio remains below 0.5 %, the impact of BGN on the total band gap width can be neglected in the present study.

Finally, an advanced model for the temperature dependence of the effective densities of states, $N_C(T)$ and $N_V(T)$, should be introduced. The simple $T^{3/2}$ -dependence, which has been found in Eq. (1.4), directly follows from the integration of the energy state density $D(E)$ within the integral (1.2) and does not consider any temperature dependence of the effective masses of electrons and holes. To account for such effects, the effective densities of states have to be written as [8]

$$N_{C/V}\left(T; \frac{m_{e/h}^*(T)}{m_0}\right) = N \times \left[\frac{m_{e/h}^*(T)}{m_0} \right]^{3/2} \times \left[\frac{T}{300\text{K}} \right]^{3/2} \quad (1.26)$$

where m_e^* and m_h^* are the effective masses of electrons in the conduction band and holes in the valence band, respectively, m_0 is the electron rest mass and $N=2.541\times10^{19} \text{ cm}^{-3}$ is a numerical factor, which collects all residual physical constants.

As discussed in [8], a change in the effective masses with temperature has to be expected from two effects. On the one hand, the energy-momentum curves themselves, from which the effective masses are deduced, change with temperature due to a change in the electron-phonon interaction energies. On the other hand, at increased temperatures, those regions of the bands are increasingly occupied which are away from the band edge and thus depart from simple parabolic shape. A multitude of experimental and theoretical results are found to be well described by the following equations for the effective masses m_e^* and m_h^* [8]:

$$\frac{m_e^*(T)}{m_0} = 6^{2/3} \left[\left(C \frac{E_{\text{gap}}(0)}{E_{\text{gap}}(T)} \right)^2 \frac{m_l}{m_0} \right]^{1/3} \quad (1.27a)$$

$$\frac{m_h^*(T)}{m_0} = \left(\frac{a + bT + cT^2 + dT^3 + eT^4}{1 + fT + gT^2 + hT^3 + iT^4} \right)^{2/3} \quad (1.27b)$$

The numerical values of the coefficients $a-i$, C and m_l/m_0 are given in [8] and displayed below.⁸ The structural difference in the analytical expressions for the electron and hole effective mass results from differences in the band structure of the conduction and the valence band. This is why the effective mass of holes in the valence band is expected to be more temperature-sensitive than that of electrons in the conduction band [8].

⁸ Coefficients in the EM equations (1.27) [8]: $C=0.1905$, $m_l/m_0=0.9163$, $a=0.4435870$, $b=0.3609528\times10^{-2}$, $c=0.1173515\times10^{-3}$, $d=0.1263218\times10^{-5}$, $e=0.3025581\times10^{-8}$, $f=0.4683382\times10^{-2}$, $g=0.2286895\times10^{-3}$, $h=0.7469271\times10^{-6}$, $i=0.1727481\times10^{-8}$.

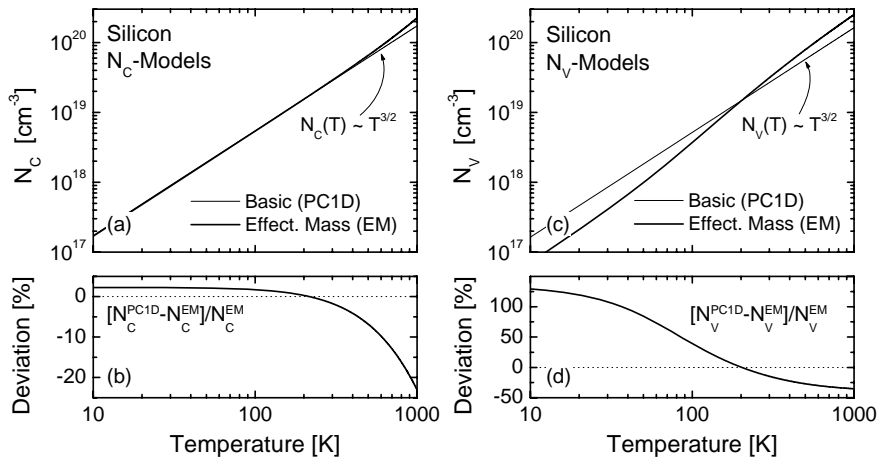


Fig. 1.7. Temperature dependence of the effective density of states (a) in the conduction band, $N_c(T)$, and (c) in the valence band, $N_v(T)$, for a basic T -model [thin solid lines, Eq. (1.4)] and an advanced T -model [thick solid lines, Eq. (1.26)] based on effective mass theory. The percentage deviation between the two models is shown for $N_c(T)$ and $N_v(T)$ in (b) and (d), respectively (lower half).

If Eqs. (1.27a) and (1.27b) are inserted in Eq. (1.26), explicit values for N_c and N_v can be calculated. The diagrams in the upper half of Fig. 1.7 display the temperature dependence of the effective densities of states in the conduction band, $N_c(T)$, and in the valence band, $N_v(T)$, respectively. To assess the relevance of the advanced $N_{c,v}$ -model based on the effective mass theory (EM), both diagrams show the effective densities of states which result from the basic [thin solid lines, Eq. (1.4)] and the advanced model [thick solid lines, Eq. (1.26)]⁹. In addition, the diagrams in the lower half of Fig. 1.7 display the percentage deviation between the models for $N_c(T)$ and $N_v(T)$, respectively.

As can be seen from Fig. 1.7a and b, up to 500 K the advanced EM model for $N_c(T)$ corresponds to the basic model within 5 % accuracy. While the overall temperature dependence of $N_c(T)$ approaches the $T^{1.5}$ power, as expected from Eq. (1.4), below 100 K, it is slightly enhanced in the intermediate temperature range from 200–500 K where it can be approximately described by a $T^{1.58}$ power law [8]. Only above 500 K, stronger deviations from the $T^{1.5}$ -dependence have to be expected. Thus, in

⁹ Note that both $N_{c,v}$ -models are used in current commercial semiconductor-device-simulation programs: while PC1D [6] uses the basic model, the advanced model is implemented in DESSIS [10].

the relevant temperature range from 100–600 K the impact of the advanced $N_C(T)$ -model is expected to be of minor importance.

In contrast, the advanced EM model for $N_V(T)$ significantly differs from the basic model in terms of both absolute values and temperature dependence. As displayed in Fig. 1.7d, the deviation between the two models reaches 30 % in the relevant temperature range from 100–600 K and is even much higher at lower temperatures. Apart from that, Fig. 1.7c shows that the overall temperature dependence of $N_V(T)$ approaches the $T^{1.5}$ power expected from the simple model only at high (above 600 K) and low (below 50 K) temperatures while being strongly enhanced in the intermediate temperature range from 200–500 K, where it can be approximately described by a $T^{1.85}$ power law [8].

Thus, in the temperature range from 100–600 K, which is relevant to the investigations of the present work, the introduction of the advanced EM models for the effective densities of states will affect the fundamental semiconductor quantities particularly through $N_V(T)$ while the changes through $N_C(T)$ are of minor importance. This difference directly reflects the structural difference which has been observed in the temperature-dependent expressions (1.27a) and (1.27b) of the effective masses of electrons and holes.

B Definition of the advanced model

Analogously to the definition of the basic and standard model in Sects. 1.2.1C and 1.2.2C, we now define an *advanced model* for the temperature dependence of the fundamental semiconductor quantities. Since the advanced model is conceived as an extension of the standard model which additionally accounts for the temperature-dependence of the band gap and the effective masses, all the equations derived for the standard model hold good in the advanced model if only E_{gap} is replaced by $E_{gap}(T)$ from Eq. (1.25) and $N_C(T)$, $N_V(T)$ by the effective-mass-based models in Eq. (1.26). The set of semiconductor parameters used as defining basis for the advanced model is listed in Table 1.1 at the end of this chapter.

C Impact of the advanced model on the basic semiconductor quantities

To assess the practical relevance of the advanced T -model, its impact on the basic semiconductor quantities should finally be investigated using derivations from Sect. 1.2.2. To visualize the impact of the advanced temperature models for $E_{gap}(T)$ and $N_{C,V}(T)$ alone, the different curves are each calculated twice in the following, under the assumption of the

standard (thin solid line) and the advanced T -model (thick solid line), and superposed in the same diagram. In addition, for some quantities the absolute deviation between the two models is plotted separately, which provides a quantitative estimate of the impact of the model extensions from Sect. 1.2.3A exclusively.

Their impact on the freeze-out effect is displayed in Fig. 1.8. Analogously to Fig. 1.2a, Fig. 1.8a shows the ionization degree f_A of boron atoms in silicon, whose temperature dependence has been calculated from Eq. (1.18) for different doping concentrations. As can be seen, the advanced T -model (thick solid lines) leads to a slight decrease in the ionization degree which directly reflects the fact that at low temperatures the density $N_V(T)$ of allowed states in the valence band is lower in the advanced than in the simple $N_V(T)$ -model (see Fig. 1.7).¹⁰ Showing the absolute deviation of the $f_A(T)$ curves for the two T -models, Fig. 1.8b reveals that the maximum f_A reduction due to the model exchange, which is given by the peak value, ranges from 10 to 6 % and decreases with increasing doping concentration.

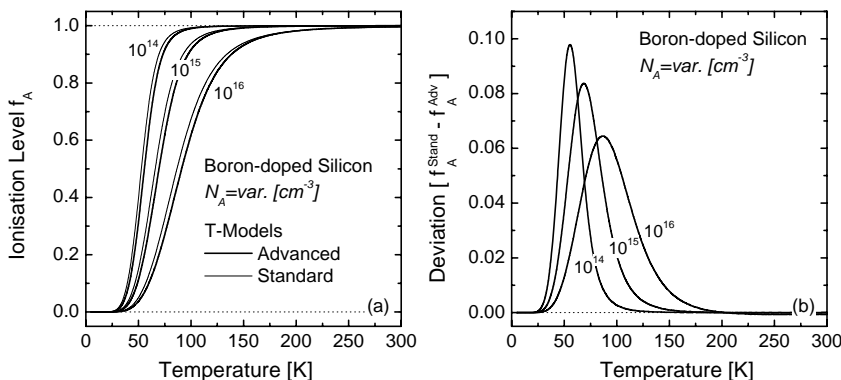


Fig. 1.8. Impact of the optimum advanced T -model on the freeze-out effect. (a) Ionization degree f_A of boron atoms in silicon calculated from Eq. (1.18) as a function of temperature for different doping concentrations under the assumption of the standard (thin solid lines) and the advanced T -model (thick solid lines). The advanced T -model leads to a slight reduction in the ionization degree. (b) Absolute deviation between corresponding $f_A(T)$ curves calculated for the two T -models.

¹⁰ An $E_{\text{gap}}(T)$ effect can be excluded since the doping level is assumed to be pinned to the adjacent band edge, its energy distance thus being temperature independent.

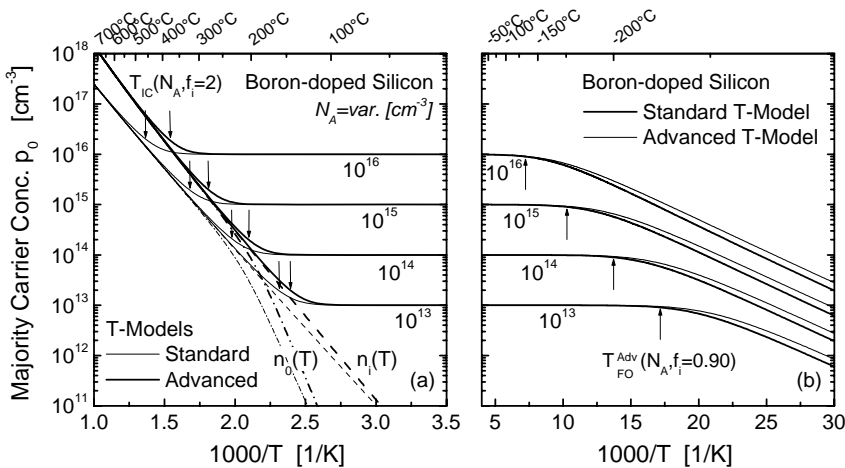


Fig. 1.9. Majority carrier concentration $p_0(T)$ in p -type silicon calculated from the composite model in Eq. (1.22) as a function of inverse temperature for different doping concentrations under the assumption of the standard (thin solid lines) and the advanced T -model (thick solid lines) for (a) high and (b) low temperatures. (a) At high temperatures the introduction of the advanced T -model induces an increase in the intrinsic carrier concentration $n_i(T)$ [dashed line, Eq. (1.5)] which is reflected in an onset of intrinsic conduction at lower temperatures. Arrow pairs indicate the IC onset temperatures T_{IC} for $f_i=2$. (b) At low temperatures the advanced T -model induces a reduction of $p_0(T)$, which reflects the decrease in the ionization degree observed in Fig. 1.8.

Figure 1.9 displays the impact of the standard (thin solid line) and the advanced T -model (thick solid line) on the majority carrier concentration $p_0(T)$ in p -type silicon, which has been calculated as a function of inverse temperature for different doping concentrations using the composite model in Eq. (1.22). At low temperatures, as shown in Fig. 1.9b, the advanced T -model induces a reduction of $p_0(T)$ which directly reflects the decrease of the ionization degree observed in Fig. 1.8. The arrows in Fig. 1.9b indicate the temperatures T_{FO} for the onset of freeze-out which are determined for the advanced T -model and an f_A threshold of 0.90. Note that the T_{FO} values are hardly affected by the T -model.

At high temperatures, as shown in Fig. 1.9a, the introduction of the advanced T -model induces an increase in the intrinsic carrier concentration $n_i(T)$ (dashed lines) which is calculated from the defining Eq. (1.5). The increase in $n_i(T)$ comes mainly from the reduced band gap width (see Fig. 1.5) and to a lesser extent from the enhanced densities of states in the valence and the conduction band (see Fig. 1.8). Since the band gap width $E_{gap}(T)$ declines continuously with increasing temperature, the model-based difference in the magnitude of $n_i(T)$ grows continuously, which can

be seen from the divergence of the $n_i(T)$ curves for the standard (thin dashed line) and the advanced T -model (thick dashed line). The increase in $n_i(T)$ due to the model exchange is directly reflected in an onset of intrinsic conduction at lower temperatures. This is shown in Fig. 1.9a by the arrow pairs, which indicate for both T -models the onset temperatures of intrinsic conduction, T_{IC} , for an excitation degree $f_i = 2$.¹¹

To allow the impact of the advanced T -model on intrinsic conduction to be assessed quantitatively, Fig. 1.10a displays the T_{IC} values, calculated from Eq. (1.21) on the basis of the advanced T -model, as a function of doping concentration for different transition factors f_i . If again $f_i = 1.10$ is defined as threshold for the transition to intrinsic conduction, the onset temperatures of intrinsic conduction range between 440 and 590 K in the relevant doping range from 10^{14} to 10^{16} cm^{-3} . Since the investigations of the present study are performed up to temperatures of 600 K, especially for the lesser doped samples a significant part of the investigated temperature range will be affected by intrinsic conduction, though the effect is present within the whole doping range. The enormous impact of only the advanced temperature models for $E_{gap}(T)$ and $N_{C,V}(T)$ becomes evident from Fig. 1.10b, which shows the absolute reduction of the onset temperatures T_{IC} due to the transition from the standard to the advanced T -model. As expected from the

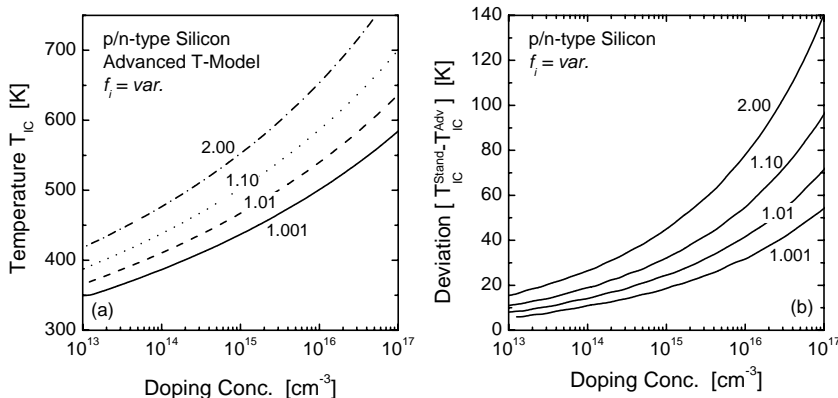


Fig. 1.10. (a) Onset temperature of intrinsic conduction T_{IC} calculated from Eq. (1.21) on the basis of the advanced T -model as a function of doping concentration for different transition factors f_i . (b) Absolute reduction of T_{IC} due to the transition from the standard to the advanced T -model as a function of doping concentration for different transition factors f_i .

¹¹ The fact that the model-based distance between the onset temperatures increases with increasing doping concentration, even on the inverse temperature scale in Fig. 1.9a, indicates a superlinear grow of the T_{IC} reduction, which is consistent with the above observations on $n_i(T)$ and is shown explicitly in Fig. 1.10b.

mentioned divergence of the $n_i(T)$ curves for both T -models (dashed lines in Fig. 1.9a), the T_{IC} reduction increases with increasing doping concentration N_A . While T_{IC} is only reduced by 20 K for a low doping of $N_A = 10^{14} \text{ cm}^{-3}$, its reduction already exceeds 50 K for a medium doping of $N_A = 10^{16} \text{ cm}^{-3}$ and almost amounts to 100 K for a high doping of $N_A = 10^{17} \text{ cm}^{-3}$. As a result, the doping dependence of the absolute T_{IC} values is reduced for the advanced T -model compared to the standard T -model. The strong T_{IC} reduction in the relevant doping range from $10^{14}\text{--}10^{16} \text{ cm}^{-3}$, due to the model exchange, and the resultant low absolute T_{IC} values, which lie significantly below the upper limit of the investigated temperature range, demonstrate the relevance of the complete advanced T -model for the analysis in the present study.

For the sake of completeness, Fig. 1.11a displays the temperature dependence of the Fermi level $E_F(T)$ in p - and n -type silicon with different doping concentrations if the advanced T -model is taken as a basis.¹² For comparison, we superposed for p -type silicon the $E_F(T)$ curves calculated in Fig. 1.4 on the basis of the standard T -model. The absolute deviation of the Fermi levels calculated for the two T -models is displayed in Fig. 1.11b.

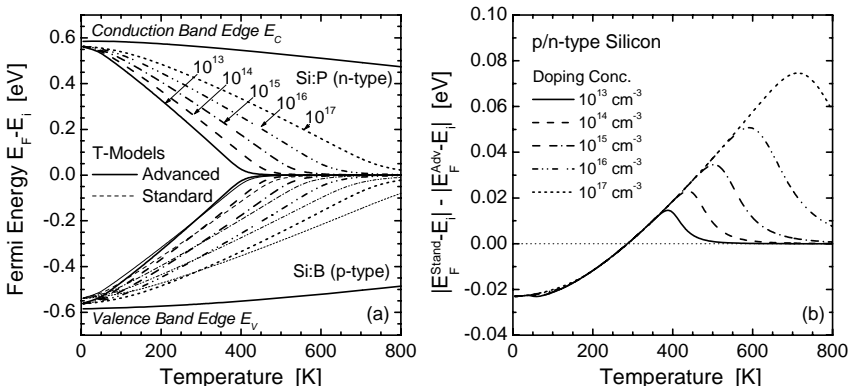


Fig. 1.11. (a) Temperature dependence of the Fermi level $E_F(T)$ in p - and n -type silicon with different doping concentrations calculated on the basis of the advanced T -model (thick lines) according to Eq. (1.24). For p -type silicon, the $E_F(T)$ curves calculated in Fig. 1.4 on the basis of the standard T -model are superposed for comparison (thin lines). (b) Absolute deviation of the Fermi levels calculated for the standard and the advanced T -model as a function of temperature for different doping concentrations.

¹² The $E_F(T)$ calculations are based on Eq. (1.24) with $p_0(T)$ given by the composite model displayed in Fig. 1.9. For symmetry reasons the intrinsic Fermi level E_i is again chosen as zero energy. The temperature dependence of the band edges is calculated from Eq. (1.6) using the advanced $E_{\text{gap}}(T)$ - and $N_{C,V}(T)$ -models from Eqs. (1.25) and (1.26).

As can be seen, in the standard T -model the distance $|E_f - E_i|$ of the Fermi level from mid-gap is underestimated below 300 K and overestimated above 300 K. This mainly reflects the under- and overestimation of the temperature-dependent silicon band gap by the assumption $E_{gap} = \text{const.}$, which the standard T -model is based on. Quantitatively, the inaccuracy of the standard T -model in determining the Fermi level ranges in the relevant doping (10^{14} – 10^{16} cm $^{-3}$) and temperature (100–600 K) range from –20 to +50 meV.

1.2.4 Tabular overview of the T -models

Since the basic, standard and advanced temperature models for the fundamental semiconductor quantities essentially differ (from each other) in the degree of complexity, they are finally compared in Table 1.1 in terms of (i) the temperature effects which are taken into account, (ii) the physical equations which are used for the calculation of the equilibrium carrier concentrations and (iii) the set of semiconductor parameters which completely defines the system. All three models will be applied in Chaps. 3 and 4 for the calculation and modeling of carrier lifetime.

Table 1.1. Comparison of the three temperature models used for the calculation of the fundamental semiconductor quantities on different levels of complexity and accuracy.

T -model	Basic	Standard	Advanced
<i>Considered temperature models</i>			
Freeze-out	NO $f_A = 1$	YES $f_A(T)$, (1.18)	YES $f_A(T)$, (1.18)
Intrinsic cond.	NO $n_i = n_i^{300K}$	YES $n_i(T)$, (1.5)	YES $n_i(T)$, (1.5)
Band gap	NO $E_{gap} = E_{gap}^{300K}$	NO $E_{gap} = E_{gap}^{300K}$	YES $E_{gap}^{Sze}(T)$, (1.25)
Eff. dens. states	YES $T^{3/2}$ model, (1.4)	YES $T^{3/2}$ model, (1.4)	YES EM model, (1.26)
<i>Parameters at 300 K</i>			
N_C^{300K}	2.8430×10^{19} cm $^{-3}$	2.8430×10^{19} cm $^{-3}$	2.8939×10^{19} cm$^{-3}$
N_V^{300K}	2.6821×10^{19} cm $^{-3}$	2.6821×10^{19} cm $^{-3}$	3.1437×10^{19} cm$^{-3}$
N_C^{300K} / N_V^{300K}	1.060	1.060	0.921
n_i^{300K}	1.0000×10^{10} cm$^{-3}$	1.0000×10^{10} cm$^{-3}$	1.0923×10^{10} cm $^{-3}$
E_{gap}^{300K}	1.1240 eV	1.1240 eV	1.1245 eV
E_{gap}^{0K}	1.1240 eV	1.1240 eV	1.1700 eV
<i>Equilibrium carrier concentrations</i>			
Majorities	$p_0 = N_A$, (1.8a)	$p_0(T)$, (1.22)	$p_0(T)$, (1.22)
Minorities	$n_0 = n_i^{300K} / N_A$	$n_0(T) = n_i(T) / p_0(T)$	$n_0(T) = n_i(T) / p_0(T)$

The numbers in parentheses refer to the defining equations of the underlying models. **Bold font** denotes the defining set of model parameters, the others being calculated on the basis of the fundamental equations (see, e.g., Sect. 1.2.1D).

1.3 Fundamentals 2: generation, recombination and carrier lifetime

Generation in semiconductors refers to the processes by which electron-hole pairs are created. The energy for the excitation of an electron from the valence to the conduction band can come from thermal processes or through the absorption of photons. *Recombination* refers to the inverse processes whereby electron-hole pairs are lost due to a spontaneous transition of an excited electron from the conduction band to an unoccupied state (hole) in the valence band. The excess energy and the change in momentum are either released as photons or phonons or transferred to other carriers, which ensures energy and momentum conservation for the individual processes of electron-hole recombination. Generally speaking, the *recombination rate* R is directly proportional to the densities of the carriers involved in the transition and to a *recombination coefficient*, which mainly reflects the quantum mechanical probability of an electron transition from the conduction to the valence band and thus depends on the individual physical processes underlying recombination. These physical processes are referred to as *recombination mechanisms*.

In thermal equilibrium, thermal generation G_0 is counterbalanced by an equilibrium recombination R_0 , leading to the equilibrium electron and hole densities n_0 and p_0 whose product is constant, $n_0 p_0 = n_i^2$, as shown in Sect. 1.2.1. Upon a constant optical excitation, the system passes into a new stationary state, where the increased total generation rate $G > G_0$ is counterbalanced by an increased total recombination rate $R > R_0$, which leads to increased non-equilibrium electron and hole densities n and p with $np > n_i^2$. As thermal equilibrium cannot be reached instantaneously after switching off the external generation source, the excess carrier densities $\Delta n = n - n_0$ and $\Delta p = p - p_0$ decay successively with the *net recombination rate* $U = R - R_0$, which is a characteristic of the individual recombination mechanisms and vanishes in thermal equilibrium. Since only this net recombination rate U is relevant to the purpose of the present work, it is often simply referred to as the recombination rate. Assuming charge neutrality and the absence of trapping centers¹³, i.e. $\Delta n = \Delta p$, the time-dependent decay of the excess carrier density $\Delta n(t)$ is defined by the following rate equation:

$$\frac{\partial \Delta n(t)}{\partial t} = -U(\Delta n(t), n_0, p_0) \quad (1.28)$$

¹³ The presence of shallow trap centers leads to inequalities between Δn and Δp , resulting in the so-called trapping effect which will be further discussed in Sects. 1.4.3C and 3.3.1A.

In general, U can be written as a polynomial in Δn , whereby the zero-order coefficient identically equals zero, as $U(\Delta n=0)$ has to vanish (thermal equilibrium). Thus, in the simplest case U is proportional to Δn . According to Eq. (1.28) the time-dependent decay of Δn then follows an exponential law. The time constant of this exponential decay represents the *recombination lifetime* – often also referred to as the *carrier lifetime* or *lifetime* – which is thus generally defined via the following equation:

$$\tau(\Delta n, n_0, p_0) := \frac{\Delta n}{U(\Delta n, n_0, p_0)} \quad (1.29)$$

As can be seen, an injection-independent carrier lifetime is only observed in the special case of $U \propto \Delta n$. However, as already indicated in Eq. (1.29), carrier lifetime will in general strongly depend on the injection density Δn as well as on the doping concentration of the semiconductor via n_0 and p_0 .

As the different physical recombination mechanisms can be considered to occur independently in the semiconductor, the total recombination rate U_{eff} is simply the sum of the individual recombination rates U_v (index v). According to Eq. (1.29), the total carrier lifetime τ_{eff} then equals the inverse sum of the reciprocal carrier lifetimes τ_v related to the individual recombination processes:

$$U_{\text{eff}} = \sum_v U_v \quad \Rightarrow \quad \frac{1}{\tau_{\text{eff}}} = \sum_v \frac{1}{\tau_v} \quad (1.30)$$

Thus τ_{eff} is always smaller than the smallest lifetime of the contributing recombination channels. The following section introduces the different recombination mechanisms observed in silicon. In addition to a discussion of the underlying physical processes, expressions for their specific $\tau_v(\Delta n, n_0, p_0)$ -dependence are presented.

1.4 Carrier recombination mechanisms

A common classification of the different recombination mechanisms distinguishes intrinsic and extrinsic mechanisms:

- *Intrinsic recombination mechanisms* are always present even in the ideal undisturbed crystal and do not depend on the specific technique used for crystal growth, being in this sense unavoidable. Depending on the way the excess energy released by the decay of an electron-hole pair is dispersed, two fundamental processes may be distinguished: *radiative band-band recombination*, if the excess energy is released as a photon,

and *Auger band-band recombination*, if the excess energy is transferred to a third carrier, the transition thus being non-radiative. Depending on the band structure of the semiconductor crystal, in both processes phonons may also be involved, to ensure momentum conservation.

- In the case of *extrinsic recombination mechanisms*, the decay of an electron-hole pair does not occur directly via a band-band transition of an electron – as in the case of the intrinsic mechanisms – but stepwise by an electron transition via a defect center with an intermediate energy level in the band gap. This process is commonly known as Shockley-Read-Hall (SRH) recombination after those who originally modeled its effect. Although this defect-mediated recombination process may in principle be removed by producing an ideal crystal of perfect purity, under real conditions it is very often the dominant process, as any imperfection of the ideal crystal structure induces defect levels, which may act as recombination centers if located within the band gap. SRH recombination can occur either through bulk defects, induced by impurities or lattice defects, or as a result of surface states, which are typically caused by dangling bonds at the wafer surface. The cases of *bulk SRH recombination* and *surface recombination* are treated separately below.

As lifetime spectroscopy aims at characterizing impurity-induced bulk defects on the basis of the SRH bulk lifetime, it is necessary to examine the relative importance of the different recombination channels in crystalline silicon, to assess the possibilities of a direct determination of this quantity. That is why the present section introduces specific expressions for the injection and doping dependence of the recombination lifetimes related to all four recombination mechanisms mentioned above.

1.4.1 Radiative recombination

Radiative band-band recombination is the direct annihilation of an electron-hole pair, involving the emission of a photon with an energy approximately equal to that of the band gap. This is in fact the inverse process to optical generation in a solar cell, as depicted in Fig. 1.12a. As the process involves a conduction band electron falling from an allowed conduction band state into a vacant valence band state (hole), the radiative recombination rate depends jointly on the concentrations of free electrons n and free holes p , which gives rise to the following expression for the net recombination rate U_{rad} :

$$U_{rad} = B (np - n_i^2) \quad (1.31)$$

The coefficient B directly reflects the quantum-mechanical probability of a radiative transition, which strongly depends on the band structure of the semiconductor. In direct semiconductors, such as GaAs, band-band transitions occur vertically in the E - k -space, which requires only the emission of a photon to conserve energy, while momentum conservation is ensured inherently. In indirect semiconductors, such as silicon, on the contrary, an electron transition from the conduction band minimum to the valence band maximum requires – due to the existing momentum difference – the simultaneous emission of a photon and a phonon, in order to conserve both momentum and energy. Due to the additional particle involved in the recombination process (three-particle process), the probability of radiative recombination is inherently reduced in indirect semiconductors compared to direct semiconductors. This is directly reflected in the value of the coefficient B , which is found in the literature to be four orders of magnitude smaller in silicon ($B=1\times10^{-14}\text{ cm}^{-3}\text{s}^{-1}$ [11]) than in GaAs ($B=3\times10^{-10}\text{ cm}^{-3}\text{s}^{-1}$ [11]).

Inserting the non-equilibrium concentrations $n=n_0+\Delta n$ and $p=p_0+\Delta p$ in Eq. (1.31) and assuming charge neutrality ($\Delta n=\Delta p$), U_{rad} takes the form of a second-order polynomial in Δn , which upon use of Eq. (1.29) yields the following general expression for the radiative recombination lifetime τ_{rad} :

$$U_{rad} = B(n_0 + p_0)\Delta n + B\Delta n^2 \Rightarrow \tau_{rad} = \frac{1}{B(n_0 + p_0) + B\Delta n} \quad (1.32)$$

In the limiting cases of low-level injection ($\Delta n \ll n_0 + p_0$) and high-level injection ($\Delta n \gg n_0 + p_0$), Eq. (1.32) further simplifies and results in two common relationships for the asymptotic dependence of τ_{rad} :

$$\tau_{rad}^{LLI} = \frac{1}{B N_{dop}} \quad \text{and} \quad \tau_{rad}^{HLI} = \frac{1}{B \Delta n} \quad (1.33)$$

As can be seen, the radiative lifetime depends on the inverse of the carrier density n ($\tau_{rad} \propto 1/n$). Therefore, under LLI conditions τ_{rad} is injection-independent, its magnitude being proportional to the inverse of the doping concentration. Under HLI conditions τ_{rad} decreases as the injection density increases, its magnitude being independent of the doping concentration.

While radiative recombination is typically the dominant recombination process in direct semiconductors, where it forms the basis for the operation of light-emitting diodes, it is considered to be small or even negligible compared to other recombination processes in indirect semiconductors, such as silicon (see Fig. 1.13 and discussion below).

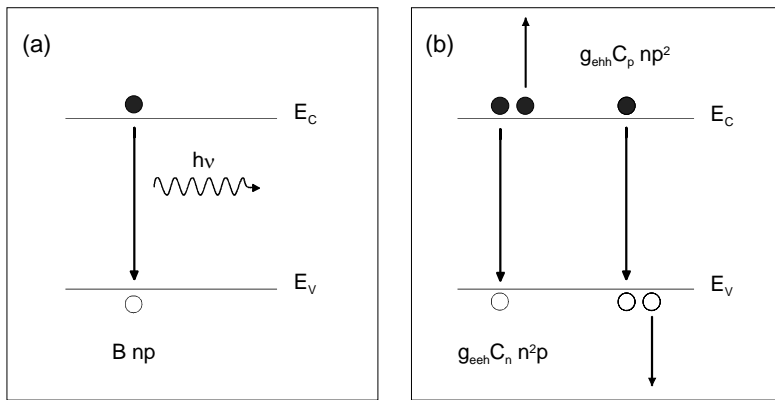


Fig. 1.12. Schematic diagram of intrinsic recombination mechanisms: (a) radiative band-band recombination and (b) Auger band-band recombination.

1.4.2 Auger recombination

Auger recombination, which is the second intrinsic recombination process, is traditionally viewed as a three-particle interaction where the energy released by the recombination of an electron-hole pair is transferred to a third free carrier, which releases its excess energy as phonons to the crystal (thermalization). This process is depicted in Fig. 1.12b. In the classical theory, the charge carriers are assumed to be non-interacting quasi-free particles [12]. Depending on the third carrier being either a conduction band electron or a valence band hole, the Auger recombination rate U_{Auger} is either proportional to n^2p (for the eeh -process) or to p^2n (for the ehh -process) [13, 14]. Thus, the net recombination rate is given by

$$U_{Auger} = C_n (n^2 p - n_0^2 p_0) + C_p (np^2 - n_0 p_0^2) \quad (1.34)$$

with C_n and C_p being the Auger coefficients of the eeh - and the ehh -process, respectively. Analogously to Eq. (1.32), a general expression for the Auger recombination lifetime τ_{Auger} may be derived from Eq. (1.34), which leads in the limiting cases of low- and high-level injection to the common relationships for the asymptotic dependence of τ_{Auger} :

LLI conditions:

$$\tau_{Auger}^{LLI,n} = \frac{1}{C_n N_D^2} \quad \text{for } n\text{-type}, \quad \tau_{Auger}^{LLI,p} = \frac{1}{C_p N_A^2} \quad \text{for } p\text{-type}. \quad (1.35)$$

HLI conditions:

$$\tau_{\text{Auger}}^{\text{HLI}} = \frac{1}{(C_n + C_p)\Delta n^2} = \frac{1}{C_a \Delta n^2} \quad \text{for } n\text{-type and } p\text{-type,} \quad (1.36)$$

where $C_a \equiv C_n + C_p$ represents the so-called ambipolar Auger coefficient. The most commonly quoted values for the Auger coefficients are those determined by Dziewior and Schmidt on *n*-type and *p*-type silicon with a doping concentration greater than $5 \times 10^{18} \text{ cm}^{-3}$: $C_n = 2.8 \times 10^{-31} \text{ cm}^6 \text{s}^{-1}$ and $C_p = 9.9 \times 10^{-32} \text{ cm}^6 \text{s}^{-1}$ [15].

As can be seen, the Auger lifetime ideally depends on the inverse square of the carrier density n ($\tau_{\text{rad}} \propto 1/n^2$). Therefore, under LLI conditions τ_{Auger} is injection-independent, its magnitude being proportional to the inverse square of the doping concentration, while under HLI conditions τ_{Auger} decreases as the injection density increases, its magnitude being independent of the doping concentration. As τ_{Auger} shows a stronger dependence on the injection level than τ_{rad} , Auger recombination will become the dominant mode of recombination in silicon for high injection levels.

A Coulomb enhancement of Auger recombination

In fact, Auger recombination is more complex than the idealized view presented above and significant departures from the Eqs. (1.35) and (1.36) have been observed experimentally.¹⁴ On the one hand the quadratic decrease in the LLI Auger lifetime with increasing doping concentration was only observed for high doping concentrations above $5 \times 10^{18} \text{ cm}^{-3}$ [15], while below $1 \times 10^{18} \text{ cm}^{-3}$ the doping dependence was found to be weaker [15], reflecting a higher Auger recombination rate than the one predicted by Eq. (1.35). On the other hand a number of experiments on weakly doped material at medium to high injection densities showed [18] that the C_a -coefficient is larger than the sum of the low-injection Auger coefficients, $C_n + C_p$, determined on highly-doped silicon (in the τ_{Auger} -regime with quadratic doping dependence) [15]. This difference was found to decrease with increasing injection density and to vanish for injection densities above $1 \times 10^{18} \text{ cm}^{-3}$ (for a comparison of the experimental C_a data see [16, p.29]. Thus, the experimental observations consistently pointed towards a mechanism which enhances Auger recombination at lower carrier densities ($< 1 \times 10^{18} \text{ cm}^{-3}$).

¹⁴ A detailed discussion may be found in [16, pp. 23–32] or [17].

The most elegant theoretical explanation for this effect has been presented by Hangleiter and Häcker with their theory of Coulomb-enhanced (CE) Auger recombination [12, 19]. Different from the traditional theory where the charge carriers involved in the recombination process are regarded as non-interacting quasi-free particles, they took into account the Coulomb interaction between mobile charge carriers. Due to the Coulomb interaction the electron density is locally increased in the vicinity of a hole and locally reduced in the vicinity of an electron. As the Auger recombination rate strongly depends on the carrier concentration, it may significantly increase due to such local inhomogeneities in the carrier density [14]. To account for this effect, the Auger coefficients C_n and C_p in Eq. (1.35) are multiplied by carrier-density-dependent enhancement factors g_{eeh} and g_{ehh} which reflect the increased probability that the three carriers involved in the recombination process will be in the same place.

LLI conditions:

$$\begin{aligned} \tau_{CE\text{-Auger}}^{LLI,n} &= \frac{1}{g_{eeh} C_n N_D^2} && \text{for } n\text{-type,} \\ \tau_{CE\text{-Auger}}^{LLI,p} &= \frac{1}{g_{ehh} C_p N_A^2} && \text{for } p\text{-type.} \end{aligned} \quad (1.37)$$

Based on the finding that the Coulomb interaction induces a spatial correlation of electron-hole pairs due to the formation of bound states (excitons), the quantum-statistical approach of Hangleiter and Häcker allowed the enhancement factors to be calculated without using any free parameter [12]. Their correlation theory revealed that the excitonic states dominate under low doping concentration, while they have been found to vanish for doping concentrations above 10^{18} cm^{-3} due to a complete screening of the electron-hole interaction. This reduction in the spatial correlation of the system with increasing majority carrier concentration directly results in a reduction of the Coulomb enhancement, which is reflected in the enhancement factors approaching 1. As a consequence, at high majority carrier densities the electrons and holes may be regarded as free particles and the theory of CE-Auger recombination passes into the traditional Auger theory. Although the CE-Auger theory allows an elegant explanation of the experimentally observed enhancement of Auger recombination, the agreement between calculated and measured LLI-Auger lifetimes has been found to be only qualitatively correct [20].

B Model for the injection dependence of CE-Auger recombination lifetime

1. Low-injection model. From a fit to the maximum LLI-Auger lifetimes measured by different groups, Altermatt et al. determined an empirical parameterization for the enhancement factors g_{eeh} and g_{ehh} , using the C_n and C_p values of Dziewior and Schmidt, and found for their doping dependence the following expressions [21]:

$$g_{eeh}(N_D) = 1 + 44 \left\{ 1 - \tanh \left[\left(\frac{N_D}{5 \times 10^{16} \text{ cm}^{-3}} \right)^{0.34} \right] \right\} \quad (1.38a)$$

$$g_{ehh}(N_A) = 1 + 44 \left\{ 1 - \tanh \left[\left(\frac{N_A}{5 \times 10^{16} \text{ cm}^{-3}} \right)^{0.29} \right] \right\} \quad (1.38b)$$

The resulting doping dependence of the CE-Auger lifetime under LLI conditions is shown in Fig. 1.13a (solid line).

2. High-injection model. As discussed in further detail in [16], a Coulomb enhancement of Auger recombination is also observed under HLI conditions, though being less pronounced than under LLI conditions. This enhancement is directly reflected in the measured values for the C_a coefficient. In spite of the scatter of these values, the value of $C_a = 1.66 \times 10^{-30} \text{ cm}^6 \text{s}^{-1}$ determined by Sinton and Swanson [22] seems to be reasonable for the purpose of the present work. On the one hand its magnitude is fully consistent with the CE-Auger theory (see [16]) and on the other hand its determination occurred in an injection range which coincides with the maximum injection range reached in the lifetime measurements of the present work. Moreover, this coefficient is also used in the commercial device simulation package PC1D [23]. Thus under HLI conditions the injection dependence of the CE-Auger lifetime can be adequately described by Eq. (1.36), as shown in Fig. 1.13b (dashed line).

3. Complete model. A model for the injection dependence of the CE-Auger lifetime has been proposed by the author in [16, 24]. To allow on the one hand a description on the basis of the general Auger model given in Eq. (1.31) and to fully consider on the other hand the findings on the Coulomb enhancement under LLI and HLI conditions, injection-dependent Auger coefficients have been defined as

$$C_n^* := g_{eeh} C_n \left(\frac{n_0}{n_0 + \Delta n} \right) + \frac{C_a}{2} \left(\frac{\Delta n}{n_0 + \Delta n} \right) \quad (1.39a)$$

$$C_p^* := g_{ehh} C_p \left(\frac{p_0}{p_0 + \Delta p} \right) + \frac{C_a}{2} \left(\frac{\Delta p}{p_0 + \Delta p} \right) \quad (1.39b)$$

using for the Auger coefficients the values already cited above: $C_n = 2.8 \times 10^{-31} \text{ cm}^6 \text{s}^{-1}$, $C_p = 9.9 \times 10^{-32} \text{ cm}^6 \text{s}^{-1}$ and $C_a = 1.66 \times 10^{-30} \text{ cm}^6 \text{s}^{-1}$. As can be seen, these effective Auger coefficients are defined as weighted mean values between the corresponding LLI-Auger coefficients and the ambipolar HLI-Auger coefficients using as weighting function the ratio of equilibrium and excess carrier density to total carrier density. Note that a similar weighting is also used in the device simulation package PC1D [23]. However, in contrast to the implementation there, our model incorporates for the LLI-Auger coefficients the doping-dependent enhancement factors given in the Eqs. (1.38a) and (1.38b) and thus fully accounts for the Coulomb enhancement under LLI conditions. Using these effective Auger coefficients, the injection-dependent CE-Auger lifetime may be calculated as

$$\tau_{CE-Auger} = \frac{n - n_0}{C_n^* \times (n^2 p - n_0^2 p_0) + C_p^* \times (np^2 - n_0 p_0^2)} \quad (1.39c)$$

which directly follows from the general expression (1.34) for the Auger recombination rate upon use of Eq. (1.29). The quality of this model has been proved in [16]. Allowing CE-Auger lifetime to be accurately determined at any injection and doping density, this model is used throughout the work.

A similar extension to all injection levels has been suggested later by Altermatt et al. [25] which involves evaluating the enhancement factors at the total free-carrier density for intermediate injection. Only recently, Kerr et al. proposed a generalized parameterization of CE-Auger lifetime that has been determined as the simplest functional form to fit experimental Auger lifetimes, measured over a broad range of injection and doping densities for n -type and p -type dopants [17]. The detailed comparison of the models, presented there, revealed only slight variations between the new parameterization and the model used here [17, p.63], which further justifies the simple approach.

C Comparison of the intrinsic recombination lifetimes

To demonstrate the relative importance of the two intrinsic recombination channels, Fig. 1.13 displays a comparison of the radiative lifetime (dash-dotted lines) with the classical (dashed lines) and the Coulomb-enhanced (solid lines) Auger lifetime. The calculations are based on the above equations, the physical parameters being chosen as indicated in the text.

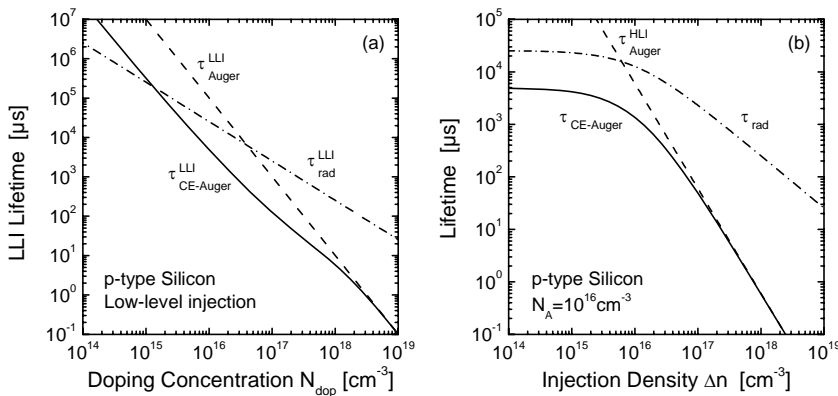


Fig. 1.13. Comparison of radiative, Auger and Coulomb-enhanced Auger recombination lifetime (a) under low-level injection as a function of the doping concentration and (b) for a 10^{16} cm^{-3} -doped sample as a function of the injection density.

Figure 1.13a shows the doping dependence of the intrinsic recombination lifetimes under LLI conditions. As can be seen, the Coulomb enhancement reduces the Auger recombination lifetime by more than an order of magnitude in a broad doping range below 10^{17} cm^{-3} . As a result, Auger recombination is the dominant intrinsic recombination channel over a much broader doping range, while radiative recombination only predominates for doping concentrations below 10^{15} cm^{-3} . However, as the radiative lifetime at that low doping concentration exceeds 100 ms, recombination is most likely completely dominated by defect-dependent SRH lifetime even in high-purity material, which shows that radiative recombination is totally screened. In contrast to that, for medium doping concentrations between $2\text{--}5 \times 10^{16} \text{ cm}^{-3}$, the CE-Auger lifetime ranges between 1500 and 300 μs , which is in the order of magnitude of real lifetime values, and thus shows that due to the Coulomb enhancement, lifetime measurements have to be aware of an impact of intrinsic recombination even under LLI conditions, at least in that doping range.

The injection dependence of the intrinsic recombination lifetimes is shown in Fig. 1.13b, for a medium doping concentration of 10^{16} cm^{-3} , which represents a typical value for the samples investigated here. As can be seen, CE-Auger recombination significantly outweighs radiative recombination at all injection levels. While a predominance of radiative recombination is theoretically possible under LLI conditions for lower doping concentrations (see above), it is impossible under HLI conditions due to the stronger Δn -dependence of the Auger lifetime [quadratic, see Eq. (1.36)] compared to the radiative lifetime [linear, see Eq. (1.33)].

Thus, the general conclusion is that radiative recombination can usually be safely ignored in the analysis of measured recombination lifetimes in silicon. CE-Auger recombination, on the contrary, will often contribute to, or even dominate, the overall effective lifetime, particularly under HLI conditions. As CE-Auger recombination is intrinsic and thus unavoidable, it defines an upper limit for the maximum bulk lifetime. Under LLI conditions, this upper limit can only be reached in the best material with the best surface passivation, as the lifetime is normally dominated by recombination through defects, as will be discussed in the next section.

1.4.3 Bulk recombination through defects (Shockley-Read-Hall)

Having seen the impact of intrinsic recombination mechanisms in the previous sections, the extrinsic recombination via defects in the bulk, which represents the recombination channel that lifetime spectroscopy is based on, is discussed in the following. While the present section focuses on the fundamental concept that describes defect recombination, including its validity for the investigations of the present work, the general expression derived for the defect-recombination lifetime will be analyzed in detail from a spectroscopic point of view in Chap. 3.

A Different roles of a defect level – a pictorial view

The presence of defects within a semiconductor, be they from impurities or crystallographic imperfections, produces discrete energy levels within the band gap. Such a defect level, which can be occupied either by an electron (occupied state) or by a hole (unoccupied state), may interact with the conduction (CB) and the valence band (VB) through four elementary processes which are displayed in Fig. 1.14. While an occupied defect level can either emit its electron into the CB (1) or capture a hole from the VB (3), an unoccupied defect level can either capture an electron from the CB (2) or emit its hole into the VB (4). Since it is conventional to describe the interaction with the CB via electrons and the interaction with the VB via holes, the direction of the solid and dashed arrows in Fig. 1.14 indicates the direction of the electron and hole transition, respectively.¹⁵ The possible two-step processes, which result from a suitable combination of these elementary events, may be divided into three classes differing in the function assigned to the defect level:

¹⁵ Note that each of the elementary processes displayed in Fig. 1.14 describes both the transition of an electron and (in opposite direction) the transition of a hole. For example, the hole capture (3) from the valence band into the localized defect state (dashed arrow) can also be regarded as an electron emission from the localized state into the valence band.

1. The defect level acts as a *recombination center*: The recombination process may be understood as a two-step capture process, whereby a free electron from the CB (2) and a free hole from the VB (3) are successively captured by the defect level and annihilate each other, or as a two-step relaxation process whereby a free electron from the CB first relaxes to the defect level (2) and then relaxes to the VB (3), where it finally annihilates a hole.
2. The defect level acts as a *generation center*: The generation process, which is just the inversion of the recombination process, may be understood as a two-step emission process, whereby the defect level successively emits an electron in the CB (1) and a hole in the VB (4) or as a two-step excitation process, whereby an electron from the VB is first excited into the defect level (4) and then excited in the CB (1). On balance, an electron-hole pair is generated.
3. The defect level acts as a *trap center*: The trapping process, which is neither recombination nor generation, is identified with those two-step processes where a carrier is captured at the defect center and subsequently injected back into the band from which it came, i.e., with the combinations (2)+(1) or (3)+(4), meaning that the defect center interacts with only one of the two bands.

Since thermal generation through a defect center only becomes relevant if there is a paucity of carriers as, e.g., in a deeply depleted space charge region [26], it can be neglected for the purpose of the present work. Whether a defect acts as a recombination or a trap center only depends on whether

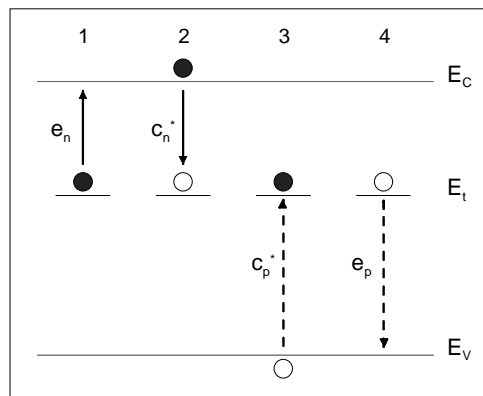


Fig. 1.14. Electron energy band diagram showing the four possible interaction mechanisms of free carriers with a defect level in the band gap: electron emission (1), electron capture (2), hole capture (3) and hole emission (4). The direction of the *solid* and *dashed arrows* indicates the direction of the electron and hole transition, respectively.

thermal reemission of a captured carrier or a second capture process occurs with higher probability and thus on the location of the Fermi level, the temperature and the capture cross-sections of the impurity [26]. This will be further discussed in Sect. 1.4.3C.

B The Shockley-Read-Hall equation

Irrespective of the exact physical mechanisms the capture and emission processes are based on, Shockley and Read [1] and Hall [2] formulated in 1952 a theory of recombination through defects from purely statistical considerations of the four elementary processes and determined the recombination rate related to a single defect level as a function of the defect, material and excitation parameters. Since this standard Shockley-Read-Hall theory (SRH theory) forms the basis of lifetime spectroscopy and thus underlies the detailed theoretical investigations in Chap. 3, the concept of its derivation should be briefly outlined following an illustrative description in [27].

1. General expressions for dn/dt and dp/dt . To determine the time rates of change of the electron density n in the CB and the hole density p in the VB, the total emission and capture due to the ensemble of defect centers has to be balanced for electrons and holes. The starting point is the capture and emission rates of a single defect center, which directly reflect the probability of the individual processes in Fig. 1.14.¹⁶ While the *emission rates* e_n and e_p for thermal emission of electrons and holes are a priori unknown physical constants, the *capture rates* c_n^* and c_p^* for electrons and holes may be expressed as

$$c_n^* = c_n n = (\sigma_n v_{th}) n \quad \text{and} \quad c_p^* = c_p p = (\sigma_p v_{th}) p \quad (1.40)$$

which has an illustrative physical explanation [26], exemplified here for electrons. If the movement of electrons within the lattice is regarded from their own frame of reference, the defect centers move randomly with the thermal velocity v_{th} while the electrons themselves are immobile. Then, with its capture cross-section σ_n , the defect center sweeps out a volume per unit time of $\sigma_n \times v_{th}$. The fact that those electrons which find themselves within that volume have a high probability of being captured, directly leads to Eq. (1.40).¹⁷

¹⁶ The electron capture rate (emission rate) represents the number of carriers captured (emitted) per second from the CB (from the defect center) and is thus given in [1/s].

¹⁷ While the electron capture rate is proportional to the density of electrons in the CB, the electron emission rate scales with the density of unoccupied electron states in the CB. Since this quantity is orders of magnitude higher than the common carrier densities, it is hardly affected by the carrier dynamics and thus included as a fixed quantity in the variable e_n .

For the transition from a single defect center to the ensemble, let N_t be the density of defect centers and f_t the probability of occupation by an electron.¹⁸ Since the total electron emission (total hole capture) is proportional to the density of occupied defect centers $N_t \times f_t$ and the total electron capture (total hole emission) to the number of unoccupied defect centers $N_t \times (1-f_t)$, the time rates of change of n and p due to generation and recombination alone may be written as

$$\left(\frac{dn}{dt} \right)_{GR} = (1) - (2) = e_n \times N_t f_t - c_n n \times N_t (1 - f_t) \quad (1.41a)$$

$$\left(\frac{dp}{dt} \right)_{GR} = (4) - (3) = e_p \times N_t (1 - f_t) - c_p p \times N_t f_t \quad (1.41b)$$

the numbers indicating the processes in Fig. 1.14. Equations (1.41a) and (1.41b) are generally valid including the special case of stationary equilibrium.

2. Detailed balancing – expressions for the emission rates e_n and e_p and SRH densities. The principle of detailed balance requires $dn/dt \equiv 0$ and $dp/dt \equiv 0$, since each process must be in equilibrium with its inverse process, irrespective of other processes. If the expressions (1.3) for the equilibrium carrier concentrations n_0 and p_0 are introduced and if the occupation probability f_t is identified with the Fermi-Dirac distribution function given in Eq. (1.1), Eqs. (1.41) allow the unknown emission rates e_n and e_p to be expressed as functions of the defect energy E_t and the capture coefficient c_n and c_p , respectively:

$$e_n = c_n n \frac{1 - f_t}{f_t} = c_n N_C \exp\left(-\frac{E_C - E_t}{k_B T}\right) =: c_n n_1 \quad (1.42a)$$

$$e_p = c_p p \frac{f_t}{1 - f_t} = c_p N_V \exp\left(-\frac{E_t - E_V}{k_B T}\right) =: c_p p_1 \quad (1.42b)$$

where N_C and N_V are the effective densities of states in the CB and VB, respectively, and E_C and E_V the energies of the CB edge and VB edge, respectively. These equations define the so-called SRH densities n_1 and p_1 , which are statistical factors and play an important role in the SRH theory:

¹⁸ Note that f_t has to be described by the more general Fermi-Dirac distribution since the Fermi level E_F may even coincide with the defect energy level E_t which makes the simplifying Boltzmann distribution invalid.

$$n_1 := N_C \exp\left(-\frac{E_C - E_t}{kT}\right), \quad p_1 := N_V \exp\left(-\frac{E_t - E_V}{kT}\right) \quad (1.43)$$

As can be seen from a comparison with Eq. (1.3), n_1 and p_1 equal the equilibrium densities of electrons and holes when the Fermi level E_F coincides with the defect energy E_t , and thus satisfy the law of mass action given in Eq. (1.5): $n_1 p_1 = n_i^2$.

3. Steady-state non-equilibrium – occupation probability and SRH recombination rate. To find an expression for the SRH recombination rate, the general case of non-equilibrium has to be considered. An increase in the electron and hole densities n and p may be realized, e.g., by optical generation. As soon as steady-state conditions are reached, the time rates of change of n and p must equal each other, since any divergence would result in a continuously increasing occupancy of the defect centers by electrons or holes. If the expressions (1.42) for e_n and e_p are inserted in the Eqs. (1.41), equating $dn/dt = dp/dt$ yields the occupation probability f_t of the defect centers as a function of the preset defect (n_1 , p_1 , c_n and c_p) and excitation (n and p) parameters. If this expression for f_t is inserted in either of the Eqs. (1.41), the net recombination rate for SRH recombination through defects takes the form

$$U_{SRH} = \left(\frac{dn}{dt} \right)_{GR} = \left(\frac{dp}{dt} \right)_{GR} = \frac{(np - n_i^2)}{[N_t \sigma_n v_{th}]^{-1}(p + p_1) + [N_t \sigma_p v_{th}]^{-1}(n + n_1)} \quad (1.44)$$

Again the driving force of the recombination process is the term $(np - n_i^2)$, which describes the deflection of the system from thermal equilibrium.¹⁹ Although derived under steady-state assumptions here, it is possible to show that this expression is also valid for transient conditions.

4. SRH lifetime. If the non-equilibrium densities are replaced by $n = n_0 + \Delta n$ and $p = p_0 + \Delta p$ and if carrier trapping is assumed to be negligible ($\Delta n = \Delta p$), it follows from Eq. (1.29) that the SRH lifetime can be expressed as

$$\tau_{SRH} = \frac{\tau_{n0}(p_0 + p_1 + \Delta n) + \tau_{p0}(n_0 + n_1 + \Delta n)}{p_0 + n_0 + \Delta n} \quad (1.45)$$

¹⁹ Depending on the non-equilibrium conditions, Eq. (1.44) leads to different net effects. If the electron and hole density is increased, e.g., by optical generation ($np > n_i^2$), Eq. (1.44) describes a net recombination of electron-hole pairs ($U_{SRH} > 0$). If the electron and hole density is decreased, e.g., in the depletion region of a reverse biased diode ($np < n_i^2$), then Eq. (1.44) describes a net generation of electron-hole pairs ($U_{SRH} < 0$)

where τ_{n0} and τ_{p0} are the capture time constants of electrons and holes which are related to the thermal velocity v_{th} , the defect concentration N_t , and the capture cross-sections σ_n and σ_p of the specific defect center in question:

$$\tau_{p0} := (N_t \sigma_p v_{th})^{-1}, \quad \tau_{n0} := (N_t \sigma_n v_{th})^{-1} \quad (1.46)$$

C Prerequisites of the standard SRH model

The derivation of the standard SRH model, as outlined above, involves a number of simplifying assumptions whose limiting character should be briefly discussed:

1. The semiconductor is non-degenerate.
2. The defect levels involved all have the same energy E_t (single-level trap).
3. The energy position of the defect level is stable, i.e., especially independent of the charge state of the impurity.
4. The impurity concentration is negligibly small compared to the background doping.
5. The relaxation times of the captured carriers are much smaller than their reemission times.

(1) The assumption of non-degeneracy is certainly valid in the wafer bulk in all practical cases though it may not be correct in diffused regions. Since the lifetime spectroscopic investigations of Chaps. 4 and 5 are performed on non-diffused bulk wafers, non-degeneracy is assumed throughout the work (see footnote 2 in Sect. 1.2.1). (2) and (3) The assumption of a stable single-level trap dominating recombination is certainly valid for the point defects investigated here but may be incorrect for precipitates or surface defects whose defect energies tend to be continuously distributed in certain regions of the band gap (see Sect. 1.4.4). The common problem of the coexistence of a deep and a shallow level, dominating carrier lifetime under different conditions, is compatible with the standard SRH model as long as both defects can be treated independently, as is the case in the investigations presented here. (4) and (5) The last two points basically ensure that the defect center acts mainly as a recombination center and that eventual trapping effects due to the defect center are negligible, $\Delta n = \Delta p$ hence being valid. In fact this is the only assumption which is less easily verified, though highly relevant since trapping effects cause distortions in the excess carrier densities which may result in significant deviations of the actual lifetime from the trapping-free SRH lifetime.

In a recent publication [3], Macdonald and Cuevas compared the standard SRH model with a more general model that explicitly accounts for trapping effects, and derived an analytical expression for a so-called critical recombination center density N_{crit} , above which standard SRH theory becomes inaccurate. This limit not only depends on the doping concentration N_{dop} and the excess carrier concentration Δn but also on the energy level E_t and the capture cross-sections σ_n and σ_p of the given recombination center, and thus represents a unification of the prerequisites 4 and 5. In parallel with the increasing dominance of trapping effects, N_{crit} decreases with decreasing N_{dop} and decreasing Δn , respectively. Thus, for a given defect center and sample, the low-injection approximation N_{crit}^{LLI} represents a lower bound for N_{crit} . For p -type doping it takes the form [3]

$$N_{crit}^{LLI} = \frac{[p_0 + p_1] \times [n_1 + (\tau_{n0} / \tau_{p0})(p_0 + p_1)]}{|p_0 - (\tau_{n0} / \tau_{p0})p_1|} \quad (1.47)$$

Macdonald showed that the standard SRH model is accurate across all injection levels when $N_t \ll N_{crit}^{LLI}$ [3]. To ensure an accuracy of the standard SRH model of 10 % under low-injection conditions, N_t has to be at least an order of magnitude smaller than N_{crit}^{LLI} [3]. For higher recombination center densities mid- and high-injection lifetime measurements may still be accurately modeled with the standard SRH model, provided the excess carrier density is high enough to ensure $N_t \ll N_{crit}(\Delta n)$. An analytical expression for the lower bound Δn_{min} of the Δn range, where the standard SRH model is still accurate within 10 %, may be directly derived from the general expression $N_{crit}(\Delta n)$ [3]. The N_{crit} criterion thus allows the validity of the standard SRH model to be accurately verified for arbitrary experimental conditions if the density and the defect parameters of the recombination center in question are known.

The application of the N_{crit} criterion to the intentionally metal-contaminated samples investigated in Chap. 4 revealed that $N_t \ll N_{crit}^{LLI}$ is fulfilled in almost all cases, which proves the validity of standard SRH theory throughout the book. The few samples which did not fulfil $N_t \ll N_{crit}^{LLI}$ have either been sorted out or subjected to a careful investigation of the experimental conditions, the modeling of the lifetime data being restricted to those Δn ranges which fulfilled $N_t \ll N_{crit}(\Delta n)$. The N_{crit} criterion thus defines for each impurity an upper limit to the tolerable contamination level, which is found to be high enough for the investigated contaminants to apply SRH-based lifetime techniques.

For clarity it should be stressed that the N_{crit} criterion only accounts for trapping effects arising from the dominating recombination center itself, termed *internal trapping*. However, trapping effects may also arise from

centers which are present in addition to the dominating recombination center and mainly act as trapping centers, this effect being distinguished by the appellation *external trapping*. In spite of an identical physical background, there is a difference between the two types of trapping effect which is important from a practical point of view [28]. While the internal trapping effect leads to hidden distortions of lifetime curves as shown in [3], the external trapping effect causes characteristic distortions of the lifetime curves which may easily be detected in the experiment, as shown in [29, 30]. As a consequence, lifetime data which are affected by internal trapping – which may be controlled only by using the N_{crit} criterion – have to be discarded [3] while those data affected by external trapping – which is detected from the characteristic distortions – may be subjected to an analytical correction [30] which allows the trapping effect to be eliminated. Since external trapping is often observed, its impact on the lifetime data and the possibilities for its elimination will be discussed in more detail in Sects. 3.3.1A and 3.5.2. Internal trapping, on the contrary, is of minor importance at least for the investigated contaminants.

D Strengthening of the standard SRH model and outlook

After the successful verification of the validity of the standard SRH model for the investigations of the present work, it should finally be stressed that expression (1.45) for the SRH lifetime includes the general dependence of SRH recombination on injection level, doping concentration, defect parameters, and temperature. The impact of these variables on the recombination activity of defect centers and on the characteristic shapes of injection- and temperature-dependent SRH lifetime curves will be investigated in detail in Sect. 3.2.

Moreover, it should be emphasized again that the SRH model results from purely statistical considerations. The fact that the microscopic aspects of recombination are completely left out of consideration within the derivation, ensures the general validity of the SRH model in describing recombination through defects. The only quantities in the SRH model which are influenced by the carrier capture processes involved in the recombination process are the capture cross-sections σ_n and σ_p . As will be shown in Sect. 3.5.1, their temperature dependence reflects a characteristic feature of the physical mechanism of carrier capture. To assess the suitability of the $\sigma(T)$ -dependence for an identification of the underlying capture mechanism Sect. 3.5.1 contains a comparison of the important capture mechanisms, which may be divided in terms of the energy dissipation process into radiative, phonon-assisted and Auger capture processes.

1.4.4 Surface recombination through defects

The surfaces or interfaces of a silicon substrate represent an abrupt discontinuity in the crystal structure, which results in a large number of partially bonded silicon atoms. Like any perturbation of periodicity, these dangling bonds give rise to a great density of recombination-active defect levels, located in the band gap near the semiconductor surface.

A Extended SRH formalism

Evidently, surface recombination is a special case of SRH recombination. Unlike bulk SRH centers, however, interface states do not normally occupy a single energy level, but are continuously distributed throughout the band gap. Thus, the interface trap density $D_{it}(E_t)$ and the capture cross-sections $\sigma_n(E_t)$ and $\sigma_p(E_t)$ are energy-dependent quantities. This has to be taken into account in an extended SRH formalism. While the SRH recombination rate of the individual interface traps is given by Eq. (1.44), the overall surface recombination rate U_s is given by integrating this expression over the entire band gap, using the interface trap density $D_{it}(E_t)$ as weighting function:

$$U_s = \left(n_s p_s - n_i^2 \right) \times \int_{E_V}^{E_C} \frac{v_{th} D_{it}(E_t) dE_t}{[n_s + n_i(E_t)] \sigma_p^{-1}(E_t) + [p_s + p_i(E_t)] \sigma_n^{-1}(E_t)} \quad (1.48)$$

Here, n_s and p_s are the electron and hole density at the surface and n_i and p_i the SRH densities given in Eq. (1.43). The calculation of the surface recombination rate U_s requires on the one hand an experimental determination of the surface parameters $D_{it}(E_t)$, $\sigma_n(E_t)$ and $\sigma_p(E_t)$ with their energy dependence and on the other hand a determination of the surface concentration n_s and p_s . In general the latter has to be performed numerically using an algorithm proposed by Girisch et al. [31], as an analytical determination of n_s and p_s fails due to a bending of the energy bands near the semiconductor surfaces, which is induced, e.g., by fixed or mobile charges in dielectric surface layers such as SiO_2 or SiN_x .

In contrast to the bulk recombination rate U_{SRH} in Eq. (1.44), the surface recombination rate U_s is a rate per unit area instead of per unit volume. This is why the definition of a surface lifetime according to Eq. (1.29) makes no sense. Alternatively, a new quantity called *surface recombination velocity* S (*SRV*) has to be defined:

$$S \equiv \frac{U_s}{\Delta n} \quad (1.49)$$

As the SRV is related to the fundamental properties of the surface defects through Eqs. (1.48) and (1.49), it is a direct measure of the recombination activity of the semiconductor surface and thus allows the quality of a surface passivation to be assessed. Illustrating how fast the carriers diffuse into the surface to recombine there, the SRV cannot exceed $S = 10^7 \text{ cm/s}$ as the thermal velocity of the carriers imposes an upper bound.

While the calculation of the doping and injection dependence of the SRV in general requires the Girisch algorithm [31], an analytical expression can only be found in the special case of a “flat band”. As the excess carrier densities at the surface are then given by $\Delta n_s = n_s - n_{s0} = p_s - p_{s0} = \Delta p_s$, the expression for U_s in Eq. (1.48) simplifies analogously to Eq. (1.45) and results by virtue of Eq. (1.49) in the formula:

$$\begin{aligned} S(\Delta n_s, n_0, p_0) &\equiv \frac{U_s(\Delta n_s, n_0, p_0)}{\Delta n_s} \\ &= \int_{E_V}^{E_C} \frac{(n_0 + p_0 + \Delta n_s) v_{th} D_{it}}{[n_0 + n_1 + \Delta n_s] \sigma_p^{-1} + [p_0 + p_1 + \Delta n_s] \sigma_n^{-1}} dE \end{aligned} \quad (1.50)$$

Because of the large number of energy-dependent variables, it is possible for the SRV to decrease, increase or remain constant as the injection level increases. The injection dependence of the SRV has been discussed in detail by Aberle [32]. A detailed discussion of the injection and doping dependence of the SRV, exemplified by an SiO_2 passivation, may also be found in [16, pp. 57–58].

B Fundamental mechanisms for surface passivation

From the formal relationship between the surface recombination rate and the surface properties given in Eq. (1.48), it can be concluded that there are two fundamental mechanisms for reducing the surface recombination rate at the semiconductor surfaces, i.e., for surface passivation:

1. Optimization of the interface properties. This involves a reduction of the interface trap density $D_{it}(E_t)$ in particular. By the use of an appropriate dielectric surface layer such as a thermally grown silicon oxide layer (SiO_2 , at 1050°C) or a plasma-deposited silicon nitride layer (SiN_x , at 350°C), many of the dangling silicon bonds are passivated with oxygen or nitrogen atoms and hydrogen atoms, which reduces $D_{it}(E_t)$ by several orders of magnitude. Each modification of the interface directly modifies the recombination-active interface states, which generally implies a change in the characteristic defect properties. It follows from Eq. (1.48) that any reduction of the capture cross-sections σ_n and σ_p results in a further reduction of the surface recombination rate and thus reduces the SRV.

2. Reduction of the surface concentrations of electrons or holes. This is a completely different approach to reduce the surface recombination rate. As both carrier types are involved in the recombination process, the highest recombination rates are achieved if electrons and holes are present at the surfaces in a ratio of $n_s/p_s \approx \sigma_p/\sigma_n$. Reducing the surface concentration of one of the two carrier types – typically that of the minority carriers – therefore results in a significant reduction of the surface recombination rate. Technologically this may be achieved in two different ways:

- *Installation of a Back Surface Field (BSF).* The incorporation of an additional doping profile in the form of a high-low-junction (n^+n or p^+p) repels the minority carriers from the surfaces. This structure is used in high-efficiency solar cells for back surface passivation.
- *Field-effect passivation.* Charges in an overlying dielectric layer establish an electrical field near the surface (band bending) which may either repel minority carriers (negative charges would repel free electrons in a p -type wafer) or invert the surface in extreme cases (large amounts of positive charges would invert the surface in a p -type wafer). These charges may either be incorporated as fixed charges in the dielectric layer or additionally deposited by means of a corona charging of the dielectric layer.

In practice, the methods for reducing the surface recombination in actual devices are based to some extent on both of these mechanisms. For a thermally grown SiO_2 layer [33] and a plasma-deposited SiN_x layer [34] the passivating properties result from both an effective reduction in the density of the interface states and a field effect passivation due to fixed positive charges within the dielectric layers. In this work a passivation by means of dielectric silicon nitride layers has been chosen as a standard. Its technological preparation and electrical characterization will be detailed in Sect. 4.2.2.

1.5 Effective lifetime and the separation of bulk lifetime

The four recombination mechanisms discussed in the previous section may occur simultaneously in a given sample. As already mentioned in Sect. 1.3, for independent processes the overall recombination rate is just the sum of the individual recombination rates, resulting in an effective lifetime τ_{eff} given by

$$\frac{1}{\tau_{\text{eff}}} = \left(\frac{1}{\tau_{\text{SRH}}} + \frac{1}{\tau_{\text{CE-Auger}}} + \frac{1}{\tau_{\text{rad}}} \right) + \frac{1}{\tau_{\text{surface}}} = \frac{1}{\tau_{\text{bulk}}} + \frac{1}{\tau_{\text{surface}}} \quad (1.51)$$

While the relative importance of the three bulk recombination channels has already been discussed in Sect. 1.4.2C and will be further discussed in Sect. 3.3.1B from a spectroscopic point of view, the present section focuses on the impact of surface recombination on the effective carrier lifetime. This is an important issue, as the lifetime spectroscopic investigations presented here aim at characterizing bulk defects, which makes an accurate determination of bulk recombination properties mandatory. This requires either a separation of bulk and surface recombination or at least a criterion to quantify the S impact for arbitrary parameter constellations.

A Approximate equations for the surface impact and its range of validity

In the limiting cases of low and high surface recombination rates, the general theory of recombination dynamics allows simple analytical expressions to be derived for the surface lifetime $\tau_{surface}$ in Eq. (1.51), and these make a direct assessment of the S impact on the effective lifetime τ_{eff} possible (for the derivation see [16, pp.64–71]). In the following these expressions are discussed for a test structure with identically passivated wafer surfaces ($S_1=S_2=S$), as this structure has been used throughout this work for the lifetime measurements.

1. For sufficiently low S values, $\tau_{surface}$ in Eq. (1.51) may be expressed as [35]

$$\frac{1}{\tau_{eff}} = \frac{1}{\tau_{bulk}} + \frac{2S}{W} \quad \text{for} \quad \frac{SW}{D_n} < \frac{1}{4} \quad (1.52)$$

For well passivated surfaces, the effective lifetime thus only depends on the recombination properties in the bulk and at the surfaces and not on the carrier diffusion towards the surfaces. Sproul showed in a detailed analysis [35] that the approximate τ_{eff} solution (1.52) is valid within 4 % over the given range of validity. Thus, for a wafer thickness $W=300\text{ }\mu\text{m}$ and a diffusion constant $D_n=30\text{ cm}^2/\text{s}$, Eq. (1.52) is valid with sufficient accuracy as long as $S<250\text{ cm/s}$.

2. For high S values, $\tau_{surface}$ in Eq. (1.51) is found to be given by

$$\frac{1}{\tau_{eff}} = \frac{1}{\tau_{bulk}} + D_n \left(\frac{\pi}{W} \right)^2 \quad \text{for} \quad \frac{SW}{D_n} > 100 \quad (1.53)$$

For badly passivated surfaces, the effective lifetime is determined by recombination in the bulk and the carrier diffusion towards the surfaces, but no longer depends on the recombination rate at the surfaces, as S is so large that all carriers reaching the surface immediately recombine.

Over the given range of validity the approximate τ_{eff} solution (1.53) is again valid to within 4 % [35]. Thus, for $W=300 \mu\text{m}$ and $D_n=30 \text{ cm}^2/\text{s}$, Eq. (1.52) is valid with sufficient accuracy if $S>10^5 \text{ cm/s}$.

3. Grivickas et al. [36] proposed the combination of these two approximate expressions for τ_{surface} as an approximation to the exact τ_{eff} solution in the whole parameter plane set up by the three relevant parameters S , W and D_n :

$$\frac{1}{\tau_{\text{eff}}} = \frac{1}{\tau_{\text{bulk}}} + \left(\frac{W}{2S} + \frac{1}{D_n} \left(\frac{W}{\pi} \right)^2 \right)^{-1} \quad (1.54)$$

The detailed analysis shows that this approximate τ_{eff} solution deviates less than 5 % from the exact τ_{eff} solution for arbitrary constellations of S , W and D [35].

B Determination of the bulk lifetime

As will be shown in Sect. 4.2.2, the quality of the SiN surface passivation used in the present work is high enough for Eq. (1.52) to be valid. This relatively simple expression implies an elegant technique to separate τ_{bulk} and S . Measuring τ_{eff} on a set of samples with different wafer thickness W and plotting the data in a $1/\tau_{\text{eff}}$ versus $1/W$ diagram, a straight line is obtained, whose slope equals $2S$ and whose axis intersection equals $1/\tau_{\text{bulk}}$. However, in practice, the errors of the τ_{bulk} determination are relatively high due to the extrapolation to infinite wafer thickness, which leads to a strong enhancement of small measurement errors. Thus being less suitable for τ_{bulk} determinations, the thickness-variation technique nevertheless allows an accurate S determination and will be applied in Sect. 4.2.2 to characterize the surface passivation quality of the SiN layers.

Once the quality of the surface passivation is known, Eq. (1.52) allows the true bulk lifetime to be extracted from the measured effective lifetime, making use of the fact that for the same surface roughness the surface passivation quality only depends on the doping type and the doping concentration, which allows the determined S values to be transferred directly to corresponding wafers.

However, the simplest way to determine bulk lifetime is to reduce the surface recombination to such an extent that the measured effective lifetime, within experimental error, only reflects contributions from the bulk, so that τ_{eff} can be directly identified with τ_{bulk} . It is evident that such an identification implies an inherent systematic error, whose magnitude sensitively depends on the constellation of the parameters τ_{bulk} , S and W .

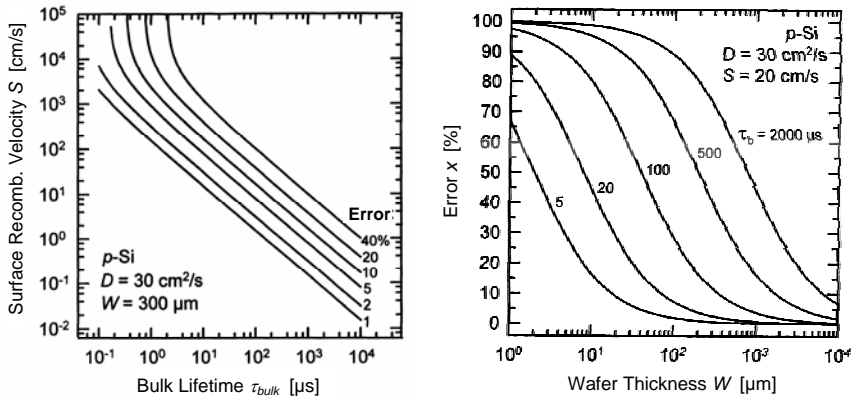


Fig. 1.15. (a) Relationship between the surface recombination velocity S and the bulk lifetime τ_{bulk} for a systematic error between 1 % and 40 %. The $p\text{-Si}$ wafer is $300 \mu\text{m}$ thick and has a diffusion constant of $30 \text{ cm}^2/\text{s}$. From [37] (b) Dependence of the systematic error x on the wafer thickness W for bulk lifetimes between 5 and $2000 \mu\text{s}$. The $p\text{-Si}$ wafer has an SRV of 20 cm/s on both surfaces and a diffusion constant of $30 \text{ cm}^2/\text{s}$. From [37]

This has been investigated by Schmidt et al. [37] and the simulation results are displayed in Fig. 1.15. To ensure accurate results over the whole parameter range, the simulations have been performed numerically using the general transcendental equation for τ_{eff} [37]. According to its significance, the percentage error is defined via the following equation:

$$\tau_{eff} / \tau_{bulk} =: 1 - x / 100 \quad (1.55)$$

Figure 1.15a shows which S values are required for a wafer with a given bulk lifetime so that τ_{eff} approaches τ_{bulk} with a certain error x . As expected, both an increase in the SRV and an increase in the bulk lifetime – due to the increased carrier diffusion length – lead to an increased influence of the surface recombination and consequently to an increase in the deviation x between τ_{eff} and τ_{bulk} . Figure 1.15b shows the strong impact of the wafer thickness W . For a fixed SRV of 20 cm/s , the error x is shown as a function of the wafer thickness for different bulk lifetimes τ_{bulk} . As expected, a decrease in the wafer thickness leads to an increase in the deviation x between τ_{eff} and τ_{bulk} , which reflects the fact that the surface impact increases with decreasing wafer thickness. In the case of a known SRV with sufficiently low S values, Eqs. (1.52) and (1.55) lead to a condition for the τ_{eff}/W ratio, for which the deviation between τ_{bulk} and τ_{eff} falls below x %:

$$\tau_{eff} / W < x / (200 S) \quad (1.56)$$

Let us assume an S value of 10 cm/s, which indeed reflects an upper bound for the SiN passivation used in the present work (see Sect. 4.2.2). If the wafer thickness ranges between 300 and 600 μm , then the effective lifetime must not exceed an upper bound of 150 to 300 μs to ensure that the deviation between τ_{eff} and τ_{bulk} remains below 10 %, which seems to be a tolerable error.

As for the metal-contaminated samples investigated in Chap. 4, the wafer thickness varies between 400–600 μm and the effective room-temperature lifetime under LLI conditions between 4–20 μs , it is evident that the measured effective lifetime can be directly identified with the bulk lifetime. Taking into account the strong temperature dependence of carrier lifetime, the impact of temperature on the accuracy of this identification will be discussed in Sect. 4.2.5C. For the standard Cz silicon samples investigated in Chap. 5, the variations of wafer thickness (100–600 μm) and effective lifetime (1–2000 μs) go beyond the parameter ranges which ensure that a 10 % error is not exceeded. Although an accurate τ_{bulk} determination would require an S correction of the measured τ_{eff} values, it will be shown that the special properties of the Cz defect allow a measurement procedure which completely eliminates the impact of surface recombination from the measured τ_{eff} data.

1.6 Chapter summary

As a basis for the following chapters, Chap. 1 introduced some fundamental concepts related on the one hand to fundamental semiconductor properties and on the other hand to the recombination lifetime, which represents the key quantity of lifetime spectroscopy.

Since the modeling of the temperature-dependent carrier lifetime will be shown in Chap. 3 to depend crucially on the exact concentrations of free carriers, their temperature dependence has been investigated in detail, considering the effects of freeze-out and intrinsic conduction and taking into account advanced temperature models for the effective densities of states as well as the temperature dependence of the energy band gap.

To ensure an accurate interpretation of the recombination lifetime, the principal recombination mechanisms in silicon have been discussed. These include the intrinsic bulk processes of radiative and Auger recombination and the extrinsic processes of recombination via defects in the bulk and at the surfaces. Taking into account the Coulomb enhancement of Auger recombination, this channel has been identified as the dominant intrinsic recombination channel over most of the parameter range. With respect to

extrinsic recombination, the fundamental concept of standard Shockley-Read-Hall (SRH) theory has been outlined, proving its validity for the investigations to be presented. The general expression for SRH lifetime deduced here represents the starting point for the detailed theoretical investigations of the potential of lifetime spectroscopy in Chap. 3. As lifetime spectroscopy aims to characterize bulk defects, an accurate determination of the bulk SRH lifetime is mandatory. The fundamental problem is that in the experiment only an effective lifetime is accessible, which reflects all the different recombination channels to a certain extent. Thus, it is especially the impact of surface recombination on the effective carrier lifetime that has been investigated, focusing on techniques to separate surface and bulk recombination and deriving a general criterion to estimate the surface passivation quality required for a direct identification of the measured effective lifetime with the bulk lifetime.

References

- [1] W. Shockley and W.T.J. Read, *Statistics of the recombinations of holes and electrons*, Phys. Rev. **87** (5), 835–42 (1952).
- [2] R.N. Hall, *Electron-hole recombination in germanium*, Phys. Rev. **87**, 387 (1952).
- [3] D. Macdonald and A. Cuevas, *Validity of simplified Shockley-Read-Hall statistics for modeling carrier lifetimes in crystalline silicon*, Phys. Rev. B (Condensed Matter and Materials Physics) **67** (7), 75203–1–7 (2003).
- [4] S.M. Sze, *Physics of Semiconductor Devices*, 2nd edn. (John Wiley & Sons, New York, 1981).
- [5] A.B. Sproul and M.A. Green, *Improved value for the silicon intrinsic carrier concentration from 275 to 375 K*, J. Appl. Phys. **70** (2), 846–54 (1991).
- [6] D.A. Clugston and P.A. Basore, *PCID version 5: 32-bit solar cell modeling on personal computers*, Proc. 26th IEEE PVSC (Anaheim, California, USA, 1997), pp. 207–10.
- [7] N.W. Ashcroft and N.D. Mermin, *Solid State Physics*, International Edition (Saunders College Publishing, New York, 1976).
- [8] M.A. Green, *Intrinsic concentration, effective densities of states, and effective mass in silicon*, J. Appl. Phys. **67** (6), 2944–54 (1990).
- [9] M.A. Green, *Silicon Solar Cells: Advanced Principles and Practice* (Center for Photovoltaic Devices and Systems, University of New South Wales, Sydney, 1995).
- [10] ISE Integrated Systems Engineering AG, *DESSIS Manual 7.0* (Zürich, 2001).
- [11] R.J. Nelson and R.G. Sobers, *Minority-carrier lifetime and internal quantum efficiency of surface-free GaAs*, J. Appl. Phys. **49**, 577 (1978).

- [12] A. Hangleiter and R. Häcker, *Enhancement of band-to-band Auger recombination by electron-hole correlations*, Phys. Rev. Lett. **65** (2), 215–18 (1990).
- [13] P.T. Landsberg, *Recombination in Semiconductors* (Cambridge University Press, 1991).
- [14] A.R. Beatti and P.T. Landsberg, *Auger effect in semiconductors*, Proc. Royal Soc. A **429**, 16 (1958).
- [15] J. Dziewior and W. Schmid, *Auger coefficients for highly doped and highly excited silicon*, Appl. Phys. Lett. **31** (5), 346–8 (1977).
- [16] S. Rein, *Untersuchung der Degradation der Ladungsträgerlebensdauer in Cz-Silizium*, Diplomarbeit, Albert-Ludwigs-Universität Freiburg (1998).
- [17] M.J. Kerr, *Surface, emitter and bulk recombination in silicon and development of silicon nitride passivated solar cells*, PhD thesis, Australien National University (2002).
- [18] P. Jonsson, H. Bleichner, M. Isberg, and E. Nordlander, *The ambipolar Auger coefficient: Measured temperature dependence in electron irradiated and highly injected n-type silicon*, J. Appl. Phys. **81** (5), 2256–62 (1997).
- [19] A. Hangleiter and R. Häcker, *Excitonic band-to-band Auger recombination in silicon*, Proc. 18th International Conf. on the Physics of Semiconductors (1987), p. 907.
- [20] R. Häcker and A. Hangleiter, *Intrinsic upper limits of the carrier lifetime in silicon*, J. Appl. Phys. **75**, 7570 (1994).
- [21] P.P. Altermatt, J. Schmidt, G. Heiser, and A.G. Aberle, *Assessment and parameterization of Coulomb-enhanced Auger recombination coefficients in lowly injected crystalline silicon*, J. Appl. Phys. **82** (10), 4938–44 (1997).
- [22] R.A. Sinton and R.M. Swanson, *Recombination in highly injected silicon*, IEEE Trans. Electron Devices **34** (6), 1380 (1987).
- [23] P.A. Basore and D.A. Clugston, *PC1D version 4 for Windows: from analysis to design*, Proc. 25th IEEE PVSC (Washington D C, 1996), pp. 377–81.
- [24] S.W. Glunz, D. Biro, S. Rein, and W. Warta, *Field-effect passivation of the SiO₂–Si interface*, J. Appl. Phys. **86** (1), 683–91 (1999).
- [25] P.P. Altermatt, J. Schmidt, M. Kerr, G. Heiser, et al., *Exciton-enhanced Auger recombination in crystalline silicon under intermediate and high injection conditions*, Proc. 16th EC PVSEC (Glasgow, UK, 2000), pp. 243–6.
- [26] D.K. Schroder, *Semiconductor Material and Device Characterization* (John Wiley & Sons, New York, 1990).
- [27] A. Schlachetzki, *Halbleiter-Elektronik* (Teubner, Stuttgart, 1990).
- [28] D. Macdonald, *Classification of trapping effects*, personal communication (2003).
- [29] D. Macdonald and A. Cuevas, *Trapping of minority carriers in multicrystalline silicon*, Appl. Phys. Lett. **74** (12), 1710–12 (1999).
- [30] D. Macdonald, R.A. Sinton, and A. Cuevas, *On the use of a bias-light correction for trapping effects in photoconductance-based lifetime measurements of silicon*, J. Appl. Phys. **89** (5), 2772–8 (2001).

- [31] R.B.M. Girisch, R.P. Mertens, and R.F. De Keersmaecker, *Determination of Si–SiO₂ interface recombination parameters using a gate-controlled point-junction diode under illumination*, IEEE Trans. Electron Devices **35** (2), 203–22 (1988).
- [32] A.G. Aberle, *Crystalline silicon solar cells – Advanced surface passivation and analysis* (University of New South Wales, Sydney, 1999).
- [33] A.G. Aberle, S. Glunz, and W. Warta, *Impact of illumination level and oxide parameters on Shockley-Read-Hall recombination at the Si–SiO₂ interface*, J. Appl. Phys. **71** (9), 4422–31 (1992).
- [34] A.G. Aberle, *Overview on SiN surface passivation of crystalline silicon solar cells*, Sol. Ener. Mater. Sol. Cells **65**, 239–48 (2001).
- [35] A.B. Sproul, *Dimensionless solution of the equation describing the effect of surface recombination on carrier decay in semiconductors*, J. Appl. Phys. **76** (5), 2851–4 (1994).
- [36] V. Grivickas, D. Noreika, and J.A. Tellesfen, *Surface and Auger recombination in silicon wafers of high carrier density*, Lithuanian Physics Journal **29** (5), 48–53 (1989).
- [37] J. Schmidt and A.G. Aberle, *Accurate method for the determination of bulk minority-carrier lifetimes of mono- and multicrystalline silicon wafers*, J. Appl. Phys. **81** (9), 6186–99 (1997).

2. Lifetime measurement techniques

2.1 Introduction

As an accurate determination of recombination lifetime is a fundamental prerequisite for lifetime spectroscopy, Chap. 2 discusses the two techniques used in the present work for measuring the effective carrier lifetime. The measurement of carrier lifetimes is based on the recombination dynamics of excess carriers which are normally generated optically. The different techniques may be classified in terms of the time dependence of the illumination and the technique used to measure the excess carrier density.

Concerning the time dependence of the illumination, three operating regimes can be distinguished. (a) The first regime involves a sharp pulse of illumination that is rapidly turned off and a subsequent determination of the excess carrier density without illumination. This is the traditional transient technique, used especially to measure high carrier lifetimes. (b) The second regime is the steady-state illumination, which is of minor importance due to the problem that the samples will quickly suffer from heating and a changing lifetime in true steady state. (c) Such effects are avoided in the third regime, where the illumination intensity is slowly reduced to zero over several milliseconds, the decay being long enough to ensure that the sample remains in steady state in terms of the recombination processes. This is the basis of the *quasi-steady-state method* first introduced by Sinton and Cuevas [1]. The major advantage of a slowly decaying illumination is that a large range of operating points can be conveniently explored. Note that the covered range of carrier densities is typically about one order of magnitude.

Obviously the first two regimes are special cases of the third, which therefore represents the general case. The detailed analysis of the recombination dynamics in all three cases is based on the continuity equation for the excess minority carriers:

$$\frac{\partial \Delta n}{\partial t} = G_{bulk}(t, x) - U_{bulk}(t, x) + \frac{1}{q} \frac{dJ_n}{dx} \quad (2.1)$$

where G_{bulk} and U_{bulk} are the photogeneration rate and the recombination rate in the bulk, Δn the excess minority carrier density and J_n the electron current density. The transport term reduces to surface recombination terms when Eq. (2.1) is integrated over the sample width because the sample is in open-circuit conditions. A generalized analysis procedure has been proposed by Nagel et al. [2]. In order to define an effective lifetime regardless of the decay time of the illumination source, they combined the bulk and surface recombination rates into an effective recombination rate U_{eff} and found, considering all the terms in Eq. (2.1), the following general expression for the effective carrier lifetime:

$$\tau_{eff} = \frac{\Delta n_{av}}{G_{av}(t) - \frac{\partial \Delta n_{av}(t)}{\partial t}} \quad (\text{general case}), \quad (2.2)$$

where n_{av} is the average excess carrier density and G_{av} the average generation rate, both calculated over the whole wafer thickness. In the extreme operating regimes, simplified τ_{eff} expressions follow directly from Eq. (2.2). In the first regime with $G \equiv 0$:

$$\tau_{eff} = \frac{\Delta n_{av}}{\frac{\partial \Delta n_{av}(t)}{\partial t}} \quad (\text{quasi-transient case}), \quad (2.3)$$

which is only valid when carrier lifetime is significantly higher than the decay time of the illumination source. In the second regime with $\partial \Delta n / \partial t \equiv 0$:

$$\tau_{eff} = \frac{\Delta n_{av}}{G_{av}(t)} \quad (\text{quasi-steady-state case}), \quad (2.4)$$

which is only valid when the carrier lifetime is significantly lower than the decay time of the illumination source.

Thus, to determine the effective lifetime it is necessary to measure the time dependence of the excess carrier density and the generation rate within the test samples (except for the transient case). The excess carrier density can be directly monitored via the photoconductance, which can be measured inductively or by means of the reflectivity of microwaves. The fundamental differences arising from these detection techniques for the lifetime measurements will be discussed in the following two sections, being dedicated to the inductively coupled *quasi-steady-state photoconductance technique* (QSSPC) and the *microwave-detected photoconductance decay technique* (MW-PCD), respectively.

A common feature of both techniques is that they are non-contacting, which makes them ideally suited for lifetime spectroscopic purposes, as partially finished devices that are free of metal contacts can be investigated, including the starting material itself, as in the present work.

2.2 Quasi-steady-state photoconductance technique (QSSPC)

The experimental apparatus used in the present work for QSSPC measurements was fabricated by Sinton Consulting and is shown in Fig. 2.1. A photographic flash lamp is used as the generation source. The sample is inductively coupled by a coil to a radio-frequency bridge, which senses changes in the permeability of the sample and therefore its conductance. A reference solar cell and an oscilloscope are used to determine the time dependence of both the excess photoconductance of the test sample $\Delta\sigma(t)$ and its illumination $I(t)$ by using appropriate calibration functions. The average excess carrier density $\Delta n_{av} = \Delta p_{av}$ in the test sample can be determined via

$$\Delta n_{av}(t) = \frac{\Delta\sigma(t)}{q(\mu_n + \mu_p)W} \quad (2.5)$$

where W is the sample thickness and μ_n and μ_p are the electron and hole mobilities. As μ_n and μ_p are themselves functions of the carrier density, the determination of Δn_{av} requires an iterative procedure on the basis of a carrier-density-dependent mobility model [3].

The illumination intensity I_{av} , measured from the calibrated reference solar cell and normally quoted in suns ($1 \text{ sun} = 1000 \text{ W/m}^2$), is a measure of the number of photons incident on the sample surface. As any real sample will only absorb a fraction f_{abs} of these available photons, the remainder being lost by reflection and transmission, the generation rate within the sample can be determined as

$$G_{av}(t) = \frac{I_{av}(t)f_{abs}N_{ph}^{1sun}}{W} \quad (2.6)$$

where N_{ph}^{1sun} is the flux of photons in solar light with an irradiance of 1 sun, which generate electron-hole pairs in the sample. As the required quantities in the general Eq. (2.2) can thus be experimentally measured, a determination of the effective lifetime is possible.

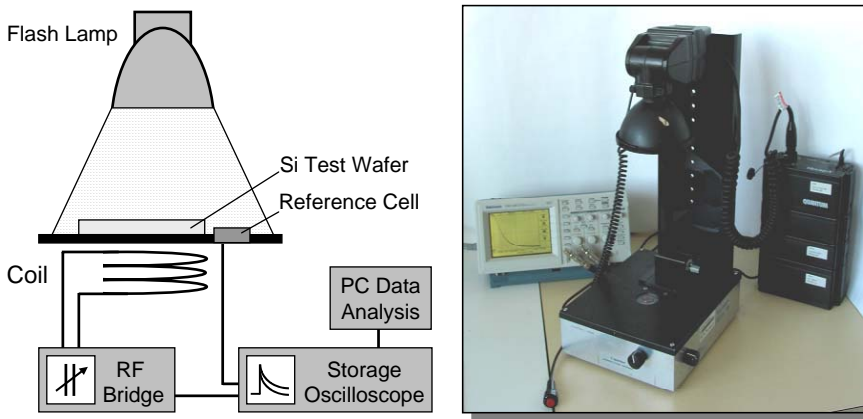


Fig. 2.1. QSSPC setup used to measure injection-dependent carrier lifetimes. *Left:* Schematic diagram of the inductively-coupled photoconductance apparatus. *Right:* WCT-100 apparatus from Sinton Consulting used in the present work.

As the decay time of the flash lamp may be varied by two orders of magnitude, the QSSPC setup allows measurements in the *transient mode* (PCD) and in the *quasi-steady-state mode* (QSSPC). The typical PCD and QSSPC traces are displayed in Fig. 2.2a and b, respectively. In conjunction with the simplified analyses given in Eqs. (2.3) and (2.4), both modes are restricted to certain lifetime ranges.¹ However, using the QSSPC mode in conjunction with the generalized analysis given in Eq. (2.2), it constitutes an excellent method for measuring a large range of carrier lifetimes (from $0.1\ \mu\text{s}$ to several ms) over a large range of carrier densities (10^{12} – $10^{17}\ \text{cm}^{-3}$, depending on the lifetime level). Thus, this technique is ideally suited for injection-dependent lifetime measurements and has been used throughout this work. Details about the calibration of the coil and the reference solar cell may be found in [4]. A fundamental advantage of inductively-coupled photoconductance measurements will be discussed in Sect. 2.3.1 in comparison with the microwave-detected measurements.

¹ Being well suited for high lifetimes, the PCD mode is less accurate for low lifetimes ($<200\ \mu\text{s}$) due to the poor cutoff time of the flash lamp. The QSSPC mode, on the contrary, is well suited for low lifetimes, but becomes increasingly invalid for high lifetimes ($>200\ \mu\text{s}$), as the steady-state assumption starts to break down.

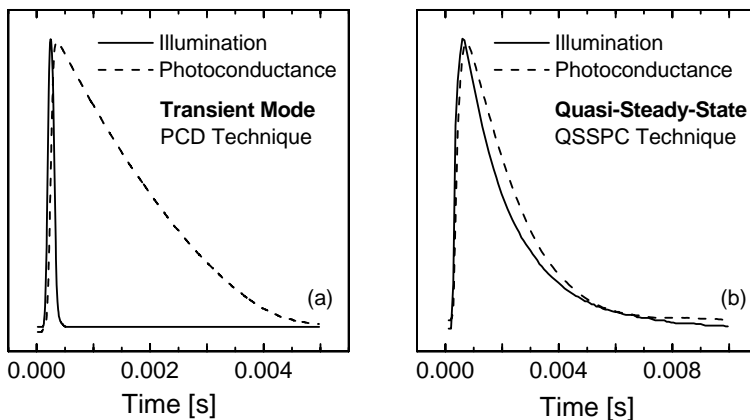


Fig. 2.2. Typical traces measured by means of the inductively-coupled QSSPC system. (a) Traces in the transient mode showing the sharp illumination peak (*solid line*) and the ensuing photoconductance decay (*dashed line*). (b) Traces in the quasi-steady-state mode, showing the uniform decay of both signals.

2.3 Microwave-detected photoconductance decay technique (MW-PCD)

The MW-PCD technique is a pure transient technique, the effective carrier lifetime being determined from the asymptotic decay of the average excess carrier density following a pulse-like excitation. This decay is monitored via the changes in the sample photoconductance [see Eq. (2.5)] which in turn is measured via changes in its microwave reflectance.

2.3.1 Microwave reflection and associated restrictions

Since the microwave reflectance is a highly non-linear function of the free carrier density [5, 6], the MW-PCD technique is restricted to use as a small signal technique. This is no barrier to performing measurements of the low-injection lifetime. However, lifetime measurements at higher carrier densities require the use of an additional steady-state bias light to generate the desired background carrier density upon which a small-signal transient pulse is superimposed and detected by the changes in the microwave reflectance. The use of a bias light involves the problem that a *differential* effective lifetime $\partial\tau_{\text{eff}}/\partial\Delta n$ is measured [7]. To determine the *actual*

effective lifetime τ_{eff} at higher carrier densities, it is thus necessary to measure the differential effective lifetime over the whole range of lower carrier densities and then integrate the resulting data. Moreover, as the reflectivity signal does not contain any information about the absolute magnitude of the excess carrier density, the bias light has to be calibrated so that the steady-state generation rate in the sample can be calculated. Since the actual carrier density depends not only on the generation rate but also on the lifetime level itself, the integration procedure has to be performed iteratively. A detailed discussion may be found in [8, p.75].

The above discussion reveals some decisive advantages of the inductively-coupled QSSPC technique compared to the MW-PCD technique. First, the carrier injection level is directly measured and requires no device simulation. Second, the QSSPC technique is a large signal technique and as such allows the actual effective lifetime to be measured directly at any range of injection levels without integrating differential quantities. And third, it offers the practical advantage that it allows accurate lifetime measurements over large injection ranges in one quick flash, in contrast to the individual measurements at each bias-light setting necessary with MW-PCD. That is why injection-dependent lifetime measurements have been performed throughout this work by means of the QSSPC technique.

However, concerning the use of the MW-PCD technique, it has to be emphasized that under low-level injection the differential lifetime directly coincides with the actual lifetime for theoretical reasons, which are further discussed in [8, p.77]. As temperature-dependent lifetime spectroscopy operates at these injection conditions (see Sect. 3.2.4), the MW-PCD technique has been used for the temperature-dependent lifetime measurements of the present work, making use of its high sensitivity and the possibility of an easy integration of the cryostat in the measurement setup (see below). The optimum measurement conditions and the interpretation of the lifetimes obtained by means of the MW-PCD technique will be discussed in detail in Sect. 4.2.5B.

2.3.2 MW-PCD measurement setup

Figure 2.3 shows a block diagram of the MW-PCD system used at Fraunhofer ISE. As its mode of operation is discussed in detail in [9–11], it is only briefly outlined here to show some special features of the system. Generated in a phase-locked microwave oscillator, microwaves of frequency of 2.8 GHz are directed over an adjustable main attenuator to a 1:1 power splitter that divides the incident microwave power into two parts. One half of the signal goes to the microwave antenna, integrated in

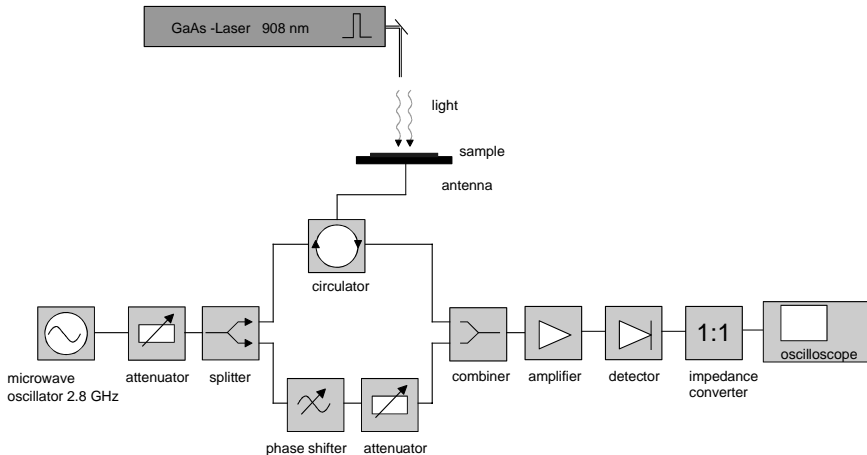


Fig. 2.3. Block diagram of the MW-PCD system used at Fraunhofer ISE. From [9]

the measurement chuck, and is thus directed at the sample, which is placed on top of the antenna. Depending on the sample conductance, the signal is reflected with varying intensity. The reflected signal is combined with the second half of the signal using a combiner. The important point is that the signal in the lower bridge branch goes to an adjustable phase shifter and an adjustable attenuator. By adjusting the phase and the amplitude in the lower bridge branch, it is possible to subtract the time-independent part of the signal coming from the sample before an amplifying step. This bridge circuit significantly increases the sensitivity of the system. The amplified signal is detected by a highly sensitive microwave detector and recorded by a storage oscilloscope. The storage oscilloscope allows subsequent PCD transients to be averaged and thus improves the signal-to-noise ratio. In the present work, 200 to 500 transients have been averaged depending on the signal quality. The recorded averaged transient is transferred to a computer and analyzed in a manually chosen time interval. The advantage of the semi-automatic analysis is that artifacts in the data can be detected, which increases the reliability significantly (for an example see Sect. 4.2.5). A characteristic transient is shown in Fig. 4.5a.

A GaAs laser diode, emitting laser pulses of 908 nm wavelength with a pulse length of 100 ns, is used as a generation source. The penetration depth in silicon amounts to 30 μm . To adjust the background injection level, the sample is illuminated with an additional bias light, whose intensity is determined by means of a calibrated cell. Using a set of gray filters the laser power coupled into the sample can be attenuated to such an extent that the small-signal condition is fulfilled at each bias position. Due to the

high detection sensitivity of the unit and the high digital resolution of the oscilloscope, the PCD decay can be measured across several orders of magnitude.

2.3.3 The cryostat

To enable temperature-dependent lifetime measurements, a liquid-nitrogen-cooled cryostat has been integrated into the existing MW-PCD setup. The special optical and electromagnetic requirements of the MW-PCD apparatus required a special design for the head of the cryostat. A schematic diagram of the cryostat is shown in Fig. 2.4. As the generation light (laser pulse and bias light) is coupled in from the top, a special window (Suprasil 300) with a high transmission coefficient in the wavelength range from 200 to 2000 nm has been used on the top side of the cryostat. The microwave itself is coupled in from the bottom side through a second window whose permeability to the microwave is uncritical. In order to ensure the high detection sensitivity of the system, the sample has been placed close above the microwave at a distance of 6 mm from the bottom of the cryostat. For good thermal contact between sample and heat exchanger, the sample is mounted on a sapphire window, being mechanically pressed against the window by a metal frame. The sapphire window is permeable to the generation light and shows a high heat conductivity especially in the low-temperature range.

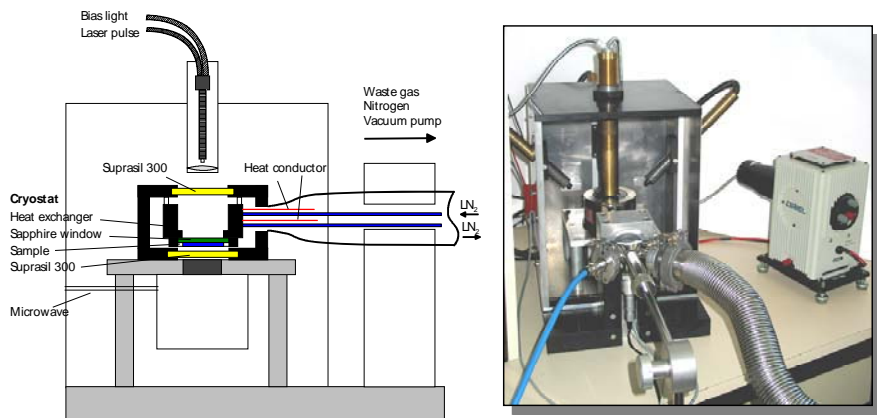


Fig. 2.4. *Left:* Schematic diagram of the cryostat and its integration in the existing MW-PCD apparatus. *Right:* MW-PCD setup with integrated cryostat used to measure temperature-dependent carrier lifetimes.

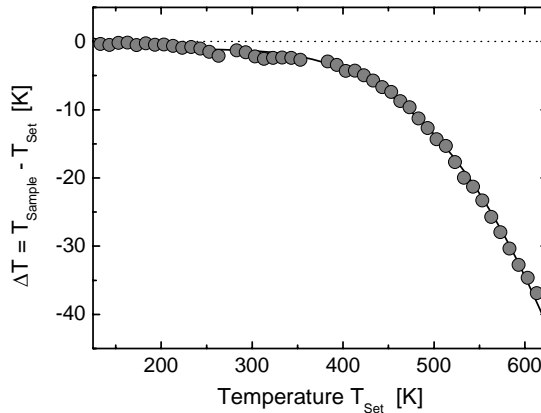


Fig. 2.5. Temperature difference between heat exchanger (set temperature) and sample. The increase in the temperature difference with increasing set temperature reflects the decreasing heat conductivity of the sapphire window the sample is mounted on and brings out the importance of measuring the temperature directly on the sample surface.

The accessible temperature range of the cryostat is adjustable from 77–650 K, a PT100 sensor integrated in the block of the heat exchanger controlling the temperature. In order to avoid the sample icing up and to ensure stable temperatures over the whole temperature range, an insulating vacuum of $p < 10^{-5}$ mbar is created by a turbo molecular pump. As a careful control of the sample temperature is mandatory, an additional PT100 sensor was placed directly on the sample surface. The need for this measure can be seen directly in Fig. 2.5, showing the temperature difference between the heat exchanger (set temperature) and the sample, measured on a standard silicon sample. While the temperature difference approaches zero below 300 K, it increases monotonically above 300 K reaching a maximum value of around 40 K at a set temperature of 600 K. This increasing temperature difference directly reflects the decreasing heat conductivity of the sapphire window with increasing temperature.

In order to exclude systematic measurement errors due to the ohmic resistance of the long sensor cables, the four-point method has been used to measure the sample temperature. Moreover, by averaging the sample temperature over the time interval (5–10 s) required to record the PCD transients, minimum variations of the sample temperature (<0.1 K) have been taken into account. It can be concluded that the sample temperature is determined with high accuracy.

References

- [1] R.A. Sinton and A. Cuevas, *Contactless determination of current-voltage characteristics and minority-carrier lifetimes in semiconductors from quasi-steady-state photoconductance data*, Appl. Phys. Lett. **69** (17), 2510–2 (1996).
- [2] H. Nagel, C. Berge, and A.G. Aberle, *Generalized analysis of quasi-steady-state and quasi-transient measurements of carrier lifetimes in semiconductors*, J. Appl. Phys. **86** (11), 6218–21 (1999).
- [3] F. Dannhäuser, *Die Abhängigkeit der Trägerbeweglichkeit in Silizium von der Konzentration der freien Ladungsträger (The dependence of carrier mobility in Si on the concentration of free charge carriers)*, Solid-State Electron. **15** (12), 1371–5 (1972).
- [4] R. Mühlhaupt, *Messung der Ladungsträgerlebensdauer in Silizium für die Prozessoptimierung bei der Herstellung von Solarzellen*, Diplomarbeit, Fachhochschule Furtwangen (2004).
- [5] U. Creutzburg, *Berührungslose Meßverfahren zur Bestimmung von Silizium-Materialeigenschaften für Solarzellenanwendungen*, Dissertation, Universität Bremen (1991).
- [6] M. Schöfthaler and R. Brendel, *Sensitivity and transient response of microwave reflection measurements*, J. Appl. Phys. **77** (7), 3162–73 (1995).
- [7] R. Brendel and M. Wolf, *Differential and actual surface recombination velocities*, Proc. 13th EC PVSEC (Nice, France, 1995), pp. 428–31.
- [8] S. Rein, *Untersuchung der Degradation der Ladungsträgerlebensdauer in Cz-Silizium*, Diplomarbeit, Albert-Ludwigs-Universität Freiburg (1998).
- [9] S.W. Glunz, *Ladungsträgerrekombination in Silicium und Siliciumsolarzellen*, Dissertation, Universität Freiburg (1995).
- [10] V. Henninger, *Ladungsträgerdynamik in dünnen Silicium-Epitaxieschichten*, Diplomarbeit, Albert-Ludwigs-Universität Freiburg (1995).
- [11] S.W. Glunz, J. Schumacher, W. Warta, J. Knobloch, et al., *Solar cells with mesh-structured emitter*, Progr. Photovolt. **4** (6), 415–24 (1996).

3. Theory of lifetime spectroscopy

3.1 Introduction

Although deep-level transient spectroscopy (DLTS) is accepted to be one of the most sensitive techniques to detect and analyze small concentrations of electrically active defects [1], defect concentrations below the detection limit of DLTS can still significantly affect carrier recombination lifetime. Due to this high sensitivity of carrier lifetime to electrically active defects, lifetime measurements can be used to characterize the material quality. Apart from detecting the presence of recombination-active defects, lifetime measurements allow a direct identification of impurities if the injection and temperature dependence of carrier lifetime is analyzed. The different approaches, which all rely on standard Shockley-Read-Hall theory (SRH theory), are referred to as *lifetime spectroscopy* (LS). Apart from its extraordinary sensitivity, the principal advantage of lifetime spectroscopy over traditional defect characterization techniques is that it uses the recombination process to analyze defect centers and thus gives insight into precisely those defects which are actually relevant to semiconductor devices such as solar cells and random-access memories.

A Previous work on lifetime spectroscopy

Some LS techniques have already been reported in the literature, although their spectroscopic potential has not been analyzed systematically up to now. Temperature-dependent lifetime measurements have been introduced as a spectroscopic technique by Shimura et al. [2] and Kirino et al. [3], who determined the defect energy level of different transition metals in silicon from data taken with a Laser/Microwave-DLTS system (LM-DLTS). Since 1990, *temperature-dependent lifetime spectroscopy* (TDLS) has been applied by several authors to determine the recombination properties of the well-known defects formed by iron in silicon [4-6] but also of other defects [7, 8].

Defect characterization from the injection dependence of carrier lifetime was first restricted to the measurement of the lifetime ratio under high- and low-level injection [9, 10]. As this quantity does not allow the

different defect parameters to be separated, Bleichner et al. [11] were the first to analyze the complete injection dependence of lifetime curves combining lifetime data from different techniques to cover a broad injection range. Since the spectroscopic evaluation of injection-dependent lifetime data turns out to be difficult due to an inherent ambiguity of the SRH parameterization, *injection-dependent lifetime spectroscopy* (IDLS) has been applied only by few authors up to now, the investigations being focused on the boron-oxygen complex in Czochralski silicon [12-14] and the iron-related defect centers [15-18]. In the case of unknown systems, the few attempts to avoid the ambiguity of IDLS by a simultaneous SRH analysis of a set of IDLS curves subject to a doping [14] or temperature [19] variation failed so far and only led to broad ranges for the defect parameters instead of a discrete solution.

It has to be concluded that, although lifetime spectroscopy might currently be one of the most sensitive diagnostic tools to identify impurities in semiconductors, it is not yet established as a standard technique for defect characterization, the spectroscopic potential of most LS techniques being unclear so far. However, the interest in lifetime spectroscopy is growing fast, first by the need for increasingly sensitive techniques to track ever diminishing quantities of impurities, which affect electronic devices due to the ever more stringent requirements, and second by the fact that the quasi-steady-state photoconductance technique, which has recently been developed by Sinton and Cuevas [20] and is already well established, is ideally suited to measure carrier lifetime over a broad injection range, thus facilitating the use of IDLS-based techniques.

B Chapter outline

The present chapter thus focuses on two issues: on the one hand on a detailed theoretical evaluation of the spectroscopic potential of the different LS techniques and on the other hand on the development of transparent data evaluation procedures to make the different LS techniques applicable as a diagnostic tool.

To disclose the possibilities and theoretical limitations of lifetime spectroscopy and to provide an overview of the characteristic features of the different LS techniques, Sect. 3.2 starts with a systematic analysis of standard SRH theory, on which lifetime spectroscopy is based. A detailed analysis of IDLS is presented in Sect. 3.3. On the basis of a newly developed routine for a transparent evaluation of IDLS data, the ambiguity of the SRH parameterization of a single IDLS curve is investigated in detail. This leads to well-founded guidelines concerning the extractable spectroscopic information. Moreover, the advanced IDLS analysis is

expanded to be applicable on a set of IDLS curves subject to a doping variation, which gives a deeper insight into simultaneous SRH analysis and reveals for the first time the possibilities and fundamental restrictions of the expanded N_{dop} -IDLS technique. TDLS is analyzed in Sects. 3.4 and 3.5. Since TDLS allows direct determination of the defect energy depth from a simple linear fit, in Sect. 3.4 improved techniques for a linear evaluation of TDLS data are developed and their spectroscopic accuracy is investigated under realistic conditions. Special attention is given to the resolution capability of TDLS since the presence of multiple recombination centers may hamper the spectroscopic result. Section 3.5 then investigates the spectroscopic potential of an advanced TDLS analysis which is based on the SRH modeling of the complete TDLS curve and thus involves a quantitative analysis of several superposed effects to ensure accurate modeling. To examine the possibility of an unambiguous and complete defect characterization on a single sample, Sect. 3.6 presents a further extension of lifetime spectroscopy which consists in the combination of the spectroscopic results obtained from IDLS and TDLS. On the basis of the advanced IDLS analysis from Sect. 3.3, Sect. 3.7 then investigates the spectroscopic potential of the T -IDLS technique which uses a set of IDLS curves measured at different temperatures as data base. With the chapter summary in Sect. 3.8 the different LS techniques are finally compared in terms of their spectroscopic potential.

3.2 General analysis of possibilities and restrictions

Since standard Shockley-Read-Hall (SRH) theory forms the basis of lifetime spectroscopy (LS), the theoretical investigation starts with a systematic analysis of the SRH equation, to demonstrate on the one hand the possibilities and basic restrictions of lifetime spectroscopy and to provide on the other hand an overview of the characteristic features of the different LS techniques. A fundamental discussion of the injection and temperature dependence of SRH lifetime has already been published by Bullis and Huff in 1997 within a review of problems associated with the interpretation of carrier lifetime [21]. In the present chapter – which is based on the results published in [22] – the general impact of the defect and material parameters on the injection and temperature dependence of SRH lifetime is investigated in more detail, showing on the one hand the variety of attainable curve shapes and evaluating on the other hand their suitability for a spectroscopic determination of defect parameters. Special emphasis is given to the fundamental difference between shallow and deep levels. From this the basic requirements for an unambiguous defect

characterization are deduced for the different LS methods. To keep the discussion as simple as possible, the theoretical analysis in this section is restricted to a single-level approach. The major results concerning the dependence of SRH lifetime on the material and defect parameters are summarized in five rules of general validity following the respective sections.

3.2.1 The Shockley-Read-Hall equation

A general description of the Shockley-Read-Hall theory (SRH theory) of carrier generation and recombination at a single defect level [23, 24] is provided in Sect. 1.4.3. Since this theory forms the basis of the different techniques of lifetime spectroscopy which will be discussed in the present chapter, the relevant equations should be repeated here. The derivation in Sect. 1.4.3B led to the following well-known expression for the SRH lifetime:

$$\tau_{SRH} = \frac{\tau_{n0}(p_0 + p_1 + \Delta n) + \tau_{p0}(n_0 + n_1 + \Delta n)}{p_0 + n_0 + \Delta n} \quad (3.1)$$

Here, $\Delta n = \Delta p$ is the excess carrier density, in the absence of carrier trapping,¹ while τ_{n0} and τ_{p0} are the fundamental capture time constants and n_0 and p_0 the equilibrium densities of electrons and holes, respectively. The so-called SRH densities n_1 and p_1 equal the equilibrium electron and hole densities when the Fermi energy E_F coincides with the energy level E_t of the recombination center and are thus given by

$$n_1 := N_C \exp\left(-\frac{E_C - E_t}{k_B T}\right), \quad p_1 := N_V \exp\left(-\frac{E_t - E_V}{k_B T}\right) \quad (3.2)$$

Here, N_C and N_V are the effective densities of states at the conduction band and the valence band edges, whose energy positions are given by E_C and E_V . Values for the different quantities are compiled in Table 1.1. The fundamental time constants τ_{n0} and τ_{p0} for the capture of electrons and holes into the defect state are proportional to the inverse product of the defect concentration N_t and the capture cross-sections σ_n and σ_p for electrons and holes:

¹ As discussed in Sect. 1.4.3C, standard SRH theory is only valid when the density of recombination centers N_t is small enough to avoid trapping effects, which cause distortions in the excess carrier densities. Then $\Delta n = \Delta p$ is a reasonable simplifying assumption. A criterion to control this prerequisite of SRH theory has been presented in Sect. 1.4.3C [25]. The validity of standard SRH theory for the investigations of the present work has been verified there.

$$\tau_{p0} := (N_t \sigma_p v_{th})^{-1}, \quad \tau_{n0} := (N_t \sigma_n v_{th})^{-1} \quad (3.3)$$

with $v_{th} = 1.0 \times 10^7 \text{ cm/s}$ [26] being the thermal velocity.

Before starting with the detailed analysis of the SRH equation and its spectroscopic use, some general features of the SRH equation should be pointed out giving insight into the potential and the basic restrictions of all *lifetime spectroscopic methods* (LS methods).

A Classification of the defect parameters

The characteristic capture cross-sections of a defect state and thus the corresponding capture time constants may differ by orders of magnitude. As the extent of the capture asymmetry is a characteristic feature of a defect state, we define a symmetry factor k

$$k \equiv \sigma_n / \sigma_p = \tau_{p0} / \tau_{n0} \quad (3.4)$$

that depends only on the defect structure but not on the absolute quantities N_t and $\sigma_{n,p}$ of the defect. Thus, k is a relative defect parameter like the energy level E_t . Replacing one of the two absolute quantities τ_{n0} and τ_{p0} by the symmetry factor k , the SRH lifetime in Eq. (3.1) becomes

$$\tau_{SRH} = \tau_{n0} \left[\frac{p_0 + p_1 + \Delta n}{p_0 + n_0 + \Delta n} + k \frac{n_0 + n_1 + \Delta n}{p_0 + n_0 + \Delta n} \right] \quad (3.5)$$

Equation (3.5) includes the general dependence of SRH lifetime on injection level, doping concentration, defect parameters and temperature. Taking a closer look at the dependence on the defect parameters, the advantage of introducing the symmetry factor k becomes obvious. The absolute defect parameters N_t and σ_n appear only as a product in the electron capture time constant τ_{n0} , which is a common factor for each of the terms contributing to τ_{SRH} , i.e., τ_{n0} is only a scaling factor for the SRH lifetime. That is why any variation of the absolute defect parameters only results in a vertical shift of the SRH lifetime curves but not in a change in their shapes. On the contrary, the relative defect parameters E_t and k only contribute to some of the terms contributing to τ_{SRH} and therefore have a crucial influence on the shapes of the SRH lifetime curves, which will be discussed in detail in the following sections.

The fundamental difference between the relative and the absolute defect parameters leads to a basic restriction for all LS methods. Only E_t and k can be determined exclusively from LS methods, while the determination of N_t and $\sigma_{n,p}$ requires an additional spectroscopic method to separate the two parameters. Nevertheless, the weakness in separating N_t and $\sigma_{n,p}$ turns

out to be one of the major advantages of all LS methods. As SRH lifetime depends on the product of N_t and $\sigma_{n,p}$ and not only on the defect concentration N_t , as for example deep-level transient spectroscopy (DLTS), all LS methods show a high sensitivity to all electrically active defects even if their concentration lies below the detection limit of DLTS. A prominent example of a very recombination-active defect center that could not be detected by DLTS measurements is the metastable defect observed in boron-doped Cz silicon [27].

B LLI- and HLI-SRH lifetime

In the limit of low-level injection (LLI: $\Delta n \ll n_0 + p_0$) Eq. (3.5) simplifies and the SRH lifetime becomes independent of the injection level:

$$\tau_{SRH}^{LLI} = \tau_{n0} \left[\left(\frac{p_0 + p_1}{p_0 + n_0} \right) + k \left(\frac{n_0 + n_1}{p_0 + n_0} \right) \right] \quad (3.6)$$

A further simplification of Eq. (3.6) is achieved for a *p*-type ($p_0 \gg n_0$) and an *n*-type ($n_0 \gg p_0$) semiconductor, respectively:

$$\tau_{SRH}^{LLI,p} = \tau_{n0} \left[\left(1 + \frac{p_1}{p_0} \right) + k \left(\frac{n_1}{p_0} \right) \right] \quad \text{for } p\text{-type,} \quad (3.7a)$$

$$\tau_{SRH}^{LLI,n} = k \tau_{n0} \left[\left(1 + \frac{n_1}{n_0} \right) + \frac{1}{k} \left(\frac{p_1}{n_0} \right) \right] \quad \text{for } n\text{-type.} \quad (3.7b)$$

Beyond this, further simplifications of the LLI-SRH lifetime result for special levels E_t of the defect state and are discussed in Sect. 3.2.2. For a summary see Table 3.1.

In the limit of high-level injection (HLI: $\Delta n \gg n_0 + p_0, n_1, p_1$) Eq. (3.5) simplifies irrespective of the position of the defect level, and the SRH lifetime becomes independent of the doping concentration and the injection level:

$$\tau_{SRH}^{HLI} = \tau_{n0} + \tau_{p0} = \tau_{n0} (1 + k) \quad (3.8)$$

Thus, SRH recombination under high-level injection is limited by the slower of the two capture processes. It should be stressed that $\tau_{SRH,HLI}$ is independent of the defect level. Note that high-level injection is normally defined by $\Delta n \gg n_0 + p_0$ irrespective of n_1 and p_1 . In some cases this standard HLI definition allows a slight injection dependence under high-level injection which can be excluded by the stronger HLI definition used here.

Table 3.1. Simplification of the LLI-SRH lifetime for special energy positions E_t of the defect for a p -type semiconductor [see Eq. (3.7a)]. All energies are measured relative to the valence band edge E_V . From [22]

Position of the defect level E_t in the band	Magnitude of the relevant densities	Recombination activity of the defect	Position of E_F in relation to E_t
<i>Deep defect level</i>			
Close to mid-gap: $E_t \rightarrow E_{gap}/2$	$p_1, n_1 \ll p_0$	$\tau_{SRH}^{LLI,p} / \tau_{n0} = 1$	$E_t >> E_F$ and $E_t \ll E_C - E_F$
<i>Shallow defect level</i>			
Close to VB edge: $E_t \rightarrow E_V$	$n_1 \ll p_0 \ll p_1$	$\tau_{SRH}^{LLI,p} / \tau_{n0} = p_1 / p_0$	$E_t \ll E_F$
Close to CB edge: $E_t \rightarrow E_C$	$p_1 \ll p_0 \ll n_1$	$\tau_{SRH}^{LLI,p} / \tau_{n0} = k (n_1 / p_0)$	$E_t >> E_C - E_F$
<i>Defect level in the transition region (between deep and shallow)</i>			
In lower band gap half	$n_1 \ll p_0 \approx p_1$	$\tau_{SRH}^{LLI,p} / \tau_{n0} = 1 + p_1 / p_0$	$E_t \approx E_F$
In upper band gap half	$p_1 \ll p_0 \approx n_1$	$\tau_{SRH}^{LLI,p} / \tau_{n0} = 1 + k (n_1 / p_0)$	$E_t \approx E_C - E_F$
Special case: $E_t = E_F$	$p_1 = p_0 \gg n_0 = n_1$	$\tau_{SRH}^{LLI,p} / \tau_{n0} = 1 + k$	$E_t = E_F$

CB: conduction band, VB: valence band.

C Normalization and recombination activity

Anticipating the detailed analysis of LLI-SRH lifetime in Sect. 3.2.2, the case of deep defect levels close to mid-gap should be discussed here. As the SRH densities n_1 and p_1 are equal by definition to the intrinsic carrier density $n_i \approx 10^{10} \text{ cm}^{-3}$ for a mid-gap trap (see Fig. 3.1), they are substantially smaller than the doping concentration and Eq. (3.7) simplifies for p -type doping to $\tau_{SRH,LLI,p} = \tau_{n0}$ and for n -type doping to $\tau_{SRH,LLI,n} = \tau_{p0}$. Thus, in the limiting case of low-level injection, recombination over a deep defect state is limited by the capture of minority carriers. This is why LLI-SRH lifetime is often called *minority carrier lifetime*. Taking a closer look at the general SRH equation (3.5), it can easily be seen that the *minority carrier capture time constant* is the absolute minimum of SRH lifetime within the whole parameter range given by the independent variables E_t , k , N_{dop} , Δn and T . As the minority carrier capture time constant additionally is a simple scaling factor of the SRH lifetime, it is a suitable quantity to normalize the SRH lifetime. With the absolute SRH lifetime being normalized for p -type doping on τ_{n0} and for n -type doping on $\tau_{p0} = k \times \tau_{n0}$ as indicated in Eq. (3.7), a relative SRH lifetime is defined that is a direct measure of the *recombination activity* of a defect under the prevailing conditions. This interpretation is based only on the special property of the minority carrier capture time constant to be the absolute minimum of the SRH lifetime. Thus, a normalized SRH lifetime of 1 signifies that the absolute SRH lifetime takes its minimum value, which is synonymous with a maximum re-

combination activity of the defect. According to the definition, increasing normalized SRH lifetimes therefore indicate a decreasing recombination activity of the defect.

This approach underlies the analysis in the Sects. 3.2.2 to 3.2.4 dealing with the impact the different parameters have on the normalized SRH lifetime and on the recombination activity of the defect, respectively.

3.2.2 Influence of the defect parameters on the SRH lifetime under LLI conditions

Before studying the impact of the defect parameters E_t and k and of the doping concentration on the injection- and temperature-dependent shape of SRH lifetime curves, we first want to summarize their impact on the SRH lifetime under LLI conditions at room temperature as these results are fundamental for the physical interpretation of the relations developed in Sects. 3.2.3 and 3.2.4. For the sake of simplicity, we restrict the following analysis to a p -type semiconductor, as the whole derivation can easily be transferred to an n -type semiconductor. Note that the numerical simulations throughout Sect. 3.2 have been performed on the basis of the basic T -model for the semiconductor quantities (see Sect. 1.2.1) whose numerical values are compiled in Table 1.1.

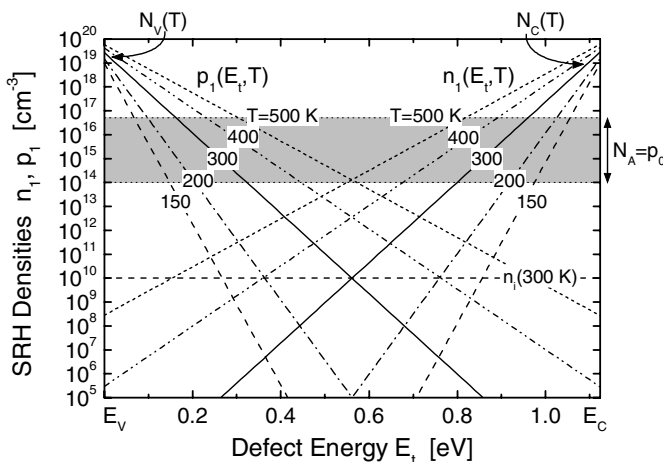


Fig. 3.1. SRH densities n_1 and p_1 as a function of the defect energy level E_t – measured from the valence band edge – for different temperatures (solid lines at 300 K). To allow their magnitude to be estimated directly, the doping region relevant to photovoltaic applications is marked in gray. From [22]

A Significance of the energy level of a defect for its recombination activity ($k=1$)

The most important parameter is the energy level E_t . To investigate its impact on the recombination activity of a defect, we first consider the case of symmetric capture cross-sections ($k=1$).

According to Eq. (3.7a) the normalized LLI-SRH lifetime for a p -type semiconductor consists of three terms:

$$\frac{\tau_{SRH}^{LLI}}{\tau_{n_0}} = 1 + \frac{p_1}{p_0} + k \frac{n_1}{p_0} \quad (3.9)$$

To get an idea of the magnitude of the two concentration ratios, Fig. 3.1 shows the SRH densities n_1 and p_1 as a function of the defect level E_t for different temperatures. For comparison the part marked in gray denotes the doping region relevant to photovoltaic applications. The temperature dependence will be discussed in Sect. 3.2.4. Regarding the magnitude of the SRH densities at 300 K (solid lines) in relation to the doping concentration, three regions for the energy level E_t may be distinguished, which are presented in Table 3.1 together with the resulting approximations of Eq. (3.9).

These three regions may be found directly in Fig. 3.2a, which shows the influence of the energy level E_t on the recombination activity of the defect states in materials with different doping concentrations. The width of the energy interval around mid-gap, in which the defects act as deep levels and show maximum recombination activity, strongly depends on the position of the Fermi level (see last column in Table 3.1) and therefore on the doping concentration.

This explains the strong doping dependence of LLI-SRH lifetime for defects in the transition region, which is given in Fig. 3.2b for different defect parameters: while shallow levels as $E_t-E_V=0.1\text{ eV}$ are active for recombination only for high doping concentrations, deep levels as $E_t-E_V=0.5\text{ eV}$ show maximum recombination activity over the whole doping region. Thus we summarize:

Rule 1: (a) Deep defects with energy levels close to mid-gap are most effective for recombination. The resulting LLI-SRH lifetime is independent of the doping concentration and equals the minority capture time constant. The SRH recombination rate is limited by the capture of minority carriers. (b) Shallow defects with energy levels several kT away from mid-gap only contribute to recombination for high doping concentrations. The correlated LLI-SRH lifetimes are strongly doping dependent.

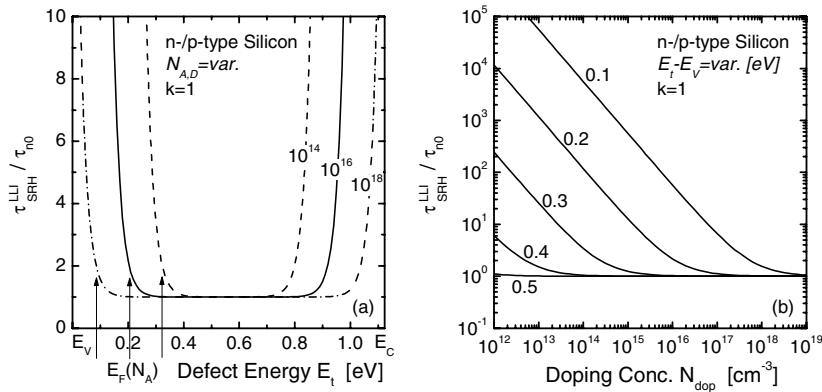


Fig. 3.2. Recombination activity of defect states with symmetric capture cross-sections for electrons and holes ($k=1$) under LLI conditions (at 300 K). (a) Impact of the energy level E_t in materials with different doping concentrations. (b) Impact of the doping concentration for defects with different energy levels E_t . Since $k=1$, the curves are valid in n - and p -type silicon.

From Fig. 3.2a it can be seen that:

Rule 2: (a) For symmetric capture cross-sections ($k=1$), defects in the lower and the upper half of the band gap which have the same energy distance ΔE_t from mid-gap show the same effectiveness for recombination. The dependence of LLI-SRH lifetime on E_t is symmetric to an axis through $E_{\text{gap}}/2$.

B Impact of capture asymmetry ($k \neq 1$) on the recombination activity

This symmetry is lost in the case of different capture cross-sections for electrons and holes. Figure 3.3a shows the impact of a variation in the symmetry factor k on the E_t -dependent shape of the LLI-SRH lifetime for a fixed doping concentration $N_A = 10^{16} \text{ cm}^{-3}$. For a qualitative understanding of the occurring changes, it has to be taken into account that a variation of k is equivalent to a variation in the hole capture cross-section σ_p , as σ_n is fixed by the normalization factor τ_{n0} . As recombination via a defect in the lower half of the band gap is limited under LLI conditions by electron capture, the corresponding recombination activity remains unchanged by a variation of k and σ_p , respectively.² In contrast, for a defect in the upper

² Note that the observed k independence of LLI-SRH lifetime for defects in the lower band gap half (in p -type silicon) does not only result from the τ_{n0} normalization but has a deeper physical background which will be discussed in more depth in Sects. 3.3.3A and 3.5.6A.

half of the band gap, hole capture is the process which limits recombination under LLI conditions. Thus, for defects with the same energy E_t in the upper band gap half, if a fixed doping concentration is assumed, one may conclude as follows: the smaller the symmetry factor k and the higher therefore the relative capture cross-section for holes, the more effective is the defect for recombination and therefore the smaller is the LLI-SRH lifetime (see Fig. 3.3a).

This has the following impact on the doping dependence of LLI-SRH lifetime which is displayed in Fig. 3.3b for an energy level $E_t-E_V=0.9\text{ eV}$ in the upper band gap half: the smaller the symmetry factor k and the higher therefore the relative capture cross-section for holes, the lower the doping concentration below which LLI-SRH lifetime increases due to a decreasing recombination activity of the defect.

Rule 2: (b) In a *p*-type semiconductor, the doping region where defects with the same energy E_t (in the upper half of the band gap) but different capture asymmetry show maximum recombination activity under LLI conditions is wider for a higher relative capture cross-section for holes, i.e., a lower symmetry factor k .

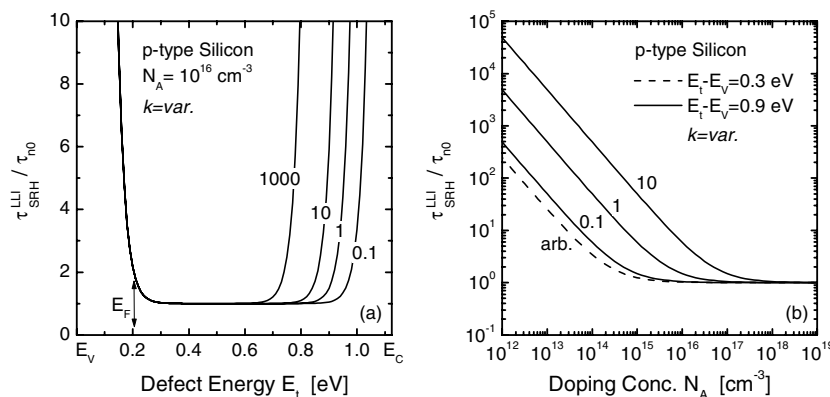


Fig. 3.3. Impact of capture asymmetry ($k \neq 1$) on the recombination activity of defect states under LLI conditions (at 300 K). (a) For defect states with continuously varied energy level E_t in material with $N_A = 10^{16} \text{ cm}^{-3}$. (b) In material with continuously varied doping concentration for defect states with a fixed shallow energy level in the upper (*solid lines*) and the lower (*dashed line*) band gap half, respectively. An asymmetry of the capture cross-sections of electrons and holes only influences the recombination activity of defect states in the upper band gap half. Since $k \neq 1$, the curves are only valid in *p*-type material, the symmetry factor being defined as $k := \sigma_n/\sigma_p$.

3.2.3 Injection-dependent SRH lifetime – IDLS

On the basis of this physical background, we will now investigate the injection and temperature dependence of the SRH lifetime, to deduce the characteristic features of injection-dependent and temperature-dependent lifetime spectroscopy (IDLS and TDLS), which will be discussed in further detail in Sects. 3.3 to 3.7 starting from the fundamentals found here. In the following two sections two kinds of parameter variations are performed: while the variation of the energy level E_t and the symmetry factor k will show the variety of attainable curve shapes, the variation of doping concentration for fixed defect parameters will give an indication of the suitability of the different curve shapes for defect analysis, i.e., for the determination of defect parameters. Special emphasis is put on the fundamental differences between deep and shallow levels.

In the following, the injection dependence of SRH lifetime will be studied first. In order to be able to compare the shapes of the injection-dependent SRH lifetime for different doping concentrations, the calculated lifetime curves are plotted versus the injection level $\eta = \Delta n / (n_0 + p_0)$ instead of the excess carrier density Δn . In addition to the restriction to a p -type semiconductor, we will further restrict the following considerations to defect levels that are close to mid-gap or in the upper half of the band gap, which allows the p_i/p_0 ratio to be neglected in all τ_{SRH} equations (since $E_t - E_V \gg E_F - E_V$). Although simplifying the discussion, this restriction still allows the fundamental impact of k variations to be deduced, since LLI-SRH lifetime is only affected for defects in the upper band gap half, as has been seen in Sect. 3.2.2B. Nevertheless, the loss of symmetry between the upper and lower half of the band gap for $k \neq 1$ has to be kept in mind. The differences arising concerning the IDLS curves for defects in both halves of the band gap will be discussed in further detail in Sect. 3.3.3A in the context of advanced IDLS analysis.

A Influence of the defect and material parameters on the injection-dependent shape of SRH lifetime

Figure 3.4a illustrates the influence of the energy level E_t on the injection dependence of the normalized SRH lifetime. The observed strong influence reflects the fact that the SRH lifetime does not depend on the energy level under HLI conditions [see Eq. (3.8)]:

$$\tau_{SRH}^{HLI} / \tau_{n_0} = 1 + k \quad (3.10)$$

while a strong dependence on the energy level exists under LLI conditions. According to Table 3.1, the LLI-SRH lifetime for the considered E_t interval is given by

$$\tau_{SRH}^{LLI}/\tau_{n0} = 1 + k (n_1/p_0) \quad (3.11)$$

From Eqs. (3.10) and (3.11) the characteristic lifetime difference between HLI and LLI can be calculated:

$$\frac{\Delta\tau_{SRH}}{\tau_{n0}} \equiv \frac{\tau_{SRH}^{HLI} - \tau_{SRH}^{LLI}}{\tau_{n0}} = k \left(1 - \frac{n_1}{p_0} \right) \quad (3.12)$$

Conditions for the E_t intervals corresponding to the three qualitatively different τ_{SRH} curves in Fig. 3.4a may be derived directly from Eq. (3.12).

Rule 3: (a) τ_{SRH} increases with η (i.e., $\Delta\tau_{SRH} > 0$) if $n_1 < p_0$. This condition is always satisfied for deep levels or more generally for all defects (in the upper band gap half) with $E_C-E_t > E_F-E_V$. (b) τ_{SRH} decreases with η (i.e., $\Delta\tau_{SRH} < 0$) if $n_1 > p_0$. This condition is satisfied for shallow levels (close to the conduction band) or more generally for all defects with $E_C-E_t < E_F-E_V$. (c) τ_{SRH} is injection-independent (i.e., $\Delta\tau_{SRH} = 0$) if $n_1 = p_0$. This is valid for a level with $E_C-E_t \approx E_F-E_V$ or for a deep level if $k \rightarrow 0$.

Figure 3.4b illustrates the influence of the symmetry factor k . For defects with the same energy level E_t the injection dependence of the SRH lifetime is stronger for higher k factors [see Eq. (3.12)]. The example of a deep level best shows the physical reasons: while SRH recombination is limited by minority capture under LLI conditions ($\tau_{SRH,LLI,p} = \tau_{n0}$), it is limited by the slower of the two capture processes under HLI conditions ($\tau_{SRH,HLI,p} = \tau_{n0} + \tau_{p0}$). Consequently, the difference between $\tau_{SRH,HLI}$ and $\tau_{SRH,LLI}$ is bigger the slower the majority capture is in relation to the minority capture, i.e., the bigger τ_{p0} is in relation to τ_{n0} and the bigger k is, respectively. For a deep level with a small symmetry factor on the other hand, minority capture is the limiting process throughout the whole injection range, and this results in a weak injection dependence of the SRH lifetime. In the case of a deep defect, the lifetime difference $\Delta\tau_{SRH}$ in Eq. (3.12) does not depend on the energy level E_t . As the normalization factor τ_{n0} equals the total LLI-SRH lifetime for deep defects, it should be possible to determine the symmetry factor k directly from $\Delta\tau_{SRH}$. This will be demonstrated in Sect. 3.3.3.

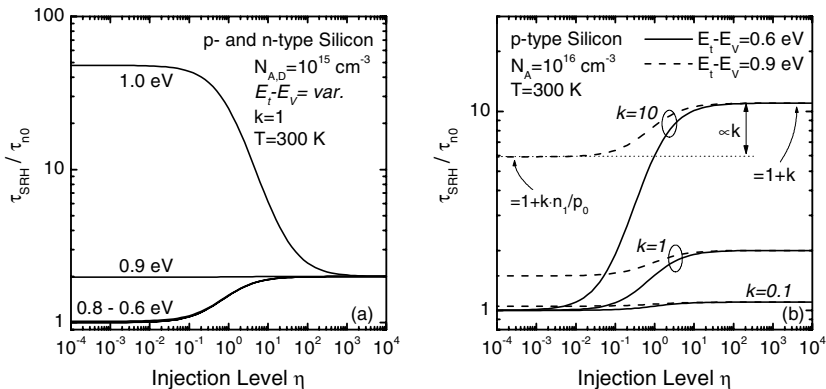


Fig. 3.4. (a) Influence of the energy level E_t on the injection dependence of the normalized SRH lifetime at 300 K for symmetric capture cross-sections ($k=1$) and a fixed doping concentration. (b) Influence of a capture asymmetry ($k \neq 1$) on the injection dependence of the normalized SRH lifetime at 300 K for deep (solid lines) and shallow (dashed lines) levels. From [22]

B Requirements for an unambiguous defect characterization from the injection-dependent shape of SRH lifetime

Concerning the applicability of IDLS for defect characterization, a major restriction arises from the fact that the characteristic shape of the injection-dependent SRH lifetime depends on three parameters: on the one hand directly on the energy level E_t (see Fig. 3.4a) and on the symmetry factor k (see Fig. 3.4b) and on the other hand indirectly on the normalization factor τ_{n0} . Although the minority capture time constant is only a scaling factor, it is not known a priori and indirectly affects the determination of k . Thus, it seems to be impossible to extract unambiguous information about the defect parameters from a single IDLS curve taken on one sample. In order to examine which is the maximum spectroscopic information that may be extracted from a single IDLS curve, the ambiguity in its SRH parameterization will be investigated in detail in Sect. 3.3.3.

Generally speaking, IDLS measurements only allow a determination of the defect parameters if the ratio n/p_0 can be varied from values above 1 to values below 1 so that the three parameter ranges pointed out in rule 3 are covered. In terms of physics, this variation is identical to a variation of the recombination activity of the defect under LLI conditions. This variation may be achieved indirectly by changing the doping concentration (see Fig. 3.5) or directly by varying the sample temperature for fixed doping concentration (see Fig. 3.6). Formally, the latter corresponds to a variation

of the SRH density n_l (see Fig. 3.1). The defect parameters may then be determined from a simultaneous fit to a set of IDLS curves for different ratios n_l/p_0 . The unambiguity of such a simultaneous IDLS analysis will be examined in Sect. 3.3.4.

The influence of the doping concentration on the injection-dependent shape of the normalized SRH lifetime is shown in Fig. 3.5 for (a) a deep and (b) a shallow level. While no variation exists for the deep level (see Fig. 3.5a), the shape changes qualitatively from a decreasing to an increasing curve for the shallow level if the doping concentration is increased (see Fig. 3.5b). This reflects the fact that for a shallow level the recombination activity under LLI conditions increases with increasing doping concentration due to the correlated movement of the Fermi level. For a deep level, on the other hand, recombination activity does not depend on the doping concentration within the whole injection range leading to the characteristic increase of SRH lifetime over the entire doping range.

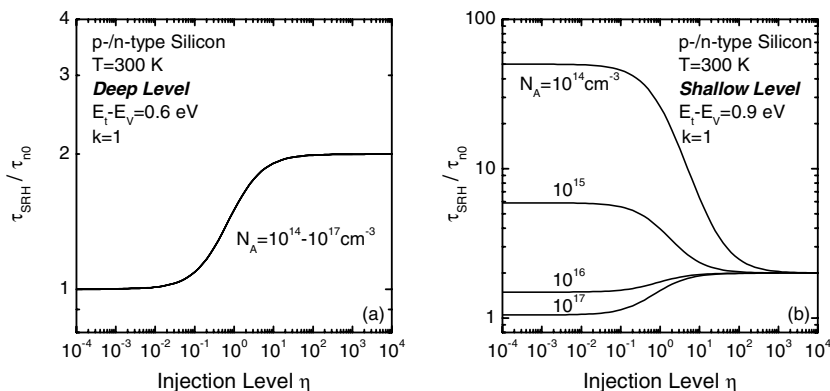


Fig. 3.5. Influence of the doping concentration on the injection dependence of the normalized SRH lifetime for (a) a deep level and (b) a shallow level with symmetric capture cross-sections ($k=1$) at 300 K.

The influence of temperature on the injection-dependent shape of SRH lifetime is shown in Fig. 3.6. In complete analogy to the variation of the doping concentration it is found that in the case of a deep level, SRH lifetime is almost independent of temperature within the whole injection range (see Fig. 3.6a). For a shallow level, however, the shape changes qualitatively from a decreasing to an increasing curve if the temperature is increased (see Fig. 3.6b). The increase in the LLI-SRH lifetime results from the fact that recombination activity of a shallow defect decreases under LLI conditions with increasing temperature (see Sect. 3.2.4). Thus we summarize:

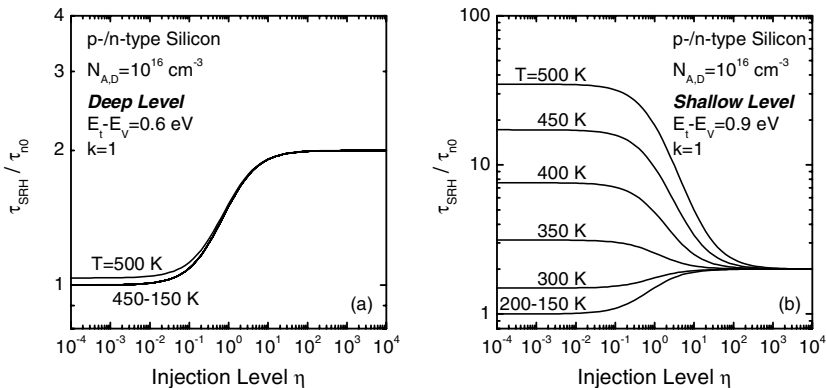


Fig. 3.6. Influence of temperature on the injection dependence of the normalized SRH lifetime for (a) a deep level and (b) a shallow level assuming symmetric capture cross-sections and a fixed doping concentration.

Rule 4: (a) For a *deep level* a variation of the ratio n_i/p_0 has no influence on the SRH lifetime under low-level injection. Thus, it has no effect on the injection-dependent shape of τ_{SRH} . For this it is irrelevant whether the ratio n_i/p_0 is changed directly by varying the sample temperature or indirectly by varying the doping concentration. (b) For a *shallow level* a variation of the ratio n_i/p_0 leads to a qualitative change of the injection-dependent shape of τ_{SRH} . For decreasing doping concentration and increasing temperature, an increase in the LLI-SRH lifetime is observed. This is due to a reduction in the recombination activity of the defect level and causes the injection-dependent shape of τ_{SRH} to turn from an increase into a decrease.

The doping and temperature dependence of IDLS curves serves as a basis for two lifetime spectroscopic techniques, N_{dop} -IDLS and T -IDLS, which will be introduced in Sects. 3.3.4 and 3.7, respectively. Using a newly developed modeling procedure for IDLS curves, their spectroscopic potential will be investigated comprehensively.

3.2.4 Temperature-dependent LLI-SRH lifetime – TDLS

As already seen in Fig. 3.6, temperature has a significant impact on LLI-SRH lifetime. The possibilities for defect characterization arising from a measurement of the temperature-dependent LLI-SRH lifetime will be discussed in the following section. To disclose the fundamental aspects, the

basic T -model for the semiconductor quantities is used (see Sect. 1.2.1). Superposed effects arising from advanced T -models will be discussed in Sect. 3.5.

A Defect characterization from the temperature-dependent shape of LLI-SRH lifetime

Considering again a defect level in the upper half of the band gap in p -type silicon, Eq. (3.7a) for the LLI-SRH lifetime reduces to

$$\tau_{SRH}^{LLI}(T) = \tau_{n0}(T) \left[1 + k \frac{n_1(T)}{p_0} \right] \quad (3.13)$$

The major contribution to the overall temperature dependence arises from the exponential temperature dependence of the SRH density n_1 . As shown in Fig. 3.1, the ratio n_1/p_0 increases with increasing temperature over several orders of magnitude. This reflects the decreasing recombination activity of the defect as the Fermi level E_F approaches mid-gap and leads to a steep increase in the LLI-SRH lifetime in the temperature range where n_1/p_0 dominates Eq. (3.13) (see previous section).

In order to see how to extract defect parameters from the lifetime data, the T -dependence of all other parameters has to be considered. Since the SRH density n_1 depends on the effective density of states N_C in the conduction band, an additional T -dependence is superimposed which can be expressed as [see Eq. (1.4)]:

$$N_C(T) = N_C^{300K} (T/300K)^{3/2} \quad (3.14)$$

Assuming that the capture cross-sections are temperature-independent, the electron capture time constant $\tau_{n0}(T)$ only depends on temperature via the thermal velocity $v_{th}(T)$ whose T -dependence may be described by [28, p.35]

$$v_{th}(T) = v_{th}^{300K} (T/300K)^{1/2} \quad (3.15)$$

with $v_{th}^{300K} = 1.0 \times 10^7 \text{ cm/s}$ being the thermal velocity at 300 K [26]. According to Eq. (3.3) the T -dependence of $\tau_{n0}(T)$ then takes the form

$$\tau_{n0}(T) = [N_i \sigma_n v_{th}(T)]^{-1} = \tau_{n0}^{300K} (T/300K)^{-1/2} \quad (3.16)$$

with τ_{n0}^{300K} being the electron capture time constant at 300 K. If the analysis is restricted at this stage to a temperature range from 150 to ~ 500 K, impurity depletion can be assumed (see Sect. 1.2.3). Since the majority carrier concentration p_0 then equals the doping concentration N_A , no T -dependence has to be taken into account for p_0 (basic T -model). The upper

bound of the T range where this simplifying assumption is accurate shows a slight doping dependence as it is given by the onset of intrinsic conduction (see Fig. 1.10a).³

This allows the overall T -dependence of the LLI-SRH lifetime to be evaluated. At sufficiently low temperatures ($T \in T_<$) the n_l/p_0 term in Eq. (3.13) can be neglected. Since the LLI-SRH lifetime then equals the electron capture time $\tau_{n0}(T)$, it is independent of the defect parameters E_t and k and exhibits a slight decrease with increasing temperature as indicated in Eq. (3.16). At a sufficiently high temperature ($T \in T_>$), however, the defect-level-dependent n_l/p_0 term becomes dominant and the simple τ_{n0} addend in Eq. (3.13) can be neglected. Using Eqs. (3.14) and (3.16), the LLI-SRH lifetime in the $T_>$ region then approaches:

$$\tau_{SRH,>}^{LLI}(T) = \tau_{n0}(T) k \frac{n_l(T)}{p_0} \propto T \times \exp\left(-\frac{E_C - E_t}{k_B T}\right) \quad (3.17)$$

which reveals that the dominant exponential T -dependence of the activation term is superimposed by a linear T -dependence arising from the T -dependent pre-factors. If the LLI-SRH lifetime is thus divided by temperature and plotted in an Arrhenius plot of $\ln(\tau/T)/T$ vs. $1/T$ as shown in Fig. 3.7, a linear increase is observed in the $T_>$ region:

$$\ln\left[\frac{\tau_{SRH,>}^{LLI}(T)}{T}\right] = \text{const.} - \frac{E_C - E_t}{k_B T} \quad (3.18)$$

As the slope of this increase in the Arrhenius plot only depends on the defect energy level and is not influenced by other defect parameters (see Fig. 3.7a and b), the evaluation of the linear Arrhenius increase allows the defect energy to be determined directly from a single measurement on one sample. This is the main advantage of TDLS compared to IDLS. However, it has to be taken into account that in an unknown system the Arrhenius increase in the LLI-SRH lifetime may either arise from the n_l/p_0 term, if the defect is located in the upper band gap half, or from the p_l/p_0 term, if the defect is located in the lower band gap half. As a consequence, the slope of the Arrhenius increases may be proportional to either $E_C - E_t$ or $E_t - E_V$, which demonstrates that a linear fit of the Arrhenius increases only yields the energy depth ΔE_t of the defect but does not provide any information about the band gap half the defect is located in.

³ As will be shown in Sect. 3.5 within a detailed analysis of superposed effects, the abrupt strong increase in p_0 due to intrinsic conduction (advanced T -model) overcompensates the exponential increase in the SRH density and thus completely screens the Arrhenius increase of the LLI-SRH lifetime.

Since the accuracy of the ΔE_t determination strongly depends on the width of the defect-dominated Arrhenius increase, which may be greatly reduced under realistic conditions, improved techniques for a linear data evaluation will be developed in Sect. 3.4 and analyzed with respect to their spectroscopic accuracy. Section 3.5 will then investigate the spectroscopic potential of an advanced TDLS analysis, being based on the SRH modeling of the complete temperature dependence of the LLI-SRH lifetime.

B Influence of the defect and material parameters on the temperature-dependent shape of LLI-SRH lifetime

Since defect characterization by means of TDLS is strictly linked with the Arrhenius increase, the question arises at which temperatures the increase has to be expected. This depends on the defect parameters E_t and k as well as on the doping concentration N_A .

The impact of the defect energy E_t on the T -dependence of LLI-SRH lifetime is shown in Fig. 3.7a for a medium doping concentration of 10^{15} cm^{-3} . As can be seen, an increasing defect energy depth ΔE_t not only increases the slope of the Arrhenius increase but also shifts the onset temperature of the Arrhenius increase to higher values. The reason for this shift is that the SRH densities are reduced by several orders of magnitude for a deep compared to a shallow level and thus necessitate higher temperatures to enter the $T_>$ region. In the limiting case of a symmetric mid-gap level, the

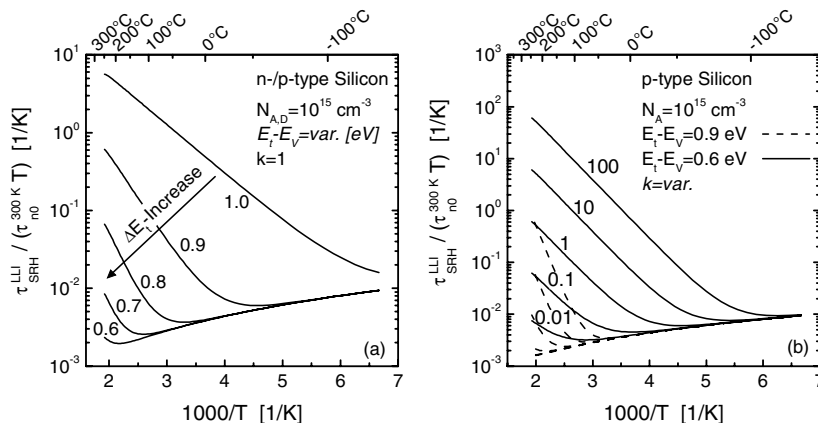


Fig. 3.7. (a) Influence of the energy level E_t on the linear Arrhenius increase of the temperature-dependent normalized LLI-SRH lifetime assuming symmetric capture cross-sections ($k=1$). (b) Influence of a capture asymmetry ($k \neq 1$) on the linear Arrhenius increase of the temperature-dependent normalized LLI-SRH lifetime for deep (dashed lines) and shallow (solid lines) energy levels near the conduction band.

Arrhenius increase vanishes completely and the slight temperature dependence of τ_{n0} dominates the whole temperature range. This demonstrates that it may be difficult to characterize deep defects by means of TDLS.

The impact of the symmetry factor k on the onset temperature of the Arrhenius increase is shown in Fig. 3.7b for shallow (solid lines) and deep (dashed lines) levels in the upper band gap half. As hole capture is the process limiting recombination via defects in the upper band gap half and as a k increase corresponds to a decrease in the relative capture cross-section for holes, the recombination activity of these defects decreases with increasing k , and this leads to lower temperatures for the onset of the Arrhenius increase. The situation changes for defects in the lower band gap half since recombination is then limited by the capture of electrons. As the electron capture cross-section remains unchanged upon variations of k due to the natural τ_{n0} normalization (see discussion in Sect. 3.2.3A), the onset temperature of the Arrhenius increase does not depend on the symmetry factor k . In the general expression (3.7a) for the LLI-SRH lifetime this is reflected by the fact that the p_1/p_0 term, which is relevant to defects in the lower band gap half, is not weighted with the symmetry factor k . The physical origin of this difference between defects in the upper and lower band gap half will be discussed in more depth in Sect. 3.5.6. Having a decisive impact on the SRH modeling of a TDLS curve, it forms the basis for an advanced TDLS analysis introduced there.

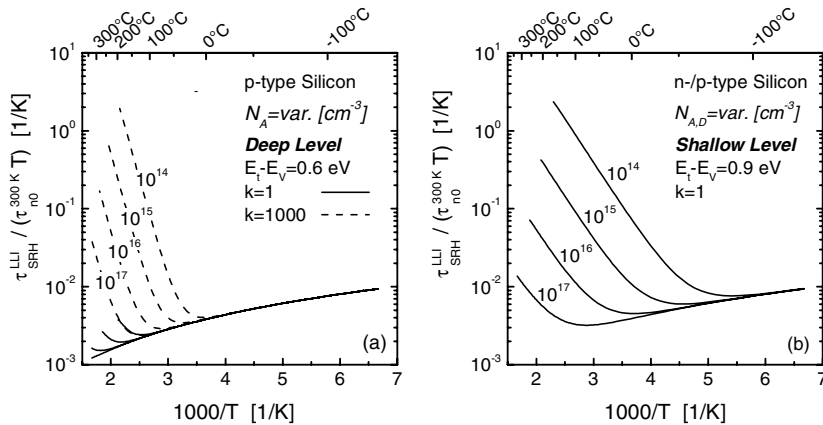


Fig. 3.8. Influence of the doping concentration on the linear Arrhenius increase of the temperature-dependent normalized LLI-SRH lifetime for (a) a deep energy level and (b) a shallow energy level near the conduction band. The *dashed lines* in (a) show that in the rare situation of a strong capture asymmetry ($k=1000$), even deep defects around mid-gap may exhibit an Arrhenius increase below 500 K which enables their characterization by means of TDLS.

Finally, Fig. 3.8 shows the impact of the doping concentration N_A for (a) a deep and (b) a shallow level. Since a reduction of the doping concentration implies a movement of the Fermi level towards mid-gap and thus causes an indirect reduction in the recombination activity of the defect, the onset temperature of the Arrhenius increase is shifted to lower temperatures for decreasing N_A . Formally, this is reflected in Eq. (3.13) by the fact that the SRH ratio n_l/p_0 becomes dominant at lower temperatures if p_0 is reduced. Thus, we summarize:

Rule 5: The shallower the energy level of a defect, the lower the slope of the Arrhenius increase of $\tau_{SRH,LLI}(T)$ and the lower the temperature of its onset. The recombination activity being indirectly reduced by a reduction of the doping concentration, the onset of the Arrhenius increase can be moved to lower temperatures.

In conclusion, the parameter variations of Figs. 3.7 and 3.8 on the one hand demonstrate that TDLS is applicable in most of the parameter ranges and reveal on the other hand two critical classes of parameter constellations: (i) mid-band-gap traps in samples of arbitrary doping concentration and (ii) arbitrary traps in highly doped samples. In both cases the linear Arrhenius increase will in general be shifted out of the accessible temperature range and screened by the beginning intrinsic conduction. Nevertheless the dashed lines in Fig. 3.8a show that in the case of high symmetry factors ($k=1000$) even deep defects around mid-gap may exhibit an Arrhenius increase below 500 K, which enables their characterization by means of TDLS. This is particularly achieved if the sample has low doping. The mutual impact of the defect parameters and the physical limitations due to intrinsic conduction being taken into account, the applicability of TDLS will be investigated in detail in Sect. 3.5.8.

3.2.5 Section summary

In Sect. 3.2, the SRH equation has been analyzed systematically to reveal the possibilities and restrictions of lifetime spectroscopy (LS) and to provide an overview of the characteristic features of the different LS techniques. The introduction of a symmetry factor k , describing the capture asymmetry of the defect state for electrons and holes, revealed some universal features, as it allows the defect parameters to be classified as relative or absolute parameters. Whereas the relative parameters E_t and k have a crucial influence on the shape of the SRH lifetime curves and can therefore be determined exclusively from LS techniques, the absolute parameters N_t and σ_n appear only as a product in the electron capture time

constant τ_{n0} , which is a scaling factor for the SRH lifetime. This prevents the separation of the absolute defect parameters on the basis of lifetime measurements, but illustrates the high sensitivity of all LS techniques to electrically active defects even if their concentration is very low, e.g., below the detection limit of DLTS.

To demonstrate the characteristic features of the injection and temperature dependence of the SRH lifetime, two kinds of parameter variations have been performed: while the variation of the defect parameters E_t and k showed the variety of attainable curve shapes, the variation of doping concentration for fixed defect parameters gave an indication of the suitability of the different curve shapes for the spectroscopic determination of defect parameters. The physical background for the observed dependence has been discussed in detail.

The fundamental requirement for an unambiguous determination of the defect parameters from lifetime spectroscopy has been found to be a variation of the recombination activity of the defect under low-level injection (LLI) conditions, which is identical to a variation of the SRH ratio n_i/p_0 and p_i/p_0 , respectively. This variation can be achieved indirectly by varying the doping concentration or directly by varying the sample temperature. As this variation is inherent in temperature-dependent measurements of the LLI-SRH lifetime, TDLS allows the defect energy depth ΔE_t to be determined directly from a single measurement on one sample, although it does not indicate directly whether the defect is located in the upper or lower half of the band gap. It has been shown that ΔE_t is directly proportional to the slope of a linear increase which the TDLS curve exhibits in an Arrhenius plot above a certain temperature. By contrast, it is generally not possible to extract unambiguous information about the defect parameters from a single IDLS curve, as the characteristic shape depends on E_t , k and τ_{n0} . As a possible solution to this ambiguity problem, it has been shown that IDLS measurements may allow the defect parameters to be determined if a set of IDLS curves, either measured on several samples with different doping concentrations (N_{dop} -IDLS) or measured on the same sample at different temperatures (T -IDLS), is subjected to simultaneous SRH analysis.

On the basis of the identified fundamental features of the injection-dependent and temperature-dependent SRH lifetime analysis, the analytical potential of the different LS techniques will be investigated in more depth in the following sections. As a guide to Chap. 3, the diagram in Fig. 3.9 summarizes the different LS techniques that will be discussed in the following sections.

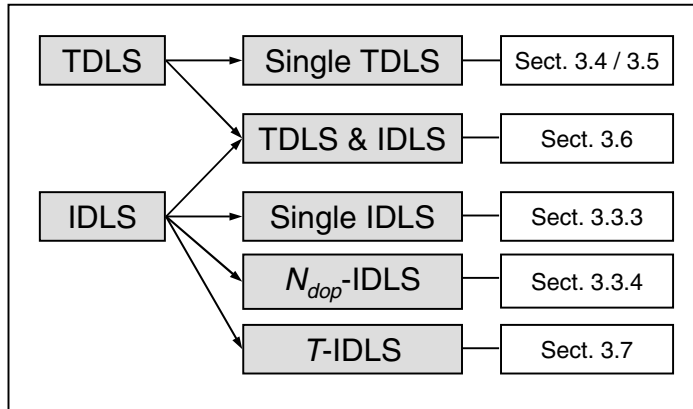


Fig. 3.9. Compilation of the different lifetime spectroscopic techniques discussed in Chap. 3.

3.3 Injection-dependent lifetime spectroscopy (IDLS): advanced analysis

As already pointed out in Sect. 3.2, injection-dependent lifetime spectroscopy (IDLS) faces the problem that the SRH parameterization of a single IDLS curve is ambiguous. This ambiguity should in principle be avoided if a set of IDLS curves measured on several samples with varying doping concentration (N_{dop} -IDLS) is subjected to a simultaneous SRH fit. However, neither the ambiguity of a single IDLS curve nor the unambiguousness of the N_{dop} -IDLS technique have been investigated so far from a theoretical point of view. The first uncertainty manifests itself in a lack of well-founded guidelines concerning the spectroscopic information which may be extracted from a single IDLS curve in spite of its ambiguity. From an experimental point of view, the N_{dop} -IDLS technique is already established [13, 18] although rarely used. The application to unknown systems revealed the problem [13] that the simultaneous SRH fit often fails, which is reflected in broad parameter ranges for the defect parameters instead of discrete solutions. This ambiguity of the spectroscopic result is most likely induced by the lack of a transparent procedure for data evaluation. Thus the present section focuses on two issues: on the one hand on the detailed theoretical evaluation of the spectroscopic potential of the simple IDLS and the extended N_{dop} -IDLS techniques and on the other hand on the development of a routine for data evaluation, which takes into account the ambiguity of the IDLS fit results and thus makes IDLS applicable as a diagnostic tool.

Since the extraction of the pure SRH lifetime is a basic requirement for IDLS investigations, we first demonstrate in Sect. 3.3.1 how the characteristic SRH shape of real IDLS curves may be distorted under LLI and HLI by the superposition of external carrier trapping and intrinsic recombination, respectively, and briefly discuss the technique of a bias correction to eliminate trapping effects from the lifetime data. As it is a common problem that IDLS curves are dominated under LLI and HLI by two different defect levels, the basic aspects of a two-defect SRH simulation are discussed in Sect. 3.3.1C.

Addressing the fundamental problem of ambiguity, we then introduce in Sect. 3.3.2 a new modeling procedure for IDLS data which is based on the determination of the associated *defect parameter solution surface* (DPSS). Since the DPSS analysis allows a transparent and comprehensive SRH analysis of IDLS and perfectly visualizes the ambiguity of IDLS fit results, it is ideally suited to evaluate the spectroscopic potential of IDLS in detail. Focusing in Sect. 3.3.3 on the DPSS of a single IDLS curve, we first discuss in Sect. 3.3.3A the physical background for its characteristic energy dependence. As a basis for the whole analysis we then develop in Sect. 3.3.3B analytical expressions for the two curves, constituting the DPSS, and discuss in Sect. 3.3.3C the impact of the defect parameters on their shape and characteristics. In order to evaluate the possibility of extracting the true defect parameters from the two DPSS characteristics of a single IDLS curve, we finally deduce in Sect. 3.3.3D analytical expressions for the different DPSS characteristics and investigate their spectroscopic value in depth in Sect. 3.3.3E. Section 3.3.3F then examines the possibility of deriving conditional equations for both defect parameters by combining the analytical expressions associated with the pair of DPSS characteristics of a single IDLS curve.

After discussing the restrictions in determining defect parameters from a single DPSS, we investigate in Sect. 3.3.4 the spectroscopic potential of the expanded N_{dop} -IDLS technique. In Sect. 3.3.4A the DPSS evaluation procedure is first expanded to be applicable to a set of IDLS curves. The resulting superposed DPSS analysis gives a deeper insight into simultaneous SRH analysis and reveals for the first time the possibilities and fundamental restrictions of the N_{dop} -IDLS technique. These are discussed in Sect. 3.3.4B. While the impact of the defect depth on the quality of the spectroscopic result is discussed in Sect. 3.3.4C, minimum requirements to achieve maximum accuracy in an N_{dop} -IDLS experiment are derived in Sect. 3.3.4D, being put to practical use by means of a special diagram. The practical advantages of the newly developed superposed DPSS analysis are then discussed in Sect. 3.3.4E.

3.3.1 Superposed effects: measurability of the injection-dependent shape of SRH lifetime

A Under LLI: superposition of external carrier trapping and bias correction

The use of injection-dependent lifetime data for spectroscopic purposes is contingent upon reliable measurements of the SRH recombination lifetime over the whole injection range. However, under low-level injection recombination, lifetime may be completely screened if additional minority carrier trapping centers are present in the semiconductor. The following discussion focuses on this *external trapping* effect, which is often observed and has to be differentiated from internal trapping, which may occasionally arise from the dominating recombination center itself as discussed in Sect. 1.4.3C. Additional trapping centers, which do not contribute to recombination but only interact with the minority band and thus lead to the external trapping effect, are well known in multicrystalline [29] and Czochralski silicon [30]. Their impact on lifetime measurements can be dramatic if photoconductance-based techniques are used as in the present work. For transient photoconductance decay measurements, the relatively slow detrapping of minority carriers causes a long tail in the photoconductance decay, feigning an extremely long lifetime, which does not represent the actual recombination lifetime but an apparent lifetime [29]. Moreover, traps may significantly influence the steady-state photoconductance of a sample. At carrier densities comparable to or below the trap density, the presence of minority carrier traps induces a relative increase in the concentration of majority carriers to guarantee charge neutrality.⁴ This leads to an increase in the steady-state photoconductance above its value when traps are absent, which in turn results in a longer apparent lifetime and thus hampers the measurement of recombination lifetimes under low injection levels [29].

To avoid distortions of the spectroscopic result obtained from an injection-dependent lifetime curve, its trap-affected part has to be rejected in the SRH simulations. However, since trap densities may be large enough to affect lifetime curves up to carrier densities of 10^{13} – 10^{14} cm⁻³, such a data cutoff results in a complete loss of the LLI part of the lifetime curve

⁴ The reason for this increase is discussed in [31]. In *p*-type, charge neutrality requires $\Delta p = \Delta n + n_T$, with n_T being the concentration of trapped excess electrons. Since the concentration Δn of free excess electrons is only determined by recombination, which operates independently of the traps, its value is the same with and without traps being present. Hence, as n_T begins to be appreciable compared to Δn , the excess hole concentration Δp becomes significantly higher than the level that would be expected without traps. Thus the reason for the Δp increase is that the traps remove some of the electrons from the recombination channel, allowing the photogenerated carriers to build up until a steady state is reached.

for the spectroscopic investigation. Thus in order to extend the range of useful data towards the LLI region, the external trapping effect has to be eliminated from the data. This can be achieved by two different methods recently discussed in the literature.

- (i) Macdonald et al. have recently found that it is possible to extract the relevant trap parameters from the measured apparent lifetime curve if a theoretical trapping model [29, 32] is fitted to the data. An accurate determination of the underlying recombination lifetime may thus be achieved by fitting the complete trapping model with SRH recombination to the data and then “turning off” the traps. This is, however, very time-consuming [33] and further increases the complexity of the fitting problem.
- (ii) An alternative approach consists in applying a bias-light correction which has been proposed by Sinton [34]. This technique attempts to eliminate the effects of traps by effectively subtracting the trap-induced excess photoconductance, the analysis then being carried out relative to this “base-line” photoconductance [33, 34]. It has to be stressed that this bias-light correction represents a purely analytical data correction and in terms of physics does not involve applying an additional bias light during the measurement. The advantage of the bias-light correction is that it is easily and quickly applied to the measured QSSPC data.

Since the present work focuses on the characterization of recombination-active defects, the second and simpler approach to eliminate the trapping effects has been favored. To demonstrate the aptitude of the bias-light correction, its basic concept and accuracy should be discussed briefly in the following.

The bias-light correction essentially consists of two steps, which are illustrated in Fig. 3.10a [33]. Displaying a linear plot of photoconductance vs. light intensity for a trap-affected sample, Fig. 3.10a shows the trapping-induced rapid increase of the photoconductance under low illumination, and also the positioning of the bias-light intensity I_{bias} at a point where it is just sufficient to fill the traps. In the first step, a corrected lifetime $\tau_{corr} = \delta(\Delta n) / \delta G$ is calculated according to the standard equations in Sect. 2.1, using for the generation δG and the excess carrier density $\delta(\Delta n)$ the values relative to the bias point, $\delta G := G(I) - G(I_{bias})$ and $\delta(\Delta n) := \Delta n - \Delta n_{bias}$, respectively. The carrier density Δn_{bias} is directly read from the original data at the bias point. As shown in Fig. 3.10a, this corrected lifetime is then directly proportional to the ratio of Δ photoconductance to Δ intensity. Because of the large imbalance between the electron and hole density in the trapping region, the minority carrier density Δn_{min} is the relevant quantity to ascribe the lifetime to. Thus in the second step, Δn_{min} is estimated at each data point. Since Δn_{min} is proportional to the “base-line”

photoconductance ($\Delta\sigma - \sigma_{trap}$), this requires an estimate of the excess photoconductance due to the traps, σ_{trap} . As shown in Fig. 3.10a, this is achieved by an extrapolation of the photoconductance vs. intensity data from above the bias point to the photoconductance axis. The fully corrected data are then plotted in the form τ_{corr} vs. Δn_{min} [33].

In recent work [33], Macdonald et al. investigated the effectiveness of this correction method and determined guidelines for its proper application. To this end, they calculated pairs of lifetime curves with and without superposed carrier trapping, using the theoretical trapping model mentioned above [29], and investigated the impact of the bias-light correction for various bias intensities. Figure 3.10b displays this analysis for an increasing lifetime curve dominated by SRH recombination via a deep center [33]. While the lowest bias value of 0.03 suns is not sufficient to eliminate the trapping effect, an increase of the bias to 0.3 suns induces a shift of the corrected curve towards the actual recombination lifetime. However, if the bias is further increased, the corrected curve starts to rise again as shown in Fig. 3.10b for 3 and 30 suns. The reason is that the carrier density at the bias point, which is displayed on the horizontal axis, then lies well above the region where trapping dominates. The fact that the extrapolation of photoconductance then reflects high-injection conditions, which do not fit to the low-injection region of interest, causes the corrected lifetime to overestimate recombination lifetime.

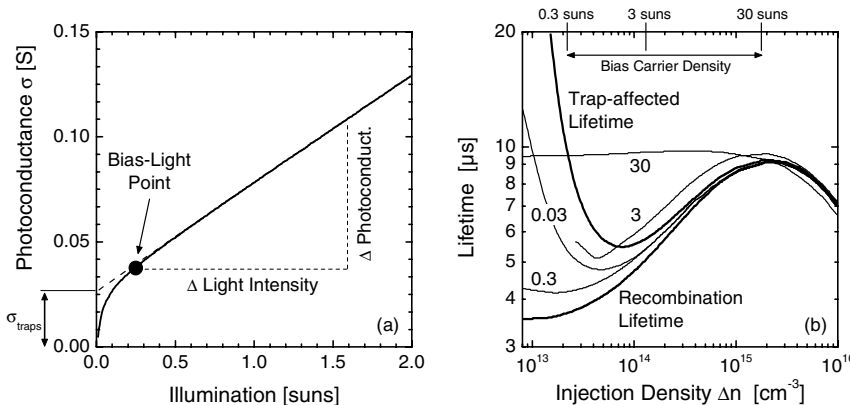


Fig. 3.10. (a) Photoconductance vs. light intensity for a sample affected by trapping. Taken from [33]. (b) Modeled lifetime dominated by SRH recombination (with $E_C - E_{SRH} = 0.4$ eV, $\sigma_n = 9 \times 10^{-15} \text{ cm}^2$, $\sigma_h = 9 \times 10^{-17} \text{ cm}^2$, $N_{SRH} = 2 \times 10^{12} \text{ cm}^{-3}$ and an additional emitter term). In the trap-affected lifetime curve a trap density of $1 \times 10^{14} \text{ cm}^{-3}$ is assumed. The impact of the bias-light correction is shown for different bias-light intensities (given in suns), the corresponding bias carrier densities being shown on the upper horizontal axis. Taken from [33].

The result from Fig. 3.10b led to the following simple rule concerning the optimum choice of the bias level: in the case of a lifetime curve which increases immediately after the trapping region with increasing Δn , the bias level has to be increased from below the measurement range until the corrected lifetime curve reaches a minimum at the lower carrier densities [33]. In the case of a lifetime curve which decreases or is constant immediately after the trapping region, similar considerations revealed a modified rule: in that case the optimum bias is found by increasing its value until the corresponding bias carrier density is at the point where the uncorrected lifetime is approximately doubled due to the traps [33]. Both guidelines reflect the endeavor to use enough bias light to fill the traps but not more. Together they allow a trap correction of arbitrary lifetime curves.

An estimate of the accuracy of the bias-light correction can be deduced directly from Fig. 3.10b [33]. For the 0.3 suns case, which represents the optimum bias correction in Fig. 3.10b, the corrected lifetime data are found to overestimate recombination lifetime only by about 15 % at the bias carrier density of $2.0 \times 10^{13} \text{ cm}^{-3}$, with improving accuracy at higher carrier densities. The uncorrected lifetime data on the contrary overestimate the true lifetime value at the same carrier density by a factor of 3 (200 %) and reach an accuracy of 15 % only at about $1.5 \times 10^{14} \text{ cm}^{-3}$. This nicely demonstrates that the correction procedure in general yields an extra order of magnitude of usable data, in terms of carrier density, than would otherwise be available [33]. To guarantee this accuracy, Macdonald et al. strictly recommended using the corrected lifetime data only above the bias carrier density (general working principle), i.e., in that region where trapping only partially affects the measurements and does not completely dominate.⁵

Taking into account the fact that the accuracy of the bias-light correction can be further improved compared to Fig. 3.10b if the increment in the bias variation is reduced around its optimum, the bias-light correction is well suited to eliminate the trapping effect from the original lifetime data. It is thus used in the present work to extend the injection range usable for spectroscopic IDLS analysis to lower injection densities whenever minority carrier trapping is observed.

⁵ At carrier densities lower than the bias carrier density the residual SRH dependence is overwhelmed by the trap-induced photoconductance, which makes the corrected data unreliable.

B Under HLI: superposition of intrinsic recombination

In addition to a possible superposition of trapping effects, whose appearance is tied to the purity of the material, defect-specific SRH recombination is always superimposed by intrinsic recombination. According to Eq. (1.51) the total bulk lifetime is given by:

$$\tau_{\text{bulk}}^{-1} = \tau_{\text{SRH}}^{-1} + \tau_{\text{CE-Auger}}^{-1} + \tau_{\text{rad}}^{-1} \quad (3.19)$$

As discussed in Sect. 1.4.2C, radiative recombination is of minor importance in silicon, whereas CE-Auger recombination may be crucial. A theoretical model for the injection dependence of $\tau_{\text{CE-Auger}}$ has been discussed in Sect. 1.4.2. In order to evaluate the impact of CE-Auger recombination on the measurability of the characteristic shape of SRH lifetime, the injection-dependent shape of total bulk lifetime has been simulated in Fig. 3.11 for different doping concentrations, SRH recombination being assumed to occur via (a) a deep level and (b) a shallow level.

In the case of a deep level, which is shown in Fig. 3.11a, the measurability of HLI-SRH lifetime strongly depends on the doping concentration. While it can be measured for doping concentrations below 10^{15} cm^{-3} , it is completely screened by CE-Auger recombination if the doping concentration reaches 10^{16} cm^{-3} . Thus, in the case of more highly doped samples the defect-specific lifetime difference $\Delta\tau_{\text{SRH}}$ cannot be determined directly. Moreover, in the case of a shallow level which is shown in Fig. 3.11b, the HLI-SRH lifetime is completely screened irrespective of the doping level

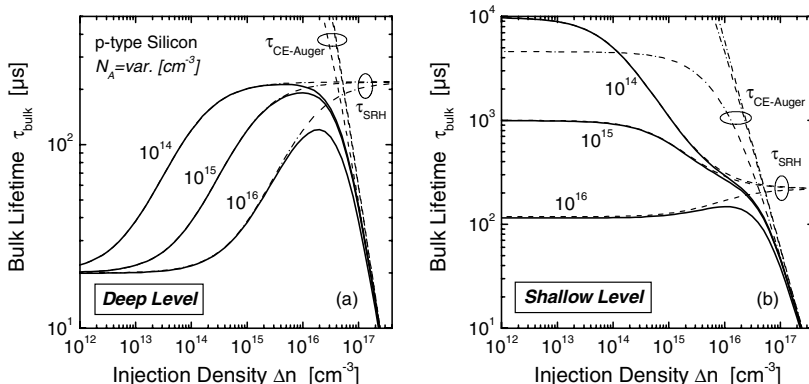


Fig. 3.11. Injection dependence of bulk lifetime (solid lines) for different doping concentrations (at 300 K) assuming that SRH recombination (dash-dotted lines) occurs via (a) a deep level at $E_i - E_V = 0.6 \text{ eV}$ and (b) a shallow level at $E_i - E_V = 0.9 \text{ eV}$, both with $k = \sigma_n / \sigma_p = 10$ and $\tau_{n0} = 10 \mu\text{s}$. The HLI region is dominated by CE-Auger recombination (dashed lines).

since the characteristic SRH decrease (or SRH increase) is shifted by about an order of magnitude to higher carrier densities, as can be seen in Fig. 3.4a. As a consequence, the step-like SRH shape is completely lost for shallow levels. Figure 3.11a and b thus illustrate that, compared to pure SRH lifetime curves, the defect-specific information in injection-dependent bulk lifetime curves is often significantly reduced by the unavoidable superposition of CE-Auger recombination.

In order to expand the injection range usable for spectroscopic IDLS analysis, CE-Auger recombination has to be eliminated from the measured lifetime data. This should be possible with adequate precision as CE-Auger recombination is a fundamental mechanism which can be simulated to a high level of accuracy, e.g., by the model used in Fig. 3.11a and b. Note that the elimination by means of a theoretical model is much simpler for the Auger than for the trapping effect since the adjustment of the model does not involve the complex determination of defect parameters from a fit, but only the insertion of the known doping concentration of the investigated sample. However, this lack of free parameters within the model implies that the correction is only as good as the Auger model description of the actually measured lifetime decrease. Irrespective of the model accuracy, the corrected lifetime curve reliably reflects the actual SRH lifetime only in that Δn region where bulk lifetime is partially affected but not completely dominated by CE-Auger recombination. At higher carrier densities, the residual SRH traces are totally screened by Auger recombination, which makes the corrected data unreliable. Because of the steep decrease in the CE-Auger lifetime, the transition region between the SRH- and Auger-dominated part of the bulk lifetime curve is about an order of magnitude wide in terms of carrier density Δn , as displayed in Fig. 3.11. Consequently the Auger correction at best pushes up the range of usable data by an order of magnitude in terms of Δn than would otherwise be available for the spectroscopic analysis. Notably for highly-doped samples the Auger correction thus increases the spectroscopic information as the extraction of the screened HLI-SRH lifetime may become possible, which can be seen in Fig. 3.11a.

In addition to the strong Auger impact under HLI conditions, CE-Auger recombination may affect the bulk lifetime in the whole injection range, as partially recognizable in Fig. 3.11b for the 10^{16} cm^{-3} -doped sample. Since CE-Auger lifetime under LLI conditions strongly decreases with increasing doping concentration (see Fig. 1.13a), this becomes relevant in highly-doped samples whenever SRH recombination is reduced either due to a shallow energy level or a low defect concentration. In these special cases, the uncertainty of the spectroscopic IDLS result is increased.

C Under HLI: superposition of a second defect level (two-defect SRH simulation)

In the case of a deep center, which dominates recombination under LLI conditions, the HLI part of the SRH lifetime curve may be screened not only by Auger recombination (see Fig. 3.11a) but also by the superposition of SRH recombination via a second shallower defect center whose decreasing SRH lifetime curve cuts the top of the increasing SRH lifetime curve associated with the deep center. Such a coexistence of a deep (dominating LLI) and a shallow (dominating HLI) defect level is reported in the literature for different impurities in silicon [14, 18] and has often been observed in the present work. Obviously, an accurate SRH modeling of the entire injection dependence then requires the consideration of two independent SRH centers, which increases the number of free model parameters from three to six. The important question is whether this doubling of the degrees of freedom further increases the ambiguity of the SRH fit result beyond the intrinsic ambiguity, which is observed for an ideal one-defect SRH simulation and will be discussed in detail in the following sections.

Analytically, the total SRH lifetime is simply calculated as the reciprocal sum of the inverse SRH lifetimes of the two defects. However, to single out a possible supplementary ambiguity coming from the defect superposition, the two-defect SRH fit has been further structured by the introduction of a weighting factor X which is defined as the ratio of the modeled LLI-SRH lifetime of only the second defect to the actual LLI-SRH lifetime of the entire system:

$$X := \tau_{SRH,D2}^{LLI} / \tau_{eff}^{LLI} \quad (3.20)$$

The benefit of the X factor is that it represents a direct measure of the impact of the second defect level on the total lifetime under LLI conditions – the impact being the higher the lower the X value is – and thus allows a transparent weighting of the impact of both defect levels under LLI. The introduction of the X factor replaces the electron capture time constant τ_{n0}^{D2} of the second defect as free parameter. An analytical expression for τ_{n0}^{D2} follows from Eq. (3.20) if Eq. (3.6) is inserted for the LLI-SRH lifetime of the second defect:

$$\tau_{n0}^{D2} := X \times \tau_{eff}^{LLI} \left/ \left(\frac{p_1^{D2} + p_0}{p_0 + n_0} + k^{D2} \frac{n_1^{D2} + n_0}{p_0 + n_0} \right) \right. \quad (3.21)$$

Equation (3.21) shows that in the modified two-defect SRH model τ_{n0}^{D2} becomes a function of the weighting factor, of the actual total lifetime under LLI and of the defect parameters of the second defect.

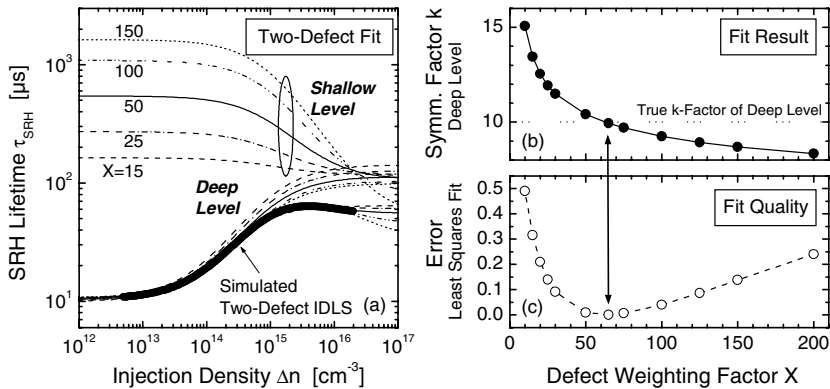


Fig. 3.12. Impact of the weighting factor X on the result of a two-defect SRH analysis. **(a)** Fitted SRH lifetime curves (lines): the preset IDLS curve (symbols) represents the total SRH lifetime in a two-level system consisting of a deep level ($E_C-E_t=0.4$ eV, $k=10$, $\tau_{n0}=10$ μs) and a shallow level ($E_C-E_t=0.2$ eV, $k=1$, $\tau_{n0}=50$ μs). The SRH fits are performed on the basis of a two-defect SRH model subject to a specified but varied weighting factor X . **(b)** SRH fit results: optimum symmetry factors k of the deep level (*upper half*) and corresponding χ^2 errors of the least squares fit (*lower half*) as a function of the weighting factor X .

The accuracy of the two-defect SRH fit is examined using as object of analysis the simulated total SRH lifetime of a two-level system consisting of a deep level at $E_C-E_t=0.4$ eV (with $k=10$ and $\tau_{n0}=10$ μs) and a shallow level at $E_C-E_t=0.2$ eV (with $k=1$ and $\tau_{n0}=50$ μs). These defect data correspond to a weighting factor $X=65$, which is a priori unknown in the experiment and should be determined from the two-defect SRH analysis. As shown in Fig. 3.12a (symbols), the range of the lifetime data used in the fit is confined in terms of Δn to $5\times10^{12}\text{--}2\times10^{16}$ cm⁻³, which represents the Δn range that normally allows a determination of the SRH lifetime in the experiment. This confinement ensures a SRH analysis under realistic conditions. In order to determine the impact of the shallow level, dominating HLI, on the fit result of the deep level, dominating LLI, the preset SRH lifetime curve (symbols) has been simulated for specified but gradually varied weighting factors X . Since the ambiguity of the single-level fit is investigated in detail in the following sections, the energy levels of both defects have been fixed on their true values, which reduced the set of free parameters from six to three variables: the k factors of both defects and the τ_{n0} value of the deep defect. Their optimum values have been determined by means of a least squares fit subject to a fixed X factor. The resulting symmetry factors k of the deep level (*upper half*) and the corresponding χ^2 errors of the least squares fit (*lower half*) are exemplified in Fig. 3.12b

as a function of the weighting factor X . Moreover, Fig. 3.12a displays the corresponding SRH lifetime curves (lines) of the deep and the shallow level as well as their superposition, calculated for different weighting factors on the basis of the optimum fit results partially displayed in Fig. 3.12b.

Due to the reduction of the fitting problem, the X -dependence, which is found in Fig. 3.12b for the optimum k factor of the deep level, directly reflects the isolated impact of the additional shallow level on the fit result of the deep level. The fact that the $\text{Chi}^2(X)$ curve exhibits a minimum demonstrates that it is possible to determine the accurate weighting factor. However, the minimum of the $\text{Chi}^2(X)$ curve is relatively broad. Without significant change in the fit quality the X factor may thus be varied between 40 and 100. Fortunately, the variation of the k factor around the optimum X value is also very weak. The broad range of possible X values thus still leads to a narrow range for the k factor, in the present case ranging from 9–11, which corresponds to a 10 % error range around its optimum k value. It can be concluded that the presence of a second defect level *does not* increase the ambiguity of the SRH simulation, which is an important result given that two-defect SRH curves are often observed.

Another important feature of the two-defect simulation is revealed by the asymmetry of the $k(X)$ and the $\text{Chi}^2(X)$ curves. While an underestimate of the X factor by a factor of 2 or more results in a significant overestimate of the true k factor, which is reflected in a steep increase of the Chi^2 value, an overestimate by a factor of 3 still leads to adequate fit results with relatively low Chi^2 values and fit parameters close to the true values. This demonstrates that it is worse if the impact of the shallow defect level on the LLI region of the superposed SRH lifetime curve is overestimated, as shown in Fig. 3.12a for $X=15$.⁶ Moreover, the relatively good spectroscopic result in the case of a serious underestimate of the impact of the shallow level, shown in Fig. 3.12a for $X=150$, implies a further possible simplification of the fitting problem. Instead of performing a two-defect fit in the whole Δn range, the LLI and MLI part of the lifetime curve may as well be fitted by a one-defect fit. Moving the upper bound of the fit range to the Δn position of the inflection point of the original lifetime curve may serve as a (conservative) criterion for the necessary reduction of the fit range. In the present case, the k factor of the deep level determined from a one-defect fit varies between 9.5 and 8.9 if the upper bound of the fit range is varied between $3 \times 10^{14} \text{ cm}^{-3}$ (inflection point) and $1 \times 10^{15} \text{ cm}^{-3}$, and thus agrees well with the true k -value even in the broader fit range.

⁶ In general it should be possible to avoid an underestimate of the weighting factor because of the related steep increase of the Chi^2 value.

In conclusion, the investigation showed that a two-defect simulation is much less critical with respect to the unambiguousness of the spectroscopic result than expected at first glance. Moreover, it turned out that the two-defect fit may be replaced by a one-defect fit in a reduced fit range if the spectroscopic investigation only aims to characterize the defect center dominating the LLI part of the superimposed lifetime curve. This is often the case, as this defect center shows the higher recombination activity under cell operating conditions and is thus the relevant level.

For clarity it has to be stressed again that the present section is an investigation with total disregard of the inherent ambiguity of an ideal one-defect SRH simulation and just focuses on additional effects arising from the superposition of a second defect level. The important features of an ideal one-defect SRH simulation will be discussed in detail in Sects. 3.3.2 to 3.3.4.

3.3.2 The defect parameter solution surface (DPSS)

A Injection-dependent lifetime spectroscopy and its fundamental restriction

In order to examine the spectroscopic information which can be gained from a single IDLS curve, the SRH modeling of a predefined IDLS curve should be investigated in more depth. The starting point of the investigation is the general expression for the injection-dependent SRH lifetime given in Eq. (3.5). Although allowing the defect parameters to be classified in a useful way, which has been discussed in Sect. 3.2.1, expression (3.5) is fairly complex and obscures the procedure for modeling an IDLS curve. Better suited as a basis for a systematic modeling of IDLS curves are the analytical expressions for the SRH lifetime under low- and high-level injection, since these quantities are characteristics of the IDLS curve which are directly extracted from the experiment. In order to guarantee maximum generality of the following derivations, these IDLS characteristics are described by their general expressions, valid for an arbitrary doping type and an arbitrary location of the defect level within the band gap. As already shown in Sect. 3.2.1B, the SRH lifetime becomes independent of the injection level in both asymptotic cases, being given under LLI conditions by

$$\tau_{SRH}^{LLI} = \tau_{n0} \left[\left(\frac{P_0 + P_1}{P_0 + n_0} \right) + k \left(\frac{n_0 + n_1}{P_0 + n_0} \right) \right] \quad (3.22)$$

and under HLI conditions by

$$\tau_{SRH}^{HLI} = \tau_{n0} + \tau_{p0} = \tau_{n0}(1+k) \quad (3.23)$$

The fundamental difference between these asymptotic cases of SRH lifetime is their dependence on the doping concentration and the defect energy which is significant under LLI conditions and is completely missing under HLI conditions. As a consequence, the lifetime difference $\Delta\tau_{SRH}$ between HLI and LLI is a third characteristic of IDLS curves, which is directly deduced from the two other characteristics given in Eqs. (3.22) and (3.23):

$$\Delta\tau_{SRH} \equiv \tau_{SRH}^{HLI} - \tau_{SRH}^{LLI} = \tau_{n0} \left(\frac{n_0 - p_1}{p_0 + n_0} + k \frac{p_0 - n_1}{p_0 + n_0} \right) \quad (3.24)$$

While the introductory discussion of the IDLS shape in Sect. 3.2.3A has been restricted for the sake of simplicity to defects in the upper band gap half, the general validity of Eq. (3.24) now allows the IDLS shape to be analyzed for defect levels in both band gap halves, which will in fact disclose a band-gap-half-dependent difference with spectroscopic relevance.

So the maximum set of independent IDLS characteristics which can be directly extracted from experiment thus consists of two quantities: $\tau_{SRH,LLI}$ and $\Delta\tau_{SRH}$ or $\tau_{SRH,LLI}$ and $\tau_{SRH,HLI}$. The fundamental problem of IDLS concerning its applicability for defect characterization arises from the fact that the characteristic shape of the injection-dependent SRH lifetime depends on three defect parameters, as already mentioned in Sect. 3.2.3B: on the one hand directly on the energy level E_t and on the symmetry factor k and on the other hand indirectly on the common pre-factor τ_{n0} . Although the minority capture time constant is only a scaling factor, it is not known a priori and indirectly affects the determination of k . Thus, being a problem with two conditional equations (for $\tau_{SRH,LLI}$ and $\Delta\tau_{SRH}$) and three unknown variables (E_t , k and τ_{n0}), the SRH modeling of a single IDLS curve does not allow one to extract unambiguous information about the defect parameters. Instead of a discrete solution a two dimensional solution surface has to be expected.

Before addressing the question of what can be learnt from the solution surface, we first want to introduce a new modeling procedure for IDLS data which allows a straightforward determination of the *defect parameter solution surface* (DPSS) and perfectly visualizes the ambiguity of IDLS fit results. On the basis of a newly developed DPSS diagram the structural properties of the defect parameter solution surface and possible experimental expansions to circumvent the identification problem will be discussed in Sects. 3.3.3 and 3.3.4, respectively.

B A potential diagram to evaluate IDLS curves and to visualize the ambiguity of extractable defect parameters

The modeling procedure to determine the defect parameter solution surface of an IDLS curve shall be developed on the basis of an experimental data set, to demonstrate the practical use from the very beginning.

Figure 3.13a depicts an IDLS curve measured on an intentionally titanium-contaminated silicon sample using the QSSPC technique. Since surface recombination is suppressed effectively by means of a high quality SiN surface passivation, the measured effective carrier lifetime (open symbols) directly reflects bulk recombination. In order to extract the pure SRH lifetime related to the titanium centers in the bulk (closed symbols) in a maximum Δn range, the measured lifetime curve has to be corrected twofold: while the superposed external carrier trapping under low-level injection ($\Delta n < 10^{13} \text{ cm}^{-3}$) is removed by means of the bias light correction discussed in Sect. 3.3.1A, the influence of intrinsic recombination under high-level injection ($\Delta n > 10^{16} \text{ cm}^{-3}$) is eliminated by simply subtracting the CE-Auger recombination channel as discussed in Sect. 3.3.1B.

As can be seen from Fig. 3.13a, the accurate SRH modeling of the extracted injection dependence over the whole injection range requires two independent SRH centers whose impact is displayed separately. While the increase of SRH lifetime up to $\Delta n = 10^{15} \text{ cm}^{-3}$ is well described by only the deep defect level (dashed line) and is hardly affected by the shallow center (dash-dotted line), the successful modeling of the observed slight decrease of SRH lifetime under HLI conditions (above $\Delta n = 10^{15} \text{ cm}^{-3}$) strongly depends on the shallow defect level. Consequently, the total SRH lifetime (solid line), which is simply calculated as the reciprocal sum of the inverse SRH lifetimes of both defects, is equally affected by both recombination centers above $\Delta n = 10^{15} \text{ cm}^{-3}$, while below, it is almost identical with the SRH lifetime curve of the deep center. This is reflected in the defect weighting factor X , whose optimum value has been determined according to Sect. 3.3.1C to be as high as $X = 150$. As the observed two-defect nature of recombination represents a standard problem of IDLS (see Sect. 3.3.1C), the defect level dominating HLI is taken into account when determining the defect parameter solution surface (DPSS), which is associated with the defect center dominating the LLI part of the IDLS curve.

For the DPSS determination the standard SRH model given in Eq. (3.5) is adjusted to the measured IDLS curve by means of a least squares optimization for specified but gradually varied energy levels E_C-E_t of the defect center dominating LLI. The resulting electron capture time constants and symmetry factors of the defect center dominating LLI and the corresponding Chi^2 errors of the least squares optimization are displayed in

Figs. 3.13b–d as a function of the energy level E_C-E_t (closed circles). The $k^{DPSS}(E_C-E_t)$ and the $\tau_{n0}^{DPSS}(E_C-E_t)$ curves, which from now on are referred to as DPSS- k and DPSS- τ_{n0} curves, are characteristic functions of the measured IDLS curve, which contain the full information about all possible SRH parameterizations and thus represent together the DPSS of the IDLS curve. In addition to the DPSS curves of the defect center dominating LLI (closed symbols), Figs. 3.13c–d show the defect parameters of the shallow defect center dominating the HLI part of the IDLS curve (open circles). These parameters were optimized once for an arbitrarily chosen shallow energy level and then kept on fixed values within the whole DPSS analysis: $E_C-E_t=0.15\text{ eV}$, $k=0.56$, $\tau_{n0}=21.7\mu\text{s}$. Note that the SRH parameterization used for the defect center dominating HLI is only one of its own defect parameter solution surface.

Some of the basic features of the DPSS curves (closed symbols) which will be analyzed in detail in Sect. 3.3.3 already manifest themselves in Fig. 3.13. First of all, it should be emphasized that the quality of the SRH fit does not change at all in a broad energy interval which is reflected by the constant Chi^2 curve displayed in Fig. 3.13b. Thus, despite the broad codomains of the DPSS- k and the DPSS- τ_{n0} curves, which cover several orders of magnitude, the DPSS parameter triplet (E_t, k, τ_{n0}) represents equivalent solutions for the SRH parameterization of the IDLS curve, a fact that visualizes the strong inherent ambiguity of a single IDLS.

The structure of the DPSS curve is distinguished by the asymmetric energy dependence for levels in the upper and the lower half of the band gap: while the DPSS curves are defined down to the valence band edge, the continuous DPSS validity range shows a broad definition gap towards the conduction band edge, where no valid parameter triplets (E_t, k, τ_{n0}) can be found. A further characteristic of the DPSS curves is the plateau region around mid-gap. While k and τ_{n0} increase and decrease, respectively, by orders of magnitude towards the edges of the DPSS validity range, both DPSS parameters become independent of the energy level around mid-gap. The physical origin of both the asymmetry and the qualitative shape of the DPSS curves will be discussed in Sect. 3.3.3.

Thus, two characteristic quantities can be directly extracted from the DPSS diagram: (i) the energy position of the DPSS definition gap and (ii) the DPSS plateau values for the defect parameters k and τ_{n0} . The existence of these characteristics raises two fundamental questions. Do the DPSS characteristics directly agree with the true defect parameters or do they at least enable their extraction from a single IDLS curve? And is the observed DPSS structure characteristic of all DPSS curves? The answer to these questions requires analytical expressions for the DPSS curves and their characteristics which will be derived in Sect. 3.3.3.

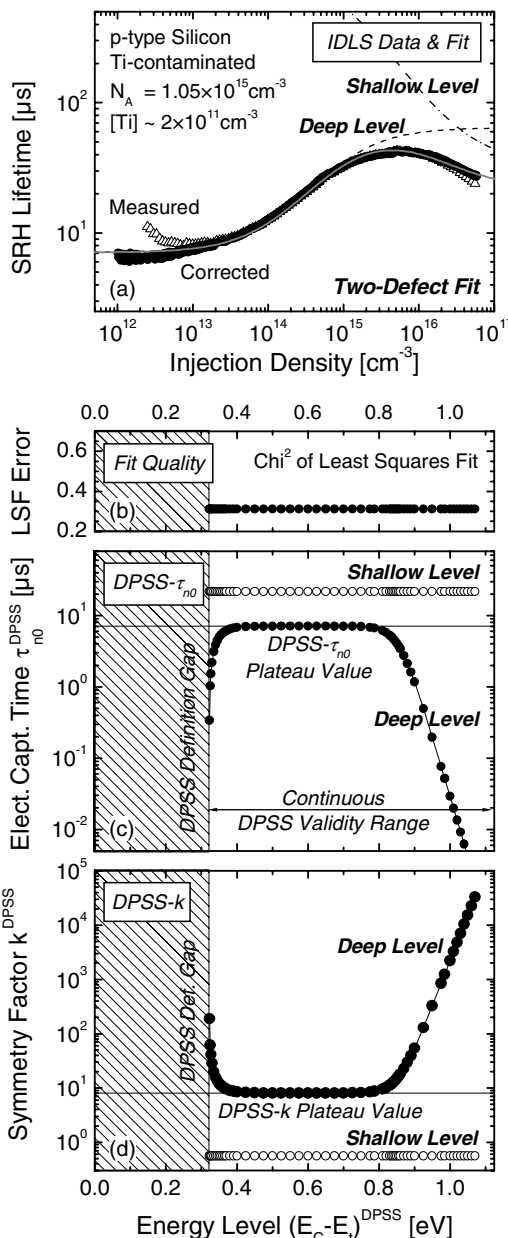


Fig. 3.13. Advanced SRH analysis of an IDLS curve measured on an intentionally titanium-contaminated silicon sample by means of the QSSPC technique. **(a)** The trapping- and Auger-corrected lifetime curve (closed symbols) can be attributed completely to SRH recombination at the titanium centers in the bulk. The accurate SRH modeling (solid line) of the measured injection dependence over the whole Δn range requires two independent SRH centers whose impact is displayed separately. **(b)-(d)** The strong ambiguity of the SRH parameterization for the deep center is visualized by means of the associated *defect parameter solution surface* (DPSS), which is determined from a least squares optimization of the standard SRH model for specified but gradually varied energy levels $E_C - E_t$ of the deep center. The Chi^2 errors of these least squares fits and the resulting electron capture time constants and symmetry factors of the deep center are displayed in **(b)-(d)**, respectively, as a function of the energy level $E_C - E_t$ of the deep center (closed circles). The DPSS curves $k^{\text{DPSS}}(E_C - E_t)$ and $\tau_{n_0}^{\text{DPSS}}(E_C - E_t)$ are characteristic functions of the measured IDLS curve which contain the full information about all possible SRH parameterizations. In the *shaded area* no valid solutions can be found. In addition to the DPSS curves of the deep center (closed circles) **(c)** and **(d)** show the defect parameters of the shallow center (open circles) which are optimized once for an arbitrarily chosen shallow energy level and then kept on fixed values within the whole DPSS analysis: $E_C - E_t = 0.15 \text{ eV}$, $k = 0.56$, $\tau_{n_0} = 21.7 \mu\text{s}$, $X = 150$.

Before starting with the theoretical analysis of the DPSS curves, the practical importance of the newly developed DPSS diagram should be summarized: first, the DPSS diagram is extracted from the measured IDLS curve in a direct and simple manner without making use of extended mathematics. Second, the DPSS analysis allows a transparent and comprehensive SRH analysis of IDLS curves and thus visualizes the strong ambiguity of the results obtained from a SRH fit of one single IDLS curve. To evaluate the suitability of the DPSS curves for an unambiguous determination of the defect parameters, the following analysis focuses on the question of how to extract the true defect parameters (i) from one single DPSS curve (see Sect. 3.3.3) and (ii) from a set of DPSS curves obtained from a set of IDLS curves which have to be fitted simultaneously (see Sect. 3.3.4).

3.3.3 Theoretical analysis I: features of the DPSS curves

Focussing in the first part of the theoretical analysis on a single pair of DPSS curves, we first discuss the physical background for their characteristic energy dependence observed in Fig. 3.13c and d. As a basis of the whole analysis we then derive analytical expressions for both DPSS curves and discuss the impact of the defect parameters on their shape and characteristics. In order to evaluate the possibility of extracting the true defect parameters from the two DPSS characteristics of a single IDLS curve, we finally derive analytical expressions for the different DPSS characteristics and investigate their spectroscopic value in depth.

A Fundamental physical difference between MinBH and MajBH defect levels

The strong and asymmetric energy dependence of the DPSS- k curve, which has been observed in Fig. 3.13d, originates from a fundamental physical difference, which is observed for defects located in the band gap half closer to the majority band (MajBH defect) and closer to the minority band (MinBH defect), respectively, concerning the sensitivity of their recombination activity to variations of the symmetry factor k .

Figure 3.14 visualizes this difference showing the influence of a capture asymmetry ($k \neq 1$) on the injection dependence of SRH lifetime calculated in Fig. 3.14a for a MinBH defect (in p -type Si: $p_i \ll n_i$) and in Fig. 3.14b for a MajBH defect (in p -type Si: $p_i \gg n_i$) with the same energy depth $\Delta E_t = 0.3$ eV. While the symmetry factor affects SRH lifetime under HLI conditions irrespective of the energy position of the defect center, an impact on the SRH lifetime under LLI conditions is only observed for defects in the MinBH.

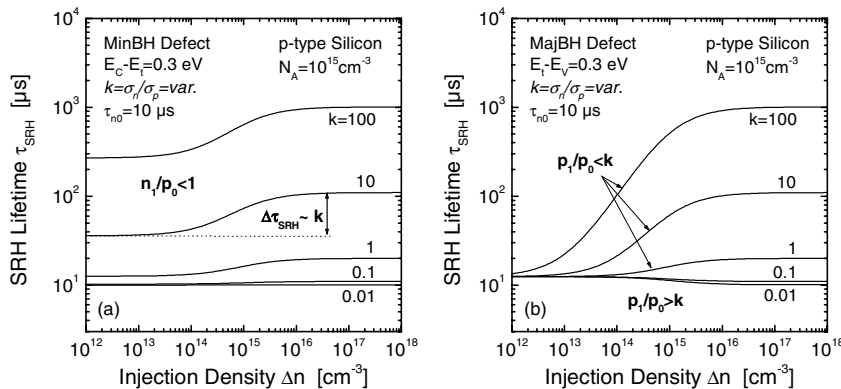


Fig. 3.14. Influence of a capture asymmetry ($k \neq 1$) on the IDLS curves at 300 K **(a)** for a MinBH defect and **(b)** for a MajBH defect with same energy depth. While the symmetry factor affects the SRH lifetime under HLI conditions irrespective of the energy position of the defect center, an impact on the SRH lifetime under LLI conditions is only observed for defects in the MajBH. As a consequence, in the case of a MinBH defect the symmetry factor k does not influence the qualitative shape of IDLS curves, i.e., $\Delta\tau_{SRH}$ being negative or positive, but only acts as proportionality factor for the characteristic lifetime difference between LLI and HLI. In contrast, in the case of a MajBH defect the symmetry factor has a strong impact on the qualitative shape of the IDLS curve.

Physical reason

The physical reason for the observed difference under LLI conditions is that recombination via a MajBH defect is completely limited by minority carrier capture since the minority band is less populated and more distant from the defect level than the majority band. For both reasons the quantum mechanical probability of minority carrier capture is reduced compared to that of majority carrier capture. Since normal capture asymmetries as shown in Fig. 3.14 cannot invert these proportions, the LLI-SRH lifetime for a MajBH defect does not depend on the symmetry factor k .⁷ On the contrary, recombination via a MinBH defect can be limited by minority or majority capture. Whether the capture of minority carriers from the slightly populated minority band or the capture of majority carriers from the distant majority band limits recombination via a MinBH defect, strongly depends on the ratio of the capture cross-sections, i.e., on the symmetry factor k .

Under HLI conditions the differences between a MinBH and a MajBH defect disappear. As the population asymmetry between the minority and

⁷ This situation only changes for $k \gg 1$ (i.e., $\sigma_p \ll \sigma_n$) when minority carrier capture is extremely enhanced compared to majority carrier capture due to a strong asymmetry in the capture cross-sections.

majority band vanishes, the SRH lifetime no longer depends on the energy level E_t but symmetrically on the pure time constants of both capture processes and thus on the symmetry factor k as already derived in Eq. (3.8) and shown in Fig. 3.14.

Quantitative analysis

A more quantitative analysis of the divergence between a MinBH and a MajBH defect which combines the discussed results under LLI and HLI can be obtained from a closer look at the analytical expression for the lifetime difference $\Delta\tau_{SRH}$. To allow a detailed and quantitative comparison of the effectiveness of both capture processes under HLI and LLI, Eq. (3.24) is simplified for a p -type semiconductor ($p_0 \gg n_0$) while any further simplification is avoided:⁸

$$\Delta\tau_{SRH}^p = \overbrace{\tau_{n0} + \tau_{p0}}^{=\tau_{SRH}^{HLI,p}} - \underbrace{\left(\tau_{n0} + \tau_{n0} \frac{p_1}{p_0} + \tau_{p0} \frac{n_1}{p_0} \right)}_{=\tau_{SRH}^{LLI,p}} \quad (3.25)$$

Analytically, the qualitative shape of the IDLS curve is directly reflected in the sign of $\Delta\tau_{SRH}$, negative and positive values being related to decreasing and increasing IDLS curves, respectively.

In the case of a MinBH defect, when the p_1 -dependent term in Eq. (3.25) vanishes ($n_1 \gg p_1$), the limitation of recombination due to minority carrier capture (in p -type: electron capture) is identical under HLI and LLI. Consequently, the qualitative shape of the IDLS curve only depends on the difference concerning the effectiveness of majority carrier capture under LLI and HLI and thus on the population statistics and the energy position E_t , but not on the symmetry factor k . If Eq. (3.25) is simplified for a MinBH defect

$$\Delta\tau_{SRH}^{p,MinBH} = k \cdot \tau_{n0} \left(1 - n_1 / p_0 \right) \quad (3.26)$$

it turns out that k only acts as proportionality factor for the characteristic lifetime difference between LLI and HLI without having any influence on its sign. The latter only depends on the magnitude of the ratio n_1/p_0 . For $n_1/p_0 < 1$, when majority capture is more effective under LLI than under HLI, the IDLS curve increases for arbitrary k while it decreases in the opposite case.

In contrast to that, in the case of a MajBH defect, when the n_1 -dependent term in Eq. (3.25) vanishes ($p_1 \gg n_1$), recombination under LLI

⁸ The τ_{n0} - and τ_{p0} -related contributions in Eq. (3.25) have to be attributed to electron and hole capture, respectively.

is limited twofold by minority carrier capture due to the asymmetric population of the bands and the energy position of the defect while no limitation due to majority carrier capture exists. Under HLI conditions on the other hand, recombination depends symmetrically on both capture processes. Comparing the effectiveness of each of the capture processes under LLI and HLI, it turns out that minority carrier capture is less effective under LLI than under HLI while it is the opposite for majority carrier capture.⁹ As a result Eq. (3.25) is simplified for a MajBH defect to

$$\Delta\tau_{SRH}^{p,MajBH} = \tau_{n0} (k - p_1/p_0) \quad (3.27)$$

Equation (3.27) reveals that the symmetry factor k is no longer a pure proportionality factor of the characteristic lifetime difference $\Delta\tau_{SRH}$, but has a direct impact on the sign of $\Delta\tau_{SRH}$ and thus on the qualitative shape of the IDLS curve: if the level-dependent part of minority carrier capture under LLI is more effective than majority carrier capture under HLI, i.e., if $\tau_{n0} \times p_1/p_0 < \tau_{p0}$ and $p_1/p_0 < k$, respectively, the IDLS curve increases while it decreases in the opposite case. In terms of the symmetry factor k , this observation corresponds to the following rule: the higher the k factor, i.e., the more effective the capture properties for minority carriers compared with those for majority carriers, the smaller the energy interval above the valence band edge in which defect energy levels E_t lead to a decreasing IDLS curve.

Impact on the DPSS structure

Against this physical background, the structure of the DPSS curve which has been determined in Fig. 3.13 can be fully understood. Given the measured IDLS curve with its characteristic lifetime increase $\Delta\tau_{SRH}$, the associated DPSS curves in Fig. 3.13 exhibit three characteristic regions. (a) As long as the energy levels E_t for the modeling of the IDLS curve are chosen from an interval around mid-gap in which the ratios n_1/p_0 and p_1/p_0 are much smaller than 1 and can thus be neglected, the resulting DPSS- k and DPSS- τ_{n0} values do not depend on the energy level E_t which leads to the observed plateau region in both DPSS curves. (b) When the assumed energy level E_t approaches the majority band edge (in p -type: the valence band edge), minority carrier capture under LLI is increasingly suppressed due to the energy position of the defect level. To avoid a qualitative change in the IDLS curve from an increasing to a decreasing shape, the deactivation of the defect has to be compensated by an enhancement of the minority carrier capture process which can be achieved by increasing the

⁹ This is reflected by a total minority capture time which is increased under LLI by the term $\tau_{n0} \times p_1/p_0$ and a total majority capture time which is increased under HLI by the term τ_{p0} .

capture cross-section of minority carriers compared to that of majority carriers and thus by increasing the capture asymmetry $k = \sigma_n/\sigma_p$. As a result, the DPSS- k curve strongly increases with decreasing energy depth of the assumed MajBH defect. Since the overall recombination activity of the defect center has to remain unchanged, the minority capture time constant τ_{n0} , which is a simple scaling factor of SRH lifetime, has to be reduced simultaneously. This leads to the strong decrease of the DPSS- τ_{n0} curve.¹⁰ (c) The situation changes when the energy level approaches the minority band edge (in *p*-type: the conduction band edge). The increasing suppression of majority carrier capture under LLI due to the energy position of the defect leads to an increase in the LLI-SRH lifetime and thus a shrinkage of $\Delta\tau_{SRH}$ as the HLI-SRH lifetime is not affected by the E_t variation. Since k acts as proportionality factor of $\Delta\tau_{SRH}$ as shown in Eq. (3.26), a compensation for the $\Delta\tau_{SRH}$ shrinkage is achieved by an increase in the k factor. However this leads to a reduction in the overall recombination activity which can be seen, e.g., in Eq. (3.23) from the related increase in the HLI-SRH lifetime. To ensure a stable overall recombination activity of the defect center, the increase in the DPSS- k curve thus has to be accompanied by a decrease in the DPSS- τ_{n0} curve. As soon as the energy level of the assumed MinBH defect falls below a characteristic value which will be determined in Sect. 3.3.3D, the DPSS curves are no longer defined. This DPSS definition gap towards the minority band has its roots in the fact that the IDLS curves which are associated with the DPSS- E_t values from this energy interval show a characteristic decrease for arbitrary k and thus cannot describe the increasing shape of the given IDLS curve, under any circumstances.

Having clarified the physical origin of the characteristic DPSS structure, we now wish to develop analytical expressions for the DPSS curves and their characteristics to enable a theoretical evaluation of the suitability of the DPSS analysis for a complete defect characterization.

B Derivation of analytical equations for the DPSS curves

K^{DPSS} and τ_{n0}^{DPSS}

Starting point for the derivation of analytical expressions for the DPSS curves are the two conditional equations (3.6) and (3.24) for the independent IDLS characteristics $\tau_{SRH,LLI}$ and $\Delta\tau_{SRH}$, whose values are directly extracted from the experiment. To enable the analytical DPSS determination, Eqs. (3.6) and (3.12) are no longer regarded as functions of the true

¹⁰ Note that the decrease of the DPSS- τ_{n0} curve directly reflects the σ_n increase, which is related to the increase in the DPSS- k curve.

defect parameters E_C-E_t , k and τ_{n0} but as function of the DPSS parameters $(E_C-E_t)^{DPSS}$, k^{DPSS} and τ_{n0}^{DPSS} . Following the experimental procedure of DPSS determination as presented in Sect. 3.3.2B, $(E_C-E_t)^{DPSS}$ is regarded as an independent variable while k^{DPSS} and τ_{n0}^{DPSS} are regarded as dependent variables, whose functional dependence on $(E_C-E_t)^{DPSS}$ should be determined. Since Eqs. (3.6) and (3.12) only exhibit an indirect E_t -dependence via the SRH densities n_1 and p_1 , the following equations are regarded as a function of n_1^{DPSS} and p_1^{DPSS} instead of $(E_C-E_t)^{DPSS}$. This simplifies the necessary transformations to determine the functional connection between the DPSS parameters and increases the clarity of the expressions derived.

In the general case of arbitrary doping type and arbitrary location of the defect level within the band gap, which is assumed whenever not specified otherwise, the set of conditional DPSS equations takes the following shape:

$$\tau_{SRH}^{LLI} = \tau_{n0}^{DPSS} \left[\left(\frac{p_0 + p_1^{DPSS}}{p_0 + n_0} \right) + k^{DPSS} \left(\frac{n_0 + n_1^{DPSS}}{p_0 + n_0} \right) \right] \quad (3.28a)$$

$$\Delta\tau_{SRH} = \tau_{n0}^{DPSS} \left[\left(1 - \frac{p_0 + p_1^{DPSS}}{p_0 + n_0} \right) + k^{DPSS} \left(1 - \frac{n_0 + n_1^{DPSS}}{p_0 + n_0} \right) \right] \quad (3.28b)$$

Solving this system of linear equations, the following analytical expressions are derived for the DPSS parameters k^{DPSS} and τ_{n0}^{DPSS} :

$$k^{DPSS} = \frac{-(p_0 + n_0) + (p_0 + p_1^{DPSS}) (1 + \Delta\tau_{SRH} / \tau_{SRH}^{LLI})}{(p_0 + n_0) - (n_0 + n_1^{DPSS}) (1 + \Delta\tau_{SRH} / \tau_{SRH}^{LLI})} \quad (3.29a)$$

$$\tau_{n0}^{DPSS} = \frac{\Delta\tau_{SRH} (n_0 + n_1^{DPSS}) - \tau_{SRH}^{LLI} (p_0 - n_1^{DPSS})}{(n_0 + n_1^{DPSS}) - (p_0 + p_1^{DPSS})} \quad (3.29b)$$

Since Eqs. (3.29a) and (3.29b) describe the dependent DPSS parameters k^{DPSS} and τ_{n0}^{DPSS} as a function of the independent DPSS parameter $(E_C-E_t)^{DPSS}$ – which only appears via n_1^{DPSS} and p_1^{DPSS} – subject to the experimentally accessible IDLS characteristics $\tau_{SRH,LLI}$ and $\Delta\tau_{SRH}$, they are the defining equations for the DPSS- k and the DPSS- τ_{n0} curve, which are associated with an IDLS curve of specified $\tau_{SRH,LLI}$ and $\Delta\tau_{SRH}$. While the DPSS- k curve only depends on the ratio $\Delta\tau_{SRH} / \tau_{SRH,LLI}$ of the IDLS characteristics, their absolute quantities insert into the expression for the DPSS- τ_{n0} curve.

Equations (3.29a) and (3.29b) contain the full dependence of the DPSS curves on the true defect parameters E_t , k and τ_{n0} although concealed behind the IDLS characteristics $\tau_{SRH,LLI}$ and $\Delta\tau_{SRH}$. The direct dependence of the DPSS curves on the true defect parameters is revealed if the IDLS

characteristics in Eqs. (3.29a) and (3.29b) are replaced by their analytical expressions which are given by Eqs. (3.28a) and (3.28b) if written for the true defect parameters E_t , k and τ_{n0} instead of the DPSS parameters. Again an increased clarity of the derived expressions is achieved if Eqs. (3.28a) and (3.28b) are treated as functions of the true SRH densities n_1 and p_1 instead of the true energy level E_C-E_t . After some transformations one ends up with the following expressions:

$$k^{DPSS} = \frac{k(-p_0 + n_0) + (p_1 + kn_1) - p_1^{DPSS}(1+k)}{(-p_0 + n_0) - (p_1 + kn_1) + n_1^{DPSS}(1+k)} \quad (3.30a)$$

$$\tau_{n0}^{DPSS} = \tau_{n0} \frac{(p_0 - n_0) + (p_1 + kn_1) - n_1^{DPSS}(1+k)}{(p_0 - n_0) + (p_1^{DPSS} - n_1^{DPSS})} \quad (3.30b)$$

Due to the direct functional connection of Eqs. (3.30a) and (3.30b) with the true defect parameters, the following theoretical investigation of the DPSS curves is completely based on these equations referred to as *DPSS equations*.

Being derived without any approximation concerning the doping type, Eqs. (3.30a) and (3.30b) in principle describe the DPSS associated with an IDLS curve for both doping types. Nevertheless, they constitute the natural set of equations only for p -type doping but not for n -type doping. As discussed in detail in Sect. 3.2.1A, the natural quantity to normalize the SRH lifetime is the minority capture time constant, which is not only a simple scaling factor for the SRH lifetime, as is the majority capture time constant as well, but also its absolute minimum. Thus, to achieve full symmetry between n - and p -type doping concerning the structure and interpretation of the DPSS, the set of conditional DPSS equations (3.28) generally has to be written in multiples of the respective minority capture time constant which implies a difference in the natural set of DPSS parameters given by $(E_C-E_t)^{DPSS}$, k^{DPSS} , τ_{n0}^{DPSS} for p -type doping and $(E_C-E_t)^{DPSS}$, k^{DPSS} , τ_{p0}^{DPSS} for n -type doping. In the above equations these requirements are met for p -type doping. For n -type doping, however, the set of conditional DPSS equations (3.28) has to be rewritten in multiples of the hole capture time constant τ_{p0}^{DPSS} . Due to the identity $\tau_{p0}^{DPSS} = k^{DPSS} \times \tau_{n0}^{DPSS}$ this is achieved without any redefinition by extracting the factor k^{DPSS} from the terms in square brackets. As a consequence, the k -dependence in Eq. (3.28) is transformed into a $1/k$ -dependence and moved from the n_1 - to the p_1 -dependent terms. If the above derivation of the DPSS equations is repeated, it turns out that the analytical expression (3.30a) for the DPSS- k curve is identically reproduced while the expression for the DPSS- τ_{p0} curve is subject to slight changes compared to the expression (3.30b) for the DPSS- τ_{n0} curve:

$$\tau_{p0}^{DPSS} = \tau_{p0} \frac{(p_0 - n_0) - (k^{-1} p_1 + n_1) + p_1^{DPSS} (k^{-1} + 1)}{(p_0 - n_0) + (p_1^{DPSS} - n_1^{DPSS})} \quad (3.31)$$

Thus, if one describes the DPSS in the case of an *n*-type semiconductor by Eqs. (3.30a) and (3.31), the structure of the DPSS fully corresponds to the structure derived from Eqs. (3.30a) and (3.30b) for a *p*-type semiconductor. The complete transfer of the results is achieved, if only the effect of the two fundamental differences between *n*- and *p*-type is taken into account. While the permutation of the minority and majority band is reflected in a transposition of both DPSS diagrams at a vertical axis through $(E_C - E_t)^{DPSS} = E_{gap}/2$, the $1/k$ -dependence of the IDLS characteristics due to the τ_{p0} normalization results in an additional transposition of only the DPSS- k diagram at a horizontal axis through $k^{DPSS} = k$. Since these two rules enable a direct and easy transfer of the DPSS results from *p*- to *n*-type doping, all DPSS curves and characteristics displayed throughout the work are calculated only for a *p*-type semiconductor according to Eqs. (3.30a) and (3.30b). The physical interpretation of the diagrams and expressions is also performed for the case of a *p*-type semiconductor although being kept in general terms by addressing electrons as minority and holes as majority carriers, which enables a direct transfer to the case of an *n*-type semiconductor.

C Impact of the defect parameters on the shape of the DPSS curves

The structure of the DPSS equations (3.30a) and (3.30b) implies a natural classification of the defect parameters in terms of their impact on the shape of the DPSS curves, which is similar to the classification deduced in Sect. 3.2.1A from their general impact on the shape of the lifetime curves. Consider that the true defect energy level E_t only appears in the DPSS equations through the related SRH densities n_t and p_t . Since the relative defect parameters E_t and k then only contribute to some of the terms in Eqs. (3.30a) and (3.30b), they have a crucial influence on the shape of both DPSS curves, which will be analyzed later in this section. In contrast, the absolute defect parameter τ_{n0} does not affect the DPSS- k curve at all and only appears as common pre-factor in the expression for the DPSS- τ_{n0} curve. Consequently, τ_{n0} only induces vertical shifts of the DPSS- τ_{n0} curve but no changes in its shape. Thus, the τ_{n0} dependence of the DPSS curves is of minor importance and will not be considered in the following.

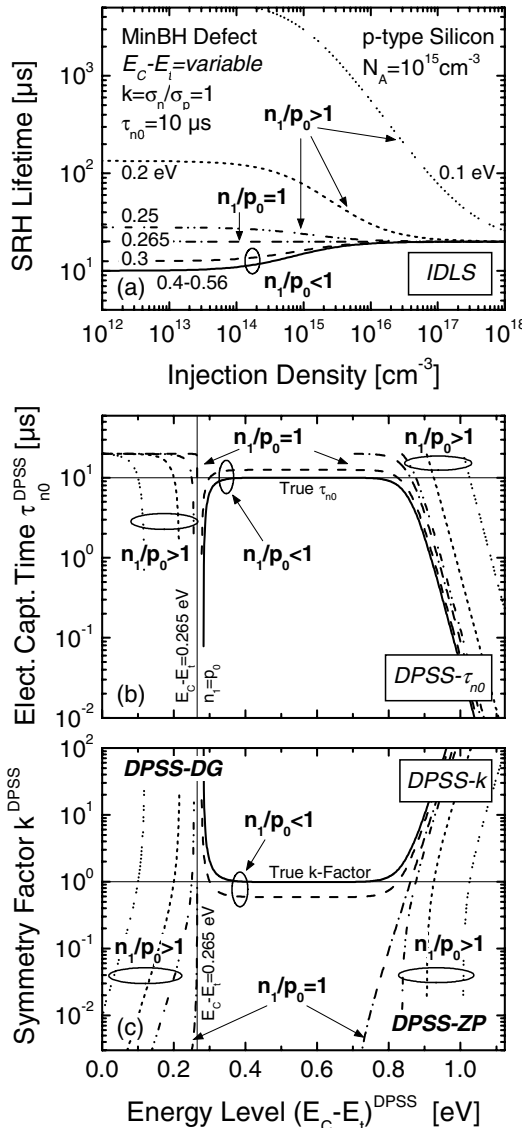


Fig. 3.15. Influence of the defect energy level E_t on the shape of the DPSS curves for symmetric capture cross-sections ($k=1$). While (a) displays IDLS curves calculated for MinBH defects with varying energy depth, (b) and (c) show the associated DPSS- τ_{n0} and DPSS- k curves calculated from Eq. (3.30). Two classes of DPSS curves have to be distinguished: DPSS curves with continuous and split range of validity.

Impact of the energy level

The influence of the defect energy level E_t on the shape of the DPSS curves is illustrated in Fig. 3.15 for symmetric capture cross-sections ($k=1$). While Fig. 3.15a displays IDLS curves calculated for MinBH defects with varying energy depth, Figs. 3.15b and c show the associated DPSS- τ_{n0} and DPSS- k curves calculated from Eq. (3.30).

The observed transition of the IDLS curves from an increasing to a decreasing shape when the defect level is moved from mid-gap to the minority band edge originates from the fact that recombination activity of a defect center does not depend on the energy level under HLI conditions [see Eq. (3.8)] while a strong dependence exists under LLI conditions [see Eq. (3.6)]: due to the increasing suppression of majority carrier capture when the energy level approaches the minority band edge, recombination activity of the defect center decreases under LLI, and this leads to the observed increase in the LLI-SRH lifetime.

As can be seen in Fig. 3.15b and c, the qualitative divergence in the shape of the IDLS curves is reflected in two classes of DPSS curves. For ratios $n_I/p_0 < 1$, i.e., for increasing IDLS curves, the DPSS curves have a continuous range of validity with a definition gap towards the conduction band and exhibit the typical tub-like structure as already observed in Fig. 3.13. However, for ratios $n_I/p_0 = 1$ and $n_I/p_0 > 1$, i.e., for constant or decreasing IDLS curves, the DPSS curves have a split range of validity with a definition gap around mid-gap and do not show any plateau region as observed for the other DPSS class. Instead of the plateau region, these DPSS curves exhibit a new DPSS characteristic: a zero point in the lower half of the band gap.

Physically the split DPSS curves originate from the fact that a decreasing IDLS curve cannot be realized for defect energy levels around mid-gap. Since recombination via a deep level is most effective under LLI conditions, which is reflected in the fact that the SRH lifetime reaches its absolute minimum (see Fig. 3.4), given by the minority capture time constant [see Eq. (3.6) for $n_I/p_0, p_I/p_0 \ll 1$], the SRH lifetime increases towards higher injection levels, irrespective of k , being limited under HLI by the sum of both capture time constants [see Eq. (3.8)]. The fundamental prerequisite for the SRH modeling of a decreasing IDLS curve is that recombination under LLI conditions is kept less effective than under HLI conditions. This is most easily achieved for shallow defect levels close to either band edge. When the assumed energy level E_t is moved from the minority (majority) band edge deeper into the band gap, majority (minority) carrier capture is enhanced due to the energy position of the defect level. In order to guarantee the fixed lifetime decrease $\Delta\tau_{SRH} < 0$ of the original IDLS curve subject to the DPSS analysis, the coupled activation of the defect has to be compensated by a suppression of the majority (minority) capture process by means of an increased (decreased) capture asymmetry k , which is related to a relative decrease of the majority (minority) capture cross-section. As a result the DPSS- k curve increases (decreases) significantly with increasing energy depth of the assumed MinBH (MajBH) defect, as observed in Fig. 3.15. If the energy depth of the assumed MinBH (MajBH)

defect exceeds a characteristic energy depth, the MinBH (MajBH) branch of the split DPSS curve is no longer defined since the IDLS curves associated with the DPSS- E_t values from that energy interval show a characteristic increase for k values that are compatible with the original IDLS curve. In the following these discrete energy positions for the MinBH and the MajBH branch of the DPSS curve are referred to as the DPSS definition gap (DPSS-DG) and DPSS zero point (DPSS-ZP), respectively.

Impact of the symmetry factor

The influence of a capture asymmetry ($k \neq 1$) on the shape of the DPSS curve is shown in Fig. 3.16 for a MajBH defect. While Fig. 3.16a displays IDLS curves which are calculated for MajBH defects at $E_t - E_V = 0.3$ eV with varying symmetry factor k , Fig. 3.16b and c show the associated DPSS- τ_{n0} and DPSS- k curves calculated from Eq. (3.30). The physical reasons for the observed changes in the shape of the IDLS curves upon k variations have been discussed in detail in Sect. 3.3.3A. Again the two classes of DPSS curves are observed. For $p_1/p_0 < k$, i.e., for increasing IDLS curves, the DPSS analysis leads to the tub-like DPSS curves with continuous range of validity. However for $p_1/p_0 > k$, i.e., for decreasing IDLS curves, the associated DPSS curves exhibit the split range of validity with a definition gap around mid-gap. Concerning the structure of the DPSS curves, the observations in Figs. 3.15 and 3.16 reveal the inherent law that decreasing IDLS curves are characterized by a split DPSS while increasing IDLS curves are characterized by a continuous DPSS.

Impact of the band gap half

From this, the impact the band gap half of the defect center has on the shape of the DPSS curves can easily be deduced. To visualize the following considerations, Fig. 3.17 displays the impact of a capture asymmetry ($k \neq 1$) analogously to Fig. 3.16 for defects of the same energy depth but located in the opposite band gap half, i.e., at $E_C - E_t = 0.3$ eV (MinBH). Since the IDLS curves for a MinBH and a MajBH defect with the same energy depth are identical for $k = 1$ (except for small numerical corrections related to small deviations between N_C and N_V), the impact of the energy level E_t on the shape of the DPSS curves, which is shown in Fig. 3.15, is the same for a symmetric MajBH defect as for a symmetric MinBH defect. This can be seen in Figs. 3.16 and 3.17, the DPSS curves for $k = 1$ (solid lines) being identical. In contrast, the impact of a capture asymmetry on the shape of the DPSS curves strongly depends on the band gap half of the defect center. Instead of the k -dependent structure of the DPSS curves associated with MajBH defects of fixed energy level but varying k factors (see Fig. 3.16), the structure of the DPSS curves associated with the corresponding MinBH defects does not depend on the k factor but only on the energy level E_t (see Fig. 3.17). For MinBH defects with $n_1/p_0 < 1$, as

shown in Fig. 3.17, the DPSS curves will be continuous, irrespective of the k value of the defect center, which reflects the k -independent increase of the IDLS curves shown in Fig. 3.14a. Correspondingly, for MinBH defects with $n_1/p_0 > 1$ the DPSS curves will be split for arbitrary k .

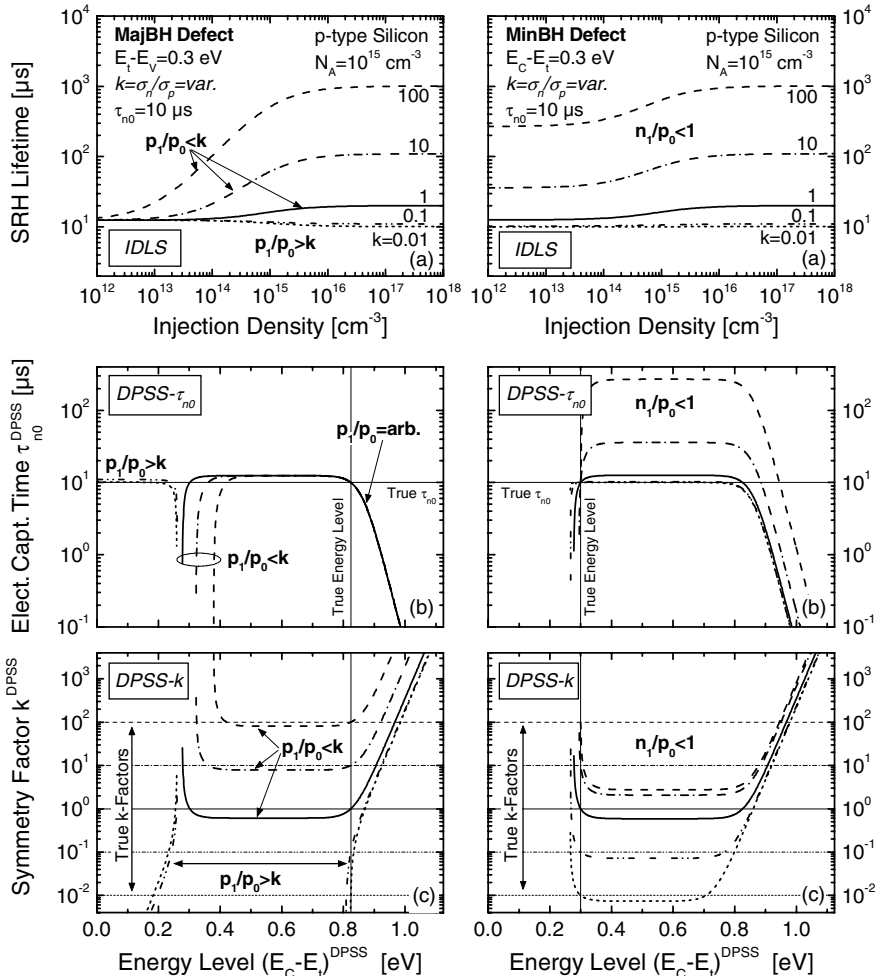


Fig. 3.16. Influence of a capture asymmetry ($k \neq 1$) on the shape of the DPSS curves for a MajBH defect. While (a) displays IDLS curves which are calculated for MajBH defects at $E_t - E_v = 0.3$ eV with varying symmetry factor k , (b) and (c) show the associated DPSS- τ_{n0} and DPSS- k curves calculated from Eq. (3.30).

Fig. 3.17. Influence of a capture asymmetry ($k \neq 1$) on the shape of the DPSS curves for a MinBH defect. While (a) displays IDLS curves which are calculated for MinBH defects at $E_C - E_t = 0.3$ eV with varying symmetry factor k , (b) and (c) show the associated DPSS- τ_{n0} and DPSS- k curves calculated from Eq. (3.30).

Since the DPSS analysis aims at determining the true defect parameters, special attention has to be given to the DPSS characteristics. Some general trends concerning the relation between the DPSS characteristics and the true defect parameters can be directly extracted from Figs. 3.15 to 3.17.

Figure 3.15c shows that the DPSS-DG energy and the DPSS-ZP energy are shifted significantly towards the minority and the majority band edge, respectively, as the energy level E_t of the true defect center approaches one of the band edges. Nevertheless, this strong E_t -dependence is only observed for shallow defect centers with $n_t/p_0 > 1$ while for deep centers with $n_t/p_0 < 1$ the DPSS-ZP is no longer defined and the E_t -dependence of the DPSS-DG energy almost vanishes. The latter directly reflects the small differences in the underlying IDLS curves. It can be concluded that a direct determination of the true defect energy from the two characteristic DPSS energies may be possible for shallow defect centers, being characterized by decreasing IDLS and split DPSS curves. The problem, when analyzing a completely unknown system, becomes obvious in Fig. 3.16c, which shows that both characteristic DPSS energies depend not only on the energy level E_t but also on the symmetry factor k of the true defect center.

For deep centers with $n_t/p_0 < 1$ or $p_t/p_0 < k$, which are characterized by increasing IDLS and continuous DPSS curves, the third DPSS characteristic, the DPSS- k value at mid-gap which is referred to as the DPSS plateau k value (DPSS-PL), seems to be most relevant. As illustrated in Fig. 3.16c, the DPSS plateau values are close to the k factors of the underlying true defect centers. Nevertheless, Fig. 3.15c shows that the quality of the correspondence between the DPSS-PL k value and the true k factor strongly depends on the energy level E_t of the true defect center, the quality being the better the deeper the energy level. In addition Fig. 3.17c shows that the k -value itself may have an impact on the quality of the correspondence.

Thus, in order to evaluate the possibility of extracting the true defect parameters from the DPSS characteristics of a single DPSS curve and to assess the accuracy of this extraction, the dependence of the DPSS characteristics on the true defect and material parameters has to be investigated systematically.

D Analytical derivation of DPSS characteristics and their dependence on the true defect parameters

On the basis of the DPSS equations (3.30), in the following section analytical expressions for all three DPSS characteristics are derived. Their dependence on the true defect parameters E_t and k is displayed from Figs. 3.20 to 3.22 and will be discussed in depth in Sect. 3.3.3E within a detailed evaluation of the spectroscopic value of the isolated DPSS characteristics.

As discussed at the end of Sect. 3.3.3B, the natural set of constitutive DPSS equations depends on the doping type. Since the expression for the DPSS- k curve is identically reproduced for both doping types, Eq. (3.30a) is taken as a basis for the following derivation which ensures the general validity of the derived expressions not only for an arbitrary location of the defect level within the band gap but also for an arbitrary doping type. Although in the physical interpretation of the derived expressions the focus is on the case of a p -type semiconductor, the expected structural differences in an n -type semiconductor will be pointed out roughly for the sake of completeness. As will be shown, these changes are fully compatible with the rules specified at the end of Sect. 3.3.3B for the transfer of DPSS diagrams.

Due to the indirect $(E_C - E_t)^{DPSS}$ -dependence of the DPSS equations (3.30) via the SRH densities n_1^{DPSS} and p_1^{DPSS} , the derivation of the characteristic DPSS energies $(E_C - E_t)^{DPSS-XX}$ from Eq. (3.30a) results in expressions for the associated SRH densities $n_1^{DPSS-XX}$ or $p_1^{DPSS-XX}$. For physical reasons these expressions are only defined for positive values, which leads directly to a parameter range of definition for the DPSS characteristics. Within this parameter range of definition the characteristic DPSS energies $(E_C - E_t)^{DPSS-XX}$, which correspond to the extracted SRH densities, can be directly deduced from Eq. (3.2) and may be written as $(E_C - E_t)^{DPSS-XX} = -k_B T \times \ln(n_1^{DPSS-XX}/N_C)$.

DPSS definition gap function

An expression for the characteristic energy position $(E_C - E_t)^{DPSS-DG}$ of the DPSS definition gap is found if the denominator of expression (3.30a) for the DPSS- k curve is equated with zero. The result for the associated SRH density is

$$n_1^{DPSS-DG} = \frac{(p_0 - n_0) + (p_1 + k n_1)}{(1 + k)} \quad (3.32)$$

For a p -type semiconductor ($n_0 \ll p_0$) expression (3.32) gets positive values irrespective of the defect parameters E_t and k . Thus, the DPSS-DG is defined within the whole parameter range. Note that the associated energy level would be located around mid-gap if the SRH density $n_1^{DPSS-DG}$ was of the order of the intrinsic carrier concentration $n_i = 10^{10} \text{ cm}^{-3}$. Since $n_1^{DPSS-DG}$ significantly exceeds n_i for realistic material and defect parameters, the DPSS-DG is located in the upper half of the band gap, i.e., in the band gap half close to the minority band for p -type doping, and may be written as $(E_C - E_t)^{DPSS-DG} = -k_B T \times \ln(n_1^{DPSS-DG}/N_C)$.

Concerning the quantitative dependence of the DPSS-DG on the material and defect parameters, one major aspect should be pointed out

here in anticipation of the detailed discussion in Sect. 3.3.3E. As can be seen from Eq. (3.32), the DPSS-DG energy only depends on the true energy level E_t for $k \times n_1 > p_0$ or $p_1 > p_0$, i.e., for shallow defect levels near both band edges. For deep levels ($n_1, p_1 \ll p_0$), however, the DPSS-DG energy becomes independent of E_t and is retained at a fixed value related to the doping concentration. This nicely explains the observations in Fig. 3.15c. It can be concluded that for shallow levels the DPSS-DG energy may at best provide a reasonable approximation for the true energy level E_t . Taking into account that the DPSS-DG simultaneously depends on both defect parameters E_t and k , the quality of the agreement between the DPSS-DG energy and the true energy is investigated in detail in Sect. 3.3.3E (see Fig. 3.6).

DPSS zero point function and its definition gap

An expression for the characteristic energy position $(E_C - E_t)^{DPSS-ZP}$ of the DPSS zero points can be deduced if the numerator of expression (3.30a) for the DPSS- k curve is equated with zero. The associated SRH density is given by

$$p_1^{DPSS-ZP} = \frac{k(-p_0 + n_0) + (p_1 + kn_1)}{(1+k)} \quad (3.33)$$

For a p -type semiconductor ($n_0 \ll p_0$), the parameter range of definition of the DPSS-ZP energy is restricted, since $p_1^{DPSS-ZP}$ becomes negative once the underlying defect center reaches an energy depth such that both related SRH densities n_1 and p_1 are small enough to fulfill the inequality $k \times p_0 > p_1 + k \times n_1$. Nevertheless, if $p_1^{DPSS-ZP}$ is positive and thus defined, $p_1^{DPSS-ZP}$ significantly exceeds n_1 except for a narrow transition region around the zero points of Eq. (3.33). Consequently, the DPSS-ZP is located in most cases in the lower half of the band gap, i.e., in the band gap half close to the majority band for p -type doping, and may be written, if defined, as $(E_t - E_V)^{DPSS-ZP} = -k_B T \times \ln(p_1^{DPSS-ZP}/N_V)$.

Since the existence of the DPSS-ZP directly correlates with the qualitative structure of the DPSS curves as observed in Sect. 3.3.3C, the exact position of its definition gap is of fundamental interest. If Eq. (3.33) for the DPSS-ZP energy is regarded as a continuous function of the true defect energy level E_t , as displayed in Fig. 3.21a, the definition gap of the DPSS-ZP function (DG/DPSS-ZP) around mid-gap is bounded by the energy positions $(E_C - E_t)^{DG/DPSS-ZP}$ of the zero points of Eq. (3.33). We arrive at an analytical expression for the associated SRH densities $n_1^{DG/DPSS-ZP}$ by equating the numerator of Eq. (3.33) with zero, then eliminating p_1 upon use of the identity $p_1 = n_1^2/n_1$ and finally solving the resulting quadratic equation for n_1 :

$$n_1^{DG/DPSS-ZP} \Big|_{+/-} = 1/2 \times \left[(p_0 - n_0) \pm \sqrt{(p_0 - n_0)^2 - 4n_i^2/k} \right] \quad (3.34)$$

The energy boundaries of the DPSS-ZP definition gap which are related to the ‘plus’ and ‘minus’ solution in Eq. (3.34) are located in the upper and the lower half of the band gap, respectively. While the DPSS-ZP is not defined for energy levels in-between these boundaries, i.e., for deep defect centers, it is defined for energy levels in the rest of the band gap, i.e., for shallow defect centers near both band edges.¹¹ The position and width of the DPSS-ZP definition gap only depend on the symmetry factor k and the doping concentration N_{dop} , whose impact is shown in Fig. 3.21a and c, respectively, and will be discussed in Sect. 3.3.3E.

Thus, only being defined for shallow levels, the DPSS-ZP energy strongly depends on the true energy level E_t in its whole range of definition, as already observed in Fig. 3.15c. The boundary conditions under which the DPSS-ZP energy provides a reasonable approximation for the true energy level E_t are investigated in detail in Sect. 3.3.3E (see Fig. 3.21) considering the simultaneous dependence of the DPSS-ZP energy on the symmetry factor k .

DPSS plateau value at $(E_C-E_t)^{DPSS}=E_{gap}/2$

An expression for the third DPSS characteristic, the DPSS plateau value $k^{DPSS-PL}$ (DPSS-PL), can be derived if expression (3.30a) for the DPSS- k curve is evaluated for $(E_C-E_t)^{DPSS}=E_{gap}/2$. Considering that both DPSS-SRH densities n_1^{DPSS} and p_1^{DPSS} are then of the order of $n_i=10^{10}\text{ cm}^{-3}$ and can thus be neglected compared to the equilibrium majority carrier concentration, expression (3.30a) can be simplified to

$$k^{DPSS-PL} = \frac{k(-p_0 + n_0) + (p_1 + k n_1)}{(-p_0 + n_0) - (p_1 + k n_1)} \quad (3.35)$$

For a p -type semiconductor ($n_0 \ll p_0$) the range of definition of the DPSS-PL directly correlates with that of the DPSS-ZP. Since the numerators of the expressions (3.35) and (3.33) are identical and the signs of the respective denominators opposite within the whole parameter range, the DPSS-PL is defined exactly in that energy region where the DPSS-ZP is not defined and vice versa. Thus, the DPSS-PL is defined in particular for deep centers as already observed in Fig. 3.15.

The significance of the DPSS-PL becomes evident if Eq. (3.35) is further approximated for the specific case of a mid-gap center. Since both

¹¹ As a consequence of the existence or non-existence of the DPSS-ZP, the DPSS curves associated with deep centers are characterized by a continuous range of validity, while those associated with shallow centers are characterized by a split range of validity.

SRH densities n_1 and p_1 can then be neglected compared to the equilibrium majority carrier concentration, the DPSS-PL equals the true symmetry factor k of the defect center. The boundary conditions under which the DPSS-PL provides such an accurate approximation to the true symmetry factor k are investigated in detail in Sect. 3.3.3E (see Fig. 3.22) considering the simultaneous dependence of the DPSS-PL on both defect parameters E_t and k .

Structural differences in the DPSS characteristics for n -type doping

Transferring the above discussion to an n -type semiconductor ($n_0 \gg p_0$), only one fundamental difference appears. Since Eq. (3.32) can have negative values for n -type doping, the DPSS-DG is no longer defined for arbitrary defect and material parameters as for p -type doping but has a restricted parameter range of definition. In contrast, the range of definition of the DPSS-ZP is no longer restricted for n -type doping as Eq. (3.33) has positive values irrespective of the defect and material parameters. Furthermore, while the exact position of the characteristic DPSS energies changes according to Eqs. (3.32) and (3.33), the band gap half remains unchanged when switching from a p -type to an n -type semiconductor.

These differences in the DPSS characteristics are in full agreement with the physically motivated geometric connection between the DPSS- k diagrams for n - and p -type doping, which has been specified at the end of Sect. 3.3.3B: while the first transposition at the vertical axis through $(E_C - E_t)^{DPSS} = E_{gap}/2$ moves both characteristics in the opposite band half, the second transposition at the horizontal axis through $k^{DPSS} = k$ permutes definition gaps into zero points and vice versa. Thus, if a DPSS- k curve is calculated for identical defect and material parameters, except for that of the doping type, the DPSS-DG in the p -type case directly corresponds to the DPSS-ZP in the n -type case, while the DPSS-ZP in the p -type case is transformed to the DPSS-DG in the n -type case. While the first pair of characteristics is defined in the whole parameter range, the second pair shows almost the same restriction in the range of definition.

This correlation between n - and p -type doping is also reflected in the third DPSS characteristic: for n -type doping the range of definition of the DPSS-PL no longer correlates with that of the DPSS-ZP but with that of the DPSS-DG. Since the denominator of expression (3.35) for the DPSS-PL and the numerator of expression (3.32) for the DPSS-DG are identical except for the sign, while the opposite parts of both ratios are positive in the whole parameter range, the DPSS-PL is defined exactly in the energy regions where the DPSS-DG is not defined and vice versa, i.e., in particular for deep centers.

Characteristic structure of the range of validity of DPSS curves

Combining the individual results from the preceding discussion of the DPSS characteristics, the impact of the defect parameters on the characteristic structure of the validity range of the DPSS curves is illustrated in Figs. 3.18 and 3.19 for a *p*-type semiconductor.

Figure 3.18 displays the structure of the DPSS validity range as a function of the true defect energy level for symmetric capture cross-sections ($k=1$). Both axes show the energy interval of the silicon band gap: while the horizontal axis displays the true energy level of the investigated defect center, the vertical axis displays the DPSS energies used for the simulation of the associated DPSS curves. The plus and minus signs indicate the DPSS energy intervals in which the associated pair of DPSS curves exists or does not exist, respectively. As can be seen from Fig. 3.18, the horizontal axis of the diagram is divided into three parts: while the DPSS curves associated with shallow defect centers close to one of the band edges exhibit a split range of validity with a definition gap around mid-gap, the DPSS curves associated with defect levels, which are located within a broad interval around mid-gap, show a continuous range of validity with a definition gap towards the conduction band.

Both classes of DPSS curves have already been observed in Figs. 3.15 and 3.16. Analytically, the range of validity is confined in the upper half of the band gap by the DPSS-DG function given in Eq. (3.32) (solid line) and in the lower half of the band gap by the DPSS-ZP function given in Eq. (3.33) (dashed line). The interval of true defect energy levels for which a continuous DPSS validity range is observed, is defined by the upper and lower energy bound of the definition gap (dotted vertical lines), the DPSS-ZP function exhibits itself around mid-gap [see Eq. (3.34)].

Since the qualitative structure of the DPSS curve thus directly correlates with the existence of the DPSS-ZP, Eq. (3.34) enables a division of the true defect parameter plane (E_t, k) in terms of the expected qualitative structure of the associated DPSS curves. Mathematically, the calculated boundaries $k(E_C-E_t)$ (solid lines) are identical with the upper and lower bound of the DPSS-ZP definition gap if Eq. (3.34) is given for k instead of n_1 . As shown by the vertical shape of the lower ZP bound, the qualitative structure of the DPSS curves associated with a MinBH defect only depends on the energy position E_t and not on the symmetry factor k of the defect center. In contrast, for a MajBH defect of medium depth the qualitative structure of the DPSS curves depends on both the exact energy position and the symmetry factor k , which can be seen from the energy dependence of the upper ZP bound. Thus, for a given but arbitrary set of defect parameters the diagram allows the qualitative structure of the associated DPSS curves to be predicted.

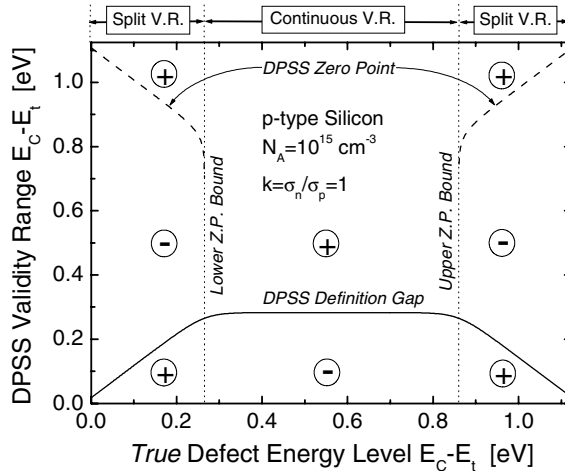


Fig. 3.18. Structure of the range of validity of the DPSS curves as a function of the true defect energy level for symmetric capture cross-sections ($k=1$) in a *p*-type semiconductor with $N_{dop}=10^{15} \text{ cm}^{-3}$. While the *horizontal axis* displays the true energy level of the investigated defect center, the *vertical axis* displays the DPSS energies used for the simulation of the associated DPSS curves. The *plus* and *minus* signs indicate the DPSS energy intervals in which the associated pair of DPSS curves exists or does not exist, respectively.

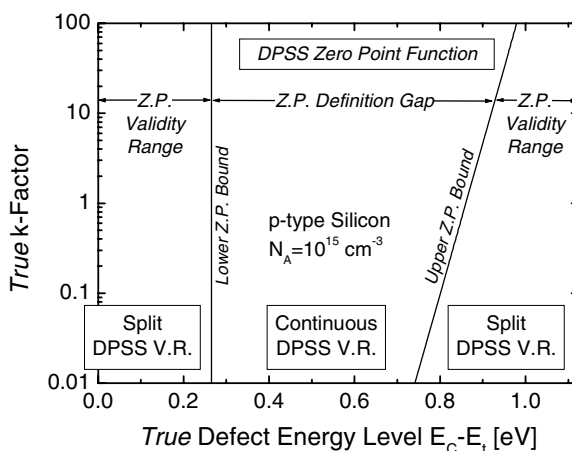


Fig. 3.19. Division of the true defect parameter plane (E_t, k) in terms of the expected qualitative structure of the DPSS curves. Mathematically, the calculated boundaries $k(E_c - E_t)$ (*solid lines*) are identical with the upper and lower bound of the definition gap existing for the DPSS zero point function given in Eq. (3.34).

E Spectroscopic value of the isolated DPSS characteristics

Against the background of the strong ambiguity of the spectroscopic results obtained from a single IDLS curve, the fundamental question is: do the DPSS characteristics associated with a specific IDLS curve allow a direct identification of the unknown defect parameters or at least a strong restriction of the DPSS? To answer this question, the dependence of all three DPSS characteristics on the defect and material parameters has to be investigated systematically, based on the results of the previous section. A suitable visualization of this complex dependence is achieved if the DPSS characteristics are plotted as continuous functions of the true energy level E_t for various symmetry factors k and for various doping concentrations N_{dop} . While the first group of curves shows the variety of the codomains of the DPSS characteristics in comparison to the true defect parameters, the second group of curves gives an indication for the optimal choice of the only adjustable material parameter with respect to the agreement between the extracted DPSS characteristic and the true defect parameter. The quality of this agreement is visualized for each DPSS characteristic in an associated error plot which displays the deviation between the extracted DPSS characteristic and the corresponding defect parameter as a function of the true energy level for both types of parameter variation. The following discussion is completely focused on a p -type semiconductor but may be easily transferred to an n -type semiconductor if the structural changes discussed in Sect. 3.3.3D are taken into account.

DPSS definition gap energy

Figure 3.20 displays the result of the above analysis for the DPSS-DG, whose energy position is shown in comparison to the true defect energy depth ΔE_t (solid straight lines in Fig. 3.20a and c). While the upper half of Fig. 3.20 shows the absolute value of the DPSS-DG energy calculated from Eq. (3.32) as a function of the true energy level E_t for (a) various k and (c) various N_{dop} , the lower half of Fig. 3.20 shows the corresponding error plots given by the absolute deviation between the DPSS-DG energy and the true energy depth ΔE_t . As estimate for the accuracy of the ΔE_t determination we prefer the absolute to the relative deviation since this avoids artificial deformations of the error curves due to a reference energy continuously varying along the horizontal axis.

As predicted in the previous section, the DPSS-DG is located in the upper half of the band gap and is defined in the whole parameter range. While the DPSS-DG energy depends linearly on the true energy depth ΔE_t for shallow levels near both band edges, it becomes independent of ΔE_t in a broad energy interval around mid-gap and is retained on a fixed value defined by k and N_{dop} . As a consequence a constant deviation between the

extracted and the true energy depth is observed in Fig. 3.20c and d for shallow levels which is as low as 20 meV if $k = 1$. For deep centers, however, the deviation increases significantly up to 300 meV when the defect level approaches mid-gap. As can be seen in Fig. 3.20a, the acceptable agreement for shallow levels is strongly affected by the symmetry factor k : for $k > 1$ the agreement improves for MinBH defects, while it degrades for MajBH defects. For $k < 1$ the opposite trend is observed. If we assume $k = 0.01$ for example, the deviation between the extracted and the true energy depth amounts to 110 meV for a shallow MinBH defect while it is reduced to almost zero for a shallow MajBH level.

Since the DPSS-DG energy does not allow an accurate determination of the defect energy depth, the question arises as to whether it provides an upper or lower bound for the true energy depth. To answer this question, we divide the horizontal axis in terms of the expected qualitative structure of the DPSS curves according to Fig. 3.19. The closed circles in Fig. 3.20a and b represent the lower and upper bound of the DPSS-ZP definition gap and thus indicate those energy positions where the qualitative structure of the underlying DPSS curve changes from split to continuous.

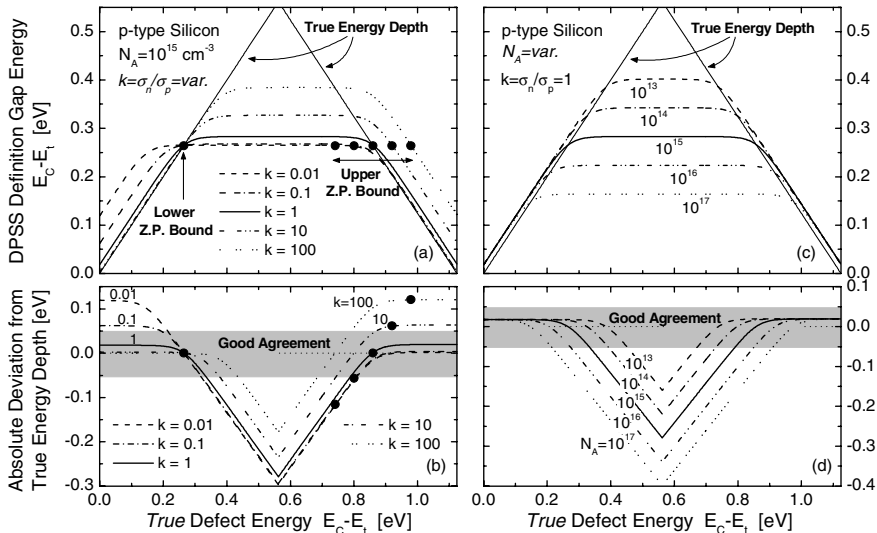


Fig. 3.20. Energy position of the DPSS definition gap and its correlation with the true defect energy level: while the *upper half* shows the absolute value of the DPSS characteristic calculated from Eq. (3.32), the *lower half* shows its absolute deviation from the true energy depth ΔE_t , both as a function of the defect energy level (**a**, **b**) for various symmetry factors and (**c**, **d**) for various doping concentrations. Representing the lower and upper bound of the DPSS-ZP definition gap, the *closed circles* indicate the energy positions where the qualitative structure of the underlying DPSS curve changes from split to continuous.

For $k=1$ it turns out that the upper and lower ZP bounds coincide with the two energy positions in Fig. 3.20a and c at which the DPSS-DG energy equals the true defect energy depth. Thus, in all split DPSS curves the true energy depth of the underlying shallow levels is overestimated, the DPSS-DG energy being an upper bound, while in all continuous DPSS curves the true energy depth of the underlying deep levels is underestimated, the DPSS-DG energy being a lower bound, even though a bad one.

Unfortunately, the situation gets more complex for $k \neq 1$. For defects in the upper band gap half the significance of the DPSS-DG energy for split and continuous DPSS curves remains unchanged for arbitrary k since first, the DPSS-DG curves intersect the ΔE_t^{true} line at the same energy for arbitrary k and second, the lower ZP bound does not depend on k . For defects in the lower half of the band gap, however, both the intersection point of the DPSS-DG curves with the ΔE_t^{true} line and the upper ZP bound strongly depend on k and no longer coincide as displayed in Fig. 3.20a. In contrast to the above classification, MajBH defects of medium depth ΔE_t exhibit for $k > 1$ continuous DPSS curves whose DPSS-DG energy is an upper rather than a lower bound for the true energy depth. For $k < 1$ on the other hand these defects exhibit split DPSS curves whose DPSS-DG energy is a lower instead of an upper bound for the true energy depth. This special situation can be observed in Fig. 3.16c which shows DPSS- k curves for MajBH defects at $E_t - E_V = 0.3$ eV with different k factors. While the DPSS-DG of the continuous DPSS- k curve for $k=100$ is located at $(E_C - E_t)^{\text{DPSS-DG}} = 0.38$ eV and thus overestimates ΔE_t^{true} , the DPSS-DG of the split DPSS- k curve for $k=0.1$ is located at $(E_C - E_t)^{\text{DPSS-DG}} = 0.25$ eV and thus underestimates ΔE_t^{true} . Since such special parameter constellations cannot be detected a priori for an unknown system, the use of the DPSS-DG as energy bound for the true defect depth is limited. Nevertheless, irrespective of the k factor of the underlying defect, the DPSS-DG energy of split DPSS curves provides an upper bound for ΔE_t^{true} whenever the DPSS-DG energy falls significantly, i.e., by around 20 %, below the energy of the lower ZP bound. This parameter only depends on the doping concentration and thus can be determined as an auxiliary quantity for a system with unknown defect center from the positive solution of Eq. (3.34). In Fig. 3.20a and c it is represented by imaginary horizontal lines through the intersection points of the DPSS-DG curves for $k=1$ with the ΔE_t^{true} lines.

Finally, Fig. 3.20c and d show that the interval of defect energies near the two band edges, in which the DPSS-DG energy agrees acceptably with the true energy depth, gets significantly wider when the doping concentration N_{dop} decreases: if N_{dop} is reduced from 10^{17} to 10^{13} cm⁻³, the width of the interval increases from 150 to 400 meV.

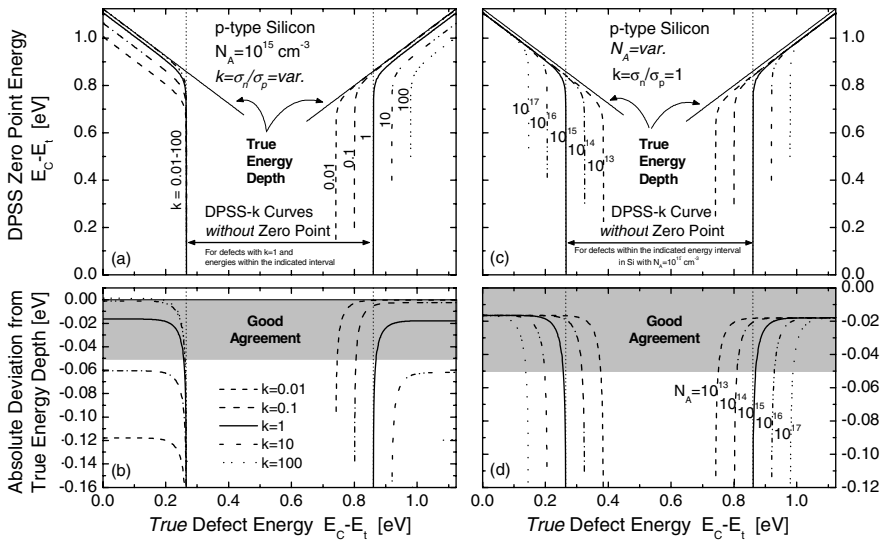


Fig. 3.21. Energy position of the DPSS zero point and its correlation with the true defect energy depth. While the *upper half* shows the absolute value of the DPSS characteristic calculated from Eq. (3.33), the *lower half* shows its absolute deviation from the true energy depth ΔE_t , both as a function of the defect energy level (a, b) for various symmetry factors and (c, d) for various doping concentrations.

DPSS zero point energy

Figure 3.21 shows the same parameter variations as Fig. 3.20 but for the DPSS-ZP, whose energy position is calculated from Eq. (3.33), and again correlated with the true energy depth ΔE_t (solid lines in Fig. 3.21a and c). The absolute deviation between the two quantities is again chosen as estimate for the accuracy of the ΔE_t determination in Fig. 3.21b and d.

As predicted, the validity range of the DPSS-ZP shows a definition gap around mid-gap. Except for defect centers from a narrow transition region adjacent to both edges of the validity range, the DPSS-ZP is located in the lower half of the band gap and depends linearly on the true energy depth ΔE_t . As a consequence, a constant deviation between the extracted and the true energy depth is observed in Fig. 3.21b and d, which is as low as 18 meV for shallow levels with $k=1$. Nevertheless, in the transition regions the deviation is strongly increased.

The major advantage of the DPSS-ZP over the DPSS-DG is that the DPSS-ZP energy provides an upper limit for the true defect energy depth ΔE_t^{true} whenever defined. Nevertheless, the spectroscopic quality of this upper bound crucially depends on the possibility of detecting a priori parameter constellations in an unknown system which lead to DPSS-ZPs

within the transition region. Two criteria actually allow such DPSS curves to be identified: (i) the absolute value of the DPSS-ZP energy and (ii) the slope of the DPSS- k curve in the DPSS-ZP. An observed DPSS-ZP lies in the transition region (i) if it is located at $(E_c - E_v)^{DPSS-ZP} = 0.7 \text{ eV}$ or deeper (*sufficient condition*) and (ii) if the slope, which the DPSS- k curve exhibits in the DPSS-ZP, is reduced (*necessary condition*). The first condition can be seen from Fig. 3.21a, c if a horizontal line is added at 0.7 eV: for none of the representative parameter constellations does the E_t -dependent part of the DPSS-ZP curves fall below that limit. The second condition can be explained from Fig. 3.15c showing the DPSS- k curves associated with symmetric MinBH defects of varying depth: while the DPSS- k curve enters the DPSS-ZP almost vertically for $n_l/p_0 > 1$, which corresponds to parameter constellations outside the transition region, it enters the DPSS-ZP with reduced slope for $n_l/p_0 = 1$, which corresponds to a parameter constellation at the edge of the validity range. Since parameter constellations producing DPSS-ZPs within the transition region can thus be identified from the structure of the DPSS curve, the DPSS-ZP is a suitable quantity to estimate the true energy depth.

As can be seen from Fig. 3.21a and b the quality of the agreement between the extracted and true energy depths is affected by the symmetry factor k : for $k > 1$ the agreement improves for shallow MinBH defects, while it degrades for shallow MajBH defects. For $k < 1$ the opposite trend is observed. That is why in an unknown system the maximum overestimate of ΔE_t^{true} by the DPSS-ZP energy has to be indicated with $\Delta E^{max} = 60\text{--}120 \text{ meV}$ depending on whether a k range from 0.1 to 10 or from 0.01 to 100 is assumed to be realistic. Since the overestimate varies between ΔE^{max} and 0 depending on the band gap half and the k domain of the unknown defect center, the DPSS-ZP energy alone allows an energy interval to be determined for the unknown energy depth, with a width ΔE^{max} that only depends on the assumption for k . The interval of possible defect depths ranges from $(E_t - E_v)^{DPSS-ZP} - \Delta E^{max}$ to $(E_t - E_v)^{DPSS-ZP}$.

As the DPSS-ZP is an interesting quantity for defect characterization, the impact of k and N_{dop} on its E_t range of definition should finally be investigated. As can be seen in Fig. 3.21b, the width of the definition gap of the DPSS-ZP function decreases with decreasing doping concentration, since both DPSS-ZP zero points given in Eq. (3.34) are shifted towards mid-gap. While both boundaries of the DG/DPSS-ZP depend on the doping concentration, only the upper bound of the DG/DPSS-ZP depends on k and is moved towards the valence band edge if k increases. Thus, the lower N_{dop} and the lower k , the broader the interval of true defect energies near both band edges, which show a DPSS-ZP and thus allow the defect energy depth to be reasonably estimated. On the other hand, since the

validity range of the DPSS-PL is completely complementary to that of the DPSS-ZP, the interval of the true defect energies which lead to a DPSS with continuous validity range, exhibiting a plateau region as major characteristic, is the broader the higher N_{dop} and k .

DPSS plateau k value

The spectroscopic information which can be gained from this third IDLS characteristic is investigated in Fig. 3.22. In comparison to the true k factors of the underlying defect center (horizontal lines) the upper half shows the absolute values of the DPSS-PL k value calculated from Eq. (3.35) as a function of the defect energy level E_t (a) for various symmetry factors k and (c) for various doping concentrations N_{dop} . The corresponding error plots are shown in the lower half of Fig. 3.22. In contrast to the energetic DPSS characteristics, the accuracy of the k determination is best described by the relative deviation between the DPSS-PL k value and the true k factor. On the one hand the single error curve is not deformed by the normalization since the reference k value does not change along the E_t axis. On the other hand, the normalization to the true k factor ensures the full comparability of the error curves for different k factors.

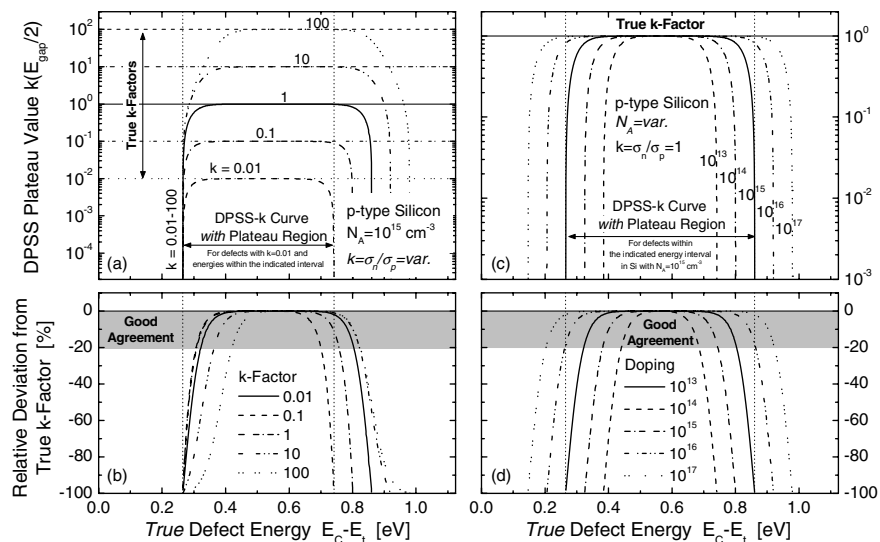


Fig. 3.22. DPSS- k plateau value at $(E_C-E)^{DPSS}=E_{gap}/2$ and its correlation with the true defect symmetry factor. While the *upper half* shows the absolute value of the DPSS characteristic calculated from Eq. (3.35), the *lower half* shows its absolute deviation from the true defect symmetry factor k , both as a function of the defect energy level (a, b) for various symmetry factors and (c, d) for various doping concentrations.

As predicted, the validity range of the DPSS-PL shows a definition gap towards both band edges. The two main characteristics of the DPSS-PL, which have a significant impact on its spectroscopic use, can be directly observed in Fig. 3.22. Whenever defined, the DPSS-PL value provides a lower bound for the true k factor of the underlying unknown defect center. In addition, in an energy interval around mid-gap, the DPSS-PL value perfectly agrees with the true k factor irrespective of the other defect and material parameters. Mathematically, the equality $k^{DPSS-PL} = k$ is attached to the two inequalities $p_1 + k \times n_1 \ll p_0$ and $p_1 + k \times n_1 \ll k \times p_0$, which follow directly from Eq. (3.35) if it is simplified for a p -type semiconductor. As a consequence of these boundary conditions the width of the energy interval with $k^{DPSS-PL} = k$ reaches its maximum for $k = 1$ and decreases with increasing capture asymmetry irrespective of whether $k > 1$ or $k < 1$. Figure 3.22a displays this trend. On the other hand the energy interval with $k^{DPSS-PL} = k$ gets broader the higher the doping concentration, as shown in Fig. 3.22c. This demonstrates the important impact of the only experimentally adjustable parameter.

In spite of this extraordinary agreement between the extracted and the true k factor over a broad parameter range, large deviations up to 100 % are observed for defect centers which are located in the transition regions adjacent to the edges of the DPSS-PL validity range. These deviations result from a strong E_r -dependence of the DPSS-PL value when one of the SRH densities n_1 or p_1 exceeds the equilibrium majority carrier concentration p_0 . Thus, as in the case of the DPSS-ZP energy, the spectroscopic quality of the extracted DPSS-PL value decisively depends on the possibility of detecting a priori critical parameter constellations in an unknown system. Unfortunately, neither the qualitative structure of the continuous DPSS curves nor the magnitude of the extracted DPSS-PL value allow an identification of the DPSS curves whose DPSS-PL value is located within the transition regions.

From these considerations the following conclusion has to be drawn: although the DPSS-PL value extracted from continuous DPSS curves may provide a perfect approximation of the true symmetry factor k , in an unknown system, the k determination from the DPSS-PL only provides a lower bound, whose actual agreement with the true symmetry factor is completely undefined, since it is impossible to distinguish a priori DPSS curves with a DPSS-PL located at the edge or in the middle of the validity range. Thus, the presented results disprove the widespread assumption that the SRH analysis of a single IDLS curve with increasing injection dependence at least allows an accurate determination of the symmetry factor k . Without any knowledge of the energy level of the underlying defect this assertion is definitely proved to be incorrect.

The detailed discussion of the practical use of the DPSS characteristics should be summarized in two guidelines. (i) The energy depth ΔE_t of an unknown defect center, on the one hand, is best estimated from the DPSS-ZP in a sample with minimum doping concentration since then the intervals of defect energies which result in reasonable ΔE_t estimates reach their maximum width. (ii) The symmetry factor k of an unknown defect center, on the other hand, is best estimated from the DPSS-PL in a sample with high doping concentration since this ensures a broad interval of defect energies around mid-gap for which the extracted $k^{\text{DPSS-PL}}$ equals the true value of the symmetry factor k and thus enhances the probability of an accurate k determination.

F Defining equations for the defect parameters from the combination of DPSS characteristics of a single pair of DPSS curves

As discussed in the previous section all three DPSS characteristics depend individually on the two unknown defect parameters E_t and k . Considered isolated from each other, each of the DPSS characteristics only acts as upper or lower bound for one of the defect parameters or defines a parameter interval of possible solutions, but does not allow a direct determination. Nevertheless, each DPSS- k curve is characterized by two DPSS characteristics, which only depend on the two unknown variables E_t and k according to Eqs. (3.32) to (3.35). Since the analytical expressions for the respective two DPSS characteristics thus provide two conditional equations for two unknown variables, the idea of deriving defining equations for both defect parameters as functions of the DPSS characteristics seems to suggest itself. Unfortunately, this attempt fails. If in the case of a continuous DPSS curve Eq. (3.32) for the DPSS-DG and Eq. (3.35) for the DPSS-PL are both solved for k and then equated, a quadratic equation for the SRH density n_I is found whose solutions equal p_0 and n_0 , respectively, and thus do not show any dependence on the initializing DPSS parameters. The fact that this solution is identically reproduced for the second combination of DPSS characteristics points towards a systematically inherent origin for this initially surprising solution and shows that the true defect parameters cannot be determined even if the information of both DPSS characteristics is combined. The physical background for this finding is clarified by the following observation. If the analytical expressions for the DPSS characteristics are derived from Eq. (3.29a) instead of Eq. (3.30a) as functions of the IDLS characteristics $\tau_{SRH,LLI}$ and $\Delta\tau_{SRH}$, the combination of two of them allows defining equations for both IDLS characteristics to be derived. In contrast to the solution for the defect parameters, these equations depend on the initializing DPSS parameters and successfully

define both IDLS characteristics. This indicates that the undefinability of the defect parameters from the DPSS characteristics is an inherent problem which results from the origin of the DPSS curves. Although perfectly visualizing the possible solutions for the SRH parameterization of a single IDLS curve, the DPSS curves are derived from the IDLS curve and thus contain the same reduced defect information.

The fact that the system formed by two DPSS characteristics is underdetermined to deduce both defect parameters can be illustrated using the example of a symmetric mid-gap center. Values for the characteristics of the associated continuous DPSS curve can be directly extracted from Figs. 3.6 and 3.22: we obtain $k^{DPSS-PL} = 1$ and $(E_C - E_t)^{DPSS-DG} = 0.28$ eV. Although $k^{DPSS-PL}$ actually equals the true k factor, it can only be interpreted as a lower bound as long as the interval of possible defect energies cannot be confined to the energy interval in which the DPSS-PL curve calculated for precisely the extracted $k^{DPSS-PL}$ displays its constant plateau region. In the present example the energy interval would have to be confined to $E_C - E_t = 0.35 - 0.75$ eV, where the relevant DPSS-PL curve for $k = 1$ exhibits its constant plateau as shown in Fig. 3.22. Thus, even if $(E_C - E_t)^{DPSS-DG}$ is interpreted as lower bound for the true energy depth, the interval of possible defect energies is not confined enough to allow the identification of the extracted $k^{DPSS-PL}$ with the true symmetry factor k . The fact that in the presented case not even one defect parameter could be determined accurately from the combined information of both DPSS characteristics shows the underdetermination of the system with respect to the true defect parameters.

G Conclusion

We may conclude that an accurate determination of the true defect parameters from a single IDLS curve definitely fails even if the DPSS analysis is applied. As a consequence, the simultaneous SRH fit of a set of IDLS curves measured on samples with varying doping concentration or on the same sample at varying temperatures, as outlined in Sect. 3.2.3B, remains the only possibility to determine the true defect parameters from IDLS. Although a successful derivation of defining equations for E_t and k from the DPSS characteristics of a single IDLS curve would have been the culmination of the DPSS analysis, the negative result does not lower its significance. On the one hand the DPSS diagram not only visualizes the possible SRH solutions but also allows the parameter intervals for both defect parameters to be significantly reduced as discussed in the previous sections. On the other hand the DPSS analysis is the ideal technique to perform the simultaneous simulation of sets of IDLS curves required for an

unambiguous determination. This will be shown in the following section for IDLS curves measured on samples with varying doping concentration and in Sect. 3.7 for a set of IDLS curves measured on the same sample at varying temperatures. The latter technique is known as *T-IDLS*.

3.3.4 Theoretical analysis II: defect characterization by analyzing a set of IDLS curves with different doping concentrations

Having discussed the basic properties of the DPSS curves and the restrictions concerning the determination of the defect parameters from a single DPSS curve, the second part of the theoretical analysis is dedicated to the transfer of the DPSS analysis to a set of IDLS curves measured on samples with different doping concentration. As outlined in Sect. 3.2.3B, a simultaneous SRH fit to such a set of IDLS curves should in principle allow an accurate determination of the true defect parameters. Nevertheless, there are only a few experiments reported in the literature which made use of this technique [13, 18]. And when applied to unknown systems [13], the simultaneous SRH fit in general failed and only led to the determination of broad parameter ranges for the defect parameters instead of discrete solutions. These problems dwell in the lack of a suitable tool for data evaluation which accommodates the complexity of SRH simulation and its ambiguity when applied to IDLS data. Since the DPSS analysis is distinguished by the required transparency of IDLS data evaluation, its application to a set of IDLS curves, which has to be fitted simultaneously, should allow the true defect parameters to be extracted. The procedure of defect parameter extraction and the achievable accuracy of the spectroscopic results are the focus of this discussion.

A Transparent procedure for the required simultaneous SRH simulation: superposition of DPSS curves obtained for a set of IDLS curves

Figure 3.23a displays a set of IDLS curves which has been calculated for samples with different doping concentrations under the assumption that recombination in all samples is limited by the same shallow SRH defect center ($E_c-E_t=0.3\text{ eV}$, $k=10$, $\tau_{n0}=10\mu\text{s}$). Instead of solving the SRH fit problem for all curves simultaneously, which would require a high-performance fit algorithm, we divide the fitting problem into two steps: in the first step we determine the pair of DPSS curves for each of the IDLS curves separately and then in the second step superpose the DPSS curves of the different samples (in two diagrams). Figure 3.23b and c show the superposition of the DPSS- τ_{n0} and DPSS- k curves, respectively, which are

associated with the IDLS curves from Fig. 3.23a and have been calculated for the theoretical analysis from Eq. (3.30). In the experiment they would have been determined by means of the procedure described in Sect. 3.3.2B. Since each DPSS curve constitutes by definition the set of equivalent solutions for the SRH parameterization of the underlying IDLS curve, the fact that all IDLS curves are induced by the same defect center should be reflected in one common intersection point of all DPSS curves in both DPSS diagrams, whose DPSS coordinates should equal the true defect parameters E_i , k and τ_{n0} .

Actually, as can be seen in Fig. 3.23b and c, the DPSS curves exhibit two common intersection points (DPSS-IP) instead of one: the expected DPSS-IP (1st) at the position of the true defect parameters and a second DPSS-IP (2nd) in the opposite half of the band gap. Since both DPSS-IPs provide equivalent SRH solutions for the simultaneous fit of the set of IDLS curves, it is important to understand how they differ from each other and how these differences affect the identification of the true defect parameters.

In both DPSS diagrams the ordinate values of the two DPSS-IPs coincide with each other and equal the true k and τ_{n0} values, respectively (horizontal lines in Fig. 3.23b and c), which enables an unambiguous determination of the true symmetry factor k and the true capture time constant τ_{n0} from each of the two DPSS-IPs. Comparing the energy positions of the corresponding DPSS-IPs in the DPSS- k and the DPSS- τ_{n0} diagram, we find coincidence for both DPSS-IPs. Thus, a full characterization of the energy positions of the two DPSS-IPs is achieved from each of the DPSS diagrams. Without loss of generality we focus in the following discussion on the DPSS- k diagram displayed in Fig. 3.23c.

A quantitative comparison of the DPSS-IP energies in Fig. 3.23c reveals that the 2nd DPSS-IP in the lower band gap half does not originate from the 1st DPSS-IP by a simple transposition at a vertical axis through $(E_C - E_i)^{DPSS} = E_{gap}/2$, which would have led to the energy position displayed by the dotted vertical line. In fact, the energy depth observed for the 2nd DPSS-IP (dashed vertical line) is 60 meV smaller than the true energy depth of the underlying defect center as shown in Fig. 3.23c by the gap between the dotted and dashed vertical line. Since the DPSS-IP providing the true energy position cannot be identified in an unknown system, the above result indicates that neither the band gap half nor the true energy depth of the underlying defect center can be identified unambiguously from an IDLS experiment with varying doping concentrations, at least not for the presented parameter constellation.

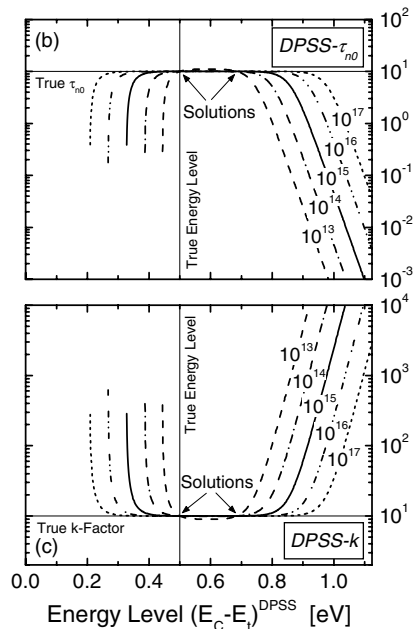
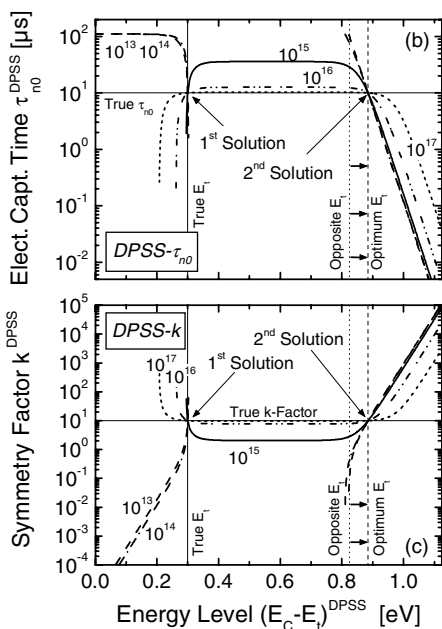
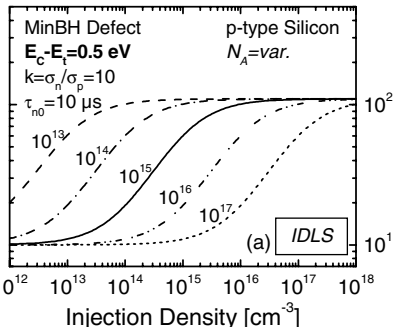
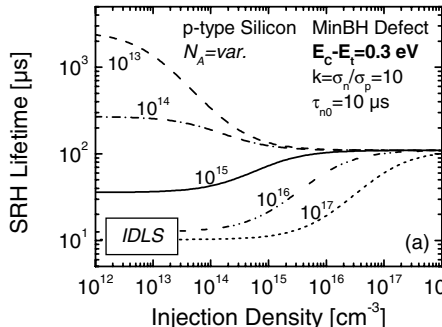


Fig. 3.23. Application of the advanced DPSS analysis to a set of IDLS curves calculated for samples with different doping concentrations N_A . In all samples recombination is assumed to be limited by the same shallow SRH defect center ($E_C - E_t = 0.3 \text{ eV}$, $k = 10$): (a) calculated IDLS curves; (b–c) superposition of the associated DPSS- τ_{n0} and DPSS- k curves calculated from Eq. (3.30). Since the different DPSS curves represent the same defect center, the true defect parameters can be extracted from the intersection points in both DPSS diagrams.

Fig. 3.24. Application of the advanced DPSS analysis to a set of IDLS curves calculated for samples with different doping concentrations N_A . In all samples recombination is assumed to be limited by the same deep SRH center ($E_C - E_t = 0.5 \text{ eV}$, $k = 10$): (a) calculated IDLS curves; (b–c) superposition of the associated DPSS- τ_{n0} and DPSS- k curves calculated from Eq. (3.30). Since all DPSS curves for the deep center show the tub-like structure with almost identical plateau values irrespective of N_A , the energy localization of the DPSS intersection points is not as accurate as for a shallow center (see Fig. 3.23).

B Possibilities and fundamental restrictions of the simultaneous N_{dop} -IDLS analysis

In order to assess the significance of the observed energy ambiguity for the spectroscopic aptitude of the simultaneous IDLS analysis, analytical expressions for the energy positions of the DPSS-IPs have to be derived. Since the DPSS-IPs equal the intersection points of the DPSS- k curve with the horizontal line representing the true k value, which will be proved by the result of the derivation, the required analytical expressions for the DPSS-IP energies are easily gained by equating Eq. (3.30a) with the true k value. We arrive after some rearranging and upon use of the identity $p_1^{DPSS-IP} = n_i^2/n_1^{DPSS-IP}$ at a quadratic equation for the associated SRH density $n_1^{DPSS-IP}$ whose solutions are given by

$$n_1^{DPSS-IP-1} = n_1 \quad (3.36a)$$

$$n_1^{DPSS-IP-2} = p_1 / k \quad (3.36b)$$

The fact that both solutions are independent of the doping concentration or related quantities confirms the observation of two sharp intersection points in the superposed DPSS diagram and ensures that the calculated intersection points equal the DPSS-IPs observed for DPSS curves with different doping concentration. Expressions for the energy positions $(E_C - E_t)^{DPSS-IP}$ of the DPSS-IPs result directly from Eq. (3.36) upon use of Eq. (3.2) and are given by:

$$(E_C - E_t)^{DPSS-IP-1} = E_C - E_t \quad (3.37a)$$

$$(E_C - E_t)^{DPSS-IP-2} = (E_t - E_V) + \underbrace{k_B T \ln \left(k \frac{N_C}{N_V} \right)}_{=: E^{corr}(k, T)} \quad (3.37b)$$

As the energy positions of both DPSS-IPs are described in terms of their distance from the conduction band, the equations (3.37) reveal that one DPSS-IP provides the true energy distance of the defect center from the conduction band while the other DPSS-IP provides a modified value for its energy distance from the valence band thus being located in the opposite half of the band gap. Equation (3.37b) displays the decisive dependence of the correction term E^{corr} , which produces the energy deviation at the 2nd DPSS-IP: a logarithmic dependence on the symmetry factor k of the defect and a linear dependence on the temperature. The temperature dependence can be neglected for the present discussion of the simultaneous IDLS analysis, since the sample temperature is always kept at room temperature. Nevertheless, this temperature dependence will be

highlighted in Sect. 3.7, in which the DPSS analysis is transferred to the simultaneous evaluation of a set of IDLS curves measured at various temperatures (called T -IDLS curves).

Highly relevant to the simultaneous IDLS analysis at room temperature is the dependence of the correction term E^{corr} on the symmetry factor k of the defect. For $k=1$, the correction term E^{corr} almost vanishes. The negligible E^{corr} value of 2 meV only reflects the slight deviation in the density of states given by the ratio $N_C/N_V=1.06$ (standard T -model [35]). Since both DPSS-IPs thus have more or less the same energy depth, the simultaneous IDLS analysis allows, for symmetric capture cross-sections, the unambiguous determination of the true energy depth but not the identification of the relevant band gap half.

For $k \neq 1$ on the other hand, the correction term is higher the stronger the capture asymmetry of the defect center is, irrespective of the k domain. For moderate capture asymmetries with σ_n and σ_p differing around one order of magnitude ($k=10$ or $k=0.1$), the energy correction term gets significant values around 60 meV, which increase to values as high as 120 meV if σ_n and σ_p differ around two orders of magnitude ($k=100$ or $k=0.01$). Thus for asymmetric capture cross-sections, the advanced DPSS analysis identifies for the defect center two possible energy positions with different energy depth. As can be seen from Eq. (3.37b), the energy correction E^{corr} is positive for $k > 1$, while it becomes negative for $k < 1$. Although the sign and magnitude of the energy correction are accessible in the experiment due to the unambiguous k -identification from both DPSS-IPs, this structural difference is of no use for the identification of the true defect position. This can be demonstrated using the situation in Fig. 3.23c. If we pretend that the defect is unknown, the spectroscopic result from Fig. 3.23c allows the following interpretations: from the ordinate values of both DPSS-IPs the value $k=10$ is unambiguously determined for the symmetry factor of the defect, which implies a positive value for the energy correction term E^{corr} . The DPSS-IPs in the upper and the lower half of the band gap are located at $E_C-E_t=0.30\text{ eV}$ and $E_t-E_V=0.24\text{ eV}$, respectively. If we identify the deeper DPSS-IP in the upper band gap half with the true energy position, $E^{corr} > 0$ moves the DPSS-IP in the lower band gap half from the opposite energy position closer to the valence band edge, which results in a reduced energy depth of the 2nd DPSS-IP. On the other hand, if we identify the shallower DPSS-IP in the lower band gap half with the true energy position, $E^{corr} > 0$ moves the DPSS-IP in the upper band gap half from the opposite energy position deeper into the band gap, which results in an increased energy depth of the 2nd DPSS-IP. Thus, depending on the true band gap half of the defect center, the DPSS-IP in the opposite band gap half exhibits an energy depth which is reduced or

increased compared to the true defect energy depth. This demonstrates the complete equivalence of both DPSS solutions. Thus, for $k \neq 1$ the simultaneous IDLS analysis allows neither an unambiguous determination of the energy depth nor an identification of the relevant band gap half.

This ambiguity in the detection of the energy level represents a fundamental restriction on the spectroscopic aptitude of simultaneous IDLS analysis, of which the current assessment in the literature is not aware [13, 18, 22]. The fact that the detection of these theoretical restrictions has only been enabled by the application of DPSS analysis elucidates once more the potential of DPSS analysis for evaluating any lifetime spectroscopic data. In spite of the ambiguity in the energy determination, it should be emphasized that the application of the superposed DPSS analysis significantly improves the quality of the spectroscopic results which can be extracted from a set of IDLS curves subject to a doping variation. The fact that the superposed DPSS analysis enables the extraction of two discrete parameter solutions for the defect center, including the true solution, represents an extraordinary reduction of the DPSS, especially since the two solutions only differ in E_t , but not in k and τ_{n0} .

C Impact of the defect depth on the spectroscopic result

Having shown above the spectroscopic value of the two discrete defect parameter solutions provided by the two discrete DPSS-IPs, we finally want to assess the accuracy with which these solutions can be extracted from the superposed DPSS diagram taking into account the full bandwidth of defect parameter constellations. The degree of precision for the localization of the DPSS-IPs depends on the divergence of the DPSS shapes within the set of DPSS curves subject to the doping variation. For the shallow defect level displayed in Fig. 3.23 the DPSS curves change qualitatively from a split to a continuous shape with increasing doping level, which enables an accurate determination of the DPSS-IPs since the DPSS curves of both classes intersect almost vertically. Considering the results on the energy and doping dependence of the DPSS characteristics presented in Sect. 3.3.3E and taking into account that their existence or non-existence directly reflects the qualitative shape of the associated DPSS curves, it turns out that the doping dependence of the qualitative DPSS shape depends decisively on the energy level E_t of the limiting defect center. Aiming at a qualitative change of the DPSS curves with varying doping level, Figs. 3.21 and 3.22 reveal the critical E_t domains for the defect level. While the DPSS curves for defect levels close to one of the band edges always exhibit a split shape, the DPSS-ZP being defined irrespective of N_{dop} , those for defect levels close to mid-gap always display

a continuous shape, the DPSS-PL then being defined irrespective of N_{dop} . Since generally only the second group of defects is recombination-active and is thus relevant to lifetime spectroscopy, we wish to evaluate what changes in the superposed DPSS diagrams have to be expected in the case of a deep level.

Analogously to Fig. 3.23, Fig. 3.24 displays the advanced DPSS analysis of a set of IDLS curves which has been calculated for samples with different doping concentrations, this time under the assumption that recombination in all samples is limited by the same deep SRH defect center ($E_C-E_t=0.5\text{ eV}$, $k=10$, $\tau_{n0}=10\mu\text{s}$). While Fig. 3.24a displays the IDLS curves, Fig. 3.24b and c show the superposition of the associated DPSS- τ_{n0} and DPSS- k curves calculated from Eq. (3.30). As expected, and in contrast to the DPSS analysis of a shallow level displayed in Fig. 3.23, all DPSS curves calculated for the deep center show, irrespective of the doping concentration, the tub-like structure with a continuous range of validity and almost identical plateau values. As a consequence the energy localization of the DPSS-IPs is not as accurate as for the shallow level, its quality strongly depending on the lowest doping concentration included in the set of samples. If the 10^{13} cm^{-3} doped sample is left out, the discrete DPSS-IPs at 0.50 and 0.69 eV disappear and the energy solution for the defect center, which can be gained from the superposed DPSS analysis, only consists of an energy interval around mid-gap ranging from 0.47 to 0.72 eV. In accordance with all previous results the extraction of the true values for the symmetry factor k and the capture time constant τ_{n0} is not affected at all by changes in the doping range.

D Derivation of minimum requirements for the necessary parameter variation within the set of IDLS curves

As has been seen from the comparison of Figs. 3.23 and 3.24, maximum accuracy for the localization of the DPSS-IPs is achieved if the investigated doping range is chosen in such a way that the set of superposed DPSS curves contains both types of DPSS curves, those with a split and those with a continuous range of validity. In order to enable simultaneous IDLS experiments which provide maximum information on a minimum number of samples, a plot is finally derived which allows the optimum doping range to be read out directly as a function of the defect parameters.

In Sect. 3.3.3D it has been shown that the qualitative structure of the DPSS curve directly correlates with the existence of the DPSS-ZP which enabled the division of the defect parameter plane (E_t , k) in terms of the expected qualitative structure of the associated DPSS curves as displayed in Fig. 3.19. Figure 3.25 shows a corresponding division of the parameter

plane set up by the defect parameter E_t and the material parameter N_{dop} . Mathematically, the calculated boundaries $N_{dop}(E_c-E_t; k)$ are identical with the upper and the lower bound of the DPSS-ZP definition gap if the defining Eq. (3.34) is this time resolved for $p_0=N_{dop}$ instead of n_1 . While Fig. 3.25a shows the (E_t, N_{dop}) division for symmetric defects ($k=1$), Fig. 3.25b shows the impact of a capture asymmetry ($k \neq 1$) on the division boundaries. While DPSS curves for parameter pairs between the two boundary curves have a continuous validity range and exhibit the characteristic plateau region, DPSS curves for all other parameter pairs have a split validity range and show a zero point instead of a plateau region.

Since the diagram directly displays the boundary doping concentration for the qualitative DPSS change as a function of the true defect energy, it allows the determination of the optimum doping range for a set of samples subject to a simultaneous IDLS analysis if there are any indications for the expected energy level and symmetry factor. This first benefit of the diagram originates from a vertical interpretation. As can be seen from Fig. 3.25a,

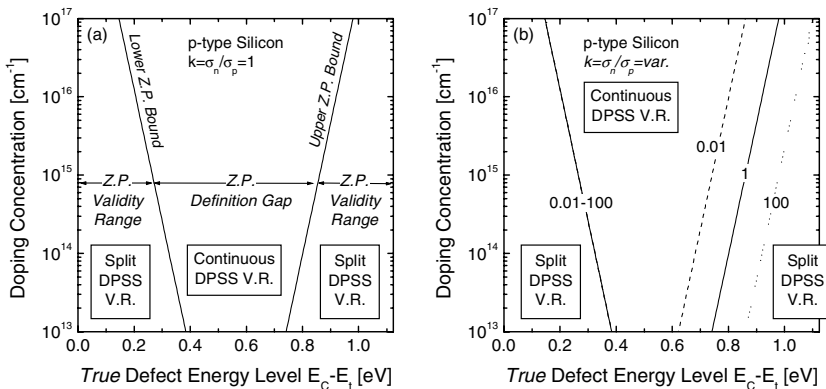


Fig. 3.25. Division of the parameter plane set up by the defect parameter E_t and the material parameter N_{dop} in terms of the expected qualitative structure of the DPSS curve. Mathematically, the calculated boundaries $N_A(E_c-E_t; k)$ are identical with the upper and the lower bound of the definition gap which exists for the DPSS zero point function and is given by Eq. (3.34). While (a) shows the (E_t, N_A) division for symmetric defects ($k=1$), (b) shows the impact of a capture asymmetry ($k \neq 1$) on the division boundaries. Since the diagram directly displays the boundary doping concentration for the qualitative DPSS change as a function of the defect energy, the benefit of the diagram is twofold. For a given defect center on the one hand, the diagram displays the optimum doping range for a simultaneous IDLS analysis which guarantees maximum accuracy of the spectroscopic results on a minimum number of samples. For a given doping range of an available set of samples on the other hand, the diagram gives information about the range of defect energies for which the simultaneous N_{dop} -IDLS analysis is highly sensitive.

the position of the optimum doping range – around the boundary doping concentration – is lowered by four orders of magnitude from 10^{17} to 10^{13} cm^{-3} if the energy depth of a symmetric defect center increases from 0.15 to 0.40 eV. For deeper defects with energies in the range of 0.4 to 0.7 eV the prerequisites to localize the DPSS-IPs with maximum accuracy can no longer be accomplished within the standard doping range down to 10^{13} cm^{-3} . The consequences for the defect characterization have been discussed in the previous section using Fig. 3.24. In addition, Fig. 3.25b shows that the position of the optimum doping range increases by two orders of magnitude if the symmetry factor k of a MajBH defect decreases by one order of magnitude. As can also be seen from Fig. 3.25b, this k -dependence is only observed for the division boundary in the MajBH, while the division boundary in the MinBH is not affected by k variations. This observation is in full agreement with the observations in Fig. 3.19 and can be understood from the physical differences between MinBH and MajBH defects, which have been discussed in Sect. 3.3.3A. The fact that for defects in the MinBH the qualitative structure of the DPSS curves only depends on E_t and N_{dop} , makes the division boundary in the MinBH universally usable.

On the other hand, if the diagrams in Fig. 3.25 are not interpreted vertically but horizontally, they give information about the range of defect energy levels which can be determined with maximum accuracy from a given doping variation of a set of samples. From this point of view, which is closer to experimental reality, the diagram defines the spectroscopic sensitivity of the simultaneous IDLS analysis depending on the doping variation of an available set of samples. Thus, the benefit of the diagram is twofold.

E Practical importance of the superposed DPSS analysis

The practical advantages of performing the simultaneous IDLS analysis by means of the superposed DPSS analysis instead of a direct SRH simulation of the whole set of IDLS curves are obvious. In contrast to the superposed IDLS diagram, the superposed DPSS diagram allows the defect parameters to be extracted directly from the DPSS-IPs. The quality of these DPSS-IPs provides a direct estimate of the accuracy and consistency of the extracted defect parameters. Thus, the bisection of the fitting problem combined with the transparency and completeness of the DPSS analysis guarantees the high reliability of the spectroscopic result. Moreover, the superposed DPSS analysis allows the impact of each of the IDLS curves on the entire spectroscopic result to be assessed separately. The latter advantage of the superposed DPSS analysis gains practical importance if we are conscious

of an experimental problem the N_{dop} -IDLS technique is confronted with: the problem of unintended variations among the samples of different doping concentration, which may affect the qualitative shape of the IDLS curves beyond the expected pure SRH effect of the doping level. The superposed DPSS analysis enables the identification of such problematic IDLS curves, which then can be eliminated from the constituting set of IDLS curves to avoid a distortion of the entire spectroscopic result. Although not unambiguous for theoretical reasons, the spectroscopic result of an N_{dop} -IDLS experiment is thus significantly improved if the proposed DPSS analysis is applied.

3.3.5 Section summary

In Sect. 3.3, the potential of IDLS has been investigated in detail. Focusing first on the measurability of SRH lifetime, it has been shown that the determination of the pure SRH lifetime often requires the elimination of superposed external carrier trapping under LLI and superposed intrinsic recombination under HLI, which may be achieved by a bias-light correction and the use of a theoretical model for CE-Auger recombination, respectively.

To allow a transparent and comprehensive SRH simulation of IDLS curves, a new modeling procedure based on the determination of the associated *defect parameter solution surface* (DPSS) has been introduced. The DPSS is defined by two curves, $k^{DPSS}(E_C-E_t)$ and $\tau_{n0}^{DPSS}(E_C-E_t)$, which result from SRH simulations of the measured IDLS curve for specified but gradually varied energy levels E_C-E_t of the defect center, with the optimal fit parameters k^{DPSS} and τ_{n0}^{DPSS} being determined by means of a least squares fit subject to a fixed energy level. The practical importance of this newly developed DPSS diagram consists in the fact that it clearly visualizes the large inherent ambiguity in the SRH parameterization of a single IDLS curve, while being extracted from the measured IDLS curve in a direct and simple manner without making use of extended mathematics.

Theoretical analysis of the DPSS curves disclosed the existence of two qualitatively different DPSS structures. While the DPSS curves associated with increasing IDLS curves have a continuous range of validity with a definition gap towards the conduction band and exhibit a tub-like structure with a plateau around mid-gap, those associated with constant or decreasing IDLS curves have a split range of validity with a definition gap around mid-gap and exhibit a zero point instead of a plateau region. It turns out that both DPSS structures are distinguished by two characteristics, whose values strongly depend on the true defect parameters. While the energy

position of the definition gap (DPSS-DG) is a common characteristic of both DPSS structures, the continuous DPSS- k curves are additionally characterized by the k value of the plateau region (DPSS-PL), whereas the split DPSS- k curves are additionally characterized by the energy position of the zero point (DPSS-ZP).

The detailed evaluation of the spectroscopic value of the individual DPSS characteristics required analytical expressions for all three of them and led to the following results, which have been visualized in three special diagrams showing the DPSS characteristics as a function of the true defect and material parameters. Concerning the energy depth ΔE_t of an unknown defect center, the DPSS-DG energy is of limited use as an energy bound. The DPSS-ZP energy, on the contrary, represents an upper bound for ΔE_t and allows an energy interval to be determined for the unknown ΔE_t , with a width that only depends on the uncertainty of k , being only 120 meV wide if the k uncertainty covers four orders of magnitude. Concerning the symmetry factor k , an accurate determination may be given by the DPSS-PL k value. However, as the study revealed, without any knowledge of the energy level of the underlying defect center, the DPSS-PL k value can only be interpreted as a lower bound for the true symmetry factor k , while the actual agreement with k is completely undefined. This important result disproves a widespread assertion that the SRH analysis of a single IDLS curve with increasing injection dependence allows at least an accurate determination of the symmetry factor k . In an IDLS curve dominated by an unknown defect center, this assertion is definitely incorrect. Nevertheless, it has been shown that the probability of an accurate k determination increases with increasing doping concentration, since the interval of defect energies around mid-gap, where the DPSS-PL and the true k value coincide, becomes broader. The failure of the attempt to deduce defining equations for E_t and k by combining the analytical expressions of the respective pairs of DPSS characteristics conclusively showed that the defect parameters definitely cannot be determined unambiguously from a single IDLS curve, even if the information of both DPSS characteristics is combined.

In the second half of the study, we thus investigated the spectroscopic potential of the expanded N_{dop} -IDLS technique, which is based on the simultaneous SRH simulation of a set of IDLS curves subject to a doping variation. The comprehensive SRH analysis of the whole set of IDLS curves by means of a superposed DPSS analysis, which was proposed in the present work, revealed a fundamental theoretical restriction of simultaneous IDLS analysis. From the fact that the superposed DPSS analysis identifies two equivalent DPSS intersection points – the true solution and a second solution in the other band gap half – it had to be concluded that

simultaneous IDLS analysis never allows the identification of the band gap half where the defect is located. Furthermore, except for symmetric capture cross-sections, even the true energy depth of the defect center cannot be determined unambiguously, since the energy depth of the additional solution is modified by the symmetry factor k . This ambiguity in the detection of the energy level represents a fundamental restriction on the spectroscopic potential of simultaneous IDLS analysis, which has not been recognized in the literature to date. Nevertheless, the superposed DPSS analysis enables two discrete parameter solutions for the defect center to be extracted, which represents an extraordinary reduction of the DPSS, especially since the two solutions only differ in E_t but not in k and τ_{n0} . This demonstrates that simultaneous IDLS analysis at least allows an accurate determination of the symmetry factor k and the capture time constant τ_{n0} . Concerning the energy solution, the study revealed greater ambiguity in the case of deep levels around mid-gap, since the superposed DPSS curves no longer intersect at two discrete energy positions but coincide along an energy interval around mid-gap.

This observation led to the finding that the energy solution is most accurately identified if the investigated doping range is chosen so that the superposed DPSS diagram contains DPSS curves with both split and continuous ranges of validity. To put this criterion to practical use, a diagram has been developed which allows the optimum doping range to be read out directly as a function of the defect parameters and thus allows N_{dop} -IDLS experiments to be designed which provide the sought results with maximum accuracy for a minimum number of samples.

Apart from enabling the detection of the theoretical restrictions of simultaneous IDLS analysis, the superposed DPSS analysis proposed here offers important practical advantages compared to a direct SRH simulation of the whole set of IDLS curves. In contrast to the superposed IDLS diagram the superposed DPSS diagram allows the defect parameters to be extracted directly from the DPSS-IPs. The quality of the DPSS-IPs provides a direct estimate of the accuracy and consistency of the extracted defect parameters. Moreover, the superposed DPSS analysis allows the impact of each of the IDLS curves on the entire spectroscopic result to be assessed separately, which is of practical importance especially in an N_{dop} -IDLS experiment, where the IDLS curves may be affected by unintended variations among the samples. Thus, in spite of the ambiguity for theoretical reasons, the quality and reliability of the spectroscopic results obtained from an N_{dop} -IDLS experiment are expected to be significantly improved if the proposed DPSS analysis is applied.

3.4 Temperature-dependent lifetime spectroscopy: improved standard analysis and its limitations

As already shown in Sect. 3.2, the major advantage of temperature-dependent lifetime spectroscopy (TDLS) compared to injection-dependent lifetime spectroscopy (IDLS) is that TDLS allows the direct determination of the defect energy depth ΔE_t on a single sample from a simple linear fit of the data. Thus TDLS has a special appeal in terms of both the extractable defect information and the low complexity of data evaluation. Nevertheless, the question of accuracy has been left out of consideration so far.

The present section is dedicated to a detailed analysis of the procedures used for the evaluation of TDLS data, the focus being on their accuracy concerning the ΔE_t determination. The limiting factor of accuracy is the width of the defect-dominated linear Arrhenius increase. Since it strongly depends on the defect and material parameters, in Sect. 3.4.1 we first identify the critical parameter constellations for which the standard analysis fails or at least becomes highly defective. It is then demonstrated that even for a moderate parameter constellation which allows the formation of the Arrhenius increase over 100 K, the accuracy of the standard analysis is limited systematically. To expand the temperature range of the linear Arrhenius increase, we introduce in Sect. 3.4.1 a procedure of data linearization which is proposed in the literature. It will be shown that the suitability of this technique depends heavily on the features of the TDLS data. While the application to ideal TDLS curves provides accurate results, large systematic errors have to be expected if the technique is applied to realistic TDLS data which show a superposed temperature dependence of the capture cross-sections. In order to minimize or even eliminate these evaluation errors, we develop in Sect. 3.4.2 two advanced procedures for data evaluation, which are based on an improved data linearization and thus still avoid the complex SRH modeling. Their potential will be discussed in detail. A third procedure based on the complete SRH modeling of the TDLS curve will be discussed in detail in the next Sect. 3.5.

Discussing in Sect. 3.4.3 the ability of TDLS to separate multiple defect levels, we finally reveal a fundamental limitation of TDLS as a whole and especially of the linearized data evaluation techniques, which unambiguously demonstrates the invalidity of the prevalent interpretation of TDLS data in the literature.

3.4.1 Basic problem of data evaluation and data linearization

A Standard analysis of TDLS data

Since the standard analysis of TDLS data which has been introduced in Sect. 3.2.4 provides the basis for the derivations of the present section, we briefly summarize the approach focusing on the overall temperature dependence of SRH lifetime and the approximations made. Assuming without loss of generality a defect level in the upper band gap half in *p*-type silicon, we found in Sect. 3.2.4 the following expression for the SRH lifetime under LLI conditions:

$$\tau_{SRH}^{LLI}(T) = \tau_{n0}(T) + \underbrace{\tau_{n0}(T) k \frac{n_1(T)}{p_0}}_{ExpTerm} \quad (3.38)$$

Since the exponential temperature dependence of the SRH density n_1 exceeds the temperature dependence of all other contributions, given by low order power laws, the complete temperature range can be divided into three regions with respect to the expected temperature dependence of LLI-SRH lifetime:

$$\begin{aligned} T \in T_{<} &\Leftrightarrow k n_1(T) \ll p_0 \Leftrightarrow \tau_{ExpTerm}(T) \ll \tau_{n0}(T) \\ T \in T_{trans} &\Leftrightarrow k n_1(T) \approx p_0 \Leftrightarrow \tau_{ExpTerm}(T) \approx \tau_{n0}(T) \\ T \in T_{>} &\Leftrightarrow k n_1(T) \gg p_0 \Leftrightarrow \tau_{ExpTerm}(T) \gg \tau_{n0}(T) \end{aligned} \quad (3.39)$$

At sufficiently low temperatures ($T \in T_{<}$), the n_1/p_0 term in Eq. (3.38) can be neglected and the LLI-SRH lifetime equals the electron capture time constant $\tau_{n0}(T)$. If the idealized case of temperature-independent capture cross-sections is chosen as a starting point, $\tau_{n0}(T)$ only depends on temperature via the thermal velocity as indicated in Eq. (3.3). The temperature dependence of LLI-SRH lifetime is thus given by

$$\tau_{SRH,<}^{LLI}(T) \approx \tau_{n0}(T) = [N_i \sigma_n v_n(T)]^{-1} \propto T^{-1/2} \quad \text{for } T \in T_{<}. \quad (3.40)$$

At sufficiently high temperatures ($T \in T_{>}$), however, the defect-dependent n_1/p_0 term becomes dominant and Eq. (3.38) approaches $\tau_{ExpTerm}$ as the simple τ_{n0} addend can be neglected:

$$\tau_{SRH,>}^{LLI}(T) \approx \tau_{ExpTerm}(T) \propto T \times \exp\left(-\frac{\Delta E_t}{k_B T}\right) \quad \text{for } T \in T_{>}. \quad (3.41)$$

As already shown in Sect. 3.2.4, the overall T -dependence of LLI-SRH lifetime in the $T_{>}$ region is then given by a superposition of the dominating

exponential T -dependence of the activation term and a linear T -dependence which arises from the temperature-dependent pre-factors $N_C(T) \propto T^{3/2}$ and $\tau_{n0}(T) \propto T^{-1/2}$ in Eq. (3.38). Equation (3.41) provides the basis for the standard TDLS analysis. If the LLI-SRH lifetime is divided by temperature and plotted in an Arrhenius plot [i.e., $\ln(\tau(T)/T)$ vs. $1/T$], the $T_>$ region exhibits a linear increase:¹²

$$\ln\left[\frac{\tau_{SRH,>}^{LLI}(T)}{T}\right] = \text{const.} - \frac{\Delta E_t}{k_B T} \quad \text{for } T \in T_>, \quad (3.42)$$

whose slope only depends on the energy depth ΔE_t and is not influenced by any other defect parameter. Thus, ΔE_t may be directly extracted from a fit of the linear increase in the Arrhenius plot.

At medium temperatures ($T \in T_{\text{trans}}$), both addends in Eq. (3.38) contribute to the LLI-SRH lifetime. This produces a smooth transition from the slightly decreasing part of the TDLS curve in the $T_<$ region to the strongly increasing part in the $T_>$ region. An example is displayed in Fig. 3.26 (closed circles). As will be shown later in this section, all three temperature regions have to be considered for the derivation of improved TDLS evaluation techniques.

B Basic problem of the evaluation of TDLS data: reduced Arrhenius increase

The accuracy of the ΔE_t determination from a linear Arrhenius fit, as proposed by the standard TDLS analysis, strongly depends on the width of the temperature range which exhibits the characteristic Arrhenius increase. As has been shown in Figs. 3.7 and 3.8 the width of this temperature range strongly depends on energy level and doping concentration since the onset temperature of the Arrhenius increase is shifted to higher values for deeper energy levels and higher doping concentrations. At high temperatures, the evaluable temperature range is confined by an additional superposed effect, which will be discussed in detail in Sect. 3.5: the abrupt onset of intrinsic conduction. The induced lifetime decrease is so great that the linear increase in the SRH density is completely screened. As can be seen from the simulated TDLS curve in Fig. 3.26 (solid circles), in the case of a 10^{15} cm^{-3} doped wafer a temperature of 500 K is found as upper limit for

¹² Although TDLS curves are always plotted versus inverse temperature, comments on their qualitative shape are always used with respect to an increase of temperature. The term “Arrhenius increase” thus refers to the increase of lifetime with increasing temperature, although the Arrhenius diagram itself displays a curve which decreases with $1/T$.

the evaluable temperature range. This intrinsic upper temperature limit strongly depends on the doping concentration N_A and decreases with decreasing N_A . The explicit calculation of both confining temperatures as functions of the material and defect parameters (see Sects. 3.5.4B and 3.5.8) reveals that, especially for defect levels close to mid-gap and highly doped samples, the temperature range exhibiting the Arrhenius increase may be reduced to such an extent that an accurate determination of the energy level is no longer possible (see Fig. 3.51).

The limitations of the standard TDLS evaluation in terms of accuracy becomes obvious from the evaluation of the simulated TDLS curve displayed in Fig. 3.26. Although the assumed energy depth and doping concentration represent medium values for both quantities, the onset of intrinsic conduction reduces the temperature range of the Arrhenius increase to such an extent that the energy depth of 0.28 eV, which is gained from a linear fit of the original data in a temperature range from 400–500 K (dashed line), underestimates the true defect depth of 0.30 eV by 20 meV. It has to be emphasized that this energy deviation of 7 % is a pure systematic error which cannot be reduced even by a further adjustment, i.e. reduction, of the fitted temperature range. This observation demonstrates that even in the temperature range from 400–500 K, where the T -normalized TDLS curve is supposed to exhibit its linear increase [and thus to equal $\tau_{ExpTerm}$ as indicated in Eq. (3.41)], the influence of the simple $\tau_{no}(T)$ addend in Eq. (3.38) cannot be completely neglected. This shows the real dimension of the transition region T_{trans} .¹³ Since the systematic deviation arising here may significantly increase for more adverse parameter constellations, an accurate application of TDLS requires improved techniques for data evaluation which avoid such effects.

¹³ The exact contribution to the systematic ΔE_t error which comes from to the de facto width of the transition region can be isolated if the simple analysis is repeated for a TDLS curve τ_{app} which is calculated for the same parameters as τ_{gen} in Fig. 3.26 but without considering intrinsic conduction, i.e., for $p_0(T) = N_A$ in the whole T range. A linear fit of τ_{app} in the T range from 400–500 K yields $\Delta E_t = 0.282$ eV compared to 0.278 eV which is obtained from a similar fit of τ_{gen} . This demonstrates that 6 % (absolute) of the determined systematic ΔE_t error of 7.3 % has to be attributed to the impact of the TDLS transition region and only 1.3 % (absolute) to the impact of the TDLS bend due to intrinsic conduction. If the T range for the linear fit of τ_{app} is reduced to 435–500 K and 475–500 K, respectively, the determined ΔE_t increases to 0.288 eV (4 % error) and 0.292 eV (2.7 % error), respectively. This gives an impression of the real dimensions of the sphere of influence of the transition region and highlights the relevance of improved techniques for the evaluation of TDLS data.

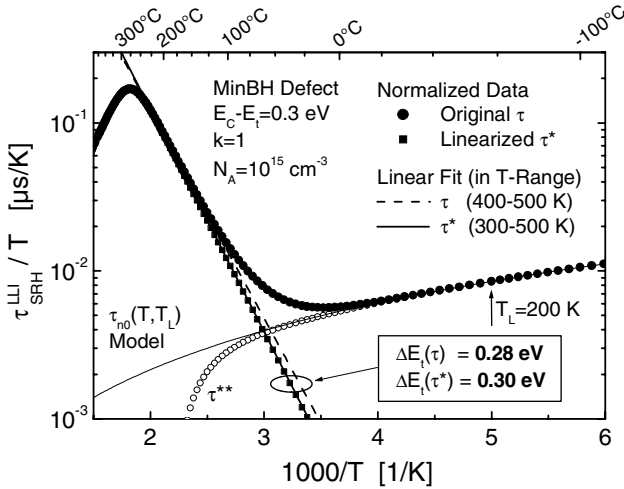


Fig. 3.26. Linearization of the TDLS transition region according to the procedure proposed in [36] demonstrated for a simulated data set. The abrupt large lifetime decrease at high temperatures is due to intrinsic conduction (see Sect. 3.5.3). The linear fit of the original (dashed line) and the linearized (solid line) Arrhenius increase reveals the necessity of the linearization in order to avoid systematic errors in the extracted defect energy depth.

C Solution: linearized data evaluation

In order to expand the temperature range of the linear Arrhenius increase, Ling and Cheng [36] proposed a procedure for a “linearization” of the transition region. As the $\tau_{n0}(T)$ term in Eq. (3.38) cannot be neglected for $T \in T_{trans}$, they proposed to define a modified lifetime $\tau^*(T)$ by subtracting $\tau_{n0}(T)$ from the measured lifetime. As the LLI-SRH lifetime measured at a temperature $T_L \in T_{<}$ equals $\tau_{n0}(T_L)$, they propose to determine $\tau_{n0}(T)$ by the following expression:

$$\tau_{n0}^*(T, T_L) := \tau_{n0}(T_L) \times \left(\frac{T}{T_L} \right)^{-0.5} = \tau_{SRH}^{LLI}(T_L) \times \left(\frac{T}{T_L} \right)^{-0.5} \quad (3.43)$$

where the modeling of the T -dependence of τ_{n0} is based on the simple theoretical T -dependence given in Eq. (3.40). Since the modified lifetime $\tau^*(T)$,

$$\tau^*(T) := \tau_{SRH}^{LLI}(T) - \tau_{n0}^*(T, T_L) = \text{const.} \times T \times \exp\left(-\frac{\Delta E_t}{k_B T}\right) \quad (3.44)$$

directly corresponds to the defect-dependent term $\tau_{ExpTerm}$ of Eq. (3.38), by definition in the whole temperature range, the energy level is extracted in

an analogous way to the standard analysis from a fit of the linear increase which theoretically covers the whole temperature range if the quantity

$$\ln\left[\frac{\tau^*(T)}{T}\right] = \text{const.} - \frac{\Delta E_t}{k_B T} \quad (3.45)$$

is plotted in an Arrhenius plot versus $1/T$. The benefit of this evaluation is demonstrated in Fig. 3.26 on the simulated TDLS curve which has already been evaluated in the previous section by means of the standard analysis. While the temperature region of the linear Arrhenius increase is narrow for the raw data covering only 400–500 K, it is greatly extended for the $\tau^*(T)$ data (closed squares) covering a temperature range twice as wide, from 300–500 K.¹⁴ This extension is directly reflected in the increased accuracy of the extracted ΔE_t value: while the linear fit of the original Arrhenius increase (dashed line) yielded $\Delta E_t=0.28$ eV and thus systematically underestimated the true defect depth, the linear fit of the linearized Arrhenius increase (solid line) accurately provides the defect energy depth of $\Delta E_t=0.30$ eV. Thus, at least in the considered case of an ideal¹⁵ TDLS curve, the linearization of the transition region completely eliminates the systematic ΔE_t error and thus significantly extends the defect and material parameter plane for which TDLS is applicable.

3.4.2 Improved techniques of data linearization

A The problem of the standard linearization: deviations from the simple $\tau_{n0}(T)$ -dependence

Ling and Cheng recommended choosing the reference point T_L as deep as possible in the $T_<$ region to ensure that the extracted lifetime is no longer influenced by the defect-dependent $\tau_{ExpTerm}$ and thus equals $\tau_{n0}(T_L)$. How-

¹⁴ Since the linearized lifetime $\tau^*(T)$ equals by definition the defect-dependent SRH term in Eq. (3.38), the complete $\tau^*(T)$ curve constitutes the linear Arrhenius increase. From a theoretical point of view the Arrhenius increase of the linearized data thus covers the whole temperature range. From a practical point of view the evaluable part of the $\tau^*(T)$ curve is limited towards lower temperatures since $\tau^*(T)$ becomes very small for $T \in T_<$. As a consequence, the quantity τ^* which is calculated in the experiment from the lifetime values measured at the temperatures T and T_L becomes defective in that temperature region since measurement errors are transferred above average. Nevertheless, this error is of minor importance in the transition region where neither of the two addends of Eq. (3.38) dominates. Thus τ^* allows a linearization of the transition region of sufficient accuracy and hence a significant extension of the temperature range for the linear fit.

¹⁵ The attribute “ideal” denotes a TDLS curve without superposed T -dependence of the capture cross-sections.

ever, it then becomes a fundamental prerequisite for the accuracy of this linearization that the temperature dependence of LLI-SRH lifetime measured for $T \ll T_c$ can be simulated by Eq. (3.43). Unfortunately, under realistic circumstances this is often not the case. The observed deviations most likely result from a temperature dependence of the capture cross-section that is not considered by the modeling in Eq. (3.43).

The linearization of such “non-ideal” but realistic TDLS curves according to Eqs. (3.43) and (3.44) leads to $\tau^*(T)$ curves that strongly depend on the choice of T_L . This problem is simulated in Fig. 3.27 for a defect level with a capture cross-section that increases exponentially with increasing temperature, as is typical of multiphonon capture.¹⁶ For comparison, the ideal data linearization labeled $\tau^{***}(T)$ which is discussed in Sect. 3.4.2E is plotted as well (solid squares). It becomes obvious that the deviation of the $\tau^*(T)$ curve from the ideal $\tau^{***}(T)$ curve increases with decreasing T_L since the modeled $\tau_{n0}(T, T_L)$ curves (thin lines) increasingly deviate in the transition region from the real $\tau_{n0}(T)$ curve (solid line).

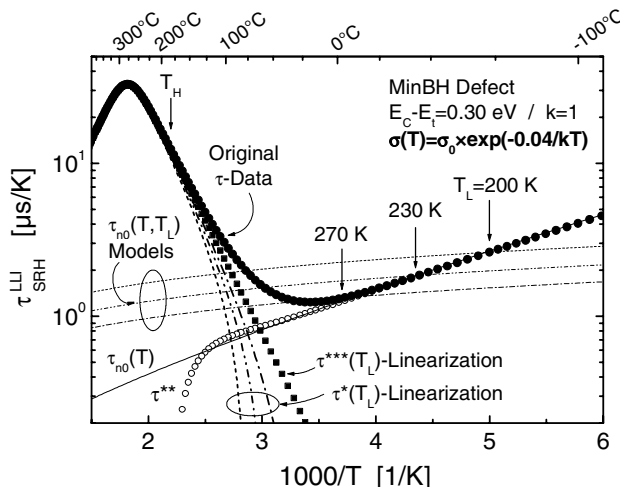


Fig. 3.27. Linearization of the TDLS transition region for a simulated data set under the assumption of a defect with temperature-dependent capture cross-sections. The quality of the procedure proposed in [36] (thick lines) strongly depends on the reference temperature T_L and the related $\tau_{n0}(T, T_L)$ -model (thin lines). For comparison, the new, optimized procedure proposed in this work is displayed (solid squares). Note that the diagram displays the lifetime curves $\tau(T)$ and not $\tau(T)/T$.

¹⁶ The assumed $\sigma(T)$ -model is $\sigma_n(T) = \sigma_\infty \times \exp(-E_\infty/k_B T)$ with an activation energy $E_\infty = 0.04$ eV which corresponds to realistic values, e.g., $E_\infty(\text{Fe}_i) = 0.043$ eV [37]. A brief overview of the different capture mechanisms and their temperature dependence will be given in Sect. 3.5.1.

In order to minimize or even eliminate these evaluation errors in the case of an additional temperature dependence for $T \in T_<$, we propose three advanced procedures for data evaluation.

B Solution 1: optimum choice of T_L by means of an iterative procedure

The first procedure aims to optimize the T_L determination while the linearization model itself remains unchanged. On the one hand T_L has to be chosen low enough to ensure that the corresponding lifetime is not yet influenced by the linear increase. On the other hand T_L has to be chosen close to the transition region T_{trans} , in order to avoid a distortion of the $\tau^*(T)$ curve due to deviations between the modeled and the measured τ_{n0} -dependence. Thus, the optimum T_L is the upper limit of the $T_<$ region.

To be able to determine this optimum T_L , an auxiliary function $\tau^{**}(T)$ is deduced from the measured data which approximates the real temperature dependence of τ_{n0} in the whole temperature range. Analogously to Eq. (3.43) the temperature dependence of $\tau_{ExpTerm}$ in Eq. (3.38) may be modeled using a lifetime value measured at a temperature T_H within the exponential regime ($T_H \in T_>$) if the temperature dependence given in Eq. (3.41) is taken into account via a function $h(T)$:

$$\tau_{ExpTerm}(T; T_H, \Delta E_t) := \tau_{SRH}^{LLI}(T_H) \times \frac{h(T)}{h(T_H)} \quad (3.46)$$

$$\text{with } h(T) := T \times \exp\left(-\frac{\Delta E_t}{k_B T}\right)$$

The auxiliary function $\tau^{**}(T)$ given by

$$\tau^{**}(T; T_H, \Delta E_t) := \tau_{SRH}^{LLI}(T) - \tau_{ExpTerm}(T; T_H, \Delta E_t) \quad (3.47)$$

then incorporates the *complete* temperature dependence of τ_{n0} (see open circles in Figs. 3.26 and 3.27). Thus, the optimum T_L lies at the temperature where the measured lifetime curve starts deviating from the $\tau^{**}(T)$ curve, since precisely up to that temperature the measured lifetime curve is not affected by $\tau_{ExpTerm}$, i.e. the Arrhenius increase. As $\tau^{**}(T)$ depends on the value of ΔE_t yet to be determined, an iterative procedure has to be used:

- Determine ΔE_t in a first approximation from the original lifetime data $\tau(T)$ using the standard analysis.
- Calculate $\tau^{**}(T; T_H, \Delta E_t)$ for a temperature $T_H \in T_>$ according to Eq. (3.47).
- Determine the optimum T_L at the separation point of $\tau(T)$ and $\tau^{**}(T)$.

- Calculate $\tau^*(T; T_L)$ using the lifetime value measured at T_L according to Eq. (3.44).
- Determine an improved value of ΔE_t from a linear fit of the linearized lifetime data $\tau^*(T)$.
- Calculate a new $\tau^{**}(T; T_H, \Delta E_t)$ using the improved ΔE_t and repeat the procedure.

Usually, a self-consistent solution is achieved after 2–3 runs. Before discussing the accuracy of the proposed iterative procedure in Sect. 3.4.2D, let us first show from a theoretical point of view how the slope of the Arrhenius increase and thus the extracted value for the energy depth ΔE_t change if the temperature dependence of an arbitrary $\sigma(T)$ -model is superposed.

C Impact of an underlying $\sigma(T)$ -model (1): theoretically expected deviation of the extracted energy from the defect energy

Evaluating the impact of a $\sigma(T)$ -model on the LLI-SRH lifetime, we want to assume that the symmetry factor $k = \sigma_n/\sigma_p$ is still independent of temperature, an assumption which is further discussed in Sects. 3.5.1C and 3.5.10. According to Eqs. (3.38) and (3.40), the temperature dependence of the capture cross-sections then only influences the LLI-SRH lifetime via the minority capture time constant τ_{n0} :

$$\tau_{n0}(T) = \frac{1}{N_i \sigma_n(T) v_{th}(T)} \propto \frac{1}{\sigma_n(T) \cdot T^{1/2}} \quad (3.48)$$

According to Eq. (3.40), the LLI-SRH lifetime directly displays this modified temperature dependence in the $T_<$ region. In the $T_>$ region, the overall temperature dependence of LLI-SRH lifetime is derived in an analogous way to Eq. (3.41) and is given by (for $T \in T_>$)

$$\tau_{SRH,>}^{LLI}(T) \approx \tau_{n0}(T) k \frac{n_1(T)}{P_0} = \text{const.} \times \frac{T}{\sigma_n(T)} \times \exp\left(-\frac{\Delta E_t}{k_B T}\right) \quad (3.49)$$

For the lifetime increase observed in an Arrhenius plot at temperatures $T \in T_>$ we thus find

$$\ln\left[\frac{\tau_{SRH,>}^{LLI}(T)}{T}\right] = \text{const.} - \left(\frac{\Delta E_t}{k_B T} + \underbrace{\ln[\sigma_n(T)]}_{=: \text{Error}} \right) \quad \text{for } T \in T_>. \quad (3.50)$$

Equation (3.50) shows that the gradient of the Arrhenius plot $\ln[\tau(T)/T]$ vs. $1/T$ is no longer directly proportional to ΔE_t but that it is modified by the temperature-dependent error term $\ln[\sigma_n(T)]$.

To quantify the implications, the error term is calculated for two types of T -dependence which represent the most important $\sigma(T)$ -models as will be discussed in Sect. 3.5.1. For an exponential temperature dependence $\sigma_n(T) := \sigma_\infty \times \exp[-E_\infty/k_B T]$, as assumed for the simulated TDLS curve in Fig. 3.27, the error term may be written as

$$\text{Error} := \ln[\sigma_n(T)] = -\frac{E_\infty}{k_B T} + \ln \sigma_\infty \quad (3.51)$$

While the temperature-independent term $\ln[\sigma_\infty]$ just leads to a vertical shift of the whole Arrhenius curve, the temperature-dependent E_∞ term modifies the overall gradient of the Arrhenius plot of $\ln[\pi(T)/T]$, leading to¹⁷

$$\Delta E_t^{\text{fit}} := \Delta E_t - E_\infty \quad (3.52)$$

This shows that the energy value ΔE_t^{fit} , which is determined from a linear fit of the Arrhenius increase, underestimates the true defect energy depth ΔE_t for purely theoretical reasons. To obtain ΔE_t , the activation energy E_∞ of the $\sigma(T)$ -model has to be added to the measured value ΔE_t^{fit} .¹⁸ But since E_∞ is unknown a priori and since a linear fit of the Arrhenius increase only yields the difference of the underlying activation energies, the separation of these energies in general fails.

For a power law temperature dependence $\sigma_n(T) = \sigma_0 \times T^\alpha$ the error term takes the form

$$\text{Error} := \ln[\sigma_n(T)] = -\alpha \ln T + \ln \sigma_0 \quad (3.53)$$

Again only the temperature-dependent term $-\alpha \ln T$ influences the gradient of the Arrhenius plot of $\ln[\pi(T)/T]$ which leads to¹⁹

$$\Delta E_t^{\text{fit}}(T) := \Delta E_t - k_B \alpha T \quad (3.54)$$

¹⁷ Equation (3.52) follows from inserting Eq. (3.51) into Eq. (3.50) and calculating the derivative $\partial/\partial[k_B T]^{-1}$. Its calculation corresponds to the procedure of a linear fit in the Arrhenius diagram.

¹⁸ Note a decisive difference with DLTS: DLTS is based on a measurement of the emission rate which is defined as $e_n(T) \propto \sigma_n(T) \times \exp(-\Delta E_t/k_B T)$. If the investigated defect exhibits an exponential $\sigma(T)$ -dependence, the Arrhenius plot of the emission rates exhibits a gradient which is proportional to the sum $\Delta E_t + E_\infty$. To obtain the true defect energy depth ΔE_t , the activation energy E_∞ of the $\sigma(T)$ -model has to be subtracted from the measured value ΔE_t^{fit} . Thus in the case of an exponential $\sigma(T)$, the DLTS result overestimates the true energy depth by E_∞ , whereas it is underestimated by the same amount by the TDLS result. This may explain deviations between the spectroscopic results of the two techniques.

¹⁹ Equation (3.54) follows from inserting Eq. (3.53) into Eq. (3.50) and calculating the derivative $\partial/\partial[k_B T]^{-1}$.

This shows that the gradient of the Arrhenius plot becomes temperature-dependent if a power-law-dependent $\sigma(T)$ -model is superposed. But since the linear temperature correction in Eq. (3.54) is proportional to Boltzmann's constant $k_B = 8.62 \times 10^{-5}$ eV/K, the gradient of the Arrhenius increase only changes by 9 meV over a temperature distance of 100 K if we assume $\alpha=1$. Thus, in most experimental cases the bending of the Arrhenius increase due to a power-law-dependent $\sigma(T)$ will not be detectable, the evaluation of the Arrhenius increase yielding an average energy $(\Delta E_t^{fit})_{av}$. The direction of the deviation between measured and true energy depth is defined by the sign of the power α :

$$\begin{aligned}\alpha > 0 &\Rightarrow (\Delta E_t^{fit})_{av} < \Delta E_t \\ \alpha < 0 &\Rightarrow (\Delta E_t^{fit})_{av} > \Delta E_t\end{aligned}\quad (3.55)$$

So for $\alpha>0$, i.e., if $\sigma_n(T)$ increases and $\tau_{n0}(T)$ decreases with temperature, the true energy depth is slightly underestimated by the extracted energy, whereas for $\alpha<0$, i.e., if $\sigma_n(T)$ decreases and $\tau_{n0}(T)$ increases with temperature, the true energy depth is slightly overestimated by the extracted energy. Nevertheless, a considerable effect is only expected for $|\alpha|>2$.

D Impact of an underlying $\sigma(T)$ -model (2): systematic errors in the energy determination due to inadequate data evaluation

The impact of an underlying $\sigma(T)$ -dependence on the accuracy of ΔE_t determination is twofold. Apart from the theoretically expected deviations of the extracted energy value, which have been discussed in the previous section, $\sigma(T)$ influences the systematic errors due to data evaluation.

In order to evaluate the accuracy of the different evaluation procedures in the case of a “realistic” TDLS curve, we determined ΔE_t from the original and linearized TDLS curves in Fig. 3.27, which represent the case of a TDLS curve with an underlying exponential $\sigma(T)$ -dependence. The necessary linear fits have been performed on the corresponding Arrhenius plots $\pi(T)/T$ which are displayed in Fig. 3.28. Table 3.2 provides an overview of the obtained spectroscopic results. The linear fit (dashed line in Fig. 3.28) of the original data (circles) in a T range from 400–500 K leads to an energy value of 0.24 eV which underestimates the energy value of $\Delta E_t/E_\infty=0.26$ eV expected from Eq. (3.52) by 8 %. In terms of both direction and magnitude, this deviation equals the one observed in Fig. 3.26, when the standard analysis has been applied to an ideal TDLS curve. As in that case, the deviation cannot be reduced by a further reduction of the fitted T range. Thus, it has to be mainly attributed to a long-range impact of the transition region.

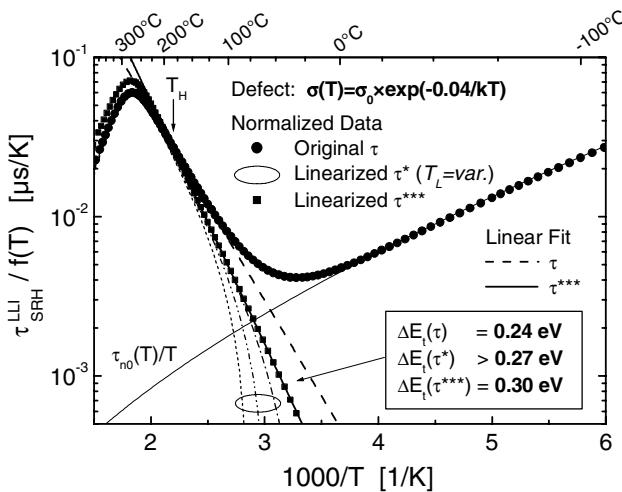


Fig. 3.28. Original and linearized TDLS data from Fig. 3.27 normalized on temperature according to Eq. (3.59). Due to the underlying activation law for the capture cross-section, the slope of the Arrhenius increase should (i) equal $\Delta E_t - E_\infty = 0.26 \text{ eV}$ for the standard T normalization with $f(T) = T$ as used for the τ_{eff} data (solid circles) and the τ^* data (thin lines) and (ii) directly provide $\Delta E_t = 0.30 \text{ eV}$ for the advanced T normalization with $f(T) = T/\sigma(T)$ as used for the τ^{***} data (solid squares). The linear fit of the differently processed Arrhenius increases reveals that the expected energy depth is systematically underestimated if the original τ_{eff} data are used (dashed line) and overestimated if the linearized τ^* data are used (fit not shown). Only the use of the optimally linearized τ^{***} data allows an accurate determination of the energy (solid line).

For the linearized τ^* data (dotted and dash-dotted lines in Fig. 3.28), we have found that the artificial bending of the τ^* curves due to the inadequate $\tau_{no}(T, T_L)$ -models leads to an overestimate of the expected energy value of $\Delta E_t - E_\infty = 0.26 \text{ eV}$ throughout the parameter variation. Apart from that, our supposition was confirmed that the accuracy of the ΔE_t determination strongly depends on (i) the choice of T_L and (ii) the fitted T range. Fitting the $\tau^*(T; T_L)$ curves for different T_L in a fixed T range from 400–500 K, we have found that the overestimate of ΔE_t increases from 4 % for the optimum $T_L = 270 \text{ K}$ to 85 % for $T_L = 150 \text{ K}$. The fact that the deviation already reaches 12 % for $T_L = 230 \text{ K}$, i.e., only 40 K below the optimum T_L , demonstrates the necessity of an optimized T_L determination. The quality of the iterative procedure for the T_L determination, which has been proposed in Sect. 3.4.2B, is demonstrated impressively by a systematic error as low as 4 %. For the optimum $\tau^*(T; T_L = 270 \text{ K})$ curve we investigated the impact of the fitted T range. If the T range is doubled from 400–500 K to 300–500 K, the error of ΔE_t increases from 4 % to 42 %, which shows the poor quality of the linearization deeper in the transition region T_{trans} , even

Table 3.2. Impact of the data evaluation procedure and the fit range on the energy depth ΔE_t determined from TDLS by a linear fit of the Arrhenius increase. The underlying TDLS curve, shown in Fig. 3.28, is simulated for a symmetric ($k=1$) defect level at $E_C-E_t=0.3$ eV, which exhibits an exponential $\sigma(T)$ -model with $E_\infty=0.04$ eV.

Evaluation procedure		Spectroscopic result				
Technique / T normalization	T_L	Fitted T range	ΔE_t^{fit}	ΔE_t error	ΔE_t expected	Comment
Original data τ_{eff} $\rightarrow f(T)=T$	—	400–500 K	0.24 eV	– 8 %	$E_t-E_\infty=0.26$ eV	E_t underestimate
Standard linearization τ^* $\rightarrow f(T)=T$	270 K (Opt.)	455–500 K	0.26 eV	0 %	$E_t-E_\infty=0.26$ eV	1. Accurate for short T range
		400–500 K	0.27 eV	+ 4 %		2. Increasing E_t overestimate with increasing T range
		350–500 K	0.30 eV	+ 15 %		
		300–500 K	0.37 eV	+ 42 %		
Advanced linearization τ^{***} $\rightarrow f(T)=T/\sigma(T)$	230 K	400–500 K	0.29 eV	+ 12 %		Increasing E_t overestimate with decreasing T_L
	200 K	400–500 K	0.30 eV	+ 15 %		
	150 K	400–500 K	0.48 eV	+ 85 %		
Advanced linearization τ^{***} $\rightarrow f(T)=T/\sigma(T)$	250 K or below	300–500 K	0.30 eV	0 %	$E_t=0.30$ eV	Accurate for arbitrary T range

for the optimized τ^* curve. On the other hand, an accurate ΔE_t determination is achieved if the fitted T range is reduced to 455–500 K. It has to be concluded that the best fit result is obtained if the actually linearized data are only used to a minimum extent within the fit. This trend reduces the presented linearization procedure to absurdity!

E Solution 2: advanced data linearization with respect to the measured $\tau_{ho}(T)$

As shown above, the TDLS evaluation procedures presented so far face the problem that, when applied to a “realistic” TDLS curve with superposed $\sigma(T)$ -model, the extracted energy value ΔE_t^{fit} often deviates significantly from the true defect energy depth ΔE_t : on the one hand due to systematic errors induced by simplifying assumptions of data evaluation (see Sect. 3.4.2D) and on the other hand due to theoretically expected changes in the Arrhenius gradient which cannot be identified from a simple linear fit of the $\ln[\tau(T)/T]$ data and are thus incorrectly attributed to the defect energy depth ΔE_t being equated with ΔE_t^{fit} (see Sect. 3.4.2C). While the proposed iterative linearization procedure successfully minimizes the first problem, the second problem remains unsolved for all the above techniques. To make an accurate determination of just the true energy depth ΔE_t

possible, the underlying T -dependence of the capture cross-sections has to be taken into account in the data evaluation.

Fortunately, the $\sigma(T)$ -model of the underlying defect can be directly extracted from the low-temperature part of the TDLS curve. According to Eq. (3.40) the LLI-SRH lifetime equals, for $T \in T_<$, the minority capture time constant τ_{n0} , whose general T -dependence is given by $\tau_{n0}(T) = [N_i \sigma_n(T) v_{th}(T)]^{-1}$. Thus, all deviations of $\tau_{SRH,<}^{LLI}(T)$ from the simple $T^{-1/2}$ -dependence, induced by the known T -dependence of $v_{th}(T)$, have to be attributed to the T -dependence of the minority capture cross-section $\sigma_n(T)$, which is thus obtained by modeling the quantity

$$[\tau_{SRH,<}^{LLI}(T) \times T^{1/2}]^{-1} \text{ or } [\tau^{**}(T) \times T^{1/2}]^{-1} \rightarrow [\tau_{n0}(T) \times T^{1/2}]^{-1} \rightarrow \sigma_n(T) \quad (3.56)$$

The accuracy in determining the $\sigma_n(T)$ -model can be increased if, instead of $\tau_{SRH,<}^{LLI}(T)$, the auxiliary function $\tau^{**}(T)$ which has been introduced in Sect. 3.4.2B is used for the modeling, since $\tau^{**}(T)$ reflects the complete temperature dependence of τ_{n0} over a broader T range.

Considering the possibility of determining an underlying $\sigma(T)$ -model from the TDLS data alone, we developed an advanced procedure for TDLS data evaluation, which follows the linearization procedure from Sect. 3.4.2B except for two important changes. The first difference is that the actually measured T -dependence of τ_{n0} is accurately modeled instead of being approximated by the simple $T^{-1/2}$ -dependence. To this end, the underlying $\sigma(T)$ -model is determined by means of the procedure described above. Analogue to Eq. (3.43), the complete $\tau_{n0}(T)$ -dependence is then developed around a lifetime value measured at a temperature $T_L \in T_<$ which leads to the following expression:

$$\tau_{n0}^{***}(T; T_L) := \tau_{SRH}^{LLI}(T_L) \times \left[\left(\frac{T_L}{T} \right)^{0.5} \frac{\sigma_n(T_L)}{\sigma_n(T)} \right] \quad (3.57)$$

The linearization of the TDLS data is achieved as before by subtracting the modeled $\tau_{n0}^{***}(T; T_L)$ curve subtracted from the original lifetime data:

$$\tau^{**}(T) := \tau_{SRH}^{LLI}(T) - \tau_{n0}^{***}(T; T_L) = \text{const.} \times f(T) \times \exp\left(-\frac{\Delta E_t}{k_B T}\right) \quad (3.58)$$

$$\text{with} \quad f(T) := T/\sigma(T)$$

It should be emphasized that, due to the correct consideration of the measured $\tau_{n0}(T)$, the linearized $\tau^{**}(T)$ curve does not depend on the choice of T_L . As can be seen from Eq. (3.58), the overall T -dependence of $\tau^{**}(T)$ is given by a superposition of the exponential T -dependence of the

activation term and the non-linear T -dependence of a function $f(T)$ which depends on $\sigma(T)$.

From this arises the second important difference between the advanced and the standard linearization procedure. Since the accurate determination of ΔE_t from an Arrhenius fit requires the Arrhenius plot of a quantity which shows the isolated T -dependence of the activation term, $\tau^{***}(T)$ is divided not only by temperature, as is done for $\tau(T)$ and $\tau^*(T)$, but also by the complete function $f(T)$. To guarantee a pinning of the Arrhenius plots, obtained from the different procedures, at a common point $\tau_{SRH}^{LLI}(T_H)/T_H$ within the Arrhenius increase, the complete normalization takes the form

$$\ln \left[\frac{\tau^{***}(T) \times f(T_H)}{f(T) \times T_H} \right] = \ln \left[\frac{\tau^{***}(T)}{T} \times \frac{\sigma_n(T)}{\sigma_n(T_H)} \right] = \text{const.} - \frac{\Delta E_t}{k_B T} \quad (3.59)$$

As can be seen, the Arrhenius gradient of such a normalized τ^{***} curve leads directly to the true defect energy depth ΔE_t without any offset. The term on the left hand side of Eq. (3.59) represents a generalized expression for the generation of the different Arrhenius plots used throughout this chapter. The function $f(T)$ only has to be equated with that T -dependence which should be eliminated from the data in each case: while $f(T) = T/\sigma(T)$ is required in the case of the advanced linearization, $f(T) = T$ has to be used in the case of the standard analysis and the simple linearization.

Figures 3.27 and 3.28 display the original and the $f(T)$ -normalized $\tau^{***}(T)$ curves (solid squares), respectively, as they result when the advanced linearization procedure is applied to the “realistic” TDLS curve with exponential $\sigma(T)$ -model. In contrast to the artificially bent τ^* curves, the τ^{***} curve is absolutely linear in the whole transition region which demonstrates the accuracy of the linearization. Note that in the experiment the linearity of the τ^{***} curve is a direct measure for the quality of the determined $\sigma(T)$ -model. As displayed in Table 3.2, a linear fit of the Arrhenius increase (solid line in Fig. 3.28) in a T range as broad as 300–500 K accurately yields the defect energy depth $\Delta E_t = 0.30$ eV. It should be emphasized that for the linearized τ^{***} curve the result of the linear Arrhenius fit depends on neither the fitted T range nor the choice of $T_L \in T_<$. It has to be concluded that the advanced linearization procedure is the most appropriate technique to evaluate TDLS data with superposed T -dependence: not only because it allows an exact determination of the true defect energy depth ΔE_t , but also because it provides the T -model of the capture cross-sections, which is an additional fingerprint of the defect, as will be discussed in Sect. 3.5.1.

F Solution 3: simulation of the complete TDLS curve

The third and last of the advanced procedures of data evaluation is the SRH modeling of the complete TDLS curve. The discussion in the previous section revealed that an accurate ΔE_t determination requires more than a linear fit of the Arrhenius plot. Although the advanced linearization procedure can be ranked among the simple evaluation techniques as it renounces a complex SRH modeling and uses a simple linear Arrhenius fit for the ΔE_t determination, it already requires the modeling of the low-temperature part of the TDLS curve to determine the underlying $\sigma(T)$ -model. Thus, the step from the advanced data linearization to the SRH modeling of the complete TDLS curve only increases to a medium extent the complexity of data evaluation, whilst allowing a tremendous increase in the extractable spectroscopic information. This will be discussed in detail in Sect. 3.5.

3.4.3 Resolution capability of TDLS

A further problem concerning the accuracy of the spectroscopic result may arise from the presence of multiple recombination-active defect levels. The following section is therefore dedicated to the resolution capability of TDLS. The focus is put on the one hand on the possibility of separating multiple defect levels and on the other hand on the error in the ΔE_t determination which has to be expected for the dominant defect if a separation fails.

A Impact of two independent defect levels on the TDLS curve

Let us consider for the sake of simplicity a system of two independent²⁰ SRH centers A and B, characterized under LLI conditions by SRH lifetimes τ^A and τ^B , respectively. According to Eq. (1.30) the overall SRH lifetime τ_{total} of the two-level system observed under LLI conditions is then given by

$$\begin{aligned} \tau_{LLI}^{total}(T) &= \left[\frac{1}{\tau_{LLI}^A(T)} + \frac{1}{\tau_{LLI}^B(T)} \right]^{-1} \\ &= \underbrace{\tau_{LLI}^A(T) \times \left[1 + \frac{\tau_{LLI}^A(T)}{\tau_{LLI}^B(T)} \right]^{-1}}_{=: \text{Deviation}^A} = \underbrace{\tau_{LLI}^B(T) \times \left[1 + \frac{\tau_{LLI}^B(T)}{\tau_{LLI}^A(T)} \right]^{-1}}_{=: \text{Deviation}^B} \end{aligned} \quad (3.60)$$

²⁰ Any interactions between defect levels such as electronic transitions are left out of consideration within this work to avoid further complicating the discussion.

Since the individual lifetimes τ^A and τ^B are added reciprocally, the overall SRH lifetime τ_{total} of the two-level system is at each temperature smaller than the smallest single lifetime, the shape of the associated superposed TDLS curve $\tau_{total}(T)$ thus being dominated in the whole temperature range by the lower of the two individual TDLS curves $\tau^A(T)$ and $\tau^B(T)$. As indicated in the second row of Eq. (3.60), $\tau_{total}(T)$ may be written as a product of the dominating single-level curve and a temperature-dependent deviation term which approaches unity as the ratio of the lifetimes of active/inactive defect approaches zero, i.e., as the difference between both single lifetimes increases towards infinity.

Concerning the overall shape of the superposed TDLS curve, three qualitatively different cases are possible. These are displayed in Fig. 3.29 for a system with a deep level A at 0.35 eV (thin solid line) and a shallow level B at 0.20 eV (thin dashed line), both assumed in the upper half of the band gap. Since defect deactivation, which is reflected in the Arrhenius increase, starts at much lower temperatures for the shallow than for the deep level, the deep level A dominates in most of the T range if both defects exhibit the same recombination activity at low temperatures, i.e., if $\tau_{n0}^A = \tau_{n0}^B$. As shown in Fig. 3.29a, the presence of the shallow level B is only reflected in a small step within the low-temperature part of the superposed TDLS curve $\tau_{total}(T)$, whereas the Arrhenius increase of $\tau_{total}(T)$ more or less equals that of $\tau^A(T)$, the deep level A thus being determined by means of TDLS. The situation changes for $\tau_{n0}^A > \tau_{n0}^B$, i.e., if the recombination activity of the deep level A is reduced compared to that of the shallow level B which is displayed in Fig. 3.29b for $\tau_{n0}^A/\tau_{n0}^B = 100$. Then, the superposed TDLS curve $\tau_{total}(T)$ is dominated by $\tau^B(T)$ up to the temperature where the Arrhenius increase of $\tau^B(T)$ intersects the low-temperature part of $\tau^A(T)$. Due to the progressive deactivation of the shallow level B, $\tau^A(T)$ dominates $\tau_{total}(T)$ at higher temperatures. As a result $\tau_{total}(T)$ exhibits a cascade structure with a first and a second step that may allow a determination of the shallow level and the deep level, respectively. The possibility of separating defect levels from such a cascade-structured TDLS curve and the achievable accuracy are investigated in Sects. 3.4.3C and 3.4.3D on the basis of a theoretical and an experimental example, respectively. If the recombination activity of the deep level A further decreases, at some stage $\tau_A(T)$ and $\tau_B(T)$ no longer intersect each other as shown in Fig. 3.29c for $\tau_{n0}^A/\tau_{n0}^B = 10^4$. In this case the shallow level B dominates in the whole T range. Since $\tau_{total}(T)$ is almost identical with $\tau^B(T)$, the shallow level B is determined by means of TDLS. As expected, TDLS does not necessarily determine the deepest defect in a system, but the one which exhibits maximum recombination activity.

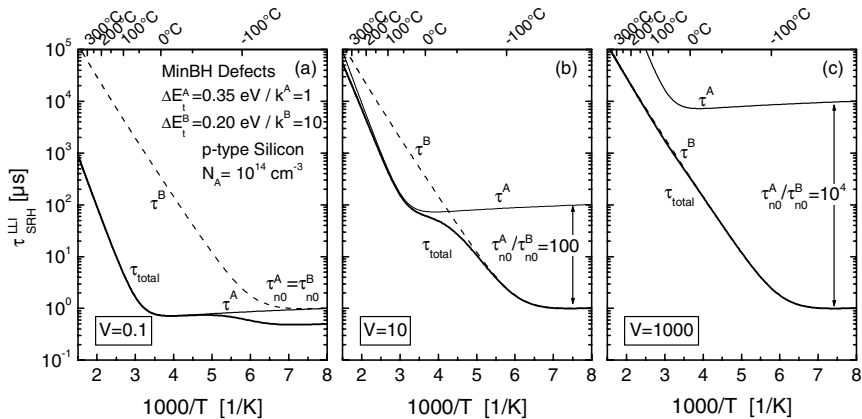


Fig. 3.29. Overall shape of a TDLS curve (thick solid line) for a system of two independent defect levels A (thin solid line) and B (thin dashed line) with different energy depths $\Delta E_t^A > \Delta E_t^B$. (a) For $\tau_{n0}^A = \tau_{n0}^B$ the deep level A dominates in most of the T range. (b) For $\tau_{n0}^A > \tau_{n0}^B$ both defects influence the Arrhenius increase of the superposed TDLS curve which exhibits a cascade structure. (c) For $\tau_{n0}^A \gg \tau_{n0}^B$ the shallow level B dominates in the whole T range. The quantity V which is defined in Eq. (3.62) has a decisive impact on the error of the Arrhenius gradient as shown in Fig. 3.31.

The fundamental problem in a real two-level system as displayed in Fig. 3.29b is the accuracy of the ΔE_t determination from the linear Arrhenius increase of the superposed TDLS curve. As can be seen in the τ^A -dominated part of $\tau_{total}(T)$, the gradient of the Arrhenius increase of $\tau_{total}(T)$ is significantly reduced compared to that of the original $\tau^A(T)$ curve. This deviation originates from the remaining impact of the shallow level B and leads to a systematic error in the extracted value for ΔE_t^A . A closer look at Fig. 3.29c reveals a similar problem in the τ^B -dominated Arrhenius increase which is there induced by a remaining impact of the deep level A present in the background.

B Accuracy of the ΔE_t determination of the dominating defect

As shown in the previous section, the Arrhenius gradient in a two-level system may significantly deviate from the accurate single-level value of the dominant defect level due to the remaining impact of the secondary defect level. Since the extent of these deviations strongly depends on the constellation of the defect parameters, the present section is dedicated to an identification of the critical actuating variables and to a quantitative estimate of the related systematic error in the ΔE_t determination of the dominant defect.

For a two-level system a theoretical estimate of this systematic ΔE_t error has been derived in the diploma thesis of T. Rehrl [38], carried out within the framework of this work. Making some restricting assumptions about the defect levels on the one hand and generalizing the ΔE_t error calculation on the other hand, we present a modified version of the derivation, which more clearly shows the fundamental dependence without significant loss of generality. Both defect levels A and B are assumed to be located in the upper band gap half of a p -type semiconductor. Concerning their relative energy position, we assume defect A to be deeper in the band gap than defect B, i.e., $\Delta E_t^A > \Delta E_t^B$ with $\Delta E_t^{A/B} := E_C - E_t^{A/B}$ describing the energy distance from the conduction band.

If the dominance of defect A is assumed first,²¹ the following expression may be derived from Eq. (3.60) for the overall lifetime increase which is observed in an Arrhenius plot at temperatures $T \in T_A, T_B$ where both individual TDLS curves exhibit their linear Arrhenius increase:

$$\begin{aligned} \ln\left[\frac{\tau_{LLI>}^{total}(T)}{T}\right] &= \ln\left[\frac{\tau_{LLI>}^A(T)}{T}\right] - \ln\left[1 + \frac{\tau_{LLI}^A(T)}{\tau_{LLI}^B(T)}\right] \\ &= \text{const.} - \frac{\Delta E_t^A}{k_B T} - \underbrace{\ln\left[1 + V \times \exp\left(-\frac{\Delta E_t^A - \Delta E_t^B}{k_B T}\right)\right]}_{=: \text{Deviation}^A(T)} \end{aligned} \quad (3.61)$$

The structure of expression (3.60) equals the one derived in Eq. (3.50) for the Arrhenius increase with a superposed $\sigma(T)$ -model. In this case, the supplementary $\ln[\dots]$ term describes the deviation of the overall Arrhenius increase in a two-level system from its linear single-level shape, with a gradient proportional to ΔE_t^A , due to the presence of the secondary defect B. The deviation term depends on two defect-specific quantities: the relative energy distance $\Delta E_t^A - \Delta E_t^B$ of both defects and a ratio V which is defined as

$$V := \frac{(\tau_{n0}^{300K})^A}{(\tau_{n0}^{300K})^B} \times \frac{k^A}{k^B} = \frac{N_t^B \sigma_n^B}{N_t^A \sigma_n^A} \times \frac{k^A}{k^B} \quad (3.62)$$

V thus essentially describes the ratio of the recombination activities of a deep(A)/shallow(B) defect level, being the higher the lower the recombination activity of the deep level A is compared to that of the shallow level B, i.e., the higher τ_{n0}^A is compared to τ_{n0}^B . In addition it depends on

²¹ The discussion below reveals that Eq. (3.61) is generally valid and not restricted to the case of dominance by defect A, which is only used as a starting point.

the ratio k^A/k^B of the symmetry factors. While the ratio k^A/k^B determines the relative horizontal position²² of the Arrhenius increases of both defects, the ratio τ_{n0}^A/τ_{n0}^B specifies their vertical distance whereas the relative energy distance $\Delta E_t^A - \Delta E_t^B$ stipulates their angle of intersection. Thus all three relative quantities describe the mutual impact of both Arrhenius increases, which explains their impact on the deviation term.

Before studying the general dependence of the deviation term on these parameters let us first consider two special cases which define its limits. For $V \ll 1$ the deviation term vanishes, since the ln-argument approaches unity, and the gradient of the overall Arrhenius increase equals ΔE_t^A , as in the case of a single deep level. This limiting case is reached irrespective of the relative energy distance $\Delta E_t^A - \Delta E_t^B$ of the two defects due to the higher recombination activity of the deep defect ($V \ll 1$).²³ The same result is obtained for similar recombination activities ($V \approx 1$) but then only if defect A is much deeper than defect B, i.e., if $\Delta E_t^A \gg \Delta E_t^B$. This situation is displayed in Fig. 3.29a. It differs from the first situation only by the small lifetime step in the T_c part of $\tau_{total}(T)$ which is not observed for $V \ll 1$, $\tau_{total}(T)$ being identical with $\tau_A(T)$ in the whole T range. A qualitatively different simplification of the deviation term in Eq. (3.61) is achieved if the defect-dependent addend in the ln-argument significantly exceeds the constant value of unity, since the deviation term is then reduced to $\ln[V] - (\Delta E_t^A - \Delta E_t^B)/(k_B T)$. In this case the Arrhenius gradient becomes equal to ΔE_t^B , which shows that the overall Arrhenius increase is completely dominated by the shallow level B. This situation is shown, e.g., in Fig. 3.29c and in general requires a reduced recombination activity of the deep level A ($V \gg 1$) combined with a limited energy difference $\Delta E_t^A - \Delta E_t^B$. In the intermediate cases the deviation term reduces the gradient of the overall Arrhenius increase below its single-level values, as shown e.g. in Fig. 3.29b, and thus yields an energy depth ΔE_t^{fit} which is reduced compared to the energy depth of the dominant defect level.²⁴

An analytical expression for this systematic error in the ΔE_t determination is arrived at if the Arrhenius gradient is calculated from Eq. (3.61):

²² The impact of the k factor on the horizontal position of the Arrhenius increase has been shown in Fig. 3.7b.

²³ Analytically, the approximation for $V \ll 1$ does not require any restrictions on $\Delta E_t^A - \Delta E_t^B$ since the $\exp(\dots)$ -term in the ln-argument is always smaller than unity due to the assumption $\Delta E_t^A > \Delta E_t^B$.

²⁴ The reduced value for the extracted energy depth ΔE_t^{fit} results from the fact that the deviation term, bigger than unity, increases monotonically with temperature, which leads to an increasing reduction of the superposed Arrhenius increase and thus to a decreased Arrhenius gradient.

$$\begin{aligned}
 & \text{Arrhenius Gradient} \\
 & =: \Delta E_t^{fit} \\
 \frac{\partial \ln[\tau/T]}{\partial [k_B T]^{-1}} & = - \left[\Delta E_t^A - \overbrace{\frac{\Delta E_t^A - \Delta E_t^B}{1 + \frac{1}{V} \times \exp\left(\frac{\Delta E_t^A - \Delta E_t^B}{k_B T}\right)}}^{\text{=:Error}(\Delta E_t^A)} \right] \\
 & = - \left[\Delta E_t^B - \overbrace{\frac{\Delta E_t^A - \Delta E_t^B}{1 + V \times \exp\left(-\frac{\Delta E_t^A - \Delta E_t^B}{k_B T}\right)}}^{\text{=:Error}(\Delta E_t^B)} \right]
 \end{aligned} \quad (3.63)$$

Equation (3.63) allows the definition of a ΔE_t^A error and a ΔE_t^B error, which describe the deviation of the extracted energy depth ΔE_t^{fit} from the true energy depth of the respective defect level. It has to be emphasized that, being based on Eq. (3.61), Eq. (3.63) is only valid for temperatures $T \in T_>^A, T_>^B$ within the Arrhenius increase of both individual TDLS curves. Due to the T -dependence of the error terms, the Arrhenius gradient calculated in Eq. (3.63) actually corresponds to the local gradient of the Arrhenius increase of $\tau_{total}(T)$.

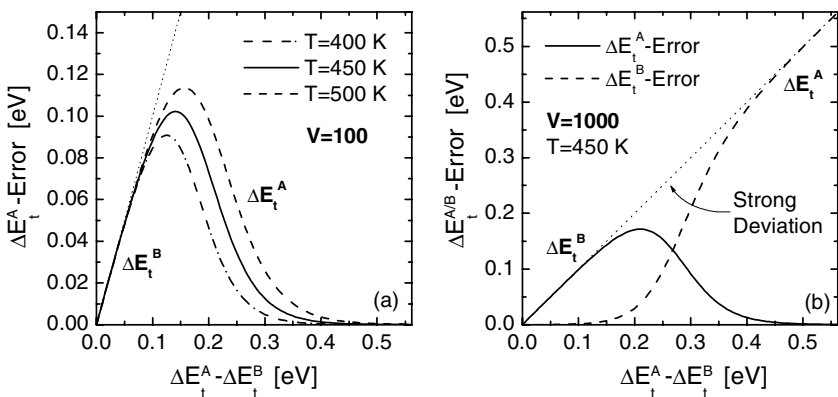


Fig. 3.30. (a) $(\Delta E_t^A - \Delta E_t^B)$ -dependence of the error in determining the energy depth ΔE_t^A of the deep level in a two-level system simulated on the basis of Eq. (3.63) for an activity ratio $V=100$ at various temperatures $T \in T_>^A, T_>^B$. The ΔE_t^A error curve at medium $T=450$ K (*solid line*) corresponds best to the situation of a linear Arrhenius fit. (b) Deviation of ΔE_t^{fit} from the energy depth of the deep (ΔE_t^A , *solid line*) and the shallow (ΔE_t^B , *dashed line*) level according to Eq. (3.63) for an activity ratio $V=1000$. The simulation is performed as in (a) at $T=450$ K. For each value of $(\Delta E_t^A - \Delta E_t^B)$ the overall Arrhenius increase is dominated by the defect level which yields the smaller energy error.

Figure 3.30a displays the local ΔE_t^A error as a function of the energy distance $\Delta E_t^A - \Delta E_t^B$ of the defects for various temperatures which are chosen high enough to fulfill the prerequisite $T \in T_s^A, T_s^B$ for most parameter constellations. The deviations among the local ΔE_t^A curves for different T values reflect a slight T -dependence of ΔE_t^{fit} , which points towards a slight bending of the Arrhenius increase in a two-level system. But without the knowledge of a secondary defect being present in the background, in general, it is not possible to detect this bending in the experiment, as will be shown in Sect. 3.4.3C using a simulated two-defect TDLS curve. A linear fit of the Arrhenius increase thus yields a medium gradient which corresponds best to the local gradient calculated at a medium temperature $T = 450$ K (solid line in Fig. 3.30a). In the remaining graphs $T = 450$ K is chosen as reference temperature.

To clarify the physical meaning of the ΔE_t^A and the ΔE_t^B errors, their dependence on the energy distance $\Delta E_t^A - \Delta E_t^B$ of the defects is compared in Fig. 3.30b for an activity ratio $V = 1000$. For low values of $\Delta E_t^A - \Delta E_t^B$ the ΔE_t^B error (dashed line) is much smaller than the ΔE_t^A error (solid line), which indicates that the overall Arrhenius increase is dominated by the shallow level B. This corresponds to the situation displayed in Fig. 3.29a. If the extracted energy ΔE_t^{fit} is compared with ΔE_t^A in spite of this B dominance, the whole energy difference between defects A and B has to be interpreted as ΔE_t^A error, which explains its linear increase for low $\Delta E_t^A - \Delta E_t^B$ values and shows that this part of the ΔE_t^A error curve lacks a sensible physical interpretation. For high values of $\Delta E_t^A - \Delta E_t^B$, however, the reverse ratio of both errors indicates dominance of the deep level A which analogously leads to artificially high values of the ΔE_t^B error. Thus, the generalized error in determining ΔE_t for the dominant level in a two-level system has to be defined at each parameter position by the minimum of the ΔE_t^A and the ΔE_t^B errors:

$$\text{Error}(\Delta E_t) := \text{Minimum}\{\text{Error}(\Delta E_t^A); \text{Error}(\Delta E_t^B)\} \quad (3.64)$$

This generalized ΔE_t error is displayed in Fig. 3.31 as a function of the energy distance $\Delta E_t^A - \Delta E_t^B$ of the two defects for different activity ratios V . According to Fig. 3.30 the parameter constellations forming the increasing and decreasing part of the ΔE_t error curves, respectively, lead to an overall Arrhenius increase of $\tau_{total}(T)$ which is dominated by the shallow level (B) and the deep level (A), respectively.

Figure 3.31 only displays ΔE_t error curves for $V > 1$ since these are the critical cases. For $V < 1$ on the contrary, the ΔE_t error approaches zero irrespective of the energy distance between the two levels. This is due to the fact that for $V < 1$ the recombination activity of the shallow level is reduced

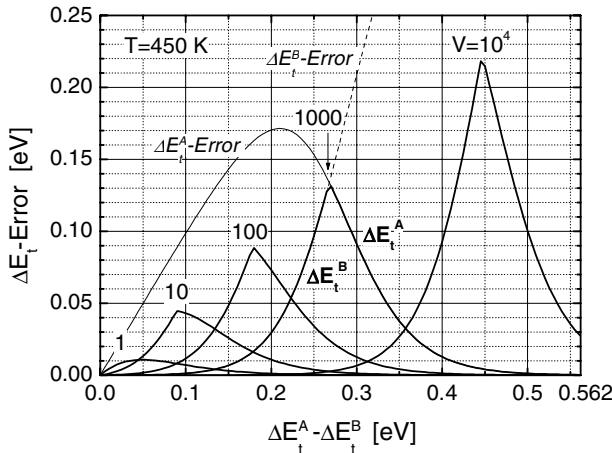


Fig. 3.31. Simulated error of the energy level ΔE_t of the dominant defect in a two-level system, if it is determined from a linear fit of the Arrhenius increase, as a function of the energy distance $\Delta E_t^A - \Delta E_t^B$ of the two defect levels for various activity ratios V . The error curves for $V \ll 1$ approach zero irrespective of the energy distance. According to Fig. 3.30 the parameter constellations forming the increasing and decreasing part of the error curves lead to an overall Arrhenius increase of $\tau_{total}(T)$, which is dominated by the shallow level (B) and the deep level (A), respectively. The simulation is performed on the basis of Eqs. (3.63) and (3.64) at $T = 450$ K, which represents a temperature within the Arrhenius increase for most parameter constellations and thus fulfills the prerequisite $T \in T_>^A, T_>^B$.

compared to that of the deep level. Since the impact of the shallow level on the superposed TDLS curve can then be neglected, $\tau_{total}(T)$ is almost identical with $\tau^A(T)$ in the whole T range which allows the energy depth ΔE_t^A of the deep level to be determined with maximum accuracy. This situation, which corresponds qualitatively to the one displayed in Fig. 3.29a, represents an important special case since it guarantees an accurate TDLS result in that half of the possible two-level systems where the deeper level exhibits the higher recombination activity.

For the other half of the possible two-level systems with $V > 1$, Fig. 3.31 allows the determination of the critical parameter constellations for which an accurate ΔE_t determination of the dominant defect level fails. If a value of 50 meV is defined as an upper limit of the tolerated systematic ΔE_t error, the linear fit of the Arrhenius increase of $\tau_{total}(T)$ always yields the energy depth of defect A or B with sufficient accuracy if $V = 1$ or $V = 10$. For $V = 100$, however, a sufficient accuracy is only achieved if the relative energy distance remains below 150 meV or exceeds 230 meV. In the first case the extracted energy corresponds to ΔE_t^B , since $\tau_{total}(T)$ is dominated by the shallow level B, similarly to the situation displayed in Fig. 3.29c. In

the second case the extracted energy corresponds to ΔE_t^A , since $\tau_{total}(T)$ exhibits a cascade structure similar to the one displayed in Fig. 3.29b, whose second step is dominated by the deep level A.

In addition Fig. 3.31 reveals a general trend concerning the dependence of the generalized energy error on the actuating variables V and $\Delta E_t^A - \Delta E_t^B$. As can be seen, with increasing V the energy distance $\Delta E_t^A - \Delta E_t^B$ at which the energy error reaches its maximum is shifted to higher values, accompanied by an increase in the maximum value itself. The shift of the peak position can easily be understood from Fig. 3.29a–c. Since an increase in V corresponds to a continued reduction in the recombination activity of the deep level compared to that of the shallow level, the impact of the shallow level B on the overall Arrhenius increase gains weight. The overall Arrhenius increase being $\tau^A(T)$ -dominated for low V values (see Fig. 3.29a), an increase in V first leads to a cascade-structured Arrhenius increase whose second step is significantly influenced by $\tau^B(T)$, even though dominated by $\tau^A(T)$ (see Fig. 3.29b). As a consequence the energy error in determining ΔE_t^A increases. As can be seen from Fig. 3.29c, a further deactivation of defect A for an unchanged energy distance between the two defect levels again leads to a qualitative change in $\tau_{total}(T)$: it no longer exhibits a cascade structure but becomes dominated by $\tau^B(T)$ in the whole T range. As a result the evaluation of the overall Arrhenius increase yields the energy ΔE_t^B , which is determined with increasing accuracy as the deactivation of the deep defect A progresses and V increases. This shows that a simple vertical interpretation of Fig. 3.31 for a fixed energy distance between the two defect levels leads to an energy error which shows a maximum value for medium V values and decreases above that. Since high energy errors are only observed if both individual TDLS curves affect the overall Arrhenius increase, their observation for $V \gg 1$ requires that either the Arrhenius increase of $\tau^A(T)$ is shifted to higher temperatures towards the Arrhenius increase of $\tau^B(T)$ or the Arrhenius increase of $\tau^B(T)$ is shifted to lower temperatures towards the Arrhenius increase of $\tau^A(T)$ (see Fig. 3.29c). Since the activity ratio V should remain unchanged, these relative displacements of the two TDLS curves cannot be achieved by a change of the symmetry factors k^A and k^B , but only by a change of the energy depths ΔE_t^A and ΔE_t^B .²⁵ The required directions of the displacements are achieved if the energy depth ΔE_t^A of the deep defect is further increased and the energy depth ΔE_t^B of the shallow defect is further reduced, i.e., if the energy distance between the two defect levels is increased. A

²⁵ Strictly speaking variations in the energy depth do not lead to a pure shift of the Arrhenius increase. They induce a shift of its onset temperature accompanied by a change of the slope which has the desired effect concerning the displacement of the increase.

closer look shows that this requirement explains not only the V -induced shift of the peak position, observed for the ΔE_t error curves in Fig. 3.31, but also the observed increase in their maximum values. Since the average gradient of the superposed Arrhenius increase deviates the more from the two underlying single-level gradients the stronger these differ from each other, the increase in the maximum energy error with increasing V is a direct consequence of the shifted peak position.

In conclusion the theoretical study of the two-level system leads to the following essential findings: even if a sample is influenced by two defect levels of comparable recombination activity, in general, TDLS is not capable of resolving the two levels in different temperature regions of the TDLS curve but only allows the dominant level to be determined. A very special parameter constellation which may allow a separation of the levels is discussed in the previous section. The accuracy of the ΔE_t determination of the dominant defect depends on two defect-specific quantities: the relative energy distance $\Delta E_t^A - \Delta E_t^B$ of the defects and the activity ratio V which essentially describes the ratio of their recombination activities. As long as the deeper level A exhibits the higher recombination activity ($V < 1$), TDLS allows an accurate determination of its energy depth ΔE_t^A irrespective of the level distance $\Delta E_t^A - \Delta E_t^B$. If the shallow level B exhibits the higher recombination activity ($V > 1$), the identification of the dominant level and the accuracy of its ΔE_t determination strongly depend on the individual parameter constellation. Here the following qualitative trend is observed: while the shallow level dominates for low level distances, the deep level does so for high level distances. For medium level distances the ΔE_t error reaches its maximum values. The boundaries of these $\Delta E_t^A - \Delta E_t^B$ regions strongly depend on the activity ratio V . It can be concluded that in most cases the accuracy of TDLS will not be affected by the presence of multiple defect levels.

C Requirements for a separation of multiple defect levels

As has been seen in the previous section, TDLS data in general only allow the dominant defect level to be extracted. If at all, a separation of multiple defect levels can only be achieved if the Arrhenius increase of the combined TDLS curve exhibits a cascade structure whose different slopes can be attributed to the Arrhenius increases of the individual defect centers. Such a TDLS cascade structure represents an exception since it is formed only for very special constellations of the parameters of both defects. An example has been presented in Fig. 3.29b. To investigate the possibilities and restrictions of a defect separation by means of TDLS on an ideal system, the simulated curve is evaluated in Fig. 3.32.

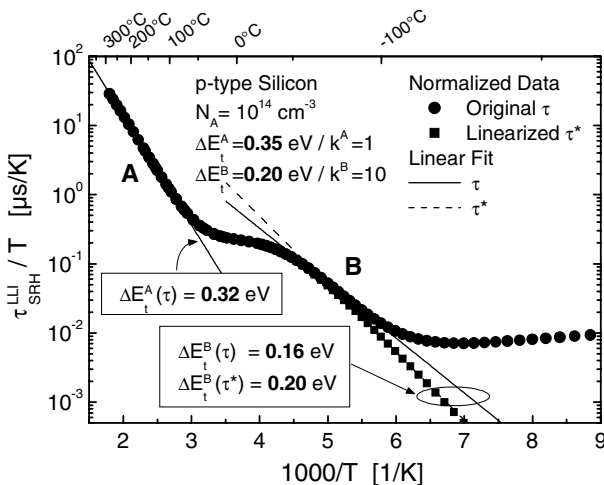


Fig. 3.32. Evaluation of the cascade-structured Arrhenius increase of the TDLS curve from Fig. 3.29b. Both steps are analyzed in an optimized T range (A:370–500 K, B:185–200 K) by means of the standard analysis (solid lines). Improved accuracy is achieved for the ΔE_t determination from step B if the linear fit (dashed line) is performed on the linearized TDLS curve (squares), which is obtained by means of the standard linearization procedure of Sect. 3.4.1C in a T range from 150–200 K.

The solid lines in Fig. 3.32 represent the standard TDLS analysis of the two steps. To minimize the impact of the transition regions, the fitted T range is optimized for both steps such that the extracted energy value reaches its maximum value. For the lower step B this optimization leads to a very short fit range from 185–200 K which demonstrates the strong impact of both transition regions. But even in this optimized fit range the linear fit of the original data yields an energy value of 0.16 eV, which significantly underestimates the true energy depth $\Delta E_t^B = 0.20$ eV of the shallow level. Improved accuracy is achieved for the ΔE_t determination from step B if the original TDLS curve (circles) is linearized (squares) by means of the standard linearization procedure of Sect. 3.4.1C. A linear fit (dashed line) of the linearized TDLS in a more than tripled T range from 150–200 K actually provides the accurate value of 0.20 eV for the shallow level. This shows that the accurate energy value of the shallow level can in principle be determined from the lower step of a cascade-structured TDLS curve, but that a sufficient accuracy absolutely requires improved techniques of data evaluation. In contrast to the lower step B, the upper step A of the TDLS curve can only be evaluated by means of the standard analysis. If the Arrhenius increase of step A is fitted linearly in an optimized T range from 370–500 K (solid line), an energy value of 0.32 eV is determined for the deep level. The standard TDLS analysis thus reveals a

systematic deviation of 0.03 eV from the true energy $\Delta E_t^A = 0.35$ eV, which corresponds to the value predicted in Fig. 3.31. Beyond that, the Arrhenius increase of step A is an example which confirms the claim in the previous section that the bending of the superposed Arrhenius increase²⁶ due to the remaining impact of a secondary defect normally cannot be detected in the experiment.

Thus for the evaluation of a cascade-structured Arrhenius increase it can be concluded: if just the gradients of the different steps of the Arrhenius increase are evaluated, the energy value ΔE_t^B of the shallow level, which is related to the lower step, is extracted with maximum accuracy by a linearization of the TDLS data while the energy value ΔE_t^A of the deep level, which is related to the upper step, has to be extracted by means of the standard analysis. The error in ΔE_t^B is given by the general evaluation error which has been derived in Sect. 3.4.2 for the ΔE_t extraction from linearized TDLS data. An additional ΔE_t^B error may result from the impact of the low-temperature part of $\tau^A(T)$ if the τ_{n0}^A/τ_{n0}^B ratio is reduced. An estimate of the systematic error of ΔE_t^A due to the presence of a secondary defect is given in Fig. 3.31. Nevertheless, a superposed evaluation error due to the long range impact of the transition region has to be taken into account (see Sect. 3.4.1B), which can reduce the extracted ΔE_t beyond the predicted systematic reduction.

To increase the accuracy of a multiple defect extraction, the TDLS curve has to be analyzed by means of a complete SRH simulation. Nevertheless, an unambiguous identification of several defect levels seems to be achieved only for a cascade structure of the Arrhenius increase in contrast to the prevalent interpretation of TDLS data in the literature [36].

²⁶ The bending of the Arrhenius increase can only be detected if the local gradient is determined at various temperatures given in brackets: 0.28 eV (365 K), 0.31 eV (390 K), 0.32 eV (425 K), 0.32 eV (465 K), 0.31 eV (515 K), 0.30 eV (570 K). While the increase of the local gradient at lower temperatures reflects the impact of the transition region, the decrease at high temperatures reflects the bending due to the secondary defect B. Since the variations of the local gradient which are induced by the bending effect do not exceed 20 meV within a T range as wide as 200 K, the bending of the Arrhenius increase due to secondary defects in the background can be neglected compared to other error sources such as underlying $\sigma(T)$ -models and measurement errors.

D Experimental example

Among the samples investigated in the present work a superposition of defect levels has been observed only once on an intentionally titanium-contaminated sample²⁷ with a *p*-type doping of $N_A = 2.3 \times 10^{15} \text{ cm}^{-3}$ whose cascade-structured TDLS curve is displayed in Fig. 3.33. To validate the accuracy of a defect separation under realistic conditions, the TDLS curve has been evaluated by means of different procedures: while Fig. 3.33a displays the evaluation of the gradients of both steps in adjusted T ranges as proposed in the previous section, Fig. 3.33b shows two different two-defect SRH simulations of the entire TDLS curve.

The boundary conditions of the fits and the spectroscopic results are summarized in Table 3.3. In spite of the pronounced cascade structure which results from the fact that the two steps are shifted against each other by 150 K, the spectroscopic results turn out not to be as unambiguous as supposed after the evaluation of the simulated curve in Fig. 3.32.

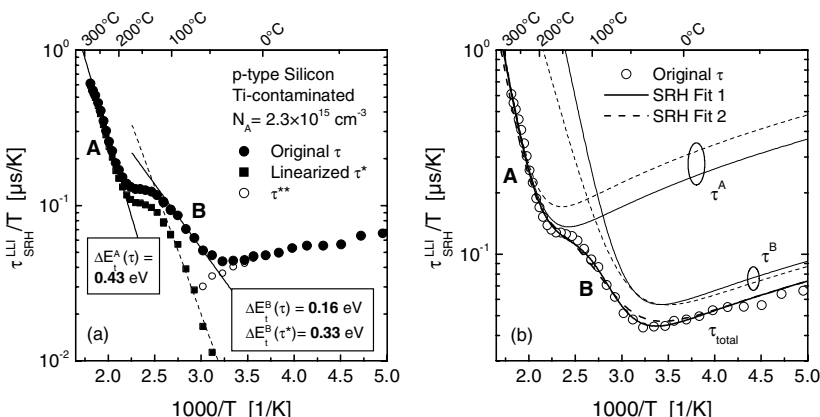


Fig. 3.33. TDLS curve with cascade-structured Arrhenius increase measured on an intentionally titanium-contaminated Si sample. **(a)** Evaluation of both steps by means of a linear fit of the Arrhenius increase in adjusted T ranges using the original (solid circles) and the linearized data (solid squares). **(b)** Two-defect SRH fit of the entire TDLS curve with all defect parameters assumed free (6 degrees of freedom: solid lines) and with ΔE_t^B fixed at the value determined from the τ^* -Arrhenius fit (5 degrees of freedom: dashed lines). While the thin lines represent the TDLS curves of each individual defect, the thick lines equal their superposition according to Eq. (3.60). The details of the fits are summarized in Table 3.3.

²⁷ The qualitative difference of the TDLS curve compared to those of the other titanium-contaminated samples (see Chap. 4) may lie in the doping concentration which is the highest for the sample with the cascade-structured Arrhenius increase. The TDLS curves of all samples have been measured by means of the MW-PCD technique.

Table 3.3. Spectroscopic results determined for the two-defect system in Fig. 3.33. The measured cascade-structured TDLS curve has been evaluated by means of different procedures.

Evaluation procedure	Defect A Fitted T range		ΔE_t^A	Defect B Fitted T range		ΔE_t^B	Comment	
Linear fit τ	490–540 K		0.40 eV	345–370 K		0.16 eV	—	
Linear fit τ^*	490–540 K		0.43 eV	330–385 K		0.33 eV	—	
	τ_{n0}^A	k^A	$E_C - E_t^A$	τ_{n0}^B	k^B	$E_C - E_t^B$	Chi^2	Comment
SRH fit 1	64 μ s	13	0.53 eV	16 μ s	395	0.45 eV	0.095	Entire T range
SRH fit 2	84 μ s	18	0.56 eV	15 μ s	6	0.33 eV	0.188	ΔE_t^B fixed at value of linear fit of τ^*

The linear fit of the Arrhenius increases of both steps yields an energy depth of $\Delta E_t^A = 0.40\text{--}0.43\text{ eV}$ for the deep level dominating the upper step A and an energy depth of $\Delta E_t^B = 0.33\text{ eV}$ for the shallow level dominating the lower step B. Here ΔE_t^B is determined from the linearized data (squares) the result obtained from the original data (circles) being much lower for the reasons mentioned before. To verify these results, we tried to simulate the entire TDLS curve using a complete two-defect SRH model with at most 6 degrees of freedom which are given by the energy levels $E_C - E_t$, the symmetry factors k and the electron capture time constants $\tau_{n0}(300\text{ K})$ of the two defects.²⁸

Since the results from the previous section suggest an accurate ΔE_t determination of the shallow level from the lower step B, we first assigned to the parameter ΔE_t^B the fixed energy value of 0.33 eV obtained by fitting the linearized Arrhenius increase of step B and thus reduced the degrees of freedom of the complete SRH simulation from 6 to 5. As can be seen from the dashed lines in Fig. 3.33b, this allows an adequate SRH simulation of the entire TDLS curve which yields an energy depth $\Delta E_t^A = 0.56\text{ eV}$ for the deep level. Nevertheless, a further improvement in the fit quality (solid lines) is achieved if all 6 defect parameters are optimized by the fit algorithm which is reflected in a reduction of the Chi^2 value by a factor 2 (see Table 3.3). As a result the shallow level is found to be located much deeper at $\Delta E_t^B = 0.45\text{ eV}$. The broad variation of the results for ΔE_t^B may partly be explained by the strong impact of defect A on step B since the recombination activity of both defects only varies by a factor $\tau_{n0}^A/\tau_{n0}^B = 5\text{--}6$. Compared to the simulated curve in Fig. 3.32 the τ_{n0}^A/τ_{n0}^B ratio is thus reduced by more than an order of magnitude. In spite of the varying values

²⁸ The details of the single-level SRH modeling will be discussed in Sect. 3.5. Since both levels are assumed to be independent, the overall lifetime of the two-level system is calculated on the basis of Eq. (3.60).

of ΔE_t^B , the two different SRH fits determine almost the same value for ΔE_t^A ranging from 0.53–0.56 eV, which can thus most likely be identified with a true energy depth ΔE_t^A of the deep level. The strong deviation between the ΔE_t^A values obtained from the SRH fit and the linear fit of the Arrhenius increase demonstrates the significant impact of the shallow level B on the Arrhenius increase of step A and reflects the systematic error of a linear evaluation in a two-level system whose amount has been estimated in Fig. 3.31.

While a deep level at 0.53–0.56 eV is not reported for titanium in the literature, an energy depth of 0.33 eV for the shallow level corresponds to the results obtained for titanium in Chap. 4. Nevertheless, the result for the shallow level is highly defective as shown above.

It has to be concluded that even in the case of a cascade-structured TDLS curve and even by extracting the defect parameters with the help of a complete SRH simulation, the spectroscopic information gained is uncertain for both defect levels. This demonstrates once more the limited resolution capability of TDLS. Due to the mutual impact of the Arrhenius increases in a real two-level system, especially the linear evaluation techniques fail to resolve the different defect energies accurately. While the linear techniques only lack accuracy in the case of a cascade-structured TDLS curve,²⁹ the determination of multiple defect levels from different linear regions in the Arrhenius plot of the original or linearized TDLS data completely fails in all other cases for the shape of the superposed TDLS curve. Thus, our investigation definitely shows the invalidity of the prevalent interpretation of TDLS data in the literature [36]. Although a data linearization leads to great improvement in the accuracy in determining the dominant defect level (see Sect. 3.4.2), it does not improve the resolution capability of TDLS.

Fortunately, the case of the simultaneous presence of defect centers of similar recombination activity is a rare exception. The strong selectivity of TDLS and the lifetime spectroscopic methods as a whole have the practical advantage that the identified impurity definitely is the one which limits recombination activity.

²⁹ This has been shown in the present section by the discrepancy of the ΔE_t^A results obtained from the linear fit and the complete SRH fit.

3.5 Temperature-dependent lifetime spectroscopy: superposed effects and advanced analysis

As shown in the previous section, a simple linear fit of the Arrhenius increase of a TDLS curve always allows an accurate determination of the defect depth ΔE_t if advanced procedures for data linearization are used. Nevertheless, the standard TDLS analysis does not provide any information about the symmetry factor $k = \sigma_n/\sigma_p$ and the band gap half the defect is located in, and thus does not allow a complete characterization of the defect center. As will be shown in the following, these restrictions can be overcome by an advanced analysis of TDLS data, based on the SRH modeling of the complete TDLS curve.

Since the accuracy of the spectroscopic result will depend directly on the accuracy of the TDLS simulation, the first half of the section is dedicated to superposed effects which may influence the observed temperature dependence of the TDLS curve. Section 3.5.1 deals once more with the temperature dependence of the capture cross-sections. Since its impact on the TDLS curve has already been discussed from a practical point of view in Sect. 3.4.2, the present discussion concentrates on the physical origin of this temperature dependence to provide an overview of the theoretically possible $\sigma(T)$ -models and also to assess the validity of a fundamental assumption concerning the consideration of the $\sigma(T)$ -dependence within the SRH model. The overview should guarantee a physically motivated simulation of the experimental TDLS curves in Chap. 4, making the determination of an additional fingerprint of the investigated defect centers possible. In Sect. 3.5.2 it is shown how superposed external carrier trapping may distort the real TDLS curve. On the basis of the standard T -model of the equilibrium carrier concentrations we then discuss in Sect. 3.5.3 the impact of freeze-out and intrinsic conduction on the TDLS curve. It turns out that intrinsic conduction strictly confines the T range of the Arrhenius increase to its upper end. As the advanced models for $N_C(T)$, $N_V(T)$ and $E_{gap}(T)$ are known from Sect. 1.2.3 to have a significant impact on the onset temperature of intrinsic conduction, their impact on the TDLS curve is investigated in Sect. 3.5.4. The relevance of the discussed extensions of SRH theory for a quantitatively correct simulation of TDLS curves is finally demonstrated in Sect. 3.5.5 by the simulation of a measured TDLS curve.

The second half of the section is dedicated to the extraction of additional defect parameters from the TDLS curve. In Sect. 3.5.6 we first investigate how the physical difference between defects in the upper and the lower half of the band gap, which has already been discussed in Sect. 3.3.3 for

IDLS, influences the TDLS curve, and disclose a fundamental difference in the unambiguity of the spectroscopic result achievable for the two groups of defects. It is then demonstrated that modeling the TDLS bend due to intrinsic conduction may increase the extractable spectroscopic information in some cases. To make a transparent SRH analysis of TDLS data possible, the analysis by means of the defect parameter solution surface (DPSS), developed for IDLS in Sect. 3.3.2, is transferred to TDLS in Sect. 3.5.7. Applying the DPSS technique to TDLS curves simulated for defects with different characteristic properties, we discuss the important aspects of modeling TDLS curves in an illustrative way, demonstrating at the same time the practical value of the DPSS analysis. Following this a diagram is developed in Sect. 3.5.8 which provides information about the applicability of TDLS depending on both the defect and material parameters and the experimental boundary conditions concerning the accessible T range. Finally the two basic assumptions of the proposed advanced TDLS analysis are discussed critically in Sect. 3.5.9. With the summary in Sect. 3.5.10 the optimum procedure for the advanced TDLS analysis is presented, including a tabular overview of the spectroscopic significance of the various parts of the TDLS curve.

3.5.1 Temperature-dependent capture cross-sections: origin, impact and relevance

As shown in Sect. 3.4.2C, the modeling of the low-temperature part of the TDLS curve allows the $\sigma(T)$ -model of the investigated impurity to be determined directly. The analysis in Sect. 3.4.2C revealed that a superposed T -dependence of the capture cross-sections has to be known to allow an accurate determination of the energy depth ΔE_t of the defect level from TDLS. But apart from this practical use of the $\sigma(T)$ -model in terms of evaluation accuracy, its knowledge has an independent physical value as it may give deeper insight into the mechanism of recombination. The reason is that the T -dependence of the capture cross-sections is one of the characteristic features of the physical mechanism of carrier capture in an impurity level. This microscopic aspect of recombination is completely left out of consideration within the purely statistical SRH model. The $\sigma(T)$ -model thus represents an additional fingerprint of the investigated impurity, which can be extracted directly from temperature-dependent lifetime measurements.

In order to guarantee a TDLS modeling, which is motivated in terms of physics, and in order to investigate the possibility of identifying special capture mechanisms by means of their $\sigma(T)$ -dependence, the characteristic

features of the important capture mechanisms reported in the literature are briefly summarized in the following. Furthermore, it is shown that different experimental conditions may imply that different capture mechanisms are effective, which could explain discrepancies between the $\sigma(T)$ -models reported in the literature for the same impurity. Concerning the impact of a $\sigma(T)$ -model on the temperature-dependent carrier lifetime, we finally discuss a fundamental assumption.

A Mechanisms of carrier capture and their characteristic features

The different physical mechanisms of carrier capture may be divided into three classes according to the process of energy dissipation when a free carrier is trapped on a defect site: (i) *radiative capture*, where the energy is dissipated into photon emission, (ii) *phonon-assisted capture*, where the energy is transformed into phonons and (iii) *Auger capture*, where the energy is transmitted to other free carriers.

Table 3.4. Characteristic features of the most important physical mechanisms of carrier capture into an impurity level.

Capture mechanism ^{Ref}	Relevant to	Capture cross-sections	
		Expected size	Expected T -model
<i>Radiative capture</i>			
Photon emission capture ^{a,b}	Not relevant in silicon	10^{-24} – 10^{-22} cm 2	$\sigma(T) = \text{const.}$
<i>Phonon-assisted capture</i>			
Multiphonon emission capture (MPE) ^c	Deep centers	below 10^{-14} – 10^{-15} cm 2	$\sigma(T) = \sigma_{\infty} \times \exp(-E_{\infty} / k_B T)$ with $\sigma_{\infty} = 10^{-14}$ – 10^{-15} cm 2 with $E_{\infty} = 0$ – 0.56 eV
Cascade capture ^{d,e}	Shallow Coulomb-attractive centers	10^{-12} – 10^{-15} cm 2	$\sigma(T) = \sigma_0 \times T^{-\alpha}$ with $\alpha = 1..4$
Two-stage model of cascade capture ^f	Deep Coulomb-attractive centers	?	$\sigma(T) \propto T^{-2} \times \exp(\Delta E / k_B T)$ with $\Delta E := E_I - E_{\infty}$ E_I = energy of excited state (1 st) E_{∞} = energy barrier of MPE (2 nd)
<i>Auger capture</i>			
Classical Auger capture ^{a,g}	Not important	below 10^{-15} cm 2	No significant T -dependence
Excitonic Auger capture ^g	Deep centers	10^{-12} – 10^{-15} cm 2	$T < 60\text{K}: \sigma(T) = \text{const.}$ $T > 60\text{K}: \sigma(T) = \sigma_0 \times T^{-\alpha} \quad \alpha > 0$

Table 3.4 (cont.)

References for the different capture mechanisms. As far as known, the authors who introduced the different mechanisms are mentioned explicitly with their original work:

- ^a Ref. [39, pp. 68,71].
- ^b Ref. [40].
- ^c Ref. [41], Henry 1977.
- ^d Ref. [42], Lax 1960.
- ^e Ref. [43, pp. 184–188], Bourgoin 1983.
- ^f Ref. [44], Gibb 1977.
- ^g Ref. [45], Hangleiter 1987.

Table 3.4 displays the characteristic features of the six capture mechanisms usually discussed in that context. In addition to the characteristic $\sigma(T)$ -models, the comparison covers the expected magnitude of the capture cross-sections, which is a measure of the capture activity and thus of the relevance of each mechanism, and the class of defect centers for which carrier capture may be induced by the respective mechanism. To elucidate the reasons for the restriction to special classes of defect centers and to motivate the T -dependence of the capture cross-sections qualitatively, the basic physical idea of each mechanism should be briefly discussed.

The *radiative capture process* into impurity levels is almost of no importance in silicon due to its indirect band structure. Basically, the energy dissipation by photon emission gives rise to characteristic lines in the luminescence spectrum which correspond to the depth of the defect level. In silicon, most impurities show no deep luminescence at all. And if observed, the luminescence is far too weak to explain recombination quantitatively [40].

The *multiphonon emission process* represents a more efficient capture process. In this model capture results from lattice vibrations which cause the crossing of the defect energy level into the conduction band and thus enable the capture of a free electron [41]. Since the equilibrium lattice coordinate and the corresponding energy of the defect level differ in the unoccupied and occupied states, the lattice is displaced a long way from its new equilibrium position immediately after capture. The jump to the new equilibrium position will release a violent lattice vibration at the defect with the associated energy loss being propagated away as localized lattice phonons. Since the multiphonon emission allows the conveyance of large excess energies, this mechanism is often used to explain capture into deep levels. As multiphonon capture of a carrier requires sufficiently large vibrations of the defect on its lattice site to initiate the transition between the free-carrier and the bound-carrier levels (vibronic coupling), the capture probability increases with temperature. The detailed analysis leads to a thermally activated behavior of the capture cross-sections with a

thermal barrier E_∞ , which a free electron in the conduction band has to overcome to be captured by the defect level [41]. Note that capture cross-sections as high as 10^{-14} – 10^{-15} cm 2 are only observed for the multiphonon process due to the described vibronic coupling whereas only the weak electron-phonon interaction would lead to a very small capture cross-section of the order of 10^{-22} cm 2 [42].

A second phonon-assisted mechanism is the *cascade capture process* introduced by Lax [42]. Under the assumption that a defect center possesses a series of closely spaced excited levels with a distance below the maximum phonon energy, a free carrier from the band can be captured by diffusing down that spectrum of excited states while losing its energy by the emission of one phonon during each step. Since the probability of reemission increases at higher temperatures, the capture cross-section decreases with increasing temperature. The detailed analysis shows that temperature dependence can be described by a power law with a negative exponent between -1 and -4 [42, 43]. The relevance of this mechanism strongly depends on the defect depth and the charge state of the impurity. It is believed to be responsible for the capture of carriers into shallow impurity levels with Coulomb attractive potential, whose hydrogen-like level scheme is ideally suited for this mechanism [42]. Although charged deep levels may possess hydrogen-like excited states within the band gap as well, at least the energy difference between the lowest excited and the ground state of the defect is so large that it cannot be overcome by the emission of a single phonon [40]. However, since the carrier is effectively trapped as soon as it gets more than the thermal energy ($k_B T$) from the band edge, the cascade process may account for the capture into deep levels [42] but not for the recombination via deep levels [40], the latter being limited by the final step. Capture into non-attractive centers cannot be explained by the cascade process. Although neutral centers may have excited levels due to the large polarizability of the neutral atom, their energy separation is generally too large to suit the cascade theory. Centers with Coulomb repulsive potential on the other hand do not possess excited states at all. In conclusion, fundamental considerations show that the cascade mechanism is only able to explain capture into a very limited class of defect centers, namely the shallow Coulomb attractive centers.

To overcome these restrictions, Gibb et al. [44] suggested a *two-stage model of cascade capture*, in which a free carrier is first captured by a cascade process into a shallow excited level E_1 of the defect center. The transition to the deeper ground state then occurs, thermally activated by a multiphonon process in a subsequent step. Using the detailed balance

theory, they found for the total capture cross-section the T -model given in Table 3.4.³⁰ While the decrease of the total capture cross-section with T^{-2} is exponentially enforced for $E_l > E_\infty$, i.e., if the energy depth of the shallow level is higher than the thermal barrier of the multiphonon process, it is exponentially attenuated in the opposite case. Although the two-stage model may account for capture into deep charged levels, it cannot explain capture into neutral and repulsive centers due to the missing series of shallow excited levels.

The last group of capture mechanisms to be mentioned are the Auger capture processes. In the *classical Auger capture process*, two independent free carriers have to meet at the impurity site, where their electron-electron interaction induces a transition of one of the carriers into a deeply bound state, while the excess energy is transferred to the other carrier which is highly excited in its respective band. The capture cross-sections of this mechanism are predicted to depend weakly on temperature and linearly on the carrier concentration [46]. But due to their relatively small size the relevance of this capture process is doubted in the literature [41].

In the most recent work on the topic of carrier capture [45, 47] Hangleiter introduced the *excitonic Auger capture mechanism* which is a decisive extension of the classical model of Auger capture. Due to an attractive Coulomb interaction, electron-hole pairs tend to form spatially localized free excitons. The model is based on the fact that a free exciton which meets the impurity always contains one particle to be captured, e.g., an electron, and one particle to take over the excess energy in an Auger process, e.g., a hole. Due to the spatial correlation of the electron and the hole within the exciton a very efficient excitonic Auger capture mechanism becomes possible. Since free excitons exist in thermal equilibrium with free electrons and holes, the T -dependence of the associated capture cross-section is governed by the thermal ionization of the excitons [45]. Below 60 K the capture cross-section is found to be independent of temperature as almost all carriers are bound as free excitons. Above 60 K the capture cross-section starts to decrease as an increasing portion of the excitons becomes thermally ionized. But as Hangleiter's theoretical and

³⁰ Note that the given T -model is only valid at higher temperatures, when the probability for thermal excitation of the captured carrier back into the adjacent band is much larger than the final capture down to the ground state. In the opposite case the total capture cross-section equals that of the cascade capture. Since a decrease in temperature not only results in a decrease in the reemission rate but also in a reduction of the capture rate due to multiphonon emission, the temperature for the transition between the two T -models is generally expected below 100 K and thus outside the temperature range investigated in the present work.

experimental results show, the cross-section of excitonic Auger capture decreases by less than an order of magnitude in a temperature range from 50 to 500 K [47], which confirms the relevance of this mechanism in the temperature range investigated in the present work. As indicated in Table 3.4 the $\sigma(T)$ -dependence can be described by a power law with a negative exponent. From the fact that the capture cross-section decreases in parallel with the portion of free excitons, Hangleiter consistently concludes that Auger capture of free carriers is much less effective than that of free excitons [45]. The fairly large capture cross-sections, which have been identified experimentally, in good agreement with theoretical calculations [47], demonstrate that excitonic Auger capture is one of the most efficient mechanisms for carrier capture into deep impurity levels. Its major advantage is that it is efficient irrespective of the charge state of the defect center and thus for both minority and majority capture. Since a complete recombination of an electron-hole pair is simply realized by two subsequent excitonic Auger processes, just as in the usual SRH model, it can be concluded that excitonic Auger capture is a very efficient mechanism for non-radiative recombination via deep impurity levels in semiconductors. Experimental evidence for this capture mechanism has been found for recombination via the deep levels associated with chromium and gold in silicon [45].

The literature survey presented in Table 3.4 does not claim to be complete but provides an overview of the most relevant capture models and thus allows a physical assessment of the $\sigma(T)$ -dependence observed experimentally in Chap. 4. Although the determination of the $\sigma(T)$ -model may lead to a significant confinement of the possible capture mechanisms, an unambiguous identification of the responsible capture mechanism requires additional information besides carrier lifetime, such as capture and emission properties of the defect center under investigation [44, 46].

B Impact of experimental conditions on the effective capture mechanism

A comparison of the capture mechanisms listed in Table 3.4 reveals one decisive distinction between excitonic Auger capture and the remaining capture mechanisms which is pointed out in [45]. Since the excitonic Auger capture mechanism requires electron-hole pairs, this mechanism only works under minority carrier injection conditions, i.e., if the sample is excited optically or by a forward biased *pn*-junction. Consequently, if no minority carriers are generated as in standard DLTS experiments, capture into deep levels has to be induced by alternative processes such as the multiphonon or the cascade mechanism. From this Hangleiter concluded

that different experimental conditions may imply that different capture mechanisms are effective, which should be directly reflected in the observed temperature dependence of the capture cross-sections.

In fact Hangleiter was able to show [46] that this view is supported by literature data mostly gained from DLTS-like experiments, which may be divided into two groups. On the one hand, all experiments where only majority carriers were present revealed a thermally activated behavior of the capture cross-sections (including zero activation energy) which indicates the multiphonon mechanism to be most likely responsible for the capture of majority carriers into the investigated deep levels. On the other hand, in the second group of DLTS experiments, where minority carriers were injected in order to investigate minority carrier capture, capture cross-sections decreasing with increasing temperature were found, following a power law. This result suggests that in the second group of experiments excitonic Auger capture might be the dominating capture mechanism. This conclusion is supported by Hangleiter's own experimental results [46]. Having found the same decrease of $\sigma(T)$ for different metal impurities in an all-optical lifetime experiment, he was able to prove the trap-Auger process directly by detecting highly excited Auger particles by means of Auger spectroscopy.

In this monograph the recombination properties of different impurities are investigated by means of carrier lifetime measurements. Since the measurement techniques used are all based on the optical injection of electron-hole pairs,³¹ the discussed excitonic Auger mechanism might be the dominating process for capture into the deep levels. The relevance of this mechanism for the investigated impurities will be analyzed in Chap. 4.

C Basic assumption concerning the impact on the TDLS curve

Concerning the impact of a $\sigma(T)$ -model on the TDLS curve, the derivations to be presented are based on the fundamental assumption that the symmetry factor k is still independent of temperature, which directly implies models with identical T -dependence for the electron and hole capture cross-sections. From a physical point of view, we thus assume that electron and hole capture into the defect level occur via the same capture mechanism.

Although this simplifying assumption represents a basic restriction concerning the degree of freedom of the fitting parameters, there are theoretical arguments to support it. Since capture mechanisms which do not

³¹ Note that these measurement conditions also reflect the operating conditions in a solar cell, which shows that the capture mechanism identified by means of lifetime spectroscopy represents the one which is relevant to recombination in the device.

depend on the charge state of the defect center, such as excitonic Auger capture, are as efficient for minority as for majority capture, there are no physical reasons to expect significant differences in the T -dependence of the two capture cross-sections, the simplifying assumption most likely being physically correct. However, for those mechanisms whose efficiency depends on the charge state of the defect center, such as the cascade mechanism, the simplifying assumption will most likely be violated. Nevertheless, even in this case the two-step nature of recombination prevents fundamental differences since a singly charged center is attractive for minority carriers and becomes at least neutral before capturing a majority carrier in the subsequent step.

The fundamental problem is that, even for most of the well investigated metal impurities, the mechanisms of the individual capture processes involved in the recombination process are still not completely understood and are often unknown [39, p.68]. Since TDLS on the other hand only allows the $\sigma(T)$ -model of the minority carrier capture cross-section to be determined experimentally, as has been shown in Sect. 3.4.2C, any T -dependence assumed for k would be quite arbitrary and thus questionable. On this background the assumption $k(T)=\text{const.}$ seems to be most reasonable. In addition, it will be shown at the end of Sect. 3.5 that even if our simplifying assumption were not correct, distortions of the spectroscopic results obtained from TDLS are only expected for defects located in the upper half of the band gap (in p -type), while the results for those located in the lower half remain accurate. The physical reasons for this phenomenon will be elucidated in the course of this section.

The impact of a temperature-dependent capture cross-section on the overall T -dependence of the TDLS curve is finally visualized in Fig. 3.34 for the two capture mechanisms which are assumed to be most relevant: (a) the multiphonon emission process and (b) the excitonic Auger capture process. To show the variety of attainable TDLS shapes, we varied the defect-specific capture parameters, namely the activation energy E_∞ for the multiphonon process and the exponent α for the excitonic Auger process, always assuming the same symmetric ($k=1$) defect center located 0.3 eV above the valence band edge. As a reference, the TDLS curve for temperature-independent capture cross-sections is displayed as well (solid line). Since the low-temperature part of the TDLS curves equals the minority capture time $\tau_{n0}(T) \propto \sigma_n(T)^{-1}$ (thin lines), its modeling according to the procedure given in Sect. 3.4.2C allows the $\sigma(T)$ -model of the capture cross-sections to be determined directly.

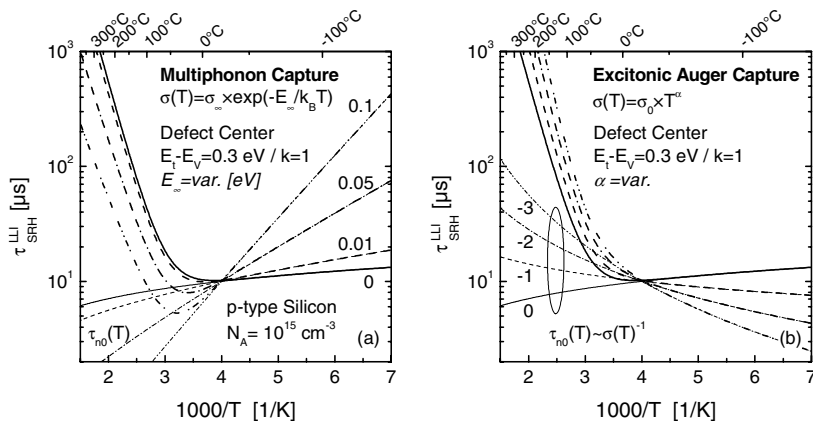


Fig. 3.34. Impact of a temperature-dependent capture cross-section on the TDLS curve if electrons and holes are captured (a) via a multiphonon emission process being simulated for a variation of the activation energy E_{∞} and (b) via an excitonic Auger capture process being simulated for a variation of the exponent α of the power law. All TDLS curves (thick lines) are calculated for the same symmetric ($k=1$) defect center located 0.3 eV above the valence band edge. Both graphs display the TDLS curve for temperature-independent capture cross-sections (solid line) as reference. The basic assumption of a temperature-independent symmetry factor k implies the same $\sigma(T)$ -model for electrons and holes being directly reflected in the T -dependence of the minority capture time $\tau_{n0}(T) \propto \sigma_n(T)^{-1}$ (thin lines).

Apart from that, the graphs visualize the distortions of the high-temperature part of the TDLS curves which have been theoretically predicted in Sect. 3.4.2C. As can be seen from Fig. 3.34a, the overall gradient of the Arrhenius increase decreases with an increasing energy barrier of the multiphonon process. This leads to the predicted underestimate of the defect depth if only the Arrhenius increase is fitted linearly in the case of a thermally activated carrier capture. Figure 3.34b gives an idea of the slight bending of the Arrhenius increase, which has been predicted for a superposed power law dependence. Nevertheless, the Arrhenius slopes are shifted almost parallel, which confirms our prediction that the distortions of the energy depth, as determined from a linear fit of the Arrhenius increase, are expected to be small in the case of a power-law-dependent $\sigma(T)$ -dependence.

3.5.2 Impact of superposed external carrier trapping

A fundamental prerequisite for an accurate determination of the $\sigma(T)$ -model by modeling the low-temperature part of the TDLS curve according to the procedure given in Sect. 3.4.2C is that this part of the TDLS curve

really follows $\tau_{n0}(T)$ and is not distorted. Unfortunately, such a distortion may arise from superposed carrier trapping at additional shallow trapping centers, which do not contribute to recombination but only interact with the minority band. The discussion again focuses on this *external trapping* effect,³² whose impact on the injection-dependent carrier lifetime has already been examined in Sect. 3.3.1A.

A simple analytical model which accounts for the external trapping effect is discussed in [48]. Assuming a minimum system of two levels, one of which plays the role of a recombination center while the other acts as trapping center (see Sect. 1.4.3A), bulk recombination is found to be described by an asymptotic lifetime τ_a which is proportional to the actual recombination lifetime τ_{SRH} and can be expressed as follows:

$$\tau_a(T) := \tau_{SRH}(T) \times \left\{ \frac{N_{trap} n_{1,trap}(T)}{[\Delta n + n_0 + n_{1,trap}(T)]^2} \right\} \quad (3.65)$$

where N_{trap} is the trap concentration and $n_{1,trap}$ the SRH density of electrons if it is assumed that the trap level is located below the conduction band. As can be seen from Eq. (3.65), the asymptotic lifetime increases for $\Delta n \rightarrow 0$, while the trapping effect weakens when the injection density Δn becomes large in accordance with the observations in Sect. 3.3.1A. Since TDLS is performed under LLI conditions, the trapping effect is expected to play a role providing the presence of an additional shallow trap level. But for which trap parameters and in which temperature range?

An estimate is given in Fig. 3.35 which displays the temperature dependence of the asymptotic bulk lifetime (dashed lines) resulting from Eq. (3.65) for a deep recombination and a shallow trapping center in the upper half of the band gap assuming LLI conditions ($\Delta n = 0$). For comparison the underlying trapping-free TDLS curve associated with the recombination center alone is displayed as well (solid line). As can be seen from the increasing gap between τ_a and τ_{SRH} , the impact of the trapping effect increases towards lower temperatures, the mid- and high-temperature part of the TDLS curve in general not being affected at all. The onset temperature at which the asymptotic lifetime τ_a starts to deviate from the actual recombination lifetime τ_{SRH} strongly depends on the parameters of the trapping center. As shown in Figs. 3.35a and b, respectively, the deeper the energy level of the trapping center and the higher the trap concentration, the

³² Note that the external trapping effect, which arises from additional defect centers mainly acting as trapping levels, has to be distinguished from internal trapping, which may occasionally arise from the dominating recombination center itself as discussed in Sect. 1.4.3C. As pointed out there, internal trapping is of minor importance for the present work.

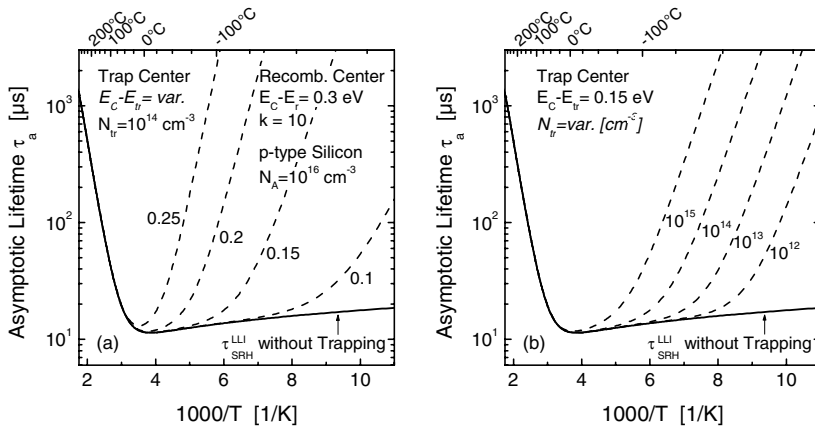


Fig. 3.35. Impact of superposed external carrier trapping on the TDLS curve. The asymptotic bulk lifetime is calculated according to Eq. (3.65) under the assumption of a two-level system formed by a deep recombination and a shallow trapping center in the upper half of the band gap. **(a)** Impact of the energy level of the trapping center at a fixed trap concentration of 10^{14} cm^{-3} . **(b)** Impact of the trap concentration for a trapping center at a fixed energy position $E_c - E_t = 0.15 \text{ eV}$.

higher the onset temperature. Beyond that, the expected deviation between τ_a and $\tau_{\text{SRH}}^{\text{LLI}}$ increases with increasing energy depth of the trapping center as the τ_a increase towards lower temperatures becomes steeper. Since trapping effects may thus completely screen the pure recombination lifetime in the low-temperature region of the TDLS curve, they have to be identified to avoid distortions of the extracted $\sigma(T)$ -model. In general, this identification is easily achieved due to the pronounced deviation of τ_a from the baseline of the underlying trapping-free TDLS curve.

3.5.3 Impact of the temperature dependence of the majority carrier concentration

Up to now, most of the considerations concerning the temperature dependence of SRH lifetime have been based on the assumption of a temperature-independent majority carrier concentration. However, this assumption is not justified in the whole T range. As has been discussed in detail in Sect. 1.2, the majority carrier concentration equals the doping concentration [$p_0(T) \equiv N_A$] only at medium temperatures, while it decreases significantly at low temperatures due to the freeze-out of doping atoms [$p_0(T) < N_A$] and increases significantly at high temperatures due to the onset of intrinsic conduction [$p_0(T) > N_A$]. Although the onset temperatures

of the two effects strongly depend on the doping concentration as shown in Figs. 1.8 and 1.10, they are predicted within the investigated T range from 100 to 600 K.³³ As the effects of freeze-out and intrinsic conduction are thus relevant to the investigations of the present study, their impact on the temperature dependence of LLI-SRH lifetime will be investigated in the following on the basis of the standard T -model whose general properties are summarized in Table 1.1.

A Impact of the freeze-out effect on the TDLS curve

According to Eq. (3.7a), the general T -dependence of the LLI-SRH lifetime in a p -type semiconductor is given by

$$\tau_{SRH}^{LLI,p}(T) = \tau_{n0}(T) \times \left[1 + \frac{p_1(T)}{p_0(T)} + k \frac{n_1(T)}{p_0(T)} \right] \quad (3.66)$$

Equation (3.66) is valid as long as $n_0(T) \ll p_0(T)$ can be assumed, and this is definitely the case in the T range of freeze-out. Since the majority carrier concentration $p_0(T)$ only influences the LLI-SRH lifetime via the two SRH terms p_1/p_0 and kn_1/p_0 , the freeze-out effect may affect the shape of the TDLS curve only in the $T_>$ region of the linear increase, where the LLI-SRH lifetime is dominated by the SRH terms, but not in the $T_<$ region, where the LLI-SRH lifetime equals $\tau_{n0}(T)$. However, since the freeze-out effect is only observed at low temperatures, its onset temperature T_{FO} does not lie within the $T_>$ region in general, the TDLS curve thus being unaffected by the freeze-out effect in the whole T range. It is only for very shallow defect levels and high symmetry factors k that the Arrhenius increase may start below T_{FO} .

These considerations are confirmed in Fig. 3.36a, which displays pairs of TDLS curves that have been simulated with (solid lines, standard T -model) and without (dashed lines, basic T -model) considering the freeze-out effect, assuming a doping concentration $N_A = 10^{16} \text{ cm}^{-3}$. While the TDLS curve of a symmetric defect center with an energy depth as low as $\Delta E_t = 0.1 \text{ eV}$ is still not affected by the freeze-out of the doping atoms, the solid and dashed lines lying on top of each other, a weak impact of the freeze-out effect is observed below -100°C if the defect depth is reduced

³³ In the relevant doping range from 10^{14} to 10^{16} cm^{-3} the onset temperature of freeze-out ranges between 100 and 225 K while that of intrinsic conduction ranges between 440 and 590 K. These values, which reflect the situation for the advanced T -model, can be extracted from Figs. 1.8 and 1.10, respectively, if we assume an ionization level $f_A = 0.99$ and an excitation degree $f_i = 1.10$ as threshold for the transition to freeze-out and intrinsic conduction, respectively.

to $\Delta E_t = 0.05$ eV or if the symmetry factor is increased to $k = 1000$, which both shift the onset of the linear Arrhenius increase towards lower temperatures. But even then the deviations within the pairs of curves are small. Since the freeze-out of doping atoms is known from Sect. 1.2 to increase with increasing doping concentration, Fig. 3.36b displays the TDLS curve of the shallow asymmetric defect level, which has been affected the most by freeze-out in Fig. 3.36a, for different doping concentrations. While the TDLS curve for the higher $N_A = 10^{17} \text{ cm}^{-3}$ shows a clear impact of the freeze-out effect up to temperatures of -50°C , the TDLS curve for the lower $N_A = 10^{15} \text{ cm}^{-3}$ is no longer affected.

In conclusion the discussion thus reveals: for most defect and material parameter constellations the TDLS curves are free from any distortions due to the freeze-out effect. This holds especially if the doping concentration is confined to the relevant doping range from 10^{14} to 10^{16} cm^{-3} . The potential impact of the freeze-out effect on the TDLS curve consists in a moderate lifetime increase at temperatures below 220 K and is only observed in more highly doped samples, which contain a shallow defect level with increased k factor. However, since such shallow asymmetric defect levels are highly unlikely to act as recombination centers, they cannot be detected by means of TDLS, the associated TDLS curves thus being hypothetical. It can be concluded that the freeze-out effect is of no practical importance for TDLS.

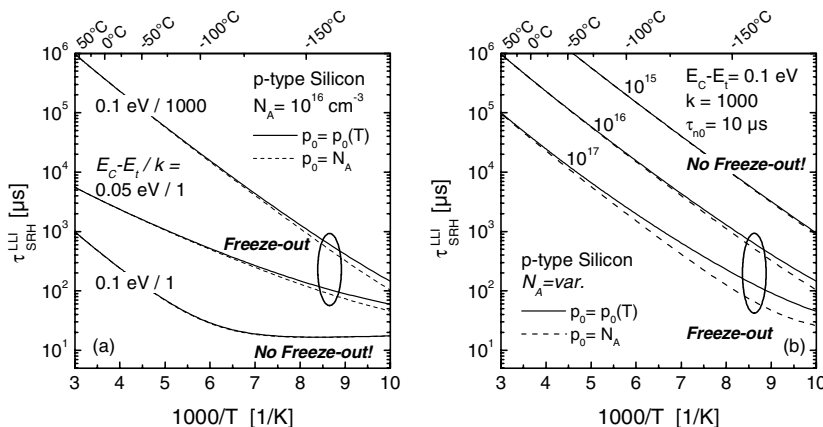


Fig. 3.36. Impact of the freeze-out effect on the TDLS curve (a) for shallow defect levels with varying defect parameters in a 10^{16} cm^{-3} -doped sample and (b) for a shallow asymmetric defect level in samples with varying doping concentration. The freeze-out effect is considered in the *solid* TDLS curves according to the standard T -model while the *dashed* curves are calculated as reference for constant $p_0 = N_A$ according to the basic T -model.

B Impact of intrinsic conduction on the TDLS curve

In contrast to freeze-out, the impact of intrinsic conduction is much more pronounced, as has already been indicated in Sect. 3.4.1B. At sufficiently high temperatures the majority carrier concentration $p_0(T)$ starts to increase exponentially with temperature, as it becomes dominated by the intrinsic carrier concentration $n_i(T)$. This is shown in Fig. 1.3. Concerning the impact on the SRH lifetime, it has to be taken into account that the minority carrier concentration $n_0(T) = n_i(T)^2/p_0(T)$ increases in parallel with $p_0(T)$ and can no longer be neglected compared to $p_0(T)$. According to Eq. (3.6) the general temperature dependence of LLI-SRH lifetime is thus given by

$$\tau_{SRH}^{LLI}(T) = \tau_{n_0}(T) \times \left[\frac{p_0(T) + p_1(T)}{p_0(T) + n_0(T)} + k \frac{n_0(T) + n_1(T)}{p_0(T) + n_0(T)} \right] \quad (3.67)$$

Since the denominator $[p_0(T) + n_0(T)]$ increases exponentially above the onset temperature of intrinsic conduction, the induced decrease in the SRH lifetime is large, as reflected in a sharp bend in the TDLS curve.

This is shown in Fig. 3.37 which displays pairs of TDLS curves which have been simulated on the basis of Eq. (3.67) with (solid lines, standard T -model) and without (dashed lines, basic T -model) considering the effect of intrinsic conduction. As can be seen, the TDLS bend due to intrinsic conduction completely screens the characteristic Arrhenius increase at higher temperatures. But due to the abrupt onset of intrinsic conduction, the remaining part of the Arrhenius increase at temperatures below the TDLS bend shows no distortions, which ensures the applicability of the simple evaluation techniques discussed in Sect. 3.4. Thus, considering the temperature dependence of the equilibrium carrier concentrations reveals that the T range exhibiting the defect-specific linear Arrhenius increase is strictly confined at its upper end by the onset of intrinsic conduction, its width thus being limited only for physical reasons.

The impact of the doping concentration is shown by the two sets of TDLS curves in Fig. 3.37a and b which have been calculated for varying doping concentration under the assumption of a defect level of (a) medium and (b) high energy depth, respectively. Reflecting the doping dependence which has been observed for the onset temperature of intrinsic conduction in Fig. 1.3b, the position of the IC-induced TDLS bend is shifted to lower temperatures as the doping concentration decreases. However, the width of the Arrhenius increase remains almost unchanged as the reduction of its T range at the upper end is partially compensated by an expansion at its lower end, which results from the whole Arrhenius increase being shifted to

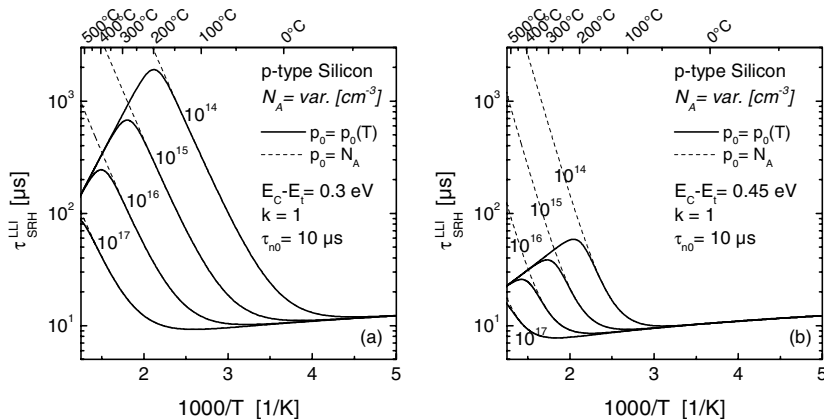


Fig. 3.37. Impact of intrinsic conduction on the TDLS curve (a) for a defect level of medium depth and (b) for a deep level in samples with varying doping concentration. The effect of intrinsic conduction is considered in the *solid* TDLS curves according to the standard T -model while the *dashed curves* are calculated as reference for constant $p_0 = N_A$ on the basis of the basic T -model.

lower temperatures with decreasing doping concentration. In contrast, the width of the Arrhenius increase decreases significantly if the defect depth is only increased from 0.3 eV to 0.45 eV, which can be seen if Fig. 3.37a and b are compared. This observation directly reflects the fact that the onset temperature of the Arrhenius increase (lower T bound) is highly sensitive to the energy depth while that of the IC-induced TDLS bend (upper T bound) is not. Since the width of the defect-specific Arrhenius increase is highly relevant to the accuracy of the TDLS result, both confining temperatures will be explicitly calculated as a function of the defect and material parameters later on in this section, after examining the impact of the advanced T -model.

3.5.4 Impact of the optimum advanced model for the temperature dependence of $N_c(T)$, $N_V(T)$, $E_{gap}(T)$ on the TDLS curve

The previous section revealed the significance of intrinsic conduction for TDLS as it strictly confines the temperature range of the defect-specific Arrhenius increase at its upper end. Since the advanced models for $N_c(T)$, $N_V(T)$ and $E_{gap}(T)$ are known from Sect. 1.2.3 to have a significant impact on the onset temperature of intrinsic conduction (IC), their impact on the TDLS curve should now be investigated.

Concerning the advanced $E_{gap}(T)$ -model, it has to be mentioned that its implementation in the T -model for TDLS is subjected to a fundamental restriction. While the temperature-induced band gap narrowing is fully considered in the calculations of the equilibrium carrier concentrations $p_0(T)$ and $n_0(T)$ to allow an accurate modeling of intrinsic conduction, it is ignored in the calculation of the SRH densities $n_1(T)$ and $p_1(T)$. The reason for the latter simplification is the lack of a widely accepted model for the movement of defect levels in a flexible band gap and level pinning, respectively. As a consequence, the temperature dependence of $n_1(T)$ and $p_1(T)$ is calculated for a constant energy distance of the defect level to both band edges which are determined for the band gap width at 300 K. Whenever the advanced T -model is used throughout this book, its application is based on this assumption.

A Comparison of TDLS curves calculated on the basis of different T -models

In order to demonstrate the impact of the different extensions of the T -model separately, Fig. 3.38a and a2 display two sets of TDLS curves which have been calculated on the basis of the optimum advanced (solid), the standard (dashed) and two intermediate T -models. The intermediate T -models are based on the standard T -model being modified by the introduction of either the advanced effective-mass-based $N_{C,V}$ -models (dash-dotted) or the advanced $E_{gap}(T)$ -model (dash-dot-dotted). To be sensitive to asymmetric effects which depend on the band gap half of the defect, the calculations are performed for a defect in the upper (MinBH, left side) and the lower (MajBH, right side) half of the band gap, assuming the same energy depth of 0.3 eV. As can be seen from Fig. 3.38a and a2, the TDLS curves associated with the different T -models only deviate from each other at temperatures above the onset of the linear Arrhenius increase.³⁴

In order to uncover the origin of the model-induced changes in the TDLS curves let us first have a look at the actuating variables $N_C(T)$, $N_V(T)$ and $p_0(T)$. Their changes under the different T -models are displayed in the lower half of Fig. 3.38, which shows for each of the three quantities the divergence of the three sub-optimal T -models from the advanced T -model, calculated in percentages as a function of inverse temperature.

Concerning the density of states in the conduction band, $N_C(T)$, Fig. 3.38d reveals a considerable effect. While the $N_C(T)$ values for the standard and the two intermediate T -models barely deviate from each other

³⁴ This is expected because of the fact that the two model extensions only affect the densities n_1 , p_1 and n_0 , p_0 .

in the whole T range, they increasingly fall below the $N_C(T)$ values for the advanced T -model as temperature increases. This effect directly results from the E_{gap} -dependence of $N_C(T)$, which the effective-mass model predicts in contrast to the basic model according to Eqs. (1.26) and (1.27a). In spite of this one-sided E_{gap} -dependence, the basic and the advanced $N_C(T)$ -model agree well with each other in the whole T range as long as $E_{gap} \equiv \text{const.}$ is assumed. This has been shown in Fig. 1.7 and is reflected in Fig. 3.38d in the parallel shape of the $N_C(T)$ curves related to the standard and intermediate T -models. But if a temperature-dependent $E_{gap}(T)$ is assumed, the $N_C(T)$ value of the effective mass model increases above the reference value for $E_{gap} \equiv \text{const.}$ if the energy gap decreases. Combining the advanced $N_C(T)$ - and $E_{gap}(T)$ -model within the advanced T -model thus leads to an additional increase of $N_C(T)$ with temperature due to temperature-induced band gap narrowing.³⁵

Concerning the effective density of states in the valence band, $N_V(T)$, Fig. 3.38d2 reveals two decisive differences in its model dependence compared to what is observed for $N_C(T)$. On the one hand the effective-mass model of $N_V(T)$ is independent of the band gap width and is thus the same for constant and temperature-dependent E_{gap} . On the other hand the absolute values of the basic and the advanced $N_V(T)$ -model differ significantly from each other, those of the effective mass model being 10–30 % higher in the relevant T range above 250 K.

Being related to $n_i(T)$ according to Eq. (1.22), the majority carrier concentration $p_0(T)$ is affected not only by $E_{gap}(T)$ but also by $N_C(T)$ and $N_V(T)$, though only in the T region of intrinsic conduction. As can be seen in Fig. 3.38c from the fairly large gap between the $p_0(T)$ curves related to the original (dashed) and the $E_{gap}(T)$ -modified (dash-dot-dotted) standard model, the increased p_0 level in the advanced T -model can be mainly attributed to the introduction of $E_{gap}(T)$. Nevertheless, the increase in the effective densities of states in both bands due to the transition from the basic to the advanced $N_{C,V}$ -models further increases the p_0 level, especially in conjunction with $E_{gap}(T)$, since, for the effective mass model, the density of states in the conduction band is higher for a reduced band gap (see discussion above).³⁶

³⁵ This additional increase of $N_C(T)$ is reflected in Fig. 3.38d in the increasing divergence of the $N_C(T)$ curves related to the three sub-optimal T -models from the zero baseline related to the advanced T -model.

³⁶ This effect is reflected in the fact that the deviation between the $p_0(T)$ curves related to the $E_{gap}(T)$ -modified standard model (dash-dot-dotted) and the advanced model (dotted zero baseline) is much bigger than the deviation between the $p_0(T)$ curves related to the original (dashed) and the $N_{CV}^{EM}(T)$ -modified (dash-dotted) standard model.

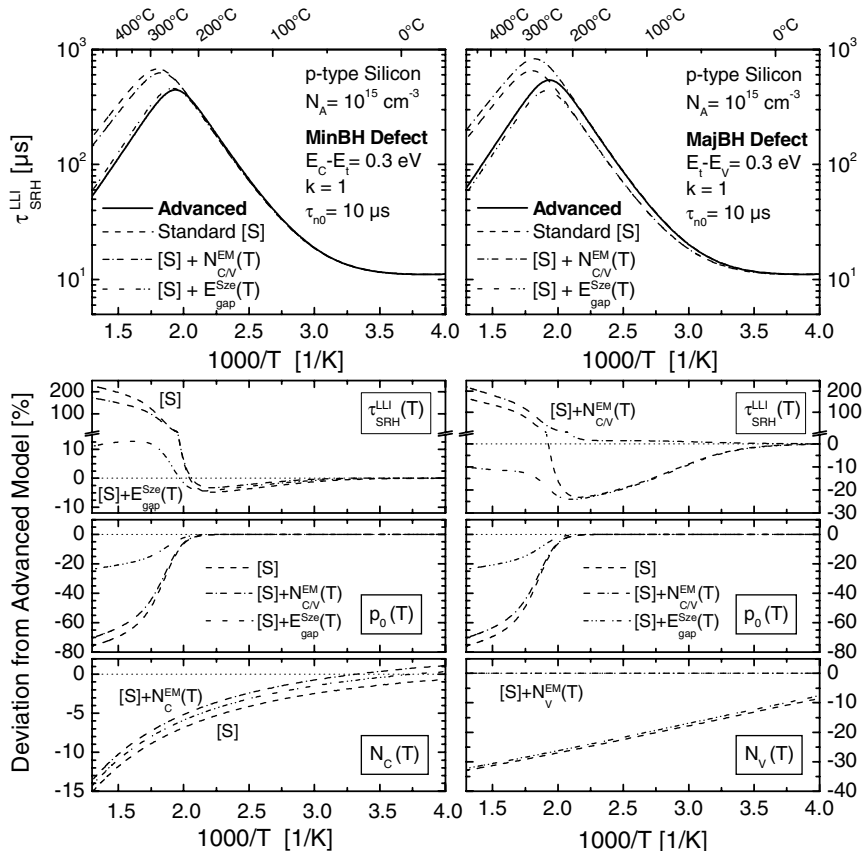


Fig. 3.38. Impact of the different extensions of the T -model on the TDLS curve of a MinBH (left) and a MajBH defect (right). **(a)** shows the absolute TDLS curves calculated for the optimum advanced (solid), the standard (dashed) and two intermediate T -models. The divergence of the three sub-optimal T -models from the advanced T -model is calculated in percentages as a function of inverse temperature for three physical quantities: **(b)** for the LLI-SRH lifetime itself, **(c)** for the majority carrier concentration and **(d)** for the relevant density of states.

For a MinBH defect the graduated increase of the p_0 level within the four models is directly reflected in a graduated decrease of the lifetime level of the IC-induced TDLS bend. As can be seen from Fig. 3.38a, the main reduction of the TDLS bend comes from the introduction of the $E_{\text{gap}}(T)$ -model while a further but much weaker reduction can be attributed to the introduction of the advanced $N_{C,V}$ -models. As a result the onset temperature and the lifetime level of the IC-induced TDLS bend are the lowest for the complete advanced T -model (solid) and the highest for the

pure standard T -model (dashed). The T position of the Arrhenius increase is more or less identical for the different models, as the relative deviations among the $N_c(T)$ curves of the different models are small. Nevertheless, a closer look at the relative lifetime deviations in Fig. 3.38b reveals that within the T range of the Arrhenius increase the lifetime level is slightly increased by 2–5 % for the advanced T -model compared to the three non-optimal models. This directly reflects the slightly increased level of the $N_c(T)$ curve related to the advanced T -model which leads to a corresponding increase in the SRH density n_1 , dominating the Arrhenius increase in the case of a MinBH defect.

For a MajBH defect the introduction of the advanced $N_{c,v}$ -models has a much stronger impact on the Arrhenius increase. The density of states in the valence band being 10–30 % higher for the effective-mass than for the basic model, the lifetime level of the TDLS curves based on the advanced $N_v(T)$ -model is increased by the same amount within the p_1 -dominated T range above the onset of the Arrhenius increase. As can be seen from Fig. 3.38a2, this model-induced vertical lifetime step directly corresponds to a shift of the whole Arrhenius increase to lower temperatures. Beyond its impact on the Arrhenius increase, the strong model dependence of $N_v(T)$ changes the graduation of the lifetime level, observed in the case of a MajBH defect for the IC-induced TDLS bend. While the reduction of the TDLS bend due to the introduction of $E_{gap}(T)$ remains unchanged, the additional introduction of the advanced $N_{c,v}$ -models leads to a slight increase of the TDLS bend instead of the decrease observed for a MinBH defect. The reason is that the additional increase of the p_0 level, which is independent of the defect and thus the same as in the case of a MinBH defect, is overcompensated by the model-induced increase of the SRH density $p_1(T)$. Consequently, the dominant SRH ratio p_1/p_0 increases due to the transition from the basic to the advanced $N_{c,v}$ -models. As a result the lifetime level of the IC-induced TDLS bend is only the second lowest for the complete advanced T -model (solid) and the second highest for the pure standard T -model (dashed).

Having shown how the shape of the TDLS curve is influenced by the individual components of the advanced T -model, Fig. 3.39 displays for a shallow and a deep level a comparison of TDLS curves which have been calculated on the basis of the standard (dashed lines) and the complete advanced (solid lines) T -model for different doping concentrations. Since the position of the TDLS maximum is obviously a characteristic quantity of the TDLS curve which defines the onset of the TDLS bend due to intrinsic conduction, the related temperature should be denoted in the following as $T_{IC-Onset}$. As expected, the introduction of the advanced T -model leads to a significant reduction of $T_{IC-Onset}$ in the whole parameter range. Beyond this

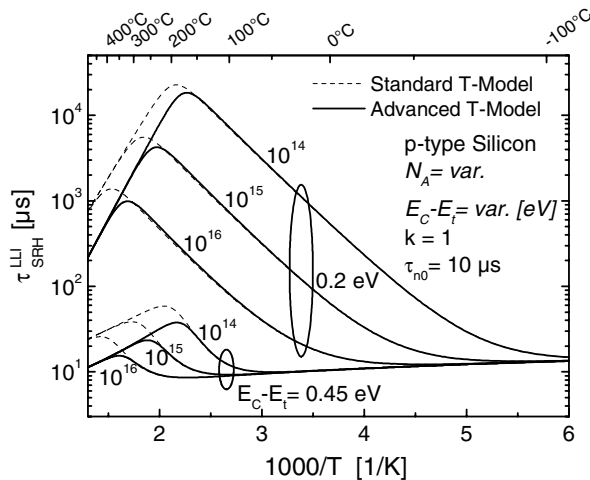


Fig. 3.39. TDLS curves for a shallow and a deep defect level calculated for different doping concentrations on the basis of the standard (dashed lines) and the optimum advanced (*solid lines*) *T*-model. Both the introduction of the optimum advanced *T*-model and a decrease in doping concentration induce a shift of the TDLS bend due to intrinsic conduction to lower temperatures.

general trend Fig. 3.39 already intimates an enhancement of the $T_{IC\text{-}Onset}$ reduction with increasing doping concentration and increasing defect depth. Both effects will be quantitatively analyzed in the following Sect. 3.5.4B. Thus especially for deep levels, the correct consideration of the effect of intrinsic conduction may reduce the Arrhenius increase to such an extent that an accurate application of TDLS becomes difficult. Having shown the strong impact of the advanced *T*-models on the shape of the TDLS curves, we will demonstrate the extraordinary performance of an SRH model based on this advanced *T*-model in Sect. 3.5.5, by application to an experimental TDLS curve.

B Impact of the defect parameters on the onset temperature $T_{IC\text{-}onset}$ of the TDLS bend due to intrinsic conduction calculated on the basis of the advanced *T*-model

As has been seen in the previous sections, the onset of the TDLS bend due to intrinsic conduction strictly confines the *T* range of the defect-specific Arrhenius increase at its upper end. To determine explicitly a value for the confining temperature $T_{IC\text{-}Onset}$, the position of the TDLS maximum has to be calculated numerically for the relevant TDLS curve.

To allow a quantitative assessment of this upper temperature limit of TDLS, Fig. 3.40a displays the $T_{IC\text{-}Onset}$ values, which have been calculated

on the basis of the advanced T -model, as a function of doping concentration for symmetric defect levels with varying energy depth. As expected, $T_{IC-Onset}$ decreases with decreasing doping concentration N_A . The significance of this doping dependence becomes evident on a numerical example. For a medium defect energy depth of 0.3 eV, a decrease in the doping concentration by only two orders of magnitude from 10^{16} to 10^{14} cm^{-3} results in a decrease of $T_{IC-Onset}$ by 150 K from 600 to 450 K, which is in good agreement with the T_{IC} values displayed in Fig. 1.10a.³⁷ But in contrast to the T_{IC} values calculated from $p_0(T)$ only, the $T_{IC-Onset}$ values, which are extracted from the final TDLS curve as upper bound of the Arrhenius increase, depend slightly on the energy depth of the underlying defect. For a medium-doped sample with $N_A = 10^{15} \text{ cm}^{-3}$, $T_{IC-Onset}$ increases by 40 K from 495 and 535 K if the energy depth increases from 0.1 to 0.5 eV. In spite of a slight enhancement of the ΔE_t -sensitivity of $T_{IC-Onset}$ with increasing N_A , the numerical example shows that the energy dependence of $T_{IC-Onset}$ is much weaker than its doping dependence. Since the TDLS investigations of the present study are performed up to temperatures of 600 K, especially the less doped samples will show a distinctive TDLS bend due to intrinsic conduction, the upper temperature limit of their Arrhenius increase being shifted far below the experimentally imposed upper temperature limit.

The relevance of the advanced T -model with respect to an accurate modeling of the position of the IC-induced TDLS bend becomes evident from Fig. 3.40b, which shows the absolute reduction of $T_{IC-Onset}$ due to the transition of the standard to the advanced T -model as a function of doping concentration for symmetric defect levels of varying energy depth. As already expected from Fig. 3.39, the reduction of $T_{IC-Onset}$ strongly increases with increasing doping concentration N_A . While $T_{IC-Onset}$ is only reduced by 25 K for a low doping of $N_A = 10^{14} \text{ cm}^{-3}$, its reduction already exceeds 65 K for a medium doping of $N_A = 10^{16} \text{ cm}^{-3}$ and amounts to 115 K for a high doping of $N_A = 10^{17} \text{ cm}^{-3}$, which reflects the results from Fig. 1.10b. These values have again been extracted for a medium energy depth of 0.3 eV. In addition, Fig. 3.40b confirms that the reduction of $T_{IC-Onset}$ due to the exchange of the T -models also increases with increasing energy depth ΔE_t . The energy depth being again varied between 0.1 and 0.5 eV, the $T_{IC-Onset}$ reduction for a medium doped sample with $N_A = 10^{15} \text{ cm}^{-3}$ varies between 30 and 55 K, i.e. by 25 K.

³⁷ The assumed doping range from 10^{14} to 10^{16} cm^{-3} being relevant to the present work, the positions of the IC-induced bend of the TDLS curves have to be expected in the T range from 450 to 600 K.

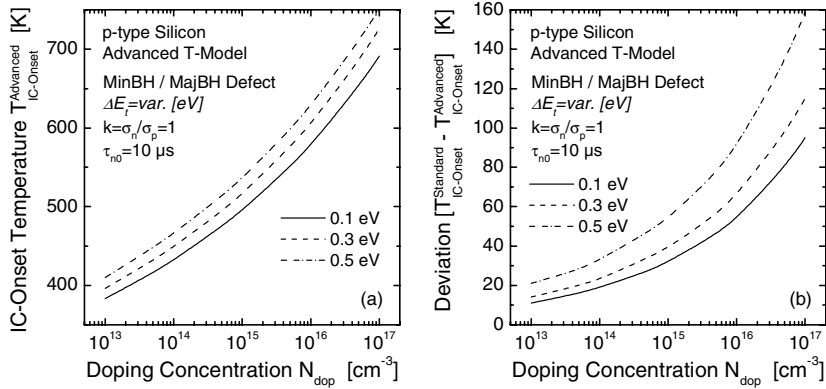


Fig. 3.40. (a) Onset temperature $T_{\text{IC-Onset}}$ of the TDLS bend due to intrinsic conduction calculated on the basis of the advanced T -model as a function of doping concentration for symmetric defect levels with varying energy depth. (b) Absolute reduction of $T_{\text{IC-Onset}}$ due to the transition from the standard to the advanced T -model as a function of doping concentration for symmetric defect levels of varying energy depth.

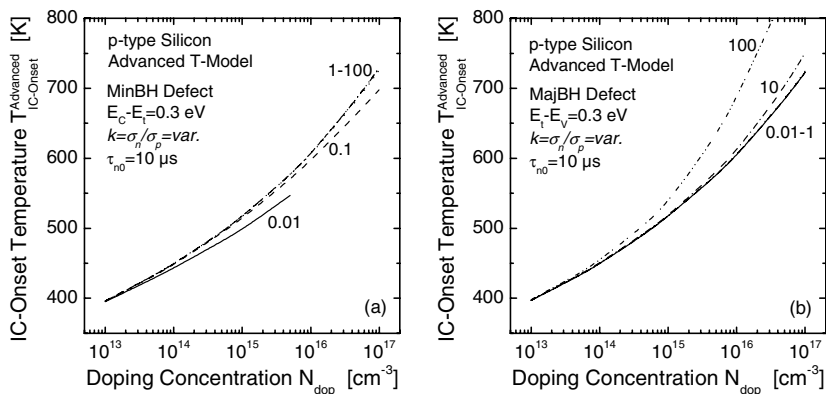


Fig. 3.41. Onset temperature $T_{\text{IC-Onset}}$ of the TDLS bend due to intrinsic conduction calculated on the basis of the advanced T -model as a function of the doping concentration (a) for MinBH defects and (b) for MajBH defects of the same energy depth but with varying symmetry factors k .

Figure 3.41 displays $T_{\text{IC-Onset}}$ values, which have been calculated for (a) MinBH defects and (b) MajBH defects of the same energy depth but with varying symmetry factors k , again as a function of the doping concentration. As can be seen, the impact of the symmetry factor k can be neglected in most of its parameter range. Only in highly doped samples are extreme symmetry factors found to affect $T_{\text{IC-Onset}}$.

In conclusion, the study revealed that the upper temperature bound $T_{IC-Onset}$ mainly depends on the doping concentration N_A , while it is only slightly affected by the energy depth ΔE_t and almost unaffected by the symmetry factor k . The strong reduction of $T_{IC-Onset}$ in the relevant doping range from 10^{14} – 10^{16} cm⁻³ due to the exchange of the T -models and the resultant low absolute values for $T_{IC-Onset}$, which lie significantly below the experimentally imposed upper temperature limit, demonstrate on the one hand that the effect of intrinsic conduction is highly relevant to the present study and on the other hand that its accurate consideration necessarily requires the complete advanced T -model. The latter will be proven in the following section by modeling an experimental TDLS curve. The benefit of the developed graphs finally consists in the fact that they provide the upper temperature limit of the Arrhenius increase for arbitrary defect and material parameters and thus allow an individual a priori selection of the temperature range, which is most interesting for spectroscopic investigation, mainly based on the knowledge of the doping concentration.

3.5.5 Experiment: accurate TDLS simulation on the basis of the advanced T -model

The relevance of the different extensions of the SRH model, which have been deduced in Sects. 3.5.1 to 3.5.4, should be demonstrated in the following by the modeling of an experimental TDLS curve which has been measured by means of the MW-PCD technique on an Mo-contaminated sample. The experimental details are given in Chap. 4. To allow the validity of SRH theory to be verified comprehensively, the lifetime measurements have been performed in a T range from 130 to 580 K as shown in Fig. 3.42. To our knowledge this is the broadest T range ever investigated: while lifetimes have been measured at lower temperatures [45], an upper temperature limit of 520 K has not been exceeded so far [36].

As can be seen from the dashed line in Fig. 3.42, the SRH model based on the basic T -model fails to describe the observed temperature dependence in the whole T range. While an adequate description is achieved at medium temperatures from 250–500 K (circles), large deviations are observed above 500 K (triangles) and below 250 K (stars).

We first focus on the correct modeling of the low-temperature part of the TDLS curve ($T < 250$ K), different SRH simulations being shown in Fig. 3.42a. Since the LLI-SRH lifetime equals the minority capture time constant $\tau_{no}(T) := [N_i \sigma_n(T) v_{th}(T)]^{-1}$ at temperatures below the onset of the Arrhenius increase, all deviations of the known T -dependence of v_{th} , which is displayed in Fig. 3.42a by the thin dashed line, have to be attributed to a

T -dependence of the capture cross-section $\sigma(T)$, as discussed in Sect. 3.5.1C. As shown by the thin solid line, the observed decrease of the capture cross-section with increasing temperature can be modeled in terms of $\sigma(T) = \sigma_0 \times T^\alpha$ with an exponent $\alpha = -1.5$. The fact that precisely the same T -dependence has been identified on a second Mo-contaminated sample, demonstrates its significance as an additional fingerprint of the defect center which reflects the mechanism of carrier capture. According to the survey of capture mechanisms in Sect. 3.5.1A, the identified $\sigma(T)$ -model either points towards a cascade capture process [42], which is only found for shallow Coulomb attractive centers, or towards an excitonic Auger capture process [45], which is observed for centers of arbitrary depth and charge state. While the cascade mechanism is unlikely to be due to an energy depth of 0.32 eV of the underlying defect center (see below), the excitonic Auger mechanism is likely to be the dominating process especially, as it is favored by the measurement conditions used, being based on the optical injection of electron-hole pairs (see discussion in Sect. 3.5.1B).

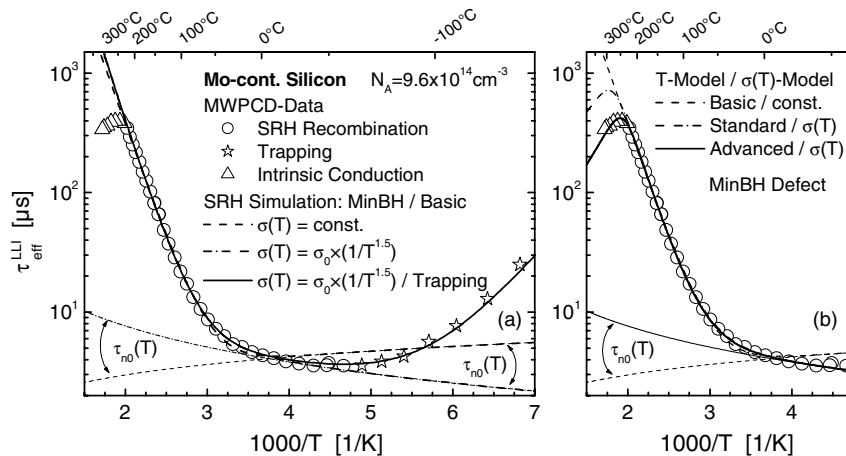


Fig. 3.42. TDLS curve measured by means of the MW-PCD technique on an intentionally Mo-contaminated silicon sample ($[Mo] = 3.7 \times 10^{11} \text{ cm}^{-3}$, $N_A = 9.9 \times 10^{14} \text{ cm}^{-3}$). **(a)** An accurate simulation of the low-temperature part from 120 to 300 K is not achieved by the standard SRH model (dashed line) but requires the insertion of a temperature-dependent capture cross-section (dash-dotted line). The lifetime increase below 200 K can be explained by superposed carrier trapping at an additional shallow level (solid line). **(b)** For an accurate simulation of the lifetime decrease above 500 K (high-temperature part), which is induced by the onset of intrinsic conduction, it is not only the temperature dependence of the majority carrier concentration (dash-dotted line) that has to be considered, but also the complete advanced T -model (solid line).

Unfortunately, the introduction of this $\sigma(T)$ -model with $\alpha=-1.5$ only improves the SRH fit in the T range from 250–200 K, while below 200 K the discrepancy between fit and data is considerable. The large increase of effective carrier lifetime below 200 K (stars) most likely originates from superposed carrier trapping, discussed in Sect. 3.5.2. In fact, as shown by the solid line in Fig. 3.42a, an accurate modeling of the measured temperature dependence down to 130 K is achieved if an additional shallow trap level at $E_C-E_t=0.15$ eV with a trap density $N_{trap}=6\times10^{14}$ cm⁻³ is assumed, the lifetime at low temperatures being identified with the asymptotic lifetime defined in Eq. (3.65). Such trapping effects are often observed at low temperatures and have to be identified to avoid distortions of the extracted $\sigma(T)$ -model which may significantly affect the modeling of the Arrhenius increase and thus the accuracy of the spectroscopic result. Since the trapping effect screens the pure recombination lifetime, the TDLS curve below 200 K is ignored in the SRH fits.

Concerning the SRH modeling of the high-temperature part of the TDLS curve ($T>500$ K), Fig. 3.42b displays the impact of the basic, standard and advanced T -model, which has been discussed in Sects. 3.5.3 and 3.5.4. Since the observed lifetime decrease above 500 K (triangles) clearly reflects the abrupt onset of intrinsic conduction, the SRH modeling using the basic T -model (dashed line) does not even allow a qualitatively correct description in that T region, as it assumes T -independent equilibrium carrier concentrations. But as can be seen from the dash-dotted line, even the consideration of their T -dependence, as in the standard T -model, only allows a SRH modeling of the TDLS bend due to intrinsic conduction, which is qualitatively but not quantitatively correct. The fact that the experimentally observed onset of intrinsic conduction is shifted to lower temperatures, points to a stronger T -dependence of $p_0(T)$ than predicted in the advanced T -model, due to the temperature-induced narrowing of the silicon band gap. In fact a perfect modeling of the TDLS curve in the whole T range is achieved if the SRH model based on the complete advanced T -model is used (solid line). The extraordinary performance of the SRH fit clearly proves the validity of this extended SRH model, which is therefore used as standard for the modeling of TDLS curves in Chap. 4.

The spectroscopic results of the individual fits will be discussed in Sect. 4.3 within the LS analysis of the molybdenum impurity. As the modeling in this section has focused on a validation of the SRH model and not on the determination of the actual defect parameters, the modeling has been restricted to MinBH defects (upper band gap half). This restriction will be removed in Sect. 4.3. The attempt to model the TDLS curve for MajBH defects (lower band gap half) reveals an even stronger impact of the chosen SRH model, as it may determine whether an SRH modeling of the TDLS

curve is possible at all. The theoretical background for this difference between MinBH and MajBH defects will be given in the following section.

3.5.6 Determination of additional defect parameters by modeling the whole TDLS curve

As has been shown in Sect. 3.4, the simple linear fit of the Arrhenius increase always allows an accurate determination of the defect depth ΔE_t , but does not provide any information about the symmetry factor $k = \sigma_n/\sigma_p$ and the band gap half the defect is located in. Based on the SRH modeling of the entire TDLS curve, the possibilities of a complete defect characterization will now be investigated, focusing on the unambiguousness of the spectroscopic result.

A Fundamental physical difference between MinBH and MajBH defect levels

A fundamental quality of TDLS, which the following discussion is based on, has already been brought out in Sect. 3.3.2A: while the slope of the Arrhenius increase only depends on the energy level E_t , its position on the $1/T$ axis is directly related to the symmetry factor k . Due to this entirely different impact of E_t and k on the shape of the TDLS curve, a fit of the entire TDLS curve should in principle allow both defect parameters to be determined.

However, concerning the sensitivity of the onset temperature $T_{Arrh-Onset}$ of the Arrhenius increase on k variations, general SRH theory leads to a fundamental difference for defects in the band half close to the majority band (MajBH defect) and close to the minority band (MinBH defect), respectively, which is illustrated in Fig. 3.43: while the onset temperature does not depend on k in the case of a MajBH defect (in p -type: $p_i \gg n_i$), a strong dependence is observed in the case of a MinBH defect (in p -type: $p_i \ll n_i$).

The physical reason for this difference is that under LLI conditions recombination via a MajBH defect is completely limited by minority carrier capture, since the minority band is less populated and further away from the defect level than the majority band, which leads to a twofold reduction of the quantum mechanical probability of minority capture compared to that of majority capture. Since normal capture asymmetries cannot invert these proportions, the TDLS curve associated with a MajBH defect does not depend on the symmetry factor k as shown in Fig. 3.43.³⁸ In contrast,

³⁸ This situation only changes for $k \gg 1$ (i.e., $\sigma_p \ll \sigma_n$) when minority carrier capture is extremely enhanced compared to majority carrier capture, due to a strong asymmetry of the capture cross-sections.

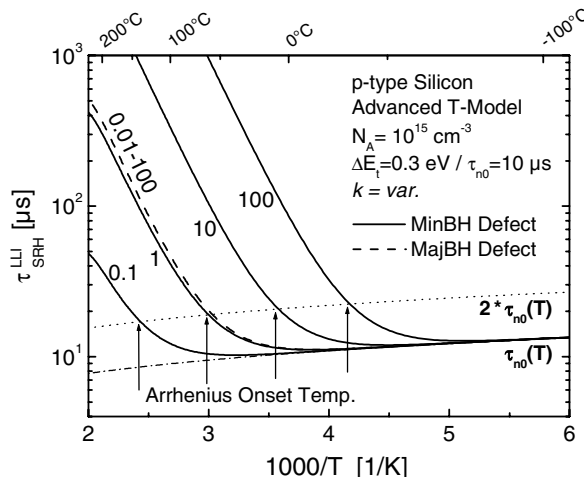


Fig. 3.43. Impact of the symmetry factor k on the Arrhenius increase of the TDLS curve for a MinBH (solid lines) and a MajBH (dashed lines) defect with an energy depth $\Delta E_t = 0.3 \text{ eV}$. While the energy level E_t from either band edge is determined from the slope of the Arrhenius increase, the modeling of its position on the $1/T$ axis often allows a determination of the symmetry factor $k = \sigma_n/\sigma_p$ and provides information about the half of the band gap in which the defect is located. The temperature where the LLI-SRH lifetime equals $2 \times \tau_{n0}(T)$ is defined as the onset temperature $T_{Arrh-Onset}$ of the linear Arrhenius increase.

recombination via a MinBH defect can be limited by minority or majority capture. Whether the capture of minorities from the slightly populated minority band or the capture of majorities from the distant majority band limits recombination via a MinBH defect strongly depends on the ratio of the capture cross-sections, i.e., on the symmetry factor k .³⁹

The difference in the k -dependence of the TDLS curves associated with MinBH and MajBH defects has a decisive impact on the SRH modeling of a TDLS curve associated with an unknown defect. Irrespective of the band gap half the unknown defect is located in, its energy depth ΔE_t^{fit} directly results from the slope of the Arrhenius increase. Assuming the defect to be located in the MinBH ($E_C - E_t = \Delta E_t^{fit}$ in p -type), an accurate SRH modeling of the entire TDLS curve⁴⁰ is always achieved as the position of the Arrhenius increase can be adjusted by an adjustment of the symmetry factor k . Assuming the defect to be located in the MajBH ($E_t - E_V = \Delta E_t^{fit}$ in

³⁹ Note that the differences in the k -dependence of the TDLS curves have the same physical origin as the differences in the k -dependence of the LLI part of IDLS curves, which have been discussed in Sect. 3.3.3A.

⁴⁰ Modeling the entire TDLS curve means modeling its complete T -dependence, i.e., slope and magnitude.

p-type), however, an accurate SRH modeling of the entire TDLS curve may completely fail because the position of the Arrhenius increase only depends on the parameters N_A and E_t , which are both fixed either from an external measurement or from the slope of the Arrhenius increase, and thus cannot be adjusted by varying k . Against the background of this finding, the following procedure for an advanced defect characterization from TDLS has been derived in the present work:

1. If the entire TDLS curve cannot be simulated assuming a MajBH defect, the defect is definitely located in the MinBH and k can be determined from an entire fit of the TDLS curve, thus allowing a complete defect characterization from TDLS alone.
2. If the entire TDLS curve can be simulated assuming a MajBH defect, the defect is most probably, although not definitely, located in the MajBH. Moreover, in the case of an underlying MajBH defect, k cannot be determined from the TDLS data alone, the TDLS curve being independent of k .

This advanced analysis of TDLS data is reported for the first time in the literature. With respect to an unambiguous identifiability from TDLS alone, the entirety of defects may thus be divided into two classes: (i) the asymmetric MinBH defects, which can be identified from TDLS alone, and (ii) the symmetric MinBH defects together with all MajBH defects, for which an unambiguous identification from TDLS alone fails, the band gap half and symmetry factor k being undetermined. But as will be shown in Sect. 3.6, even for the second group of defects a complete defect characterization can be achieved if the ambiguous spectroscopic results from the TDLS curve and the corresponding room-temperature IDLS curve are combined.

B Significance of an accurate modeling of the TDLS bend due to intrinsic conduction

Although based on a complete SRH fit, the advanced spectroscopic evaluation of TDLS curves has so far been restricted to the T range below $T_{IC-Onset}$. Nevertheless, an accurate modeling of the TDLS bend due to intrinsic conduction may significantly improve the spectroscopic result. To disclose the impact of the defect parameters on the T -dependence of the TDLS decrease, the general expression (3.67) for the T -dependence of LLI-SRH lifetime has been approximated for the T range of intrinsic conduction ($T > T_{IC-Onset}$), where $p_0(T) = n_0(T) \equiv n_i(T)$ can be assumed:

$$\tau_{SRH}^{LLI,IC}(T) = \tau_{n_0}(T) \times \left[\frac{1}{2}(1+k) + \frac{p_1(T)}{2n_i(T)} + k \frac{n_1(T)}{2n_i(T)} \right] \quad (3.68)$$

As expected and shown by Eq. (3.68), the observed decrease of the TDLS curve is determined by the dominant SRH ratio as long as its magnitude exceeds the constant addend (first term in brackets). Both SRH density (denominator) and intrinsic carrier concentration (numerator) are dominated by an exponential T -dependence following $\exp(-\Delta E/k_B T)$ with characteristic energies given by the energy depth ΔE_t of the defect and the half band gap width $E_{gap}/2$, respectively. Since $\Delta E_t < E_{gap}/2$, the denominator of the dominant SRH ratio increases more weakly with temperature than the numerator, which leads to an overall exponential decrease of the TDLS curve with temperature, the dominant term taking the form⁴¹

$$\tau_{SRH}^{LLI,IC}(T) \propto \exp\left(\frac{E_{gap}/2 - \Delta E_t}{k_B T}\right) \quad (3.69)$$

Equation (3.69) shows that the characteristic energy of the exponential TDLS decrease due to intrinsic conduction is just given by the energy distance of the defect level from mid-gap. This finding is directly reflected in Fig. 3.44, which shows the impact of the defect energy level E_t on the shape of the TDLS decrease for (a) MinBH defects and (b) MajBH defects with the same symmetry factor $k=10$. As expected from Eq. (3.69), the slope of the TDLS decrease flattens with increasing energy depth ΔE_t irrespective of the band gap half of the defect. For a mid-gap trap with $\Delta E_t = E_{gap}/2$, the T -dependence of the TDLS decrease vanishes according to Eq. (3.69), which is actually reflected in Fig. 3.44a and b in TDLS curves with an almost horizontal shape in the T range above $T_{IC-Onset}$. Thus, the shape of the TDLS decrease above $T_{IC-Onset}$ provides redundant spectroscopic information about the energy depth ΔE_t of the defect.

The impact of the symmetry factor k is shown in Fig. 3.45. In the case of a MinBH defect, as displayed in Fig. 3.45a, the peak value of the TDLS curve increases with increasing symmetry factor k , which directly results from the position of the Arrhenius increase being k -dependent. Moreover, k variations mainly induce a vertical shift of the whole TDLS decrease without changing its shape. In the case of a MajBH defect, on the other hand, the peak value of the TDLS curve is almost independent of the symmetry factor k , which reflects the k independence of the Arrhenius increase. However, Fig. 3.45b reveals for a MajBH defect a partial k -dependence of the TDLS decrease above $T_{IC-Onset}$: while the decrease as a

⁴¹ Note that Eq. (3.69) neglects superposed weaker contributions to the overall T -dependence which arise from the effective densities of states and $\tau_{n0}(T)$ and result in slight deviations from a pure linear decrease of LLI-SRH lifetime in an Arrhenius plot. In addition, Eq. (3.69) is only valid in that T range in which the LLI-SRH lifetime from Eq. (3.68) is not yet dominated by the constant addend but only by the relevant SRH ratio.

whole is almost independent of k for $k < 1$, its slope starts to flatten out with increasing k as soon as $k > 1$.

The reason for this flattening can be directly deduced from Eq. (3.68). A closer look at the T -dependence of both SRH ratios reveals a fundamental difference. Since the dominant SRH ratio depends on the defect energy depth ΔE_t which is by definition smaller than $E_{gap}/2$, it decreases

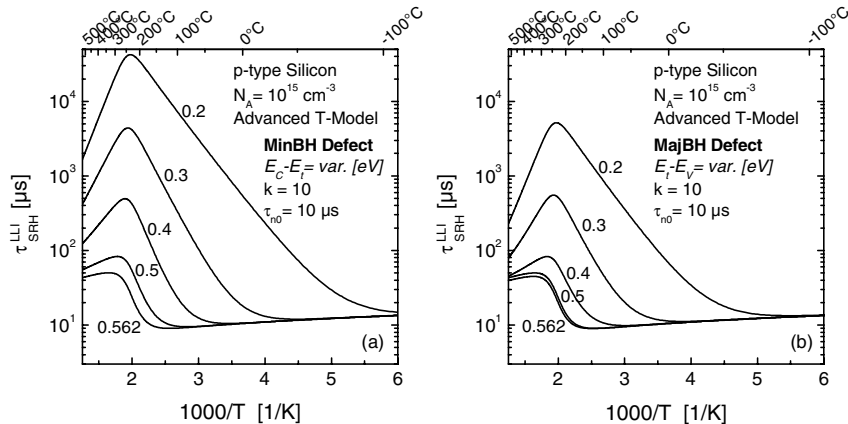


Fig. 3.44. Impact of the defect energy level E_t on the shape of the TDLS bend due to intrinsic conduction (a) for a MinBH defect and (b) for a MajBH defect. With increasing defect depth the slope of the TDLS bend flattens out for MinBH and MajBH defects.

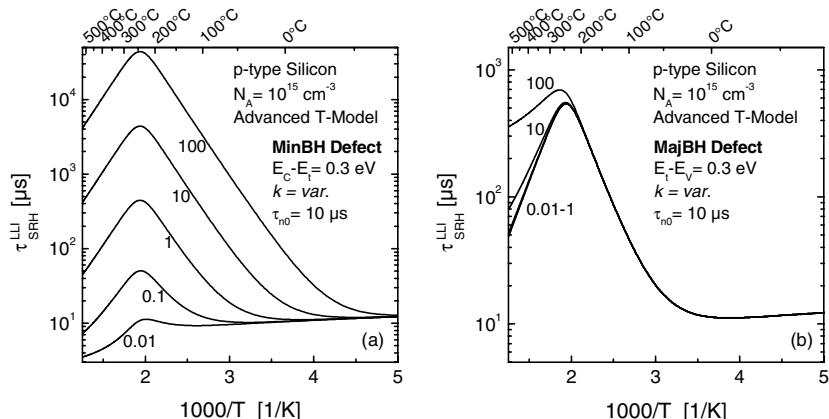


Fig. 3.45. Impact of the defect symmetry factor k on the shape of the TDLS bend due to intrinsic conduction (a) for a MinBH defect and (b) for a MajBH defect. Only for MajBH defects does the slope of the TDLS bend depend on k and flatten out with increasing k .

exponentially with temperature according to Eq. (3.69), the exp-argument being positive. In contrast, the subordinate SRH ratio, which has been neglected so far, depends on the energy distance of the defect level from the more distant band, i.e. $E_{gap}-\Delta E_t$. Since this energy difference is by definition bigger than $E_{gap}/2$, the subordinate SRH ratio shows an exponential increase with temperature instead of a decrease,⁴² though on a lower level than the dominant SRH ratio. As a consequence, both ratios approach each other in terms of magnitude as the temperature increases. Nevertheless, their difference in magnitude is in general too big to be significantly altered or even inverted by the opposite T -dependence alone. This is why the TDLS decrease of MinBH defects has not been affected by the subordinate p_1/n_i ratio. The situation changes for MajBH defects as here the subordinate n_1/n_i ratio directly scales with the symmetry factor k . Being increased for $k=100$, for example, by two orders of magnitude above its normal value, the subordinate n_1/n_i ratio affects the TDLS decrease in its whole range of definition, as shown in Fig. 3.45b. The fact that its impact increases with increasing temperature due to the opposite T -dependence is reflected in the increasing gap between the TDLS curves for $k=100$ and $k=1$ and leads to a reduced slope of the TDLS decrease in an Arrhenius plot. It is obvious that the k -dependence of the TDLS decrease becomes the stronger the deeper the MajBH defect is as the difference in magnitude between n_1 and p_1 declines.

The fact that a k -dependence of the TDLS decrease due to intrinsic conduction is particularly observed for MajBH defects is of practical importance as precisely these defects do not allow a k determination from the Arrhenius increase, as shown in Sect. 3.5.6A. Thus it can be concluded that the inclusion of the TDLS bend in the SRH modeling may allow a k determination in the case of a MajBH defect and thus an increase in the spectroscopic information. This procedure will be especially successful for deeper MajBH defects with higher symmetry factors k .

Apart from that, accurate modeling of the TDLS bend due to intrinsic conduction may serve as consistency check of the externally determined material parameter N_{dop} . The essential characteristic for this is the position of the TDLS bend, rather than its shape, since $T_{IC-Onset}$ strongly depends on the doping concentration N_{dop} , while being hardly affected by the defect parameters E_t and k (see Sect. 3.5.4B). In order to assess the impact of an error in the doping concentration on the spectroscopic result obtained from

⁴² The overall T -dependence of the subordinate SRH ratio is described by a similar expression as given in Eq. (3.69). Only the characteristic energy changes to $E_{gap}/2 - (E_{gap}-\Delta E_t)$, which makes the exp-argument negative and thus leads to the discussed increases in the subordinate SRH ratio with temperature.

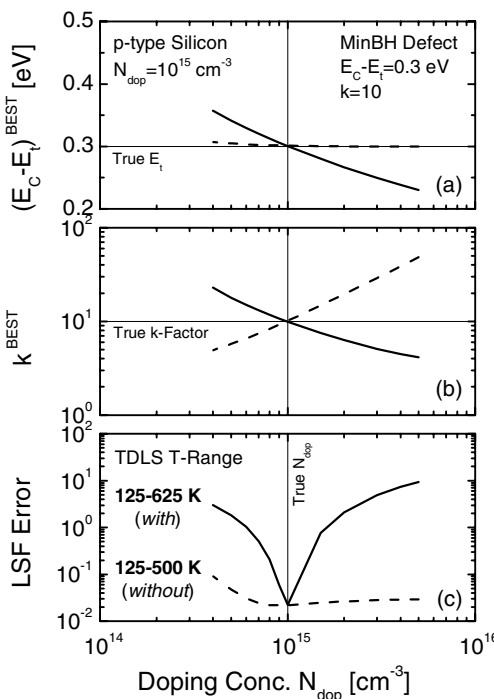


Fig. 3.46. Impact of an error in the doping concentration on the TDLS fit result with (solid lines) and without (dashed lines) considering the TDLS bend due to intrinsic conduction in the SRH modeling. The underlying TDLS curve has been calculated for a MinBH defect at $E_c - E_t = 0.3 \text{ eV}$ with $k = 10$ in a 10^{15} cm^{-3} doped sample. (a,b) Defect parameters E_t and k determined from least squares fits of this TDLS curve for specified but gradually varied values of the doping concentration. (c) Related χ^2 errors of these least squares fits displayed as a function of N_{dop} . As shown by the pronounced minimum of the solid χ^2 curve, the inclusion of the TDLS bend in the SRH modeling makes an independent cross-check of the doping concentration possible and thus prevents an unrecognized transfer of an N_{dop} error to the defect parameter k .

TDLS, a predefined TDLS curve has been analyzed by means of least squares fits for specified but gradually varied values of N_{dop} . The optimum defect parameters E_t and k , which have been extracted from the individual fits, and the related χ^2 errors of the fit are displayed as functions of N_{dop} in Fig. 3.46a, b and c, respectively. To bring out the relevance of modeling the TDLS bend, the least squares fits have been performed with (solid lines) and without (dashed lines) including the TDLS bend in the SRH modeling. As can be seen, an error in N_{dop} particularly affects the accuracy of the k determination while E_t only changes with N_{dop} if the TDLS bend is included in the SRH modeling (solid line). But this additional tendency to error is only apparent since for a SRH simulation, including the TDLS bend (solid line), the N_{dop} -dependent χ^2 curve exhibits a pronounced minimum, which indicates the true doping concentration. In contrast, if the TDLS bend is neglected in the SRH modeling (dashed line), the associated χ^2 curve is flat in a broad doping range, thus impeding the identification and control of the true doping concentration. Without being detectable, each error in determining N_{dop} is directly transmitted to the defect parameter k , while E_t is almost unaffected.

It can be concluded that the measurement and modeling of the TDLS bend due to intrinsic conduction is of some importance for an accurate advanced defect characterization from TDLS. On the one hand, it may increase the spectroscopic information in the case of MajBH defects. On the other hand it allows the doping concentration to be cross-checked independently and thus prevents an unrecognized transfer of an N_{dop} error to the defect parameter k . This consistency check of the determined material and defect parameters greatly increases the reliability of the spectroscopic TDLS result.

3.5.7 Defect parameter solution surface of TDLS curves (DPSS)

Having seen how to extract the maximum defect information from TDLS, we now want to address the important issue of spectroscopic accuracy. In order to quantify the accuracy of the defect parameters determined from TDLS, the tolerance of the fitting model towards slight fluctuations of the fitting parameters has to be investigated. To perform this investigation with maximum transparency, the analysis by means of the defect parameter solution surface (DPSS), which has been developed for IDLS in Sect. 3.3.2, is transferred to TDLS. Applying the DPSS technique to TDLS curves simulated for defects with different characteristic properties, we discuss the important aspects of modeling TDLS curves in an illustrative way, demonstrating at the same time the practical value of the DPSS analysis.

A Case 1: asymmetric MinBH defect with constant capture cross-section (result: E_c, k)

The procedure of DPSS analysis and its basic characteristics should be derived using the TDLS curve displayed in Fig. 3.47a (symbols) which has been calculated for an asymmetric MinBH defect at $E_c-E_t=0.3$ eV with $k=10$. As expected from Sect. 3.5.6A, an accurate SRH fit of the TDLS curve is only achieved for a MinBH defect (solid line) while the SRH modeling with a MajBH defect fails (dashed-dotted line).

Analogously to the DPSS analysis of IDLS curves presented in Sect. 3.3.2, the DPSS diagram associated with the TDLS curve is determined from SRH simulations of the preset TDLS data for specified but gradually varied energy levels E_c-E_t of the defect center, with the optimal k factors being determined by means of a least squares fit subject to a fixed energy level. The resulting symmetry factors k^{DPSS} and the corresponding Chi^2 errors of the least squares fit are displayed in Fig. 3.47b and c as a function of the energy level E_c-E_t (solid lines). Both curves together represent the DPSS of the TDLS curve and are referred to as the DPSS- k and DPSS- Chi^2 curves.

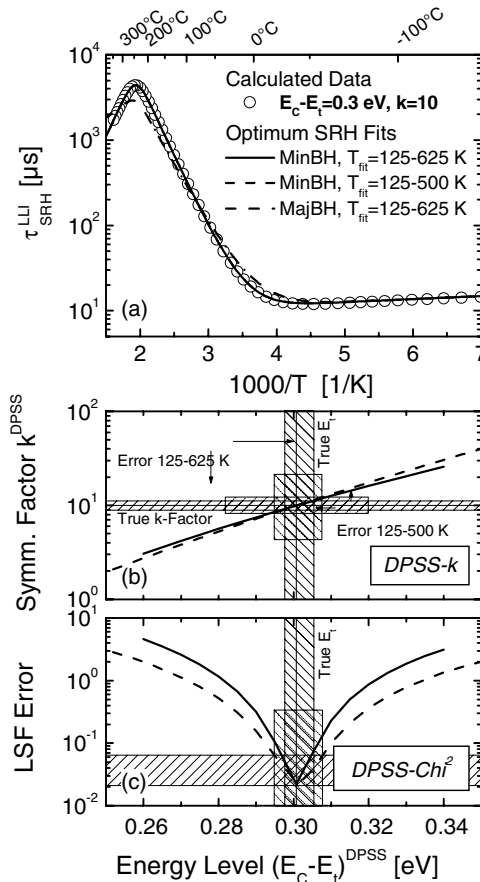


Fig. 3.47. Case 1: Advanced DPSS analysis of a TDLS curve calculated for an asymmetric MinBH defect. (a) As expected, the SRH modeling of the TDLS curve with a MajBH defect fails (*dash-dotted line*). (b, c) The DPSS- χ^2 curve allows the true defect parameters to be identified from the position of its minimum and an error for the extracted defect parameters to be estimated from its width. The DPSS analysis for the MinBH defect is performed *with* (*solid lines*) and *without* (*dashed lines*) considering the TDLS bend due to intrinsic conduction within the SRH modeling of the TDLS curve. While the optimum value for the defect parameters is not affected by a variation of the considered temperature range, the error of the extracted defect parameters is reduced if the TDLS bend due to intrinsic conduction is enclosed in the SRH modeling of the TDLS curve (*shaded areas*).

The practical value of the DPSS diagram of the TDLS curve is twofold: while the position of the minimum of the DPSS- χ^2 curve allows the identification of the true defect parameters from the DPSS- k curve, the width of the DPSS- χ^2 curve makes possible an error estimate for the extracted defect parameters. If an upper limit for the tolerated least squares error is defined, the ranges of acceptable values for the defect parameters can be graphically deduced from the DPSS diagram, as shown by the shaded areas in Fig. 3.47b and c.

A further strength of the proposed DPSS analysis is that it allows a direct quantitative comparison of the spectroscopic results if the SRH model or the boundary conditions of the fit are varied. As an example Fig. 3.47b and c display the impact of the considered T range, the two pairs of DPSS curves being determined with (125–625 K, solid lines) and without (125–500 K, dashed lines) considering the TDLS bend due to

intrinsic conduction within the SRH modeling of the TDLS curve. As can be seen from the coincidence of both DPSS- Chi^2 minimums, the optimum values for the defect parameters are not affected by a variation of the considered T range. The only difference is the steeper shape of the solid DPSS- Chi^2 curve which demonstrates that the error of the extracted defect parameters can be reduced if the TDLS bend due to intrinsic conduction is included in the SRH modeling of the TDLS curve. Depending on the quality of the TDLS data, this reduction may be stronger than shown in Fig. 3.47b and c for an ideal TDLS curve.

B Case 2: asymmetric MajBH defect with constant capture cross-section (result: ΔE)

To demonstrate the impact of the differences between MinBH and MajBH defects (see Sect. 3.5.6) on the DPSS analysis, a TDLS curve which has been calculated for an asymmetric MajBH defect at $E_t-E_V=0.3\text{ eV}$ with $k=10$ is analyzed in Fig. 3.48. Again the DPSS analysis is performed without (left) and with (right) considering the TDLS bend due to intrinsic conduction within the SRH modeling. As expected from Sect. 3.5.6A, an accurate SRH modeling of the TDLS curve is possible with a MinBH (dashed line) and a MajBH defect (solid line) even if the TDLS bend is included (see Fig. 3.48a and a2).

Let us first consider the DPSS diagram on the left side of Fig. 3.48, which is associated with the reduced TDLS curve (125–500 K). While the energy depth of the two solutions is almost the same with $(E_C-E_t)^{S1}=0.31\text{ eV}$ and $(E_t-E_V)^{S2}=0.30\text{ eV}$, the k factor differs by almost an order of magnitude. Since both solutions are identical in quality, which is manifested in similar minimum values of both DPSS- Chi^2 curves, an identification of the true band gap half and k factor of the defect center is not possible. The qualitative shape of the DPSS curves reflects the fundamental difference between MinBH and MajBH defects discussed in Sect. 3.5.6A. The steep DPSS- k and the narrow DPSS- Chi^2 curves observed for the MajBH solution directly arise from the fact that the onset temperature of the Arrhenius increase is independent of k for a MajBH defect. Analogously, the existing k -dependence for a MinBH defect leads to a moderate slope of the DPSS- k curve and to a broader DPSS- Chi^2 curve. Thus, concerning the accuracy of the extracted defect parameters, the following pattern is found: while the defect parameters of the MinBH solution are both determined with sufficient accuracy, the MajBH solution only allows an accurate E_t determination while the k determination in general fails, the extracted k range being several orders of magnitude wide.

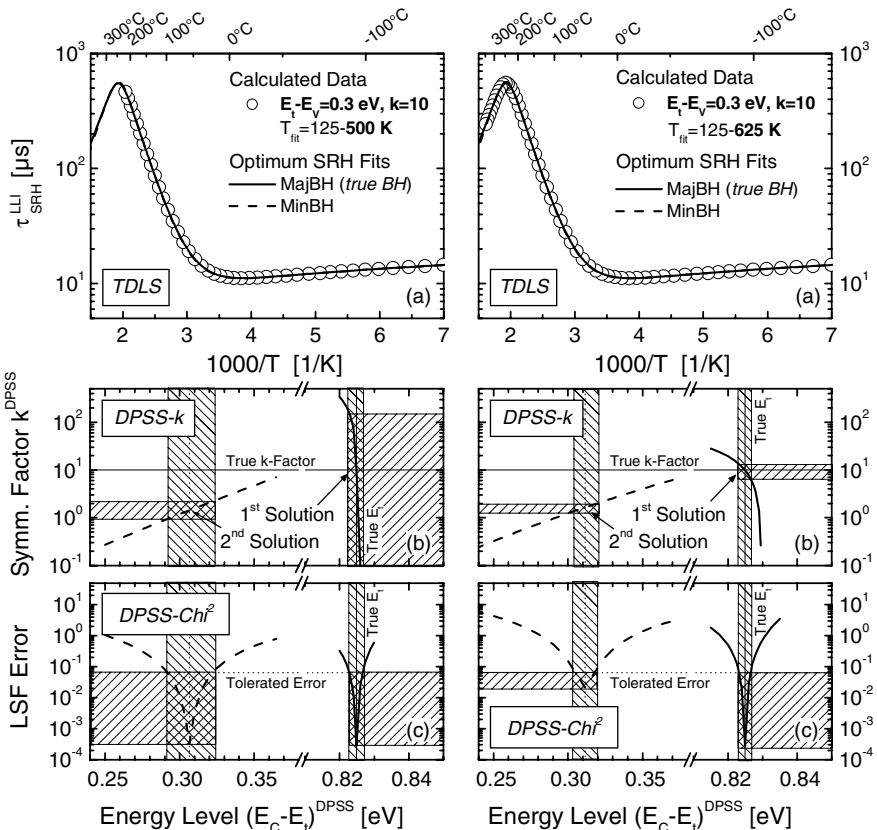


Fig. 3.48. Case 2: Advanced DPSS analysis of a TDLS curve calculated for an asymmetric MajBH defect without (*left*) and with (*right*) considering the TDLS bend due to intrinsic conduction in the SRH modeling. **(a)** Even if the TDLS bend is included, an accurate modeling of the TDLS curve is possible with a MinBH (*dashed line*) and a MajBH defect (*solid line*). **(b, c)** The DPSS analysis shows that the energy depth of the two solutions is almost the same while the k factor differs by almost an order of magnitude. Whereas the optimum values of the defect parameters are not affected by a variation of the considered T range, the errors of the extracted defect parameters are significantly reduced, especially for the MajBH solution, if the TDLS bend due to intrinsic conduction is included in the SRH modeling of the TDLS curve. In principle, the comparison of the two minimum values of the DPSS- Chi^2 curve allows the true band gap half of the defect center to be identified. However, this identification fails in the case of a reduced fit range, since then both solutions are identical in quality.

If the TDLS bend is considered within the SRH modeling of the TDLS curve, the associated DPSS diagram exhibits some decisive changes which are displayed on the right side of Fig. 3.48. In principle, the observed divergence of the DPSS- Chi^2 minimum allows the defect level in the lower half

of the band gap to be identified.⁴³ Nevertheless, with a superposed measurement error this difference will most likely disappear. Thus, the modeling of the TDLS bend will not in general help to find the true solution of two possible TDLS solutions. Whereas the effect of the increased T range of SRH modeling is negligible for the absolute values of the defect parameters extracted at the two DPSS- Chi^2 minimums, it is not for the estimated errors. Apart from the slight reduction in the E_t and k error of the MinBH solution already observed in Fig. 3.47, the consideration of the TDLS bend leads to a large reduction in the k error of the MajBH solution, especially towards higher k values. Note that this improvement does not result from a further improvement of the E_t determination but from a flattening of the DPSS- k curve due to the k -dependent shape of the TDLS decrease (see Fig. 3.45). Thus, an accurate modeling of the TDLS decrease due to intrinsic conduction may in fact provide the k information in the case of a MajBH defect.

C Case 3: MinBH defect with temperature-dependent capture cross-section

The impact of a superposed temperature-dependence of the capture cross-sections is finally analyzed in Fig. 3.49. The TDLS curve displayed in Fig. 3.49a (symbols) has been calculated for an asymmetric MinBH defect at $E_C-E_t=0.3\text{ eV}$ with $k=10$ with temperature-dependent capture cross-sections, the $\sigma(T)$ -model being assumed as $\sigma(T)=\sigma_0 \times T^{-2}$. The DPSS analysis is performed with (solid lines) and without (dashed lines) considering the correct $\sigma(T)$ -model. Note that in the case of an SRH modeling with $\sigma=\text{const.}$ (dashed lines) the considered T range has been restricted to $T>200\text{ K}$ to avoid artificially high Chi^2 values due to the self-evident inadequacy of the simple SRH model in the T range below.

Analogously to the results in Fig. 3.47, the SRH modeling with a MajBH defect completely fails, regardless of whether or not the $\sigma(T)$ -model is considered (not shown in Fig. 3.49a). As can be seen from Fig. 3.49b and c, the DPSS solution is significantly falsified if the underlying $\sigma(T)$ -dependence is ignored. For the assumed $\sigma(T)$ decrease with

⁴³ The increase of the DPSS- Chi^2 minimum of the MinBH solution, which is observed under the expansion of the considered T range, results from the fact that the preset TDLS curve exhibits a TDLS decrease of reduced slope due to the asymmetry ($k=10$) of the underlying MajBH defect (see Fig. 3.45). If the modeling is performed on the basis of a MinBH defect, this kind of a flatter TDLS decrease cannot be realized by an adjustment of k but only by an increase in the defect depth (see Figs. 3.45 and 3.44), which worsens the modeling of the Arrhenius increase. In fact the E_t value of the optimum MinBH solution slightly increases from 0.306 eV (without TDLS bend) to 0.311 eV (with TDLS bend).

increasing temperature, which represents a realistic case, the extracted energy level is shifted 60 meV deeper into the band gap and the extracted k factor is increased by an order of magnitude. This demonstrates the significance of a correct modeling of the low-temperature part of the TDLS curve with respect to an accurate determination of defect parameters E_t and k .

In conclusion, the three examples demonstrate that the newly developed DPSS analysis allows a transparent and comprehensive SRH analysis of TDLS data, which provides a quantitative estimate of the accuracy of the spectroscopic result and visualizes all fundamental aspects of modeling TDLS curves.

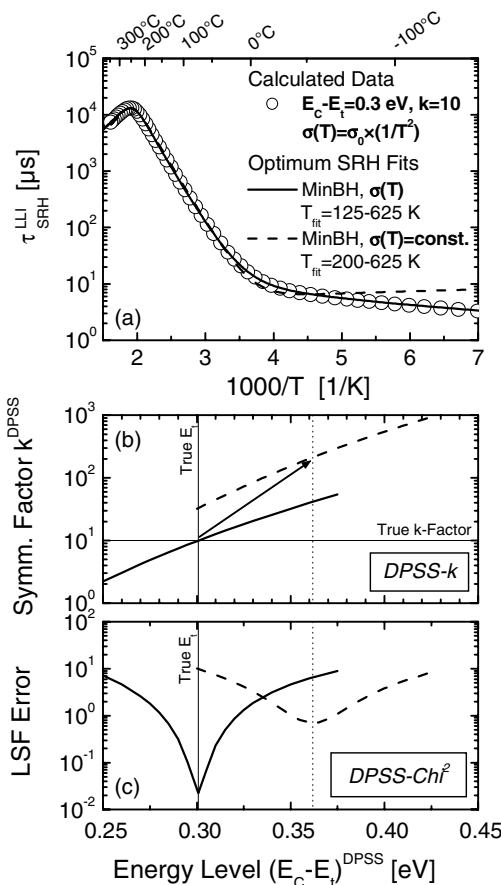


Fig. 3.49. Case 3: Advanced DPSS analysis of a TDLS curve calculated for an asymmetric MinBH defect with temperature-dependent capture cross-section. The DPSS analysis is performed with (solid lines) and without (dashed lines) considering the correct $\sigma(T)$ -model. If the underlying $\sigma(T)$ -dependence is ignored, the DPSS solution is significantly falsified.

3.5.8 Applicability of TDLS: onset temperature and width of the linear Arrhenius increase

Since the Arrhenius increase contains most of the defect-specific information, the accuracy or even applicability of TDLS strongly depends on the width of the T range which exhibits the Arrhenius increase. While a small Arrhenius increase will only affect the accuracy of the spectroscopic result if the advanced TDLS analysis on the basis of an entire SRH modeling is applied, it may lead to a complete break-down of TDLS if simple evaluation techniques on the basis of a linear fit are used. As already shown, the T range of the Arrhenius increase is confined for purely physical reasons: at its lower end by the SRH statistics, which define an onset condition, and at its upper end by the onset of intrinsic conduction. While the upper T bound $T_{IC-Onset}$ has already been calculated in Sect. 3.5.4B, the lower T bound $T_{Arrh-Onset}$ has not yet been quantified. To allow a quantitative estimate of the Arrhenius width for arbitrary defect and material parameters and hence a division of the parameter plane in terms of the applicability of TDLS, the onset temperature $T_{Arrh-Onset}$ of the Arrhenius increase is determined in the following as a function of the defect and material parameters.

As shown graphically by the dotted line in Fig. 3.43, $T_{Arrh-Onset}$ is defined as that temperature at which the LLI-SRH lifetime is enhanced by a factor 2 above the corresponding value of the minority capture time $\tau_{n0}(T)$, which represents the baseline of the TDLS curve.⁴⁴ Analytically, the defining condition is thus given by

$$1 + \underbrace{\frac{p_1(T_{Arrh-Onset})}{p_0} + k \times \frac{n_1(T_{Arrh-Onset})}{p_0}}_{=1} ! = 2 \quad (3.70)$$

which follows directly from Eq. (3.7a) for a *p*-type semiconductor. From Eq. (3.70), $T_{Arrh-Onset}$ has been calculated numerically in Fig. 3.50 as a function of doping concentration (a) for symmetric defect levels with varying energy depth ΔE_t and (b) for asymmetric MinBH (solid) and MajBH (dashed) defect levels of same energy depth with varying symmetry factor k .

As can be seen from Fig. 3.50a and b, $T_{Arrh-Onset}$ increases with increasing doping concentration N_A , increasing energy depth ΔE_t and decreasing symmetry factor k , which has already been qualitatively discussed in Sect. 3.2.4. The significance of the impact of these three factors becomes evident from three numerical examples: (i) For a symmetric defect level

⁴⁴ According to Sect. 3.2.1, $\tau_{n0}(T)$ represents at each temperature the absolute minimum of the SRH lifetime and is thus a suitable reference to estimate the lifetime enhancement.

with medium energy depth of 0.3 eV, an increase in the doping concentration by only two orders of magnitude from 10^{14} to 10^{16} cm^{-3} results in an increase in $T_{\text{Arrh-Onset}}$ by 130 K from 280 to 410 K. As can be seen from the divergence of the curves in Fig. 3.50a, this doping dependence of $T_{\text{Arrh-Onset}}$ becomes stronger as the energy depth increases.⁴⁵ (ii) On the other hand, a slight increase in the defect depth from 0.2 to 0.4 eV yields an increase in $T_{\text{Arrh-Onset}}$ by almost 200 K from 235 to 430 K, if a medium-doped sample with $N_A = 10^{15} \text{ cm}^{-3}$ is assumed. Consistently with (i), this energy dependence of $T_{\text{Arrh-Onset}}$ becomes stronger as the doping concentration increases.⁴⁶ (iii) Finally, a k -dependence of $T_{\text{Arrh-Onset}}$ is only observed for MinBH defects (solid lines) but not for MajBH defects (dashed line), as discussed in Sect. 3.5.6A. If we thus assume a MinBH defect at 0.3 eV in a 10^{15} cm^{-3} -doped sample, a decrease in the symmetry factor by only two orders of magnitude from 10 to 0.1 causes an increase in $T_{\text{Arrh-Onset}}$ by 130 K from 280 to 410 K, which corresponds precisely to the changes in (i) induced by an increase in N_A by the same amount. As can be seen from the divergence of the curves in Fig. 3.50b, the k -dependence of $T_{\text{Arrh-Onset}}$ also becomes stronger as the doping concentration increases.⁴⁷ It has to be concluded that all three factors have a strong impact on $T_{\text{Arrh-Onset}}$, the impact of the energy depth nevertheless being the strongest.

Combining the results for $T_{\text{Arrh-Onset}}$ with the results for $T_{\text{IC-Onset}}$ determined in Sect. 3.5.4B, we are now able to calculate the width of the T range exhibiting the Arrhenius increase:

$$\Delta T_{\text{Arrh}} := T_{\text{IC-Onset}} - T_{\text{Arrh-Onset}} \quad (3.71)$$

Figure 3.51 displays ΔT_{Arrh} as a function of doping concentration again (a) for symmetric defect levels with varying energy depth ΔE_t and (b) for asymmetric MinBH (solid) and MajBH (dashed) defect levels with varying symmetry factor k and same energy depth. Since both confining temperatures increase approximately uniformly with increasing doping concentration, the doping dependence of ΔT_{Arrh} is much weaker than that of $T_{\text{Arrh-Onset}}$ and $T_{\text{IC-Onset}}$. As can be seen from Fig. 3.51a, the doping dependence of ΔT_{Arrh} changes from a slight decrease for deep energy levels

⁴⁵ Upon an N_A increase from 10^{14} to 10^{16} cm^{-3} , $T_{\text{Arrh-Onset}}$ only increases by 60 K for a shallow level with 0.1 eV while the increase amounts to 185 K for a deep level with 0.5 eV, assuming both levels to be symmetric.

⁴⁶ Upon a ΔE_t increase from 0.2 to 0.4 eV, $T_{\text{Arrh-Onset}}$ only increases by 165 K for a low doping of 10^{14} cm^{-3} while the increase amounts to 230 K for a high doping of 10^{16} cm^{-3} .

⁴⁷ Upon a k decrease from 10 to 0.1, $T_{\text{Arrh-Onset}}$ only increases by 90 K for a low doping of 10^{14} cm^{-3} while the increase amounts to 200 K for a high doping of 10^{16} cm^{-3} , assuming a MinBH defect at 0.3 eV in both cases.

with $\Delta E_t > 0.35$ eV to a slight increase for shallow defect levels with $\Delta E_t < 0.35$ eV, which directly reflects the fact that in contrast to the ΔE_t -independent doping dependence of $T_{IC-Onset}$ (see Fig. 3.41a), the doping dependence of $T_{Arrh-Onset}$ varies with the energy depth ΔE_t , being enhanced for deep levels and attenuated for shallow levels (see Fig. 3.50a).

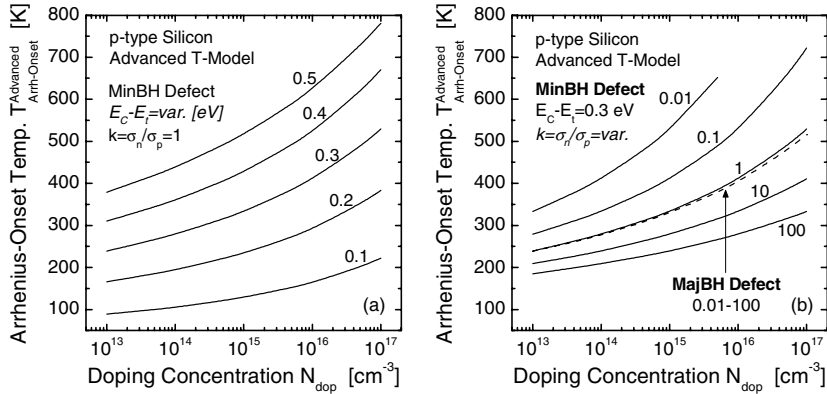


Fig. 3.50. Onset temperature $T_{Arrh-Onset}$ of the linear Arrhenius increase of TDLS as a function of doping concentration. (a) Impact of the energy level E_t for symmetric defects. (b) Impact of a capture asymmetry ($k \neq 1$) for MinBH (solid) and MajBH (dashed) defects with same energy depth $\Delta E_t = 0.3$ eV.

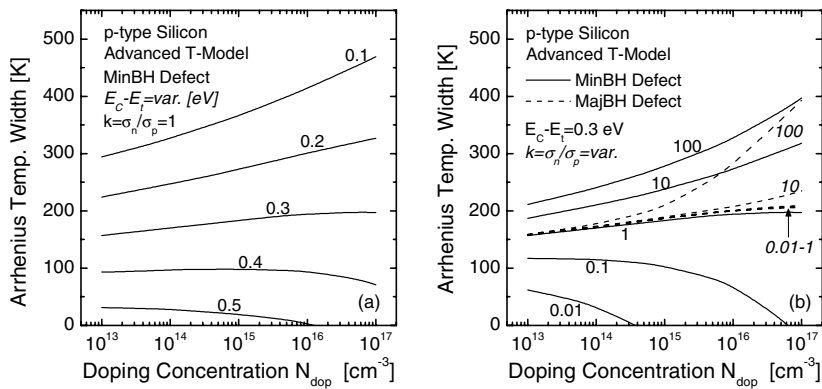


Fig. 3.51. Width of the temperature range of the linear Arrhenius increase as a function of doping concentration. (a) Impact of the energy level E_t for symmetric defects. (b) Impact of a capture asymmetry ($k \neq 1$) for MinBH (solid) and MajBH (dashed) defects with the same energy depth $\Delta E_t = 0.3$ eV. The width of the Arrhenius T range is defined as $\Delta T_{Arrh} := T_{IC-Onset} - T_{Arrh-Onset}$ and calculated from the values of $T_{IC-Onset}$ and $T_{Arrh-Onset}$ which are displayed in Figs. 3.40, 3.41 and 3.50, respectively. The higher ΔT_{Arrh} , the higher the accuracy of the E_t determination from the TDLS.

In contrast to the weak doping dependence, ΔT_{Arrh} strongly depends on the defect parameters, since the E_t - and k -dependence of $T_{Arrh-Onset}$ (see Fig. 3.50) is much stronger than that of $T_{IC-Onset}$ (see Fig. 3.41). The strength of the ΔT_{Arrh} reduction with increasing energy depth ΔE_t and decreasing symmetry factor k becomes evident from the ΔT_{Arrh} values, which are expected in a medium-doped sample with $N_A = 10^{15} \text{ cm}^{-3}$: if the energy depth of a symmetric defect level increases slightly from 0.2 to 0.4 eV, the width of the Arrhenius T range reduces by 175 K from 275 to 100 K (see Fig. 3.51a). On the other hand if we assume a MinBH defect at 0.3 eV, a decrease in the symmetry factor k by only two orders of magnitude from 10 to 0.1 causes a reduction of ΔT_{Arrh} by 140 K from 240 to 100 K (see Fig. 3.51b).

Moreover, Fig. 3.51 reveals the critical parameter constellations concerning the applicability of TDLS. For the minimum width of the Arrhenius T range, which still allows an accurate spectroscopic result, empirical values of 50 K and 100 K, respectively, have been found in the present work depending on whether the advanced or a linear evaluation technique is used. Focusing on the advanced analysis, Fig. 3.51 shows that an accurate TDLS analysis fails for defect levels around mid-gap ($\Delta E_t \geq 0.5 \text{ eV}$) and for shallower levels if their symmetry factor is strongly reduced ($\sigma_n \ll \sigma_p$). In both cases the Arrhenius increase may completely vanish if the doping concentration becomes high enough. It should be emphasized that this restriction of the parameter intervals with respect to applicability of TDLS originates for purely physical reasons. Further restrictions may arise from experimental boundary conditions due to a limitation of the accessible T range.

In conclusion, Figs. 3.50 and 3.51 together allow the position and width of the Arrhenius increase to be estimated for arbitrary defect and material parameters. The benefit of this newly developed combined diagram is threefold: (i) For given defect and material parameters, the combined diagram allows the relevant temperature range of the TDLS measurement to be selected a priori and provides information about the general suitability of TDLS in terms of spectroscopic accuracy. (ii) For a given defect center to be analyzed, the combined diagram makes the determination of the optimum doping concentration possible, which allows an accurate modeling of both the Arrhenius increase and the low-temperature part of the TDLS curve. (iii) For a given doping concentration of a sample with unknown defects, the combined diagram provides information about the range of defect energies for which an accurate TDLS analysis is possible. All this information becomes more important the greater the limitation of the experimentally accessible T range. While the first two points are relevant from a scientific point of view if TDLS is applied on intentionally

contaminated samples as in the present work, the last point is relevant from a practical point of view if TDLS is used as diagnostic tool.

3.5.9 Discussion of the fundamental assumptions of TDLS theory

As demonstrated in Sect. 3.5.5, accurate SRH modeling of TDLS curves is achieved if the advanced models discussed in Sects. 3.5.1 to 3.5.4 are taken into account for the different superposed effects. However, the SRH modeling is based on two fundamental assumptions: the temperature-independence of (i) the symmetry factor k and (ii) the energy distances of the defect level to both band edges. Although simplifying the fitting problem, these assumptions are the most suitable theoretical basis for the SRH modeling of TDLS curves. This should be demonstrated in the following by qualitatively investigating the changes in the TDLS analysis which have to be expected if these assumptions are abandoned.

A Assumption 1: temperature-independent symmetry factor k

The assumption of a temperature-independent symmetry factor k directly implies models with identical T -dependence for the electron and hole capture cross-sections, $\sigma_n(T)$ and $\sigma_p(T)$, which in turn requires electrons and holes to be captured into the defect level via the same capture mechanism. As discussed in detail in Sect. 3.5.1C, the validity of this assumption strongly depends on the type of the physical mechanism which dominates capture into a defect level.

The fact that this assumption may be invalid, raises the question as to how the TDLS curve changes if there is a difference in the T -dependence of the electron and hole capture cross-section of a defect, i.e., if the k factor is no longer a constant but a function of temperature. A closer look at the LLI-SRH lifetime reveals that the expected changes strongly depend on the band gap half the defect is located in. This can be seen from Eqs. (3.72a) and (3.72b), which represent the LLI-SRH lifetime for a p -type semiconductor, assuming a defect in the lower (MajBH) and the upper (MinBH) band gap half, respectively, with the k factor being replaced by the hole capture time constant τ_{p0} :

$$\tau_{SRH}^{LLI,p,MajBH}(T) = \tau_{n0}(T) \times \left[1 + \frac{p_1(T)}{p_0(T)} \right] \quad (3.72a)$$

$$\tau_{SRH}^{LLI,p,MinBH}(T) = \tau_{n0}(T) + \tau_{p0}(T) \frac{n_1(T)}{p_0(T)} \quad (3.72b)$$

For MajBH defects no changes are expected. Since the LLI-SRH lifetime depends on neither the symmetry factor k nor the majority capture time constant [$\tau_{p0}(T)$ in p -type] but only on the minority capture time constant [$\tau_{n0}(T)$ in p -type] in the whole temperature range, as shown in Eq. (3.72a), the proposed advanced TDLS analysis yields accurate spectroscopic results even if the k -assumption should be invalid.

For MinBH defects, however, both $\sigma(T)$ -models are relevant to the shape of the TDLS curve, as can be seen from Eq. (3.72b). While the low-temperature part of the TDLS curve (below $T_{Arrh-Onset}$) is still dominated by the minority capture time constant [$\tau_{n0}(T)$ in p -type], the high-temperature part (above $T_{Arrh-Onset}$) is dominated by the majority capture time constant [$\tau_{p0}(T)$ in p -type]. Only in the transition region around $T_{Arrh-Onset}$ are both capture time constants relevant. Since the proposed advanced TDLS analysis transfers the $\sigma(T)$ -model, determined from the low-temperature part of the TDLS curve, to its high-temperature part, the spectroscopic result, obtained for a MinBH defect, deviates all the more from reality the stronger the difference in the T -models of the capture cross-sections. However, as long as these T -models do not show a qualitative difference, i.e., that one capture cross-section is increasing while the other is decreasing with temperature, the E_t error should not exceed the errors found in Sect. 3.4.2D for the TDLS evaluation by means of the standard linearization, which are still acceptable.

In fact, there is no possibility of increasing the spectroscopic accuracy of the TDLS analysis. Taking into account an independent T -model for the majority carrier capture cross-section as additional degree of freedom facilitates the accurate SRH modeling of the TDLS curve but at the same time reduces its unambiguity. Even though the T -model of the minority carrier capture cross-section can still be extracted accurately from the low-temperature part of the TDLS curve, the unambiguous determination of defect parameters from the high-temperature part fails. Since the shape of the Arrhenius increase depends on both the T -model of the majority carrier capture cross-section and the energy level E_t of the defect, neither of the two defect characteristics can be extracted unambiguously.

Thus even in the only critical case of MinBH defects with differing T -models for the capture cross-sections, the proposed advanced TDLS analysis is still the most suitable theoretical basis for the SRH modeling. In all other cases, i.e., for arbitrary MajBH defects and for MinBH defects with identical T -models for the capture cross-sections, the proposed TDLS analysis yields accurate spectroscopic results.

B Assumption 2: temperature-independent energy depth ΔE_t

The second basic assumption has been pointed out in Sect. 3.5.4. Although the temperature-induced band gap narrowing $E_{gap}(T)$ has to be considered in the calculation of $p_0(T)$ and $n_0(T)$ to ensure an accurate modeling of the TDLS bend due to intrinsic conduction (see Sect. 3.5.5), it is completely ignored in the calculation of the SRH densities $n_i(T)$ and $p_i(T)$. Due to the lack of a widely accepted model for the movement and pinning of defect levels in a flexible band gap, the proposed advanced TDLS analysis proceeds instead on the assumption that the energy distances of the defect level to both band edges are constant throughout the whole T range and given by the values determined for the band gap width at 300 K (see Sect. 3.5.4).

Against the background that the band gap width E_{gap} decreases by almost 100 meV in the T range from 300 to 600 K (see Fig. 1.5), the extent of this simplification becomes evident. But what changes in the TDLS curve have to be expected from a temperature-induced movement of the defect level within the band gap? Since the energy level only influences the TDLS curve via the SRH densities, changes only have to be expected in the high-temperature part of the TDLS curve (above $T_{Arrh-Onset}$). Taking into account that any change in the defect energy depth ΔE_t is exponentially amplified due to the fact that it occurs within the activation term of the SRH densities, it becomes evident that these changes strongly depend on the reference point for level pinning, which may be one of the band edges or mid-gap.

Fortunately, if the defect level is pinned to the nearer band edge, the TDLS curve will be completely unaffected by a temperature-induced movement of the energy level, since the energy distance which is relevant to the dominant SRH density remains unchanged. However, if the defect level is pinned to the more distant band edge or mid-gap, the energy distance of the dominant SRH density will decrease with increasing temperature, being reflected in a bending of the Arrhenius increase with continuously reduced slope. Thus, neglecting the unknown temperature-induced movement of the energy level in the SRH modeling, as done in the present work, may at worst lead to an underestimate of the defect depth that is expected at 300 K. Nevertheless, it should be possible to detect this problematic case from the described bending of the Arrhenius increase. On the other hand, whenever the lifetime increase in the Arrhenius plot is linear, the defect level is most likely pinned to the nearer band edge, which guarantees an accurate E_t determination by means of the proposed TDLS analysis. The fact that none of the TDLS curves measured in the present work showed a smooth bending of the Arrhenius increase towards lower slopes justifies

the simplifying assumption of fixed defect energy distances in retrospect, and points towards a pinning of the defect levels to the nearer band edge.

It has to be concluded that the assumptions which the proposed advanced TDLS analysis is based on are not only motivated from a physical point of view but also from a result-oriented point of view.

3.5.10 Section summary

In Sects. 3.4 and 3.5, the spectroscopic potential of TDLS has been investigated in detail. A major advantage of TDLS is that it allows the defect energy depth ΔE_t to be determined directly from a linear fit of the Arrhenius increase measured on a single sample. Since linear evaluation techniques still represent the standard approach in the literature, we analyzed their accuracy concerning ΔE_t determination in the first part of the study (see Sect. 3.4). As the width of the linear Arrhenius increase is the limiting factor concerning accuracy, expanding the T range of the Arrhenius increase at its lower bound by means of data linearization is a suitable approach to improve accuracy. However, the suitability of a linearization technique proposed in the literature has been proved to be very limited as it only provides accurate ΔE_t results for ideal TDLS curves, but leads to strong systematic ΔE_t errors if applied to realistic TDLS curves, which show a superposed T -dependence of the capture cross-sections. To solve this problem, we proposed two advanced procedures for data evaluation, one of them consisting of an optimization of the existing linearization technique, still disregarding an underlying $\sigma(T)$ -dependence, the other one consisting of an improved data linearization, taking an underlying $\sigma(T)$ -dependence fully into account. While the systematic ΔE_t error is completely eliminated by the second technique, the first technique also proved to minimize it efficiently.

As the presence of multiple recombination-active defect levels may also affect the accuracy of the spectroscopic determination, we investigated the resolution capability of TDLS (see Sect. 3.4). The study of a two-level system led to the essential finding that, even if a sample is influenced by two defect levels of comparable recombination activity, TDLS is not in general capable of resolving the two defect levels in different T regions of the TDLS curve but only allows the dominant level to be determined. Detailed analysis of the accuracy of the ΔE_t determination of the dominant level identified the relative energy distance of the defects and the ratio of their recombination activities as the decisive quantities, but proved that in most cases the accuracy of TDLS will not be affected by the presence of multiple defect levels. Moreover, it has been shown that an unambiguous

identification of several defect levels may only be achieved for very special parameter constellations, which lead to a cascade-structured Arrhenius increase, while for all other shapes of the superposed TDLS curve, the determination of multiple defect levels from different linear regions in the original or linearized Arrhenius increase fails completely. Thus, our investigation unambiguously demonstrated the invalidity of the prevalent interpretation of TDLS data in the literature and proved that data linearization only improves the accuracy in determining the dominant level but does not improve the resolution capability of TDLS.

As the linear TDLS evaluation techniques do not provide any information about the symmetry factor k and the band gap half of the defect, in the second half of the study (see Sect. 3.5) we investigated the possibility of complete defect characterization by means of advanced TDLS analysis, based on the SRH modeling of the entire TDLS curve. The accuracy of the spectroscopic result being directly related to the accuracy of the TDLS modeling, we investigated superposed effects, which were expected to influence the temperature dependence of the TDLS curve. This was in particular the temperature dependence (i) of the capture cross-sections, (ii) of external carrier trapping and (iii) of the equilibrium carrier concentrations. Concerning the capture cross-sections, we focussed on the physical origin of the temperature dependence and presented an overview of the $\sigma(T)$ -models of the most relevant capture mechanisms. On the basis of this overview the $\sigma(T)$ -dependence observed experimentally in Chap. 4 may be classified according to physical criteria, and thus provide an additional fingerprint of the investigated defect centers, which gives insight into the relevant capture mechanism. However, it has been shown that superposed external carrier trapping may hinder an accurate determination of the $\sigma(T)$ -model from the low-temperature part of the TDLS curve, as it may completely screen the recombination lifetime at very low temperatures. Fortunately, trapping effects turned out to be easy to identify, which ensures that distortions in the extracted $\sigma(T)$ -model can be avoided. Concerning the temperature dependence of equilibrium carrier concentrations, the freeze-out effect at low temperatures proved to be of no practical importance for TDLS, while the onset of intrinsic conduction (IC) at high temperatures turned out to strictly confine the T range of the defect-specific Arrhenius increase at its upper end, as it leads to a sharp decrease in the TDLS curve. Investigating the impact of the advanced T -models for $N_C(T)$, $N_V(T)$ and $E_{gap}(T)$ on the TDLS curve, we found as a major result that considering the temperature-induced narrowing of the silicon band gap significantly reduces the onset temperature of the IC-induced TDLS bend, $T_{IC-Onset}$. Its absolute values are thus identified to range well below the experimentally imposed upper temperature limit (in the relevant doping

range), which demonstrates that the effect of intrinsic conduction is highly relevant to TDLS modeling.

The consideration of all these superposed effects led to an advanced configuration of the SRH model. Its validity has been verified comprehensively by simulating an experimental TDLS curve over a broad T range from 130 to 580 K. While the accurate modeling of the low-temperature part required both a $\sigma(T)$ -model and the assumption of an additional shallow trap center, the accurate modeling of the IC-induced TDLS bend could only be achieved if, in addition, the SRH model was based on the complete advanced T -model as proposed in Sect. 1.2, its validity being clearly proven by the extraordinary performance of the SRH fit.

The detailed investigation of the possibilities for extracting additional defect parameters from such an SRH fit of the entire TDLS curve is summarized in Table 3.5, which on the one hand provides an overview of the defect and material parameters which have been identified to influence the different parts of the TDLS curve (central part of Table 3.5), and on the other hand indicates which of the different parts and characteristics of the TDLS curve allow an identification of the individual defect parameters (right-hand part of Table 3.5).

Table 3.5. Impact of the various defect and material parameters on the different parts of the TDLS curve. This impact in some cases depends on the band gap half of the underlying defect as indicated by the code words (see below). The last two columns indicate the defect parameters which are routinely determined from the individual parts and characteristics of the TDLS curve assuming an underlying MinBH and MajBH defect, respectively.

TDLS part	Characteristic	Influencing parameters				Extractable parameters	
		N_{dop}	E_t	k	$\sigma(T)$	Trap	MinBH def.
Very low- T region	Onset temp.					Both	$N_{t,trap}$
	Slope					Both	$\Delta E_{t,trap}$
Low- T region	Shape				Both	$\sigma(T)$ -model	
Arrhenius increase	Onset temp.	Both	Both	Min		$k + \text{BGH}$	—
	Slope			Both		Energy depth ΔE_t	
High- T region	Onset temp.	Both	Both	Both		N_{dop} (Control)	
IC-induced TDLS bend	Slope		Min	Maj	Both	—	k (if $k > 10$)

Both = Common impact for a MinBH and MajBH defect.

Maj = Impact only for a MajBH defect.

Min = Impact only for a MinBH defect.

BGH = Band gap half.

IC = Intrinsic conduction.

Trap = Superposed external carrier trapping.

- As the trapping-free low-temperature part of the TDLS curve is unaffected by other defect parameters, its modeling allows the underlying $\sigma(T)$ -model to be determined directly. This knowledge is important as it influences the whole T range.
- The $\sigma(T)$ -model being known, the slope of the Arrhenius increase allows an accurate determination of the defect energy depth ΔE_t .
- Concerning the onset temperature of the Arrhenius increase, i.e., its position on the $1/T$ axis, the study revealed a general dependence on N_{dop} and ΔE_t and an additional k -dependence which, however, is only observed for defects in the MinBH and not for defects in the MajBH. This fundamental physical difference between MinBH and MajBH defects turned out to have a decisive impact on the spectroscopic information which may be extracted from a TDLS curve with an unknown defect center. As TDLS curves associated with MajBH defects (and symmetric MinBH defects) can be simulated both for an assumed MajBH and for an assumed MinBH defect, unambiguous identification from TDLS alone fails, the band gap half and the k factor of the underlying defect being undetermined. However, as TDLS curves associated with (asymmetric) MinBH defects cannot be simulated for an assumed MajBH defect but only for an assumed MinBH defect, both the band gap half and the symmetry factor k may be determined from an entire fit of the TDLS curve, thus allowing complete defect characterization from TDLS alone. The theoretical analysis thus shows that the spectroscopic information which may be extracted from TDLS alone depends on the band gap half of the underlying defect center, being reduced for defects located in the MajBH.
- Moreover, the study revealed that the consideration of the TDLS bend due to intrinsic conduction may lead to a further improvement in the spectroscopic results obtained from TDLS. On the one hand it may increase the spectroscopic information in the case of a MajBH defect, as the slope of the TDLS bend has then been found to depend on the k factor (see Table 3.5). On the other hand, as the onset temperature of the TDLS bend turned out to depend mainly on the doping concentration (see Table 3.5), modeling the TDLS bend additionally allows an independent cross-check of the doping concentration and thus prevents unrecognized transfer of an N_{dop} error to the defect parameter k . This consistency check of the determined material and defect parameters greatly increases the reliability of the TDLS result.

Both the possibility of complete defect characterization from TDLS alone and the possibility of gaining additional identifying information from the TDLS bend due to intrinsic conduction are reported for the first time and will be verified experimentally in Chap. 4.

To allow transparent and comprehensive SRH analysis of TDLS data, the analysis applying the defect parameter solution surface (DPSS) has been transferred to TDLS. The practical value of the newly developed DPSS diagram consists in the fact that it directly provides a quantitative estimate of the accuracy of the TDLS results and clearly visualizes all fundamental aspects of modeling TDLS curves, as has been demonstrated with several examples.

Based on the observation that the temperature range of the Arrhenius increase is confined for purely physical reasons, we finally developed a new diagram which allows the position and width of the Arrhenius increase to be estimated for arbitrary defect and material parameters. As the accuracy or even applicability of TDLS strongly depends on the width of the Arrhenius increase, the diagram allows an a priori assessment of the suitability of TDLS for arbitrary boundary conditions and is thus of practical importance. It reveals that TDLS is applicable with high accuracy over the whole parameter plane except for defect levels around mid-gap and MinBH defects with strongly reduced k factors. Further restrictions may arise due to limitations on the experimentally accessible T range, and can be determined directly from the diagram.

As the advanced TDLS analysis proposed in the present work is superior to the linear TDLS evaluation techniques in terms of both accuracy and completeness of the spectroscopic results, it defines a new standard for defect characterization from TDLS and has been used throughout the work presented here. However, in the future when TDLS is used in combination with lifetime mapping units to generate spatially resolved “ ΔE_t maps” of samples with an inhomogeneous defect distribution (e.g., multicrystalline silicon samples), the simplicity of data evaluation will gain importance. As the improved linear evaluation techniques proposed here are a good compromise between simplicity and accuracy, they are ideally suited for that purpose.

3.6 Combination of the results from TDLS and IDLS: combined DPSS analysis

An unambiguous identification of defect centers from the measurements on a single sample is a basic requirement of the general applicability of lifetime spectroscopy as a diagnostic tool. As demonstrated in Sect. 3.5, TDLS allows such an unambiguous defect characterization if the defect center is located in the MinBH. However, the spectroscopic result becomes ambiguous if the defect center is located in the MajBH. In contrast, IDLS never allows an unambiguous identification, as has been visualized in Sect. 3.3 by means of the two-dimensional DPSS associated with each IDLS curve. To avoid this ambiguity in the spectroscopic results obtained from the isolated analysis of IDLS and TDLS, the results from both techniques will be combined in the following.

Such a combination of the spectroscopic results from IDLS and TDLS can be realized simply by a superposition of the associated DPSS diagrams. An accurate determination of the defect parameters should then be achieved from the common intersection point of the two DPSS- k curves associated with the TDLS and the IDLS curve.

Figures 3.52 and 3.53 display the combined DPSS diagram for a MinBH defect and a MajBH defect, respectively, both being assumed to have the same energy depth $\Delta E_t = 0.3$ eV and to be asymmetric with $k = 10$. While the DPSS curves associated with TDLS (solid lines) are directly taken from Figs. 3.47 and 3.48, respectively, those associated with IDLS (dashed lines) are calculated according to the DPSS equations given in Sect. 3.3.3B.

A Combined DPSS analysis of TDLS and IDLS: asymmetric MinBH defect

As can be seen from Fig. 3.52, the superimposed DPSS diagram for an underlying asymmetric MinBH defect in fact exhibits a single intersection point (star) of the two DPSS- k curves associated with TDLS (solid line) and IDLS (dashed line), whose coordinates directly correspond to the true defect parameters. Since for a MinBH defect an unambiguous defect characterization is thus achieved independently from TDLS alone and also from the combination of TDLS and IDLS, the quality of the spectroscopic results can be directly controlled from the accuracy with which the DPSS- k intersection point and the minimum of the DPSS- χ^2 curve, obtained for the TDLS fit, coincide.

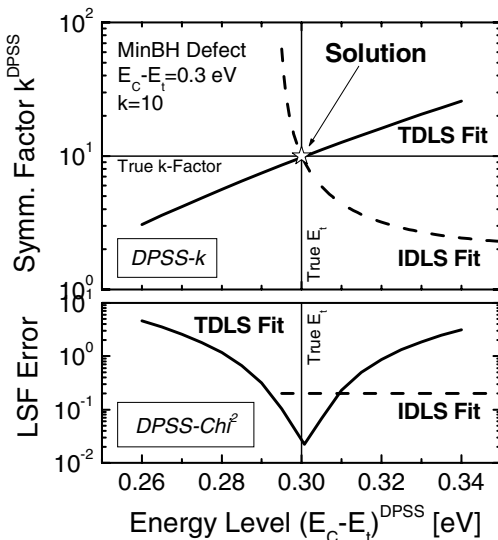


Fig. 3.52. Combined DPSS analysis of TDLS and IDLS for an asymmetric MinBH defect. Direct identification of the true defect parameters from the single common intersection point of the DPSS- k curves (star). A measure of the consistency with the independent unambiguous result from TDLS alone (see Fig. 3.47) is the accuracy with which the DPSS- k intersection point and the DPSS- χ^2 minimum coincide. While the TDLS-DPSS curves (solid lines) are taken from Fig. 3.47, the IDLS-DPSS curves (dashed lines) are calculated from the DPSS equations in Sect. 3.3.3B.

B Combined DPSS analysis of TDLS and IDLS: asymmetric MajBH defect

In the case of a MajBH defect or a symmetric MinBH defect, the situation changes slightly. Since the TDLS curve can then be simulated just as well for a MinBH as for a MajBH defect, its DPSS consists of two branches (see Sect. 3.5.7B). As shown in Fig. 3.53 for an underlying asymmetric MajBH defect, the superimposed DPSS diagram then exhibits two intersection points of the DPSS- k curves associated with TDLS and IDLS (white stars), only one of them representing the true solution. The physical assessment of these intersection points has to take into account the fact that only the DPSS- k curve associated with the IDLS curve (dashed line) displays equivalent solutions for the SRH parameterization, whereas the DPSS- k curve associated with the TDLS curve (solid line) contains solutions of varying accuracy. As a consequence, that of the two DPSS- k intersection points has to be identified with the true solution, which deviates least from the corresponding DPSS- χ^2 minimum in terms of energy. The accuracy of this coincidence is again a measure for the quality of the spectroscopic result. However, in this case the verification of the coincidence is an essential part of the procedure to identify the true solution in the combined DPSS diagram, whereas it is a simple consistency check between the results of two independent techniques in the case of an asymmetric MinBH defect (see Fig. 3.52).

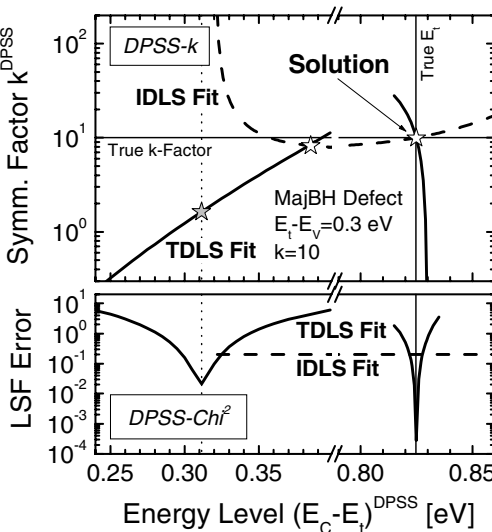


Fig. 3.53. Combined DPSS analysis of TDLS and IDLS for an asymmetric MajBH defect. That of the two DPSS- k intersection points (indicated by white stars) has to be identified with the true solution which deviates least from the corresponding DPSS- χ^2 minimum in terms of energy. A measure for the quality of the spectroscopic result is the accuracy of this coincidence. While the TDLS-DPSS curves (solid lines) are taken from Fig. 3.48, the IDLS-DPSS curves (dashed lines) are calculated from the DPSS equations in Sect. 3.3.3B.

Against this background the combined DPSS diagram in Fig. 3.53 yields the following spectroscopic result: since the DPSS- k intersection point in the upper half of the band gap strongly deviates from the corresponding DPSS- χ^2 minimum in terms of the energy position, the TDLS solution in the upper half of the band gap has to be rejected for reasons of inconsistency. This has already been indicated by the divergence of the two DPSS- χ^2 minimum of the TDLS fit.⁴⁸ In the lower half of the band gap, however, the energy positions of both the DPSS- k intersection point and the minimum of the DPSS- χ^2 curve coincide. Thus, the combined DPSS analysis allows an unambiguous identification of the underlying defect center in the MajBH which has been possible neither from IDLS nor from TDLS. Moreover, the sharp intersection point of the DPSS- k curves allows an accurate determination of the symmetry factor k , which cannot be achieved from pure TDLS analysis due to the k independence of the Arrhenius increase for defects in the MajBH, being reflected in the steep shape of the DPSS- k curve in that band gap half.

⁴⁸ In fact, Fig. 3.53a shows that the energy level of the MinBH solution of TDLS already lies in the DPSS definition gap of the IDLS curves, which demonstrates that a modeling of the IDLS curve with the optimum MinBH parameters of TDLS completely fails, i.e. even qualitatively.

C Significance of the combined DPSS diagram

Since the discussion above covers all the possible cases concerning the parameters of the defect center, it can be concluded that lifetime spectroscopy always allows a complete defect characterization on one single sample if the data from TDLS and IDLS are combined. Moreover, it has been demonstrated that the newly developed DPSS diagram allows a transparent and comprehensive SRH analysis of IDLS and TDLS data and makes it possible to evaluate the accuracy and consistency of the defect parameters determined from different lifetime spectroscopic curves that are dominated by the same defect center. Thus, the combination of TDLS and IDLS on the basis of the DPSS analysis defines a new standard of advanced lifetime spectroscopy.

3.7 Temperature- and injection-dependent lifetime spectroscopy (*T-IDLS*)

In Sect. 3.3.4 it has already been shown that the strong inherent spectroscopic ambiguity of a single IDLS curve may be avoided almost entirely by the expanded N_{dop} -IDLS technique, which is based on a simultaneous SRH analysis of a set of IDLS curves measured on samples with different doping concentrations. As outlined in Sect. 3.2.3B, similar or even better results are expected if the temperature is varied instead of the doping concentration, which leads to a second expanded IDLS technique, the temperature- and injection-dependent lifetime spectroscopy (*T-IDLS*). This relatively new technique has recently been applied by Schmidt et al. to identify the defect properties of aluminum in Cz-Si [19]. But in spite of the increased information on the Δn - and T -dependence of carrier lifetime, only broad value ranges for the defect parameters have been found instead of a discrete solution. To answer the question as to whether this is primarily due to the lack of a transparent procedure of data evaluation or to theoretical restrictions, the present section aims at a detailed analysis of the spectroscopic potential of *T-IDLS*.

For clarity it should be stressed that the *T-IDLS* technique is treated as an expansion of the IDLS technique in the sense that the set of IDLS curves is “small” due to broad temperature steps between the individual measurements, which makes a simultaneous IDLS analysis mandatory. It is evident that a quasi-continuous temperature increment between the different *T-IDLS* curves would allow the extraction of a TDLS curve from the LLI part of the IDLS curves and thus the application of the TDLS & IDLS technique, whose potential has been discussed in the previous

section. However, the T -IDLS technique should be understood as an alternative to TDLS, which avoids time-consuming temperature ramping. The quasi-continuous-temperature-increment approach has not been in the focus of the present work, as its spectroscopic evaluation and potential has already been covered by the considerations in Sect. 3.6. Since under these boundary conditions the T -IDLS technique has to be treated exactly like the N_{dop} -IDLS technique, the following evaluation of its spectroscopic potential makes use of the findings of Sect. 3.3.4 and follows the argumentation given there.

3.7.1 Defect characterization by analyzing a set of IDLS curves measured at various temperatures

From a practical point of view the T -IDLS technique has two important advantages compared to the N_{dop} -IDLS technique. First, the set of T -IDLS is measured on a single sample, which ensures an identical defect structure in all T -IDLS curves. In contrast, the N_{dop} -IDLS technique faces the problem that unintended variations among the samples can affect the qualitative shape of the IDLS curves beyond the expected pure SRH effect of the doping level and thus distort the overall spectroscopic result.⁴⁹ Second, in contrast to the doping concentration, the temperature, as an experimentally controlled parameter, may be adjusted almost arbitrarily, which allows an optimum arrangement of the set of T -IDLS curves for a wider range of defect parameters.

A Limited potential for simplifying the simulation procedure

This includes the possibility of determining the transition temperature T_0 at which the injection dependence of the T -IDLS curve disappears, as the T -IDLS curves turn over from an increasing to a decreasing shape as temperature increases (see Fig. 3.6). To assess the spectroscopic information which may be gained from this particular temperature, an analytical expression for the characteristic lifetime difference between HLI and LLI has to be derived. Using the general expressions (3.7a) and (3.8) for the LLI and HLI lifetimes, the lifetime difference is found to be given by

⁴⁹ Such distortions may arise from technological variations either during the contamination process or during the surface passivation process, or they may have a physical origin as the nature of the defect center may change due to interactions with the dopant [as for example in the case of an iron contamination (see Sect. 4.6)].

$$\begin{aligned}\Delta\tau_{SRH}(T) &\coloneqq \tau_{SRH}^{HLI}(T) - \tau_{SRH}^{LLI}(T) \\ &= \tau_{n_0}(T) \times \left[k \times \left(1 - \frac{n_1(T)}{p_0} \right) - \frac{p_1(T)}{p_0} \right]\end{aligned}\quad (3.73)$$

which is valid for arbitrary defect levels in a *p*-type semiconductor. Equating $\Delta\tau_{SRH}$ with zero, which reflects the situation at T_0 , leads to two different conditions for the SRH densities depending on whether the n_1/p_0 or the p_1/p_0 term is dominant in Eq. (3.73), i.e., whether the underlying defect center is located in the MinBH or in the MajBH.

For a MinBH defect,

$$n_1(T_0) = p_0 \quad \Rightarrow \quad E_C - E_t = -k_B T_0 \times \ln \left[\frac{p_0}{N_C(T_0)} \right] \quad (3.74a)$$

For a MajBH defect,

$$p_1(T_0) = k \times p_0 \quad \Rightarrow \quad E_t - E_V = -k_B T_0 \times \ln \left[\frac{k \times p_0}{N_V(T_0)} \right] \quad (3.74b)$$

Upon use of Eq. (3.2), the conditions for the SRH densities (left) directly yield expressions for the defect energy level E_t (right). Equations (3.74a) and (3.74b) reveal a fundamental difference between MinBH and MajBH defects. In the case of a MinBH defect [see Eq. (3.74a)], the energy level E_t is the only unknown parameter the transition temperature T_0 depends on, which allows an unambiguous E_t determination from knowledge of T_0 alone. However, in the case of a MajBH defect [see Eq. (3.74b)], the transition temperature depends on both the energy level E_t and the symmetry factor k . As both parameters are unknown a priori, none of them can be determined from the knowledge of T_0 . It has to be concluded that, as long as the band gap half of the defect center is unknown, it is impossible to extract any spectroscopic information from the transition temperature T_0 . Thus, the determination of the defect parameters once again requires the simultaneous SRH simulation of the whole set of *T*-IDLS curves, as in the case of the N_{dop} -IDLS technique.

B Simultaneous SRH simulation by advanced DPSS analysis – transfer of results and outline of the necessary expansions of DPSS analysis

As shown in Sect. 3.3.4 for the N_{dop} -IDLS analysis, such a simultaneous SRH simulation is realized with maximum transparency by means of the superposed DPSS analysis. The expected modifications in the interpretation of the DPSS diagrams and the necessary expansions of the DPSS

analysis should be outlined using Fig. 3.54, which shows the DPSS analysis of a set of T -IDLS curves that has been calculated according to the general SRH equation (3.5) for a symmetric MinBH defect at $E_C-E_i=0.3$ eV. While Fig. 3.54a shows the original IDLS curves,⁵⁰ Figs. 3.54b and c show the superposition of the associated DPSS- τ_{n0} and DPSS- k curves, which have been calculated for the theoretical analysis from the Eqs. (3.30a) and (3.30b), respectively. In the experiment, the pairs of DPSS curves would be determined for each of the T -IDLS curve separately by means of the procedure described in Sect. 3.3.2B.

Analogously to the findings for the DPSS analysis of a doping variation, the DPSS- k curves intersect each other in two common intersection points (DPSS-IP) at the true (upper half) and an alternative (lower half) energy position, whose ordinate values coincide and thus enable a determination of the true symmetry factor k (see Fig. 3.54c). However, these DPSS-IPs are no longer observed in the DPSS- $\tau_{n0}(T)$ diagram (see Fig. 3.54b). The theoretical reason is the temperature dependence of true electron capture time $\tau_{n0}(T)$ via the thermal velocity $v_{th}(T)$ [see Eq. (3.3)], which prevents an intersection of the individual DPSS- $\tau_{n0}(T)$ curves at the position of the true defect energy level. Thus, the DPSS- $\tau_{n0}(T)$ diagram is of no use for the determination of the energy solutions. However, it may be used to determine the actual temperature dependence of $\tau_{n0}(T)$ if the DPSS- $\tau_{n0}(T)$ values at the energy positions of the DPSS- k intersection points are extracted and plotted versus temperature, as shown in Fig. 3.54d (closed symbols). In the present case the temperature dependence of the extracted $\tau_{n0}(T)$ values can be described in terms of a power law with $\alpha=-0.5$, which directly reflects the well-known temperature dependence of $v_{th}(T)$. It is evident that in the experiment all deviations from this simple temperature dependence can be directly attributed to a temperature dependence of the capture cross-sections which represent the only additional source for a temperature dependence of $\tau_{n0}(T)$. Thus, the advanced DPSS analysis of a set of T -IDLS curves allows an accurate and transparent extraction of the temperature model for the capture cross-sections. This will be discussed in detail in a forthcoming publication.

If the true temperature dependence of $\tau_{n0}(T)$ is known, the DPSS- $\tau_{n0}(T)$ curves can be normalized to 300 K. As expected and shown in Fig. 3.54e, the resulting DPSS- $\tau_{n0}(300\text{ K})$ curves intersect each other in two common intersection points which are located at the same energy positions as the

⁵⁰ Under HLI conditions the individual T -IDLS curves do not approach the same value, as the electron capture time $\tau_{n0}(T)$ depends on temperature via the thermal velocity $v_{th}(T)$. This directly implies a temperature dependence of the HLI-SRH lifetime, given according to Eq. (3.8) by $\tau_{n0}(T)\propto(1+k)$.

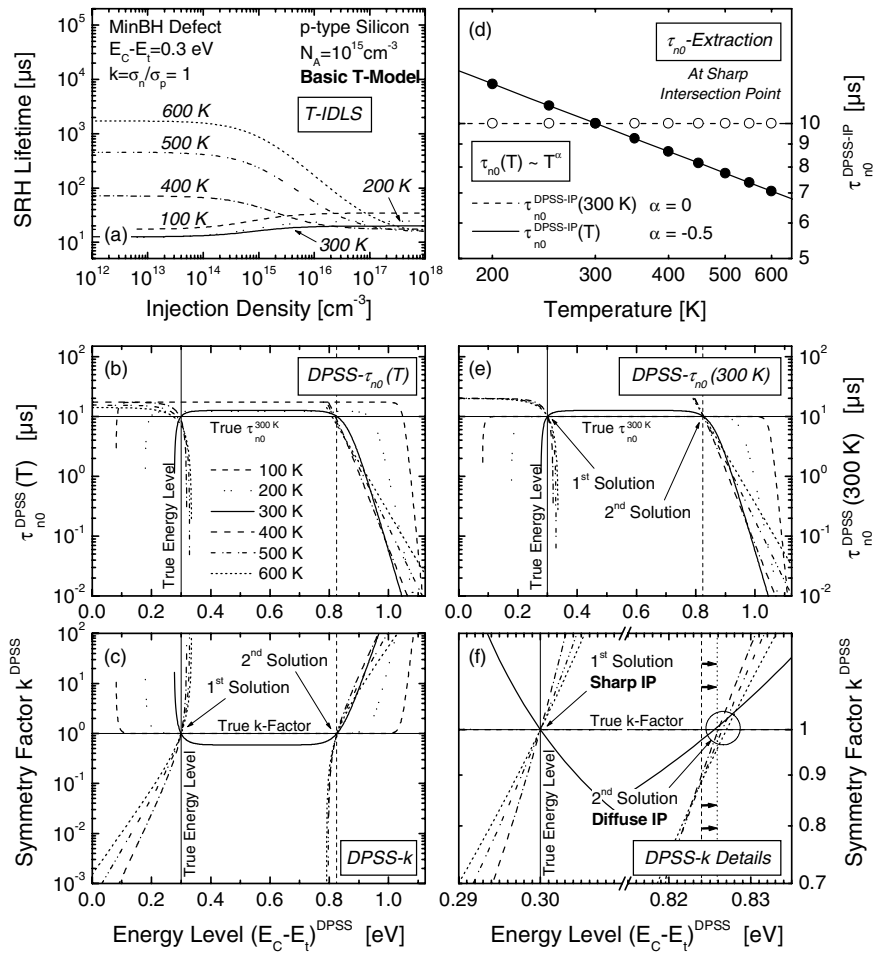


Fig. 3.54. Transfer of the advanced DPSS analysis on a set of T-IDLS curves. (a) IDLS curves calculated for different temperatures on the basis of the basic T -model for a symmetric MinBH defect at $E_c - E_t = 0.3 \text{ eV}$. (b,c) Superposed DPSS diagram associated with the set of T-IDLS curves [calculated from Eqs. (3.30a) and (3.30b)]. While the DPSS- k curves exhibit the expected two intersection points at the true and an alternative energy position, which yield the true symmetry factor, the DPSS- $\tau_{n0}(T)$ curves do not cross each other at these energy positions due to a direct temperature dependence of $\tau_{n0}(T)$ via $v_{th}(T)$. (e) Normalized DPSS- $\tau_{n0}(300 \text{ K})$ curves. After subtraction of the $v_{th}(T)$ -dependence two sharp intersection points are observed. (d) Temperature dependence of the DPSS- τ_{n0} values which are extracted at the true energy position from the original DPSS- $\tau_{n0}(T)$ (closed symbols) and the normalized DPSS- $\tau_{n0}(300 \text{ K})$ curves (open symbols). The original DPSS- $\tau_{n0}(T)$ curves show the expected temperature dependence of $v_{th}(T)$. (f) Details of the DPSS- k intersection points. Only the DPSS-IP at the true energy position is sharp (upper half), while the alternative DPSS-IP becomes diffuse (lower half).

intersection points of the DPSS- k curves. Thus, the DPSS- τ_{n0} (300 K) diagram represents the equivalence of the DPSS- τ_{n0} diagram obtained for a doping variation. However, it is of minor importance for experimental applications as its determination requires knowledge of an underlying $\sigma(T)$ -dependence.

Zooming into the intersection points of the DPSS- k diagram finally reveals an important difference between the DPSS diagrams of a temperature and a doping variation. As can be seen from Fig. 3.54e, in the case of a temperature variation only the intersection point located at the position of the true energy level is sharp while the intersection point in the opposite band half becomes diffuse. The physical reasons for this effect and its impact on the DPSS analysis and the spectroscopic result will be discussed in the following section.

3.7.2 Possibilities and restrictions of the simultaneous T-IDLS analysis

As the observed diffuseness in the 2nd DPSS-IP, located in the band gap half opposite to that of the underlying defect level, is the major difference between the *T*-IDLS and the N_{dop} -IDLS technique, its impact on the spectroscopic *T*-IDLS result should be investigated quantitatively, in particular, to answer the question as to whether or not exclusion of the second DPSS solution and hence unambiguous identification of the true parameter solution can actually be achieved.

A Uncertainty in the second DPSS-IP: reason, magnitude and optimum coordinates

A simple approach to estimate quantitatively the uncertainty of the 2nd DPSS-IP is to determine analytical expressions for the energy positions of the intersection points of an individual DPSS- k curve with the horizontal line representing the true k factor. This has already been done in Sect. 3.3.4B. As shown by the Eqs. (3.37a) and (3.37b), the two intersection points have been localized on the one hand at the position of the true defect energy level and on the other hand at an energy position in the opposite band gap half which has been found to deviate from the particular energy position showing the same energy depth as the defect level. This deviation has been described by an energy correction term E^{corr} given by the following analytical expression:

$$E^{corr}(k, T) := k_B T \times \ln \left[k \times \frac{N_C(T)}{N_V(T)} \right] \quad (3.75)$$

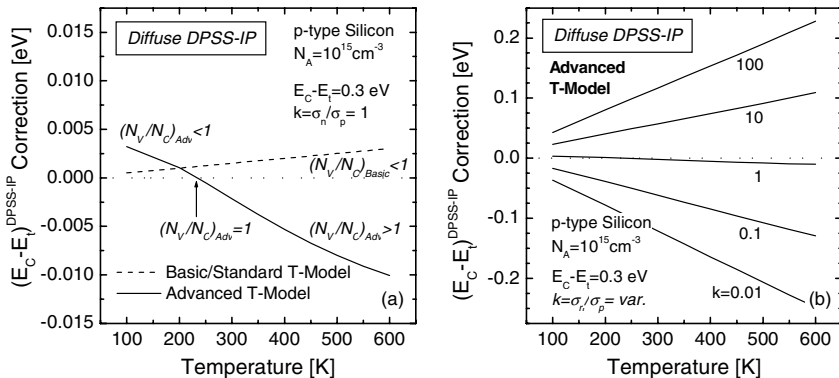


Fig. 3.55. Magnitude of the energy correction which is expected in the band half of the diffuse DPSS-IP for the intersection of the DPSS- k curve and the k horizontal as a function of temperature calculated according to Eq. (3.75). **(a)** Impact of the different T -models for a defect with symmetric electron and hole capture cross-sections ($k=1$) and **(b)** impact of a capture asymmetry for the advanced T -model.

While the doping independence of the E^{corr} term ensured a common 2nd DPSS-IP in the DPSS- k diagram of an N_{dop} -IDLS experiment, its temperature dependence demonstrates that the DPSS- k curves associated with a set of T-IDLS curves reach the true k factor at different energy positions, which directly leads to the observed uncertainty in the 2nd DPSS-IP.

As can be seen from Eq. (3.75), the energy correction term exhibits on the one hand a twofold temperature dependence via a linear term and the ratio of the densities of states and on the other hand a logarithmic dependence on the symmetry factor k . As the temperature dependence of E^{corr} provides a direct measure for the uncertainty in the 2nd DPSS-IP, it has been calculated in Fig. 3.55 for different parameter constellations. Figure 3.55a shows the impact of the model chosen for the density of states assuming a symmetric defect level ($k=1$). For the basic $N_{C,V}$ -models with the well known $T^{1.5}$ -dependence, the energy correction varies only slightly with temperature. As the N_C/N_V ratio is temperature-independent, the observed variation between 1–3 meV completely reflects the impact of the linear temperature dependence of E^{corr} . For the advanced effective-mass-based $N_{C,V}$ -models, however, the temperature dependence of E^{corr} is much more pronounced due to the then temperature-dependent N_C/N_V ratio and varies in the temperature range from 100 to 600 K between +5 and -10 meV. The change in the sign of E^{corr} directly results from a crossover of the $N_C(T)$ - and the $N_V(T)$ -models at 235 K (see Fig. 1.7). The impact of this model-induced uncertainty on the structure of the 2nd DPSS-IP is shown explicitly

in the superposed DPSS- k diagram of Fig. 3.56a, which has been calculated for a symmetric MinBH defect at $E_C-E_t=0.3\text{ eV}$, taking the advanced T -model as a basis for the semiconductor quantities. As the advanced T -model has been proved in Sect. 3.5.5 to be necessary for accurate modeling of TDLS curves, it also has to be taken into account for the modeling of T -IDLS curves and is thus taken as a basis for the following considerations.

As can be seen from Fig. 3.55b, the impact of the k factor on the magnitude and temperature dependence of E^{corr} is much stronger than that of the $N_{C,V}$ -models. As the k factor is a logarithmic scaling factor of E^{corr} , the observed temperature dependence of E^{corr} becomes stronger the higher the capture asymmetry is, regardless of whether $k>1$ or $k<1$. Thus a higher capture asymmetry directly implies a higher uncertainty in the 2nd DPSS-IP. A quantitative measure of the uncertainty of the 2nd DPSS-IP is given by the standard deviation of the E^{corr} values, which may be determined for the individual DPSS- k curves included in the investigated set. For a typical set of T -IDLS curves, taken in a medium temperature range between 200 and 500 K (in 50 K steps), the so-defined uncertainty increases from 4 meV (for $k=1$) to 45 meV (for $k=100$) and 52 meV (for $k=0.01$), respectively. Thus even under real conditions an identification of the diffuse DPSS-IP seems to be possible for high k factors, while it will become difficult for k factors close to 1. The situation may be improved by an expansion of the investigated temperature range, as the uncertainty then increases further.

In view of such uncertainties, the localization of the 2nd DPSS-IP requires calculating the standard deviation of the set of DPSS- k curves as a function of the DPSS energy. While the optimum energy position⁵¹ is reasonably localized where the standard deviation reaches its minimum, the optimum k factor is identified with the average k value of the DPSS- k curves at that energy position. Note that the standard deviation of this average k value provides an additional measure for the uncertainty of the 2nd DPSS-IP (in the k direction). As can be seen from the exemplifying DPSS- k diagrams in Fig. 3.56, the energy position of the 2nd DPSS-IP deviates from the particular energy position, which shows the same energy depth as the defect level, being located in the opposite band gap half (opposite energy position). This effective energy shift of the 2nd DPSS-IP basically reflects the average energy correction E^{corr} of the individual DPSS- k curves included in the underlying set.

⁵¹ Note that the energy correction term E^{corr} is a purely theoretical quantity which is not accessible for unknown defect parameters, whereas the optimum energy position represents the quantity which is extracted under real conditions for the 2nd DPSS-IP from the DPSS- k diagram.

Table 3.6. Quantitative impact of the symmetry factor k on the position, uncertainty and total shift of the defect parameters determined for the diffuse 2nd DPSS-IP in comparison with the true ones.

True defect parameters		Energy of 2 nd DPSS-IP (diffuse)			k factor of 2 nd DPSS-IP (diffuse)		
k	ΔE_t	Position	Uncertainty	Shift	Position	k^{IP-2}	Uncertainty
		ΔE_t^{IP-2}	$StDev(E^{corr})$	$\Delta E_t^{IP-2}-\Delta E_t$		k^{IP-2}	$StDev(k^{IP-2})$
100	300 meV	232 meV	45 meV	-68 meV	27.46	126 %	-73 %
10	300 meV	242 meV	21 meV	-58 meV	7.59	37 %	-24 %
1	300 meV	306 meV	4 meV	6 meV	0.98	6 %	-2 %
0.1	300 meV	392 meV	28 meV	92 meV	0.14	114 %	+37 %
0.01	300 meV	467 meV	52 meV	167 meV	0.11	200 %	+955 %

The simulations reflect the situation in a DPSS- k diagram associated with a set of T-IDLS curves taken between 200 and 500 K in 50 K steps if a MinBH defect at $E_C-E_t=0.3$ eV in p -type silicon with $N_A=10^{15}$ cm⁻³ is assumed. The values result from averaging this set of curves as defined in the text.

To demonstrate the decisive impact of the k factor on the quality of the spectroscopic T-IDLS result, we simulated the optimum E_t and k coordinates of the 2nd DPSS-IP according to the above procedure for a typical set of T-IDLS curves (taken between 200 and 500 K in 50 K steps) assuming a MinBH defect at $E_C-E_t=0.3$ eV, whose symmetry factor has been varied from 0.01 to 100. The coordinates with the respective uncertainties are displayed in Table 3.6. As can be seen, the achievable T-IDLS results change qualitatively with the magnitude of the capture asymmetry and may be classified into three groups:

- For almost symmetric capture cross-sections ($k=1$), the uncertainty of the 2nd DPSS-IP is negligible (in the E_t and k directions). As a result the DPSS analysis identifies *two sharp* DPSS-IPs, whose energy depths and k factors almost coincide. Analogously to the N_{dop} -IDLS technique, the T-IDLS technique then allows the true defect energy depth and the true k factor to be determined, while the band gap half of the defect remains unknown.
- For high enough capture asymmetries ($k \geq 10$ or $k \leq 0.1$), the uncertainty of the diffuse DPSS-IP is expected to exceed an experimental error. Thus even under real conditions the DPSS analysis will identify *one sharp* and *one diffuse* DPSS-IP. As the T-IDLS analysis then allows an unambiguous identification of the true solution, a complete defect characterization may be achieved.
- However, moderate capture asymmetries ($0.1 < k < 1$ or $1 < k < 10$) make identification of the diffuse DPSS-IP questionable, the uncertainty lying only in the range of an experimental error. As the total energy shift may

already be significant, neither the energy depth nor the band gap half of the defect can be unambiguously identified from the T -IDLS analysis, analogously to the N_{dop} -IDLS analysis. In addition, the T -IDLS result may suffer from a reduced accuracy in the k determination, as the k value of the diffuse DPSS-IP may also deviate from the true k factor.

It is obvious that the range of critical k factors leading to such an ambiguous T -IDLS result (point 3) strongly depends on the accuracy achievable in the measurements. Moreover, it is found to depend strongly on the choice of temperature range, as will be demonstrated in the following section.

B Possibility of identifying the diffuse 2nd DPSS-IP

Up to now only the magnitude of uncertainty expected in a fixed temperature range from 200 to 500 K has been used as a criterion to assess the identifiability of the diffuse 2nd DPSS-IP. To assess the general impact of the temperature range itself, a closer look has to be taken at the structure of the DPSS- k diagram in the 2nd DPSS-IP. As an example, Figs. 3.56a and b show two superposed DPSS- k diagrams in the vicinity of the DPSS-IPs which have been simulated for temperatures between 100 and 600 K assuming a MinBH defect at $E_C-E_t=0.3$ eV with symmetric ($k=1$) and asymmetric ($k=10$) capture cross-sections, respectively. As expected from the previous section, the deviation of the optimum coordinates of the 2nd DPSS-IP from the true defect parameters ΔE_t and k is significantly higher if a capture asymmetry is assumed. In parallel the uncertainty in the 2nd DPSS-IP increases greatly.

To give deeper insight into the fundamental requirements which ensure an identification of the diffuse DPSS-IP, the DPSS- k curves are divided into two groups according to their qualitative structure: the tub-like DPSS- k curves with a continuous range of validity are shown in blue (100–300 K) and the split DPSS- k curves with a definition gap around mid-gap are shown in red (400–600 K).⁵² As can be seen from Fig. 3.56a and b, if the whole set of DPSS- k curves is used (blue and red curves), an identification of the diffuse DPSS-IP can be achieved in both cases from a theoretical point of view, as the divergence of the individual curve shapes is then high enough in the 2nd DPSS-IP (see Fig. 3.56a and b).

⁵² As derived in Sect. 3.3.3C, the continuous DPSS curves are related to increasing IDLS curves while the split DPSS curves are related to decreasing IDLS curves. As the IDLS curves change with increasing temperature from an increasing to a decreasing shape, the associated DPSS curves change from a continuous to a split structure.

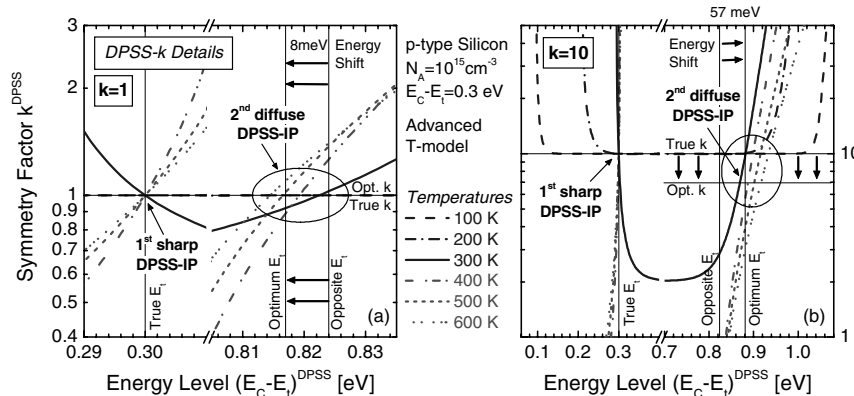


Fig. 3.56. Intersection points of the DPSS- k curves simulated according to Eq. (3.30a) for a set of T-IDLS curves assuming a MinBH defect at $E_C - E_t = 0.3$ eV with (a) symmetric and (b) asymmetric capture cross-sections. The absolute E_t and k shift and the uncertainty in the 2nd diffuse DPSS-IP increase with increasing capture asymmetry. An unambiguous T-IDLS result requires an identification of the diffuse 2nd DPSS-IP, which may be achieved if the chosen temperature range allows both continuous and split DPSS- k curves (blue and red curves). If the DPSS analysis has to be based on only continuous (blue curves) or only split (red curves) DPSS- k curves due to a restriction of the accessible temperature range, the T-IDLS result becomes ambiguous even for higher k factors, as the uncertainty of the 2nd DPSS-IP then almost vanishes. The new positions of the 2nd DPSS-IP, observed for the two subsets of DPSS- k curves, differ significantly from each other.

However, if the DPSS analysis has to be based on only the continuous (blue curves) or only the split (red curves) DPSS- k curves due to a restriction of the accessible temperature range, the T-IDLS result becomes ambiguous even for higher k factors, as the uncertainty of the 2nd DPSS-IP then almost vanishes even for the higher k factor. As can be seen from Fig. 3.56, the new positions of the 2nd DPSS-IP, observed for the two subsets of DPSS- k curves, differ significantly from each other.

- For *only continuous DPSS- k curves* (blue curves), the new 2nd DPSS-IP provides the true k factor while it still deviates from the opposite energy position for $k \neq 1$. As the 1st and the 2nd DPSS-IP thus coincide in the k factor,⁵³ the T-IDLS analysis at least allows the k factor of the defect

⁵³ The k coincidence of the two DPSS-IPs is ensured by the fact that both DPSS-IPs of a set of continuous DPSS- k curves are connected at low enough temperatures by the horizontal plateau region of the low-temperature DPSS- k curve, whose plateau value coincides with the true k factor. This may be achieved in a broad range of defect energies E_t if the minimum temperature is low enough, as the E_t range for which the plateau value of the continuous DPSS- k curves equals the true k value becomes broader the lower the temperature, as has been observed in Fig. 3.22 for a minimum doping concentration.

to be determined while an unambiguous identification of the energy depth and the band gap half of the defect fails.

- For *only split DPSS- k curves* (red curves), however, the new 2nd DPSS-IP shifts significantly in the E_t and k directions compared to the 2nd DPSS-IP determined for the whole set of DPSS- k curves. As can be seen from Fig. 3.56b, for $k \neq 1$, the optimum k position of the 2nd DPSS-IP is reduced by an order of magnitude while the optimum E_t position is shifted towards the opposite energy position. The direction and amount of these shifts will certainly depend on the defect parameters, as can be seen from the differences for $k=1$ in Fig. 3.56a. Thus, for only split DPSS- k curves, the T -IDLS analysis yields two equivalent solutions, whose energy depths and k factors will in general differ from each other, thus preventing unambiguous identification of all defect parameters.

Thus, concerning ambiguity, the spectroscopic T -IDLS result is equivalent to an N_{dop} -IDLS result if the DPSS analysis is based on only continuous DPSS- k curves, and provides less information if the DPSS analysis is based on only split DPSS- k curves.

Although the impact of the temperature range on the ambiguity of the T -IDLS result has to be further investigated to verify the results of the present section in the whole parameter range, the exemplifying discussion is representative. Thus, the study reveals that an unambiguous identification of the diffuse DPSS-IP and an unambiguous T -IDLS result are only achieved if the temperature range is chosen in such a way that the set of DPSS- k curves contains both types of DPSS- k curves, those with split and those with continuous range of validity. In other words, an unambiguous T -IDLS result is only achieved if the transition of the IDLS curves from an increasing to a decreasing shape is observed in the accessible temperature range (see Sect. 3.7.1A). Although this is the necessary condition for an identification of the diffuse DPSS-IP, in the case of low uncertainties (for k factors close to one) an identification of the diffuse DPSS-IP may only be achieved if temperature covers a maximum range (see Fig. 3.56a).

C Impact of the defect energy depth on the spectroscopic result

Up to now, the evaluation of the spectroscopic potential of T -IDLS presupposed the existence of two discrete parameter solutions and focused on the possibility of identifying the diffuse solution in order to allow an unambiguous defect characterization based on the sharp solution. However, concerning the existence of these two discrete parameter solutions, the T -IDLS technique is subjected to the same restrictions as the N_{dop} -IDLS technique. As shown in Sect. 3.3.4C, only the localization of discrete DPSS-IPs already requires a qualitative change of the DPSS shapes within

the set of DPSS curves, whose realization has been found to be critical for deep levels around mid-gap.

To demonstrate the impact of this problem for the spectroscopic *T*-IDLS results, Figs. 3.57 and 3.58 display the advanced DPSS analysis of a set of *T*-IDLS curves, which has been calculated for temperatures between 100 and 600 K, under the assumption that recombination is limited by a shallow defect center ($E_C-E_t=0.3$ eV, $k=1$, $\tau_{n0}=10\mu\text{s}$) and a deep defect center ($E_C-E_t=0.5$ eV, $k=1$, $\tau_{n0}=10\mu\text{s}$), respectively. While the graph (a) displays the *T*-IDLS curves,⁵⁴ the graphs (b) and (c) show the superposition of the associated DPSS- $\tau_{n0}(T)$ and DPSS- k curves calculated from Eq. (3.30a).

As can be seen from Fig. 3.57c, the DPSS analysis of the shallow level yields the two expected discrete parameter solutions. Their positions are localized with high precision⁵⁵ as the continuous (100–300 K) and split (400–600 K) DPSS curves intersect almost vertically. Note that a blow-up of the DPSS- k diagram in the vicinity of the two DPSS-IPs has already been shown in Fig. 3.56a.

Although discrete parameter solutions are also found for the deep center, Fig. 3.58c reveals the expected difference in the structure of the DPSS- k diagram: within a broad temperature range from 100 to 400 K the DPSS- k curves are found to exhibit a tub-like structure with a continuous range of validity and almost identical plateau values. However, if the upper temperature limit is chosen high enough, the DPSS curves deviate from this structure even for a deep level: while the 500 K curve is still continuous but already shows a reduced plateau value, the 600 K curve is split. It is evident that the quality of the energy localization of the two DPSS-IPs strongly depends on the DPSS curves obtained for these two highest temperatures. If the upper temperature limit is reduced below 500 K (as in the commercial setup used in [19]), the discrete DPSS-IPs at 0.50 and 0.62 eV disappear and the energy solution for the defect center, which can be obtained from the superposed DPSS analysis, only consists of an energy interval around mid-gap ranging from 0.48 to 0.64 eV. Note that the extraction of the true value for the symmetry factor k is not affected at all by changes of the temperature range.

⁵⁴ Note that the multiple crossovers of the *T*-IDLS curves under HLI conditions result from the temperature dependence of $\tau_{n0}(T)$ via $v_{th}(T)$, while the reduction of the LLI lifetime observed at high temperatures arises from the onset of intrinsic conduction, which is taken into account in the advanced *T*-model used for the simulations.

⁵⁵ As the theoretically related uncertainty in the 2nd DPSS-IP is small for $k=1$ (see Fig. 3.56a), it does not affect precision in localizing the 2nd solution.

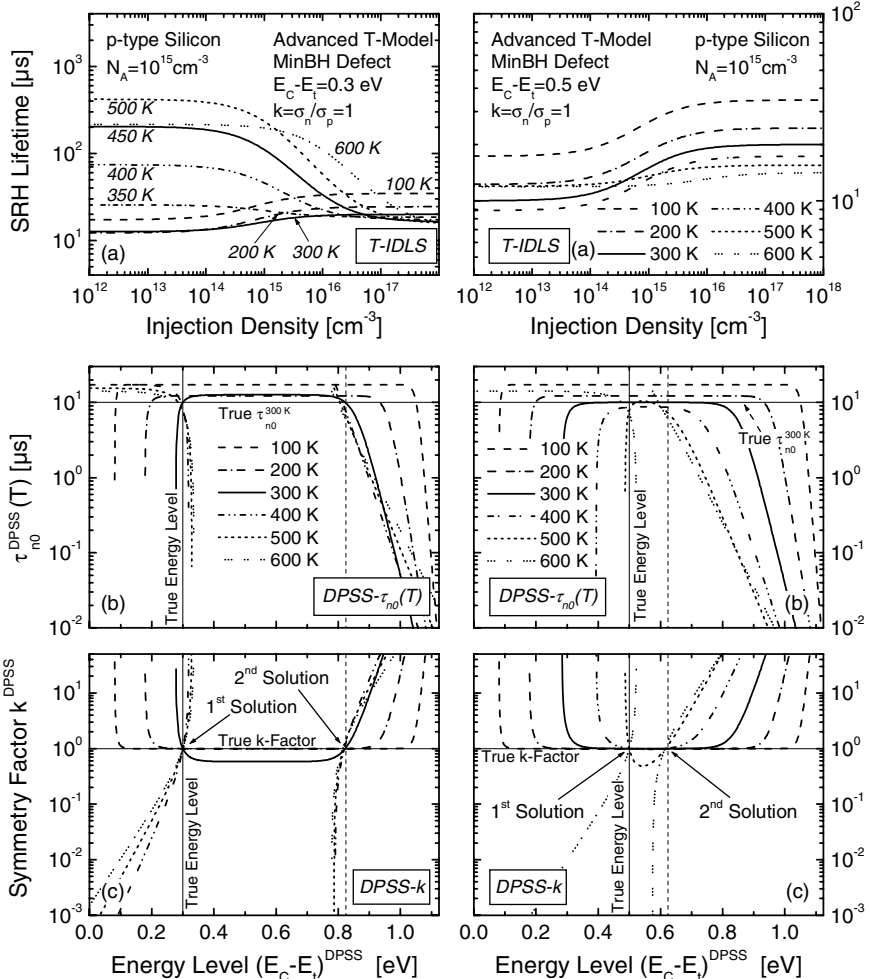


Fig. 3.57. Application of the advanced DPSS analysis to a set of T-IDLS curves calculated at various temperatures on the basis of the advanced *T*-model under the assumption that recombination is limited by a shallow SRH center ($E_C - E_i = 0.3 \text{ eV}$, $k = 1$): (a) calculated T-IDLS curves; (b–c) superposition of the associated DPSS- $\tau_{n0}(T)$ and DPSS- k curves calculated from Eq. (3.30a). As the uncertainty in the 2nd DPSS-IP almost vanishes for this parameter constellation (for a blow-up of the DPSS-IPs see Fig. 3.56a), the T-IDLS analysis determines two equivalent solutions.

Fig. 3.58. Application of the advanced DPSS analysis to a set of T-IDLS curves calculated at various temperatures on the basis of the advanced *T*-model under the assumption that recombination is limited by a deep SRH center ($E_C - E_i = 0.5 \text{ eV}$, $k = 1$): (a) calculated T-IDLS curves; (b–c) superposition of the associated DPSS- $\tau_{n0}(T)$ and DPSS- k curves calculated from Eq. (3.30a). Without the DPSS curves for 500 and 600 K, the DPSS analysis would identify a solution interval around mid-gap instead of the two discrete solutions, thereby greatly increasing the ambiguity in the T-IDLS result.

D Derivation of minimum requirements for the necessary temperature variation within the set of T-IDLS curves

As has been seen, the *T*-IDLS technique is in principle capable of providing an unambiguous spectroscopic result. However, the unambiguity of the *T*-IDLS result has been proved to depend strongly on the investigated temperature range, as the existence of two discrete DPSS-IPs (see Sect. 3.7.2C) and the identifiability of the diffuse DPSS-IP (see Sect. 3.7.2B) can only be ensured if the investigated temperature range is chosen in such a way that the set of superposed DPSS curves contains both types of DPSS curve, those with a split range of validity and those with a continuous one. In order to enable *T*-IDLS experiments which provide maximum information on a minimum number of temperature steps, a plot is finally derived which allows the optimum temperature range to be read off directly as a function of the defect and material parameters.

The fact that the qualitative structure of the DPSS curve directly correlates with the existence of the DPSS zero point (see Sect. 3.3.3D), allows the parameter plane set up by the defect energy level E_t and the temperature T to be divided in terms of the expected qualitative structure of the associated DPSS curve. This division is shown in Fig. 3.59. (Note that Fig. 3.25 shows the corresponding diagram for a division of the parameter plane set up by E_t and N_{dop} .) Mathematically, the calculated boundaries $T(E_C - E_t; k, N_{dop})$ are identical with the upper and the lower bound of the definition gap of the DPSS zero point (DPSS-ZP) function and have been determined from the defining Eq. (3.34).⁵⁶ While Fig. 3.59a shows the impact of a capture asymmetry ($k \neq 1$) on the division boundaries of the (E_t, T) division, Fig. 3.59b shows the impact of the doping concentration for symmetric capture cross-sections ($k = 1$). While DPSS curves for parameter pairs below the boundary curve have a continuous validity range and exhibit the characteristic plateau region, DPSS curves for parameter pairs above the boundary curve have a split validity range and show a zero point instead of a plateau region.

The observed energy dependence of the division boundaries may easily be understood if it is taken into account that split DPSS curves are related to decreasing IDLS curves (see Sect. 3.3.3C). As decreasing IDLS curves require a SRH ratio n_1/p_0 or p_1/p_0 greater than one, the boundary temperature, above which the DPSS validity range gets split, increases with increasing energy depth, i.e., decreasing n_1 and p_1 (see Fig. 3.59a and b), as well as with increasing doping concentration (see Fig. 3.59b). As a consequence,

⁵⁶ As an analytical expression for $T(E_C - E_t)$ cannot be deduced from Eq. (3.34), the simulation has been based on the inverse function given by $(E_C - E_t) = -k_B T \times \ln(n_1^{DG/DPSS-ZP} / N_C)$.

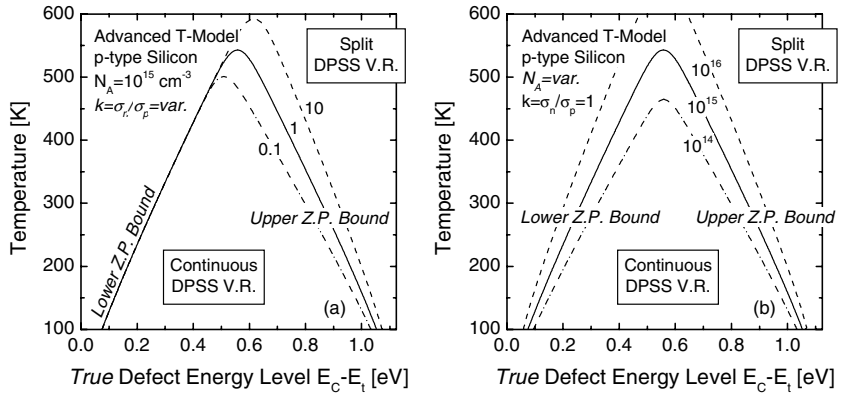


Fig. 3.59. Division of the parameter plane set up by the energy level E_t and the temperature T in terms of the expected qualitative structure of the DPSS curve. Mathematically, the calculated boundaries $T(E_c - E_t; k, N_{\text{dop}})$ are identical with the upper and the lower bound of the definition gap which exists for the DPSS zero point function and are given by Eq. (3.34). While (a) shows the impact of a capture asymmetry ($k \neq 1$) on the division boundaries, (b) shows the impact of the doping concentration for symmetric capture cross-sections ($k = 1$). Since the diagram directly displays the boundary temperature for the qualitative DPSS change as a function of the defect energy, the benefit of the diagram is twofold. For a given defect center on the one hand, the diagram displays the optimum temperature range for a simultaneous T -IDLS analysis, which guarantees maximum accuracy of the spectroscopic results on a minimum number of temperature steps. For a given temperature range of the system used for lifetime measurements on the other hand, the diagram gives information about the range of defect energies, to which the simultaneous T -IDLS analysis is highly sensitive.

with increasing temperature the defect energy range around mid-gap leading to continuous DPSS curves gets smaller. Above a certain maximum temperature, which depends on the defect symmetry factor (see Fig. 3.59a) and the doping concentration (see Fig. 3.59b), all DPSS curves have a split validity range – and exhibit a zero point instead of the characteristic plateau region – irrespective of the actual energy level of the defect, which results theoretically from the fact that the definition gap of the DPSS zero point function vanishes.

Since the diagram directly displays the boundary temperature for the qualitative DPSS change as a function of the true defect energy, it allows the optimum temperature range for a T -IDLS experiment to be determined if there are any indications of the expected energy level and symmetry factor. This first benefit of the diagram originates from a vertical interpretation. As can be seen from Fig. 3.59a, the position of the optimum temperature range – around the boundary temperature – increases by 400 K, from 120 to 520 K, if the energy depth of a symmetric defect center increases from

0.1 to 0.5 eV. If a T range up to 600 K is accessible, Fig. 3.59a and b show that an accurate T-IDLS result can even be achieved for mid-gap traps as their optimum temperature range is also included as long as the k factor does not exceed $k=10$ (for $N_A=10^{15} \text{ cm}^{-3}$) and the doping concentration $N_A \approx 5 \times 10^{15} \text{ cm}^{-3}$ (for $k=1$). Note that such an accurate characterization of mid-gap traps cannot be achieved by the N_{dop} -IDLS technique based on the standard doping range down to 10^{13} cm^{-3} . For very shallow defect levels below 0.1 eV from either band edge, the boundary temperature falls below 100 K. As a consequence, all DPSS curves determined in a T range from 100 to 600 K have a split validity range, which makes accurate characterization difficult. However, with respect to recombination activity, these defect levels are of minor importance. Beyond this, Fig. 3.59b shows that the position of the optimum temperature range increases for an increasing symmetry factor k of a MajBH defect. This k -dependence is only observed for the division boundary in the MajBH, while the division boundary in the MinBH is not affected by k variations. This observation is in full agreement with the observations in Fig. 3.19 and can be understood from the physical differences between MinBH and MajBH defects, which have been discussed in Sect. 3.3.3A. The fact that, for defects in the MinBH, the qualitative structure of the DPSS curves only depends on E_t and N_{dop} makes the division boundary in the MinBH universally usable.

On the other hand, if the diagrams in Fig. 3.59 are not interpreted vertically but horizontally, they give information about the range of defect energy levels, which can be determined with maximum accuracy for a given accessible temperature range. From that point of view, which is closer to experimental reality, the diagram defines the spectroscopic sensitivity of the T-IDLS technique as a function of the accessible temperature range. Assessing the need for a temperature expansion in an existing lifetime measurement system, the diagram provides a quantitative estimate of the physical benefit in terms of the defect parameter range with maximum detection precision. If this physical benefit is compared with technical costs, the diagram provides a valuable document to support decision-making. The horizontal and vertical interpretations show that the benefit of the diagram is twofold.

3.7.3 Section summary

Section 3.7 investigated the potential of the expanded T-IDLS technique which is based on the simultaneous SRH simulation of a set of IDLS curves determined at different temperatures. The comprehensive SRH analysis of the whole set of T-IDLS curves by means of the superposed

DPSS analysis, introduced in Sect. 3.3, revealed a fundamental difference with the N_{dop} -IDLS technique: instead of two equivalent solutions, the T -IDLS technique identifies one sharp and one diffuse DPSS intersection point, reflecting the true solution and a second solution in the opposite band gap half, respectively. This led to the conclusion that, from a theoretical point of view, the T -IDLS technique allows unambiguous defect characterization.

However, the study revealed that the magnitude of uncertainty in the diffuse DPSS-IP increases with increasing capture asymmetry and is almost negligible for symmetric capture cross-sections. Thus, for capture asymmetries close to one, the unambiguity of the T -IDLS result strongly depends on the achievable measurement accuracy. Moreover, the study revealed that the identifiability of the diffuse DPSS-IP and an unambiguous T -IDLS result are only achieved if the temperature range is chosen such that the set of DPSS- k curves contains both types of DPSS- k curve, those with a split range and those with a continuous range of validity. If the DPSS analysis has to be based on only one type of DPSS- k curves due to a restriction of the accessible temperature range, the T -IDLS result becomes ambiguous even for higher capture asymmetry, as the uncertainty in the 2nd DPSS-IP almost vanishes. It turned out that the spectroscopic T -IDLS result is comparable to the N_{dop} -IDLS result for only continuous DPSS- k curves and exhibits an even higher ambiguity for only split DPSS- k curves.

Finally, it has been shown that the qualitative change of the DPSS shapes within the set of DPSS curves is not only important for the identifiability of the diffuse DPSS-IP but is also essential to ensure the existence of two discrete energy solutions (DPSS-IPs). To put this criterion to practical use, a diagram has been developed which allows the optimum temperature range to be read off directly as a function of the defect and material parameters and thus allows T -IDLS experiments to be designed, which provide the sought results with maximum accuracy for a minimum number of samples.

3.8 Chapter summary and conclusion

In Chap. 3, the potential of lifetime spectroscopy has been investigated from a theoretical point of view. The detailed analysis of SRH theory identified the energy level E_t and the capture symmetry factor $k = \sigma_n/\sigma_p$ as the two defect parameters that are accessible by means of lifetime spectroscopy. The fact that SRH lifetime scales with the product $N_t \times \sigma_n$ of the defect concentration and the minority capture cross-section prevents the

separation of these two defect parameters on the basis of lifetime measurements. However, at the same time, it ensures the high sensitivity of all LS techniques to electrically active defects even if their concentration is very low, e.g., below the detection limit of DLTS. Moreover, lifetime spectroscopy turned out to be selective with regard to the defect level with the highest recombination activity, bringing the practical advantage that the identified impurity is definitely the one which limits material quality. An important point is that the extractable defect parameters E_t and k provide a full picture of how an impurity affects device performance and thus represents the set of defect parameters which is relevant to solar cell simulations. The identification of these parameters has been shown to require the analysis of the temperature and injection dependence of carrier lifetime, which led to the basic TDLS and IDLS techniques and several related LS techniques that have been investigated in depth.

To allow a transparent and comprehensive SRH simulation of TDLS and IDLS curves, a new modeling procedure based on the determination of the *defect parameter solution surface* (DPSS) has been introduced. The practical importance of the newly developed DPSS diagram is diverse. Being extracted from the original LS curves in a simple and direct manner, the DPSS diagram visualizes the strong inherent ambiguity of the SRH parameterization of a single IDLS curve. Moreover, a simple superposition of the associated DPSS diagrams allows the consistency of the spectroscopic results obtained from different LS curves which are dominated by the same defect center to be evaluated, regardless of whether these curves have been measured on different samples or by different LS techniques. That is why the simultaneous SRH analysis of a set of IDLS curves, which is required for the N_{dop} -IDLS and the T -IDLS techniques, is performed with maximum transparency by means of a superposed DPSS analysis, which has been newly developed in the presented work. Since the various DPSS diagrams also allow the precision of the spectroscopic results obtained to be estimated quantitatively, the proposed DPSS analysis is a very versatile tool for data evaluation in lifetime spectroscopy which may set a new standard.

The theoretical analysis of the DPSS curves gave a deeper insight into the possibilities and restrictions of the different LS techniques and led to several important findings which are compiled in Table 3.7 and will be discussed briefly. (For a more detailed survey of the features of the individual techniques, refer to the respective section summaries referenced in the last column.)

Table 3.7. Spectroscopic potential of the different LS techniques. The *symbols* indicate which of the four characteristic defect parameters (symmetry factor, energy depth, band gap half, $\sigma(T)$ -model) actually can be determined (see below). The sections containing detailed information about the respective techniques are referenced in the last column, the *page numbers* referring to the respective section summary.

Technique	No. of samples	Ambiguity	Special conditions	k	ΔE_t	BH	$\sigma(T)$	Section (Page)
IDLS	Single	Solution surface	Increasing IDLS	\textcircled{R}_A	$\textcircled{\times}$	$\textcircled{\times}$	$\textcircled{\times}$	Sect. 3.3.3 (p. 134)
		Strong ambiguity	Decreasing IDLS	$\textcircled{\times}$	\textcircled{R}_B	$\textcircled{\times}$	$\textcircled{\times}$	
N_{dop} -IDLS	Three or more	Two solutions		✓	$\textcircled{\times}$	$\textcircled{\times}$	$\textcircled{\times}$	Sect. 3.3.4 (p. 144)
T-IDLS	Single	One solution		✓	✓	✓	✓	Sect. 3.7 (p. 247)
TDLS	Single	Two solutions	MajBH defect	\textcircled{R}_C	✓	$\textcircled{\times}$	✓	Sect. 3.5 (p. 223)
		One solution	MinBH defect	✓	✓	✓	✓	
TDLS & IDLS	Single	One solution		✓	✓	✓	✓	Sect. 3.6 (p. 231)

BH = Band gap half.

✓ = Accurately determinable.

\textcircled{R} = Only parameter range determinable.

$\textcircled{\times}$ = Undeterminable.

The parameter ranges are defined by:

\textcircled{R}_A = A lower bound for the k factor.

\textcircled{R}_B = An upper (and sometimes an additional lower) bound for the energy depth.

\textcircled{R}_C = An upper bound for the k factor, the latter only being accessible if the TDLS bend due to intrinsic conduction is measured and modeled.

The parameters extracted from single IDLS curves have been found to be highly ambiguous, which proved to be unavoidable even if the information contained in two newly found DPSS characteristics was exploited. The achievable confinement of the defect parameters turned out to depend significantly on the qualitative structure of the IDLS curve. While the continuous DPSS, associated with increasing IDLS curves, provides a lower bound for the k factor given by the DPSS- k plateau value but no confinement of the defect energy depth, the split DPSS associated with decreasing IDLS curves provides an upper bound for the defect energy depth from either band edge but no confinement of the k factor. In addition, a lower ΔE_t bound may be deduced if the spectroscopic information of the DPSS- k zero point is evaluated.

Contrary to the prevalent opinion in the literature, it has been shown that this ambiguity problem cannot be completely avoided if a set of IDLS curves subject to a doping variation is analyzed simultaneously. For the expanded

N_{dop} -IDLS technique, the superposed DPSS analysis revealed the existence of two equivalent solutions. As these solutions were found to coincide only in the k factor, neither the band gap half nor the energy depth of the defect level can be determined unambiguously, which represents a general drawback of this technique. Nevertheless, N_{dop} -IDLS allows the extraction of two discrete parameter solutions for the defect center, which represents an extraordinary reduction of the DPSSs associated with the single IDLS curves and at least allows an accurate determination of the symmetry factor k . The ambiguity of the energy solution has been found to increase for deep levels around mid-gap, as the DPSS- k curves then no longer intersect at two discrete energy positions but coincide along an energy interval around mid-gap.

An important discovery was that an unambiguous spectroscopic result can be achieved if the simultaneous SRH simulation is performed on a set of IDLS curves determined at different temperatures. The reason is that the superposed DPSS analysis identifies one sharp and one diffuse DPSS solution for the expanded T -IDLS technique. As the solutions have thus been found to be no longer equivalent in the case of a temperature variation, T -IDLS allows unambiguous defect characterization. However, the lack of ambiguity of the T -IDLS result has been proved to depend heavily on the investigated temperature range, as both the existence of two discrete DPSS-IPs and the identifiability of the diffuse DPSS-IP can only be ensured if the investigated temperature range is chosen such that the set of superposed DPSS curves contains both types of DPSS curves, those with a split range and those with a continuous range of validity. If the DPSS analysis has to be based on only one type of DPSS- k curve due to a restriction of the accessible temperature range, the T -IDLS result becomes ambiguous, the result being comparable to or even worse than the N_{dop} -IDLS result in terms of ambiguity.

The defect energy depth ΔE_t can always be determined accurately from TDLS. Although ΔE_t can be extracted from a simple linear fit of the Arrhenius increase, newly developed techniques of data linearization turned out to be necessary to achieve correct results. An important discovery was that even a complete defect characterization may be achieved from TDLS alone if the entire TDLS curve is subjected to SRH modeling. However, the lack of ambiguity of the spectroscopic result obtained from this advanced TDLS analysis has been found to depend on the band gap half of the underlying defect center. While defects located in the MinBH are characterized unambiguously, two equivalent TDLS solutions are expected for defects located in the MajBH, which prevents an unambiguous identification of the k factor and the band gap half of these defect centers. While the k factor of the MajBH solution has been found to be completely undetermined if the TDLS curve covers a normal T range, the study revealed for the first time

that the consideration of the TDLS bend due to intrinsic conduction allows at least the determination of an upper bound for k and sometimes even more. However, for an accurate modeling of the IC-induced TDLS bend (high-temperature part), it turned out to be mandatory that the SRH model is based on the advanced T -model proposed here, which has been validated directly by simulating an experimental TDLS curve. Finally, as the accurate modeling of the low temperature part of the TDLS curve directly yields the $\sigma(T)$ -model for the defect center, TDLS provides an additional fingerprint which gives insight into the relevant capture mechanism.

To avoid the remaining ambiguity of the above LS techniques, we introduced a new LS technique which combines TDLS and IDLS. In fact, it can be demonstrated that the combined TDLS & IDLS technique always allows an unambiguous and complete defect characterization on a single sample in the whole range of defect parameters. This important discovery guarantees the general applicability of lifetime spectroscopy as a diagnostic tool. As the combined analysis may be performed with maximum transparency by simple superposition of the associated DPSS diagrams, the combined TDLS & IDLS technique sets a new standard for advanced lifetime spectroscopy.

Comparing the different LS techniques in terms of their spectroscopic potential reveals that a temperature variation is mandatory to identify the defect parameters unambiguously. While the combined TDLS & IDLS technique and the T -IDLS technique always allow unambiguous defect characterization, the TDLS technique does so in half of the defect parameter range (MinBH defects) and provides at least the defect energy depth ΔE_t in the other half (MajBH defects). As the energy level has been the only tabulated defect fingerprint up to now, knowledge of ΔE_t may in many cases suffice to identify an unknown defect center. Although it delivers two equivalent solutions, the N_{dop} -IDLS technique is interesting for industrial application as it operates at room temperature.

As the complete picture of the spectroscopic potential of the different LS techniques achieved in the present chapter has been obtained primarily by the use of the proposed DPSS analysis, this new evaluation technique is likely to constitute the basis of further developments in the field of lifetime spectroscopy. To verify the theoretical predictions, the different LS techniques will be applied on intentionally metal-contaminated samples in the following chapter.

References

- [1] D.V. Lang, *Deep-level transient spectroscopy: A new method to characterize traps in semiconductors*, J. Appl. Phys. **45** (7), 3023–32 (1974).
- [2] F. Shimura, T. Okui, and T. Kusama, *Noncontact minority-carrier lifetime measurement at elevated temperatures for metal-doped Czochralski silicon crystals*, J. Appl. Phys. **67** (11), 7168–71 (1990).
- [3] Y. Kirino, A. Buczkowski, Z.J. Radzimski, G.A. Rozgonyi, et al., *Noncontact energy level analysis of metallic impurities in silicon crystals*, Appl. Phys. Lett. **57** (26), 2832–4 (1990).
- [4] Y. Hayamizu, T. Hamaguchi, S. Ushio, T. Abe, et al., *Temperature dependence of minority-carrier lifetime in iron-diffused p-type silicon wafers*, J. Appl. Phys. **69** (5), 3077–81 (1991).
- [5] A. Kaniava, A.L.P. Rotondaro, J. Vanhellemont, U. Menczigar, et al., *Recombination activity of iron-related complexes in silicon studied by temperature dependent carrier lifetime measurements*, Appl. Phys. Lett. **67** (26), 3930–2 (1995).
- [6] S.W. Johnston and R.K. Ahrenkiel, *Measurement of the temperature-dependent recombination lifetimes in photovoltaic materials*, 15th NCPV Photovoltaics Program Review (Denver, CO, USA, 1999), pp. 505–10.
- [7] H. Daio, A. Buczkowski, and F. Shimura, *Lifetime study of metastable surface recombination centers in n-type silicon wafers*, J. Electrochem. Soc. **141** (6), 1590–3 (1994).
- [8] M. Ichimura, H. Tajiri, T. Ito, and E. Arai, *Temperature dependence of carrier recombination lifetime in Si wafers*, J. Electrochem. Soc. **145** (9), 3265–71 (1998).
- [9] G. Ferenczi, T. Pavelka, and P. Tütto, *Injection level spectroscopy: a novel non-contact contamination analysis technique in silicon*, Jpn. J. Appl. Phys. **30** (12B), 3630–3 (1991).
- [10] T.S. Horányi, P. Tüttő, and C. Kovacsics, *Identification possibility of metallic impurities in p-type silicon by lifetime measurement*, J. Electrochem. Soc. **143** (1), 216–20 (1996).
- [11] H. Bleichner, P. Jonsson, N. Keskitalo, and E. Nordlander, *Temperature and injection dependence of the Shockley-Read-Hall lifetime in electron irradiated n-type silicon*, J. Appl. Phys. **79** (12), 9142–8 (1996).
- [12] R. Falster and G. Borionetti, *The application of minority carrier lifetime techniques in modern Cz-Silicon*, in *Recombination Lifetime Measurements in Silicon*, ed. by F.R.B. D.C. Gupta, and W.M. Hughes [American Society for Testing and Materials (ASTM), Chelsea, MI, 1998], Vol. 1, pp. 226–249.
- [13] J. Schmidt, C. Berge, and A.G. Aberle, *Injection level dependence of the defect-related carrier lifetime in light-degraded boron-doped Czochralski silicon*, Appl. Phys. Lett. **73** (15), 2167–9 (1998).
- [14] J. Schmidt and A. Cuevas, *Electronic properties of light-induced recombination centers in boron-doped Czochralski silicon*, J. Appl. Phys. **86** (6), 3175–80 (1999).

- [15] D. Walz, J.-P. Joly, and G. Kamarinos, *On the recombination behaviour of iron in moderately boron-doped p-type silicon*, Appl. Phys. A **62** (4), 345–53 (1996).
- [16] N. Keskitalo, P. Jonsson, K. Nordgren, H. Bleichner, et al., *Temperature and injection dependence of the Shockley-Read-Hall lifetime in electron-irradiated p-type silicon*, J. Appl. Phys. **83** (8), 4206–12 (1998).
- [17] R.K. Ahrenkiel, B.M. Keyes, and S. Johnston, *Injection level lifetime spectroscopy of impurities in semiconductors*, Surface Engineering **16** (1), 54–60 (2000).
- [18] D. Macdonald and A. Cuevas, *Lifetime spectroscopy of FeB pairs in silicon*, Proc. 11th Workshop on Crystalline Silicon Solar Cell Materials and Processes (East Park, Colorado, 2001), pp. 24–31.
- [19] J. Schmidt, *Temperature- and injection-dependent lifetime spectroscopy for the characterization of defect centers in semiconductors*, Appl. Phys. Lett. **82** (13), 2178–80 (2003).
- [20] R.A. Sinton and A. Cuevas, *Contactless determination of current-voltage characteristics and minority-carrier lifetimes in semiconductors from quasi-steady-state photoconductance data*, Appl. Phys. Lett. **69** (17), 2510–2 (1996).
- [21] W.M. Bullis and H.R. Huff, *Interpretation of carrier recombination lifetime and diffusion length measurements in silicon*, J. Electrochem. Soc. **143** (4), 1399–405 (1996).
- [22] S. Rein, T. Rehrl, W. Warta, and S.W. Glunz, *Lifetime spectroscopy for defect characterization: Systematic analysis of the possibilities and restrictions*, J. Appl. Phys. **91** (3), 2059–70 (2002).
- [23] W. Shockley and W.T.J. Read, *Statistics of the recombinations of holes and electrons*, Phys. Rev. **87** (5), 835–42 (1952).
- [24] R.N. Hall, *Electron-hole recombination in germanium*, Phys. Rev. **87**, 387 (1952).
- [25] D. Macdonald and A. Cuevas, *Validity of simplified Shockley-Read-Hall statistics for modeling carrier lifetimes in crystalline silicon*, Phys. Rev. B (Condensed Matter and Materials Physics) **67** (7), 75203–1–7 (2003).
- [26] A. Goetzberger, B. Voß, and J. Knobloch, *Sonnenenergie: Photovoltaik* (Teubner Studienbücher Physik, Stuttgart, 1994).
- [27] S.W. Glunz, S. Rein, W. Warta, J. Knobloch, et al., *On the degradation of Cz-silicon solar cells*, Proc. 2nd WCPEC (Vienna, Austria, 1998), pp. 1343–6.
- [28] S.M. Sze, *Physics of Semiconductor Devices*, 2nd edn. (John Wiley & Sons, New York, 1981).
- [29] D. Macdonald and A. Cuevas, *Trapping of minority carriers in multicrystalline silicon*, Appl. Phys. Lett. **74** (12), 1710–12 (1999).
- [30] J. Schmidt, K. Bothe, and R. Hezel, *Oxygen-related minority-carrier trapping centers in p-type Czochralski silicon*, Appl. Phys. Lett. **80** (23), 4395–7 (2002).
- [31] D. Macdonald, *Recombination and trapping in multicrystalline silicon solar cells*, PhD thesis, Australien National University (2001).
- [32] J.A. Hornbeck and J.R. Haynes, *Trapping of minority carriers in silicon. (I) P-type silicon*, Phys. Rev. **97**, 311 (1955).

- [33] D. Macdonald, R.A. Sinton, and A. Cuevas, *On the use of a bias-light correction for trapping effects in photoconductance-based lifetime measurements of silicon*, J. Appl. Phys. **89** (5), 2772–8 (2001).
- [34] R.A. Sinton, *Possibilities for process-control monitoring of electronic material properties during solar-cell manufacture*, Proc. 9th Workshop on the Role of Impurities and Defects in Silicon Device Processing (Golden, CO, 1999), pp. 67–73.
- [35] P.A. Basore and D.A. Clugston, *PC1D version 4 for Windows: From analysis to design*, Proc. 25th IEEE PVSC (Washington D C, 1996), pp. 377–81.
- [36] C.H. Ling and Z.Y. Cheng, *An improved analysis for the determination of trap levels in silicon from laser microwave photoconductive decay measurements*, Appl. Phys. Lett. **71** (22), 3218–20 (1997).
- [37] K. Graff, *Metal Impurities in Silicon-Device Fabrication*, 2nd edn. (Springer-Verlag, Berlin, 2000).
- [38] T. Rehrl, *Temperaturabhängige Lebensdauerspektroskopie (TDLS) zur Defektanalyse in Silizium*, Diplomarbeit, Universität Regensburg (2001).
- [39] M.A. Green, *Silicon Solar Cells: Advanced Principles and Practice* (Center for Photovoltaic Devices and Systems, University of New South Wales, Sydney, 1995).
- [40] A. Hangleiter, *Nichtstrahlende Rekombination über tiefe Störstellen in Silizium*, Dissertation, Universität Stuttgart (1985).
- [41] C.H. Henry and D.V. Lang, *Nonradiative capture and recombination by multi-phonon emission in GaAs and GaP*, Phys. Rev. B (Solid State) **15** (2), 989–1016 (1977).
- [42] M. Lax, *Cascade capture of electrons in solids*, Phys. Rev. **119** (5), 1502–23 (1960).
- [43] J. Bourgoin and M. Lannoo, *Point defects in semiconductors II. Experimental aspects* (Springer-Verlag, Berlin, West Germany, 1983).
- [44] R.M. Gibb, G.J. Rees, B.W. Thomas, B.L.H. Wilson, et al., *A two stage model for deep level capture*, Philosophical Magazine **36** (4), 1021–34 (1977).
- [45] A. Hangleiter, *Nonradiative recombination via deep impurity levels in silicon: Experiment*, Phys. Rev. B **35** (17), 9149–61 (1987).
- [46] A. Hangleiter and R. Häcker, *Excitonic band-to-band Auger recombination in silicon*, Proc. 18th International Conf. on the Physics of Semiconductors (1987), p. 907.
- [47] A. Hangleiter, *Nonradiative recombination via deep impurity levels in semiconductors: The excitonic Auger mechanism*, Phys. Rev. B **37** (5), 2594–604 (1988).
- [48] E. Gaubas, J. Vanhellemont, E. Simoen, C. Claeys, et al., *Study of oxygen related recombination defects in Si by temperature-dependent lifetime and EBIC measurements*, Proc. 7th GADEST'97 (Spa, Belgium, 1997), pp. 155–60.

4. Defect characterization on intentionally metal-contaminated silicon samples

4.1 Introduction

After the theoretical potential of lifetime spectroscopy has been investigated in detail in Chap. 3, the present chapter aims to present the practical application of the various LS techniques. To allow a verification of the theoretical predictions and a critical assessment of the spectroscopic results, intentionally metal-contaminated samples have been chosen for this investigation.

Due to their great technological importance, metallic impurities in silicon have been the subject of a large body of work especially in the early 1980s, but even up to the present time [1, 2], with the intention of characterizing their electronic properties in order to better understand, and hopefully reduce, their impact on devices. Among the different experimental techniques which have been developed to measure the energy level and the capture cross-sections, deep-level transient spectroscopy (DLTS) is by far the most widely used. This is reflected in extended tables on the energy levels of impurities in silicon as measured using DLTS. Due to the high precision of DLTS in determining E_i , these values are ideally suited to cross-check the results obtained from lifetime spectroscopy.

However, in spite of the intensive investigations in the past, our knowledge of most metallic impurities is insufficient to estimate their impact on recombination and solar cell performance. Although DLTS allows the majority-carrier capture cross-section to be determined, these results are tainted with large uncertainties for fundamental reasons [1, 2] (see, e.g., Sect. 4.6.1A). Concerning the minority-carrier capture cross-sections, only poor information is available at present, as their experimental determination is even more complicated [1, 2]. Thus the symmetry factor k is unknown or at least uncertain for most of the metal-induced defect levels, which impedes estimation of their recombination activity. As many metallic impurities give rise to several defect levels within the silicon band gap, even an identification of the relevant defect level, which dominates recombination, fails.

As lifetime spectroscopy allows both a direct determination of the symmetry factor k and an identification of the relevant defect level (see Chap. 3), it is ideally suited to fill this gap. Thus, the current LS investigations on metal-contaminated samples aim on the one hand to complete our knowledge of the defects related to the metallic impurities, which is highly relevant to photovoltaics, and on the other hand to confirm the spectroscopic potential of the different LS techniques in order to demonstrate the general applicability of lifetime spectroscopy as a diagnostic tool.

Section 4.2 discusses the technological and experimental boundary conditions of the LS investigations to demonstrate the suitability of the samples, the surface passivation and the measurement and evaluation procedure to allow an accurate determination of the recombination lifetime related to the metal point defects in the bulk. Sections 4.3–4.6 then present the lifetime spectroscopic investigations performed on molybdenum-, titanium-, nickel- and iron-contaminated samples. Each section starts with a short summary of the technological importance and the known defect properties of the respective impurity before presenting the standard evaluation by means of TDLS, IDLS and the combination of both. Section 4.4 presents an exemplifying N_{dop} -IDLS investigation on a set of titanium-contaminated samples. The impact of the doping type on the recombination activity of the defect levels is shown in Sect. 4.5 on the two nickel-contaminated samples. The application of lifetime spectroscopy to metastable defect systems is demonstrated in Sect. 4.6 where both defect configurations of an iron contamination, interstitial iron and iron-boron pairs, are investigated. It is shown how the metastability of the iron system may be used to extract additional spectroscopic information, which is not in general accessible by means of lifetime spectroscopy. The results obtained are of special practical importance, as the most sensitive commercial technique to detect and determine iron contamination in silicon relies heavily on the defect parameters of both defect states.

Finally, Sect. 4.7 presents a detailed comparison of the experimental and methodological results of the present chapter. On the one hand a concise overview of the defect parameters determined in the previous sections is given and the impurities are compared with respect to their recombination activity and their impact on solar cell performance. On the other hand all methodological aspects which are illustrated in the different graphs, containing the LS results of the present chapter, are summarized in a tabular overview and discussed for each of the LS techniques separately. The overview should allow the reader to find quick experimental proof of the various qualities and restrictions of lifetime spectroscopy predicted in Chap. 3.

4.2 Experimental details

For an accurate characterization of bulk defects induced by the different transition metals by means of lifetime spectroscopy, it is essential to ensure on the one hand a defined incorporation of the metal impurities during contamination and on the other hand an accurate determination of the bulk recombination properties. To demonstrate that the LS investigations of the present work perfectly satisfy these two fundamental experimental prerequisites, the present section focuses on the technological and experimental boundary conditions.

In Sect. 4.2.1 the crystallographic properties of the investigated impurities and the contamination processes used are critically assessed to show that the intentionally contaminated samples are ideally suited for the LS investigations, as a homogeneous and electrically active incorporation of the metal-impurities can be guaranteed. Since a direct measurement of the bulk recombination lifetime requires an effective reduction of the impact of surface recombination, Sect. 4.2.2 focuses on silicon nitride used as a surface passivation. After a short description of the technological process, the passivation quality is accurately characterized using the method of thickness variation. It is demonstrated that this purely experimental technique allows results of high precision at low preparation cost, if an industrial infeed grinder is used for sample preparation. Additional aspects which make silicon nitride a suitable passivation for the purpose of the present work are briefly discussed. Section 4.2.3 deals with the procedure applied to determine the doping concentration, as this parameter has been proved in Chap. 3 to have a decisive impact on the LS curves and the spectroscopic LS result. Summarizing the results from Sect. 3.3.1, Sect. 4.2.4 then presents a guideline for an accurate spectroscopic evaluation of IDLS data, including both the data pre-analysis to eliminate distorting effects from the measured IDLS curves and the SRH modeling itself. Dealing with TDLS, Sect. 4.2.5 finally introduces a special procedure for the lifetime measurements by means of the MW-PCD technique, which guarantees an accurate determination of the recombination lifetime under LLI. The expected impact of surface recombination on the TDLS curves is examined in more depth, and brief instructions for an accurate spectroscopic evaluation of TDLS data are given at the end.

4.2.1 Sample preparation I: intentional metal contamination

Sample preparation in an experiment with the aim of investigating metals in silicon is critical as it has to be ensured that the intentionally introduced

impurities (i) remain dissolved to be electrically active and (ii) occur evenly throughout the bulk of the wafer, as this is essential for accurate lifetime measurements.

A Problem

Due to the extremely low solubility of all transition metals at room temperature, their deliberate introduction requires a high-temperature step. The critical process step is the cooling at the end of the heat treatment as the dissolved metal becomes increasingly supersaturated due to an exponential decrease of the solubility with decreasing temperature. Basically there are three possible reactions to avoid this supersaturation: (i) the impurities may precipitate in the bulk, (ii) they may diffuse out to the specimen surface and form precipitates there or (iii) they remain dissolved within the volume. Which of these processes dominates strongly depends on the process conditions and the properties of the respective impurity. Precipitation and outdiffusion¹ both require a sufficiently high diffusivity of the impurity atoms and sufficiently low cooling rates, since the impurity atoms have to diffuse within the cooling period to the nuclei and surfaces. In addition, precipitation in the bulk requires a sufficiently high concentration of impurity atoms, in the case of a homogeneous nucleation mechanism, and the presence of foreign nuclei, such as lattice defects and other impurity precipitates, in the case of a heterogeneous nucleation mechanism. By contrast, impurities will remain dissolved within the volume if either their diffusivity is low or the applied cooling rates are high (quenching).

The problems arising from outdiffusion and precipitation in the bulk or at the surfaces are twofold. On the one hand these processes may reduce the concentration of desired dissolved impurities below the detection limit. On the other hand they result in non-uniform defect distributions which may distort the lifetime measurements if the precipitates are electrically active. For both reasons precipitation and outdiffusion have to be avoided or at least carefully controlled during sample preparation.

B Impurities investigated and their crystallographic properties

To assess the relevance of these processes for the impurities investigated, their crystallographic properties and their behavior under heat treatment

¹ Outdiffusion additionally requires a phase change of the impurity at the surface to avoid back-diffusion. This phase change may consist in precipitation, evaporation or another reaction with the ambient atmosphere.

should be briefly discussed. Being the decisive quantities, the solubilities and diffusivities of the investigated transition metals are listed in Table 4.1, each displayed for two different temperatures (data taken from [1, pp. 22/28]).

Since *titanium* is the 3d transition element with the lowest known solubility and diffusivity (see Table 4.1), it scarcely forms precipitates. Thus once introduced, titanium will be present in a dissolved state, being incorporated on interstitial lattice sites [1].

Although *molybdenum* belongs to the medium-fast-diffusing 4d transition metals, the existence of precipitates has not yet been reported [1]. From experience it is known that electrically active molybdenum is rather insensitive to the annealing process as it neither disappears into precipitates during low-temperature annealing nor requires quenching to become electrically active. Molybdenum is assumed to occupy interstitial sites in the silicon lattice [1].

Since *iron* belongs to the moderately fast-diffusing 3d transition metals and exhibits high solubilities in silicon at high temperatures, it tends to precipitate during slow cooling from high temperatures and during subsequent low-temperature anneals, while it remains electrically active during quenching and moderately fast cooling [1]. However, since iron only precipitates via a heterogeneous nucleation mechanism, outdiffusion and precipitation depend on the presence of nucleation centers formed by lattice defects, other impurity precipitates or Si/SiO₂ interfaces and thus may be effectively suppressed in monocrystals, which are pure except for the iron contamination. Dissolved iron occupies interstitial lattice sites while iron on substitutional sites is unstable [1].

Table 4.1. Solubilities and interstitial diffusivities of the investigated transition metals in intrinsic silicon (taken from [1, pp. 22/28]). For comparison the solubilities are given at 900 and 1100°C and the diffusivities at 30 and 900°C. The values have been recalculated using the Arrhenius law and the parameterization given in [1, pp. 22/28]. Experimental data are available in the given T region. The *values in parentheses* correspond to extrapolations. The values for molybdenum have not been measured but are estimated according to the neighboring elements.

Metal	Solubility			Diffusivity		
	T region [°C]	S (900°C) [cm ⁻³]	S (1100°C) [cm ⁻³]	T region [°C]	D (30°C) [cm ² /s]	D (900°C) [cm ² /s]
Ti	950 ... 1200	2.7×10^{11}	2.2×10^{13}	600 ... 1150	(9.9×10^{-36})	1.9×10^{-10}
Mo	Estimated	$> 3.6 \times 10^{13}$		Estimated	$< 5.0 \times 10^{-17}$	$< 2.7 \times 10^{-7}$
Fe	900 ... 1200	4.3×10^{13}	2.9×10^{15}	30 ... 1200	6.4×10^{-15}	1.6×10^{-6}
Ni	500 ... 950	7.4×10^{16}	(8.4×10^{17})	800 ... 1300	(3.1×10^{-11})	1.9×10^{-5}

Nickel belongs to the fast-diffusing 3d transition metals and at high temperatures exhibits the second-highest solubility of the 3d metals in silicon [1].² As a consequence nickel precipitates almost quantitatively even during quenching of the sample from high temperatures. The precipitation takes place via a homogeneous nucleation mechanism which does not require foreign nuclei. Due to a fast outdiffusion to the surfaces during the cooling period, nickel precipitates are mainly formed at the wafer surfaces and only to a small extent in the bulk [1]. The residual nickel can be situated on both interstitial and substitutional lattice sites. However, since interstitial nickel diffuses very fast even at room temperature (see Table 4.1), it is not expected to be present at room temperature because of its outdiffusion and precipitation. In contrast, substitutional nickel diffuses very slowly. Thus substitutional nickel is expected to exist at room temperature, though its fraction may be small compared to the total nickel content. Graff et al. [1] showed that the fraction of electrically active substitutional nickel amounts to 0.01–1 % of the respective solubility, which still allows defect concentrations of 10^{12} – 10^{14} cm⁻³ due to the very high solubilities (see Table 4.1).

C Contamination processes used

Having identified iron and nickel as critical impurities concerning their electrically active incorporation in the silicon lattice, we now want to describe the contamination processes used and discuss their efficiency in providing samples with the required defect distributions.

The most elegant approach is to perform the metal contamination during crystal growth. This technique has been applied to realize contamination with molybdenum, titanium and iron, the samples being commercially manufactured by Wacker Siltronic. For deliberate contamination, the elemental metal has been added to the silicon melt before pulling a monocrystalline Cz-Si crystal. The incorporation of metal atoms into the silicon lattice during crystal growth is completely determined by segregation. Outdiffusion of the metal contaminant to the surfaces during the solidification process (cooling down) is effectively suppressed due to the small surface/volume ratio of the silicon rod and at most leads to a radial variation of the defect concentration by 5–15 % over the crystal diameter [3]. Since a careful adjustment of the pulling conditions³ allows a precipitation of the metal impurities in the bulk to be avoided, it is ensured

² Only copper exhibits a higher solubility.

³ The critical parameters are the pulling velocity and the temperature gradient at the interface between liquid and solid phase [3].

that the impurity atoms remain dissolved and thus electrically active within the whole contaminated crystal [3]. The axial distribution of the final concentration of dissolved metal impurities can be directly calculated from the metal quantity weighed into the melt using the segregation coefficients for the different metals which are known from the literature. The defect concentrations given in the following have been determined by Wacker from such calculations [3].⁴ Since the axial variation of the impurity concentration over a typical wafer thickness can be neglected, the defect distribution in the wafers finally cut from these crystals is completely uniform. Thus in terms of both the configuration and the homogeneity of the incorporated metallic impurity atoms, these wafers are ideally suited for lifetime spectroscopic investigations of defined metal impurities.

Alternatively the metal contamination may be achieved by a thermal indiffusion. This technique has been applied at the University of Berkley to produce the nickel-contaminated samples investigated in Sect. 4.5. Here elemental nickel has been deposited on the surface of high-purity float zone wafers by spin-coating a nickel-contaminated solution. In a subsequent high-temperature step the nickel has been diffused into the wafer bulk. In spite of the applied rapid cooling of the samples in air, it is impossible to avoid the outdiffusion of nickel to the surfaces due to the high diffusivities (see Sect. 4.2.1B). To remove the expected surface layers containing the nickel precipitates, several microns of silicon were finally etched from the wafers, which also allowed the surfaces to be cleaned from residuals of the spin-coated layer. So in the etched samples the distribution of the nickel defects is also expected to be uniform, which ensures accurate lifetime measurements.

4.2.2 Sample preparation II: surface passivation and its quality

For accurate characterization of bulk defects by means of lifetime spectroscopy, an accurate determination of the bulk recombination properties is mandatory. This in turn requires reducing the impact of surface recombination to such an extent that the measured effective lifetimes, within experimental error, reflect only contributions from the bulk. As theoretically demonstrated in Sect. 1.5, this is not too difficult for high defect concentrations due to the related low bulk lifetime, but becomes more challenging as the contamination level decreases. To allow accurate LS investigations in a

⁴ The theoretical calculations of the defect concentration are at least accurate to within a factor of 3. This uncertainty is quite irrelevant for lifetime spectroscopy since the LS investigations aim at the determination of the relative and not the absolute defect parameters (see Sect. 3.2.1A).

maximum range of defect concentrations, in the present work a high-quality silicon nitride has been used for surface passivation. The following section briefly describes the technological process applied and accurately characterizes the quality of the SiN surface passivation used.

A Technology: deposition of silicon nitride using a PECVD system

The deposition of the silicon nitride films has been performed by means of plasma-enhanced chemical vapor deposition (PECVD). Using a direct PECVD reactor, the mixture of processing gases is excited in the microwave cavity within the deposition chamber, the plasma being in contact with the samples. It is known from the literature [4] that in such a direct plasma the electronic properties of the Si:SiN interface crucially depend on the plasma excitation frequency. To avoid an ion bombardment of the wafer surface during the deposition, which generally results in significant surface damage and poor quality of the passivation layers, the excitation frequency has to be chosen well above the plasma frequency of 4 MHz, as then the ions can no longer follow the exciting field. Working at microwave frequency 13.6 MHz, the direct PECVD reactor at Fraunhofer ISE [5, 6] satisfies this requirement and is thus ideally suited for the deposition of high-quality passivation layers.

After a standard RCA clean of the wafer surfaces, which has been preceded by an optional etching step to remove surface damage when necessary,⁵ the silicon nitride films have been deposited onto both wafer surfaces at a temperature of 350°C with a deposition time of 10 min. As processing gases silane (SiH_4), nitrogen (N_2) and hydrogen (H_2) have been used, the hydrogen being important for an efficient passivation of defect states at the interface. The “passin” process used (for further details see [6, 7]) results in silicon-rich amorphous silicon-nitride films of 72 nm thickness with a high refraction index of around 2.8. The process is distinguished by its excellent homogeneity over a large area of 9 inches in diameter [7]. In order to optimize the electrical properties of Si:SiN interface, the SiN-coated wafers were finally sintered at 425°C for 20 min in an N_2H_2 atmosphere. This final sintering step has been proved in [6] to further improve surface passivation quality. The effectiveness of the nitride films in passivating the surfaces has always been controlled using high-purity FZ control samples of similar resistivity.

⁵ While the metal-contaminated samples investigated in Chap. 4 were routinely etched back by 30 µm from both surfaces using an acid etch, the Cz samples investigated in Chap. 5 were only subjected to this etching step if they were not commercially polished or bright-etched.

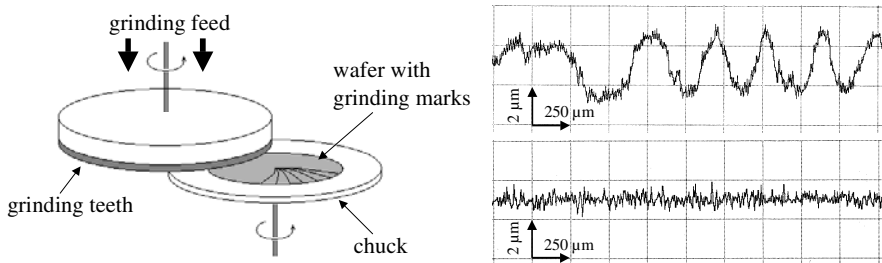


Fig. 4.1. (a) Schematic diagram of purely mechanical infeed grinding [8]. (b) Optical surface profile scans of a chemically polished wafer “from the box” (top) and of a ground and KOH-etched (6 μm) wafer [9].

B Method of thickness variation: sample preparation with an infeed grinder

As discussed in Sect. 1.5B, an elegant technique to determine the surface recombination velocity is the method of thickness variation, because it is purely experimental and does not require any theoretical assumptions. A fundamental prerequisite for the accuracy of this technique is a set of wafers whose thickness varies over a broad range and whose surfaces are identical in their crystallographic and electronic quality. While the half-manual grinding and polishing processes used for such experiments up to now have been limited in both factors [10, 11], the industrial infeed grinder used in the present work is an excellent tool to produce wafers of a thickness down to 40 μm and planar surfaces of highly reproducible quality. Figure 4.1a shows the principle of the purely mechanical grinding process, the infeed grinder built up at Fraunhofer ISE is based on [9]. The wafer is held by vacuum on a microporous chuck. The grinding occurs by a fast-rotating wheel (1000–6000 RPM) with grinding teeth at its outer diameter, which is lowered onto the wafer surface. To guarantee a homogeneous grinding of the whole wafer surface, the chuck with the wafer rotates itself at a much lower speed (40–200 RPM) in the opposite direction. A permanent rinsing of the chuck with deionized water during the grinding process washes away the abrasive material and cools the system. The abrasion rates may be varied between 0.1 and 5.0 $\mu\text{m}/\text{s}$, which allows short processing times. The precision of the grinding process manifests itself in a total thickness variation over the wafer of less than 1 μm , which is achieved irrespective of the amount of abrasion, the final thickness and the initial surface topography. This ensures planar and parallel surfaces of identical and reproducible quality. An important point is that, using an optimized grinding process developed at Fraunhofer ISE in the diploma

thesis of H. Kampwerth [8], the crystallographic surface damage caused by the grinding process may be confined to an extraordinarily shallow top layer of 1 µm depth. This is achieved by combining a rough-grinding with a fine surface finish, the latter being applied to grind off the last 20 µm. However, as the damage is mainly due to subsurface cracks, which are electrically active, a final damage removal step is necessary to obtain the crystallographically perfect surfaces which are required for an investigation of the surface recombination properties of a passivating layer.

For the thickness variation experiment we used high-purity FZ silicon wafers to ensure a maximum impact of surface recombination in the measured effective lifetimes. Moreover, it has been proved that the wafers within a set came from the same ingot, when possible even from neighboring positions, to avoid disturbing variations in the bulk lifetime within the wafer set. Sample preparation made use of the optimized grinding process (for details see [8]), which has been applied to both wafer surfaces to guarantee identical properties. The variation of the final wafer thickness (after etching) typically covered a range from 40 to 140 µm. To remove the grinding-induced damage layer, the ground wafers were etched back 5–10 µm from each side using a 40 % KOH etch at 80°C. The etch removal was chosen higher than necessary, as this allowed the average surface roughness to be reduced even when an anisotropic KOH etch was used. The high optical quality of the resulting surfaces is visualized in Fig. 4.1b, which shows an optical scan of the surface profile achieved (bottom) in comparison to the surface profile of an industrially shiny-etched wafer (top). As the surfaces are additionally damage-free, due to the final etching step, and identical within the whole wafer set used for the thickness variation, due to the high reproducibility of the surface preparation scheme, they are ideally suited as a starting point for the S-investigation. For this, the whole set of wafers has been passivated with silicon nitride according to the procedure described in Sect. 4.2.2A.⁶

C Method of thickness variation: characterization of the SiN surface passivation

The lifetime measurements have been performed by means of the QSSPC technique in a broad injection range from 1×10^{14} to $2 \times 10^{17} \text{ cm}^{-3}$. Figure 4.2a displays the injection-dependent lifetime curves measured on a set of $1 \Omega\text{cm}$ wafers with six different thicknesses. The fact that the $\tau_{\text{eff}}(\Delta n)$ curves are shifted to lower values with decreasing wafer thickness directly

⁶ To guarantee absolute comparability of the passivation scheme, the initial RCA clean has been included.

reflects the increasing impact of surface recombination on the effective carrier lifetime. Under high injection densities ($\Delta n > 5 \times 10^{16} \text{ cm}^{-3}$), the gradation between the different $\tau_{\text{eff}}(\Delta n)$ curves becomes continuously smaller, as the effective carrier lifetime is increasingly dominated by CE-Auger bulk recombination, while the impact of surface recombination declines. The observed lifetime increase under low injection densities originates from superposed external carrier trapping (see Sect. 3.3.1A). As the trapping effect completely screens the recombination lifetime, its onset ($\Delta n < 2 \times 10^{14} \text{ cm}^{-3}$) defines a lower bound for the injection range, in which an accurate determination of the surface recombination velocity (SRV) may be achieved.

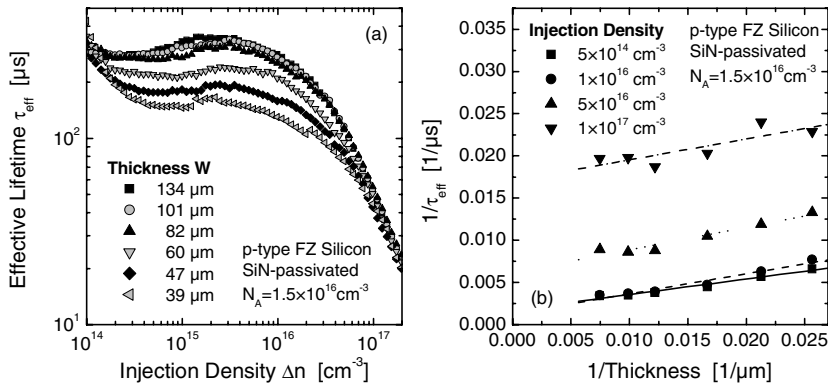


Fig. 4.2. Experimental characterization of the silicon nitride used as surface passivation by means of the method of thickness variation (here for a bulk resistivity of $1 \Omega\text{cm}$). (a) Injection dependence of the effective carrier lifetime measured by means of the QSSPC technique on the individual samples: the lifetime level decreases with decreasing sample thickness. (b) Effective lifetimes of the different samples at the same injection density plotted in a $1/\tau_{\text{eff}} - 1/W$ plot, exemplified for four different injection densities. The slope of the linear fits equals $2S$. (c) Injection dependence of the surface recombination velocity S of the SiN passivation, as it results from the linear fits of the τ_{eff} data sets associated with the different injection densities. Note that this determination is purely experimental and does not require any theoretical assumption.

To obtain the injection-dependence of the SRV, it is necessary to generate τ_{eff} data sets to fixed injection levels from the six $\tau_{eff}(\Delta n)$ curves in the whole injection range (with a fine Δn gradation), which requires an interpolation of all lifetime curves using the same interpolation nodes. As exemplified in Fig. 4.2b for four different injection densities, the extracted τ_{eff} data sets are plotted in a $1/\tau_{eff}$ - $1/W$ diagram. According to Eq. (1.52), the slope of a linear fit to the individual data sets directly yields the SRV at the respective injection level (slope = $2S$).⁷ This evaluation applied to the entity of τ_{eff} data sets finally results in the $S(\Delta n)$ curve displayed in Fig. 4.2b. The given errors result directly from the linear fit and thus represent a direct measure of the degree of linear correlation within the τ_{eff} data sets. The fact that the observed linear correlation is good in the whole injection range (see Fig. 4.2b) proves the reliability of the determined $S(\Delta n)$ curve and demonstrates the high reproducibility of the surface quality which may be achieved by means of an optimized grinding process.

D Quality of the SiN surface passivation: injection and doping dependence of the SRV

As the passivation quality of the silicon nitride is known to depend on both the injection and the doping density, the injection dependence of the SRV has been determined experimentally from thickness variation experiments, as shown in Fig. 4.2, for five different doping concentrations ranging from 1×10^{14} to $7 \times 10^{16} \text{ cm}^{-3}$. The individual experiments have all been performed on high-purity *p*-type FZ silicon using wafer sets of 5–8 samples with thickness varying between 40–140 μm . The resulting $S(\Delta n)$ curves are displayed in Fig. 4.3.

The fact that a low SRV of 50 cm/s represents the upper bound throughout the whole injection and doping range under investigation demonstrates the excellent quality of the silicon-nitride passivation used in the present work. For an intermediate doping concentration of $1 \times 10^{16} \text{ cm}^{-3}$ (circles) excellent SRV values of 10 cm/s are reached in the whole injection range, SRV being almost injection-independent. Under LLI conditions SRV is found to be strongly doping-dependent, decreasing as the doping concentration decreases. While a maximum value of 50 cm/s is determined on a $0.25 \Omega\text{cm}$ sample ($N_A = 7 \times 10^{16} \text{ cm}^{-3}$, squares), minimum values below 0.1 cm/s are found for an $8 \Omega\text{cm}$ sample ($N_A = 1 \times 10^{15} \text{ cm}^{-3}$, triangles), the

⁷ Moreover the intercept of the linear fit with the vertical axis yields the bulk lifetime (intercept = $1/\tau_{bulk}$). However, due to the extrapolation to an axis ($W \rightarrow \infty$), the τ_{bulk} error is much higher than the S error.

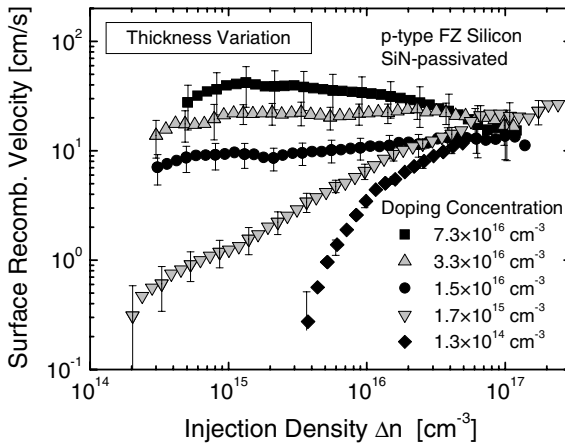


Fig. 4.3. Injection dependence of the surface recombination velocity of the silicon nitride used in this work for *p*-type silicon with different doping concentrations. *S* values have been determined altogether from thickness variations (see Fig. 4.2) realized on high-purity FZ silicon wafers. Each wafer set contained 5–8 samples with thickness varying between 40 and 140 μm . Note that these results are purely experimental and do not rely on any theoretical assumption (for details see [8]).

values of the 100 Ωcm sample ($N_A = 1 \times 10^{14} \text{ cm}^{-3}$, diamonds) being even lower, though not measurable under LLI due to superposed trapping effects (see Sect. 4.2.2C). Under HLI conditions, however, SRV becomes doping-independent, the different SRV curves all approaching the same value of 10–20 cm/s. As a consequence of the differences between LLI and HLI, the injection dependence of SRV is stronger for the less than for the more highly doped samples. While SRV increases significantly with increasing injection density for the less doped samples (though on a very low level), a slight decrease is observed for the more highly doped samples.

The observed qualitative trends are compatible with theoretical predictions in the literature if surface recombination is assumed to be dominated by a field effect due to positive charges in the isolating layer, which has consistently been proved to be the case for silicon nitride films [12]. The observed strong doping dependence of the SRV under LLI conditions (in *p*-type silicon) directly results from the charge-induced band bending near the surfaces which leads to a reduction of the hole (majority) carrier density at the interface. While the surface is only in depletion for higher doping concentrations, it is in inversion for lower doping concentrations. The depletion of majority carriers due to band bending increases the LLI-SRV compared to the flat band case, as the doping-related imbalance between electrons and holes is reduced at the surfaces, which directly

results in increased surface recombination. In the inversion case, however, recombination is completely limited by the hole (majority) capture due to the strong imbalance between the two carrier types, which results in a strong reduction of the LLI-SRV compared to the depletion case in more highly doped samples. Thus the doping dependence of the SRV under LLI directly reflects the field effect. Under HLI conditions, however, both carrier types are present in equilibrium at the surfaces, which implies that surface recombination is no longer limited by the availability of one carrier type (field effect) but only by the capture properties of the defect continuum at the interface. As a consequence SRV under HLI conditions no longer depends on the doping concentration. A detailed modeling of the injection-dependent SRV curves in Fig. 4.3 is expected to reveal some of the recombination properties of the defect continuum at the Si:SiN interface and hence to give deeper insight into the physical mechanism of surface recombination. However, as the investigation of surface recombination was not in the focus of the present work, we refrained from such a modeling.

It should be emphasized again that the results from Fig. 4.3 are purely experimental and do not rely on any theoretical assumption. However, they only prove the excellent passivation quality of the silicon nitride for $\Delta n > 10^{14} \text{ cm}^{-3}$, while the continuation of the SRV curves for $\Delta n < 10^{14} \text{ cm}^{-3}$ could not be determined in the experiment due to superposed carrier trapping. A qualitative estimate of the possible injection dependence of SRV under LLI is gained from the injection dependence which has been measured and calculated in the literature for the SRV of similar SiN films [6, 12]. This comparison suggests that the SRV of the more highly doped samples increases moderately for $\Delta n < 10^{14} \text{ cm}^{-3}$, while the SRV of the less doped samples is expected to saturate at a minimum value. In view of the extraordinarily low SRV values determined for $\Delta n > 10^{14} \text{ cm}^{-3}$, which reflect the overall quality of the silicon nitride used, this remaining uncertainty about the passivation quality under LLI conditions is of minor importance for the purposes of the present work. This is reinforced by the fact that the injection dependence of bulk lifetime observed in the LS investigations of the present work always reached its minimum in the injection range below 10^{14} cm^{-3} , which directly implies a reduced sensitivity of the measured effective carrier lifetime on surface recombination in that Δn region. Thus, it is justified to identify the measured effective lifetime with bulk lifetime in the whole injection range, provided the overall lifetime level is not too high.

E Suitability of the SiN passivation for the purposes of this work

Summarizing the results from the last sections and adding results from some pretests not shown in graphs, the essential properties of the silicon nitride passivation used are compiled in the list below:

1. Very low SRV in the whole doping and injection range.
2. High spatial homogeneity and good reproducibility.
3. Long term stability.
4. Stability upon illumination (0.1 W/cm^2 for 48 h).
5. Stability upon temperature treatments up to 425°C .
6. Low deposition temperature and short deposition time (350°C for 10 min).

While the good reproducibility of the SiN films (point 1) guarantees the validity of the SRV curves determined in Fig. 4.3 for the data of the whole work, the low SRV values (point 2) allow a direct measurement of the bulk lifetime in most cases of the present work. As the SiN films are stable upon illumination and low-temperature annealing (points 3–5), they are ideally suited for TDLS investigations in the T range from -170 to 330°C and for dynamical experiments to investigate reversible defect transformations upon annealing and illumination. Finally, the low temperature and short time required for the deposition (point 6) avoid irreversible and unwanted transformations of the bulk defects, such as precipitation or outdiffusion, which can occur if higher temperature processes such as a thermal oxidation (1050°C) are used. As high-temperature processes are not needed for surface passivation, their impact on the bulk properties can be investigated, as will be shown for the Cz-specific defect (see Chap. 5). Altogether it can be concluded that the silicon nitride film used in the present work perfectly satisfies the requirements which a surface passivation used for LS investigations of bulk defects has to meet.

4.2.3 Determination of the doping concentration

As has been shown in Figs. 3.5 and 3.8, the doping concentration N_A has a decisive impact on the qualitative shape of the IDLS and TDLS curves. Thus, an accurate N_A determination is mandatory to ensure accurate spectroscopic results. The most common technique is to calculate N_A from resistance measurements as shown in the schematic diagram in Fig. 4.4a. Using the four-point probe technique, we measured the sample resistance V/I in addition to the sample thickness W and calculated the volume resistivity ρ according to the standard equations [13], taking into account the well-known correction factors for a finite sample size [13]. To ensure maximum precision also on smaller samples, we did not only consider the

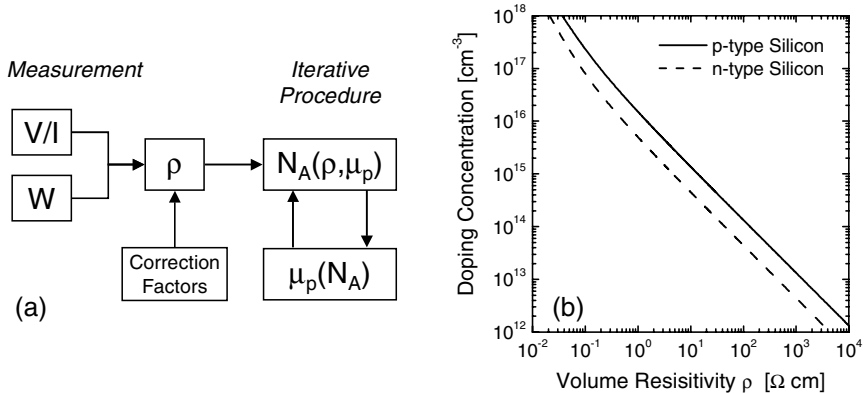


Fig. 4.4. (a) Schematic diagram of the procedure to determine the doping concentration from resistance measurements based on the four-point probe technique (exemplified for *p*-type doping). (b) Doping concentration as a function of resistivity calculated from the iterative procedure on the basis of the mobility model used in PC1D (version 5.8) [14].

correction for sample thickness, as commercially implemented in the four-point probe systems, but also the corrections for lateral sample dimensions and for the placement of the probes relative to the sample edges. The expressions used may be found in [13, p.5]. Assuming a *p*-type doping, the relation between volume resistivity ρ and doping concentration N_A may be written as

$$\frac{1}{\rho} = q\mu_p N_A \quad (4.1)$$

with the elementary charge q and the hole (majority carrier) mobility μ_p . As the mobility itself is a function of the doping concentration, the calculation of N_A from ρ requires an iterative procedure. Using for $\mu_p(N_A)$ the standard mobility model implemented in the device simulation software PC1D (version 5.8) [14], the iterative procedure finally results in the $N_A(\rho)$ curve displayed in Fig. 4.4b (solid line).⁸ Throughout this work the doping concentration of the investigated samples has been determined according to the complete procedure displayed in Fig. 4.4a.

Instead of using the four-point probe technique, the dark resistivity can also be determined inductively on the calibrated QSSPC stage. The good agreement of the results from both techniques proved the accuracy of the

⁸ The fact that the corresponding $N_D(\rho)$ curve for *n*-type doping (dashed line) is shifted to lower values directly results from the electron mobility being higher than the hole mobility.

adopted method. If one is aware of the fact that the position of the TDLS bend due to intrinsic conduction mainly depends on the doping concentration, modeling the experimental TDLS data probably represents the most sensitive cross-check of N_A as has been demonstrated in Sect. 3.5.6B. Altogether, an accurate knowledge of the doping concentration is thus ensured.

4.2.4 IDLS – measurement and modeling procedure

A Covered injection range

The IDLS measurements have been performed by means of the QSSPC technique, which has been described in Sect. 2.2. In principle the technique allows lifetime measurements in an injection range from 10^{12} – 10^{17} cm⁻³. However, there is often a limitation of the accessible injection range at its lower end because of superposed carrier trapping. Moreover, the maximum injection density which may be achieved in the experiment varies with the lifetime level. As accurate QSSPC measurements require a complete covering of the coil to ensure the validity of the conductivity calibration, IDLS investigations could only be performed on samples which exceeded a minimum size of 30×30 mm².

B Procedure of IDLS data pre-analysis

In order to guarantee that the IDLS curves subject to the advanced SRH analysis reflect the recombination properties of only the defect states related to the impurity under investigation, the measured IDLS curves have to be pre-analyzed prior to the actual SRH analysis. This pre-analysis primarily aims to detect and eliminate possible superposed effects, which cause deviations of the measured IDLS curve from the pure SRH lifetime. Most effects have already been discussed in Sect. 3.3.1. Based on the findings there, the course of the pre-analysis should be briefly delineated in the following.

Surface recombination. As mentioned in Sect. 4.2.2D, the effectiveness of the surface passivation of the contaminated samples has been verified on high-purity FZ control samples of similar resistivity, which were subjected to the same etching, cleaning and passivation treatments. To exclude surface effects in the IDLS curves measured on the intentionally contaminated samples, the analysis has been restricted to those samples whose effective carrier lifetimes were in the whole Δn range at least an order of magnitude lower than the effective lifetimes of the corresponding control sample. It is in fact this constraint which in principle defines a lower limit for the contamination level of each impurity, as lower contamination levels

would result in surface-affected lifetime measurements. Nevertheless, due to the high quality of the applied SiN surface passivation (see Sect. 4.2.2D) almost none of the investigated metal-contaminated samples has been significantly affected by surface recombination.

Carrier trapping. At low injection densities SRH recombination may be screened by superposed external carrier trapping. As discussed in Sect. 3.3.1A, distortions arising from external trapping are easily identified from an abrupt lifetime increase towards low injection densities. If the measured IDLS curve is only distorted in the Δn region below 10^{13} cm^{-3} , the trap-affected data are simply discarded. If a broader Δn region is affected, the trapping effect is analytically eliminated from the data by means of the bias-light correction [15] discussed in Sect. 3.3.1A. This allows the range of usable data to be extended by about an order of magnitude in terms of Δn , the lower bound being given by the carrier density at the bias point (see Sect. 3.3.1A).

Intrinsic recombination. At high enough injection densities, SRH recombination is always screened by CE-Auger recombination which manifests itself in a steep lifetime decrease in the measured IDLS curve. Since CE-Auger recombination is accurately described by the theoretical model given in Sect. 1.3.1 and since this model is easily adjusted to the measured data, CE-Auger recombination is routinely subtracted from the measured IDLS curves, even if the steep lifetime decrease is not reached.⁹ As discussed in Sect. 3.3.1B, this may push the range of usable data reflecting SRH recombination by about an order of magnitude higher in terms of Δn .

SRH model – validity check. The validity of standard SRH theory is verified on the basis of the N_{crit} criterion [16] discussed in Sect. 1.4.3C. To exclude hidden distortions of the SRH lifetime curve due to internal trapping arising from the recombination center itself, the LS investigations are restricted to samples which fulfill $N_t \ll N_{crit}^{LLI}$. The N_{crit} criterion thus in principle defines for each impurity an upper limit on the tolerable contamination level N_t . For a few critical samples with $N_t > N_{crit}^{LLI}$, the IDLS analysis is restricted to those Δn ranges which fulfill $N_t \ll N_{crit}(\Delta n)$. It should be emphasized that these critical samples cannot be investigated by means of TDLS, as this technique operates under LLI conditions, i.e., in the injection range where distortions due to internal trapping have to be expected.

⁹ The CE-Auger-corrected lifetime curve reflects the SRH lifetime and directly results from $1/\tau_{SRH} = 1/\tau_{eff} - 1/\tau_{CE\text{-}Auger}$.

C Procedure for spectroscopic evaluation of IDLS data

Once the pure SRH lifetime, related only to the defect states of the impurity under investigation, is extracted in a maximum Δn range (steps 1–3) and verified to reflect only the recombination properties of these defect states (step 4), the boundary conditions for the SRH model have to be adjusted, which represents the first step of the spectroscopic IDLS analysis. The problem is that an accurate SRH simulation of experimental IDLS curves in the whole Δn range often requires two independent SRH centers.

SRH model – adjustment. As discussed in Sect. 3.3.1C, the use of a two-defect SRH model requires for reasons of transparency the introduction of a defect weighting factor X , which allows careful control over the relative impact of both defect levels on the LLI part of the lifetime curve. In order to determine the optimum X factor, the two-defect SRH model is adjusted to the IDLS curve by means of a least squares fit for specified but gradually varied X factors, assuming a deep level around mid-gap and a shallow level near one of the band edges, whose exact energies are arbitrary but fixed. The optimum X factor is then identified at that point where the overall least squares error of the fit reaches its minimum (see Fig. 3.12b).

Since the spectroscopic IDLS investigations aim primarily to completely characterize the defect level dominating the LLI part of the lifetime curve, an alternative to the two-defect SRH simulation is a one-defect SRH simulation in a reduced Δn range. In this case the upper bound of the fitted Δn range has to be determined. The accuracy of this simplification and its robustness towards variations of the upper bound of the fit range have been demonstrated in Sect. 3.3.1C. Note that a one-defect simulation in the presence of a second defect level is only applied if the impact of the second defect is limited to a small Δn region under HLI. The fitted Δn range is then chosen as broad as possible while still allowing an accurate one-defect simulation of the measured data.

DPSS analysis. The detailed SRH analysis of the IDLS curve finally consists in the determination of the defect parameter solution surface (DPSS) which is associated with the defect level dominating the LLI part of the IDLS curve. The DPSS analysis is performed according to the procedure described in Sect. 3.3.2B, taking into account the boundary conditions of the SRH model, determined within the pre-analysis. If a two-defect SRH model is required, the parameters of the second defect are optimized once within the pre-analysis and then kept at fixed values within the whole DPSS analysis.

There are two reasons why the spectroscopic IDLS investigations are primarily focused on the characterization of the defect level dominating LLI. On the one hand, it is the relevant defect level for photovoltaic appli-

cations, as it dominates recombination under cell operating conditions. On the other hand, it is the relevant defect level for a combined analysis of IDLS and TDLS, since TDLS operates under LLI conditions. According to Sect. 3.6, an unambiguous identification of the defect level dominating LLI should thus be achievable.

4.2.5 TDLS – measurement and modeling procedure

A Relevant and covered T range, applied T cycles

Although the Arrhenius increase of a TDLS curve contains most of the defect-specific information, the detailed analysis in Sect. 3.5 revealed the importance of the low- and the high-temperature part for an accurate spectroscopic TDLS result: while the low-temperature part allows an underlying $\sigma(T)$ -model to be detected (see Fig. 3.34), the high-temperature part, which is dominated by intrinsic conduction, may provide additional spectroscopic information (see Fig. 3.48). In the relevant doping range from 10^{14} to 10^{16} cm^{-3} the onset temperature of the Arrhenius increase has been found to vary between 200 and 300 K for a shallow symmetric defect level with $\Delta E_i = 0.2 \text{ eV}$, being higher for deeper levels (see Fig. 3.50), while the onset temperature of the TDLS bend due to intrinsic conduction has been predicted between 450 and 600 K (see Fig. 3.40). In view of these theoretical limits on the T range of the Arrhenius increase, the T range from 100 to 600 K, which is experimentally accessible with the cryostat used in the present work, is proved to be sufficiently large to allow accurate TDLS investigations of arbitrary defect levels, since, in addition to the Arrhenius increase, both the low- and high-temperature parts of the TDLS curve are always accessible.

Problems concerning the use of TDLS may arise from temperature-induced changes of the defect configuration, which may be caused by a metastable defect structure (reversible effect) or by impurity precipitation (irreversible effect), respectively. In order to detect such defect transformations, which is important to avoid distortions of the spectroscopic TDLS result, TDLS data have been routinely recorded during both the heating and the cooling cycles throughout the work. Whenever the applied temperature cycles are not explicitly discussed, the displayed TDLS curves have been identically reproduced in both cycles, which clearly indicates a stable defect structure. Metastable defect structures, on the other hand, as they are observed, e.g., for the Cz-specific (see Sect. 5.5) or the iron-related (see Sect. 4.6) defects, are directly reflected in a hysteresis of these two TDLS curves measured subsequently, which may give deeper insight into the defect structure.

B Impact of the injection level on TDLS curves: optimum measurement conditions

The TDLS measurements have all been performed by means of the MW-PCD technique, described in Sect. 2.3. As the injection conditions of the lifetime measurement there have to be adjusted manually via a steady-state bias light, whose intensity may be varied from 0–2 suns, the question arises as to which is the optimum bias intensity. As TDLS is based on the fundamental prerequisite of low-level injection, the lifetime measurements should ideally be performed under zero bias, though small bias values can be tolerated as the SRH lifetime is predicted to be constant under LLI conditions.

However, the adjustment of the optimum bias level may become crucial if external carrier trapping is superposed, which is often the case. As discussed in Sect. 3.3.1A, trapping effects may completely screen the recombination properties of the defect center under LLI conditions and thus have to be detected and avoided to avoid distortions of the TDLS curve. Using the PCD technique, superposed carrier trapping can easily be detected from the qualitative shape of the PCD transients, as the relatively slow detrapping of minority carriers causes a long tail in the photoconductance decay as soon as the excess carrier density falls below a threshold value given by the trap density. The zero-bias PCD transient displayed in Fig. 4.5a represents an example (circles). To avoid the trapping effect in the PCD signal, the traps have to be saturated with carriers injected by a steady-state bias light. In the present case a trapping-free mono-exponential photoconductance decay (triangles) is achieved for a bias illumination with 0.025 suns (=2.5 V), which represents a typical value and shows that the bias intensities required for trap saturation are very low. The fact that the slope of the trapping-free transient (triangles) nearly coincides with the slope of the starting decay of the trapping-affected transient (circles), shows that this part of the distorted PCD transient basically reflects the recombination properties of the defect.

The effective carrier lifetimes extracted from the starting and the mono-exponential decays are displayed in Fig. 4.5b as a function of the applied bias intensity. While the strong lifetime increase above 3V bias (gray triangles) directly reflects the injection dependence of the SRH lifetime, being characteristic of the underlying defect center at 30°C, the slight lifetime decrease observed below 2V bias (gray circles) reveals that the carrier lifetimes extracted from the starting decay of trapping-affected PCD transients are still enhanced due to the superposed trapping effect.¹⁰ As a

¹⁰ Since there is no other physical mechanism which can produce a decreasing injection dependence of carrier lifetime under LLI conditions, the observed decrease definitely has to

consequence, the required recombination lifetime under LLI conditions has to be identified with the lifetime value reached in the minimum of the bias variation (black star). Being extracted from a trapping-free PCD transient, this value definitely represents the pure recombination lifetime, the LLI condition still being satisfied, as the applied bias intensity is low (<0.1 suns). The bias variation provides a simple criterion to prove the LLI condition for the optimum bias position. If a slight increase in the bias intensity above its optimum value does not result in a significant change of carrier lifetime, as in the present case (see Fig. 4.10b), the determined bias position is proved to be localized in the LLI region, as theory only predicts an injection independence of the SRH lifetime there (see Sect. 3.2.3).¹¹

Having proved the quality of the lifetime determination at an intermediate temperature of 30°C , the impact of temperature on the bias variation and the optimum result has to be examined. As the trapping effect becomes stronger at low temperatures, the required bias level to ensure its avoidance increases with decreasing temperature. At very low temperatures the trapping effect may become so strong that it dominates the whole PCD transient, whose mono-exponential decay then reflects the asymptotic lifetime introduced in Sect. 3.5.2. Although the trapping effect then becomes undetectable in the PCD signal, it is easily identified in the final TDLS curve as discussed in detail in Sect. 3.5.2. However, it has to be emphasized that the special problem of undetected carrier trapping may only occur at very low temperatures. At high temperatures, on the other hand, the trapping effect in general completely vanishes, which allows the LLI-SRH lifetime to be accurately measured under zero bias.

Concerning the satisfaction of the LLI condition, the use of a bias light implies the problem that the resulting injection level strongly depends on the lifetime level itself, which may vary by more than an order of magnitude within the TDLS curve.¹² As the lifetime level is low in the low-temperature part of the TDLS curve, the LLI condition is easily fulfilled even at elevated bias levels, which may be required to avoid trapping effects

be attributed to superposed carrier trapping in spite of the fact that the carrier lifetimes are determined from the starting decay of the PCD transients. Note that extracting the lifetime values from the tail of the PCD transients would result in a much stronger decrease, as it is known for trapping-affected QSSPC data (see, e.g., Fig. 4.10a).

¹¹ Strictly speaking the SRH lifetime is predicted to be injection-independent under both LLI and HLI conditions. However, as HLI conditions can be excluded, the observed injection independence unambiguously identifies the optimum bias point to be located in the LLI region.

¹² Apart from the relative changes of the lifetime level within the TDLS curve, the overall lifetime level depends on the defect concentration. If superposed carrier trapping requires the use of a bias light, the LLI condition is more easily satisfied in samples with higher defect concentration due to the then reduced lifetime level.

(see above). However, at high temperatures, the LLI condition has to be carefully controlled due to a strongly increasing lifetime level within the Arrhenius increase. Fortunately, in most cases this problem sorts itself out, as a bias illumination is no longer required due to the disappearance of the trapping effect (see above).

In conclusion, the accurate determination of LLI-SRH lifetime requires a small variation of the bias light (under low intensities) at each temperature. Whenever trapping effects are observed, the LLI-SRH lifetime has to be

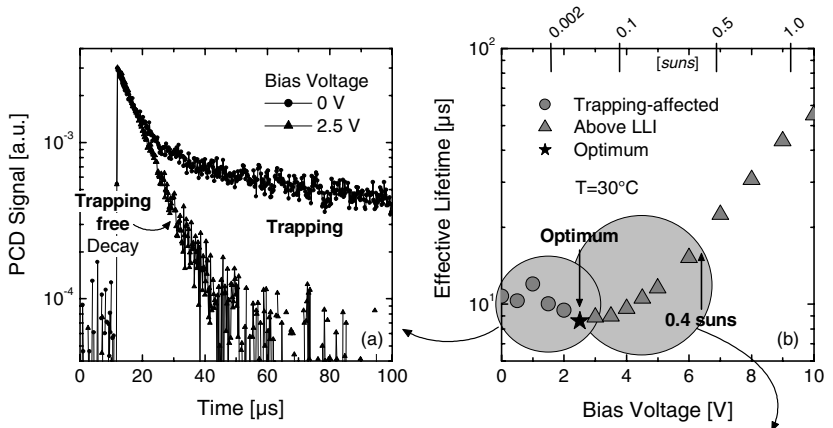


Fig. 4.5. Optimum conditions for the PCD lifetime measurements. (a) Characteristic shapes of PCD transients: distortions due to superposed carrier trapping (*circles*) can and have to be avoided by applying a bias light of low intensity (*triangles*). (b) Effective carrier lifetime at 30°C as a function of the bias voltage (the corresponding bias intensities are indicated on the *top axis*): the minimum lifetime value of this variation is identified with the LLI-SRH lifetime that TDLS is based on (optimum). (c) Impact of the illumination conditions on the TDLS curve (*T*-normalized). The bias light intensity being kept at a fixed value of 0.4 suns (*gray circles*) instead of being adjusted to its optimum value at each temperature step [*black circles*, making use of the procedure shown in (b)], this leads to a significant distortion of the Arrhenius increase, as the LLI condition is no longer ensured [*big circle* in (b)]. The measurements have been performed on a titanium-contaminated sample.

identified with the lifetime minimum of the bias variation. Only in the trapping-free temperature range can the LLI-SRH lifetime be directly determined for zero bias. This measurement procedure is adopted throughout the work. It should be emphasized again that the applied procedure of an optimized bias illumination allows a physical elimination of the trapping effect and thus ensures an accurate experimental determination of the recombination lifetime under LLI conditions in the whole temperature range.

To demonstrate the relevance of the bias optimization, Fig. 4.5c shows two TDLS curves which have been measured subsequently on the same sample, the bias level first being optimized at each temperature according to the described procedure (black circles) and second being kept at a fixed value of 0.4 suns (gray circles). As can be seen, the second simplified procedure leads to a significant distortion of the Arrhenius increase,¹³ as the LLI condition is no longer fulfilled over the whole temperature range. This is exemplified for 30°C by the bias variation displayed in Fig. 4.5b (big gray circle). Thus accurate spectroscopic TDLS results are only achieved if the proposed procedure to determine the LLI-SRH lifetime is applied as in the present work.

A final remark concerns the correct interpretation of the lifetime data obtained from a bias-dependent measurement technique such as the PCD technique used. As mentioned in Sect. 2.3, bias-dependent lifetime measurements actually result in differential recombination parameters which may deviate significantly from the true physical recombination parameters [11, pp. 74-78]. However, deviations between the differential and physical recombination parameters only have to be expected under medium and high injection levels, whereas under low injection levels both quantities coincide for theoretical reasons [11, p. 77]. This ensures that the lifetime values measured for the TDLS curves are not distorted by this measurement problem, but direct reflect the physical recombination lifetime.

C Impact of surface recombination on TDLS curves

However, it has to be kept in mind that the measured carrier lifetimes represent effective lifetimes. As the impact of surface recombination strongly depends on the lifetime level, which increases by more than an order of magnitude within the TDLS curves due to the thermally-induced deactivation of the bulk defect centers, the impact of surface recombination on the TDLS curves has to be investigated separately in spite of the excellent surface passivation quality of the silicon nitride films used (see Fig. 3.3).

¹³ The observed discrepancy between the two TDLS curves varies with temperature just as the injection dependence of SRH lifetime does (see Fig. 3.6b).

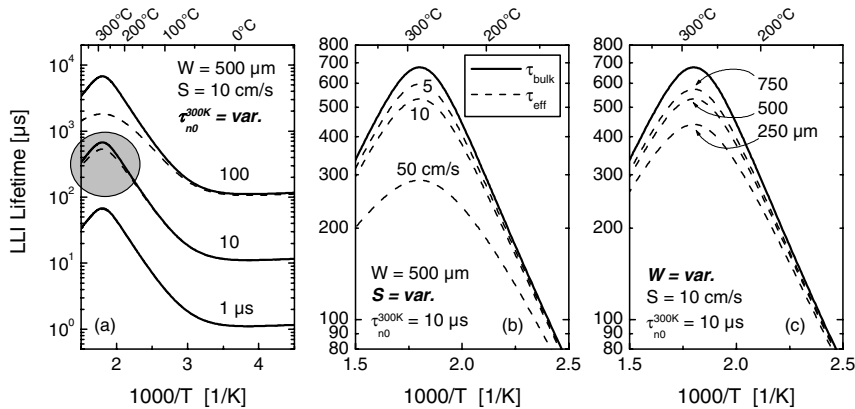


Fig. 4.6. Impact of surface recombination on the TDLS curve. The bulk lifetime (*solid lines*) is calculated for a symmetric defect level at $E_C-E_t=0.3$ eV in *p*-type silicon with a doping concentration of $N_A=10^{15}$ cm $^{-3}$. The effective lifetime (*dashed lines*) is calculated according to Eq. (4.2). Based on the assumption of a temperature-independent SRV, the calculations represent worst-case estimates of the surface impact. (a) Impact of the lifetime level for a medium SRV and wafer thickness. (b) Impact of the SRV for a medium wafer thickness and lifetime level. (c) Impact of the wafer thickness for a medium SRV and lifetime level.

A quantitative estimate of the surface impact may be directly achieved from Eq. (1.52), which accurately describes the relation between the measured effective lifetime and the actual bulk lifetime if the SRV is sufficiently low. Thus the temperature dependence of the effective lifetime measured under LLI has been calculated according to

$$\frac{1}{\tau_{eff}^{LLI}(T)} = \frac{1}{\tau_{SRH}^{LLI}(T)} + \frac{2S}{W} \quad (4.2)$$

assuming a temperature-independent SRV. A comparison of the real (dashed lines) and the ideal (solid lines) TDLS curves, based on the effective lifetime and the pure SRH lifetime, respectively, is displayed in Fig. 4.6, assuming a *p*-type doping of $N_A=10^{15}$ cm $^{-3}$. The underlying LLI-SRH lifetime has been calculated for the purposes of example for a symmetric defect level at $E_C-E_t=0.3$ eV using the general SRH equation (3.6) on the basis of the advanced *T*-model (see Sect. 3.5.4).

As expected, the deviations between the real and the ideal TDLS curves significantly depend (a) on the overall lifetime level [given by $\tau_{n0}(300$ K)], (b) on the magnitude of the SRV and (c) on the wafer thickness. The impact of all three variables is displayed separately in the three diagrams,

the two other variables always being fixed at an intermediate value. To ensure that the simulations directly reflect the experimental situation in the present work, these intermediate values have been chosen as follows: the intermediate thickness of $W=500\text{ }\mu\text{m}$ represents an average value, as the thickness of the individual TDLS samples varied between 400–600 μm . The intermediate SRV of $S=10\text{ cm/s}$ represents an upper bound for the SRV of the silicon nitride, as only samples with a doping concentration below $5\times10^{15}\text{ cm}^{-3}$ have been investigated by means of TDLS (see Fig. 4.3). In spite of the experimental uncertainty of the SRV under LLI (see Sect. 4.2.2D), this upper bound seems to be conservative in the relevant doping range, as the SRV values determined in the transition region between low and medium injection densities have been found to be lower by an order of magnitude (see Fig. 4.3). Finally, the intermediate lifetime level of $\tau_{n0}(300\text{ K})=10\text{ }\mu\text{s}$ represents once again an average value, as the lifetime level of the investigated samples varied at room temperature from 4–20 μs .

For the intermediate values $S=10\text{ cm/s}$ and $W=500\text{ }\mu\text{m}$, Fig. 4.6 reveals that only those parts of the TDLS curve which exceed a lifetime threshold of 300 μs are affected by surface recombination. As can be seen from Fig. 4.6a, the achievable accuracy of the TDLS investigation may be directly related to the measured room temperature (RT) lifetime, which is mainly determined by the contamination level, and allows a trisection of the lifetime range. While the TDLS curves for RT lifetimes around 1 μs are completely unaffected by surface recombination, those for RT lifetimes around 10 μs already show a slight reduction in the high-temperature part of the TDLS curve but still exhibit an almost unaffected Arrhenius increase. However, for RT lifetimes around and above 100 μs , massive distortions of the Arrhenius increase have to be expected, which makes accurate TDLS analysis impossible. As the lifetime level at the onset temperature of intrinsic conduction (“TDLS peak”) depends significantly on the position of the Arrhenius increase (see Figs. 3.44 and 3.45), all variations of the defect and material parameters which move the Arrhenius increase to higher temperatures will reduce the T range, in which the TDLS curve is affected by surface recombination and vice versa.

However, all these considerations are based on the assumption of a temperature-independent SRV. Although the temperature-dependence of SRV has not been measured in this work, a simple theoretical argument allows one to estimate how the SRV changes with temperature. As surface recombination occurs via a continuum of defect states at the Si:SiN interface and is thus subject to SRH theory (see Sect. 1.4.4), it has to be expected, analogously to SRH recombination via bulk defects, that the recombination activity of the interface traps will decrease with increasing

temperature, which should be directly reflected in a decreasing SRV. Although the degree of the temperature-induced SRV improvement cannot be quantified, it may at least be concluded that the SRV does not increase above its room-temperature value. This directly implies that the TDLS curves calculated for $S = 10 \text{ cm/s}$, which has been found as an upper bound for the room-temperature SRV over the doping range relevant to TDLS, represent a very conservative worst case estimate concerning the impact of surface recombination on the TDLS curves in the present work. Thus the actual threshold lifetime above which surface recombination starts to affect the measured TDLS curve, i.e., the temperature-dependent effective lifetime, most probably lies significantly higher than $300 \mu\text{s}$, which has been determined from Fig. 4.6 under the assumption of a temperature-independent $S = 10 \text{ cm/s}$. As a consequence, not only the TDLS curves for RT lifetimes around $1 \mu\text{s}$, but also those for RT lifetimes around $10 \mu\text{s}$ should be completely unaffected by surface recombination and should thus allow an accurate application of the advance TDLS analysis. As all TDLS curves measured in the present work belong to one of these two classes, any impact of surface recombination on the TDLS curves can most probably be excluded throughout the work. However, a surface impact should be easily identified in a TDLS curve as it is supposed to result in a vertical gap between the measured and the modeled “TDLS peaks”, the position of the two peaks being identical (see Fig. 4.6). The fact that such deviations between the measured and modeled TDLS bend due to intrinsic conduction have not been observed supports the conclusion of the present section that surface effects are not relevant to the TDLS investigations of the present work.

D Procedure for spectroscopic evaluation of TDLS data

In the previous sections it has been shown that the measured effective lifetime under LLI is affected neither by superposed carrier trapping, which can be excluded by the use of an optimized measurement procedure (see Sect. 4.2.5B), nor by surface recombination, whose impact proved to be negligible for the high-quality silicon nitride passivation and the contamination levels relevant to the present work (see Sect. 4.2.5C). As the impact of intrinsic recombination can generally be excluded under LLI conditions (see Sect. 3.3.1B), the measured effective LLI lifetime reflects pure SRH recombination via the defect centers in the bulk and can thus be directly identified with the LLI-SRH lifetime in the whole temperature range. Hence, the measured TDLS curves can be directly subjected to a detailed SRH analysis. This is done by means of the advanced TDLS analysis developed in Sect. 3.5, whose procedure should be briefly summarized in the following:

1. SRH modeling for a MinBH defect (model optimization). Accurate modeling of the TDLS curve typically requires an optimization of the SRH model configuration which is performed on the basis of an assumed MinBH defect, as an optimum MinBH fit can always be achieved due to the additional degree of freedom (see Sect. 3.5.6A).

- **Carrier trapping (at very low temperatures).** Although carrier trapping can be excluded in most of the T range by the optimized measurement procedure, it may be unavoidable at very low temperatures (see Sect. 4.2.5B). However, as discussed in Sect. 3.5.2, trapping is easily identified in measured TDLS curves, as it results in a strong increase of the asymptotic lifetime, which allows the trapping-free T range to be accurately identified.
- **$\sigma(T)$ -model.** As discussed in Sect. 3.5.1, the underlying temperature dependence of the capture cross-sections is accurately determined by modeling the low-temperature part of the TDLS curve in that T region where trapping effects can be excluded.
- **Advanced T -model.** The SRH model, used as a standard for TDLS modeling, does not only take into account the respective $\sigma(T)$ -dependence of the underlying defect center, but is in addition based on the advanced T -model (see Sect. 3.5.4). The validity of this model configuration, which is often referred to as the *advanced SRH model*, has already been demonstrated in Sect. 3.5.5 and will be further confirmed.
- **N_{dop} control.** The accuracy with which the measured position of the TDLS bend due to intrinsic conduction coincides with the position predicted on the basis of the advanced T -model allows an independent cross-check of the doping concentration and thus prevents unrecognized transfer of N_{dop} inaccuracies to the defect parameter k . (see Sect. 3.5.6B)

2. SRH modeling for a MajBH defect. By using the optimized SRH model configuration determined from the MinBH fit, we make the attempt to model the TDLS curve assuming a MajBH defect. If this attempt fails, the defect is unambiguously identified in the MinBH. Otherwise, the TDLS analysis yields two equivalent solutions for the defect parameters, one in each band gap half (see Sect. 3.5.6A).

3. Determination of the DPSS diagram. To estimate the accuracy of the spectroscopic TDLS results quantitatively, we finally determine the associated DPSS diagram according to the procedure described in Sect. 3.5.7, which allows direct extraction of tolerance bands for the determined defect parameters E_t and k . Moreover, the DPSS diagram is used to evaluate the consistency of the spectroscopic results obtained from TDLS and IDLS with maximum transparency (see Sect. 3.6).

4.3 Molybdenum

Molybdenum belongs to the 4d transition metals, which have in the past been less thoroughly investigated than the 3d transition metals.¹⁴ Since molybdenum tends neither to precipitate nor to pair with other impurities, it is incorporated in electrically active form on interstitial lattice sites [1]. This well defined defect structure gives rise to a simple electronic structure, which consists of only one donor level in the lower half of the silicon band gap, whose energy level has been consistently characterized as $E_t - E_V = 0.30 \text{ eV}$ by different authors [1, 17]. Thus, from a physical point of view, the molybdenum contamination in silicon represents an ideal system to assess the performance of lifetime spectroscopy and to verify the theoretical predictions. Concerning the capture properties, only the majority capture cross-section has been determined so far, as for most metal impurities. Since the important characteristic of the capture asymmetry is thus unknown for the molybdenum donor level, the lifetime spectroscopic investigation also aims to fill this gap in our knowledge of the defect properties of molybdenum.

From a technological point of view, molybdenum is of minor importance as there are no serious contamination sources known in a modern production line [1]. However, a molybdenum contamination may be introduced during the pulling process of Cz crystals. Only recently the heat shields of the Cz pullers have been identified as a potential source [18]. But due to the limited sensitivity of the standard diagnostic tools, it has not been possible to sort out its significance conclusively. A clarification should be achievable by means of lifetime spectroscopy in a similar way to the investigation presented in the following.

4.3.1 Advanced TDLS analysis

The lifetime spectroscopic investigation is performed on two samples, which have been contaminated with molybdenum during crystal growth, as discussed in Sect. 4.2.1. The samples are investigated by conducting a pure TDLS analysis (see Sect. 4.3.1), a pure IDLS analysis (see Sect. 4.3.2), and the combined analysis of TDLS and IDLS (see Sect. 4.3.3). In Sect. 4.3.4, the lifetime spectroscopic results are finally compared with DLTS results, measured on a parallel sample and obtained from the literature.

¹⁴ The reason is that almost all of the main impurities detected in wafers during device production belong to the 3d transition metals [1].

A Superposed effects and their impact on the MinBH/MajBH modeling

Figure 4.7 shows the TDLS curve which has been measured by means of the MW-PCD technique on an intentionally molybdenum-contaminated silicon sample. If advanced TDLS analysis is applied, the accuracy of the defect parameter determination strongly depends on the accuracy of the SRH fit. The accuracy of different configurations of the SRH model have already been investigated in Sect. 3.5.5, the modeling there focusing on a validation of the SRH model and thus being restricted to MinBH defects.

The two major results of this investigation are displayed in Fig. 4.7a and should be summed up here briefly. Concerning the low-temperature part of the TDLS curve ($T < 260$ K), it turned out that accurate modeling is not achieved for the simple SRH model (thin dashed line in Fig. 4.7a) but requires the insertion of a temperature-dependent capture cross-section (thin solid line in Fig. 4.7a). The observed decrease in the capture cross-section with increasing temperature follows a power law given by $\sigma(T) = \sigma_0 \times T^\alpha$ with an exponent $\alpha = -1.5$. Giving insight into the physical mechanism of carrier capture (for a survey see Sect. 3.5.1A), this $\sigma(T)$ -model has been found to be characteristic either for a cascade capture process [19], which is only relevant to shallow Coulomb-attractive centers, or for an excitonic Auger capture process [20], which is observed for centers of arbitrary depth and charge state. However, since the cascade mechanism is unlikely due to an energy depth of 0.32 eV of the underlying molybdenum defect center (see below), the excitonic Auger mechanism has been identified to be the dominant process, in all likelihood, especially as it is favored by the measurement conditions used, being based on the optical injection of electron-hole pairs (see discussion in Sect. 3.5.1B). Concerning the high-temperature part of the TDLS curve ($T > 500$ K), it has been shown in Sect. 3.5.5 that an accurate SRH modeling of the observed TDLS bend due to intrinsic conduction (open triangles in Fig. 4.7) is achieved on the basis of neither the basic T -model (dashed line) nor the standard T -model (dash-dotted line) but requires the complete advanced T -model (solid line) as a basis. The reason is that the observed low onset temperature for intrinsic conduction cannot be explained by the T -dependence of the equilibrium carrier concentrations $p_0(T)$ and $n_0(T)$ alone (see Sect. 3.5.3), but also necessitates as well the consideration of the temperature-induced narrowing of the silicon band gap $E_{gap}(T)$ (see Sect. 3.5.4).

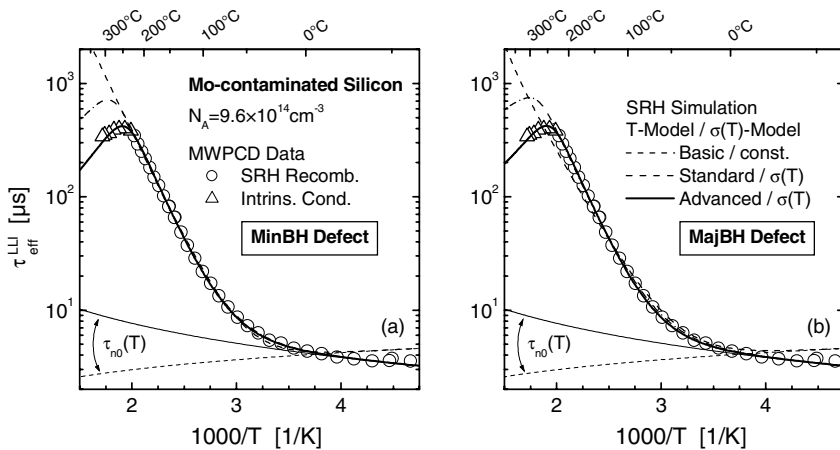


Fig. 4.7. TDLS curve (symbols) measured by means of the MW-PCD technique on an intentionally Mo-contaminated silicon sample ($[Mo] = 1.2 \times 10^{11} \text{ cm}^{-3}$, $N_A = 9.6 \times 10^{14} \text{ cm}^{-3}$) and different SRH simulations (lines). An accurate simulation below 260 K requires the insertion of a T -dependent capture cross-section (thin solid line). An accurate simulation of the Arrhenius increase requires (b) for MajBH defects the $\sigma(T)$ -model, while (a) for MinBH defects $\sigma = \text{const.}$ suffices. For an accurate modeling of the lifetime decrease above 500 K, induced by intrinsic conduction, not only the T -dependence of the majority carrier concentration (dash-dotted lines) has to be considered, but also the complete advanced T -model (solid lines).

Table 4.2. Extracted defect parameters (*bold numbers*) if the modeling of the TDLS curve in Fig. 4.7 is performed for different modifications of the SRH model (*first and second column*) assuming a MinBH defect and a MajBH defect, respectively. For each model those T regions were ignored in which the model does not allow even a qualitatively correct fit. Since the given χ^2 values are thus artificially reduced for fits on a reduced T range, the *numbers in parentheses* give the χ^2 values which were post-calculated for the whole T range from 210–580 K.

T-Model	$\sigma(T)$	Fitted T range [K]	MinBH defect			MajBH defect				
			$E_C - E_t$ [eV]	k	χ^2	Quality L M H	$E_t - E_V$ [eV]	k	χ^2	Quality L M H
Basic	Const.	260–500	0.34	5.1	0.05 (26)	$\times + \times$	0.28	arb.	0.73 (5.7)	$\times - \times$
Standard	$\propto 1/T^{1.5}$	210–500	0.31	1.2	0.05 (6.6)	$+ + \times$	0.31	arb.	0.05 (7.5)	$+ + \times$
Advanced	$\propto 1/T^{1.5}$	210–580	0.32	1.4	0.06	$+ + +$	0.32	~8	0.05	$+ + +$
Advanced	Const.	260–580	0.36	9.5	0.23 (0.6)	$\times + +$	0.29	~185	0.41 (0.8)	$\times - +$
		260–500	0.34	5.0	0.06 (0.9)	$\times + \times$				

The quality of the SRH fits is classified in:

L = Low-temperature region ($T < 260$ K).

M = Medium-temperature region ($T = 260$ –500 K).

H = High-temperature region ($T > 500$ K).

The attributes are:

$+$ = Good fit quality.

$-$ = Bad fit quality.

\times = T region not considered in the LSF optimization.

The details of the individual fits of the TDLS curve based on the different modifications of the SRH model are summarized in Table 4.2. In particular, these are the T boundaries of the fitting region, the quality of the fit and the extracted defect parameters. To avoid artificial distortions of the spectroscopic results, those T regions were ignored in the individual fits where the model under investigation did not even allow a qualitatively correct description of the observed T -dependence of carrier lifetime.

As long as the TDLS modeling is performed for a MinBH defect (see Fig. 4.7a), as done in the delineated model optimization of Sect. 3.5.5, the different configurations of the SRH model only affect the accuracy of the SRH fit in the low- or high-temperature region of the TDLS curve, while the Arrhenius increase itself is accurately described by either of the model variations, the set of defect parameters being individually optimized.¹⁵ However, according to Sect. 3.5.6, the attempt to model the TDLS curve for a MajBH defect is one of the decisive steps of the advanced TDLS analysis (see Fig. 4.7b). As expected from the reduced number of degrees of freedom of the SRH model in the case of an assumed MajBH defect, the model configurations, especially depending on whether the underlying $\sigma(T)$ -model is considered or not, gain a strong impact on the modeling of the linear Arrhenius increase. As shown by the dashed lines in Fig. 4.7a and b, the basic SRH model with temperature-independent capture cross-sections only allows a correct modeling of the Arrhenius increase for a MinBH defect, while that for a MajBH defect fails. The fact that the Arrhenius slope of the least-squares-optimized MajBH fit significantly deviates from the measured Arrhenius slope¹⁶ is reflected in a Chi^2 value of the MajBH fit which is increased by more than an order of magnitude compared to that of the MinBH fit (see first row in Table 4.2). From this observation it has been concluded in a previous work [21] that the relevant defect level of molybdenum is located in the upper half of the band gap. However, if the $\sigma(T)$ -model extracted from the low-temperature part of the TDLS curve is introduced into the SRH analysis, the electron capture time constant $\tau_{n0}(T)$, which is a simple scaling factor of the SRH lifetime, no longer decreases with increasing temperature (dashed line) but exhibits a slight increase (thin solid line). Since the two configurations of the SRH

¹⁵ This is reflected in similar Chi^2 values of around 0.05 for the different MinBH fits (see Table 4.2).

¹⁶ Whenever the SRH modeling is based the basic T -model, the fitted T range is reduced to 260–500 K. Since the IC-induced TDLS bend is thus ignored in the fit, the observed underestimate of the Arrhenius slope in the case of a MajBH defect purely results from an “incorrect” position of the measured Arrhenius increase on the $1/T$ axis. Provided the SRH model used considers all superposed effects (which is not the case for the basic T -model used here), such a fit result strictly indicates that the defect is not located in the MajBH.

model on the basis of the basic and the standard T -model are identical except for the T range of the IC-induced TDLS bend, the dash-dotted lines in Fig. 4.7a and b show that only the introduction of the additional T -dependence of $\tau_{n0}(T)$ allows the linear Arrhenius increase to be accurately modeled for both a MinBH and a MajBH defect with an energy depth of 0.31 eV. Since the quality of both fits is more or less the same, an unambiguous identification of the band gap half is no longer possible (see second row in Table 4.2).

A perfect modeling of the TDLS curve in the whole T range, including the Arrhenius increase and the TDLS bend due to intrinsic conduction, is achieved if the advanced T -model *and* the underlying $\sigma(T)$ -dependence are taken into account in the SRH model (solid lines in Fig. 4.7). Using this optimum model configuration, which is referred to in the following as the *advanced SRH model*, the equivalent MinBH and MajBH solutions for the molybdenum level are found to be located at the same energy depth $\Delta E_t = 0.32$ eV, though differing in the k factor by almost an order of magnitude (see third row of Table 4.2).

B DPSS analysis of the TDLS curve

In order to quantify the accuracy of the defect parameters determined for the MinBH and the MajBH solution, the tolerance of the fitting model towards slight fluctuations of the fitting parameters has to be investigated. This investigation is performed with maximum transparency by means of the DPSS analysis which has been introduced in Sect. 3.5.7. The defect parameter solution surface of the TDLS curve is defined by both the curves, DPSS- k and DPSS- Chi^2 , which are determined from least squares fits of the measured TDLS curve for specified but gradually varied energy levels E_C-E_t of the defect center. The pair of DPSS curves displayed as solid lines in Fig. 4.8b and c is obtained when the underlying SRH modeling of the TDLS curve is performed in the maximum T range from 210 to 580 K on the basis of the advanced SRH model, which has been identified as optimum in the previous section.

For the investigated molybdenum impurity, the DPSS diagram nicely illustrates the fact that the solutions obtained in the upper and the lower half of the band gap are identical in quality. This prevents an identification of the true band gap half and thus an identification of the symmetry factor k , which may be given by 1.4 and ~ 8 , respectively (white stars). However, since the two DPSS- Chi^2 minimums are located at almost the same distance from the nearest respective band edge, at least the energy depth of the molybdenum level is unambiguously determined with $\Delta E_t = 0.32$ eV.

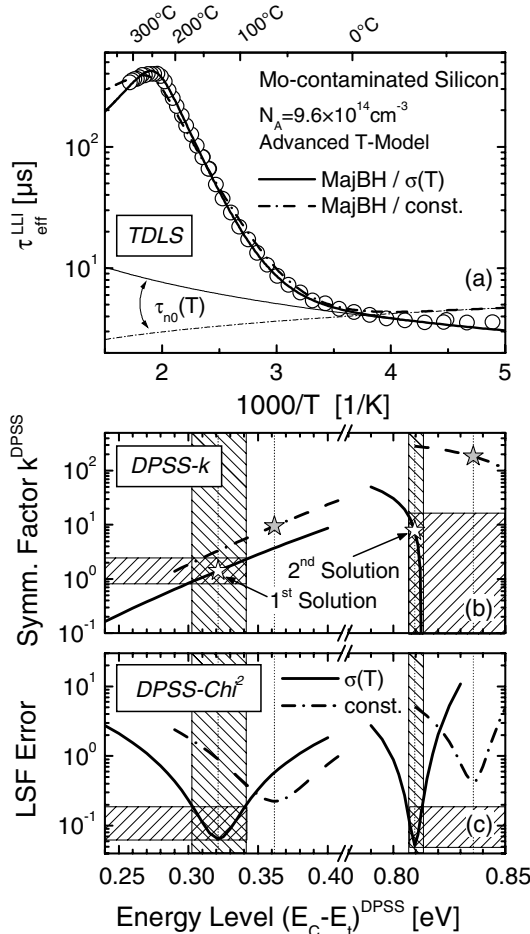


Fig. 4.8. Advanced SRH analysis of the TDLS data from Fig. 4.7 by means of the defect parameter solution surface (DPSS). The SRH modeling is based on the advanced T -model (optimum) with (solid lines, white stars) and without (dash-dotted lines, gray stars) taking into account the underlying $\sigma(T)$ -model. Comparing the minimum values of the displayed DPSS- Chi^2 curves allows the identification of both the best configuration of the SRH model and the true band gap half of the defect center. An error for the extracted defect parameters may be estimated from the width of each DPSS- Chi^2 curve (shaded areas).

The qualitative shape of the DPSS curves directly reflects the fundamental difference between MinBH and MajBH defects discussed in Sect. 3.5.6A. The steep DPSS- k and the narrow DPSS- Chi^2 curve observed for the MajBH solution directly arise from the fact that the onset temperature of the Arrhenius increase is independent of k for a MajBH defect. Analogously, the existing k -dependence for a MinBH defect leads to a moderate slope of the DPSS- k curve and to a broader DPSS- Chi^2 curve. This qualitative difference of the two DPSS branches finds expression in the errors of the extracted defect parameters, which may be deduced from the DPSS diagram. If a least squares error, which is increased by a factor of 3 above its optimal value of 5.5×10^{-2} , is defined as tolerable, the ranges of acceptable values are found to be given for the MinBH solution by $E_C - E_t = 0.30 - 0.34 \text{ eV}$ and $k = 0.9 - 2.3$ and for the MajBH solution by $E_t - E_V = 0.312 - 0.318 \text{ eV}$ and

$k=0.07\text{--}15$. This is illustrated in Fig. 4.8b and c by the shaded areas. As can be seen, for the MinBH solution, the two defect parameters are extracted with sufficient accuracy. For the MajBH solution, however, only the E_t determination is accurate while the k determination is uncertain. Actually, the branch of the DPSS- k curve in the lower band gap half only yields an upper bound for the possible k values. As discussed in Sect. 3.5.7B, this k confinement is directly related to the SRH modeling of the TDLS bend due to intrinsic conduction. Thus, if the TDLS bend had been ignored in the SRH fit, the k range for the MajBH solution would have been significantly expanded towards higher k values, the k uncertainty being even higher.

Since the use of the advanced T -model has been found in Sect. 3.5.4 (Fig. 3.38) to influence the position of the Arrhenius increase for MajBH defects, the actual impact of the $\sigma(T)$ -model on the final spectroscopic TDLS result is still unknown. This is why an additional pair of DPSS curves has been determined (dash-dotted lines), the TDLS curve being modeled for $\sigma=\text{const.}$ on the basis of the advanced T -model in a T range from 260 to 580 K as displayed in Fig. 4.8a. As can be seen from the DPSS- χ^2 curve in Fig. 4.8c, the advanced T -model enables a MinBH and MajBH fit of similar accuracy even if the $\sigma(T)$ -model is ignored, which has not been possible on the basis of the basic T -model¹⁷ (dashed lines in Fig. 4.7a and b). However, in spite of the reduced T region of the fit, the minimum χ^2 values achieved for the simplified model configuration (dash dotted lines) are increased by almost an order of magnitude compared to those achieved for the optimum model configuration (solid lines). This definitely identifies the advanced SRH model as the optimum. If the underlying $\sigma(T)$ -dependence is ignored, the MinBH solution is shifted 40 meV deeper into the band gap while the MajBH solution moves 30 meV towards the valence band edge (see gray stars in Fig. 4.8b and fourth row in Table 4.2). This large shift of the extracted defect parameters of both solutions demonstrates the significance of an accurate consideration of the $\sigma(T)$ -model.

¹⁷ A comparison of the spectroscopic results obtained for $\sigma=\text{const.}$ on the basis of the basic and the advanced T -model (see Table 4.2) reveals that a transition to the advanced T -model decreases the χ^2 value of the MajBH fit by almost a factor of 2 (from 0.73 to 0.41), while it increases the χ^2 value of the MinBH fit by almost a factor of 5 (from 0.05 to 0.23). As a result, the introduction of the advanced T -model alone enables MinBH and MajBH solutions of similar accuracy (see Fig. 4.8c). The improved quality of the MajBH fit can be mainly attributed to the fact that the Arrhenius increase slightly shifts to lower temperatures upon the transition to the effective-mass-based $N_{C,V}$ -models used within the advanced T -model (see Sect. 3.5.4). The decreased quality of the MinBH fit, however, results from the expansion of the fit range. This is confirmed by the fact that the basic and advanced T -models yield almost identical spectroscopic results if the T range affected by intrinsic conduction is ignored in both fits (fifth row in Table 4.2). The physical reason for the reduced quality of the MinBH fit is discussed along with Fig. 4.27.

In addition to the physical result, the investigation in Fig. 4.8 demonstrates a further strength of the DPSS analysis. Since the DPSS is a characteristic which depends on both the data set and the fitting model, the comparison of the DPSS- Chi^2 curves associated with the same TDLS curve but different fitting models always allows the best fitting model to be identified transparently.

C DPSS analysis of TDLS curves associated with different samples

In order to cross-check the spectroscopic results obtained for the molybdenum level so far, a second molybdenum-contaminated sample (Mo2) with a slightly increased doping concentration and a greatly increased defect concentration has been subjected to TDLS. Since the difference in the defect concentration induces a vertical shift of the two TDLS curves (see Sect. 3.2.1A), both lifetime curves have been normalized to the same lifetime value at 230 K, to ensure a direct identification of their spectroscopically relevant changes and similarities. The normalized TDLS curves are displayed in Fig. 4.9a.

At very low temperatures both samples exhibit a large lifetime increase (open stars) which may be attributed to superposed external carrier trapping (see Sect. 3.5.2). If the lifetime at low temperatures is identified with the asymptotic lifetime defined in Eq. (3.65), accurate modeling may be achieved in both cases for an additional shallow trap level at $E_C-E_t=0.15$ eV (thin lines).¹⁸ The lower temperature for the onset of carrier trapping in the more highly doped sample is directly reflected in a reduced density of trap centers, given by 6×10^{14} cm⁻³ in Mo1 (see Sect. 3.5.5) and 1×10^{14} cm⁻³ in Mo2. However, since the trapping effect screens the recombination lifetime, the affected T regions below 210 K (Mo1) and 180 K (Mo2), respectively, continue to be ignored in the SRH fit.

Since both TDLS curves coincide in the T range from 210 to 295 K,¹⁹ precisely the same T -dependence of the capture time constant $\tau_{n0}(T)$ (thin solid line) is found on both samples. This proves that the extracted $\sigma(T)$ -model with $\sigma(T)\propto T^{-1.5}$ definitely represents an additional fingerprint of the molybdenum level, which reflects the mechanism of carrier capture. Taking into account the decisive impact of the underlying $\sigma(T)$ -dependence on the TDLS result, which has been shown in Sects. 4.3.1A and B, this confirmation of the $\sigma(T)$ -model greatly increases the reliability of the spectroscopic results.

¹⁸ Note that the trap levels may reside either in the bulk or at the SiN/Si interface.

¹⁹ In the T range from 210 to 295 K, the carrier lifetime directly represents the minority carrier capture time $\tau_{n0}(T)$ since it is affected neither by carrier trapping (observed below 210 K) nor by the Arrhenius increase (observed above 295 K).

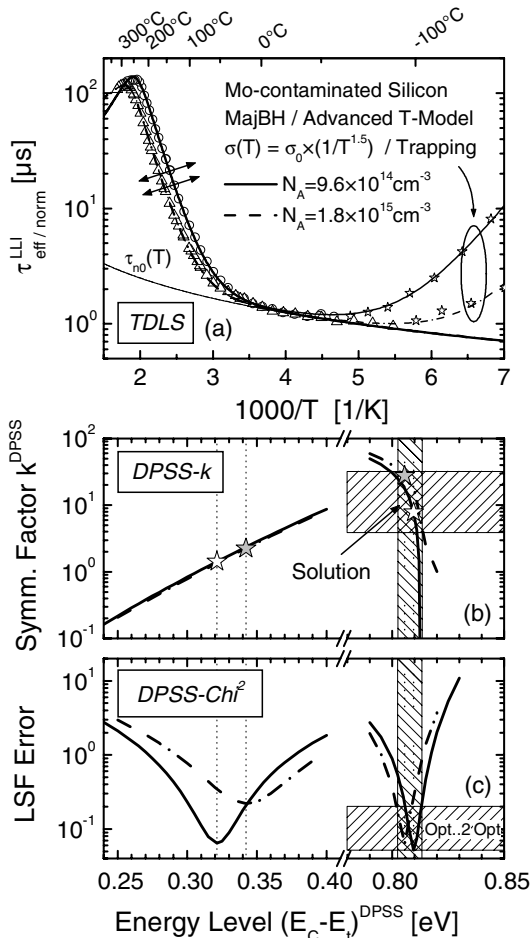


Fig. 4.9. Superposed DPSS analysis of TDLS curves measured on two molybdenum-contaminated samples with different doping and defect concentrations. (Note that the TDLS curves are normalized on the same lifetime value at 230 K.) The underlying SRH analysis is performed on the basis of the configuration of the SRH model which has been identified in Fig. 4.8 as the optimum. The predicted doping shift of the TDLS Arrhenius increase and the general validity of the $\sigma(T)$ -model used are shown in (a). From the coincidence of the DPSS- χ^2 minimum of the two samples in the MajBH, displayed in (c), the true band gap half of the defect center is identified. Due to the steep slopes of the DPSS- χ^2 curves in the MajBH, the defect energy level is determined with high accuracy while the accuracy of the k determination is reduced due to the strong E_i -dependence of the DPSS- k curves.

As expected for samples with the same contaminant, the Arrhenius increases of both TDLS curves are parallel, their common slope being directly related to the energy level of the molybdenum center. The fact that the Arrhenius increase and the onset of the lifetime decrease due to intrinsic conduction are shifted to higher temperatures for the more highly doped sample directly reflects the doping effect predicted in Figs. 3.8 and 3.37, respectively.

The quantitative spectroscopic analysis is suitably performed by means of the DPSS analysis, since a superposition of the two DPSS diagrams allows a direct and transparent verification of the consistency of the spectroscopic

results obtained from both TDLS curves.²⁰ Based on the DPSS analysis of the less doped sample presented in the previous section, Figs. 4.9b and c display the superposed DPSS diagram if the modeling of both TDLS curves is performed by means of the advanced SRH model considering the underlying common $\sigma(T)$ -model. The details of the fits and the spectroscopic results are summarized in Table 4.3 for both samples. As can be seen from Fig. 4.9b, the achieved accuracy of the SRH fit is nearly the same for both samples. Taking into account the fact that the fitted T range for the additional more highly doped sample covers 400 K, ranging from 190 to 590 K, the fit quality is remarkable and demonstrates the good performance of the SRH model configuration used. Moreover, for the more highly doped sample the Chi^2 value of the MajBH solution is decreased by almost a factor of 4 compared to the Chi^2 value of the MinBH solution, which points towards a localization of the relevant molybdenum level in the lower band gap half.

This assumption is strongly supported by the fact that the DPSS- Chi^2 minimums of the two samples nearly coincide in terms of their energy position for the MajBH solution, while they deviate by 20 meV for the MinBH solution. If the energy values of the two MajBH solutions are averaged, the energy of the relevant molybdenum level is determined with high accuracy to be $E_t - E_V = 0.317 \pm 0.003$ eV. However, it has to be stressed that the energy difference of the two MinBH solutions is too small to allow the upper band gap half to be definitely excluded as a possible location of the molybdenum level.

Table 4.3. Spectroscopic results (***bold numbers***) obtained from the advanced DPSS analysis of two TDLS curves measured on two different molybdenum-contaminated samples (see Fig. 4.9). Note that the SRH modeling is based on the advanced T -model, which has been identified in Fig. 4.7 as the optimum configuration of the SRH model. The underlying $\sigma(T)$ -model is found to be identical for both samples. The coincidence of the DPSS- Chi^2 minimums of the two samples in the MajBH points towards a localization of the defect level in the lower band gap half.

Material parameter ID	Fit parameter		$\sigma(T)$	Fitted T range [K]	MinBH defect		MajBH defect	
	N_A [cm ⁻³]	N_t [cm ⁻³]			$E_C - E_t$ [eV]	k	Chi^2	$E_t - E_V$ [eV]
Mo1	9.6×10^{14}	1.2×10^{11}	Advanced	$\propto 1/T^{1.5}$	210–580	0.321	1.4	0.06
Mo2	1.8×10^{15}	1.5×10^{12}	Advanced	$\propto 1/T^{1.5}$	190–590	0.342	2.3	0.22

²⁰ For independent TDLS curves dominated by the same defect level, the minimums of the associated DPSS- Chi^2 curves are expected to coincide in terms of their energy position either in the MinBH or the MajBH, which identifies the true energy position of the defect level. At this point the DPSS- k curves are expected to intersect in a common intersection point which yields the true k factor.

Unfortunately the agreement of the k factors within the two pairs of solutions does not clarify the situation (white and gray stars). While the k values of the MinBH solutions deviate by less than a factor of 2, those of the MajBH solutions deviate by more than a factor of 3. The assessment of this result has to take into account the fact that the k determination exhibits a high precision in the case of the MinBH solution, while it is subject to a strong inherent uncertainty in the case of the MajBH solution (see previous section). Against this background the observed k discrepancy between the MajBH solutions must not be overvalued and at least does not contradict a localization of the molybdenum level in the lower band gap half.

It can be concluded that the spectroscopic results obtained from the two independent TDLS curves are consistent and point towards a localization of the molybdenum level in the lower band gap half. Nevertheless, even the combined analysis of the TDLS curves does not allow an unambiguous identification of the true band gap half and an accurate determination of the symmetry factor k .

4.3.2 Advanced IDLS analysis

In order to show unambiguously which of the two solutions obtained from the advanced TDLS analysis provides the true defect parameters, the less doped molybdenum-contaminated sample of the TDLS investigation (Mo1) has been subjected to an IDLS experiment.

A Superposed effects and data pre-analysis

Figure 4.10a displays the IDLS curve measured by means of the QSSPC technique (open symbols). In the following, the necessary IDLS pre-analysis outlined in Sect. 4.2.4A should be presented in more detail, its presentation in the following sections being reduced to the results only. As can be seen from the large lifetime increase towards low injection densities, the measured lifetime curve (open symbols) is affected by superposed carrier trapping, which completely screens SRH recombination for injection densities below $2 \times 10^{13} \text{ cm}^{-3}$. To eliminate the trapping effect, the lifetime data have been corrected by means of the bias-light correction (see Sect. 3.3.1A [15]) whose impact is displayed in Fig. 4.10a for different bias intensities (lines). According to the guidelines given in Sect. 3.3.1A, the optimum correction is achieved for 0.1 suns (closed symbols) since then the corrected lifetime curve reaches a minimum under LLI. With a corresponding bias carrier density of $3.7 \times 10^{12} \text{ cm}^{-3}$, the range of lifetime data reliably reflecting SRH recombination and thus usable for the IDLS

analysis is increased by almost an order of magnitude in terms of Δn . Since surface recombination is negligible due to the combined effect of a high-quality surface passivation, a low lifetime level and a high sample thickness²¹ and since intrinsic CE-Auger recombination does not affect the lifetime data for carrier densities up to $1 \times 10^{16} \text{ cm}^{-3}$ due to the low lifetime level, the trapping-corrected lifetime curve (closed symbols) reflects SRH recombination via the molybdenum centers in the bulk over the whole Δn range.

As can be seen from Fig. 4.10b, the accurate SRH modeling of the measured injection dependence in the whole injection range requires two independent SRH centers whose impact is displayed separately. While the increase in the SRH lifetime up to $\Delta n = 2 \times 10^{14} \text{ cm}^{-3}$ is well described by the deep defect level alone and is hardly affected by the shallow level, the

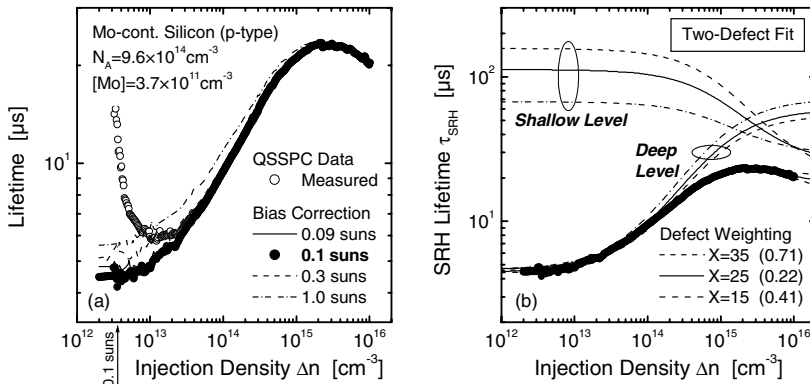


Fig. 4.10. IDLS curve measured by means of the QSSPC technique on the same molybdenum-contaminated sample as investigated in Fig. 4.7. (a) Elimination of the trapping effect under LLI (*open symbols*) by the bias-light correction, shown for different bias-light intensities (*lines*). The optimum correction is achieved for 0.1 suns (*closed circles*). With a corresponding bias carrier density of $3.7 \times 10^{12} \text{ cm}^{-3}$, the range of data reflecting SRH recombination is increased by an order of magnitude. (b) Accurate SRH modeling using a two-defect SRH model. The impact of the two independent SRH centers is displayed separately for different defect weighting factors X . The optimum two-defect fit is achieved for $X=25$, reflected in the minimum least squares error of the fit (given in parentheses).

²¹ In the present case the measured effective carrier lifetimes are not affected by surface recombination for two reasons. On the one hand, surface recombination is effectively suppressed by the high-quality SiN surface passivation used ($S \leq 20 \text{ cm/s}$). On the other hand, the impact of the surfaces itself is strongly reduced due to a high sample thickness of $600 \mu\text{m}$ and a low lifetime level of at most $30 \mu\text{s}$ (corresponding to a maximum diffusion length of $330 \mu\text{m}$).

successful modeling of the observed slight decrease in the SRH lifetime above $\Delta n = 2 \times 10^{15} \text{ cm}^{-3}$ strongly depends on the shallow defect level. In view of the doping concentration of $9.6 \times 10^{14} \text{ cm}^{-3}$, it becomes obvious that the shallow defect level affects the measured lifetime curve in the whole region of medium and high injection densities, which makes a two-defect SRH simulation mandatory.

As discussed in Sect. 3.3.1C, an accurate determination of the defect parameters from a two-defect SRH model requires the determination of the optimum defect weighting factor X , which describes the relative impact of both defect levels on the LLI part of the superimposed lifetime curve. For this the two-defect SRH model has been fitted to the measured IDLS curve for varying X factors, the deep and the shallow level being arbitrarily assumed at $E_C - E_t = 0.5 \text{ eV}$ and $E_C - E_t = 0.2 \text{ eV}$, respectively.²² The resulting IDLS curves are displayed in Fig. 4.10b for three different X factors. The least squares errors related to these fits are given in the legend of Fig. 4.10b by the figures in brackets. As can be seen, the least squares error reaches its minimum for $X = 25$, which is thus identified as the optimum defect weighting factor (solid lines). The impact of a defective X factor on the spectroscopic result obtained for the deep level is nicely illustrated in Fig. 4.10b. Since the impact of the shallow level on the superimposed lifetime curve depends on the injection density, its overall increase with decreasing X factor leads directly to steeper SRH curves for the deep level. As a consequence, the extracted k factor of the deep level (for the assumed $E_C - E_t = 0.5 \text{ eV}$) increases from 11 to 14 if the X factor decreases from 35 to 15. A 40 % deviation of the X factor from its optimum value is thus reflected in an average deviation of only 12 % in the k factor of the deep level. This demonstrates the reduced error-proneness of the spectroscopic result to X errors, which has already been observed in Sect. 3.3.1C and highlights the reliability of the results from a two-defect SRH fit.

B DPSS analysis of the IDLS curve

Although the IDLS analysis reveals the coexistence of a deep and a shallow level in the case of the molybdenum impurity, only the deep level dominating the LLI part of the lifetime curve is relevant to the combined analysis of TDLS and IDLS, since TDLS operates under LLI conditions. Due to the

²² The possibility of performing the determination of the optimum defect weighting factor X for defect levels with almost arbitrary energy levels results directly from the ambiguity of the SRH parameterization of an IDLS curve. As long as the chosen pair of energy levels can be related for a suitable pair of k factors with an increasing and a decreasing IDLS curve, any variation of the E_t values for fixed X factor only leads to a change in the optimum k factors, while the associated IDLS curves remain unchanged.

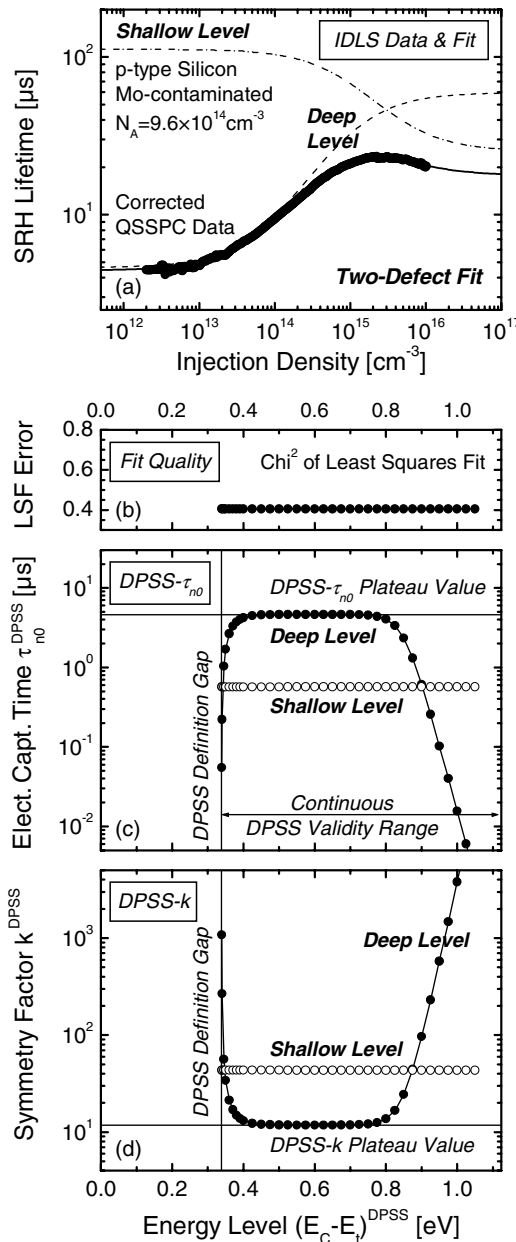


Fig. 4.11. Advanced DPSS analysis of the IDLS curve measured on the less doped molybdenum-contaminated sample, which has been pre-analyzed in Fig. 4.10. (a) Measured IDLS curve after elimination of superposed carrier trapping (symbols), accurately modeled by an optimized two-defect SRH fit with $X = 25$ (solid line). (b–c) Defect parameter solution surface of the defect center dominating the LLI part of the IDLS curve (closed symbols). The DPSS analysis is based on the modeling procedure introduced in Sect. 3.3.2B. The defect parameters of the shallow center (open symbols) are optimized once for $X = 25$ and an arbitrarily chosen $E_C - E_t = 0.15 \text{ eV}$ and then kept on fixed values ($k = 0.56$, $\tau_{n0} = 21.7 \mu\text{s}$) within the whole DPSS analysis.

strong inherent ambiguity of the SRH parameterization of an IDLS curve (see Sect. 3.3.2), its detailed spectroscopic evaluation requires determination of the defect parameter solution surface associated with the defect

center dominating the LLI part of the IDLS curve. The DPSS analysis is performed according to the procedure described in Sect. 3.3.2B. Using a two-defect SRH model, the defect parameters of the second shallow defect center dominating HLI are optimized once for an arbitrarily chosen shallow energy level and the optimum defect weighting factor $X=25$ and then kept at fixed values throughout the whole DPSS analysis (open symbols). The resulting DPSS diagram of the defect center dominating LLI is displayed in Fig. 4.11c–d (closed symbols). It should be emphasized again that in spite of the broad codomains of the DPSS- k and the DPSS- τ_{n0} curves, which cover several orders of magnitude, the DPSS parameter triplets (E_t, k, τ_{n0}) represent equivalent solutions for the SRH parameterization of the IDLS curve. This is reflected in the constant DPSS- Chi^2 curve in Fig. 4.11b and nicely illustrates the strong inherent ambiguity of the spectroscopic IDLS result. As expected for an increasing IDLS curve (see Sect. 3.3.3C), the DPSS exhibits the tub-like structure with a continuous range of validity and a definition gap towards the conduction band. The two DPSS characteristics are the energy value of the DPSS definition gap (DPSS-DG) and the plateau value of the DPSS- k curve (DPSS-PL), whose values are determined from Fig. 4.11d as $(E_C - E_t)^{\text{DPSS-DG}} = 0.339 \text{ eV}$ and $k^{\text{DPSS-PL}} = 11.8$. By definition, the DPSS-PL value represents a lower bound for the true k factor, which definitely proves a capture asymmetry for the relevant molybdenum level. However, for $k \neq 1$ it has been shown in Sect. 3.3.3E that the DPSS-DG energy may be an upper and lower bound for the true energy depth of the underlying defect level, which prevents a confinement of the possible ΔE_t values from the IDLS result alone.

4.3.3 Combined DPSS analysis of TDLS and IDLS

To avoid the ambiguity of the spectroscopic results obtained from the isolated analyses of IDLS and TDLS, the results of the two techniques should finally be combined. This is simply realized by a superposition of the associated DPSS diagrams, shown in Fig. 4.12 for the less doped molybdenum-contaminated sample (Mo1). As discussed in Sect. 3.6B, an unambiguous identification of the defect parameters is achieved from the intersection points of the two DPSS- k curves associated with TDLS (solid lines) and IDLS (dashed lines). Since the DPSS- k curve associated with TDLS contains solutions of varying accuracy, the quality of the two observed DPSS- k intersection points (white stars) depends significantly on their energy distance from the corresponding minimum of the DPSS- Chi^2 curve related to TDLS, which is shown in the lower half of Fig. 4.12. The exact coordinates of the DPSS- k intersection points are given in Table 4.4.

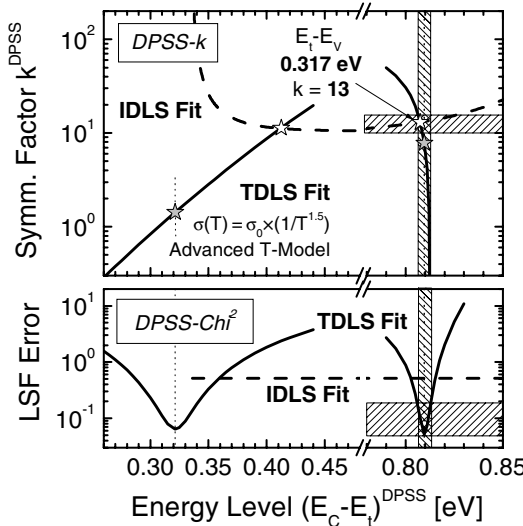


Fig. 4.12. Superposition of the DPSS diagrams associated with the TDLS (solid lines) and IDLS (dashed lines) curve of the molybdenum-contaminated sample with $N_A = 9.6 \times 10^{14} \text{ cm}^{-3}$ (Mo1) displayed in Figs. 4.8 and 4.11, respectively. Unambiguous determination of both molybdenum defect parameters from the intersection point of the DPSS- k curves in the MajBH (white star). The coincidence of this intersection point with the minimum of the DPSS- χ^2 curve related to TDLS (gray star) manifests the accuracy of the determination and the need to use the proposed advanced SRH model for the modeling of the TDLS data.

Since the energy position of the DPSS- k intersection point in the upper band gap half deviates as much as 90 meV from the energy position of the corresponding DPSS- χ^2 minimum, the TDLS solution in the upper band gap half has to be rejected for reasons of inconsistency.²³ In the lower band gap half, however, the energy positions of both the DPSS- k intersection point and the minimum of the DPSS- χ^2 curve perfectly coincide. It can be concluded that the relevant molybdenum level is definitely located in the lower band gap half. From the DPSS- k intersection point, the energy level is determined as $E_t - E_v = 0.317 \text{ eV}$, which precisely confirms the mean energy value determined in Sect. 4.3.1C from the combined analysis of two independent TDLS curves. The quality of the E_t determination from the

²³ As can be seen from Fig. 4.12 the MinBH solution of the TDLS analysis definitely has to be excluded since its energy value lies within the definition gap and its k value below the plateau value of the DPSS- k curve associated with the IDLS curve. For both reasons a modeling of the IDLS curve with these defect parameters completely fails, even qualitatively, which demonstrates the inconsistency between TDLS and IDLS in the case of the MinBH solution.

Table 4.4. Overview of the spectroscopic results obtained on the molybdenum-contaminated sample with $N_A = 9.6 \times 10^{14} \text{ cm}^{-3}$ (Mo1) by means of the different LS techniques: TDLS alone (see Fig. 4.8), IDLS alone (see Fig. 4.11) and the combination of TDLS and IDLS (see Fig. 4.12). Optimum values (*bold font*) and error intervals (*standard font*) are determined from advanced DPSS analysis. The final LS result is *shaded gray*.

Technique	Boundary conditions	MinBH defect $E_C - E_t$ [eV]	k	MajBH defect $E_t - E_V$ [eV]	K
TDLS	Advanced / $\sigma(T)$ -model	0.321 (0.30–0.34)	1.4 (0.9–2.3)	0.315 (0.31–0.32)	7.8 (0.1–15)
IDLS	Two-defect fit	IDLS fit at E_t^{TDLS} impossible		0.315 (E_t^{TDLS})	14.5
IDLS & TDLS	DPSS-IP	0.413	11.3	0.317	13.0
Final result		—	—	0.317 ± 0.005	13 ± 3

combined DPSS analysis of TDLS and IDLS is manifested in the high accuracy observed for the coincidence of the DPSS- k intersection point and the DPSS- Chi^2 minimum (see Table 4.4). The fact that the DPSS- k curves intersect almost vertically allows an accurate determination of the symmetry factor k , which could not be achieved from the pure TDLS analysis due to the steep shape of the DPSS- k curve in the MajBH (see Sect. 4.3.1B). For the molybdenum level, $k=13$ is found. Due to the vertical intersection of the DPSS- k curves, the E_t error of the combined result may be directly identified with the small E_t error of the TDLS analysis deduced in Sect. 4.3.1B, while the k error may be identified with the k error of the IDLS analysis, which is estimated to be 20 %. Both errors are indicated in Fig. 4.12 by the shaded areas. In conclusion, the combined DPSS analysis of TDLS and IDLS reveals that the relevant molybdenum level is definitely located in the lower band gap half at $E_t - E_V = (0.317 \pm 0.005)$ eV, showing an electron/hole capture cross-section ratio $k = 13 \pm 3$.

4.3.4 Comparison with results in the literature and discussion

The lifetime spectroscopic result of the present study is in good agreement with an energy level $E_t - E_V = 0.30$ eV reported in the literature for a molybdenum donor level [1, 17]. This result was obtained from DLTS measurements. The slight shift of the lifetime spectroscopic result to deeper energy values might originate from the fact that the standard DLTS analysis does not take into account any $\sigma(T)$ -dependence. In fact, if the $\sigma(T)$ -dependence is neglected in the SRH simulation of the TDLS curve, the energy level of the MajBH solution is shifted to a lower value of $E_t - E_V = 0.29$ eV, as indicated in the fourth line in Table 4.2. This approach to explain the observed slight E_t deviation is further confirmed by the result of a DLTS

measurement which has been performed on a parallel Mo-contaminated sample.²⁴ Neglecting $\sigma(T)$ in the DLTS analysis, we find an energy level $E_r-E_V=0.29\text{ eV}$, which agrees perfectly with the LS result extracted under the same boundary conditions. Nevertheless, a consistent modeling of the TDLS and IDLS curve fails under these simplified conditions, as can be seen from a comparison of the dash-dotted TDLS-related DPSS- k curve in Fig. 4.8 (determined for $\sigma=\text{const.}$) with the IDLS-related DPSS- k curve in Fig. 4.12. Since the perfect coincidence of the TDLS and IDLS results found in Fig. 4.12 thus definitely proves that the accurate consideration of any underlying $\sigma(T)$ -dependence is indispensable for an accurate spectroscopic result, the accuracy of the LS result (present work) can be assessed as being even higher than the accuracy of the DLTS result reported in [1, 17].

Beyond the confirmation of known defect parameters, the lifetime spectroscopic result makes the determination of an unknown defect parameter possible. Since standard DLTS measurements are “blind” for exchange processes with the minority band, only the majority (hole) capture cross-section $\sigma_p=6\times10^{-16}\text{ cm}^2$ has been determined for the molybdenum donor level [1], while the electron capture cross-section σ_n is unknown from DLTS. Since the ratio k of the two capture cross-sections is directly determined from lifetime spectroscopy, the missing capture cross-section can be determined by combining the results of DLTS and lifetime spectroscopy. Calculating the product $\sigma_n=k\times\sigma_p$, we find a value of $\sigma_n=(7.8\pm1.8)\times10^{-15}\text{ cm}^2$ for the unknown electron capture cross-section of the molybdenum donor level.

4.3.5 Conclusion

The lifetime spectroscopic investigations on the set of two molybdenum-contaminated samples unambiguously identified the molybdenum donor level as the recombination-active molybdenum level. In good agreement with DLTS results reported in the literature, the energy level is determined as $E_r-E_V=(0.317\pm0.005)\text{ eV}$. Concerning the capture properties, a value of $k=13\pm3$ is found for the unknown symmetry factor, which reveals an enhancement of electron capture. Using the hole capture cross-section σ_p known from the literature, the k factor allows the unknown electron capture cross-section to be determined as $\sigma_n=(7.8\pm1.8)\times10^{-15}\text{ cm}^2$. The capture cross-section has been found to be temperature-dependent with $\sigma(T)\sim T^{-1.5}$, which points towards the excitonic Auger capture process

²⁴ The DLTS system used for the measurements is based on the box-car technique, introduced by Lang [22]. The technical details of the system are described in [23].

being the relevant capture mechanism. Thus, the experimental results complete our knowledge of the defect properties of the molybdenum defect and give new insight into the physical mechanism underlying recombination.

The quality and reliability of the spectroscopic result manifests itself in the fact that it has been precisely reproduced on the one hand on two different samples and on the other hand by means of two independent LS techniques. The perfect coincidence of the results, obtained from TDLS alone and the combination of TDLS and IDLS, also demonstrates the excellent performance of both lifetime spectroscopic methods. It should be emphasized that this coincidence is due to the advanced SRH model used for the modeling of the TDLS curve. Thus, the result definitely proves that an accurate consideration of an underlying $\sigma(T)$ -dependence is indispensable to obtain an accurate spectroscopic result.

4.4 Titanium

Titanium, which belongs to the 3d transition metals, cannot be excluded as contaminant in modern production lines since it is used as a constituent in modern contact systems [1]. This defines its technological importance. The surface of silicon wafers may be contaminated during sputtering or by mechanical contact, while an electrochemical segregation of titanium from contaminated chemical solutions is unlikely since the electronegativity of titanium is reduced compared to silicon [1]. Such a surface contamination is easily introduced into the bulk during a subsequent high-temperature step. Due to its low diffusivity and solubility, titanium rarely forms precipitates and is definitely in a dissolved state (see Sect. 4.2.1B). The electrically active incorporation on interstitial lattice sites gives rise to three deep energy levels: a donor and an acceptor state in the upper band gap half, and a double donor state in the lower band gap half [1]. As indicated in Table 4.5, values for the energy levels and the cross-sections for capture from the nearer band edge have already been determined by means of standard DLTS. But as reliable data for the second capture cross-section are missing for all three levels, the ranking of the levels with respect to their recombination activity is still an open question. From a physical point of view, the lifetime spectroscopic investigation on the titanium-contaminated samples thus aims to identify the relevant defect level and to complete our knowledge of its electronic properties. From a methodological point of view, it aims at a further verification of the theoretical predictions made for lifetime spectroscopy, especially as the set of three samples allows an N_{dop} -IDLS experiment to be realized.

Table 4.5. Electronic properties of interstitial titanium in silicon as they are known from the literature. The given defect parameters are taken from [1] and represent averages of the data from different authors.

Defect	Type	Energy [eV]	Capture cross-sections		E_∞ [eV]	Technique
			σ_p [cm ²]	σ_n [cm ²]		
Ti _i	Acceptor	$E_C - 0.08$?	3.5×10^{-14}	—	DLTS
Ti _i	Donor	$E_C - 0.27$?	1.3×10^{-14}	0.004	DLTS
Ti _i	Double donor	$E_V + 0.28$	1.9×10^{-16}	?	0.040	DLTS

4.4.1 Advanced N_{dop} -IDLS analysis

The lifetime spectroscopic investigation is performed on a set of three samples, which have been contaminated with titanium during crystal growth (see Sect. 4.2.1). The LS analysis of the TDLS and IDLS data measured on these samples is divided into three parts. Since the doping concentration of the samples varies by half an order of magnitude between 6.3×10^{14} and 1.1×10^{15} cm⁻³, it is possible to subject the IDLS data of all three samples to an N_{dop} -IDLS analysis (see Sect. 4.4.1). In addition, the data of the individual samples are analyzed by the pure TDLS analysis (see Sect. 4.4.2) and the combined TDLS and IDLS analysis (see Sect. 4.4.3), as already demonstrated in the previous section on the molybdenum-contaminated sample. The investigation of three different samples and the application of three different LS techniques allows a comprehensive consistency check of the spectroscopic results obtained for titanium (see Sect. 4.3.4).

A IDLS curves and validity of the SRH model

Figure 4.13a shows the IDLS curves which have been measured by means of the QSSPC technique on the three titanium-contaminated silicon samples. Since surface recombination can be neglected due to the high-quality SiN surface passivation used and since superposed external carrier trapping and CE-Auger recombination have been eliminated where necessary within the data pre-analysis (see Sect. 4.2.4A), the displayed IDLS curves directly reflect the pure SRH lifetime related to the titanium centers in the bulk. The significant differences in the average lifetime level mainly result from a titanium concentration varying by 4 orders of magnitude among the samples (see labels in Fig. 4.13a).²⁵

²⁵ Note that the titanium concentrations displayed in Fig. 4.13a are calculated values specified by Wacker Siltronic (see Sect. 4.2.1C).

In view of such high defect concentrations, the validity of standard SRH theory has to be scrutinized. As discussed in detail in Sect. 1.4.3C, standard SRH theory is only valid when the density of recombination centers N_t is small enough to avoid internal trapping effects. This may be controlled by calculating the critical recombination center density N_{crit}^{LLI} according to Eq. (1.47) [16], as has been done for the investigated samples on the basis of the defect parameters which are finally extracted from the LS experiment.²⁶ With the doping concentration varying by only half an order of magnitude from 6.3×10^{14} to $1.1 \times 10^{15} \text{ cm}^{-3}$, a narrow range from 1.7 to $1.9 \times 10^{14} \text{ cm}^{-3}$ is determined for the corresponding values of N_{crit} . The two samples with lower contamination levels of 2×10^{10} and $2 \times 10^{11} \text{ cm}^{-3}$ easily satisfy the criterion $N_t \ll N_{crit}$ and thus allow an accurate modeling with standard SRH theory for all injection levels. Even for the sample with the highest titanium and lowest doping concentration ($[\text{Ti}] = 2 \times 10^{13} \text{ cm}^{-3}$, $N_A = 6.85 \times 10^{14} \text{ cm}^{-3}$), N_{crit} is about one order of magnitude larger than N_t , which ensures that trapping effects under low injection impact on the measurement by no more than 10 % [16]. The complete analysis [16] reveals that down to $\Delta n = 1.7 \times 10^{13} \text{ cm}^{-3}$, an accurate modeling with standard SRH theory should be achieved. While the IDLS data may easily be confined to this Δn range without significant loss of information (see Fig. 4.13a), an accurate analysis of TDLS data becomes impossible as TDLS operates under low-level injection, i.e., in the critical Δn region. This is why the least doped titanium sample has not been subjected to a TDLS experiment.

B Superposed DPSS analysis of the IDLS curves

For the spectroscopic evaluation of the IDLS curves, the boundary conditions of the SRH model first have to be adjusted. For all three samples the accurate SRH modeling (thick lines) of the measured injection dependence over the whole Δn range requires two independent SRH centers, whose impact is displayed separately for the sample with the lowest titanium concentration (closed circles). As can be seen in Fig. 4.13a, up to $\Delta n = 5 \times 10^{14} \text{ cm}^{-3}$ the total SRH lifetime (gray dashed line) is well described by only a deep level (black dashed line), while above it is equally affected by both recombination centers. The negligible impact of the shallow level under low injection levels is reflected in a high optimum defect weighting factor $X = 30$, which has been determined according to Sect. 3.3.1C. The same trend is observed for the two other samples, which has explicitly been

²⁶ Note that according to Eq. (1.47) N_{crit} not only depends on the doping concentration N_{dop} and the excess carrier concentration Δn , but also on the defect parameters E_t and k . The required N_{crit}^{LLI} represents the lower bound for N_{crit} and is independent of Δn .

shown for the highest-doped titanium sample (closed squares) within the introduction of the DPSS analysis in Sect. 3.3.2B (see Fig. 3.13).

In spite of the coexistence of a deep and a shallow titanium level revealed here, the N_{dop} -IDLS experiment focuses on the determination of the deep level dominating the LLI part of the IDLS curves. This allows in the end a comparison with the spectroscopic results obtained from TDLS, since TDLS is only sensitive to those defect levels which are active under LLI conditions. Due to the strong inherent ambiguity of the SRH parameterization of a single IDLS curve (see Sect. 3.3.2), a comprehensive SRH analysis of the whole set of IDLS curves is only achieved by the superposed DPSS analysis introduced in Sect. 3.3.4. This requires for each of the IDLS curves separately the determination of the defect parameter solution surface which is associated with the defect center dominating the LLI part of the IDLS curve. This determination is performed on the basis of the procedure described in Sect. 3.3.2B. Using the required two-defect SRH model for the modeling, the second defect level dominating HLI was assumed in all three IDLS curves to be located at $E_C - E_t = 0.15$ eV. The remaining defect parameters were then optimized once for each IDLS curve and kept on fixed values within the whole DPSS analysis (horizontal lines in Fig. 4.13c and d).²⁷

The resulting DPSS- τ_{n0} and DPSS- k curves associated with the defect center dominating LLI are superposed in Figs. 4.13c and d, respectively. As expected for increasing IDLS curves, all three defect parameter solution surfaces exhibit the tub-like structure with a continuous range of validity and a definition gap towards the conduction band (see Sect. 3.3.3C). The corresponding DPSS- Chi^2 curves are displayed in Fig. 4.13b. Their energy independence again shows that the parameter triplets (E_t , k , τ_{n0}) of each DPSS represent equivalent solutions for the SRH parameterization of the respective IDLS curves.

As predicted in Sect. 3.3.4, the three DPSS- k curves intersect in two common intersection points located in the upper and the lower band gap half. Representing by definition the two possible solutions for a simultaneous SRH parameterization of the whole set of IDLS curves, they are indicated in the DPSS- k diagram as 1st and 2nd solution (see Fig. 4.13d).

²⁷ It should be mentioned that it has not been possible to find a unique set of defect parameters for the shallow level. A further expansion of the presented DPSS analysis on the second level in a two defect fit should solve this problem. Nevertheless, the accuracy of this determination will be limited, since the modeling is based on those parts of the measured IDLS curves which show the highest uncertainty due to the superposition of CE-Auger recombination. As shown in Fig. 3.13, CE-Auger recombination affects the IDLS curves under HLI conditions already on a medium lifetime level which is often met in the experiment.

Since both solutions are equivalent, it cannot be decided which of them reflects the true defect parameters E_C-E_t and k of the underlying titanium level. This reflects the remaining ambiguity expected for any N_{dop} -IDLS experiment.

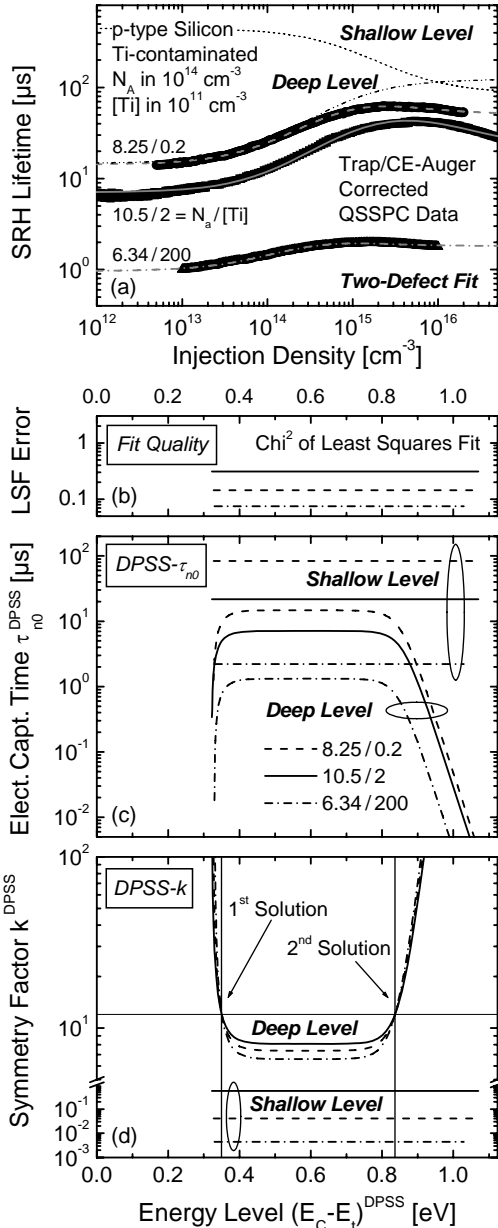


Fig. 4.13. IDLS investigation of a set of intentionally titanium-contaminated silicon samples with different doping concentrations. (a) The SRH modeling (lines) of the measured lifetime curves (symbols) requires two independent SRH centers whose impact is displayed separately for the sample with the lowest titanium concentration (closed circles). (b-d) Advanced DPSS analysis. The DPSS curves associated with the deep center are determined separately for each IDLS curve, the defect parameters of the shallow center being kept at optimized fixed values ($E_C-E_t=0.15$ eV, k and τ_{n0} as indicated in c and d). Information about the true defect parameters of the deep titanium level can be extracted from the intersection points of the superposed DPSS- k curves. The existence of two intersection points in the superposed DPSS- k diagram reflects the unavoidable remaining ambiguity of the spectroscopic IDLS result.

In contrast with the predictions, no such common intersection points are observed in the DPSS- τ_{n0} diagram (see Fig. 4.13c). The common intersection of the DPSS- τ_{n0} curves is prevented by the different contamination levels in the three samples, which induces an additional vertical shift among the DPSS- τ_{n0} curves, the τ_{n0} level growing as the contamination level decreases. Since variations of the defect concentration within the set of samples normally cannot be excluded, only the DPSS- k diagram may be exploited with respect to the energy positions of the DPSS intersection points under realistic conditions. The DPSS- τ_{n0} diagram, on the other hand, may indeed be used to detect such variations since all deviations of the DPSS- τ_{n0} curves at the energy positions of the DPSS- k intersection points have to be attributed to variations in the defect concentration.

C Computational method to determine the DPSS intersection points

It is obvious that the final spectroscopic result depends on the accuracy with which the coordinates of the DPSS- k intersection points are determined. Since the narrow range of doping concentrations among the investigated samples is reflected in only slight variations concerning the associated DPSS- k curves, the exact localization of the intersection points necessitates a special procedure.

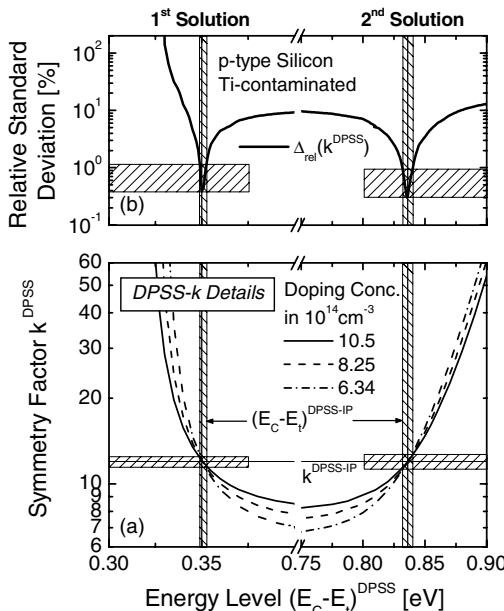


Fig. 4.14. Computational method for an accurate determination of the DPSS intersection points under realistic conditions. (a) Details of the DPSS- k diagram of Fig. 4.13d in the vicinity of the two intersection points. (b) Relative standard deviation $\Delta_{\text{rel}}[k]$ of the DPSS- k curves as a function of defect energy (solid line). While the energy positions of the $\Delta_{\text{rel}}[k]$ minima directly reflect the optimum positions of the intersection points in the DPSS- k diagram, their width allows an error estimate for the extracted defect parameters of both solutions (shaded areas).

A computational method consists in calculating the relative standard deviation $\Delta_{\text{rel}}[k]$ of the DPSS- k curves as a function of the DPSS energy. This requires averaging the k values of all three DPSS- k curves at each energy position. Figure 4.14 displays the resulting $\Delta_{\text{rel}}[k](E_C-E_t)$ curve (upper half) together with the details of the DPSS- k diagram (from Fig. 4.13d) in the vicinity of the two intersection points (lower half). The practical value of this expanded DPSS diagram of the N_{dop} -IDLS experiment is twofold. On the one hand the energy positions of the $\Delta_{\text{rel}}[k]$ minima directly correspond to the optimum positions of the intersection points in the DPSS- k diagram and thus allow an accurate determination of the two parameter solutions which may be extracted from an N_{dop} -IDLS experiment for the underlying defect center. On the other hand, reflecting the sharpness of the intersection points, the width of the $\Delta_{\text{rel}}[k]$ minima enables an error estimation for the extracted defect parameters of both solutions. If an upper limit for the tolerated $\Delta_{\text{rel}}[k]$ error is defined, the ranges of acceptable values for both defect parameters can be deduced graphically from the DPSS diagram as shown by the shaded areas in Fig. 4.14a and b.

D Assessment of the spectroscopic result

In the present case the DPSS-IP in the upper band gap half is determined at $E_C-E_t=0.350\text{ eV}$ and $k=12.1$, while that in the lower band gap half is determined at $E_t-E_V=0.289\text{ eV}$ and $k=12.0$. The accuracy of both solutions manifests itself in the narrow tolerance bands displayed in Fig. 4.14 (shaded areas). Even if the upper bound of the tolerated $\Delta_{\text{rel}}[k]$ error is assumed to be three times its optimum value, which may be regarded as a conservative estimate, E_t errors below 0.005 eV and k errors below 0.7 are found for the defect parameters. This reflects the sharp intersection points of the DPSS- k curves observed in Fig. 4.14b.

The spectroscopic results are fully consistent with the theoretical predictions of Sect. 3.3.4. On the one hand the k factors of the two solutions coincide, which allows the capture asymmetry of the underlying titanium center to be unambiguously determined as $k=12$. On the other hand, as expected for $k \neq 1$, both solutions differ in terms of their energy depth. The theoretical study in Sect. 3.3.4B revealed that this energy deviation²⁸ may be described by an energy correction term E^{corr} which depends logarithmically on the symmetry factor k . Using the analytical expression in Eq. (3.37b), E^{corr} is calculated as 0.062 eV in the present case (for $k=12$),

²⁸ In the present context the energy deviation denotes the difference in the energy depth of the two DPSS-IPs.

which accurately reflects the experimentally observed energy deviation of 0.061 eV and thus confirms the predicted k -dependence of E^{corr} .

Since the two solutions are equivalent – which is reflected in the nearly identical $\Delta_{\text{rel}}[k]$ errors – neither the energy depth nor the band gap half of the underlying titanium center can be determined unambiguously from the N_{dop} -IDLS experiment.

To estimate the accuracy of the N_{dop} -IDLS technique, the extracted energies have been compared with the energies of known titanium levels reported in the literature (see Table 4.5). Concerning the MajBH solution, its energy $E_t-E_V=(0.289\pm 0.005)$ eV agrees perfectly with the energy of the titanium double donor level which has been determined by means of DLTS as $E_t-E_V=(0.28\pm 0.01)$ eV [1]. Although the MinBH solution at $E_C-E_t=0.35$ eV might be attributed to the titanium acceptor level known to be located at $E_C-E_t=0.27$ eV [1], the significant energy difference of 80 meV shows that the MinBH solution probably has to be excluded. It may be concluded that the N_{dop} -IDLS experiment most likely identifies the titanium double donor level as the titanium level with highest recombination activity. The agreement of the energy values obtained from LS and the DLTS is remarkable.

It is all the more remarkable if the unfavorable boundary conditions of the N_{dop} -IDLS experiment are taken into account. In detail these were: (i) the superposition of a second shallow defect level in the IDLS curves, (ii) a minimum doping variation of half an order of magnitude, and (iii) an enormous variation of the defect concentration by four orders of magnitude. The last two points in particular made it completely impossible to detect the characteristic doping shift of the IDLS curves directly from the lifetime plot in Fig. 4.13a. The fact that the superposed DPSS analysis developed in the present work is completely unaffected by such critical boundary conditions demonstrates its extraordinary capability to realize the simultaneous SRH analysis of a set of IDLS curves. Allowing a transparent and comprehensive modeling of the N_{dop} -IDLS experiment which significantly improves the quality and reliability of the spectroscopic result, the DPSS analysis proposed in the present work can be highly recommended, especially for the analysis of N_{dop} -IDLS data.

4.4.2 Advanced TDLS analysis

To identify the true solution among the two N_{dop} -IDLS solutions by means of lifetime spectroscopy alone, without the aid of spectroscopic data from the literature (as done in the previous section) and to investigate the consistency of the different LS techniques, the samples with medium and low con-

tamination levels have been subject to a TDLS investigation. The third sample with the highest contamination level could not be investigated by means of TDLS, as standard SRH theory is invalid under low-level injection due to internal trapping at the titanium centers (see discussion in Sect. 4.4.1A).

A DPSS analysis of the TDLS curves

Figures 4.15a and 4.16a display the TDLS curves of the two samples which have been measured by means of the MW-PCD technique in a T range from 130 to 580 K (Ti-I) and 150 to 590 K (Ti-II), respectively. Before starting with the spectroscopic analysis of the TDLS curves, let us first adjust the boundary conditions of the SRH model.

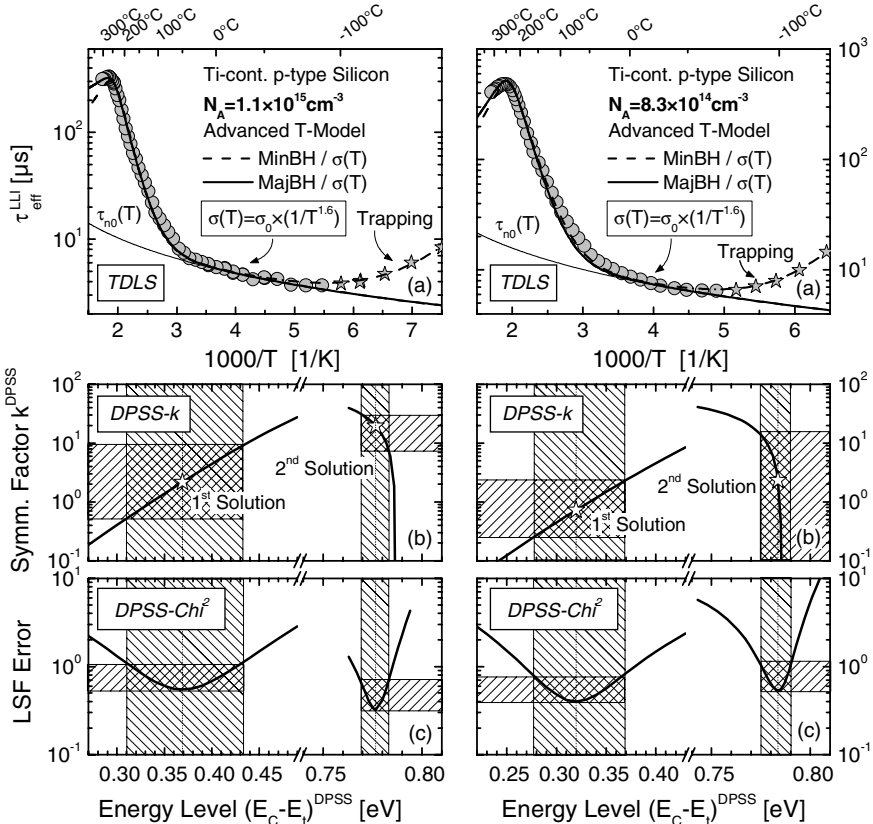
Towards very low temperatures both samples exhibit a significant lifetime increase (stars), which may be attributed to superposed external carrier trapping (see Sect. 3.5.2). In both cases an accurate modeling may be achieved for an additional shallow trap level²⁹ if the lifetime at low temperatures is identified with the asymptotic lifetime defined in Eq.(3.65) (dash-dotted lines). However, since the trapping effect screens recombination lifetime, the affected T regions below 180 K (Ti-I) and 200 K (Ti-II) are ignored in the SRH fit.

An accurate SRH modeling of the trapping-free low-temperature part of the TDLS curves ($200 \text{ K} < T < 310 \text{ K}$) again requires the introduction of a temperature-dependent capture cross-section. As shown by the thin solid lines in Figs. 4.15a and 4.16a, the observed increase of the minority capture time $\tau_{no}(T)$ with increasing temperature reflects a decreasing capture cross-section, which can be modeled in terms of $\sigma(T) = \sigma_0 \times T^\alpha$ with an exponent $\alpha = -1.6$. The fact that both samples exhibit the same $\sigma(T)$ -dependence underlines its meaning as an additional fingerprint of the titanium center, which gives insight into the physical mechanism of carrier capture.³⁰ Being almost the same as for the molybdenum center, the identified $\sigma(T)$ -model points towards either a cascade capture process [19] or an excitonic Auger capture process [20]. Since the expected defect depth of 0.28–0.35 eV is again too deep to allow capture via the cascade

²⁹ In the more highly doped sample (Ti-I) an accurate modeling of the trapping-affected T region below 180 K is achieved for a shallow trap level at $E_C - E_t = 0.10 \text{ eV}$ assuming a trap density of $3.5 \times 10^{15} \text{ cm}^{-3}$. In the less doped sample (Ti-II) the shallow trap level has to be chosen at $E_C - E_t = 0.13 \text{ eV}$ with a trap density of $1.5 \times 10^{15} \text{ cm}^{-3}$, which leads to the observed onset of trapping at 200 K. Note that the trap levels may reside either in the bulk or at the Si/SiN interface.

³⁰ A survey of the capture mechanisms and the expected $\sigma(T)$ -models is given in Sect. 3.5.1A.

mechanism, the excitonic Auger mechanism is most likely the dominating capture process, especially as it is favored by the measurement conditions used, which are based on the optical injection of electron-hole pairs (see discussion in Sect. 3.5.1B). Concerning the TDLS bend due to intrinsic conduction above 520 K (Ti-I) and 500 K (Ti-II), respectively, an accurate modeling of its T position and level again requires the advanced T -model.



Figs. 4.15 and 4.16. TDLS investigation of two intentionally titanium-contaminated silicon samples. (a) The SRH modeling of the measured lifetime data (symbols) is performed for a MinBH (dashed lines) and a MajBH defect (solid lines) on the basis of the advanced T -model, the underlying T -dependence of the capture cross-section being described by the same $\sigma(T)$ -model. The lifetime increase towards very low temperatures (stars) originates from superposed carrier trapping at an additional shallow level and can be described by an asymptotic lifetime as defined in Eq. (3.65) (dash-dotted lines). (b,c) Advanced DPSS analysis of the TDLS curve based on the optimum configuration of the SRH model. The similar Ch^2 values of the DPSS- Ch^2 minimum in the MinBH and MajBH prevent an unambiguous identification of the band gap half the defect center is located in. The errors in the extracted defect parameters (shaded areas) are estimated for tolerated Ch^2 values of twice their optimum values.

Table 4.6. Spectroscopic TDLS results obtained on the two intentionally titanium-contaminated silicon samples investigated in Figs. 4.15 and 4.16. The defect parameters are determined from an SRH fit (DPSS analysis) (i) within the whole T range on the basis of the advanced T -model (*upper half*) and (ii) within a reduced T range on the basis of the basic T -model (*lower half*), the underlying $\sigma(T)$ -model being taken into account in both cases. *Shaded gray* are the average defect parameters of the two samples obtained for both model configurations.

Material / Fit parameter ID	MinBH defect			MajBH defect		
	$E_C - E_t$ [eV]	k	Chi^2	$E_r - E_V$ [eV]	k	Chi^2
Advanced T -model / $\sigma(T) \sim 1/T^{1.6}$ / with IC-induced TDLS bend	0.344 ± 0.035	1.5 ± 1.0	0.43	0.344 ± 0.005	11.0 ± 12.0	0.47
Ti-I	1.1×10^{15}	2.1×10^{11}	180–580 K	0.369	2.2	0.55
Ti-II	8.3×10^{14}	1.5×10^{10}	200–590 K	0.320	0.7	0.40
Basic T -model / $\sigma(T) \sim 1/T^{1.6}$ / without IC-induced TDLS bend	0.281 ± 0.020	0.24 ± 0.10	0.05	0.335 ± 0.005	arb.	0.34
Ti-I	1.1×10^{15}	2.1×10^{11}	180– 520 K	0.295	0.3	0.06
Ti-II	8.3×10^{14}	1.5×10^{10}	200– 500 K	0.268	0.2	0.03

As can be seen from Figs. 4.15a and 4.16a, if both the underlying $\sigma(T)$ -dependence and the advanced T -model are taken into account in the SRH model, this configuration again being referred to as the *advanced SRH model*, the TDLS curves of the two samples can be modeled just as well for a MinBH defect (dashed lines) as for a MajBH defect (solid lines). To enable a transparent spectroscopic evaluation of the TDLS curves, the two lower graphs of Figs. 4.15 and 4.16a display the associated defect parameter solution surfaces which have been determined on the basis of the advanced SRH model using the DPSS analysis proposed in Sect. 3.5.7. As can be seen from the DPSS- Chi^2 curves, the MinBH and MajBH solutions of the two TDLS curves are similar in quality, which prevents an identification of the true solution from the respective TDLS curves individually. However, a comparison of the spectroscopic TDLS results obtained for the two samples (see Table 4.6) shows that the energies of the two MajBH solutions nearly coincide, while the energies of the MinBH solutions differ by almost 0.04 eV. This observation clearly points towards the MajBH solution as the true solution, although it does not suffice to exclude the MinBH solution. Averaging the defect parameters of the two samples, the MinBH and MajBH solutions are found to be located at the same energy depth of 0.34 eV, the average E_t value being determined with a higher standard deviation for the MinBH than for the MajBH solution. With regard to the symmetry factor k , the capture cross-sections are found to be almost symmetric in the case of the MinBH solution ($k=1.5$) and

enhanced for electrons in the case of the MajBH solution ($k \sim 11$). An assessment of the accuracy of these two k factors has to keep in mind the fundamental difference³¹ between MinBH and MajBH defects discussed in Sect. 3.5.6A, which increases the uncertainty of the MajBH solution beyond the value of the standard deviation determined by averaging the results of the two samples.

B Reduced fit quality and its impact on the E_t determination

Although the DPSS- Chi^2 minimums are primarily used to identify the true solution from a relative comparison, their absolute values directly reflect the overall quality of the SRH fits and thus allow systematic errors of the SRH modeling to be detected, though not identified.³² In the present case enhanced absolute Chi^2 values in the range of 0.32 to 0.55 reveal a medium quality of the SRH fits, which queries the accuracy of the spectroscopic TDLS results. A visual inspection of the fitted TDLS curves shows that the slope of the fitted curves slightly overestimates the actually measured Arrhenius slope in both cases (see Figs. 4.15a and 4.16a), meaning that the energy depth extracted from TDLS is too high.

At least for the MinBH solution the discrepancy between the measured and the fitted Arrhenius slope arises indirectly from modeling the TDLS bend. Since the position and slope of the Arrhenius increase are adjusted separately by independent parameters (E_t and k) for a MinBH fit, an accurate modeling of the Arrhenius increase is achievable whenever E_t and k are not confined by other boundary conditions. Such a confinement may arise from modeling the TDLS bend if the SRH model configuration used is not appropriate for the measured data.

Since the origin of the slight model inadequacy could not be identified, its impact on the E_t determination has at least to be estimated quantitatively, which requires determining the actual E_t value from an accurate fit of the Arrhenius increase alone. According to the above reflection on the theoretical quality of MinBH fits, this should be achieved by a SRH modeling of the TDLS curve which ignores the TDLS bend due to intrinsic conduction in both the data and the model. This requires on the one hand a reduction of the upper bound of the fitted T range down to 520 K (Ti-I) and

³¹ For a MajBH defect, a limited k confinement can only be achieved from modeling the TDLS bend due to intrinsic conduction, as the T position of the Arrhenius increase is independent of k .

³² Since the E_t and k errors deduced graphically from the DPSS curve result from assuming a tolerated reduction of the fit quality relative to its optimum value, they do not (or only partly) reflect systematic errors of the optimum fit itself.

500 K (Ti-II), and on the other hand the use of the basic instead of the advanced T -model. The underlying $\sigma(T)$ -model has still to be taken into account to ensure a direct comparability of the energies extracted by means of the simplified and the advanced SRH modeling.³³

Exemplified by the more highly doped titanium sample (Ti-I), a comparison of the TDLS curves modeled by means of the simplified (thick solid lines, $T = 180\text{--}520$ K) and the advanced SRH model (dash-dotted lines, $T = 180\text{--}580$ K) is displayed in Figs. 4.17a and b, assuming a MinBH and a MajBH defect, respectively. For both samples, the spectroscopic results of the simplified modeling are displayed in the lower half of Table 4.6. As expected, ignoring the TDLS bend in the fit allows the Arrhenius increase to be accurately modeled if a MinBH defect is assumed (see Fig. 4.17a). For both samples, the quality of this fit is reflected in a χ^2 value which is reduced by almost an order of magnitude compared to the χ^2 value of the advanced SRH modeling in the whole T range (see Table 4.6).³⁴

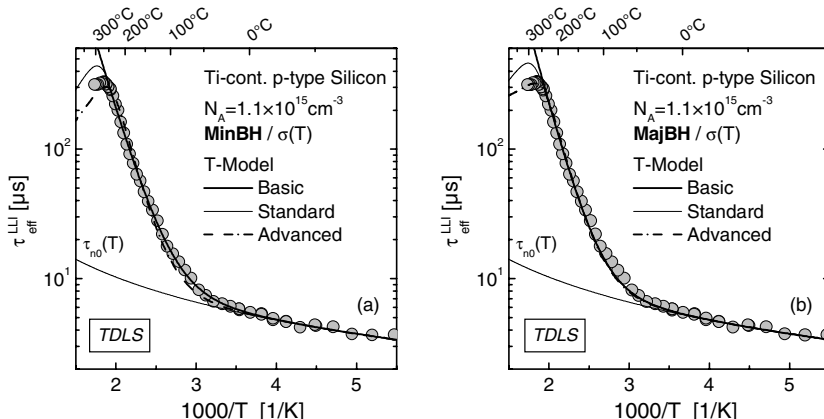


Fig. 4.17. Impact of the basic, the standard and the advanced T -model on the SRH modeling of the TDLS curve (a) for a MinBH defect and (b) for a MajBH defect shown as an example for the sample of Fig. 4.15 (Ti-I). Note that the TDLS bend due to intrinsic conduction ($T > 520$ K) is only considered in the SRH fits based on the advanced T -model. The underlying $\sigma(T)$ -model is assumed as in Fig. 4.15.

³³ Ignoring the $\sigma(T)$ -model only in the simplified SRH model would modify the extracted E_t value irrespective of the fit quality and thus make it unsuitable for estimating the ΔE_t discrepancy.

³⁴ For a direct comparison, the χ^2 values of the advanced SRH fits have to be recalculated for the reduced T range. While the χ^2 values of both MajBH solutions remain almost unchanged, those of the MinBH solutions are reduced by only 0.1 units. This confirms that the least square errors displayed in Table 4.6 mainly reflect the limited accuracy of the SRH fits in the T range of the Arrhenius increase.

On average, the accurate modeling of the Arrhenius increase results in a defect depth of 0.28 eV, which shows that the advanced SRH modeling in the whole T range overestimates the energy depth of the titanium center by approximately 0.06 eV due to the discrepancy in the slope of the measured and fitted Arrhenius increase. In parallel to the energy, the average k factor of the MinBH solution is reduced by almost an order of magnitude to $k=0.2$ for the simplified SRH fit. In contrast, if a MajBH fit is assumed, the simplified modeling in the reduced T region does not significantly change the quality of the SRH fit in the T region of Arrhenius increase (see Fig. 4.17b). For both samples this is reflected in only a slight reduction of the Chi^2 values and an almost unchanged E_t value which is reduced by only 0.01 eV to $E_t-E_V=0.335$ eV (for the simplified SRH fit).

It has to be stressed that, in spite of the accuracy of the MinBH fit, the results of the simplified SRH modeling only allow an accurate determination of the energy depth, which has to be expected for the titanium level on the basis of the $\sigma(T)$ -model determined from the low-temperature part of the TDLS curve. The attempt to use the results for an identification of the true band gap half may be misleading, as the observed accuracy has been achieved by a reduction of the TDLS information and not by an elimination of the model inadequacy. This will be shown in Sect. 4.4.3 within the combined analysis of TDLS and IDLS.

C Origin of model inadequacy

To get an idea of the physical origin of the observed inadequacy of the advanced SRH model, Figs. 4.17a and b additionally display the TDLS curves modeled on the basis of the standard T -model (thin solid lines).³⁵ Since both the T position and the level of the IC-induced TDLS bend are overestimated, it is unlikely that the observed model inadequacy results from the advanced T -model. This estimate is supported by the observed high quality of the TDLS fits (in the whole T region), which is achieved on the basis of the advanced T -model for all samples with other contaminants.

Another possible error source for the slight model inadequacy may be the simplifying assumptions made with respect to the consideration of an underlying $\sigma(T)$ -dependence within the SRH model. On the one hand the symmetry factor k is assumed to be temperature-independent, which directly implies identical $\sigma(T)$ -models for the electron and hole capture. The validity of this assumption has been discussed in detail in Sect. 3.5.9A

³⁵ The standard T -model has been introduced in Sect. 1.2.2 and considers the intrinsic conduction as it results from the pure T -dependence of p_0 , n_0 without taking into account the T -induced narrowing of the band gap.

from a theoretical point of view. On the other hand it is assumed that the $\sigma(T)$ -model extracted from the low-temperature part of the TDLS is also valid in the high-temperature part. Although allowing consistent results for the other impurities investigated in the present work, the second assumption in particular has to be queried in the case of titanium. Doubts arise from a comparison of the extracted $\sigma(T)$ -model with results from the literature. While the TDLS investigation unambiguously identified a power-law-dependent $\sigma(T)$ decrease which has been attributed to capture via the excitonic Auger mechanism (see Sect. 4.4.2A), standard DLTS investigations in the literature identified for the two deep titanium levels³⁶ an exponential $\sigma(T)$ increase which is characteristic of capture via multiphonon emission (see Table 3.4). The activation energies of the capture process have been determined as $E_{\infty}=0.004\text{ eV}$ for the donor level and $E_{\infty}=0.04\text{ eV}$ for the double donor level (see Table 4.5). Although the observed discrepancy between TDLS and DLTS may arise from the fact that the two techniques are sensitive to the opposite capture processes,³⁷ it is more likely that it results from the different injection conditions of the two techniques, which has been discussed in detail in Sect. 3.5.1B. In agreement with general observations in [20], this would imply for the titanium level that carrier capture via the excitonic Auger mechanism is more effective than via the multiphonon emission mechanism, excitonic Auger capture thus being the dominant capture process whenever minority carriers are present (TDLS conditions). However in the absence of minority carriers (standard DLTS conditions), carrier capture is still dominated by multiphonon emission. Strictly speaking, the dominance of excitonic Auger capture in the TDLS experiment is only detected at low temperatures. The important point is that the two capture mechanisms, which have been identified to be relevant to the titanium level under different injection conditions, exhibit an opposite T -dependence, implying that the effectiveness of excitonic Auger capture decreases while that of multiphonon capture exponentially increases with increasing temperature. Consequently, provided that the capture cross-sections of the two mechanisms do not differ too much in magnitude at room temperature, it may be possible that the multiphonon

³⁶ Since a donor and a double donor level are the only deep titanium levels (see Table 4.5), one of them represents the recombination-active defect center observed in LS.

³⁷ At least in the case of the titanium double donor level, which is located in the lower band gap half, the discrepancy between TDLS and DLTS could also arise from the determination of different capture cross-sections. While TDLS always determines the minority capture cross-section (here, electrons), DLTS determines the cross-section for capture from the nearer band (here, holes). However, the implied T -dependence of the k factor would not affect the SRH modeling, as the TDLS curve related to this MajBH defect would be completely unaffected by k .

capture reaches or even exceeds the effectiveness of the excitonic Auger capture within the investigated T range. Since such a change in the underlying capture process directly affects the T -dependence of the measured TDLS curve and cannot be considered in the SRH model, it might be the reason for the observed slight inadequacy of the advanced SRH model.

D Conclusion

Since none of the SRH model configurations is satisfactory within the whole T range of the TDLS curve, we chose the advanced SRH model as the best approximation for further considerations, keeping in mind that in the special case of the titanium samples the average energy depth of $\Delta E_t = 0.34 \text{ eV}$ extracted for both TDLS solutions is too deep, and tainted with some uncertainty.

4.4.3 Combined DPSS analysis of TDLS and IDLS

So far an unambiguous identification of the band gap half of the relevant titanium level has been achieved neither by the N_{dop} -IDLS nor by the TDLS investigations, since each of the techniques determined two equivalent solutions. To avoid this remaining ambiguity, the results obtained from TDLS and IDLS should finally be combined, which is simply realized by a superposition of the associated DPSS diagrams.

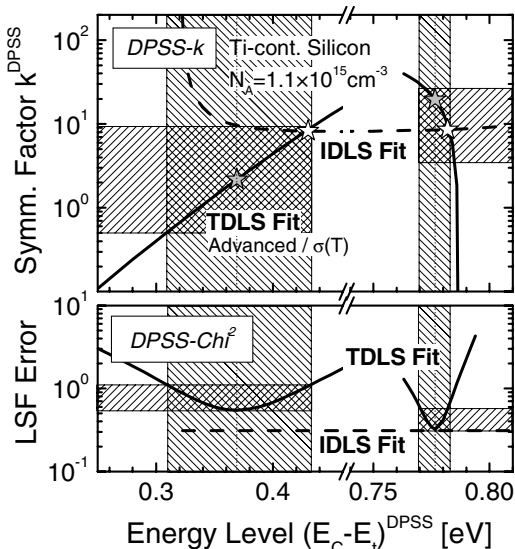


Fig. 4.18. Superposition of the DPSS diagrams associated with the TDLS (solid lines) and IDLS (dashed lines) curve of the titanium-contaminated sample Ti-I, the original DPSS diagrams being displayed in Figs. 4.15 and 4.13, respectively. Unambiguous determination of the titanium defect parameters from the intersection point of the DPSS- k curves in the MajBH (white star). The coincidence of this intersection point with the minimum of the DPSS- Chi^2 curve related to TDLS manifests the accuracy of the determination.

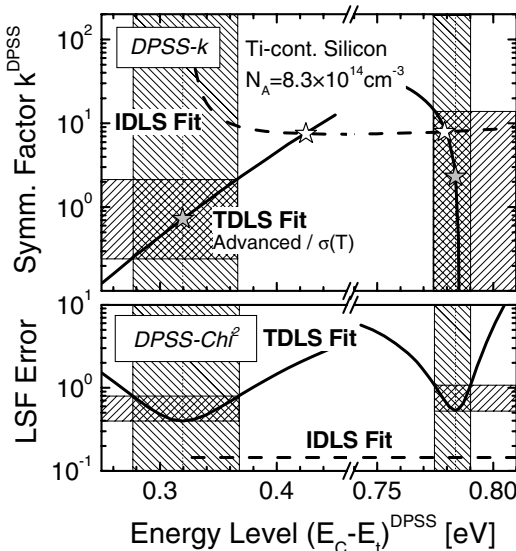


Fig. 4.19. Superposition of the DPSS diagrams associated with the TDLS (solid lines) and IDLS (dashed lines) curve of the titanium-contaminated sample Ti-II, the original DPSS diagrams being displayed in Figs. 4.16 and 4.13, respectively. Unambiguous determination of the titanium defect parameters from the intersection point of the DPSS- k curves in the MajBH (white star). The coincidence of this intersection point with the minimum of the DPSS- Chi^2 curve related to TDLS manifests the accuracy of the determination.

Figures 4.18 and 4.19 show the superposed DPSS diagrams for the high-doped (Ti-I) and medium-doped (Ti-II) titanium samples, respectively. As discussed in Sect. 3.6B, an unambiguous identification of the defect parameters is achieved from the intersection points of the DPSS- k curves associated with TDLS (solid lines) and IDLS (dashed lines). Since the DPSS- k curve associated with TDLS contains solutions of varying accuracy, the quality of the observed two DPSS- k intersection points (white stars) significantly depends on their energy distance from the corresponding minimum of the DPSS- Chi^2 curve related to TDLS. The exact coordinates of the DPSS- k intersection points are given in Table 4.7, where they are compared with the spectroscopic results obtained from the isolated analysis of TDLS and IDLS.

Since the energy position of the DPSS- k intersection point in the upper band gap half deviates by as much as 60 meV (Ti-I) and 100 meV (Ti-II) from the energy position of the corresponding DPSS- Chi^2 minimum, both diagrams consistently show that the TDLS solution in the upper band gap half has to be rejected for reasons of inconsistency. The extent of this inconsistency is particularly pronounced for Ti-II (see Fig. 4.19). Since the MinBH solution of TDLS lies with its energy value in the definition gap and with its k value below the plateau value of the DPSS- k curve associated with the IDLS curve, a modeling of the IDLS curve with these defect parameters completely fails, even qualitatively, which proves that the MinBH solution of TDLS definitely has to be excluded. In the lower band gap half, however, the energy positions of the DPSS- k intersection point and the minimum of

the DPSS- Chi^2 curve perfectly coincide in both diagrams. It can be concluded that the relevant titanium level is definitely located in the lower band gap half. This finding is supported by the fact that the DPSS- k intersection points in the lower band gap half nearly coincide for both samples (see Table 4.7). Averaging the defect parameters obtained from the two MajBH intersection points, the energy level of the titanium level is determined as $E_t-E_V=0.345\text{ eV}$ and the symmetry factor as $k=8.3$. Since the DPSS- k curves intersect almost vertically, the symmetry factor is determined with high accuracy, which could not be achieved from pure TDLS analysis due to the steep shape of the DPSS- k curve in the MajBH (see Sect. 4.3.1B).

However being aware of the unchangeable systematic error of the TDLS modeling, which has been found in the previous section to result in an overestimate of the true defect depth, the reliability of the combined result has to be critically scrutinized. If an accurate modeling of the whole TDLS curve can be achieved, it is expected from the observations in Sect. 4.4.2B that the associated DPSS- k curve in the MajBH is shifted horizontally towards the valence band edge. The impact of such a horizontal shift on the DPSS- k intersection point in the MajBH is easily assessed due to the vertical intersection of the DPSS- k curves, which implies that the E_t value of the intersection point mainly results from the TDLS analysis while its k value mainly results from the IDLS analysis. Consequently, any improvement in the TDLS modeling should be directly reflected in a reduction of the energy depth of the DPSS- k intersection point while its k factor should remain more or less unaffected.

Table 4.7. Overview of the spectroscopic results obtained on the two titanium-contaminated samples by means of the different LS techniques: TDLS alone, IDLS alone and the combination of TDLS and IDLS. The *parameter ranges in parentheses* behind the TDLS results indicate the error intervals determined from the advanced DPSS analysis.

Technique	Boundary conditions	MinBH defect E_C-E_t [eV]	k	MajBH defect E_t-E_V [eV]	k
Ti-I ($N_A = 1.1 \times 10^{15} \text{ cm}^{-3}$)	—	—	—	0.343 ± 0.010	8.6 ± 1.7
TDLS	Advanced / $\sigma(T)$ -model	0.369 (0.31–0.43)	2.2 (0.5–8.9)	0.348 (0.34–0.36)	19.6 (8.6–31)
IDLS	Two-defect fit	0.369 (E_t^{TDLS})	9.6	0.348 (E_t^{TDLS})	8.5
IDLS & TDLS	DPSS-IP	0.430	8.2	0.343	8.6
Ti-II ($N_A = 8.3 \times 10^{14} \text{ cm}^{-3}$)	—	—	—	0.346 ± 0.010	7.9 ± 1.6
TDLS	Advanced / $\sigma(T)$ -model	0.320 (0.28–0.37)	0.7 (0.3–2.2)	0.341 (0.33–0.35)	2.3 (10^{-6} –14)
IDLS	Two-defect fit	IDLS fit at E_t^{TDLS} impossible	impossible	0.341 (E_t^{TDLS})	8.0
IDLS & TDLS	DPSS-IP	0.425	7.5	0.346	7.9
Preliminary result		—	—	0.345 ± 0.010	8.3 ± 1.7

Any doubts as to whether such changes still allow an unambiguous identification of the band gap half, are cleared up by a simple consideration. Since the energy depth of an accurate MinBH fit of the TDLS curve will definitely be reduced below $E_c - E_t = 0.34$ eV, the improved MinBH solution will lie within the DPSS definition gap of the IDLS curves for at least one sample (Ti-II) but more likely for both. Apart from that, the simplified TDLS modeling in Sect. 4.4.2B revealed that in the case of the MinBH solution a reduced defect depth of the fit directly implies a further reduction of the optimum k factor (below the DPSS- k plateau values of the IDLS curves). Both trends show that the extent of the inconsistency of TDLS and IDLS in the MinBH may only increase upon an improved TDLS fit, which definitely proves the invalidity of the TDLS MinBH solution. Thus, in spite of the slight inadequacy of the TDLS modeling, the combined analysis of TDLS and IDLS allows the recombination-active titanium level to be unambiguously localized in the lower band gap half.

Apart from its significance for the characterization of the titanium center, the spectroscopic result reveals a fundamental requirement of TDLS. In order to guarantee reliable TDLS results, it is required to measure and model the TDLS curve over the whole T range, including the low- and high-temperature part. While the low-temperature part is required to configure the SRH model with respect to an underlying $\sigma(T)$ -dependence, the modeling of the TDLS bend due to intrinsic conduction (high-temperature part) on the basis of the advanced T -model allows model inconsistencies to be detected which may otherwise be undetected. The TDLS investigations on the titanium samples impressively demonstrated the serious impact that such undetected model inconsistencies may have on the spectroscopic result. Modeling the TDLS curves in a reduced T range on the basis of the simplified SRH model, the MinBH solution would have been identified with the true solution, although it can be unambiguously excluded by means of the combined analysis of TDLS and IDLS. As a consequence the titanium donor level would have been erroneously identified with the recombination-active titanium level by means of TDLS. Such a misinterpretation of the TDLS data is avoided if the TDLS curves are modeled over the whole T range by means of the advanced SRH model.

4.4.4 Comparison of results and discussion

A Comparison of LS results

Table 4.8 displays a comparison of the spectroscopic results obtained on the set of titanium-contaminated samples by means of the different LS techniques. For pure TDLS and for the combination of TDLS and IDLS,

those values are displayed which have been determined on the average of two samples, whereas the N_{dop} -IDLS result is based on all three samples. As the uncertainty of the TDLS results due to the unchangeable inadequacy of the advanced SRH model is only partly reflected in the E_t and k errors graphically deduced from the DPSS diagram, the symbol next to each value indicates its reliability.

While neither N_{dop} -IDLS nor TDLS allowed the band gap half to be identified, the combined analysis of TDLS and IDLS unambiguously revealed that the recombination-active titanium level is localized in the lower band gap half (see Sect. 4.4.3). However, since the quantitative spectroscopic results related to the TDLS curves are affected by the unchangeable systematic error of the TDLS modeling (see Sect. 4.4.2B), the defect parameters of the titanium level are determined with highest precision from the MajBH solution of the N_{dop} -IDLS experiment (see Sect. 4.4.1D). The recombination-active titanium level is thus found to be located at $E_t - E_V = (0.289 \pm 0.005)$ eV above the valence band edge, showing an electron/hole capture cross-section ratio $k = 12 \pm 1$. It has to be emphasized that this unambiguous spectroscopic result is obtained only from lifetime spectroscopy, the different LS techniques being combined.

The defect parameters finally extracted from the N_{dop} -IDLS experiment are confirmed by two observations. The energy level, on the one hand, is in good agreement with an energy depth of $\Delta E_t = 0.28$ eV which has been determined from an accurate modeling of only the Arrhenius increase of the TDLS curves, using the simplified SRH model in a reduced T range (see Sect. 4.4.2B). The symmetry factor, on the other hand, agrees well with the average capture asymmetry of $k = 11$ found for the TDLS MajBH

Table 4.8. Overview of the spectroscopic results obtained on the set of titanium-contaminated samples by means of the different LS techniques: TDLS alone, the combination of TDLS and IDLS and N_{dop} -IDLS. The numbers in the second column indicate the numbers of samples the results are averaged on. Optimum values (*bold font*) and error intervals (*standard font*) are extracted from advanced DPSS analysis. In addition, the symbol next to each value indicates its reliability: ✓ = high reliability, ⊗ = low reliability. The low reliability of the TDLS energies result from the unchangeable systematic deviation between the modeled and the measured slope of the Arrhenius increase, which is reflected in increased Chi^2 values of the optimum TDLS fits (see Table 4.6).

Technique	Av	Boundary conditions	MinBH defect			MajBH defect		
			$E_C - E_t$ [eV]	k		$E_t - E_V$ [eV]	k	
TDLS	2	Adv. / $\sigma(T)$	0.344 ± 0.035	⊗	1.5 ± 1.0	⊗	0.344 ± 0.005	⊗ 11.0 ± 12.0 ✓
IDLS & TDLS	2	—	No solution!	✓			0.345 ± 0.010	⊗ 8.3 ± 1.7 ✓
N_{dop} -IDLS	3	2-defect fit	0.350 ± 0.002	✓	12.1 ± 0.6	✓	0.289 ± 0.005	✓ 12.0 ± 0.7 ✓
Final result			—	✓ —			0.289 ± 0.005	✓ 12.0 ± 0.7 ✓

solution. Since the k factor of the MajBH solution arises mainly from a modeling of the TDLS bend due to intrinsic conduction, it is the only TDLS result that is less affected by the observed systematic error of the TDLS modeling and thus reliable. Both observations reflect the consistency of the LS results which is otherwise hidden due to the unchangeable inadequacy of TDLS modeling.

B Comparison with experimental DLTS results

To confirm the analytical result obtained from lifetime spectroscopy, all three titanium-contaminated materials have been analyzed by means of DLTS³⁸ using parallel samples which have been prepared from the same wafers used in the LS investigation. The study revealed two interesting results.

First, the DLTS spectrum measured on material Ti19 allowed the identification of a titanium level in the lower band gap half at $E_i-E_V=(0.290\pm 0.005)$ eV. The good agreement with DLTS results from the literature (see Table 4.5) on the one hand shows that the titanium contaminant is incorporated in the silicon lattice as predicted, which ensures the suitability of the titanium samples to characterize lifetime spectroscopy. The excellent agreement with the final LS result on the other hand demonstrates the high precision of the energy determination achieved by means of lifetime spectroscopy, and verifies the direct comparability of the spectroscopic results obtained from both techniques.

However, such a successful detection of titanium by means of DLTS has only been achieved on the material with highest titanium concentration (Ti19: $[Ti]=2\times 10^{13}$ cm⁻³). In contrast, no DLTS peak has been detected in the DLTS spectra of the two other materials with lower titanium concentrations of 2×10^{10} and 2×10^{11} cm⁻³. The negative DLTS result reveals that the lower contamination levels already lie below the detection limit of DLTS³⁹ although they are high enough to significantly reduce carrier lifetime ($\tau_{LL}^{DLTS}=7-14\mu s$ at 300 K). This observation impressively demonstrates one of the major advantages of lifetime spectroscopy over DLTS. Since

³⁸ The DLTS measurements have been performed at Fraunhofer ISE. The experimental setup and the box-car data evaluation technique used are described in detail in [24].

³⁹ Strictly speaking the sensitivity of DLTS depends on the ratio N_i/N_A , which is determined for the two critical samples to 2×10^{-4} (Ti-I) and 2×10^{-5} (Ti-II). Taking into account the fact that the DLTS sensitivity limit is normally specified at $N_i/N_A>1\times 10^{-5}$, our DLTS results reveal a slightly reduced sensitivity of the DLTS system used. However, since sample Ti-II almost reaches the widely accepted sensitivity limit of DLTS, the experimental results still prove that lifetime spectroscopy exhibits a higher sensitivity to recombination-active defect levels than DLTS.

the sensitivity of lifetime spectroscopy depends on the product $\sigma_n \times N_t$ and not on the defect concentration N_t alone as for DLTS, lifetime spectroscopy is highly sensitive to electrically active defect levels even if their concentration lies below the detection limit of DLTS, as shown for the medium- and low-contamination titanium samples. The accuracy of the LS results and its extraordinary sensitivity make lifetime spectroscopy a highly sensitive diagnostic tool to detect those defect levels which are relevant to photovoltaic applications.

C Comparison with results from the literature and discussion

The energy of the titanium level which is consistently determined as $E_t - E_V = (0.289 \pm 0.005)$ eV from lifetime spectroscopy (see Sect. 4.4.4A) and $E_t - E_V = (0.290 \pm 0.005)$ eV from DLTS (see Sect. 4.4.4B) perfectly agrees with the energy of the titanium double donor level which has been determined in the literature as $E_t - E_V = (0.28 \pm 0.01)$ eV using standard DLTS [1]. Concerning the magnitude of the capture cross-sections of the titanium double donor level, DLTS only allowed the hole capture cross-section to be determined as $\sigma_p = 1.9 \times 10^{-16} \text{ cm}^2$ [1], while the electron capture cross-section σ_n is still unknown. Since the electron/hole capture cross-section ratio is accurately determined from lifetime spectroscopy as $k = 12 \pm 1$, the missing capture cross-section can be determined by combining the results from lifetime spectroscopy and DLTS. Calculating the product $\sigma_n = k \times \sigma_p$, we find a value of $\sigma_n = (2.3 \pm 0.2) \times 10^{-15} \text{ cm}^2$ for the unknown electron capture cross-section of the titanium double donor level.

Comparing the recombination parameters of the two deep titanium levels reveals an interesting aspect of the recombination via titanium-related centers. From the literature, the titanium donor level in the upper band gap half is known to be located at $E_C - E_t = 0.27$ eV and to exhibit an electron capture cross-section $\sigma_n = 1.3 \times 10^{-14} \text{ cm}^{-3}$ [1]. The fact that lifetime spectroscopy identifies the double donor level in the lower band gap half as the level with highest recombination activity, in spite of a similar energy depth and an electron capture cross-section reduced by almost an order of magnitude, directly implies that the unknown hole capture cross-section of the titanium donor level must be very low ($\sigma_p < 10^{-17} \text{ cm}^{-3}$) and the corresponding symmetry factor very high ($k > 1000$), respectively. This at first surprising result demonstrates impressively that standard DLTS results, consisting of the energy level and the cross-section for the capture process from the nearer band, are not sufficient to assess the recombination activity and thus the relevance of a defect level. A further limitation arises from the fact that capture cross-sections determined from DLTS are tainted with a relatively high uncertainty, as the determination requires an extrapolation

of the Arrhenius plot to zero inverse temperature, i.e. infinite temperature. Both underline the practical importance of the relative defect parameters E_t and k determined from lifetime spectroscopy. Being determined with high precision, E_t and k allow the recombination activity of the associated defect center to be assessed in detail.

4.4.5 Conclusion

From an experimental point of view the lifetime spectroscopic investigations on the set of titanium-contaminated samples unambiguously identified the titanium double donor level as the recombination-active titanium level. In good agreement with DLTS results reported in the literature, the energy level is determined at $E_t-E_V=(0.289\pm 0.005)$ eV. Concerning the capture properties, a value $k=12\pm 1$ is found for the unknown symmetry factor, which reveals an enhancement of the electron capture. Using the hole capture cross-section σ_p known from the literature, the k factor allows the unknown electron capture cross-section to be determined as $\sigma_n=(2.3\pm 0.2)\times 10^{-15}$ cm², which completes our knowledge of the electronic properties of the titanium double donor level. DLTS investigations on parallel samples precisely confirmed the energy level determined from lifetime spectroscopy. The fact that two of the titanium samples turned out to have defect concentrations below the detection limit of DLTS, demonstrated on the one hand the relevance of titanium as a lifetime-killing contaminant and on the other hand the extraordinary sensitivity of lifetime spectroscopy to electrically active defect levels, which represents one of the major advantages of lifetime spectroscopy over DLTS.

From a methodological point of view the study revealed the excellent performance of N_{dop} -IDLS. Provided that the simultaneous SRH analysis of the set of IDLS curves is realized by means of the superposed DPSS analysis proposed in the present work, N_{dop} -IDLS allows spectroscopic results of remarkable precision even if the boundary conditions of the experiment are unfavorable. In full agreement with theoretical predictions, the N_{dop} -IDLS analysis determines two equivalent solutions. Since these solutions only coincide in the k factor, neither the band gap half nor the energy depth of the defect level can be determined unambiguously from N_{dop} -IDLS. The true solution has been identified from a combination of IDLS and TDLS.

The TDLS investigations on the titanium samples led to a small but unchangeable systematic error in the TDLS modeling, which could most likely be attributed to an undetected change in the underlying $\sigma(T)$ -dependence. To identify such model inadequacies, which is essential to assess the

reliability of TDLS results, it is shown to be mandatory that the TDLS curve is measured over the whole T range – including the low-temperature region and the TDLS bend due to intrinsic conduction – and that it is modeled on the basis of the complete advanced SRH model. Modeling TDLS curves in a reduced T range with a simplified configuration of the SRH model may lead to a significant misinterpretation of the TDLS data in spite of a high quality of the fit. Consequently, whenever accurate SRH modeling can be achieved within the whole T range, precise spectroscopic TDLS results are guaranteed. While the accurate modeling of the Arrhenius increase (reduced T region) may be regarded as a *necessary condition* for a precise result, the accurate modeling in the whole T range on the basis of the advanced SRH model represents the *sufficient condition*.

4.5 Nickel

Nickel, which belongs to the fast-diffusing 3d transition metals, is one of the main impurities in device production. Nickel is a component of steel which is widely used in the production of equipment. As contamination takes place by simple mechanical contact of the wafers with such equipment, it may easily arise during production and processing of wafers. As discussed in Sect. 4.2.1B, nickel precipitates almost quantitatively even when quenching the sample from high temperatures. As a consequence, only small residual quantities between 0.01 and 1 % of the respective solubility remain dissolved and form electrically active defects. However, due to the very high solubilities of nickel, this still allows defect concentrations of 10^{12} – 10^{14} cm $^{-3}$, which demonstrates that nickel defects cannot be ignored with respect to a deterioration of device performance. Although dissolved nickel may be situated on interstitial and substitutional lattice sites, only slow-diffusing substitutional nickel is expected to exist at room temperature as interstitial nickel diffuses very fast even at room temperature and thus disappears by outdiffusion and precipitation [1]. The electrically active incorporation of nickel on substitutional lattice sites gives rise to three energy levels: a double acceptor and an acceptor state in the upper band gap half and a donor state in the lower band gap half [1]. As indicated in Table 4.5, values for the energy levels and the cross-sections for capture from the nearer band edge have already been determined by means of standard DLTS. But as reliable data for the second capture cross-section are missing for all three levels, the ranking of the levels with respect to their recombination activity is still an open question. Thus the lifetime spectroscopic investigation on nickel-contaminated samples aims to identify the relevant defect level and to complete our knowledge of its

Table 4.9. Electronic properties of substitutional nickel in silicon as they are known from the literature. The given defect parameters are taken from [1] and represent averages of the data from different authors.

Defect	Type	Energy [eV]	Capture cross-sections			Technique
			σ_p [cm ²]	σ_n [cm ²]	E_∞ [eV]	
Ni _s	Double acceptor	$E_C - 0.07$?	5.4×10^{-18}	—	DLTS
Ni _s	Acceptor	$E_C - 0.39$?	5.6×10^{-17}	—	DLTS
Ni _s	Donor	$E_V + 0.17$	1.1×10^{-15}	?	—	DLTS

electronic properties. Moreover, since the set of nickel samples consists of a *p*-type and an *n*-type sample of similar doping concentration, the impact of the doping type on the recombination activity can be investigated. However, due to the low sample size, it has only been possible to perform TDLS measurements.

4.5.1 TDLS analysis of a *p*-type sample

As pointed out in Sect. 4.2.1C, the nickel samples have been prepared at the University of Berkley by thermal indiffusion. To ensure accurate lifetime measurements, the expected surface layers containing the unavoidable nickel precipitates have been removed by etching several microns of silicon from the contaminated wafers before passivating the surfaces with SiN. Parallel control samples without any nickel contamination have been processed on both material types. Since both nickel-contaminated samples exhibit room-temperature lifetimes which lie more than an order of magnitude below the lifetime of the corresponding control sample, it may be concluded that the lifetime data measured on both nickel-contaminated samples are affected neither by surface recombination nor by residual bulk defects, and thus reflect almost entirely the effect of the nickel-related defects.

A Thermal stability of the nickel defect

Figure 4.20 shows the temperature-dependent low-injection lifetime for an intentionally nickel-contaminated *p*-type silicon sample. The three curves displayed have been measured during an initial heating up to 600 K (open circles), a subsequent cooling down to 160 K (closed circles) and a final re-heating up to 600 K (gray circles). The observed increase of carrier lifetime after the first heating step most likely results from an incomplete nickel precipitation during sample preparation. The second heating step reveals no further lifetime change and identically reproduces the TDLS curve of the cooling step, which suggests that the initial heating cycle was sufficient

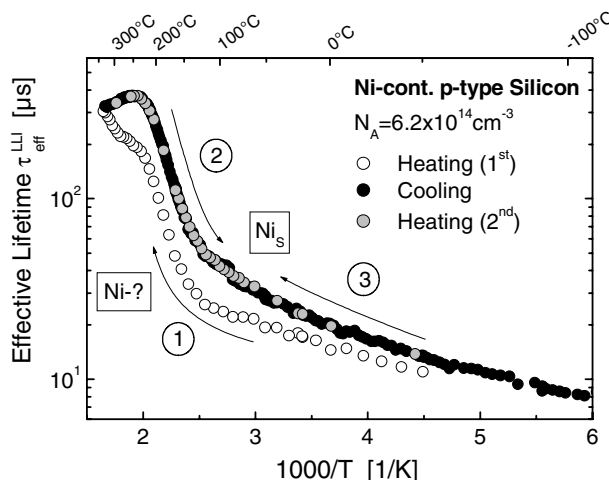


Fig. 4.20. Temperature-dependent low-injection lifetime of an intentionally nickel-contaminated *p*-type silicon sample after heating (open circles), cooling (black circles) and re-heating (gray circles). The permanent change in the lifetime after the first heating is most likely due to an incomplete precipitation during sample preparation.

to complete the precipitation process. The fact that the lifetime increases after precipitation, brings evidence that the nickel precipitates are electrically inactive, as assumed in the literature, and thus do not affect the lifetime measurements.⁴⁰ Due to the complete outdiffusion and precipitation of highly mobile, interstitially dissolved nickel during the first heating step, the thermally stable TDLS curve (solid circles) is expected to be related to substitutional nickel, known to diffuse very slowly. This consideration also holds for the *n*-type sample whose TDLS curves showed the same irreversible change upon heating and cooling as observed in Fig. 4.20 for the *p*-type sample.

B Advanced DPSS analysis of the TDLS curve

Since an accurate TDLS analysis necessarily requires a stable defect structure and a constant defect concentration over the whole *T* range, only the thermally stable TDLS curve recorded during cooling has been subjected to the SRH analysis. The measured lifetime data cover a broad *T* range from 160 to 600 K, whose upper temperature limit corresponds to the

⁴⁰ Note that the residual precipitates are most likely formed near the surfaces, whose influence on the effective carrier lifetime is very limited due to the high sample thickness of around 730 μm.

highest temperature the carrier lifetime has been measured at so far.⁴¹ Both the measured (symbols) and the modeled (lines) TDLS curves are displayed in Fig. 4.21a.

As can be seen, the high-temperature part of the TDLS curve ($T > 500$ K) is well described if the SRH model is based on the advanced T -model. This demonstrates once again that accurate modeling of the TDLS bend due to intrinsic conduction requires one to consider the temperature-induced narrowing of the silicon band gap $E_{gap}(T)$ when calculating the temperature-dependent equilibrium carrier concentrations $p_0(T)$ and $n_0(T)$.

Concerning the low-temperature part of the TDLS curve ($T < 360$ K), the modeling completely fails for $\sigma = \text{const.}$ (thin dashed line). Since the measured TDLS data are not affected by carrier trapping and thus equal the minority capture time $\tau_{n0}(T)$ in the broad T range from 160 to 360 K, the underlying $\sigma(T)$ -model can be determined with high precision (see Sect. 3.5.1C). As shown by the thin solid line, the observed decrease of the capture cross-section with increasing temperature can be modeled in terms of $\sigma(T) = \sigma_0 \times T^\alpha$ with an exponent $\alpha = -2.4$. According to the survey of capture mechanisms in Sect. 3.5.1A, the identified $\sigma(T)$ -model either points towards a cascade capture process [19] or an excitonic Auger capture process [20]. While the cascade mechanism is unlikely due to a high energy depth of 0.40 eV of the underlying defect center (see below), the excitonic Auger mechanism is likely to be the dominant process, favored by the measurement conditions used, which are based on the optical injection of electron-hole pairs (see discussion in Sect. 3.5.1B).

Thus a perfect modeling of the TDLS curve in the whole T range from 160 to 600 K is achieved if both the advanced T -model and the underlying $\sigma(T)$ -dependence are taken into account in the SRH model (see thick solid line in Fig. 4.21a). The spectroscopic evaluation of the TDLS curve is performed with maximum transparency by means of the DPSS analysis. If we use the optimum model configuration, which is again referred to as the *advanced SRH model*, the defect parameter solution surface associated with the TDLS curve takes the shape displayed in Fig. 4.21b and c. As can be seen from the two DPSS- Chi^2 minimums, the advanced SRH model allows the TDLS curve to be modeled for a defect in the upper and the lower band gap half. Since the MinBH and the MajBH solutions are identical in quality, the pure TDLS analysis does not allow an identification of the true solution. Thus, the relevant nickel level may either be located 0.40 eV below the CB edge or 0.42 eV above the VB edge, which at least

⁴¹ To our knowledge, concerning measured carrier lifetimes, an upper temperature limit of 520 K has not been exceeded in the literature so far [25].

gives a reasonable estimate of its energy depth. Concerning the symmetry factor k , the two solutions differ much more due to the fundamental difference between MinBH and MajBH defects discussed in Sect. 3.5.6A. While the capture cross-sections of the MinBH solution are found to be almost symmetric ($k=0.7$), the branch of DPSS- k curve related to the MajBH solution only yields an upper bound for the possible k factors ($k<0.6$). Note that the k confinement to lower k values is achieved owing to the modeling of the TDLS bend due intrinsic conduction (see Sect. 3.5.7B), the expected k uncertainty being even higher for a reduced T range. The errors in the extracted defect parameters are again estimated using the DPSS diagram and tolerating a least squares error of twice its optimal value. The ranges of acceptable values are visualized in Fig. 4.21b and c by the shaded areas and displayed in Table 4.10 by the parameter intervals in brackets given in addition to the actual defect parameters.

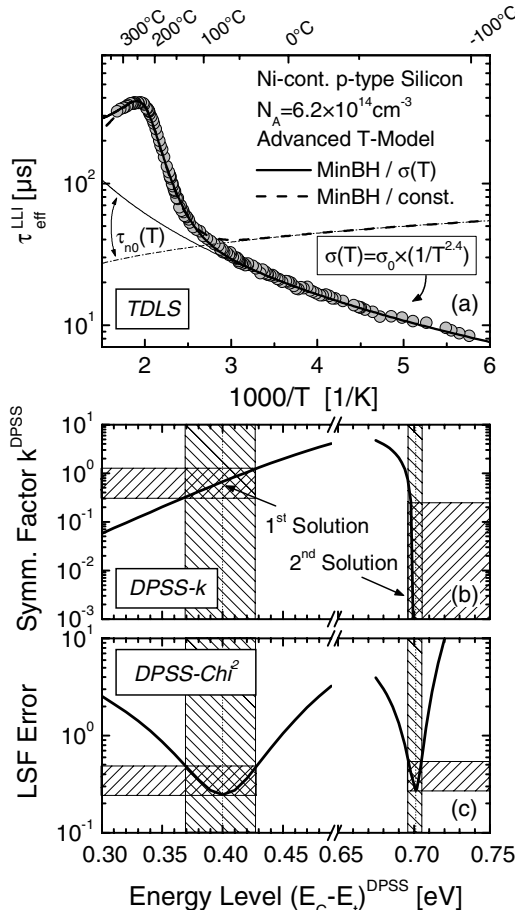


Fig. 4.21. TDLS investigation on an intentionally nickel-contaminated p -type silicon sample. (a) The SRH modeling of the measured lifetime data (symbols) is based on the advanced T -model with (solid lines) and without (dashed lines) taking into account the underlying $\sigma(T)$ -model. (b,c) Advanced DPSS analysis of the TDLS curve based on the optimum configuration of the SRH model. The minimum values of the displayed DPSS- χ^2 curves being equal, an unambiguous identification of the band gap half the defect is located in is not possible.

In order to investigate the impact of the $\sigma(T)$ -model on the spectroscopic result, the TDLS curve has finally been modeled for $\sigma=\text{const.}$, the advanced T -model still being taken into account. The arising SRH fit assuming a MinBH defect is displayed in Fig. 4.21a (dashed line). The fitted T range has been reduced to 360–600 K to avoid artificial distortions of the spectroscopic result due to structural differences between the modeled and the observed T -dependence.⁴² The spectroscopic results obtained for the MinBH and the MajBH solution are displayed in Table 4.10. Though still possible, the modeling for a MajBH defect leads to a fit whose quality is reduced by a factor of 3 compared to that for a MinBH defect. Thus ignoring the underlying $\sigma(T)$ -dependence would lead to an identification of the relevant nickel level in the upper band gap half. Due to the actual strong $\sigma(T)$ -dependence, which is considered in the advanced SRH fit, the MinBH solution of the simplified SRH fit (with $\sigma=\text{const.}$) is shifted 60 meV deeper into the band gap and exhibits a symmetry factor k which is increased by almost an order of magnitude. The qualitative change of the DPSS structure and the strong quantitative shift of the extracted defect parameters both demonstrate the significance of an accurate modeling of the $\sigma(T)$ -dependence.

Table 4.10. Spectroscopic TDLS results obtained on the two intentionally nickel-contaminated silicon samples investigated in Figs. 4.21 and 4.22, respectively. Optimum values (*bold font*) and error intervals (*standard font*) are determined from advanced DPSS analysis. *Shaded gray* are the optimum parameters of the two different nickel levels found to be most recombination-active in *p*-type (*upper half*) and *n*-type (*lower half*) silicon, respectively.

Fit parameters		Fitted T -model	Defect in upper BGH E_C-E_t [eV] k Chi^2			Defect in lower BGH E_t-E_V [eV] k Chi^2		
Ni1: <i>p</i> -type, $N_A = 6.2 \times 10^{14} \text{ cm}^{-3}$		<i>MinBH</i>			<i>MajBH</i>			
Advanced	$\propto 1/T^{2.4}$	160–600 K	0.400 ± 0.030	0.7 (0.3–1.3)	0.25	0.424 ± 0.004	< 0.64 No restriction	0.27
Advanced	Const.	360–600 K	0.461	5.6	0.13	0.403	11.9	0.38
Ni2: <i>n</i> -type, $N_D = 1.8 \times 10^{14} \text{ cm}^{-3}$		<i>MajBH</i>			<i>MinBH</i>			
Advanced	$\propto 1/T^{2.5}$	100–550 K	TDLS fit in MajBH impossible!			0.189 ± 0.060	3500 (890–12900)	0.12

BGH = band gap half

⁴² Note that below 360 K the simplified SRH model does not even allow a qualitatively correct description of the observed T -dependence of carrier lifetime.

C Comparison with results in the literature and discussion

Since the pure TDLS experiment yields two equivalent solutions for the underlying defect center, the true solution may only be identified from a comparison of the extracted energies with the energies of known nickel levels, reported in the literature. A closer look at Table 4.9 reveals that the energy level of the MinBH solution, which is determined as $E_C-E_t=(0.40\pm 0.03)\text{ eV}$, is in good agreement with the energy level $E_C-E_t=(0.39\pm 0.02)\text{ eV}$, which is reported in the literature for a deep acceptor level related to substitutional nickel [1]. This result was obtained from DLTS measurements. Since the acceptor level is the only deep level known for substitutional nickel (see Table 4.9), it is identified with the help of TDLS to be the nickel level with the highest recombination activity in *p*-type silicon. The implicit assumption that the recombination-active defect states originate from substitutional nickel is confirmed by the fact that none of the defect levels frequently reported for different nickel complexes [17] fits any of the energies extracted from TDLS.

From the fact that the energy depth of the nickel acceptor level is accurately determined for the advanced SRH model and significantly overestimated for the simplified SRH model (with $\sigma=\text{const.}$) (see Table 4.10), it can be concluded that the consideration of an underlying $\sigma(T)$ -dependence is mandatory for an accurate spectroscopic TDLS result. This in turn requires a measurement of the TDLS curve down to sufficiently low temperatures, as the $\sigma(T)$ -model has to be determined from the low-temperature part of the TDLS curve. Since the low-temperature part of the investigated TDLS curve exhibits an extraordinary width of 200 K, the model for the observed distinctive *T*-dependence of the capture cross-sections is determined with very high precision. The TDLS analysis thus allows the excitonic Auger capture to be identified for the first time as the dominant capture mechanism of the nickel acceptor level.

Concerning the magnitude of the capture cross-sections of the nickel acceptor level, DLTS only allowed the electron capture cross-section $\sigma_n=5.6\times 10^{-17}\text{ cm}^2$ to be determined [1], while the hole capture cross-section is still unknown. Since the considerations above unambiguously identified the MinBH solution of the TDLS analysis as the true solution, TDLS alone yields an accurate determination of the symmetry factor $k=0.7\pm 0.5$, which shows that the capture cross-sections of the nickel acceptor level are almost symmetric. Combining the results of TDLS and DLTS and calculating the ratio $\sigma_p=\sigma_n/k$, the unknown hole capture cross-section of the nickel acceptor level is determined as $\sigma_p=(8.0\pm 5.7)\times 10^{-17}\text{ cm}^2$.

4.5.2 TDLS analysis of an *n*-type sample

Figure 4.22a2 displays the TDLS curve of the nickel-contaminated *n*-type silicon sample, which has been measured in a broad T range from 90 to 550 K. Note that the lower temperature limit corresponds to the minimum sample temperature which has been reached with the cryostat used. Since the *n*-type sample showed the same irreversible change of carrier lifetime upon heating and cooling as the *p*-type sample (see Fig. 4.20), the thermally stable TDLS curve recorded during cooling from 550 K has again been chosen for the SRH analysis.

A Advanced DPSS analysis of the TDLS curve

The remarkable lifetime increase in the low-temperature region from 90 to 310 K (dark gray symbols) may be attributed to a decrease in the capture cross-section with increasing temperature. Since the measured TDLS data are again free from superposed carrier trapping and thus equal $\tau_{n0}(T)$ below 310 K, it is possible to determine the underlying $\sigma(T)$ -model with high precision. As shown in Fig. 4.22a2 (solid line), the modeling again reveals a power law dependence $\sigma(T) = \sigma_0 \times T^\alpha$ with an exponent $\alpha = -2.5$.

Since the spectroscopic TDLS result critically depends on the modeling of the high-temperature part of the TDLS curve ($T > 310$ K, light gray symbols), this temperature region is displayed in more detail in Fig. 4.22a. Taking into account the advanced T -model and the underlying $\sigma(T)$ -dependence, an accurate SRH modeling of both the Arrhenius increase ($T > 310$ K) and the TDLS bend due to intrinsic conduction ($T > 450$ K) is achieved if a MinBH defect in the lower band gap half⁴³ is assumed (solid line). Since the SRH modeling for a MajBH defect completely fails (dashed line), TDLS alone allows an unambiguous identification of the relevant defect center in the lower band gap half. With $E_r - E_V = 0.19$ eV and $k = 3500$ (see Table 4.10), the defect level is found to be quite shallow and unusually asymmetric with respect to the capture of electrons and holes. However since the E_r - and k -dominated Arrhenius increase of the TDLS curve is very short, the respective T region being less than 100 K wide (see Fig. 4.22a), the accuracy of the spectroscopic result is limited. In the associated DPSS diagram shown in Fig. 4.22b and c, this is directly reflected in the flatter shape of the DPSS- Chi^2 curve. Tolerating a least squares error of twice its optimum value, the ranges of acceptable values (shaded areas) are as broad as 0.14–0.25 eV for the energy level and 900–12900 for the symmetry factor.

⁴³ Due to the *n*-type doping, the lower band gap half has to be identified with the MinBH and the upper band gap half with the MajBH.

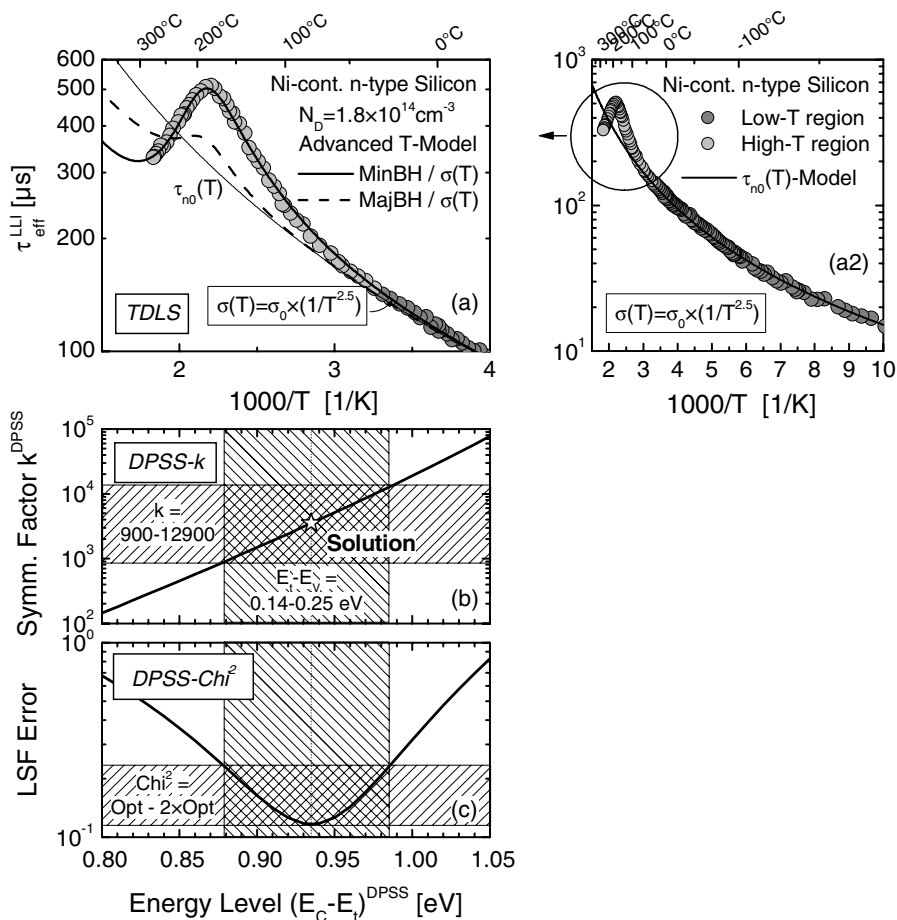


Fig. 4.22. TDLS investigation on an intentionally nickel-contaminated *n*-type silicon sample. (a2) The remarkable lifetime increase in the low-temperature region from 90 to 310 K (dark gray symbols) reveals a strong *T*-dependence of the capture cross-sections. (a) Taking into account the underlying $\sigma(T)$ -model, an accurate SRH modeling of the high-temperature part from 310–550 K (light gray symbols) is only achieved for a MinBH defect (solid line) on the basis of the advanced *T*-model. The failure of the SRH modeling for a MajBH defect (dashed line) allows an unambiguous identification of the relevant defect center in the lower band gap half (see Table 4.10). (b,c) Error estimation of the extracted defect parameters by means of the advanced DPSS analysis (shaded areas).

B Comparison with results in the literature and discussion

The determined energy level $E_i - E_V = (0.19 \pm 0.06) \text{ eV}$ is in good agreement with an energy level $E_i - E_V = (0.17 \pm 0.01) \text{ eV}$ reported in the literature for a shallow donor level related to substitutional nickel [1]. Since none of the

defect levels frequently reported for different nickel complexes [17] fits the extracted energy, the Ni_s-donor level is unambiguously identified to be the nickel level with highest recombination activity in *n*-type silicon.

Since it is too shallow to be electrically active, the recombination activity of the nickel donor level results from two characteristics: a large hole capture cross-section $\sigma_p = 1.1 \times 10^{-15} \text{ cm}^2$ known from DLTS, which ensures an effective capture of minorities (holes) from the slightly populated valence band; and the strong capture asymmetry disclosed here, which guarantees a further increased capture probability for majorities (electrons) from the distant conduction band. Combining the results from TDLS (k) and DLTS (σ_p) and calculating the product $\sigma_n = k \times \sigma_p$, the unknown electron capture cross-section of the nickel donor level is determined as $\sigma_n = 3.9 \times 10^{-12} \text{ cm}^2$. Due to the high k uncertainty (see Table 4.10), the error interval ranges from $9.8 \times 10^{-13} \text{ cm}^2$ to $1.4 \times 10^{-11} \text{ cm}^2$. Since the accuracy of DLTS in determining capture cross-sections is known to be limited, a further unknown error arises from σ_p .

Moreover, TDLS reveals a distinctive T -dependence of the capture cross-sections of the identified nickel donor level. Although the $\sigma(T)$ -model equals the one determined for the nickel acceptor level (on the *p*-type sample), the conclusions to be drawn with respect to the underlying capture mechanism differ: due to the low energy depth of the nickel donor level, either the excitonic Auger capture [20] or the cascade capture process [19] may be the dominant process of carrier capture. The fact that carrier capture may even be governed by both processes at once may explain the large capture cross-sections observed for the donor level.

4.5.3 Conclusion

As expected, the study of nickel-contaminated samples shows that the electrically active nickel levels originate from substitutional nickel. However, TDLS reveals that, depending on the doping type, the carrier lifetime is limited by two different nickel levels: in *p*-type silicon by a deep acceptor level at $E_C - E_t = (0.40 \pm 0.03) \text{ eV}$ and in *n*-type silicon by a shallow donor level at $E_t - E_V = (0.19 \pm 0.06) \text{ eV}$. The quality of the TDLS results manifests itself in the perfect agreement of the extracted energies with DLTS results reported in the literature. This agreement is due to the extraordinary quality of both the measured TDLS data and the applied SRH modeling. Without being screened by external carrier trapping, the TDLS curves reflect the recombination properties of the respective nickel levels down to temperatures of 160 K (*p*-type) and 90 K (*n*-type), respectively, and thus allow an accurate determination of the underlying $\sigma(T)$ -models.

These TDLS curves are accurately modeled over the whole T range, which is as wide as 440 K (p -type) and 460 K (n -type), if the advanced configuration of the SRH model is used.

In addition to the identification of relevant nickel levels, the TDLS analysis yields for both levels the symmetry factors k and thus completes our knowledge of their electronic properties. While the capture cross-sections of the acceptor level are found to be almost symmetric ($k=0.7$), those of the donor level are found to be unusually asymmetric ($k=3500$), the capture cross-section for electrons being enhanced compared to that for holes. In fact it is the strong capture asymmetry of the donor level, which explains why the ranking of the acceptor and the donor level with respect to their recombination activity is inverted in n -type compared to p -type silicon. The observation that the dominant defect level of a given impurity may change with the doping type, shows that a simple transfer of the defect parameters of an impurity to a sample with opposite doping type may lead to an erroneous estimate of the material quality.

The relevance of nickel with respect to a deterioration of device performance is reflected in the low room-temperature lifetime of $20\mu\text{s}$ observed for the p -type sample. In spite of a strong tendency to disappear into electrically inactive precipitates, the remaining fraction of substitutional nickel may be high enough to affect carrier lifetime significantly due to the high solubilities of nickel.

4.6 Iron

Iron, which belongs to the moderately fast diffusing 3d transition metals, is one of the main impurities in device fabrication. Its technological importance arises on the one hand from the many sources of iron contamination during wafer processing and on the other hand from its detrimental effects on device performance even at very low concentrations.

While iron contamination during crystal growth may be excluded for today's monocrystalline silicon, it is still a relevant problem for multicrystalline silicon [26], which is used for photovoltaic devices. Moreover, iron contamination may easily occur during wafer processing, since any mechanical contact of the wafer surface with iron or stainless steel (production equipment) and any liquid-phase contact with iron-contaminated solutions will produce an almost unlimited contamination source for a subsequent high-temperature step. Once introduced into the wafer bulk, iron either forms precipitates or remains dissolved, which depends on the cooling cycle (see Sect. 4.2.1). While iron precipitates are responsible for

increased leakage currents and reduced breakdown resistances and thus may reduce production yields, dissolved and thus electrically active iron represents the most common lifetime-killing contaminant. Dissolved iron is incorporated on an interstitial lattice site and gives rise to only a single deep donor level in the lower band gap half. In boron-doped *p*-type silicon interstitially dissolved iron (Fe_i^+) tends to form pairs with the shallow boron acceptors (B_s^-). These iron-boron pairs (FeB) are bound together by Coulomb attraction and give rise to a donor level in the lower and an acceptor level in the upper band gap half. Since the two defect configurations of iron, Fe_i and FeB, are both detrimental for the material quality and coexist at room temperature, they are both relevant from a practical point of view. In silicon device technology, considerable interest in the exact recombination properties of the two defect states arises from the fact that the most sensitive technique for detecting iron contamination and determining its total concentration is based on a quantitative analysis of the well-established difference in the low-injection recombination strength of Fe_i ions and FeB pairs (see Sect. 4.6.2A). Since iron is probably the most accurately characterized and well understood metallic impurity in silicon, the study is well suited to provide further confirmation of the potential of lifetime spectroscopy for the characterization of impurities in semiconductors. However, in spite of intensive studies in the past, there are still open questions that lifetime spectroscopy may provide answers to.

As a starting point, Sect. 4.6.1 thus provides a short overview of the recombination properties of the two iron-related defect configurations and critically assesses the accuracy with which the individual recombination parameters have been determined in the literature. Being relevant to experimental design, the fundamental aspects of defect transformation are briefly discussed in Sect. 4.6.2. The actual impact of the defect transformation on temperature- and injection-dependent lifetime measurements is investigated within a pilot experiment in order to identify the optimum measurement conditions and pretreatments which enable TDLS and IDLS curves that are dominated – as far as possible – by either the Fe_i defect or the FeB defect, but not by both configurations at once. The quality of the optimum TDLS and IDLS curves with respect to the purity of the underlying defect configuration is examined quantitatively on the basis of empirical relations from the literature. The detailed LS investigations to determine the recombination parameters of the interstitial iron (Fe_i) and the iron-boron pair (FeB) are presented in Sects. 4.6.3 and 4.6.4, respectively. Both studies are based on a single iron-contaminated boron-doped silicon sample, which is investigated by conducting a pure TDLS analysis, a pure IDLS analysis and a combined analysis of TDLS and IDLS. Section 4.6.5 finally evaluates the additional information contained in the combined

system of the Fe_i - and FeB-dominated IDLS curves to gain deeper insight into the recombination parameters of the iron-boron pair.

4.6.1 Previous work and special physical properties

Intensive studies in the past have revealed markedly different recombination properties for the Fe_i ion and the FeB pair. Based on two recent reviews published independently by Graff [1] and Istratov et al. [2], these results are to be summarized in the following (i) to identify those recombination parameters which have been determined with high precision and should definitely be confirmed in the present study, and (ii) to pose open questions lifetime spectroscopy may provide answers to. Table 4.11 presents an overview of the recombination parameters determined for both defect states, containing the average values from the review articles [1, 2] as well as the individual results from the few original studies based on lifetime spectroscopy.

A Electrical properties of the Fe_i defect

Interstitially dissolved iron forms two charge states, a neutral and a positively-charged state, which give rise to a single donor level in the lower band gap half [2]. In numerous studies using DLTS, Hall effect and electron paramagnetic resonance (EPR), its energy level has been consistently determined as $E_t - E_V = (0.385 \pm 0.010)$ eV [1, 2].⁴⁴ DLTS studies revealed that the hole capture is thermally activated with a barrier energy $E_\infty = (0.045 \pm 0.005)$ eV [2], which clearly indicates that holes are captured by the Fe_i^0 center via the multiphonon emission mechanism (see Sect. 3.5.1A). As pointed out in [2], the activation energy E_∞ has been determined quite consistently by different authors, although the absolute values of the underlying hole capture cross-sections $\sigma_p(T)$ varied by more than an order of magnitude. This strong scatter in the $\sigma_p(T)$ data directly reflects the large uncertainty of capture cross-sections determined by means of DLTS, which is inherently produced by the required extrapolation of emission-rate data to an axis. To achieve maximum accuracy in determining the magnitude of σ_p , Istratov et al. [2] determined a new parameterization of the exponential T -dependence of the hole capture cross-section, which is based on a least squares fit of all $\sigma_p(T)$ data published to date.⁴⁵

⁴⁴ The given energy value represents the average of the two average values determined by Istratov et al. [2] and Graff [1] (see Table 4.11).

⁴⁵ Fitting the experimental $\sigma_p(T)$ data with the expression $\sigma_p(T) = \sigma_{p0} \times \exp(-E_\infty/k_B T)$, Istratov et al. determined the free model parameters as $\sigma_{p0} = (3.9 \pm 0.5) \times 10^{-16} \text{ cm}^2$ and $E_\infty = (0.045 \pm 0.005)$ eV [2].

Table 4.11. Electronic properties of interstitial iron (Fe_i) and iron-boron pairs (Fe_iB_s) in silicon. Values with the label [Av] represent average values of results from various techniques and authors, as published in two review articles. All other values come from original studies using different LS techniques (see *reference list*). The uncertainty in the knowledge of the individual recombination parameters of the two iron defect configurations is indicated by the symbols (see *table notes*), which thus reflect the open questions.

Defect type	Energy [eV]	Capture cross-sections σ_p [cm^2] σ_n [cm^2]			k	E_∞ [eV]	Technique [Ref.]
Fe _i Donor	$E_V + 0.38$ [Av] $E_V + 0.39$ [Av]	7.0×10^{-17} [Av] —	4.0×10^{-14} [Av] —	570 —	0.045 —	Average [a] Average [b]	
<i>Reliability</i>	✓	✓	⊗	⊗	✓		
FeB Donor	$E_V + 0.10$	2.0×10^{-14}	4.0×10^{-13}	20	—	Average [a]	
FeB Acceptor	$E_C - 0.27$ [Av]	2.0×10^{-15} [c]	1.6×10^{-15} [c]	0.8	—	Average [b]	
	$E_C - 0.26$ [Av]	3.0×10^{-14} [e]	2.5×10^{-15} [e]	0.08	—	Average [a]	
	$E_C - 0.26$ [??]	2.0×10^{-15}	1.6×10^{-15}	0.8	—	[c]	
	$E_C - 0.29$	—	—	—	—	TDLS [d]	
	$E_C - 0.30$	3.0×10^{-14}	2.5×10^{-15}	0.08	—	N_{dop} -IDLS [e]	
	$E_C - 0.23$	2.0×10^{-15}	3.0×10^{-14}	15	—	N_{dop} -IDLS [f]	
<i>Reliability</i>	⊗	⊗	⊗	⊗	—		

✓ = Results from the literature consistent and accurate.

⊗ = Results from the literature inconsistent and/or uncertain.

[a] = Ref. [2], Istratov 1999.

[b] = Ref. [1], Graff 2000.

[c] = Ref. [27], Zoth 1990.

[d] = Ref. [28], Hayamizu 1991.

[e] = Ref. [29], Walz 1996.

[f] = Ref. [30], Macdonald 2001.

Using this parameterization, the hole capture cross-section of Fe_i at 300 K results in $\sigma_p = 7.0 \times 10^{-17} \text{ cm}^2$, which represents the most reliable value available to date. By contrast, the electron capture cross-section of Fe_i has been determined less accurately in the literature. The investigations being restricted to 300 K, nothing is known about the capture mechanism for electrons. Moreover, since the average room-temperature value of $\sigma_n = 4.0 \times 10^{-14} \text{ cm}^2$ is based on only two studies, it is much less reliable than the value for σ_p . As a consequence, the resulting symmetry factor $k = \sigma_n/\sigma_p = 570$ of the Fe_i donor level is tainted with a large uncertainty.

Since lifetime spectroscopy allows a direct and accurate k determination, the present study should provide an improved knowledge of both the capture symmetry factor k and the electron capture cross-section σ_n . The quality of the LS result may be assessed from the extracted energy level E_∞ ,

which should accurately confirm the average result from the literature. In spite of the intensive studies on the Fe_i defect in the past, determination of its recombination parameters E_t and k by means of lifetime spectroscopy has never been attempted, as far as we know.

B Electrical properties of the FeB defect

As summarized in [2], there is strong evidence from various studies using DLTS, Hall effect, EPR and FTIR that the FeB pair in silicon forms three charge states – a neutral, a positively- and a negatively-charged state – which give rise to a shallow *donor level* near the valence band edge and a deep *acceptor level* near the conduction band edge. While the donor level is known to be located at $E_t-E_V=0.1\text{ eV}$ [2], the acceptor level has been determined on average at $E_C-E_t=(0.26\pm 0.03)\text{ eV}$ [2]. The few lifetime spectroscopic studies [28–30] already performed on the FeB defect consistently identified the acceptor level as the dominant recombination center. But as can be seen from the spectroscopic results compiled in Table 4.11, only the energy level is known with some precision, while the results for the capture cross-sections and the symmetry factor are very inconsistent.

Hayamizu et al. [28] examined the temperature dependence of the LLI lifetime and demonstrated in a detailed SRH analysis that their data could only be adequately described by a relatively deep level around 0.29 eV, coinciding with the energy depth of the FeB acceptor level determined in previous DLTS experiments. The temperature dependence of LLI lifetime was reproduced in a later experiment by Kaniava et al. [31] but led to useless spectroscopic results for the FeB defect as the characteristic shape of the lifetime curve was completely misinterpreted (see Sect. 4.6.2B). Using a set of iron-diffused wafers of intermediate resistivities, Walz et al. [29] investigated the injection dependence of the recombination lifetime at room temperature. They also found that a modeling on the basis of the deep acceptor level described their experimental data significantly better than a modeling on the basis of the shallow donor level. Assuming the acceptor level at $E_C-E_t=0.29\text{ eV}$ and fitting the IDLS curves simultaneously, they were able to determine values for the capture cross-sections of the acceptor level⁴⁶ and found a capture asymmetry $k < 1$ (see Table 4.11). Five years later, Macdonald et al. [30] repeated this experiment under improved conditions, studying wafers with a broader range of resistivities in a broader

⁴⁶ Both IDLS studies [29, 30] determined the parameter set $(E_t, \sigma_n, \sigma_p)$ instead of (E_t, k, τ_{n0}) for the FeB defect, since a determination of the defect concentrations $[\text{FeB}]$ and $[\text{Fe}_i]$ was part of the modeling. For this modified IDLS analysis, the total iron concentration had to be determined separately.

injection range. They obtained the best fit result for a defect level at $E_C-E_t=0.23\text{ eV}$ and found a reversed asymmetry of the capture cross-sections ($k>1$, see Table 4.11).⁴⁷ The assessment of the quality of the spectroscopic results obtained from the two IDLS studies [29, 30] reveals a critical point. Since the SRH modeling of the IDLS curves had to be based on the combined effect of the FeB acceptor level and the Fe_i donor level, it was essential to make assumptions about the recombination parameters of the Fe_i donor level, as a simultaneous determination of both defect levels could not be achieved, the data being underdetermined. But as pointed out in the previous section, from the literature, only $E_i(\text{Fe}_i)$ and $\sigma_p(\text{Fe}_i)$ are known with high precision whereas the values available for $\sigma_n(\text{Fe}_i)$ and $k(\text{Fe}_i)$, respectively, are tainted with a large uncertainty. As a consequence, the spectroscopic results obtained for the FeB acceptor level are tainted with this uncertainty, which the present study reveals to be significant (see Sect. 4.6.3). Since the two studies were performed in 1996 and 2001, respectively, they differ in their assumptions about the Fe_i recombination parameters, which may partly explain the mentioned discrepancies in the recombination parameters determined for the FeB acceptor level (see Table 4.11).

In view of these uncertainties and discrepancies in the results of the previous studies, the present study aims at a complete characterization of the FeB acceptor level – reducing the assumptions from the literature to a minimum – (i) to prove its dominance as recombination center compared to the FeB donor level and (ii) to elucidate which of its capture cross-sections is actually enhanced, i.e., whether $k>1$ or $k<1$.

4.6.2 Defect transformation and its effect on carrier lifetime

As both defect configurations of iron are metastable, the planning of experiments to determine the recombination properties of the Fe_i and the FeB defect requires a detailed knowledge of the defect transformation between the two states. Fortunately, extensive studies in the literature on the kinetics of defect transformation gave quite a complete picture.

Since the *association kinetics* of FeB pairs may be described as a diffusion-limited trapping of mobile iron donors (Fe_i^+) by immobile boron acceptors (B_s^-), the association process is thermally activated, being limited

⁴⁷ Curiously, their data did not actually allow an unambiguous identification of the FeB acceptor level as dominant recombination center, as a satisfactory SRH modeling was also achieved for the FeB donor level at $E_t-E_V=0.1\text{ eV}$. However, using a physical argument from Brotherton et al. [32], Macdonald et al. were able to reject this result.

by the diffusion barrier E_{mig} of interstitial iron. Due to the electrostatic bond of the FeB pairs, the *dissociation kinetics* are determined by the potential barrier for a jump of the Fe_i ion away from the nearest-neighbor position of the boron atom. Thus, the dissociation process is also thermally activated, being limited by the dissociation energy E_{diss} . As $E_{diss} > E_{mig}$, the association process dominates at lower temperatures ($T < 100^\circ\text{C}$), while the dissociation process dominates at higher temperatures ($T > 150^\circ\text{C}$). As a consequence, the FeB pairs represent the stable defect configuration in thermal equilibrium at room temperature. It is known from the literature that the dissociation reaction of FeB pairs is also enhanced by minority carrier injection, which may be realized either by illumination or by the application of a forward bias. The observed stimulation of pair dissociation upon these treatments is explained by a recombination-enhanced defect reaction (REDR), which assumes that the energy released during recombination at the FeB center is entirely converted to vibrations of the defect and thus enables its dissociation. As summarized in the schematic diagram of Fig. 4.23, pair dissociation may thus be induced thermally, optically or by minority carrier injection, while pair association requires the sample to relax in the dark at temperatures well below 100°C .

For an accurate spectroscopic analysis of the two defect configurations it is essential (i) to prepare pure states, where the sample is dominated by only one of the two defect configurations, and (ii) to conserve these states during TDLS and IDLS measurements, i.e., to avoid movements of the equilibrium position between the two defect configurations during the measurements.⁴⁸ While the first prerequisite requires a suitable optical or thermal pretreatment of the sample, the second necessitates a careful choice of the conditions used for the lifetime measurements, because the varied measurement parameters, temperature and injection density (illumination), stimulate the defect transformation in both directions (see Fig. 4.23). To identify the optimum measurement conditions and pretreatments for a TDLS and an IDLS investigation of the Fe_i and the FeB defect, respectively, the impact of temperature and illumination on the injection- and temperature-dependent carrier lifetime is studied in a pilot experiment. After a qualitative discussion of the observed effects, the quality of the optimum TDLS and IDLS curves with respect to the purity of the underlying defect configuration is examined quantitatively on the basis of empirical relations from the literature. The whole investigation is performed on an iron- and boron-doped silicon sample with $[\text{B}_s] = 2.9 \times 10^{14} \text{ cm}^{-3}$ and $[\text{Fe}] = 2.9 \times 10^{12} \text{ cm}^{-3}$.

⁴⁸ Note that any change in the defect concentration within a TDLS or IDLS curve prevents its spectroscopic evaluation, since the quantitative SRH analysis fails.

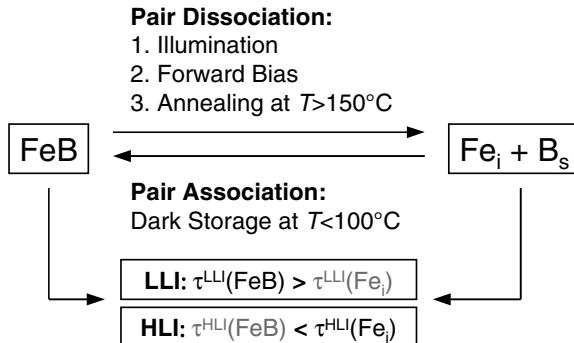


Fig. 4.23. Schematic diagram of the defect transformation between interstitial iron (Fe_i) and iron-boron pairs (Fe_iB_s) showing the different processes known to induce the association and dissociation of FeB pairs. The recombination activity of the two metastable defect states strongly depends on the injection level, being higher for the Fe_i defect under LLI conditions and for the FeB defect under HILI conditions.

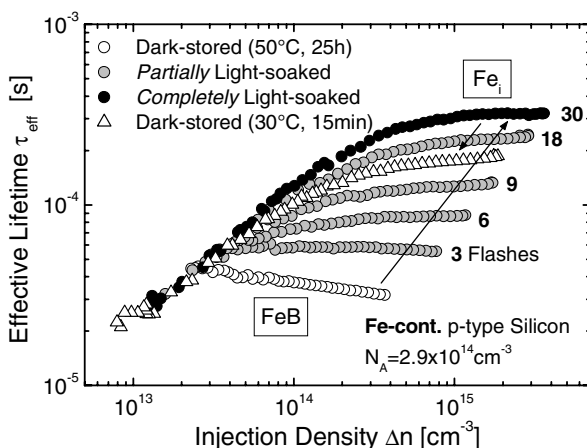


Fig. 4.24. Effect of light soaking on the injection-dependent carrier lifetime measured by means of the QSSPC technique on an intentionally iron-contaminated boron-doped *p*-type silicon sample ($[\text{Fe}] = 2.9 \times 10^{12} \text{ cm}^{-3}$, $N_A = [\text{B}] = 2.9 \times 10^{14} \text{ cm}^{-3}$). Starting from a slightly decreasing IDLS curve after a dark storage for 25 h at 50°C (white circles), which is mainly induced by FeB pairs, the IDLS curve becomes steeper with an increasing number of flashes (with maximum power). The qualitative change of the IDLS curves (gray circles) originates from the optical dissociation of the FeB pairs. The asymptotic IDLS curve reached after 30 flashes (black circles) may be attributed mainly to the Fe_i defect. Storage in the dark again decreases the IDLS curve (white triangles), reflecting the re-association of FeB pairs. At the crossover point of the two asymptotic IDLS curves (black and white circles), the carrier lifetime remains unchanged upon defect transformation, which reflects an identical recombination activity of the FeB and the Fe_i defect (at that special Δn).

A Effect of the defect transformation on the injection-dependent carrier lifetime

Figure 4.24 displays the impact of light soaking on the injection-dependent carrier lifetime at room temperature measured on the iron-contaminated sample by means of the QSSPC technique. Being the stable defect configuration at room temperature, FeB pairs dominate the initial IDLS curve (open circles) which has been measured after dark storage for 25 h at 50°C. The observed slight decrease points towards the shallow level expected for the FeB defect. Flashing the sample in-between the lifetime measurements with maximum power of the QSSPC flash (peak intensity = 25 W/cm², decay time = 1.9 ms), the IDLS curve becomes steeper with an increasing number of flashes (gray circles). The qualitative change in the IDLS curve directly results from the optical dissociation of FeB pairs. As can be seen, the light-soaked IDLS curves approach an asymptotic shape, which is achieved after 30 flashes (black circles) and mainly reflects the recombination properties of the Fe_i defect. A subsequent storage in the dark again leads to a decrease in the IDLS curve (open triangles) which is induced by a re-association of FeB pairs.

Comparing the two asymptotic IDLS curves before and after dissociation reveals a characteristic feature of the two iron-related defects, which is well known from the literature [2]: while the Fe_i defect exhibits higher recombination activity under LLI conditions, the FeB defect does so under HLI conditions. Consequently, dissociation of FeB pairs leads to a lifetime decrease under LLI conditions and to a lifetime increase under HLI conditions. At the crossover point of the two IDLS curves, which is identified in Fig. 4.24 at 2×10^{13} cm², the carrier lifetime remains unchanged upon defect transformation, which reflects an identical recombination activity of the FeB and the Fe_i defect. In a very recent publication [33], Macdonald et al. deduced some general features of the crossover point and suggested its identification as a criterion to detect iron contamination in silicon. Starting from these results, the crossover point will be exploited in Sect. 4.6.5 to gain deeper insight into the recombination properties of the FeB pairs.

B Effect of the defect transformation on the temperature-dependent carrier lifetime

Figure 4.25 displays the impact of light soaking and temperature on the temperature-dependent carrier lifetime under LLI conditions measured on the iron-contaminated sample by means of the MW-PCD technique. If the sample is kept in the dark before (for 25 h at 50°C) and in-between the lifetime measurements, the TDLS curve (open circles) exhibits an unusual S-shape during ramping-up ①, which is reproduced during ramping-down

② if the sample is kept in the dark. The unusual lifetime decrease between 95 and 155°C may be attributed to thermal dissociation ① (thermal re-association ②) of FeB pairs, as an increasing portion of Fe_i reduces the effective carrier lifetime due to the higher recombination activity of the Fe_i defect under LLI conditions (see previous section). This interpretation is strongly supported by the fact that the S-shape completely disappears if the ramping-down is not performed in the dark but under strong illumination ($I_{bias} = 0.3 \text{ W/cm}^2$) in-between the lifetime measurements (closed circles). If the dissociation of FeB pairs is stimulated optically, their thermal re-association below 155°C can obviously be avoided. It can be concluded that TDLS curve ③ is dominated by the Fe_i defect in the whole T range. The coincidence of the TDLS curves ① and ③ above 155°C proves a dominance of the Fe_i defect in that temperature region even under dark conditions. However, below 95°C the dark TDLS curves ①② are dominated by the FeB defect. Further proof of the assumed FeB dominance is provided by the fact that the lifetime level of the dark TDLS curves ①② is significantly higher than that of the Fe_i -dominated TDLS curve ③, which directly reflects the lower recombination activity of the FeB defect under LLI conditions.

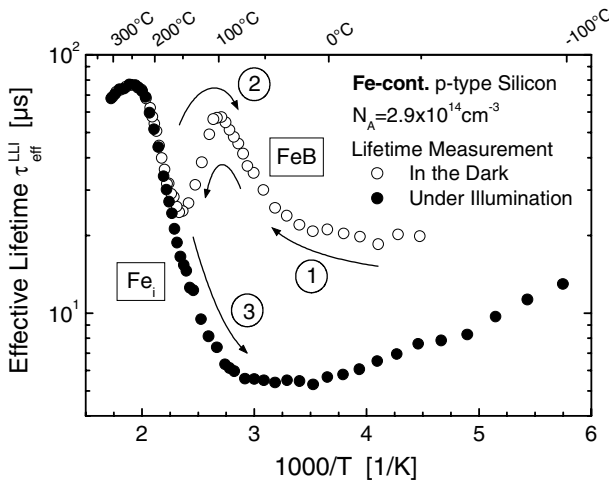


Fig. 4.25. Effect of light soaking and temperature on the temperature-dependent carrier lifetime under low-level injection, measured by means of the MW-PCD technique on the intentionally iron-contaminated p -type silicon sample investigated in Fig. 4.24. If the sample is kept in the dark in-between the lifetime measurements, the TDLS curve (open symbols) exhibits a peak at 100°C which is reproduced during ramping-up ① and ramping-down ②. The unusual lifetime change between 100 and 150°C may be attributed to thermal dissociation ① (thermal re-association ②) of FeB pairs. If the sample is illuminated with a maximum bias light ($I_{bias} = 0.3 \text{ W/cm}^2$) in-between the lifetime measurements, thermal re-association of the FeB pairs during ramping-down ③ is avoided, the TDLS curve (closed symbols) thus reflecting the Fe_i defect.

While the S-shape of the dark TDLS curves ①② has already been observed in two earlier TDLS studies [28, 31], the qualitative change of the TDLS curves upon illumination has not been reported so far. Following the argumentation given above, the qualitative change unambiguously disproves the interpretation of the S-shape given by Kaniava et al. [31]. They explained the peak around 100°C by superimposed temperature-dependent carrier trapping and attributed the Arrhenius increase in the high-temperature region to another deep level of the FeB pair, which is definitely incorrect. The practical importance of the observed qualitative change of the TDLS curves upon illumination is that it represents a new fingerprint of iron contamination. As there is no other contaminant known to show such a behavior, measuring the temperature-dependent lifetime in the dark and under strong illumination provides a very robust criterion to detect iron in silicon.

C Quality of the LS curves after dark storage: paired fraction before dissociation

Although there is no doubt that keeping the sample in the dark before and during the measurement results in IDLS and TDLS curves which are dominated by the FeB defect in the complete injection range and the lower T range, respectively, the purity of the FeB defect state has to be investigated quantitatively in both LS curves to assess their suitability for spectroscopic analysis.

The equilibrium fraction of FeB pairs before dissociation may be estimated according to the following empirical relation [34]:

$$\frac{[FeB]}{[Fe_i]} = C_1 N_A \times \exp\left(\frac{U_1}{k_B T}\right) \quad (4.3)$$

with $C_1 = 10^{23} \text{ cm}^3$ and $U_1 = 0.65 \text{ eV}$. For the present sample with $N_A = 2.9 \times 10^{14} \text{ cm}^{-3}$ this results in 99.6% present as FeB pairs at 300K. However, the time required for the sample to reach thermal equilibrium at room temperature is determined by the kinetics of pair association. It is known from the literature that an excess Fe_i concentration generated by thermal or optical dissociation re-associates according to a mono-exponential decay with a characteristic time τ_{assoc} , which depends on both doping concentration and temperature [27]:

$$\tau_{assoc} = \frac{C_2}{N_A} T \times \exp\left(\frac{U_2}{k_B T}\right) \quad (4.4)$$

The two empirical constants are given by $C_2=4.3\times10^5\text{ cm}^{-3}\text{K}^{-1}\text{s}$ and $U_2=0.68\text{ eV}$. For the present sample, Eq. (4.4) yields a value of 33 h for the association time constant at room temperature, which implies that the density of FeB pairs reaches 99 % of its equilibrium value after 150 h. To reduce the required relaxation time, we increased the dark-storage temperature. At 50°C an acceptable relaxation time of 25 h is achieved ($\tau_{assoc}=5.4\text{ h}$). As the equilibrium fraction of FeB pairs still amounts to 97.6 % according to Eq. (4.3), the dark-storage conditions chosen in the present study (25 h at 50°C) ensure almost complete pairing and are thus adequate to prepare the FeB state.

In addition to the pretreatment, the measurement process itself has to be examined as it may cause significant dissociation of FeB pairs. As for the illumination, the assessment of its impact can be based on the results of a recent study by Macdonald et al. [33]. Using for IDLS measurements the same QSSPC system as in the present study, they convincingly demonstrated that the required flashing of the sample with a xenon lamp does not induce pair dissociation as long as the peak intensity is kept below 5 W/cm². As this value has not been exceeded in the present study, the IDLS curve measured after dark storage (open triangles in Figs. 4.24 and 4.33a) purely reflects the recombination properties of the FeB pairs.

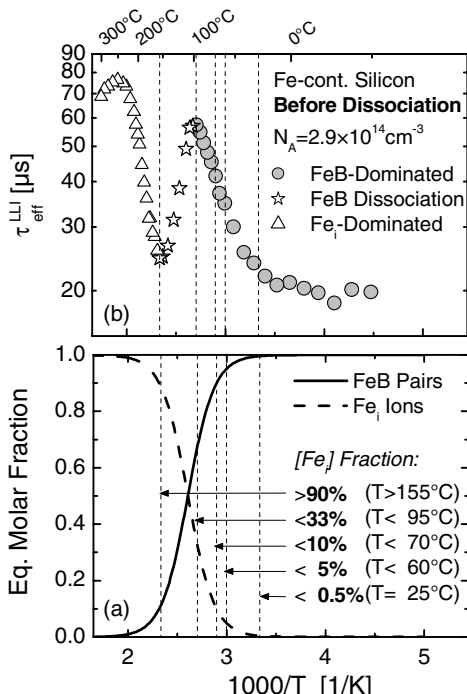


Fig. 4.26. (a) Equilibrium portions of FeB pairs (solid line) and Fe_i ions (dashed line) as a function of temperature, only taking into account thermal dissociation. The calculations are based on the empirical Eq. (4.3), considering the low doping concentration of the sample under investigation. (b) Impact of the thermal dissociation of FeB pairs on the TDLS curve measured in the dark (① in Fig. 4.25). The vertical lines indicate different threshold values of the equilibrium [Fe_i] portion. Being negligible at room temperature, it increases to 33 % at 95°C (TDLS peak) and thus significantly affects the Arrhenius increase of the FeB-dominated part of the TDLS curve (gray circles).

Since the illumination used for measurement of the LLI lifetime by means of the MW-PCD technique is much weaker (below 0.01 W/cm^2), optical dissociation can be even more surely excluded for the TDLS curve (open circles in Fig. 4.25). However, in the case of TDLS the impact of thermal dissociation has to be taken into account. As shown in Fig. 4.26a, the temperature dependence of the equilibrium portions of FeB pairs (solid line) and Fe_i ions (dashed line) can be determined on the basis of the empirical Eq. (4.3) considering the low doping concentration of the investigated sample. Both curves are displayed as a function of inverse temperature to enable a direct assignment of the calculated equilibrium portions to the dark TDLS curve ①, which is displayed in Fig. 4.26b for comparison.

The quantitative analysis confirms the interpretation of the qualitative TDLS shape given in Sect. 4.6.2B. Since the equilibrium portion of Fe_i increases in the T range from 95°C (TDLS peak) to 155°C (TDLS valley) from 33 % to 90 % and since the Fe_i ion is the center of higher recombination activity under LLI conditions, the lifetime decrease observed above 95°C (open stars) is definitely due to thermal dissociation of FeB pairs. Since the equilibrium portion of Fe_i exceeds 90 % above 155°C , the high-temperature part of the dark TDLS curve (open triangles) definitely reflects the recombination properties of the Fe_i defect and not of another deep level of the FeB defect as assumed by Kaniava et al. [31]. Unfortunately, thermal dissociation not only influences the high-temperature part of the dark TDLS curve. As the equilibrium portion of Fe_i continuously increases from negligible 0.5 % at 25°C to 33 % at 95°C (TDLS peak), it becomes evident that the Arrhenius increase of the FeB-dominated part of the dark TDLS curve is significantly affected by thermal dissociation, which impedes an accurate TDLS analysis of the FeB defect (see Sect. 4.6.4A).

It has to be concluded that an accurate spectroscopic analysis of the FeB defect may only be achieved from the room-temperature IDLS curve which has proved to reflect the pure FeB state.

D Quality of the LS curves after illumination: paired fraction after dissociation

Finally, let us investigate the quality of the IDLS and TDLS curves which were measured after strong illumination of the sample. To assess their suitability for a spectroscopic analysis of the Fe_i defect, the portion of iron which is interstitial after optical dissociation has to be estimated quantitatively.

It is known from the literature that the dissociation rate increases linearly with the injection density [2], so the intensity of the steady-state illumination used for optical dissociation has been chosen as high as 0.1 W/cm^2 or above. To get an impression of the dissociation kinetics, the dissociation

time constant τ_{diss} , being characteristic of the mono-exponential decay of FeB pairs upon illumination, has been determined for the present sample. Using an illumination with 0.1 W/cm^2 , τ_{diss} values of 9.5 min at 25°C and 3 min at 75°C have been found. The observed decrease of τ_{diss} with increasing temperature reflects a weak thermal activation of the process of optical dissociation, which is also reported in the literature [2]. Moreover, the short dissociation times demonstrate the high reaction velocities of optical dissociation, which ensures an efficient dissociation of FeB pairs in the whole T range. In a recent publication [33] Macdonald et al. demonstrated convincingly that a strong optical steady-state illumination with 0.1 W/cm^2 in fact results in almost complete dissociation of FeB pairs. This observation ensures that carrier lifetimes measured after optical dissociation are only influenced by the Fe_i defect, provided the post-dissociation measurement is performed quickly enough to avoid repairing.

In the case of IDLS, this prerequisite is easily realized by illuminating the sample on the QSSPC stage with an additional bias light of 0.1 W/cm^2 , which is switched off directly before flashing the sample for the lifetime measurements.

In the case of TDLS, the sample is illuminated in the whole T range with a maximum bias light of 0.3 W/cm^2 between subsequent lifetime measurements. However, to guarantee LLI conditions of the TDLS curve, the lifetime measurements themselves are performed at the minimum bias light intensity excluding trapping effects (see Sect. 4.2.5B). On the average it is possible to realize the lifetime measurements with a delay of approximately 10 seconds after switching off the strong bias light. The efficiency of this measurement routine to suppress a repairing depends on temperature, the T range being roughly divided into three parts:

- **$T < 30^\circ\text{C}$:** As the repairing time constant τ_{assoc} of the present sample is as high as 33 h at room temperature and further increases towards lower temperatures, a repairing (within the delay of 10 s) can be almost excluded in the low-temperature part of the TDLS curve.
- **$T = 30\text{--}150^\circ\text{C}$:** As the repairing time constant significantly decreases with increasing temperature, being as low as 17 min at 100°C , repairing becomes more critical in this intermediate T range of the TDLS curve. However, at 100°C the quantitative estimate from Eq. (4.4) still reveals a 99.0 % portion of Fe_i after 10 s in the dark, which demonstrates the adequacy of the measurement procedure to suppress repairing.⁴⁹

⁴⁹ The fact that according to Eq. (4.4) an increase in the doping concentration by an order of magnitude directly results in a decrease of τ_{assoc} by the same amount, demonstrates the suitability of low-doped samples for investigations of the Fe_i state.

- **$T > 150^\circ\text{C}$:** Although the repairing time constant decreases to values below 1.5 min above 150°C , repairing can be completely neglected in the high-temperature part of the TDLS curve as temperature becomes an additional driving force for dissociation, the equilibrium FeB portion at 150°C being as low as 15 % (see Fig. 4.26).

It can be concluded that the TDLS curve measured under illumination is affected in the whole T range by the Fe_i defect alone and is thus ideally suited for its spectroscopic analysis. The same holds for the room-temperature IDLS curve.

4.6.3 Defect configuration of interstitial iron (Fe_i^+)

Having successfully verified the quality of the TDLS and IDLS curve measured after optical dissociation, we may now turn our attention to their spectroscopic analysis to determine the recombination parameters of the Fe_i defect.

A Advanced TDLS analysis: consideration of the complete Range

Figure 4.27a displays TDLS curve ③, which reflects the recombination properties of the Fe_i defect in the whole T range from 175 to 580 K. As a starting point for the spectroscopic analysis, let us first determine the optimum configuration of the SRH model. As can be seen in Fig. 4.27a, the high-temperature part of the TDLS curve ($T > 500$ K) is well described if the SRH model is based on the advanced T -model. Concerning the low-temperature part ($T < 285$ K), an accurate SRH modeling fails for $\sigma = \text{const.}$ (thin dotted line) and requires the introduction of a temperature-dependent capture cross-section. Being free of superimposed carrier trapping, the measured TDLS data equal the minority capture time constant $\tau_{n0}(T)$ in the T range from 175 to 285 K (dark gray circles), which allows an accurate determination of the underlying $\sigma(T)$ -model (see Sect. 3.5.1C). The observed $\tau_{n0}(T)$ decrease reflects an exponential increase of the capture cross-section with temperature, which can be modeled in terms of $\sigma(T) = \sigma_0 \times \exp(-E_\infty/k_B T)$. Fitting this exponential $\sigma(T)$ -model to the data (thin solid line), the activation energy of the capture process is determined as $E_\infty = 0.024$ eV. According to the survey of capture mechanisms in Sect. 3.5.1A, the identified $\sigma(T)$ -model unambiguously shows that carrier capture into the Fe_i defect occurs via the multiphonon emission mechanism [35]. This is a fundamental difference with the other contaminants investigated so far, which all showed a power-law-dependent decrease of the capture cross-sections, most likely reflecting the excitonic Auger capture mechanism [20].

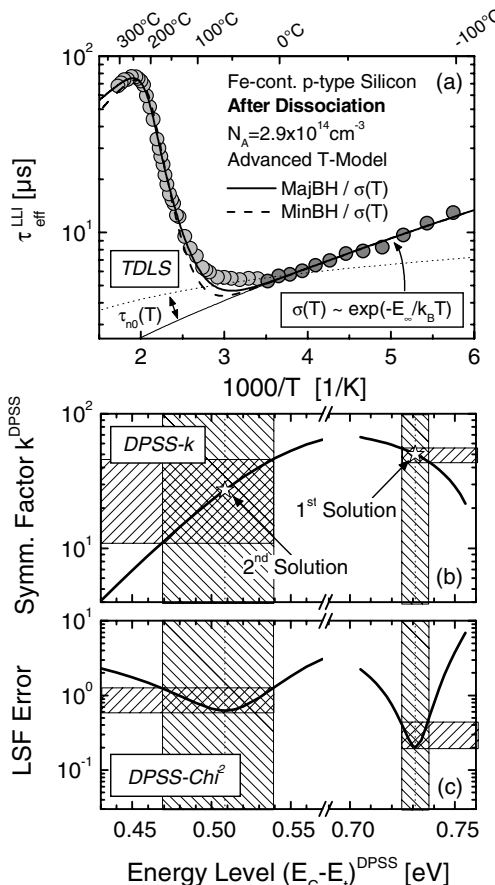


Fig. 4.27. Advanced DPSS analysis of the Fe_i -dominated TDLS curve ③ taking into account the data in the whole T range (175–580 K). (a) While accurate modeling below 285 K (dark gray circles) requires the insertion of an exponential $\sigma(T)$ -model (thin solid line), accurate modeling of the IC-induced TDLS bend above 500 K necessitates the advanced T -model. Taking into account both the underlying $\sigma(T)$ -model and the advanced T -model, the SRH modeling is performed for a MinBH (dashed line) and a MajBH defect (solid line). (b,c) As the minimum values of the DPSS- χ^2 curve differ significantly, the Fe_i -related defect level is unambiguously localized in the lower band gap half. The errors in the extracted defect parameters (shaded areas) are estimated for tolerated χ^2 values of twice their optimum values. The accurate k determination for the MajBH solution only becomes possible because the TDLS bend due to intrinsic conduction is measured and modeled over a broad T range from 500–580 K.

Using the optimum configuration of the SRH model (advanced SRH model), which takes into account both the underlying $\sigma(T)$ -model and the advanced T -model, the SRH modeling of the TDLS curve is performed for a MinBH (dashed line) and a MajBH defect (solid line) as displayed in Fig. 4.27a. To enable a transparent spectroscopic evaluation of the TDLS curves, Figs. 4.27b and c display the associated defect parameter solution surface, which has also been determined on the basis of the advanced SRH model. Since the DPSS- χ^2 minimum in the MajBH is reduced by more than a factor of three compared to the DPSS- χ^2 minimum in the MinBH, the MajBH solution can be identified as the true solution. TDLS alone thus allows a complete characterization of the Fe_i -related defect level, which is localized in the lower band gap half at $E_t - E_V = (0.393 \pm 0.005) \text{ eV}$ and found to exhibit a capture asymmetry of $k = 50 \pm 5$. The errors in the extracted defect parameters are estimated from the DPSS diagram tolerating a least

squares error of twice its optimum value (shaded areas in Figs. 4.27b and c). As can be seen, both parameters of the MajBH solution are determined with high precision. While the E_t precision is characteristic of any MajBH solution (see Sect. 3.5.7B), the precision in the k determination directly results from modeling the distinctive TDLS bend due to intrinsic conduction, which has been measured over a broad T range from 500 to 580 K. This will be demonstrated below.

An overview of the defect parameters in the two solutions is displayed in Table 4.12. Although the MinBH solution can be excluded, its much higher energy depth of 0.51 eV is surprising at first sight. However, this result is a direct consequence of including the IC-induced TDLS bend in the SRH modeling. As shown in Sect. 3.5.6B, the slope of the TDLS bend always depends on E_t but is independent of k in the case of a MinBH defect. Modeling the complete TDLS curve for a MinBH defect, the energy value E_t thus has to be determined in such a way that it optimizes both the slope of the Arrhenius increase and the slope of the TDLS bend. If the measured TDLS curve is actually related to a defect level in the MajBH and exhibits a flattened slope of the TDLS bend due to a high k factor ($k > 10$), as in the present case, the modeling for a MinBH defect may lead to an overestimate of the energy depth. However, this is directly reflected in an increased Chi^2 value of the MinBH fit, which indeed enabled the identification of the MajBH solution as the true one in the present case.

Having a closer look at the MajBH fit in Fig. 4.27a, it can be seen that the modeled TDLS curve (solid line) perfectly describes the measured data (circles) in the whole T range except for the onset region of the Arrhenius increase at around 60°C, where the measured lifetime data are slightly underestimated by the fit. As this T range has been identified in Sect. 4.6.2B to be the only critical T range with respect to a complete suppression of the re-association of FeB pairs in the short time interval between switching off

Table 4.12. Overview of the defect parameters extracted from the Fe_t -dominated TDLS curve ③ (Figs. 4.27–4.29) on the basis of different modifications of the SRH model assuming a MinBH and MajBH defect, respectively. For fits on the basis of a reduced T range (***bold numbers***), the *numbers in brackets* give the Chi^2 values which were recalculated for the complete T range (175–580 K) to make them comparable. The best fit is *shaded gray*.

T -model	$\sigma(T)$	Fitted T range [K]	MinBH defect			MajBH defect		
			E_C-E_t [eV]	k	Chi^2	E_t-E_V [eV]	k	Chi^2
Advanced	$E_\infty=24$ meV	175–580	0.509	27.2	0.63	0.393	50.1	0.20
Advanced	Const.	255 –580	0.510	16.4	0.13 (0.7)	0.413	27.3	0.03 (0.6)
Basic	$E_\infty=24$ meV	175 – 500	0.374	0.74	0.15 (1.7)	0.391	arb.	0.18 (2.5)
Basic	Const.	255 – 500	0.408	1.06	0.05	0.412	arb.	0.05

the dissociation light and taking the lifetime measurement, the observed underestimate most likely results from a slight increase in the measured carrier lifetime above its value for the fully dissociated sample due to a slight reduction in the Fe_i portion below 100 %.

B Advanced TDLS analysis: impact of model simplifications due to a reduced T -range

In the following we wish now to demonstrate that an accurate modeling of the low- and high-temperature parts of the TDLS curve is essential to obtain an accurate spectroscopic result. For this purpose the advanced DPSS analysis is repeated twice, in the SRH modeling disregarding one of the two T regions at a time (see Figs. 4.28 and 4.29). The defect parameters of the optimum solutions are summarized in Table 4.12.

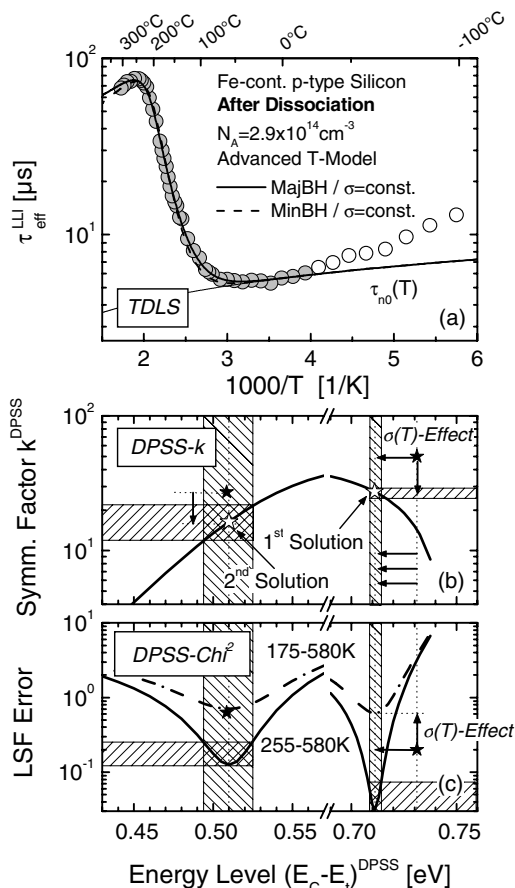


Fig. 4.28. Second DPSS analysis of the Fe_i -dominated TDLS curve (③ disregarding its low-temperature part ($T < 255 \text{ K}$, open circles)). (a) Assuming $\sigma = \text{const.}$, the SRH modeling is performed for a MinBH (dashed line) and a MajBH defect (solid line), still being based on the advanced T -model. (b,c) The significant difference in the minimum values of the DPSS- Chi^2 curve (solid line) still allows the MajBH solution to be unambiguously identified as the true one. To visualize the impact of the model simplification on the spectroscopic results, the DPSS diagram also displays the optimum SRH solutions achieved in Fig. 4.27 on the basis of the complete advanced SRH model (black stars). Since the original DPSS- Chi^2 curve (solid line) only reflects the fit quality in the reduced T range from 255–580 K, it is recalculated for the complete T range from 175–580 K (dash-dotted line) to make it comparable with the Chi^2 values determined in Fig. 4.27.

Disregarding the low-temperature part of the TDLS curve ($T < 255$ K, open circles) directly implies a simplification of the SRH model. Still based on the advanced T -model, it no longer considers the underlying $\sigma(T)$ -dependence but assumes $\sigma = \text{const}$. As can be seen from Fig. 4.28a, in the reduced T range from 255 to 580 K (gray circles), the simplified SRH model allows the data to be accurately fitted for both a MinBH defect (dashed line) and a MajBH defect (solid line). To visualize the impact of this first model simplifications on the spectroscopic result, Figs. 4.28b and c display the DPSS determined on the basis of the simplified SRH model (solid lines) together with the optimum SRH solutions determined on the basis of the advanced SRH model (black stars, from Fig. 4.27). Due to the significant difference between the minimum values of the DPSS- χ^2 curve (solid line in Fig. 4.28c), the simplified SRH model still allows an unambiguous identification of the Fe_i -related defect level in the lower band gap half, but yields a deeper energy and a lower k factor (see Fig. 4.28b). As expected from Sect. 3.4.2C, the determined energy depth ΔE_t of the defect level increases by approximately the activation energy $E_\infty = 0.024$ eV of the capture process, while the k factor is reduced by a factor two. Since the original DPSS- χ^2 curve (solid line) only reflects the fit quality in the reduced T range from 255 to 580 K, it has been recalculated for the complete T range from 175 to 580 K (dash-dotted line) to make it comparable with the DPSS- χ^2 values determined in Fig. 4.27c on the basis of the advanced SRH model (black stars). Being dominated by the inadequacy of the SRH model at low temperatures, the minimums of the recalculated DPSS- χ^2 curve (dash-dotted line) are increased and show the same value, which no longer allows the true solution to be identified.

If the high-temperature part of the TDLS curve is disregarded ($T > 580$ K, open circles), i.e., if the modeling is performed without considering the TDLS bend due to intrinsic conduction, it seems reasonable to base the SRH model on the simple (basic) T -model and not on the advanced T -model, while the underlying $\sigma(T)$ -dependence is still taken into account. As can be seen from Fig. 4.29a, in the reduced T range from 175 to 500 K (gray circles), the simplified SRH model allows the data to be accurately fitted for a MinBH defect (dashed line) and for a MajBH defect (solid line). To visualize the impact of this second model simplification on the spectroscopic result, Figs. 4.29b and c again display the DPSS determined on the basis of the modified simplified SRH model (solid lines) in comparison to the optimum SRH solutions determined on the basis of the advanced SRH model (black stars, from Fig. 4.27). For the MajBH solution the fit quality upon use of the simplified and the advanced SRH models is almost the same. While the energy depth ΔE_t remains almost unchanged, the k determination completely fails if the IC-induced TDLS bend

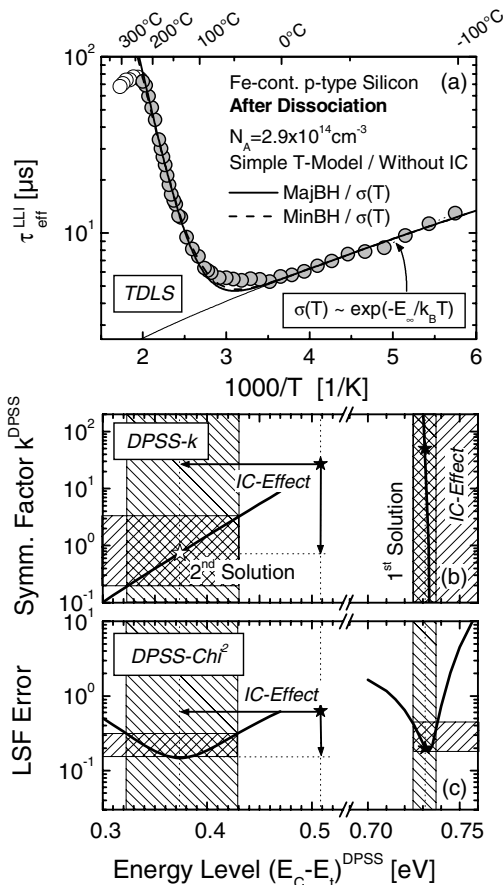


Fig. 4.29. Third DPSS analysis of the Fe_i -dominated TDLS curve ③ disregarding its high-temperature part ($T > 500 \text{ K}$, open circles). (a) Using the simple (basic) T -model as a basis, the SRH modeling is performed for a MinBH (dashed line) and a MajBH defect (solid line) still taking into account the underlying $\sigma(T)$ -model. (b,c) The minimum values of the DPSS- Chi^2 curve being equal, an identification of the true TDLS solution is not possible. Moreover, the k factor of the MajBH solution is completely undetermined, which reflects the independence of the simplified MajBH fit on this quantity. To visualize other impacts of the model simplification on the spectroscopic results, the DPSS diagram also displays the optimum SRH solutions achieved in Fig. 4.27 on the basis of the complete advanced SRH model (black stars).

is disregarded. Reflecting the k independence of the Arrhenius increase for a MajBH defect (see Sect. 3.5.6A), the DPSS- k curve in the lower band gap half becomes vertical, which prevents any k confinement. This nicely illustrates that the flat shape of the DPSS- k curve in Fig. 4.27b, which allowed the precise k determination for the MajBH solution, is only due to the fact that the IC-induced TDLS bend has been measured and modeled in the broad T range from 500 to 580 K. For the MinBH solution the use of the simplified SRH model without consideration of the IC-induced TDLS bend leads to a significant improvement in the fit quality, which is accompanied by a large reduction in the energy depth by 140 meV and a large reduction in the k factor by more than an order of magnitude (see Table 4.12). The significant change in the MinBH solution is due to the fact that, disregarding the IC-induced TDLS bend in the modeling, the energy value E_t only optimizes the measured slope of the Arrhenius increase and is no longer

influenced by the slope of the TDLS bend (see discussion in Sect. 4.6.3A). As expected, the energy depth of the two solutions becomes almost the same and no longer shows the strong discrepancy observed in Fig. 4.27b (see Table 4.12). However, due to the improved quality of the simplified MinBH fit, the minimum values of the DPSS- Chi^2 curve become equal, which no longer allows the true solution to be identified from the TDLS data alone. While the energy depth may still be estimated from the similar ΔE_t values found for the two solutions, the band gap half and the k factor of the Fe_i defect are completely undetermined.

To sum up, the study of the TDLS modeling brought out the decisive impact that an accurate consideration of the low- and the high-temperature parts of the TDLS curve may have on the overall spectroscopic result. While disregarding the low-temperature part and an underlying $\sigma(T)$ -dependence, respectively, may significantly affect the accuracy of the E_t and k determination in the MinBH and the MajBH, ignoring the high-temperature part, i.e., the TDLS bend due to intrinsic conduction, prevents any k confinement for the MajBH solution and can hinder – in the case of an underlying MajBH defect – the identification of the band gap half. It has to be stressed that in the present case, disregarding both the low- and the high-temperature part of the TDLS curve, it would have been impossible to determine only one of the defect parameters of the Fe_i defect accurately, the band gap half and the k factor being completely undetermined (see last row in Table 4.12). In view of this significant loss of spectroscopic information, it has to be concluded that impurities in unknown systems can only be identified reliably from TDLS if both the low- and the high-temperature parts of the TDLS curve are considered in the measurement and the modeling.

C Advanced IDLS analysis

Although TDLS alone already allowed a complete characterization of the Fe_i defect, the sample has been subjected to an IDLS experiment to cross-check the results obtained.

To guarantee a complete dissociation of the FeB pairs, the IDLS curve displayed in Fig. 4.30a has been measured after strong optical illumination with 0.1 W/cm^2 for 60 min and is thus dominated only by the Fe_i defect (see Sect. 4.6.2D). Being free of superposed external carrier trapping, the Auger-corrected⁵⁰ IDLS curve (gray circles) reflects the recombination properties of the Fe_i defect over the whole injection range. As can be seen

⁵⁰ The decrease of the original lifetime curve (open circles) for injection densities above $1 \times 10^{16} \text{ cm}^{-3}$ arises mainly from CE-Auger recombination and is eliminated by means of the procedure discussed in Sect. 4.2.4C.

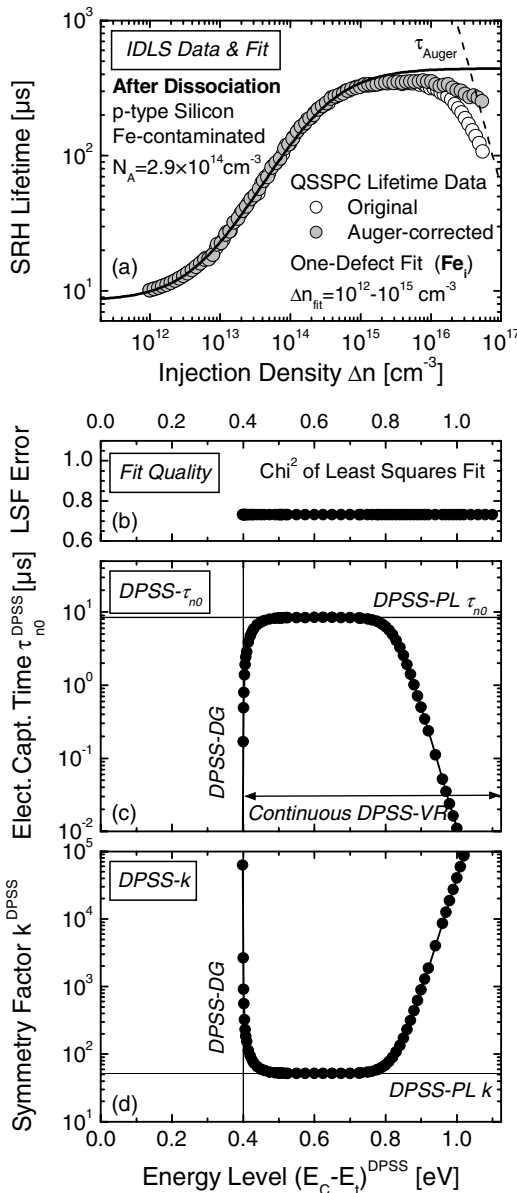


Fig. 4.30. Advanced DPSS analysis of the Fe_i -dominated IDLS curve. (a) To ensure a complete dissociation of the FeB pairs, the IDLS curve is measured after an illumination step with a halogen lamp (0.1 W/cm^2 , 60 min) (open circles). An accurate SRH modeling (line) of the Auger-corrected IDLS curve (gray circles) is achieved in a broad Δn range from $10^{12}-10^{15} \text{ cm}^{-3}$ for a single defect level. (b-d) Associated defect parameter solution surface determined on the basis of a one-defect SRH fit [see (a)].

from Fig. 4.30a, an accurate SRH modeling (line) of the measured injection dependence is achieved in a broad Δn range from $10^{12}-10^{15} \text{ cm}^{-3}$ for a single defect level. Since this defect level clearly dominates the whole range of low and medium injection densities, which is the relevant Δn range for a comparison with TDLS, and since the observed deviations

under high injection densities are small and mainly restricted to the Auger-corrected part of the IDLS curve, we chose $2 \times 10^{15} \text{ cm}^{-3}$ as an upper bound for the fitted Δn range and performed the modeling on the basis of a one-defect SRH model (see Sect. 4.2.4C).

Due to the strong inherent ambiguity in the SRH parameterization of a single IDLS curve (see Sect. 3.3.2), its detailed spectroscopic evaluation requires determination of the associated defect parameter solution surface, using the procedure described in Sect. 3.3.2B. The resulting DPSS- τ_{n0} and DPSS- k curves are displayed in Fig. 4.30c and d. The energy independence of the corresponding DPSS- Chi^2 curve in Fig. 4.30b, shows once again that the DPSS parameter triplets (E_i, k, τ_{n0}) represent equivalent solutions for the SRH parameterization of the IDLS curve. As expected for an increasing IDLS curve, the DPSS exhibits the tub-like structure with a continuous range of validity and a definition gap towards the conduction band (see Sect. 3.3.3C). The two DPSS characteristics are the energy value of the DPSS definition gap (DPSS-DG) and the plateau value of the DPSS- k curve (DPSS-PL), whose values are determined from Fig. 4.30d as $(E_C - E_i)^{\text{DPSS-DG}} = 0.400 \text{ eV}$ and $k^{\text{DPSS-PL}} = 51.5$. By definition, the DPSS-PL value represents a lower bound for the true k factor, which definitely proves a capture asymmetry for the Fe_i-related defect level. However for $k \neq 1$, it has been shown in Sect. 3.3.3E that the DPSS-DG energy may be both an upper and a lower bound for the true energy depth of the underlying defect level, which prevents one from narrowing down the possible ΔE_i values from the IDLS result alone.

D Combined DPSS analysis of TDLS and IDLS

To verify the consistency of the spectroscopic results obtained from the IDLS and the TDLS analysis, the associated DPSS diagrams simply have to be superposed as shown in Fig. 4.31.

Although the intersection points (white stars) of the two DPSS- k curves associated with TDLS (solid lines) and IDLS (dashed lines) reflect consistent parameter solutions, their quality significantly depends on their energy distance from the corresponding minimum of the DPSS- Chi^2 curve related to TDLS, which reflects the varying accuracy of the solutions contained in the DPSS- k curve associated with TDLS. The exact coordinates of the DPSS- k intersection points are given in Table 4.13 in comparison to the spectroscopic results obtained from the isolated analyses of TDLS and IDLS.

Since the DPSS- k intersection point in the lower band gap half deviates in its energy position by 40 meV from the corresponding DPSS- Chi^2 minimum, it has to be rejected for reasons of inconsistency, which demonstrates in accordance with the reduced fit quality of the TDLS MinBH solution (see

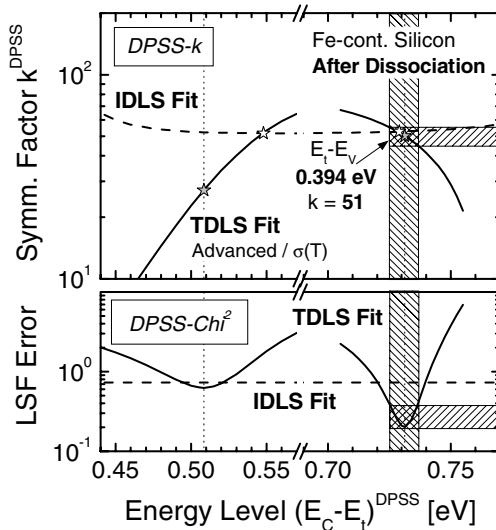


Fig. 4.31. Superposition of the DPSS diagrams associated with the Fe_i -dominated TDLS (solid lines) and IDLS (dashed lines) curve of the iron-contaminated sample. The original DPSS diagrams are displayed in Fig. 4.27 and Fig. 4.30, respectively. Unambiguous determination of the defect parameters of interstitial iron from the intersection point of the DPSS- k curves in the MajBH (white star). The coincidence of this intersection point with the minimum of the DPSS- Chi^2 curve (gray star) manifests the accuracy of the determination. Note that a consistent determination of the Fe_i parameters is achieved by two independent LS techniques: TDLS alone and the combination of TDLS and IDLS.

Sect. 4.6.3A) that the Fe_i -related defect level cannot be located in the upper band gap half. In the lower band gap half, on the other hand, the energy positions of the DPSS- k intersection point and the minimum of the DPSS- Chi^2 curve coincide perfectly, which proves the finding from TDLS that the Fe_i -related defect level is located in the lower band gap half. From the DPSS- k intersection point (white star) the energy level and the symmetry factor of the Fe_i defect are determined as $E_i - E_V = 0.395 \text{ eV}$ and $k = 53$, respectively, which well confirms the results obtained from TDLS alone (gray star). To assess the importance of the observed coincidence for the quality of the spectroscopic result, it has to be taken into account that the DPSS- k intersection point is located in the flat plateau region of the DPSS- k curve related to IDLS. For this reason its energy position is mainly determined from TDLS⁵¹ whereas its k value mainly results from IDLS.

⁵¹ This is due to the fact that only the DPSS- k curve related to TDLS exhibits a significant energy dependence in the environments of the intersection point, whereas the DPSS- k curve related to IDLS is almost energy-independent.

Table 4.13. Overview of the spectroscopic results obtained for the Fe_i defect by investigating the iron-contaminated sample with the different LS techniques: TDLS alone (see Fig. 4.27), IDLS alone (see Fig. 4.30) and the combination of TDLS and IDLS (see Fig. 4.31). Optimum values (*bold font*) and error intervals (*standard font*) are determined from advanced DPSS analysis. The final LS result is *shaded gray*.

Technique	Boundary conditions	MinBH defect E_C-E_t [eV]	k	MajBH defect E_t-E_V [eV]	k
TDLS	Advanced / $\sigma(T)$ -model	0.509 (0.47–0.54)	27.2 (11–46)	0.393 (0.40–0.39)	50.1 (45–55)
IDLS	One-defect fit	0.509 (E_t^{TDLS})	52.2	0.393 (E_t^{TDLS})	52.7
IDLS& TDLS	DPSS-IP	0.548	51.6	0.395	52.5
Final result		—	—	0.394 \pm 0.005	51 \pm 5

Bearing in mind that TDLS alone precisely determined the symmetry factor for the MajBH solution as $k=50$ (see Sect. 4.6.3A), this observation reveals that the k factor has been reproduced by two independent techniques, TDLS and IDLS, which proves the high reliability of the obtained result. Averaging the defect parameters obtained from TDLS alone (gray star) and the combined analysis of TDLS and IDLS (white star), the Fe_i defect is localized in the lower band gap half at $E_t-E_V=(0.394\pm 0.005)$ eV with a symmetry factor $k=51\pm 5$. Being identified with the errors in the pure TDLS result, the errors in this final result have been estimated conservatively (shaded areas in Fig. 4.31). The quality and reliability of the result manifests itself in the high accuracy with which the individual solutions of the two independent techniques coincide (see Fig. 4.31a). Moreover, the self-consistency of the obtained results demonstrates the excellent performance of both lifetime spectroscopic techniques.

E Comparison of the LS results with the literature and discussion

In agreement with the results from the literature which have been summarized in Sect. 4.6.1A, lifetime spectroscopy identified the Fe_i-related donor level in the lower band gap half. Concerning the energy level E_t , the determined value of $E_t-E_V=(0.394\pm 0.005)$ eV is in excellent agreement with the average value of $E_t-E_V=(0.385\pm 0.010)$ eV found in the literature [1, 2] (see Sect. 4.6.1A). Taking into account the fact that the energy level of the Fe_i defect is the best-determined Fe_i parameter in the literature and considering that the energy level is the only defect parameter that both techniques, LS and DLTS, are capable of determining with high accuracy, the coincidence of the E_t results from LS (present study) and DLTS (literature) represents an excellent confirmation of the high reliability of the LS result.

However, concerning the symmetry factor k , the determined value of $k=51\pm 5$ is more than an order of magnitude lower than the value of $k=570$, which can be calculated from the average values of the electron and hole capture cross-sections known from the literature (see Sect. 4.6.1A). In spite of this large deviation, the LS result is believed to be more reliable than the DLTS-based result from the literature. From a general point of view this is due to the fact that LS sensitively depends on k and thus allows direct access. DLTS on the contrary, only allows indirect access via the capture cross-sections and faces the problem that the σ determination is tainted by a relatively large uncertainty. In addition to these theoretical aspects, the LS result has to be favored in terms of experimental reproducibility. While the measured k value has been precisely reproduced by two independent LS techniques (see Sect. 4.6.3D), the calculated k value had to be based on σ_n results from the literature which are poorly confirmed and therefore uncertain (see Sect. 4.6.1A). The symmetry factor k thus being well determined from LS but significantly changed compared to the literature, recalculating the electron capture cross-section σ_n to remove the existing uncertainty with respect to its magnitude suggests itself. Using the well confirmed average value of $\sigma_p=7.0\times 10^{-17}\text{ cm}^2$ (at 300 K) for the hole capture cross-section and calculating the product $\sigma_n=k\times\sigma_p$, we find a value of $\sigma_n=(3.6\pm 0.4)\times 10^{-15}\text{ cm}^2$ (at 300 K) for the electron capture cross-section of the Fe_i donor level.

In agreement with results from the literature, TDLS revealed an exponential T -dependence of the capture cross-section which shows that carrier capture into the Fe_i donor level occurs via the multiphonon emission mechanism. However, the activation energy of the capture process has been determined as $E_\infty=0.024\text{ eV}$ and is thus found to be slightly reduced compared to the value of $E_\infty=0.043\text{ eV}$ reported in the literature [1]. As the $\sigma(T)$ results in the literature come from standard DLTS, they refer to the hole (majority) capture cross-section σ_p , whereas the $\sigma(T)$ results from TDLS actually refer to the electron (minority) capture cross-section σ_n . Thus the observed deviation in E_∞ might indicate that, even though the T -models of the two capture cross-sections are identical in terms of their qualitative structure, they may differ slightly in terms of their activation energy E_∞ . However, as the Fe_i donor level is located in the lower band gap half, a difference in the $\sigma(T)$ -models would not affect the TDLS modeling as discussed in Sect. 3.5.9A. Experimentally, this is clearly shown by the excellent self-consistency of the obtained LS results.

In conclusion, the LS study on the Fe_i defect gave new insight into the recombination properties of the Fe_i donor level and demonstrated the excellent performance of lifetime spectroscopy.

4.6.4 Defect configuration of iron-boron pairs (FeB)

After the successful characterization of the Fe_i defect, the following section focuses on the characterization of the defect related to iron-boron pairs (FeB). As discussed in detail in Sect. 4.6.2C, investigating the FeB state faces the problem that even optimized dark-storage conditions ensure complete pairing of iron only in the room-temperature IDLS curve, while the TDLS curve is significantly affected by thermal dissociation, even in its FeB-dominated part. Although IDLS alone thus allows accurate spectroscopic analysis of the FeB defect, we start with a rather qualitative analysis of the TDLS curve, which aims at estimating the impact of the unavoidable dissociation on the spectroscopic result and at delimiting the FeB recombination parameters.

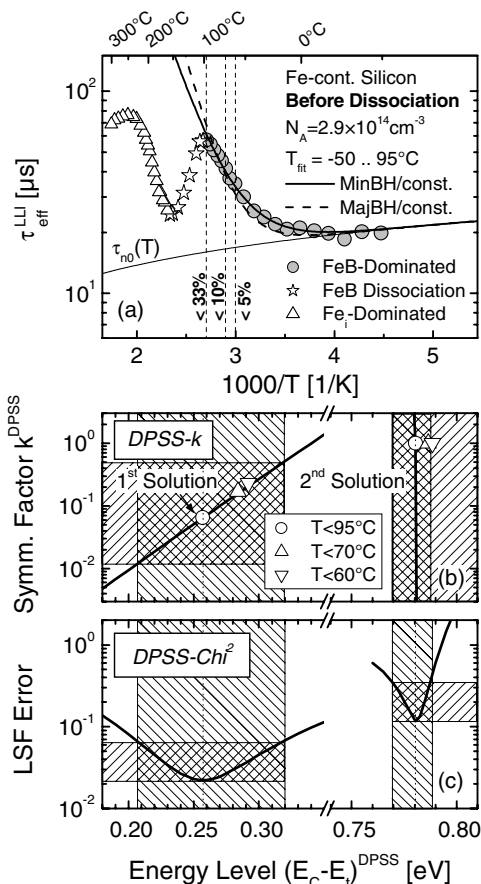


Fig. 4.32. Advanced DPSS analysis of the FeB-dominated part (gray circles) of TDLS curve ① (see Fig. 4.25), which is measured after a 25 h dark storage at 50°C, the sample being kept in the dark in-between the measurements. (a) The equilibrium portion of thermally dissociated FeB pairs is indicated for three temperatures (vertical dashed lines, for details see Fig. 4.26). As the $[\text{Fe}_i]$ portion cannot actually be neglected above 60°C, the performed one-defect SRH modeling on the basis of the advanced T -model and $\sigma = \text{const}$. only allows a qualitative estimate of the FeB defect parameters. (b,c) In addition to the DPSS curves (solid lines), which are determined on the basis of a SRH fit in the whole T range from -50 to 95°C (gray circles), the DPSS- k diagram displays the results of the optimum SRH fits (open symbols) if the upper bound of the fitted T range is reduced as indicated by the vertical lines in (a).

A TDLS analysis

Figure 4.32a displays TDLS curve ① which has been measured under dark conditions. Although the TDLS curve is dominated by FeB pairs in the T range below 95°C (gray circles), its Arrhenius increase is affected by a continuously increasing equilibrium portion of Fe_i due to thermal dissociation, whose magnitude is indicated for three temperatures (vertical dashed lines). For details see Fig. 4.26.

Since the Fe_i portion cannot actually be neglected above 60°C, as it then exceeds 5 %, the one-defect SRH modeling performed on the basis of the advanced T -model and $\sigma = \text{const.}$ only allows the FeB defect parameters to be estimated qualitatively. If the whole T range from -50 to 95°C is included in the fit (gray circles), the modeled TDLS curves for a MinBH (solid line) and a MajBH defect (dashed line) take the shapes displayed in Fig. 4.32a. The associated defect parameter solution surface is shown in Fig. 4.32b and c (solid lines). As can be seen, if thermal dissociation is neglected up to 95°C, TDLS determines the FeB level either as $E_C - E_t = 0.26 \text{ eV}$ or as $E_t - E_V = 0.34 \text{ eV}$. While the symmetry factor for the MinBH solution is found to be very low ($k = 0.07$), it is completely undetermined for the MajBH solution. However, the fact that the minimum values of the DPSS- Chi^2 curve differ by almost an order of magnitude, clearly points towards a localization of the FeB level in the upper band gap half.

An evaluation of the uncertainty in the extracted defect parameters has to consider two sources: the pure modeling error and the systematic error arising from the disturbance by Fe_i . As the Arrhenius increase of the FeB-dominated TDLS curve is only partially accessible, the modeling error is higher than usual, which is reflected in DPSS- Chi^2 curves of enhanced width. Tolerating a Chi^2 value of three times its optimum value, the tolerance bands of the MinBH solution are deduced from the DPSS diagram to be as broad as 0.21–0.32 eV for $E_C - E_t$ and 0.01–0.5 for k , respectively (shaded areas in Fig. 4.32).

Table 4.14. Overview of the defect parameters extracted from the FeB-dominated part of TDLS curve ① (see Fig. 4.32) for a MinBH and a MajBH defect, if the upper bound of the fitted T range and thus the upper bound of the tolerated equilibrium portion of Fe_i ions is varied.

T -model	$\sigma(T)$	Fitted T range	[Fe_i] portion	MinBH defect			MajBH defect		
				$E_C - E_t$	k	Chi^2	$E_t - E_V$	k	Chi^2
Advanced	Const.	-50 ... 95°C	< 33 %	0.257 eV	0.065	0.02	0.344 eV	arb.	0.12
Advanced	Const.	-50 ... 70°C	< 10 %	0.284 eV	0.17	0.013	0.338 eV	arb.	0.025
Advanced	Const.	-50 ... 60°C	< 5 %	0.292 eV	0.23	0.018	0.336 eV	arb.	0.016

A simple consideration elucidates the expected impact of the systematic error. As the Fe_i defect is the center of higher recombination activity under LLI conditions, its increasing portion leads to an Arrhenius increase with reduced slope and thus results in an underestimate of the FeB energy depth if affected T regions are included in the fit. To quantify this effect, the DPSS- k diagram in Fig. 4.32b also displays the results of optimum SRH fits (open symbols) if the upper bound of the fitted T range – and thus the upper bound of the tolerated equilibrium portion of Fe_i – is reduced as indicated by the vertical lines in Fig. 4.32a. The defect parameters resulting from these fits are compiled in Table 4.14. If the upper T bound is reduced from 95 to 60°C, which corresponds to a significant reduction of the tolerated Fe_i portion from 33 % to 5 %, the energy depth of the MinBH solution in fact increases from 0.26 to 0.29 eV, being accompanied by an increase in the k factor from 0.07 to 0.5. The energy depth of the MajBH solution, on the other hand, remains almost unchanged and is determined in all three fits around 0.34 eV. The observed insensitivity towards variations of the fitted T range directly results from the fact that the position of the Arrhenius increase only depends on the energy level E_t but not on the symmetry factor k in the case of a MajBH defect (see Sect. 3.5.6A), which implies that the modeling of the onset region alone already allows a relatively robust E_t determination. This observation gains special importance in the present case as the onset region of the Arrhenius increase is observed below 50°C, which ensures that it is almost unaffected by thermal dissociation and thus purely reflects the properties of the FeB level. Consequently, the E_t value determined for the MajBH solution is not expected to change significantly in an ideal TDLS curve dominated only by FeB pairs in the whole T range, which will allow a decisive conclusion below.

In spite of an increasing modeling uncertainty with decreasing width of the Arrhenius increase, the TDLS results obtained from the modeling on the reduced T ranges allow some important confinements of the recombination parameters expected for the FeB defect. (i) **Band gap half:** Although the difference in the minimum values of the DPSS- Chi^2 curve vanishes for the 60°C fit (see Table 4.14), the relevant band gap half may be identified by comparing the energies obtained for the MinBH and MajBH solution in terms of their magnitude with the energies of the two eligible FeB defect levels known from the literature: the donor level at $E_t - E_V = 0.1$ eV and the acceptor level at $E_C - E_t = (0.26 \pm 0.03)$ eV (see Sect. 4.6.1B). As the energy depth of the MajBH solution is determined with high reliability to be as deep as 0.34 eV, the shallow donor level can definitely be excluded as dominant recombination center, which unambiguously identifies the upper band gap half to be relevant. (ii) **Energy depth:** This is further supported by the fact that the energy depth found for the MinBH solution varies

between 0.26 and 0.29 eV, which nicely coincides with the energy interval from 0.23 to 0.29 eV known for the acceptor level. However, the TDLS modeling suggests the acceptor level to be located rather in the upper than in the lower half of the E_t interval from the literature. (iii) **k factor:** Finally, even at the upper bound of the uncertainty interval for k (see Fig. 4.32b), TDLS unambiguously suggests a symmetry factor $k < 1$, i.e., an enhancement of the hole capture compared to the electron capture.

B Advanced IDLS analysis

As TDLS only allowed a qualitative estimate of the recombination parameters of the FeB pair, the sample has been subjected to a room-temperature IDLS experiment. To guarantee a complete pairing of iron, the IDLS curve displayed in Fig. 4.33a has been measured after an optimized dark storage for 25 h at 50°C and is thus dominated only by the FeB pairs (see Sect. 4.6.2C). Superposed external carrier trapping has been eliminated from the measured data by means of the bias-light correction (see Sect. 3.3.1A). The optimum correction has been achieved for a low bias intensity of 0.1 suns, which allowed the recombination lifetime to be reliably determined down to the associated bias carrier density of $\Delta n_{Bias} = 2 \times 10^{13} \text{ cm}^{-3}$ (gray circles). Reflecting the recombination properties of only the FeB pair, the measured injection dependence can be accurately modeled in the whole injection range from 2×10^{13} to 10^{16} cm^{-3} for a single defect level, as shown in Fig. 4.33a by the solid line. The comprehensive spectroscopic analysis of the IDLS curve again requires the determination of the associated defect parameter solution surface, which is displayed in Fig. 4.33b–d. As expected for a decreasing IDLS curve, the DPSS exhibits a split range of validity with a definition gap around mid-gap (see Sect. 3.3.3C). In this case the DPSS characteristics are given by the two energy values confining the range of validity: the DPSS definition gap (DPSS-DG) in the upper half and the DPSS zero point (DPSS-ZP) in the lower half, whose values are determined from Fig. 4.33d as $(E_c - E_t)^{DPSS-DG} = 0.280 \text{ eV}$ and $(E_t - E_v)^{DPSS-ZP} = 0.300 \text{ eV}$.

As shown in Sect. 3.3.3E, the spectroscopic values of the two quantities differ significantly. While the DPSS-DG energy may be an upper or lower limit for the true energy depth with $k \neq 1$, the DPSS-ZP definitely provides an upper limit for the true energy depth of the FeB pairs. At first glance, this property of the DPSS-ZP does not provide additional information about the underlying defect center as the DPSS-DG energy is even lower than the DPSS-ZP energy, which shows that the DPSS validity range itself allows a stronger confinement of the possible energy levels. However, using the energy depth $\Delta E_t^{DPSS-ZP}$ of the DPSS-ZP, it is possible to determine an energy interval for the unknown energy depth ΔE_t^{true} of the defect (see Sect. 3.3.3E).

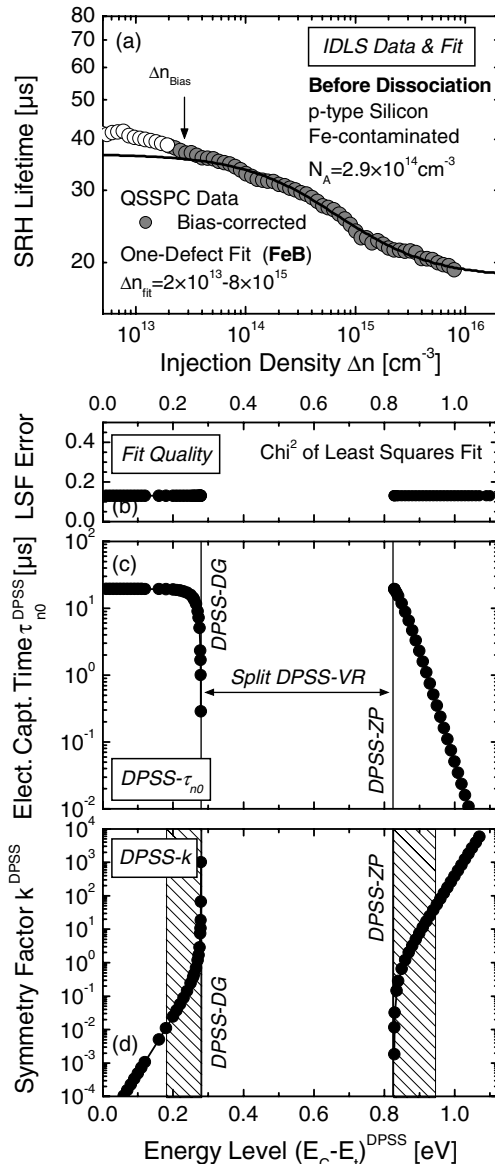


Fig. 4.33. Advanced DPSS analysis of the FeB-dominated IDLS curve. (a) To ensure a complete binding of interstitial Fe_i in FeB pairs, the IDLS curve is measured after a 25 h dark storage at 50°C. Superposed external carrier trapping is eliminated by means of the bias-light correction. Using an optimum bias intensity of 0.1 suns, the corrected lifetime data are reliable down to the associated bias carrier density of $\Delta n_{\text{Bias}} = 2 \times 10^{13} \text{ cm}^{-3}$ (gray circles). An accurate SRH modeling (line) of the trapping-corrected IDLS curve is achieved in the whole Δn range from $2 \times 10^{13}-10^{16} \text{ cm}^{-3}$ for a single defect level. (b-d) Associated defect parameter solution surface determined on the basis of a one-defect SRH fit [see (a)]. Using the spectroscopic information contained in the DPSS zero point (DPSS-ZP) allows a further confinement of the DPSS parameter solutions possible for the FeB defect [shaded areas in (d)].

This approach makes use of the fact that $\Delta E_t^{DPSS-ZP}$ overestimates ΔE_t^{true} by a constant amount, which only depends on the symmetry factor and the band gap half of the defect level but not on the energy depth itself. This maximum precision of the upper energy limit is achieved almost within the whole defect parameter range except for two small intervals of defect energies, which are located at the edges of the validity range of the DPSS-

ZP. For these special parameter constellations, which luckily can be identified from the shape of the DPSS- k curve, the deviation between $\Delta E_t^{DPSS-ZP}$ and ΔE_t^{true} increases dramatically and thus makes $\Delta E_t^{DPSS-ZP}$ useless as an upper limit for ΔE_t^{true} (for a detailed discussion see Sect. 3.3.3E). In the present case, the fact that the DPSS- k curve shows an almost vertical slope in the DPSS-ZP allows such critical parameter constellations to be excluded and thus ensures maximum precision of the upper energy limit $\Delta E_t^{DPSS-ZP}$. As a conservative assessment of the TDLS result still allows a k confinement to 0.01–1, the maximum overestimate of ΔE_t^{true} by $\Delta E_t^{DPSS-ZP}$ can be directly extracted from Fig. 3.12b and is found to be $\Delta E^{max} = 0.12$ eV.

Thus, using the spectroscopic information contained in the DPSS-ZP, the range of possible defect energies reduces to those parts of the DPSS definition range which lie within an energy interval⁵² 0.18–0.30 eV from either band edge. These intervals are displayed in Fig. 4.33d by the shaded areas. It becomes evident that the expanded DPSS analysis allows a significant confinement of the DPSS parameter solutions which in fact have to be taken into account for the FeB pair. While the initial DPSS- k curve allowed no k confinement at all, the symmetry factor is found to be limited to $k > 0.01$ in the MinBH and to $k < 50$ in the MajBH if the additional DPSS-ZP information is taken into account. Moreover, the finding of a lower bound of 0.18 eV for the defect energy depth provides further proof that the shallow FeB donor level – known to be located at $E_t - E_V = 0.1$ eV – definitely has to be excluded as the dominant recombination center.

C Comparison of LS results with the literature and discussion

In spite of the inherent ambiguity of the IDLS results and the experimental uncertainty of the TDLS results, lifetime spectroscopy allowed some important confinements of the recombination parameters expected for the FeB pair. As pointed out in Sect. 4.6.4A, the rough comparison of the TDLS energies obtained for the MinBH and MajBH solution with the known energies of the two eligible FeB levels allowed the shallow FeB donor level at $E_t - E_V = 0.1$ eV to be excluded as the dominant recombination center and thus unambiguously identified the upper band gap half to be relevant. This result is confirmed by the finding of a lower bound of 0.18 eV for the energy depth of the FeB level, if the spectroscopic information contained in the zero point of the DPSS- k curve related to IDLS is evaluated (see Sect. 4.6.4B). Thus both techniques consistently – but indirectly – identify

⁵² The range of possible defect energy depths is confined at its upper bound by $\Delta E_t^{DPSS-ZP}$ itself and at its lower bound by $\Delta E_t^{DPSS-ZP} - \Delta E^{max}$ (see Sect. 3.3.3E). Using $\Delta E_t^{DPSS-ZP} = 0.30$ eV and $\Delta E^{max} = 0.12$ eV directly results in the indicated interval.

the deep FeB acceptor level in the upper band gap half as the dominant recombination center. Concerning its energy level E_t , IDLS provides an energy interval from 0.18–0.28 eV below the conduction band. Though tainted with a higher uncertainty, the E_t results from TDLS are consistent and strongly suggest the acceptor level to be located at the upper end of the E_t interval from IDLS. Concerning the symmetry factor k , even a conservative assessment of the TDLS results allows a k confinement to 0.01–1, the lower bound being confirmed by the IDLS results.

However, due to the remaining ambiguity of the IDLS results, the accurate determination of the recombination parameters of the FeB pair requires the use of a result from the literature for either the energy level or the symmetry factor. To ensure a reasonable choice, Fig. 4.34 shows a comparison of the IDLS results obtained in the present study (line) with the spectroscopic results reported in the literature (filled symbols), whose origin and limited quality have been discussed in detail in Sect. 4.6.1B. As can be seen, our results strongly suggest intermediate defect parameters for the FeB level close to the ones determined by Zoth et al. [27]. As the k results from the literature scatter over a broad range which covers two orders of magnitude, their uncertainty far exceeds the uncertainty observed for E_t , which clearly points towards a lifetime spectroscopic determination of k on the basis of a chosen E_t . In a recent review [2], an average value of $E_C - E_t =$

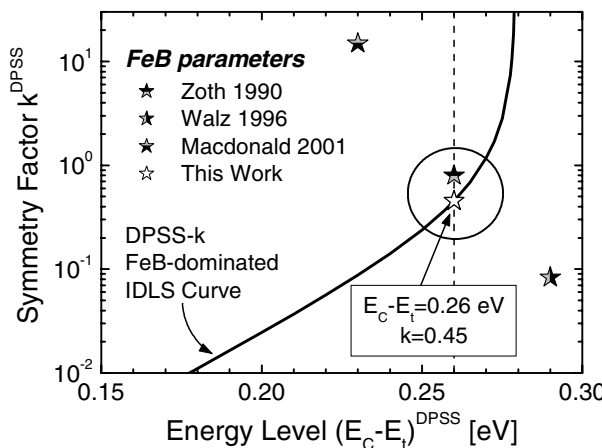


Fig. 4.34. Comparison of the DPSS- k curve associated with the FeB-dominated IDLS curve (line, see Fig. 4.33) with the FeB parameters known from the literature [27, 29, 30] (filled stars, see Table 4.11). Though ambiguous, our results suggest intermediate defect parameters for the FeB level close to the ones determined by Zoth et al. [27]. Assuming the average E_t value from the literature [2], the optimum k factor may be directly extracted from the DPSS- k curve (white star).

(0.26 ± 0.03) eV has been determined for the energy of the FeB acceptor level. As this value represents the best determination available to date and is fully consistent with the TDLS and IDLS results of the present study, it has been used as a basis to determine the k factor of the FeB acceptor level from the DPSS- k curve related to IDLS. As shown in Fig. 4.34 (white star), its optimum value is found to be $k = 0.45$.

Although the average value for the energy of the FeB acceptor level from the literature is reliable, its exact verification by means of lifetime spectroscopy would be desirable. This may be achieved on the one hand by a complete modeling of the dark TDLS curve considering the creeping defect transformation (see Sect. 4.6.2C). However, such a modeling requires accurate knowledge of the total Fe concentration, which may be determined, e.g., by means of DLTS, and necessitates assumptions about the pairing energy, which clearly introduces a new uncertainty into the spectroscopic TDLS result and thus calls the suitability of this approach into question. On the other hand, as room-temperature IDLS measurements circumvent the problem of defect transformation, a confirmation of the FeB parameters may be more easily achieved by an improved N_{dop} -IDLS experiment which (i) should ideally be based on IDLS curves affected by the FeB defect only or (ii) should at least use the new set of defect parameters found here for the Fe_i defect in the SRH modeling if a complete suppression of pair dissociation fails for some reason. In any case it is strictly recommended to use the superposed DPSS analysis for data evaluation to ensure maximum transparency of the spectroscopic results.

4.6.5 Additional information from a combined analysis of the FeB- and Fe_i -dominated IDLS curves

While the lifetime spectroscopic results of the present work combined with reliable σ_p results from the literature gave a complete picture of the recombination properties of the Fe_i defect (see Sect. 4.6.3E), the knowledge of the recombination properties of the FeB defect is still incomplete. Although the energy level and the symmetry factor of the FeB defect could be determined by means of lifetime spectroscopy (see Sect. 4.6.4), the magnitude of its capture cross-sections is still unknown as the results from the literature are highly inconsistent and thus scarcely reliable (see Table 4.11). This inconsistency of the σ results is directly reflected in the strong k scatter observed in Fig. 4.34 and has been discussed in Sect. 4.6.1B. Although it is in general impossible to estimate the absolute magnitude of the capture cross-sections from lifetime spectroscopy if the defect concentration is unknown, it is possible in the case of iron. Due to the fact that the iron content may be deliberately cycled between being completely present as

either FeB pairs or as Fe_i ions, the combined analysis of the two associated IDLS curves provides additional information, which may be exploited in the present case of an intentionally iron-contaminated sample to determine the unknown capture cross-sections of the FeB defect. This additional spectroscopic information is made accessible via two characteristics of the superposed IDLS diagram, which may be extracted in a direct manner and should be introduced in the following.

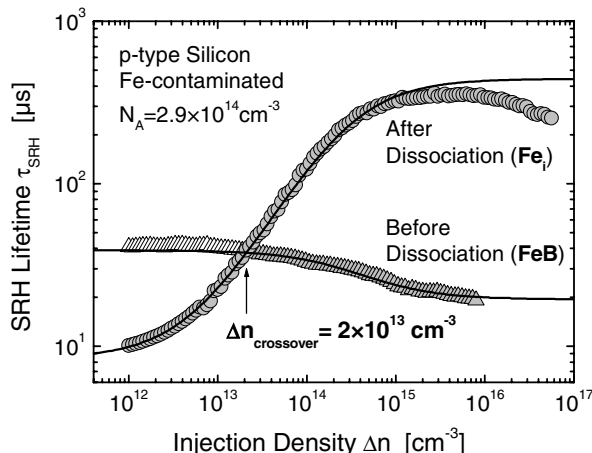


Fig. 4.35. Measured IDLS curves before (purely FeB-dominated, *triangles*) and after (purely Fe_i -dominated, *circles*) optical dissociation showing the crossover at $\Delta n = 2 \times 10^{13} \text{ cm}^{-3}$. The *lines* represent optimum one-defect SRH fits (see Figs. 4.30 and 4.33).

A First characteristic: crossover point

Figure 4.35 displays the superposed IDLS diagram for the present sample, showing the IDLS curves measured before and after optical dissociation, which are purely dominated by FeB pairs (triangles) and Fe_i ions (circles), respectively. The first characteristic may be identified with the particular excess carrier density $\Delta n_{\text{crossover}}$ at which the two IDLS curves cross over, i.e., at which the carrier lifetime remains unchanged upon dissociation. As can be seen from Fig. 4.35, this crossover is observed at $2 \times 10^{13} \text{ cm}^{-3}$ for the investigated sample. The existence of such a crossover directly results from the markedly different recombination properties of the FeB and the Fe_i defect and is well known in the literature [36, 37]. In a very recent publication [33], Macdonald et al. disclosed the important feature of the crossover that its Δn position is independent of the total iron concentration and the relative populations before and after dissociation. Additionally

postulating a doping independence – which will be critically scrutinized at the end of Sect. 4.6.5 – Macdonald et al. presented $\Delta n_{crossover}$ as a robust fingerprint of iron in silicon and suggested its measurement as a fast technique for iron detection.

It is obvious that a spectroscopic use of the crossover makes an analytical expression for $\Delta n_{crossover}$ mandatory. As [33] only presents an approximate expression for $\Delta n_{crossover}$, the general expression should be briefly deduced following the procedure in [33]. Allowing states with arbitrary relative populations of FeB and Fe_i before and after dissociation, Macdonald et al. were able to demonstrate that the general condition, under which the effective lifetimes of both states are equal, is equivalent to the simple statement that [33]

$$\tau^{FeB}(N, \Delta n_{crossover}) = \tau^{Fe_i}(N, \Delta n_{crossover}) \quad (4.5)$$

Being generally valid, Eq. (4.5) demonstrates that the crossover point is located at that excess carrier density where the lifetime due to any density N of FeB pairs equals the lifetime due to the same density of Fe_i ions. Expressing both lifetimes by the general SRH model given in Eq. (3.5), expression (4.5) may be solved for $\Delta n_{crossover}$. With the only simplifying assumption being the assumption of a *p*-type doping, the general expression for $\Delta n_{crossover}$ is found to be: (4.6)

$$\Delta n_{crossover} = -\frac{[p_0 + p_1^{FeB} + k^{FeB} n_1^{FeB}] - (\sigma_n^{FeB} / \sigma_n^{Fe_i}) \times [p_0 + p_1^{Fe_i} + k^{Fe_i} n_1^{Fe_i}]}{[1 + k^{FeB}] - (\sigma_n^{FeB} / \sigma_n^{Fe_i}) \times [1 + k^{Fe_i}]} \quad (4.6)$$

As expected, the crossover position is independent of the defect concentrations but strongly depends on the defect parameters of the FeB and the Fe_i defect. In addition to the dependence on the relative defect parameters E_t (via n_t , p_t) and k , Eq. (4.6) reveals an impact of the absolute magnitude of the electron capture cross-section of both defect states. Moreover, Eq. (4.6) predicts a doping dependence of $\Delta n_{crossover}$, whose relevance will significantly depend on the magnitude of the defect parameters.

Since the true set of defect parameters should predict the crossover at the correct position, this characteristic may be used to control the quality of the different parameter sets determined in the literature for the FeB defect (see Table 4.11). For the present sample with $N_A = 2.9 \times 10^{14} \text{ cm}^{-3}$, the crossover is predicted (i) at $1 \times 10^{13} \text{ cm}^{-3}$ for the FeB parameters of Walz et al., (ii) at $5 \times 10^{13} \text{ cm}^{-3}$ for the FeB parameters of Zoth et al. and (iii) at $1 \times 10^{14} \text{ cm}^{-3}$ for the FeB parameters of Macdonald et al. The best agreement with the experimentally observed position at $2 \times 10^{13} \text{ cm}^{-3}$ is thus achieved for the parameter set of Walz et al., while that of Macdonald et al. overestimates the crossover position by almost an order of magnitude.

It is obvious that the accurate modeling of the observed crossover position may be used in the case of an intentionally iron-contaminated sample to determine one missing defect parameter, provided the others are known (see Sect. 4.6.5C). Considering the spectroscopic results obtained so far, this unknown parameter is the electron capture cross-section of the FeB pair.

B Second characteristic: constant (Δn -independent) iron concentration

Zoth and Bergholz showed that, by measuring the lifetime before (τ_0) and after (τ_l) pair dissociation under LLI conditions, the total iron concentration (in cm^{-3}) can be found by [27]:

$$[\text{Fe}]_{\text{total}} = C \times \left(\frac{1}{\tau_l^{\text{LLI}}} - \frac{1}{\tau_0^{\text{LLI}}} \right) \quad (4.7)$$

The pre-factor C was determined empirically to be $3.19 \times 10^{12} \text{ cm}^{-3}$ for silicon wafers of dopant density $1-3 \times 10^{15} \text{ cm}^{-3}$ [27]. Being the most sensitive technique available for detecting iron contamination, this technique is widely used in commercial applications for contamination control. Its robustness largely results from the use of the difference of the inverse lifetimes before and after dissociating the FeB pairs, which cancels out the impact of other recombination channels, provided they are not altered by the dissociation step. However, the use of this technique faces two restrictions, as the result obtained from Eq. (4.7) is not entirely valid if the lifetime is measured under mid- to high-injection or if the dopant density is well outside the range $1-3 \times 10^{15} \text{ cm}^{-3}$.

In a very recent publication [33], Macdonald et al. proposed a significant extension of this technique. Making use of the recombination parameters of both FeB pairs and Fe_i , they determined the pre-factor C for arbitrary doping and injection density, which enables an [Fe] determination at any Δn position of the pair of IDLS curves according to

$$[\text{Fe}]_{\text{total}} = C(\Delta n, p_0) \times \left(\frac{1}{\tau^{\text{FeB}}(\Delta n)} - \frac{1}{\tau^{\text{Fe}_i}(\Delta n)} \right) \quad (4.8a)$$

$$\text{with } C(\Delta n, p_0) = \frac{1}{(p_0 + \Delta n) \times (Q^{\text{FeB}} - Q^{\text{Fe}_i}) \times v_{th}} \quad (4.8b)$$

$$\text{with } Q^X(\Delta n, p_0) = \frac{\sigma_n^X}{p_0 + \Delta n (1 + k^X) + p_1^X + k^X n_1^X} \quad (4.8c)$$

for $X = \text{FeB}, \text{Fe}_i$.

The general analytical expression for the C factor displayed in Eqs. (4.8b) and (4.8c) is obtained in a straightforward way by expressing the difference of the inverse lifetimes before and after dissociation in Eq. (4.8a) upon use of the standard SRH model given in Eq. (3.5) and solving the resulting equation for the defect concentration N_r . The deduced C expression is valid for the simplest case⁵³, where 100 % of the iron is paired before dissociation and 100 % interstitial afterwards, which is given in the present study as demonstrated in Sect. 4.6.2.

The expanded technique increases the reliability of the determined iron concentration in two ways. On the one hand it allows the C factor to be accurately adjusted to the respective measurement conditions. On the other hand – whenever IDLS curves are available in both defect states – the expanded technique allows the iron concentration $[Fe]$ to be determined at various points throughout the whole injection range and thus enables the determination of an average value $[Fe]_{AV}$, which is less sensitive to measurement errors than the values at the individual Δn positions. It is obvious that only Δn -independent $[Fe]$ curves are reasonable in terms of physics if $[Fe]$ is determined as a “function of the injection density”. By generalizing the derivation of Eq. (4.8b), it can easily be shown that impure states before and after dissociation, i.e., states which are still affected by both defect configurations and not by either Fe_i or FeB , cannot induce a Δn -dependence of the $[Fe]$ curve, but only lead to a vertical shift of the whole $[Fe]$ curve and thus to an error in the absolute iron concentration. As a consequence, any observed Δn -dependence of the calculated $[Fe]$ curve unambiguously has to be attributed to an inaccuracy in the defect parameters used for the calculation of the pre-factor C .

As an example, we calculated the iron concentration of the present sample in a maximum injection range⁵⁴ from 5×10^{13} to $1 \times 10^{16} \text{ cm}^{-3}$ according to Eqs. (4.8a–c), using the Fe_i parameters determined in Sect. 4.6.3 and the FeB parameters published by Macdonald et al. (white circles) and Walz et al. (gray circles), respectively. The results are shown in Fig. 4.36 together with the results for an optimized set of FeB parameters (black circles) which will be determined in the following section. The uncertainty in $[Fe]$ has been calculated by assuming a 10 % uncertainty in each lifetime

⁵³ Note that the value of C for other cases is just as easily calculated. However, it may be difficult to precisely realize other cases experimentally.

⁵⁴ The restriction of the $[Fe]$ determination to the injection range from 5×10^{13} to $1 \times 10^{16} \text{ cm}^{-3}$ minimizes the uncertainties in $[Fe]$. Below $5 \times 10^{13} \text{ cm}^{-3}$ the uncertainty in $[Fe]$ strongly increases as the lifetime difference at a given injection level becomes very small when approaching the crossover point. Above $1 \times 10^{16} \text{ cm}^{-3}$ its increase is caused by the onset of CE-Auger recombination which caps the magnitude of the effective lifetime.

measurement. The fact that both literature-based [Fe] curves (white and gray circles) exhibit a Δn -dependence which exceeds the uncertainty limits clearly demonstrates the invalidity of the two sets of FeB parameters available in the literature. Nevertheless, it is instructive to compare the average values $[Fe]_{Av}$ of the two [Fe] curves which are determined as $2 \times 10^{12} \text{ cm}^{-3}$ (gray circles, Walz et al.) and $2 \times 10^{13} \text{ cm}^{-3}$ (white circles, Macdonald et al.), respectively. The deviation being as high as an order of magnitude directly reflects the strong dependence of the C factor on the parameters of the FeB defect, which underlines the practical importance of an accurate characterization of the FeB level.

It is evident that the Δn independence of [Fe], required physically, represents a second criterion, which may be used in the case of an intentionally iron-contaminated sample to determine one missing defect parameter provided the others are known (see Sect. 4.6.5C). However, for the parameter optimization aimed at in Sect. 4.6.5C, the qualitative criterion has to be transformed into a numerical quantity. Since any Δn -dependence of the [Fe] values is directly reflected in an increased standard deviation $\Delta[Fe]_{Av}$ of the average value $[Fe]_{Av}$, the relative standard deviation $\Delta[Fe]_{Av}/[Fe]_{Av}$ is the simplest numerical quantity reflecting the qualitative shape of the [Fe] curve. Obviously, the optimum defect parameter set has to minimize this second characteristic.

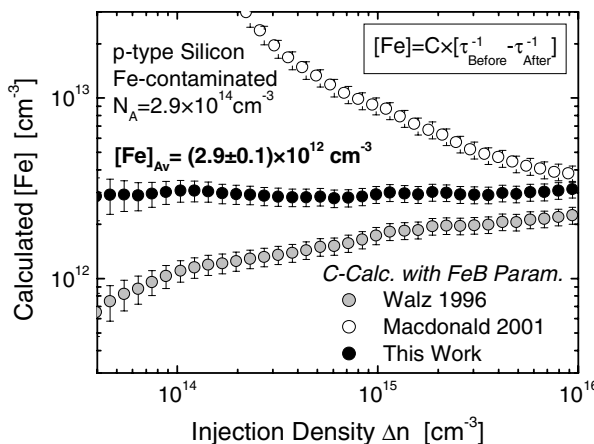


Fig. 4.36. Iron concentration $[Fe]_{\text{total}}$ calculated according to the Eqs. (4.8a–c), assuming different parameter sets for the FeB defect. For the Fe_i defect the parameters determined in Sect. 4.6.3 are used ($E_C-E_t=0.394 \text{ eV}$, $k=51$, $\sigma_p=7 \times 10^{-17} \text{ cm}^2$, $\sigma_n=3.6 \times 10^{-15} \text{ cm}^2$). The Δn independence of [Fe], required physically, is not achievable for the two FeB parameter sets known from the literature [29, 30], but for an intermediate parameter set close to the one determined by Zoth et al. [27] (see Sect. 4.6.5C).

C Determination of the FeB capture cross-sections

Since the knowledge of the recombination parameters of the FeB defect is so far restricted to the energy level and the k factor, both known from lifetime spectroscopy, the additional information contained in the two characteristics of the superposed IDLS diagram should be used to determine the unknown capture cross-sections of the FeB defect. It has to be emphasized that this approach, which inverts the procedure of iron detection [33], is only justified if the sample under investigation has been intentionally contaminated with iron as in the present case.

For this purpose, both characteristics are calculated as a function of the FeB electron capture cross-section σ_n^{FeB} , the calculations being based on the Fe_i defect parameters determined in Sect. 4.6.3 ($E_C-E_i=0.394\text{ eV}$, $k=51$, $\sigma_p=7\times10^{-17}\text{ cm}^2$, $\sigma_n=3.6\times10^{-15}\text{ cm}^2$) and the FeB defect parameters determined in Sect. 4.6.4 ($E_r-E_V=0.26\text{ eV}$, $k=0.45$). Note that the hole capture cross-section σ_p^{FeB} is varied in proportion to the electron capture cross-section σ_n^{FeB} as the k factor is kept at the fixed value determined by means of lifetime spectroscopy. While the crossover position $\Delta n_{crossover}$ is calculated according to Eq. (4.6), the average iron concentration $[\text{Fe}]_{Av}$ and its relative standard deviation $\Delta[\text{Fe}]_{Av}/[\text{Fe}]_{Av}$ are determined by averaging the individual $[\text{Fe}]$ values, calculated according to the Eqs. (4.8a–c), in a Δn range from 5×10^{13} to $1\times10^{16}\text{ cm}^{-3}$ (see Fig. 4.36). The resulting σ_n^{FeB} -dependence of all three quantities is displayed in Fig. 4.37a–c.

Since $\Delta[\text{Fe}]_{Av}/[\text{Fe}]_{Av}$ reaches its minimum at the same σ_n^{FeB} where the calculated and the observed Δn positions of the crossover coincide (gray star), the optimum values of the FeB capture cross-sections are determined to be $\sigma_n=2.5\times10^{-15}\text{ cm}^2$ and $\sigma_p=5.5\times10^{-15}\text{ cm}^2$ (vertical dashed line). Using this optimized set of FeB parameters, the average iron concentration $[\text{Fe}]_{Av}$ is determined as $(2.9\pm0.1)\times10^{12}\text{ cm}^{-3}$ (see Fig. 4.37b). The underlying $[\text{Fe}]$ values calculated at the individual Δn positions are displayed in Fig. 4.36 (black circles). As expected for a relative standard deviation of less than 3 % (see Fig. 4.37c), the calculated $[\text{Fe}]$ values are independent of Δn within the uncertainty limits, which proves that in terms of physics the spectroscopic result for the FeB defect is reasonable.⁵⁵

Beyond providing the optimum values for the capture cross-sections, Fig. 4.37 visualizes the practical importance of an accurate determination

⁵⁵ In spite of the perfect consistency of the spectroscopic FeB results, a confirmation of the calculated $[\text{Fe}]_{Av}$ by an independent technique would be an excellent verification. An appropriate technique is DLTS. Unfortunately, due to the problem of defect transformation, such a DLTS experiment is far from being a standard measurement and thus could not be performed yet.

of the FeB parameters, since any error in the FeB capture cross-sections linearly affects the calculated $[Fe]_{Av}$ and superlinearly affects the predicted Δn position of the crossover. Both quantities are overestimated if the FeB capture cross-sections are underestimated and vice versa. As can be seen from the shape of the $\Delta[Fe]_{Av}/[Fe]_{Av}$ curve in Fig. 4.37b, an underestimate of the FeB capture cross-sections may be directly detected from a strong Δn -dependence of the calculated $[Fe]$ values, whereas the Δn -dependence induced by an overestimate is much weaker. Thus an overestimate of the FeB capture cross-sections is more easily detected from the implied underestimate of the observed $\Delta n_{crossover}$.

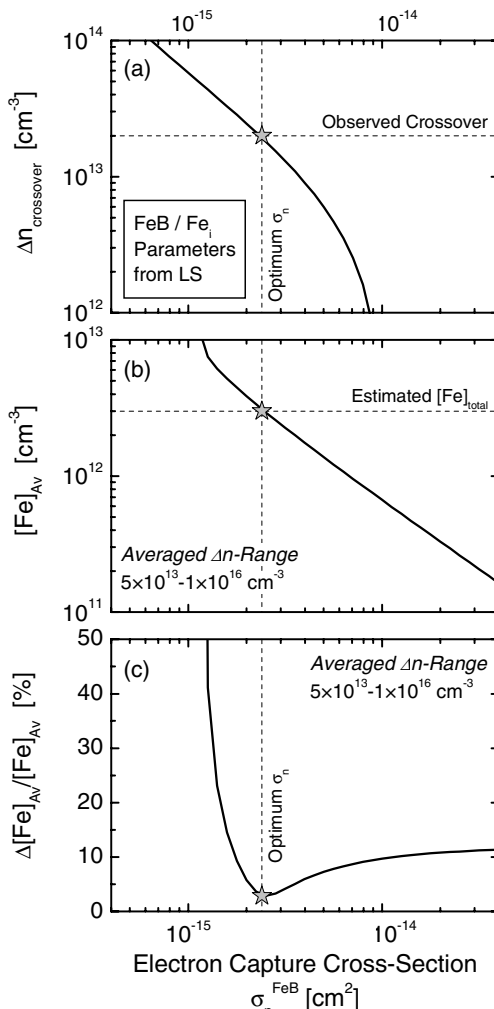


Fig. 4.37. Determination of the FeB capture cross-sections by evaluating the additional information contained in the combined system of the Fe_i - and FeB-dominated IDLS curves. The diagram displays three quantities which are calculated as a function of the FeB electron capture cross-section on the basis of the Fe_i defect parameters determined in Sect. 4.6.3 ($E_i-E_V=0.394$ eV, $k=51$, $\sigma_p=7\times10^{-17}$ cm 2 , $\sigma_h=3.6\times10^{-15}$ cm 2) and the FeB defect parameters determined in Sect. 4.6.4 ($E_C-E_i=0.26$ eV, $k=0.45$): (a) The Δn position of the IDLS crossover calculated according to Eq. (4.6). (b) The iron concentration calculated according to the Eqs. (4.8a–c) and averaged in the Δn range from 5×10^{13} – 1×10^{16} cm $^{-3}$ (see Fig. 4.36). (c) The standard deviation of the calculated iron concentration determined in the Δn range from 5×10^{13} – 1×10^{16} cm $^{-3}$ in percentages of its average value. The fact that the experimentally observed Δn position of the crossover and the minimum standard deviation of $[Fe]_{total}$ are obtained for the same σ_n^{FeB} allows the FeB capture cross-sections to be determined at $\sigma_n=2.5\times10^{-15}$ cm 2 and $\sigma_p=5.5\times10^{-15}$ cm 2 (vertical dashed line).

D Discussion

A comparison of the σ results obtained in the present study with those from the literature shows (see Table 4.11) that the electron capture cross-section $\sigma_e = 2.5 \times 10^{-15} \text{ cm}^2$ coincides with that determined by Walz et al. [29]. However, the hole capture cross-section $\sigma_h = 5.5 \times 10^{-15} \text{ cm}^2$ represents an intermediate value which is almost an order of magnitude smaller than that of Walz et al. [29] and slightly higher than that determined by Macdonald et al. [30] and Zoth et al. [27].

When assessing the quality of the spectroscopic result it is important to verify its consistency with experimental observations from the literature. While it is impossible to verify whether the new set of defect parameters for the Fe_i and the FeB defect enables an adequate SRH modeling of the IDLS curves published in the literature [29, 30], the crossover position represents a quantity which can be directly extracted from the data and easily simulated on the basis of the new parameter set, thus allowing a simple consistency check.

Having investigated iron-contaminated samples with a doping concentration around 10^{16} cm^{-3} , Macdonald et al. determined the Δn position of the crossover at $2 \times 10^{14} \text{ cm}^{-3}$ [30]. Calculations on the basis of a different parameter set for the Fe_i and the FeB defect, confirmed this position and led to the postulate that the position of the crossover is independent of the doping concentration as long as $N_A < 1.5 \times 10^{17} \text{ cm}^{-3}$. As the present study on a much less doped sample with $N_A = 3 \times 10^{14} \text{ cm}^{-3}$ unambiguously identified the Δn position of the crossover at $2 \times 10^{13} \text{ cm}^{-3}$, the postulated doping independence of the crossover position definitely proved to be incorrect, and with it the set of defect parameters which led to this postulate. In contrast, combining the observations of the two studies, there is experimental evidence that the crossover position increases by an order of magnitude if the doping concentration increases from 3×10^{14} to 1×10^{16} . This doping dependence should be reflected by the true set of defect parameters. To verify the validity of our spectroscopic result, we thus calculated the crossover position in the more highly doped samples investigated in [33] on the basis of the complete set of recombination parameters determined in the present work for the Fe_i and the FeB defect. Using the general expression (4.6), the crossover position in the two samples is theoretically predicted at $1.4 \times 10^{14} \text{ cm}^{-3}$ (for $N_A = 1.5 \times 10^{16} \text{ cm}^{-3}$) and $2.0 \times 10^{14} \text{ cm}^{-3}$ (for $N_A = 2.2 \times 10^{16} \text{ cm}^{-3}$), respectively, which precisely coincides with the experimentally observed crossover positions at $1.3 \times 10^{14} \text{ cm}^{-3}$ and $2.0 \times 10^{14} \text{ cm}^{-3}$. The consistency achieved with experimental observations from the literature nicely confirms the validity of the spectroscopic result obtained in the present study for the Fe_i and the FeB defect.

Moreover, it has to be concluded that the doping dependence of the crossover position is much stronger than assumed in [33]. Although the crossover position is not a fixed number, its measurement still allows a fast and unambiguous identification of iron in silicon as $\Delta n_{crossover}$ may be accurately predicted for arbitrary doping concentrations. However, these calculations have to be performed on the basis of the general expression (4.6), since the approximated equation for $\Delta n_{crossover}$ given in [33] is invalid if the changed capture asymmetries of both defect centers are taken into account. For the same reason, the C factors given in [33] have to be recalculated on the basis of the Eqs. (4.8a–c) to guarantee an accurate determination of the iron concentration by means of the extended technique.

4.6.6 Conclusion

The LS investigation of the iron-contaminated *p*-type sample aimed at a complete characterization of both the Fe_i and the FeB defect to verify well-known parameters and to redetermine others which are tainted with a high uncertainty in spite of the intensive studies on iron in the past. Facing the problem of defect transformation, both defect states have been carefully prepared in IDLS and TDLS.

Concerning the defect related to interstitial iron, the LS study unambiguously identified the Fe_i donor level in the lower band gap half and determined its energy level as $E_t - E_V = (0.394 \pm 0.005)$ eV and its symmetry factor as $k = 51 \pm 5$. The fact that two independent techniques, TDLS alone and the combination of TDLS and IDLS, led to the same spectroscopic result, demonstrates the quality and reliability of the defect parameters found. While the E_t value is in excellent agreement with the average E_t value reported in the literature, the capture asymmetry of the donor level proved to be an order of magnitude lower than determined from the capture cross-sections published in the literature. Using a well-confirmed average value from the literature for the hole capture cross-section, the k factor allowed the poorly confirmed electron capture cross-section to be recalculated, which led to a room-temperature value of $\sigma_n = (3.6 \pm 0.4) \times 10^{-15} \text{ cm}^2$. Moreover, the observed exponential $\sigma(T)$ -dependence revealed that electron capture into the Fe_i donor level is thermally activated with a barrier energy $E_\infty = 0.024$ eV, which shows that the multiphonon emission mechanism is the dominant capture mechanism not only for holes – as known from the literature – but also for electrons.

Concerning the defect related to the iron-boron pair, the LS study unambiguously identified the deep FeB acceptor level in the upper band gap half as the dominant recombination center. The TDLS and IDLS

results being fully consistent with the average energy value of $E_C-E_t = (0.26 \pm 0.03)$ eV known from the literature, the symmetry factor has been determined as $k=0.45$, which represents an intermediate k value compared to the widely scattered k results reported in the literature and shows that hole capture is slightly enhanced compared to electron capture. Exploiting the additional spectroscopic information, which is provided by a combined analysis of the IDLS curves measured before (FeB-dominated) and after (Fe_i-dominated) pair dissociation, we were able to determine the unknown capture cross-sections of the FeB defect and found $\sigma_h = 2.5 \times 10^{-15}$ cm² and $\sigma_p = 5.5 \times 10^{-15}$ cm².

Concerning the crossover position of the IDLS curves measured before and after pair dissociation, the present study provided experimental proof of a significant doping dependence. The fact that this doping dependence is accurately predicted on the basis of the new parameter set for the Fe_i and FeB defects further confirms the validity of the spectroscopic result and validates the use of the crossover position as a fingerprint of iron in silicon. Moreover, the study revealed a new fingerprint of iron consisting in the qualitative change of the TDLS curve upon illumination. Not being reported for any other contaminant, it represents a very robust criterion to unambiguously identify iron in silicon.

From an experimental point of view, the LS study on the iron-contaminated sample thus allowed a complete characterization of the Fe_i donor level and the FeB acceptor level, and gave a new and deeper insight into their recombination properties. As the most sensitive commercial technique to detect and determine iron contamination in silicon heavily relies on the Fe_i and FeB defect parameters, the spectroscopic results are of special practical importance.

From a methodological point of view, especially the LS study on the Fe_i defect demonstrated the excellent performance of lifetime spectroscopy, shown on the one hand in the perfect consistency of the spectroscopic results obtained from different LS techniques and on the other hand in the perfect agreement of the E_t results obtained from LS (present study) and DLTS (literature). Within a comparative study on the TDLS modeling, it was demonstrated that an accurate spectroscopic TDLS result is only achieved if the low- *and* the high-temperature part of the TDLS curve are considered in the SRH modeling. To ensure a reliable identification of impurities in unknown systems by means of TDLS, it is thus strictly recommended to choose the investigated T range broad enough to make both T regions accessible.

4.7 Detailed comparison of results

As the LS investigations on the intentionally metal-contaminated samples aimed on the one hand to verify the theoretical predictions made for the various LS techniques in Chap. 3 and on the other hand to fill gaps in our knowledge of the recombination properties of the different transition metals, the experimental and methodological results should finally be summarized and compared in two separate sections.

4.7.1 Comparison of experimental results: defect parameters

The first part of the comparison aims at a concise overview of the defect parameters found, to highlight special results and reveal common trends. General aspects concerning the quality and reliability of the results are discussed. Finally, the impurities are compared with respect to their recombination activity and their impact on the solar cell performance is exemplified for a high-efficiency cell structure.

A Overview of the defect parameters determined

The defect parameters of the different transition metals determined in the present study are compiled in Table 4.15. The different LS techniques that the displayed results are based on are indicated on the right. An overview of the detailed results from the individual LS techniques may be found for each impurity referenced in the first column in the table.

For all impurities, lifetime spectroscopy allowed an unambiguous identification of the recombination-active defect level and accurately determined its energy level E_t and its symmetry factor k . This result is of special practical importance for impurities with more than one defect level in the band gap [indicated by (*) in Table 4.15], as only the identification of the relevant defect level, achieved in the present work, allows realistic predictions of how the impurity influences solar cell performance. Although completely describing the recombination properties of the impurities, the LS result also gave deeper insight into their capture properties. As the mostly DLTS-based studies in the literature primarily investigated exchange processes with the nearer band, only the corresponding capture cross-section has been known with some precision (shaded gray in Table 4.15). The combination of these σ results from the literature with the k results from LS allowed the determination of the capture cross-section for the capture from the distant band, which up to now has been unknown or at least uncertain for the impurities investigated in the present study. In the case of the FeB

Table 4.15. List of the defect parameters determined by means of lifetime spectroscopy for the recombination-active levels of the metal contaminants under investigation. The different LS techniques applied are marked by ✓ (see *table notes*). The tables containing the overview of the spectroscopic results obtained for the different impurities from the individual LS techniques are referenced in the *first column* with their table number and page number (in parentheses). *Bold font* denotes the optimum values for the defect parameters and *standard font* their error intervals determined from the advanced DPSS analysis.

Impurity Details	Defect type Lattice site	Energy [eV]	Capture cross-sections				Techniques
			k	σ_p [cm ²]	σ_n [cm ²]	$\sigma(T)$	① ② ③ ④ ⑤ ⑥
Ti Table 4.8 (322)	Doub. donor (interst.) (*)	$E_V + \mathbf{0.289}$ ± 0.005	12 ± 1	1.9×10^{-16} [L]	2.3×10^{-15} $\pm 0.2 \times 10^{-15}$	$T^{-1.6}$	✓ ✓ ✓ ✓ ✓ ✓
Mo Table 4.4 (301)	Donor (interst.)	$E_V + \mathbf{0.317}$ ± 0.005	13 ± 3	6.0×10^{-16} [L]	7.8×10^{-15} $\pm 1.8 \times 10^{-15}$	$T^{-1.6}$	✓ ✓ ✓ ✓ ✓ ✓
Fe Table 4.13 (360)	Donor (interst.)	$E_V + \mathbf{0.394}$ ± 0.005	51 ± 5	7.0×10^{-17} [L]	3.6×10^{-15} $\pm 0.4 \times 10^{-15}$	$E_\infty =$ 24 meV	✓ ✓ ✓
FeB Sect. 4.6.4 (362)	Acceptor (int./sub.) (*)	$E_C - \mathbf{0.260}$ [L] ± 0.030	0.45 0.01–1	5.5×10^{-15}	2.5×10^{-15}	—	✓ ✓
Ni (p-Si) Table 4.10 (331)	Acceptor (subst.) (*)	$E_C - \mathbf{0.400}$ ± 0.030	0.7 0.3–1.3	8.0×10^{-17} $\pm 5.7 \times 10^{-17}$	5.6×10^{-17} [L]	$T^{-2.4}$	✓
Ni (n-Si) Table 4.10 (331)	Donor (subst.) (*)	$E_V + \mathbf{0.189}$ ± 0.050	3500 890– 12900	1.1×10^{-15} [L]	4×10^{-12} $1–10 \times 10^{-12}$	$T^{-2.5}$	✓

① = TDLS alone.

② = IDLS.

③ = Combination of TDLS and IDLS.

④ = N_{dop} -IDLS.

⑤ = T -IDLS (see [38]).

⑥ = DLTS, only given if DLTS has been applied to parallel samples.

[L] Values for the capture cross-sections, which are taken from the literature (*shaded gray*).

(*) Impurities which give rise to other defect levels within the band gap, which the LS study indirectly identified to be irrelevant in terms of recombination activity.

interst. = Interstitial defect.

subst. = Substitutional defect.

int./sub. = Defect complex with an interstitial and a substitutional component.

defect, the special correlation between the Fe_i and the FeB defect even made it possible to determine the magnitude of both capture cross-sections, which in general is impossible when applying lifetime spectroscopy if the defect concentration is unknown.

The quality and reliability of the defect parameters that have been found is demonstrated on the one hand by the perfect consistency of the spectroscopic results obtained from the different LS techniques and on the other hand by the perfect agreement of the E_i results obtained from LS (present study) and DLTS (literature). This has been discussed in detail in the con-

clusions presented at the end of each section dealing with the individual metals. Concerning the symmetry factor k , for most impurities, reference values from the literature did not exist, as the k factor is not accessible by any of the standard techniques and as the knowledge of the capture cross-sections has been incomplete in most cases (see above). An exception represented once again the iron-related defect centers which have undergone intensive studies in the past. However, in the case of the Fe_i defect the capture asymmetry proved to be an order of magnitude lower than determined from the capture cross-sections published in the literature. In the case of the FeB defect, the capture asymmetry was found to be given by an intermediate value compared to the widely scattered k results reported in the literature. The fact that lifetime spectroscopy provided new and deeper insights into the recombination properties of the Fe_i and FeB defects is of special practical importance, as the most sensitive commercial technique to detect and determine iron contamination in silicon heavily relies on the parameters of both defect states.

A comparison of the LS results obtained for the different impurities reveals a general trend concerning the capture asymmetry of the recombination-active defect level (see Table 4.15). While defects in the lower band gap half (MajBH in p -type) exhibit $k > 1$, i.e. an enhanced electron (minority) capture cross-section, defects in the upper band gap half (MinBH in p -type) exhibit $k < 1$, i.e. an enhanced hole (majority) capture cross-section. This trend is confirmed on the n -type sample whose MinBH defect in the lower band gap half exhibits $k > 1$, i.e. an enhanced electron (majority) capture cross-section. The fact that the dominant defect level of the nickel impurity changed with the doping type showed that a simple transfer of the defect parameters of an impurity to a sample with opposite doping type may lead to an erroneous estimate of the material quality. Moreover, the study revealed that the capture cross-sections of most defects are temperature-dependent. Under the given boundary condition of minority carrier injection, carrier capture into most defect levels has been found to be most probably dominated by excitonic Auger capture [$\sigma(T)$ decreasing according to a power law]. The only exception represented once again the Fe_i defect which proved to be dominated by the multiphonon emission capture mechanism [exponential $\sigma(T)$ increase].

B Comparison with respect to recombination activity

As the recombination properties of the defect levels are fully characterized by the defect parameters determined here, the investigated impurities should finally be compared with regard to their recombination activity, to allow a quantitative estimate of their harmfulness.

This is achieved by calculating the SRH lifetime for the different impurities according to the general SRH equation (3.5) using the parameter sets of Table 4.15 and assuming the same defect concentration. To take the impact of the operating conditions into account, the SRH lifetime is reasonably calculated as a function of the injection density. The resulting curves for an intermediate defect concentration $N_t = 5 \times 10^{12} \text{ cm}^{-3}$ are displayed in Fig. 4.38a, assuming a *p*-type silicon sample with a doping concentration of 10^{16} cm^{-3} . While the lifetime level under LLI conditions directly reflects the magnitude of the electron capture cross-section, the markedness of the injection dependence reflects the magnitude of the capture asymmetry (see Fig. 3.4b). As can be seen, the lifetime curves cross over due to the differing k factors of the impurities, which clearly demonstrates that the ranking of the impurities with respect to their harmfulness depends significantly on the operating conditions. However, Fig. 4.38a identifies molybdenum as the worst and nickel as the least harmful contaminant, as these two contaminants exhibit the highest and lowest recombination activity, respectively, in most of the injection range. To get a realistic picture of the impurity-induced limitations of the bulk performance, Fig. 4.38a also shows for each impurity the total bulk lifetime (thick lines), which takes into account superimposed CE-Auger recombination (dotted line).⁵⁶ While impurity-specific SRH recombination (thin lines) dominates the whole range of low and medium injection densities, its impact vanishes under high injection densities, bulk lifetime then being completely limited by the unavoidable CE-Auger recombination.

To get an impression of the bulk performance which has to be expected for different contamination levels, Fig. 4.38b shows the total bulk lifetime (thick lines) for the different impurities as a function of the defect concentration, assuming an intermediate injection density of $\Delta n = 10^{15} \text{ cm}^{-3}$, which is close to cell operating conditions (vertical dashed line in Fig. 4.38a). As expected, the bulk lifetime is completely limited by intrinsic CE-Auger recombination for low contamination levels and decreases linearly with the defect concentration above an impurity-specific N_t threshold. This decrease is due to the linear N_t -dependence of the SRH recombination rate [see Eqs. (3.1) and (3.3)]. If the minimum bulk lifetime that is necessary to achieve maximum efficiency for a given cell structure is known, Fig. 4.38b allows one to determine the impurity-specific threshold value of the defect concentration which may be tolerated without loss of cell performance.

⁵⁶ While the injection dependent CE-Auger lifetime is calculated according to Eq. (1.39), the total bulk lifetime is given by $1/\tau_{\text{bulk}} = 1/\tau_{\text{SRH}} + 1/\tau_{\text{CE-Auger}}$.

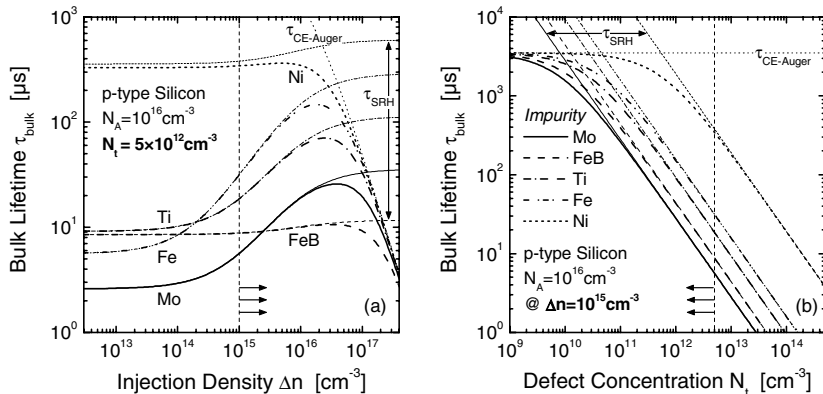


Fig. 4.38. Bulk lifetime for contamination with the different metal impurities investigated in the present work (a) as a function of the injection density for an intermediate $N_t = 5 \times 10^{12} \text{ cm}^{-3}$ and (b) as a function of the defect concentration for an intermediate $\Delta n = 10^{15} \text{ cm}^{-3}$, which is close to cell operating conditions. While the SRH lifetime (thin lines) is calculated according to the general SRH equation (3.5) using the defect parameter sets found here by means of lifetime spectroscopy (see Table 4.15), the total bulk lifetime (thick lines) additionally includes CE-Auger recombination (dotted line), which is calculated according to Eq. (1.39) and limits the total bulk lifetime under high injection levels and low contamination levels.

C Impact on the solar cell performance

As the defect parameters determined thus give a complete picture of how the investigated impurities affect the recombination lifetime under arbitrary operating conditions, they constitute the basis for realistic predictions of the solar cell performance in the presence of contamination.

As an example, the efficiency decrease due to a contamination with the different impurities has been simulated as a function of the defect concentration assuming a high-efficiency RP-PERC cell structure on a wafer with 300 μm thickness and a *p*-type base doping of 10^{16} cm^{-3} [39]⁵⁷. The simulation has been performed with PC1D (version 5.8) [14] using the N_t -dependent bulk lifetime curves of Fig. 4.38b, which approximately describe

⁵⁷ A schematic diagram of the RP-PERC cell structure (= Random Pyramid Passivated Emitter and Rear Cell) is shown in Fig. 5.33. Characteristics of the cell are: a front surface texturization with random pyramids, photolithographically defined evaporated front contacts, an oxide passivated homogeneous emitter, an oxide rear passivation, local ohmic aluminum point contacts at the rear side and no rear diffusion. The parameters for an analytical description of this cell type such as the doping profiles, the recombination parameters and the optical characteristics are well known [40, 41].

bulk recombination at cell operating conditions as being based on an intermediate $\Delta n = 10^{15} \text{ cm}^{-3}$. Figure 4.39a displays the relative efficiency decrease expected for the different impurities, the curves being normalized on a maximum efficiency of 20.9 %, which is achieved in the Auger limit of bulk lifetime under low contamination levels.⁵⁸ The area shaded gray in Fig. 4.39b is shown in detail in Fig. 4.39b to determine the threshold values of the defect concentration, which lead to an efficiency reduction to 95 % of the maximum value (dashed horizontal line). As can be seen from the key to Fig. 4.39b, the threshold values cover almost two orders of magnitude ranging between $3 \times 10^{11} \text{ cm}^{-3}$ for molybdenum and $2 \times 10^{13} \text{ cm}^{-3}$ for nickel, which directly reflects the harmfulness of a molybdenum contamination. It has to be emphasized that the magnitude of these threshold values depends on both the chosen cell structure and the operating conditions. However, using the defect parameters found in the present work, the threshold values may be determined for arbitrary boundary conditions.

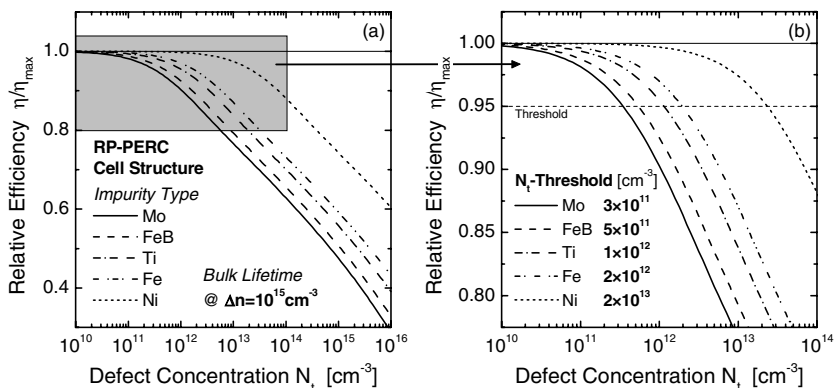


Fig. 4.39. Relative reduction of the solar cell efficiency as a function of the defect concentration for different metal contaminants. The area *shaded gray* in (a) is shown in detail in (b) together with the threshold defect concentrations which lead to an η reduction to 95 % of the maximum value (*dashed horizontal line*). The simulations are based on the corresponding bulk lifetime curves from Fig. 4.38b, whose N_t -dependence has been calculated for an intermediate injection density of $\Delta n = 10^{15} \text{ cm}^{-3}$, which is close to cell operating conditions. Moreover, the simulation assumes a high-efficiency RP-PERC cell structure on a $300 \mu\text{m}$ -thick wafer with a *p*-type base doping of 10^{16} cm^{-3} , which is illuminated with 0.1 W/cm^2 . Under these boundary conditions a maximum efficiency of 20.9 % is achieved in the Auger limit of the bulk lifetime.

⁵⁸ Under the given boundary conditions the RP-PERC cell reaches $V_{OC} = 662 \text{ mV}$, $I_{SC} = 39.6 \text{ mA/cm}^2$ and $FF = 79.6 \%$ in the Auger limit of bulk lifetime, which results in a maximum efficiency of 20.9 %.

4.7.2 Comparison of methodological results: verification of theoretical predictions

Table 4.16 presents an overview of all methodological aspects of lifetime spectroscopy which are illustrated in the different graphs containing the experimental LS results of the presented work. The comparison of the methodological aspects of the results that have been obtained for the different impurities (see last column) by means of the same LS technique reveals the fundamental qualities and restrictions of the different LS techniques and thus illustrates the validity of the various theoretical predictions made in Chap. 3. For this purpose, the different LS techniques define the main structure of the overview, which is further subdivided into sections labelled from A to J. The main results of these ten fields will be briefly discussed in the following. To allow the experimental proof of the individual effects to be found quickly, the corresponding graphs are referenced in the second column with their figure and page numbers (in parentheses).

Section A – Expanded T range: To verify the validity of SRH theory comprehensively, the TDLS investigations were made in a T range from 100 to 600 K, which to our knowledge is the broadest T range ever investigated. While lifetimes have been investigated at lower temperatures [20], an upper temperature limit of 520 K had not been exceeded so far [25].

Section B – Advanced TDLS modeling: It has been shown that accurate modeling of entire TDLS curves in this expanded T range requires an advanced configuration of the SRH model. On the one hand, all contaminants showed a temperature-dependent capture cross-section, which dominates the low-temperature part of the TDLS curve, but is still relevant within the whole T range. As the recombination lifetime may be screened at very low temperatures by superposed carrier trapping, which has been observed in two cases, trapping-affected T regions have to be identified and ignored in the SRH modeling to ensure an accurate determination of the underlying $\sigma(T)$ -dependence. On the other hand an accurate modeling of the TDLS bend due to intrinsic conduction (high-temperature part) has only been achieved for all experimental TDLS curves if the SRH model has been based on the advanced T -model. This observation unambiguously demonstrates that the observed low onset temperatures for intrinsic conduction cannot be explained by the temperature dependence of the equilibrium carrier concentrations $p_0(T)$, $n_0(T)$, alone but also requires consideration of the temperature-induced narrowing of the silicon band gap. The inadequacy of simpler T -models has been explicitly demonstrated for two samples. Using the advanced configuration of the SRH model proposed in this monograph, accurate TDLS modeling is achieved in T ranges as broad as 460 K. The predicted doping dependence of both the T position of the Arrhenius in-

crease and the onset temperature for intrinsic conduction has been proven experimentally with a set of molybdenum-contaminated samples.

General – Significance of the DPSS analysis: The evaluation of all lifetime spectroscopic data has been performed using the newly developed DPSS analysis. Allowing transparent and comprehensive SRH analysis, the DPSS analysis made it possible to evaluate the consistency of the spectroscopic results obtained (i) from different LS techniques for the same sample and (ii) from the same LS technique for different samples (with the same contaminant). A quantitative estimate of the precision of the determined defect parameters was deduced directly from the various DPSS diagrams. Moreover, the DPSS analysis turned out to be ideally suited for comparative studies to investigate the impact of different boundary conditions of the SRH modeling on the spectroscopic result, which gave deeper insight into the basic requirements of some of the LS techniques.

Section C – Ambiguity and unambiguity of TDLS: The ambiguity of the results obtained from TDLS has been shown to depend on the band gap half where the underlying defect center is located. While unambiguous defect characterization from TDLS alone has been achieved for the defect levels located in the MinBH (upper band gap half in *p*-type), it failed for those located in the MajBH (lower band gap half in *p*-type). The existence of two equivalent TDLS solutions (in the upper and the lower band gap half) prevented the identification of the symmetry factor *k* and the band gap half of the defect center, but still allowed the determination of its energy depth, as the depth of both solutions has been found to be the same within measurement errors. However, in the case of the Fe_i defect, TDLS alone allowed unambiguous identification although the defect level is located in the lower band gap half. This was only possible because the TDLS bend due to intrinsic conduction had been measured and modeled over a broad *T* range. All these observations are fully consistent with the theoretical predictions made for TDLS.

Section D – Impact of the fitted *T* range on the results extracted from TDLS: Comparative studies on TDLS modeling revealed the decisive impact that an accurate consideration of the low-temperature and high-temperature part of the TDLS curve may have on the overall spectroscopic result. While ignoring an underlying $\sigma(T)$ -dependence (low-temperature part) may significantly affect the accuracy of the *E*, and *k* determination for the MinBH and the MajBH solution, disregarding the TDLS bend due to intrinsic conduction (high-temperature part) prevents any *k* confinement for the MajBH solution. Moreover, in the case of an underlying MajBH defect, modeling the TDLS curve in a reduced *T* range with a simplified configuration of the SRH model may also affect the decision on which of

Table 4.16. Methodological aspects of lifetime spectroscopy illustrated in the various diagrams containing the experimental LS results of the presented work. The different LS techniques give the structure that underlies the overview (see *table notes*). The impurities used for validating the different LS techniques and LS effects are indicated in the *last column*. Figures are referenced with the figure number and page number (in parentheses). Figures are referenced with the figure number and page number (in parentheses).

	Graph (page)	Technique	Category	Methodological aspect / validated effect	Imp.
A	Fig. 4.21 (330)	TDLS	T range	Highest temperature: $T = 600$ K	Ni- <i>p</i>
	Fig. 4.22 (334)	TDLS	T range	Lowest temperature: $T = 90$ K	Ni- <i>n</i>
	Fig. 4.22 (334)	TDLS	T range	Broadest T range: $\Delta T = 460$ K (90–550 K)	Ni- <i>n</i>
B	Fig. 3.42 (201)	TDLS	Trapping	Superposed carrier trapping below 200 K	Mo
	Fig. 4.15 (312)	TDLS	Trapping	Superposed carrier trapping below 180 K	Ti
	Fig. 3.42 (201)	TDLS	$\sigma(T)$	$\sigma(T)$ decrease (power law): excitonic Auger capture	Mo
	Fig. 4.15 (312)	TDLS	$\sigma(T)$	$\sigma(T)$ decrease (power law): excitonic Auger capture	Ti
	Fig. 4.21 (330)	TDLS	$\sigma(T)$	$\sigma(T)$ decrease (power law): excitonic Auger capture → determination over a broad T range (160–360 K)	Ni- <i>p</i>
	Fig. 4.22 (334)	TDLS	$\sigma(T)$	$\sigma(T)$ decrease (power law): excitonic Auger / cascade capture → determination over a broad T range (90–310 K)	Ni- <i>n</i>
	Fig. 4.27 (351)	TDLS	$\sigma(T)$	$\sigma(T)$ increase (exponential): multiphonon emission capture	Fe
	Fig. 5.19 (430)	TDLS	$\sigma(T)$	$\sigma(T)$ decrease (power law): excitonic Auger capture	Cz
	Fig. 3.42 (201)	TDLS	IC bend	Variation of T -model: advanced = optimum	Mo
C	Fig. 4.17 (315)	TDLS	IC bend	Variation of T -model: advanced = optimum	Ti
	Fig. 4.9 (293)	TDLS	Special	Doping shift of the Arrhenius increase and the IC onset	Mo
	Fig. 4.8 (290)	TDLS	DPSS	Ambiguous result: equivalent MinBH and MajBH solutions	Mo
	Fig. 4.15 (312)	TDLS	DPSS	Ambiguous result: equivalent MinBH and MajBH solutions	Ti
	Fig. 4.21 (330)	TDLS	DPSS	Ambiguous result: equivalent MinBH and MajBH solutions	Ni- <i>p</i>
	Fig. 4.22 (334)	TDLS	DPSS	Unambiguous result: MinBH solution	Ni- <i>n</i>
	Fig. 4.27 (351)	TDLS	DPSS	Unambiguous result: MajBH solution	Fe
D	Fig. 4.32 (362)	TDLS	DPSS	Unambiguous result: MinBH solution	FeB
	Fig. 5.19 (430)	TDLS	DPSS	Unambiguous result: MinBH solution	Cz
	Fig. 4.8 (290)	TDLS	DPSS	DPSS with/without considering low- T part [$\sigma(T)$ model]	Mo
E	Fig. 4.28 (353)	TDLS	DPSS	DPSS with/without considering low- T part [$\sigma(T)$ model]	Fe
	Fig. 4.29 (355)	TDLS	DPSS	DPSS with/without considering high- T part (bend due to IC)	Fe
	Fig. 4.10 (296)	IDLS	Special	Data pre-analysis: bias correction, optimization of two-defect fit	Mo
F	Fig. 4.11 (298)	IDLS	DPSS	Continuous DPSS	Mo
	Fig. 4.13 (307)	IDLS	DPSS	Continuous DPSS	Ti
	Fig. 4.30 (357)	IDLS	DPSS	Continuous DPSS	Fe
	Fig. 4.33 (366)	IDLS	DPSS	Split DPSS	FeB
	Fig. 5.20 (432)	IDLS	DPSS	Continuous DPSS	Cz
G	Fig. 4.12 (300)	IDLS & TDLS	DPSS	Unambiguous result: MajBH solution → only from combined DPSS analysis	Mo
	Fig. 4.18 (318)	IDLS	DPSS	Unambiguous result: MajBH solution (on two samples)	Ti
	Fig. 4.19 (319)	& TDLS	DPSS	Unambiguous result: MajBH solution (on two samples) → only from combined DPSS analysis	

Table 4.16. (cont.)

	Graph (Page)	Technique	Category	Methodological aspect / validated effect	Imp.
G	Fig. 4.31 (359)	IDLS & TDLS	DPSS	Unambiguous result: MajBH solution → from two independent techniques	Fe
	Fig. 5.21 (433)	IDLS & TDLS	DPSS	Unambiguous result: MinBH solution → from two independent techniques	Cz
H	Fig. 4.13 (307)	N_{dop} -IDLS	DPSS	Superposed DPSS diagram (only continuous DPSS) → ambiguous result: two equivalent intersection points	Ti
	Fig. 4.14 (308)	N_{dop} -IDLS	DPSS	Computational method to determine the DPSS-IPs	Ti
I	Sect.4.4.4B (323)	LS	Sensitivity	Detection of impurity concentrations below the detection limit of DLTS	Ti

- (A) Expanded T range.
- (B) Advanced TDLS modeling.
- (C) Ambiguity and unambiguity of TDLS.
- (D) Impact of the fitted T range on the spectroscopic TDLS result.
- (E) IDLS data pre-analysis.
- (F) Inherent ambiguity of IDLS (DPSS structure).
- (G) Unambiguity of TDLS & IDLS (combined DPSS analysis).
- (H) Ambiguity of N_{dop} -IDLS (superposed DPSS analysis).
- (I) High sensitivity of lifetime spectroscopy.

the TDLS solutions is regarded as the true solution. While disregarding the TDLS bend may prevent unambiguous identification of the MajBH solution, as shown for the Fe_i defect, disregarding an underlying $\sigma(T)$ -dependence may even lead to an erroneous identification of the MinBH solution, as shown for the Mo defect. In view of this significant loss of spectroscopic information and the danger of a misinterpretation of the TDLS data, it has to be concluded that impurities in unknown systems can only be identified reliably from TDLS if both the low-temperature and the high-temperature parts of the TDLS curve are considered in the modeling. Thus, for an accurate TDLS analysis it is strongly recommended to choose the investigated T range broad enough to make both T regions accessible.

Section E – IDLS data pre-analysis: Concerning IDLS, it has been shown that accurate spectroscopic evaluation generally requires pre-analysis of the measured lifetime data with the aim of detecting and eliminating possible superposed effects such as carrier trapping under LLI and CE-Auger recombination under HLI, to extract the pure SRH lifetime related to the respective impurity over a maximum Δn range. Moreover, it turned out that an accurate SRH modeling of IDLS curves over the whole Δn range often requires a two-defect approach, only the defect level dominating LLI being relevant to the LS investigation.

Section F – Ambiguity of IDLS (DPSS structure): The significant inherent ambiguity of the spectroscopic results obtained from single IDLS curves has been visualized by means of the associated defect parameter solution surfaces. As expected, samples with an increasing IDLS curve showed a continuous DPSS with a definition gap towards the conduction band, which allowed the extraction of a lower bound for the k factor given by the DPSS- k plateau value, but no confinement of the defect energy depth. The only decreasing IDLS curve observed for the FeB defect, on the other hand, exhibited the expected split DPSS with a definition gap around mid-gap and a zero point in the lower band gap half. The spectroscopic information extracted here allowed a significant confinement of the DPSS solutions to be taken into account and thus allowed narrow ranges for the possible E_t and k values to be determined from IDLS alone.

Section G – Unambiguity of TDLS & IDLS: In agreement with the theoretical predictions, the combined DPSS analysis of TDLS and IDLS led to an unambiguous identification of the defect parameters of the underlying impurity whenever applied and irrespective of the position of the defect level in the band gap. The fact that the relevant intersection point of the DPSS- k curves related to TDLS and IDLS always coincided with great accuracy with the corresponding minimum of the TDLS-related DPSS- Chi^2 curve demonstrates the high quality of the spectroscopic results obtained from the combined LS technique. Moreover, in those cases where TDLS alone had already led to an unambiguous determination of the defect parameters, the result of the combined LS technique represented an independent confirmation, the observed self-consistency being proof of the good performance of both LS techniques.

Section H – Ambiguity of N_{dop} -IDLS: The performance of the N_{dop} -IDLS technique has been demonstrated on a set of titanium-contaminated samples. Provided that superposed DPSS analysis is used for the simultaneous SRH analysis of the set of IDLS curves, N_{dop} -IDLS has proved to provide results of remarkable precision, even if the boundary conditions of the experiment are unfavorable. Maximum precision is achieved if the DPSS- k intersection points are determined on the basis of a computational method which has been developed specially for the evaluation of superposed DPSS diagrams and allows the accuracy of the N_{dop} -IDLS result to be estimated quantitatively. In full agreement with the theoretical predictions, the N_{dop} -IDLS analysis determined two equivalent solutions. Since these solutions only coincided in the k factor, neither the band gap half nor the energy depth of the defect level could be determined unambiguously by means of the N_{dop} -IDLS technique, which represents a general drawback of this LS technique. However, using the combined LS technique for the identification of the true

solution, the extracted defect energy level is found to be in excellent agreement with E_i results from the literature.

Section I – High sensitivity of lifetime spectroscopy: The extraordinary sensitivity of lifetime spectroscopy to electrically active defect levels has been proven conclusively by a comparative DLTS study on the set of titanium-contaminated samples. It revealed a defect concentration below the detection limit of DLTS in two of the three samples, while precisely confirming the energy level determined in the LS study, on the third sample.

It has to be concluded that the experimental findings are fully consistent with the theoretical predictions made in Chap. 3 and verified almost all the different methodological aspects of lifetime spectroscopy.

4.8 Chapter summary

In the present chapter, the different LS techniques have been applied to intentionally metal-contaminated samples. Always allowing an unambiguous identification of the recombination-active defect level and an accurate determination of its energy level E_i and its symmetry factor k , the LS study filled gaps in our knowledge of the defect properties of molybdenum, titanium and nickel and provided new and deeper insight into the recombination properties of the Fe_i and FeB defects. The results on the iron-related defects are of special practical importance as the most sensitive commercial technique to detect and determine an iron contamination in silicon relies heavily on the parameters of both defect states. An overview of the determined defect parameters and a brief discussion of common trends may be found in Sect. 4.7.1, including a comparison of the investigated impurities with respect to their recombination activity which identified molybdenum as the worst and nickel as the least harmful impurity.

From a methodological point of view, the experimental LS results are in full agreement with the theoretical predictions of Chap. 3. The investigation confirmed that lifetime spectroscopy always allows complete defect characterization on a single sample if TDLS and IDLS are combined. As predicted, TDLS alone proved to yield unambiguous results for MinBH defects while two equivalent solutions were obtained for most MajBH defects. Moreover, it has been demonstrated consistently that for an accurate modeling of the entire TDLS curve in an expanded T range from 100 to 600 K, it is essential that the SRH model is based on the proposed advanced T -model and considers the $\sigma(T)$ -model of the respective impurity. Both aspects proved to have a significant impact on the spectroscopic result and have not been considered in previous studies. Unambiguous

identification failed when the N_{dop} -IDLS technique was applied, as the superposed DPSS analysis led to the two predicted solutions which allowed only the k factor to be determined. However, the superposed DPSS analysis proposed here determined these solutions with remarkable precision, even if the boundary conditions were unfavorable, a result which has not been achieved in comparable experiments so far. As the newly developed DPSS diagram guaranteed a comprehensive SRH analysis of TDLS and IDLS data and made it possible to evaluate the accuracy and consistency of the results from different LS curves with maximum transparency, it contributes decisively to the performance of the different LS techniques and thus sets a new standard for data evaluation in advanced lifetime spectroscopy. A detailed comparison of the methodological aspects of the LS investigations may be found in Sect. 4.7.2 including a tabular overview of all methodological aspects which are illustrated in the different graphs.

The excellent consistency of the spectroscopic results obtained from the different LS techniques and their good agreement with DLTS-based E_t results from the literature conclusively proved the excellent performance of lifetime spectroscopy and the high reliability of the defect parameters determined. In conclusion, the results of the present chapter demonstrate impressively that, in terms of both physical understanding and technical implementation, lifetime spectroscopy is ready to be applied as a highly sensitive diagnostic tool in the semiconductor industry.

To illustrate the successful application of lifetime spectroscopy, it will be used in the following chapter to analyze a defect center in Cz silicon with well-known detrimental effects, although all attempts to determine its electrical properties have failed so far.

References

- [1] K. Graff, *Metal Impurities in Silicon-Device Fabrication*, 2nd edn. (Springer-Verlag, Berlin, 2000).
- [2] A.A. Istratov, H. Hieslmair, and E.R. Weber, *Iron and its complexes in silicon*, Appl. Phys. A **A69** (1), 13–44 (1999).
- [3] W. Zulehner, *Growth conditions of the metal-contaminated Cz-Si crystals*, personal communication (2000).
- [4] T. Lauinger, A.G. Aberle, and R. Hezel, *Comparison of direct and remote PECVD silicon nitride films for low temperature surface passivation of p-type crystalline silicon*, Proc. 14th EC PVSEC (Barcelona, Spain, 1997), pp. 853–856.
- [5] R. Lüdemann, *Plasmatechnologie für die Photovoltaik*, Dissertation, Universität Konstanz (1998).

- [6] H. Maeckel, *Herstellung und Charakterisierung von Siliziumnitridschichten zur Passivierung von Siliziumoberflächen*, Diplomarbeit, Albert-Ludwigs-Universität Freiburg (1999).
- [7] J.Y. Lee, *Rapid thermal processing of silicon solar cells – passivation and diffusion*, Dissertation, Albert-Ludwigs-Universität Freiburg (2003).
- [8] H. Kampwerth, *Analyse von Solarzellen und Ladungsträgerrekombination mittels Dickenvariation*, Diplomarbeit, Albert-Ludwigs-Universität Freiburg (2004).
- [9] H. Kampwerth, S. Rein, and S.W. Glunz, *Pure experimental determination of surface recombination properties with high reliability*, Proc. 3rd WCPEC (Osaka, Japan, 2003), pp. 1073–6.
- [10] E. Yablonovitch, D.L. Allara, C.C. Chang, T. Gmitter, et al., *Unusually low surface-recombination velocity on silicon and germanium surfaces*, Phys. Rev. Lett. **57** (2), 249–52 (1986).
- [11] S. Rein, *Untersuchung der Degradation der Ladungsträgerlebensdauer in Cz-Silizium*, Diplomarbeit, Albert-Ludwigs-Universität Freiburg (1998).
- [12] J. Schmidt, *Untersuchungen zur Ladungsträgerrekombination an den Oberflächen und im Volumen von kristallinen Silicium-Solarzellen*, Dissertation, Universität Hannover (1998).
- [13] D.K. Schroder, *Semiconductor Material and Device Characterization* (John Wiley & Sons, New York, 1990).
- [14] P.A. Basore and D.A. Clugston, *PC1D version 4 for Windows: From analysis to design*, Proc. 25th IEEE PVSC (Washington D C, 1996), pp. 377–81.
- [15] D. Macdonald, R.A. Sinton, and A. Cuevas, *On the use of a bias-light correction for trapping effects in photoconductance-based lifetime measurements of silicon*, J. Appl. Phys. **89** (5), 2772–8 (2001).
- [16] D. Macdonald and A. Cuevas, *Validity of simplified Shockley-Read-Hall statistics for modeling carrier lifetimes in crystalline silicon*, Phys. Rev. B (Condensed Matter and Materials Physics) **67** (7), 75203–1–7 (2003).
- [17] L. Börnstein, *Semiconductors* (Springer-Verlag, Berlin, 2002).
- [18] T. Jester, *Molybdenum contamination during Cz crystal growth: Heat shields*, Discussion on R&D challenges in Si-PV (13th workshop on crystalline silicon solar cell materials and processes, Vail, Colorado) (2003).
- [19] M. Lax, *Cascade capture of electrons in solids*, Phys. Rev. **119** (5), 1502–23 (1960).
- [20] A. Hangleiter, *Nonradiative recombination via deep impurity levels in silicon: Experiment*, Phys. Rev. B **35** (17), 9149–61 (1987).
- [21] S. Rein, P. Lichtner, W. Warta, and S.W. Glunz, *Advanced defect characterization by combining temperature- and injection-dependent lifetime spectroscopy (TDLS and IDLS)*, Proc. 29th IEEE PVSC (New Orleans, Louisiana, 2002), pp. 190–3.
- [22] D.V. Lang, *Deep-level transient spectroscopy: A new method to characterize traps in semiconductors*, J. Appl. Phys. **45** (7), 3023–32 (1974).

- [23] J. Isenberg, *DLTS-Charakterisierung von mc-Silizium und Barrièreschichten für die kristalline Silizium Dünnschichtsolzelle*, Diplomarbeit, Universität Karlsruhe (TH) (2000).
- [24] J. Isenberg, J. Dicker, and W. Warta, *Analysis of the effect of diffusion length distributions on global solar cell parameters by simplified 2D modelling*, Proc. 17th EC PVSEC (Munich, Germany, 2001), pp. 1571–4.
- [25] C.H. Ling and Z.Y. Cheng, *An improved analysis for the determination of trap levels in silicon from laser microwave photoconductive decay measurements*, Appl. Phys. Lett. **71** (22), 3218–20 (1997).
- [26] D. Macdonald, *Recombination and trapping in multicrystalline silicon solar cells*, PhD thesis, Australien National University (2001).
- [27] G. Zoth and W. Bergholz, *A fast, preparation-free method to detect iron in silicon*, J. Appl. Phys. **67** (11), 6764–71 (1990).
- [28] Y. Hayamizu, T. Hamaguchi, S. Ushio, T. Abe, et al., *Temperature dependence of minority-carrier lifetime in iron-diffused p-type silicon wafers*, J. Appl. Phys. **69** (5), 3077–81 (1991).
- [29] D. Walz, J.-P. Joly, and G. Kamarinos, *On the recombination behaviour of iron in moderately boron-doped p-type silicon*, Appl. Phys. A **62** (4), 345–53 (1996).
- [30] D. Macdonald, A. Cuevas, and J. Wong-Leung, *Capture cross-sections of the acceptor level of iron-boron pairs in p-type silicon by injection-level dependent lifetime measurements*, J. Appl. Phys. **89** (12), 7932–7939 (2001).
- [31] A. Kaniava, A.L.P. Rotondaro, J. Vanhellemont, U. Menczigar, et al., *Recombination activity of iron-related complexes in silicon studied by temperature dependent carrier lifetime measurements*, Appl. Phys. Lett. **67** (26), 3930–2 (1995).
- [32] S.D. Brotherton, P. Bradley, and A. Gill, *Iron and the iron-boron complex in silicon*, J. Appl. Phys. **57** (6), 1941–3 (1985).
- [33] D.H. Macdonald, L.J. Geerligs, and A. Azzizi, *Iron detection in crystalline silicon by carrier lifetime measurements for arbitrary injection and doping*, J. Appl. Phys. **95** (3), 1021–8 (2004).
- [34] L.C. Kimerling and J.L. Benton, *Electronically controlled reactions of interstitial iron in silicon*, Physica **116B**, 297–300 (1983).
- [35] C.H. Henry and D.V. Lang, *Nonradiative capture and recombination by multi-phonon emission in GaAs and GaP*, Phys. Rev. B (Solid State) **15** (2), 989–1016 (1977).
- [36] T. Pavelka, *Problems and possibilities of comparing different lifetime measuring instruments and techniques*, in *Recombination Lifetime Measurements in Silicon*, ed. by F.R.B.D.C. Gupta, and W.M. Hughes [American Society for Testing and Materials (ASTM), Chelsea, MI, 1998], Vol. 1, pp. 206–216.
- [37] R. Falster and G. Borionetti, *The application of minority carrier lifetime techniques in modern Cz-Silicon*, in *Recombination Lifetime Measurements in Silicon*, ed. by F.R.B.D.C. Gupta, and W.M. Hughes [American Society for Testing and Materials (ASTM), Chelsea, MI, 1998], Vol. 1, pp. 226–249.

- [38] S. Rein, S. Diez, and S.W. Glunz, *Temperature- and injection-dependent lifetime spectroscopy (T-IDLS): Advanced analysis*, Proc. 19th EC PVSEC (Paris, France, 2004), pp. 219–22.
- [39] J. Knobloch, S.W. Glunz, V. Henninger, W. Warta, et al., *21 % efficient solar cells processed from Czochralski grown silicon*, Proc. 13th EC PVSEC (Nice, France, 1995), pp. 9–12.
- [40] S.W. Glunz, J. Knobloch, C. Hebling, and W. Wetling, *The range of high-efficiency silicon solar cells fabricated at Fraunhofer ISE*, Proc. 26th IEEE PVSC (Anaheim, California, USA, 1997), pp. 231–4.
- [41] J. Dicker, *Analyse und Simulation von hocheffizienten Silizium Solarzellstrukturen für industrielle Fertigungstechniken*, Doktorarbeit, Universität Konstanz (2003).

5. The metastable defect in boron-doped Czochralski silicon

5.1 Introduction

At present 90 % of worldwide solar cell production is based on boron-doped crystalline silicon, 40 % of the market share going to Czochralski-grown monocrystalline silicon (Cz-Si) and 50 % to cast multicrystalline silicon (mc-Si) [1]. Efficiencies well above 20 % achieved over a broad range of different Cz-Si materials have demonstrated the potential of Cz silicon [2]. However, the main problem of solar cells manufactured on standard boron-doped Cz silicon is that their efficiency degrades under illumination from a high initial value to a stable final value. As the efficiency loss amounts to 1–2 % (absolute) in high-efficiency solar cells, the understanding of this effect and its technological reduction or avoidance are of special practical importance.

This effect, which was first discovered by Fischer and Pschunder in 1973 [3], is due to the activation of a *Cz-specific metastable defect*, which results in a strong reduction of bulk carrier lifetime [2–6]. The observation that both illumination and application of a forward bias in the dark [2, 7] result in an exponential lifetime degradation, approaching a stable final value (see Fig. 5.1a), leads to the conclusion that the transformation of the defect into its active state is carrier-induced and not photon-induced. The lifetime degradation can be completely reversed by a short annealing step at around 200°C (see Fig. 5.1b). This anneal process transforms the metastable defect into a passive state with very low recombination activity, reflected in high carrier lifetimes. The degradation/annealing cycle, i.e., the transformation between the active and passive state of the defect, is fully reversible (see Fig. 5.1c). Although progress has been made in the past few years with respect to our physical understanding of the metastable defect, its nature has not been clarified convincingly up to now.

Concerning the multitude of experimental findings and the different models proposed for the metastable defect in the past years, a comprehensive overview has been published by Schmidt et al. [8]. Against this background, we directly focus in the following on the contributions to the present

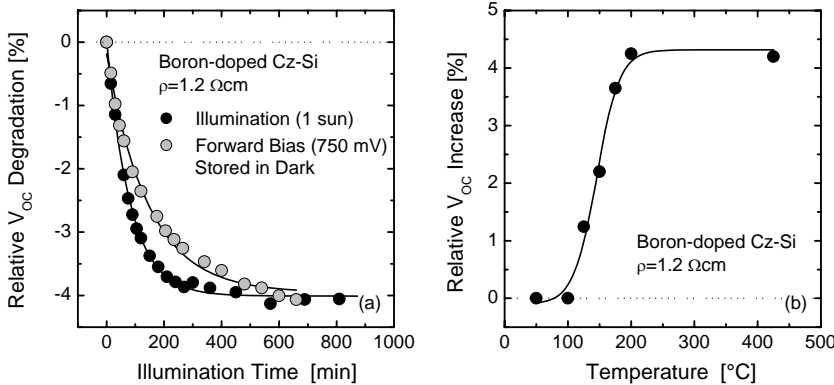


Fig. 5.1. Fundamentals of the degradation effect in boron-doped Cz silicon shown for the open-circuit voltage V_{OC} of a high-efficiency solar cell. Note that V_{OC} is directly related to bulk lifetime [9]. (a) Relative V_{OC} degradation upon illumination with 100 mW/cm^2 ($= 1 \text{ sun}$) (black circles) and upon application of a forward bias voltage of 750 mV , the cell being stored in the dark (gray circles). To ensure identical starting conditions, the cells were annealed at 200°C before degradation ($V_{OC,0} = 655 \text{ mV}$). From [2]. (b) Relative V_{OC} recovery due to an anneal at different temperatures. An anneal at 200°C allows the initial V_{OC} value and the initial cell efficiency to be recovered. From [2]. (c) Relative V_{OC} change after repeated alternating illumination in a suntester (30 h , 100 mW/cm^2 , AM1.5) and annealing (20 min , 200°C): the degradation/anneal cycle is fully reversible.

understanding of the metastable defect, which have arisen from the present work, discussing the different models and previous results when a comparison with our findings seems relevant.

With the aim of identifying the metastable defect, the following topics are examined in the present work. As a starting point Sect. 5.2 investigates qualitatively the impact of the characteristic contaminants in standard Cz silicon on the degradation effect, in order to identify the major components of the metastable defect. As a basis for the following investigations the normalized defect concentration N_t^* is introduced as a new quantity. In order to get insight into the microscopic structure of the metastable defect,

Sect. 5.3 examines the quantitative correlation of the defect concentration N_t^* with the contaminants identified to be relevant. As defect transformation is one of the major characteristics of the metastable defect, Sect. 5.4 investigates the kinetics of defect formation and annihilation quantitatively, in order to give deeper insight into the underlying physical mechanism. Section 5.5 is devoted to the electronic structure of the Cz defect. As the defect could not be detected by means of standard techniques but exhibits a high recombination activity, advanced lifetime spectroscopy, developed in the previous chapters, is ideally suited for this investigation.

The experimental findings on the defect properties lead to different strategies to reduce or even avoid the metastable defect. One of them is the permanent material improvement due to high-temperature anneals, which is discussed in Sect. 5.6. Finally, Sect. 5.7 presents an empirical model for the doping dependence of carrier lifetime in boron-doped Cz silicon, which is based on a comprehensive lifetime study and is shown to allow realistic predictions of cell performance.

5.2 Analysis I: major components

As a starting point for the analysis, the impact of the characteristic contaminants in standard Cz silicon on the degradation effect has been investigated qualitatively in order to identify the major components of the Cz-specific defect.

5.2.1 Intentionally oxygen-contaminated float zone silicon

Since interstitial oxygen is one of the most prominent contaminants in Cz silicon, the impact of oxygen has been investigated in an ideal system, in which superposed effects from residual defects could be excluded. Oxygen-doped float zone silicon, provided by the Wacker Siltronic company, represents such an ideal system.

Three different FZ materials with base resistivities between 6.5 and $8\Omega\text{cm}$ were investigated, two of them intentionally doped with oxygen. The oxygen concentration has been determined as $4\times10^{17}\text{ cm}^{-3}$ (for *n*-type FZ-Si) and $5\times10^{17}\text{ cm}^{-3}$ (for *p*-type FZ-Si), hence in the typical range for Cz silicon. For comparison a standard boron-doped Cz-Si material with $1.7\Omega\text{cm}$ and $[\text{O}_i]=6\times10^{17}\text{ cm}^{-3}$ has been included in the experiment.

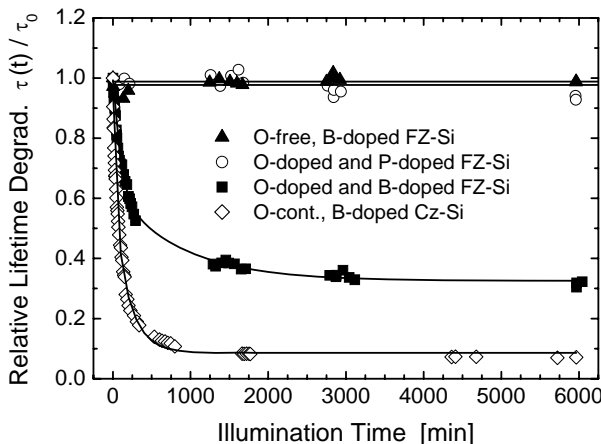


Fig. 5.2. Lifetime degradation in oxygen-free and oxygen-doped *p*- and *n*-type FZ silicon in comparison with the degradation in standard Cz silicon (open diamonds). A clear correlation of the degradation effect with oxygen and boron is revealed. After an annealing step at 230°C for 20 min (at $t=0$), the samples are degraded by illumination with a halogen lamp (intensity = 50 mW/cm²).

Figure 5.2 shows the results of time-dependent lifetime measurements on the SiN-passivated wafers. To ensure identical starting conditions, the samples were annealed at 230°C prior to the degradation experiment. Thus, in all samples the defect was deactivated at the time $t=0$. Then the wafers were degraded with white light of 50 mW/cm² intensity and measured repeatedly during the degradation. While the boron- and oxygen-doped FZ wafer (solid squares) showed a lifetime degradation comparable to the boron-doped oxygen-contaminated Cz wafer (open diamonds), both the oxygen-free boron-doped FZ wafer (solid triangles) and the phosphorus- and oxygen-doped FZ wafer (open circles) did not show such a degradation. This strongly suggests that boron and oxygen are involved in the Cz-specific defect center.

5.2.2 Modified Czochralski silicon

To confirm this hypothesis, special Cz silicon materials grown by Shin-Etsu have been investigated within an international joint research project [10]: on the one hand *magnetic Cz silicon* (MCz) with strongly reduced oxygen content, achieved by applying a magnetic field during the pulling process, and on the other hand *gallium-doped Cz silicon*, grown by means of the standard Cz process, in which case boron was replaced as a dopant.

Table 5.1. Classification of different material systems in terms of the appearance of the light-induced lifetime degradation.

Material	Interstitial oxygen	Dopant	Lifetime degradation	Reference
Boron-doped FZ	No	Boron	No	
Boron- and oxygen-doped FZ	Yes (10.8 ppma)	Boron	Yes	This work
Phosphorus- and oxygen-doped FZ	Yes (8.4 ppma)	Phosphorus	No	This work
Phosphorus-doped Cz	Yes	Phosphorus	No	Yoshida et al., 1996 [4] Schmidt et al., 1997 [5]
Boron-doped MCz	Very low (<1 ppma)	Boron	No	Joint research, 1999 [10, 11]
Gallium-doped Cz	Yes (13.2 ppma)	Gallium	No	Schmidt et al., 1997 [5] Joint research, 1999 [10, 11]

Both oxygen-free boron-doped *p*-type MCz silicon and oxygen-contaminated gallium-doped *p*-type Cz silicon showed no lifetime degradation¹ and excellent stable lifetimes close to the intrinsic limit (see Sect. 5.7.1). The fact that the degradation effect has not been observed in gallium-doped but only in boron-doped Cz silicon ensures that the Cz-specific defect actually depends on boron and not on the position of the Fermi level.

All these observations, summarized in Table 5.1, justify the hypothesis that boron and oxygen are the major components of the metastable defect underlying the Cz-specific lifetime degradation.

5.2.3 Normalized defect concentration

Using lifetime measurements to investigate the impact of oxygen and boron on the metastable defect quantitatively (see Sect. 5.3) and to examine the kinetics of defect transformation (see Sect. 5.4), the concentration of the metastable defect has to be determined from the measured carrier lifetimes. Let us denote the initial effective lifetime after an anneal above 200°C by τ_0 , the stable effective lifetime after an illumination with AM1.5 for at least 24 h by τ_d , and the effective lifetime in an arbitrary illumination state by $\tau(t)$ with $\tau(t) \in [\tau_d, \tau_0]$. Assuming that (i) the metastable Cz defect is completely deactivated after the anneal step and completely activated after the illumination step and that (ii) no additional recombination channels are

¹ For details on this material study see [10, 11].

affected by the anneal/illumination cycle, a normalized defect concentration² $N_t^*(t)$ in an arbitrary illumination state can be determined by (5.1)

$$N_t^*(t) := \frac{1}{\tau(t)} - \frac{1}{\tau_0} = \left(\frac{1}{\tau_{Cz}(t)} + \frac{1}{\tau_{res}} \right) - \frac{1}{\tau_{res}} = N_t(t) \times f(\sigma_n, \sigma_p, E_t; \Delta n, T)$$

where $N_t(t)$ is the concentration of the Cz-specific defect activated in the current illumination state, $1/\tau_{Cz}(t)$ is the corresponding SRH recombination rate and $1/\tau_{res}$ the recombination rate of all other recombination channels, including surface recombination as well as SRH recombination via other defects possibly contained in the bulk. The maximum defect concentration is got for $\tau(t) = \tau_d$.

It should be emphasized that, although effective lifetimes are measured in the following experiments, the plotted lifetime differences are only affected by SRH recombination via the Cz-specific defect in its active state. A fundamental prerequisite for the complete elimination of all other recombination channels from the lifetime difference defined in Eq. (5.1) is that the effective lifetimes in both states are measured at the same injection level Δn and the same temperature T , since the recombination rates of most recombination channels strongly depend on both. An equation for the factor f in Eq. (5.1) can be derived directly from the general SRH equation (3.5), although f cannot be determined quantitatively, since the electron capture cross-section σ_n of the defect is unknown. As f depends not only on the defect parameters σ_n , σ_p and E_t , but also on the measurement conditions Δn and T , an analysis of the time dependence of $N_t^*(t)$ requires the same Δn and T for all N_t^* . This principle was considered in all dynamic experiments carried out in Sect. 5.4.

To avoid screening of bulk recombination by surface recombination, all samples investigated in the following sections have been passivated with a low-temperature PECVD-SiN which is deposited at 350°C and leads to an excellent surface recombination velocity below 10 cm/s (see Sect. 4.2.2D). Its stability upon the anneal/degradation cycle has been controlled on float zone reference wafers, whose effective carrier lifetime did not change either after an annealing step of 20 min at 425°C or after a 36 h illumination step under 1 sun AM1.5, the latter reflecting the experimental conditions used in Sect. 5.3 for the determination of the maximum defect concentration N_t^* .

² An error estimate for this quantity may be found in [12].

5.3 Analysis II: quantitative correlation with different impurities

To give insight into the microscopic structure of the metastable defect in Cz silicon, the quantitative impact of the interstitial oxygen $[O_i]$ and the substitutional boron $[B_s]$ concentration on the normalized defect concentration N_t^* has been examined carefully on 30 different Cz materials from various manufacturers. This had not yet been done convincingly, because in previous studies of this topic either the measurement conditions [6, 12] or the database [13] had not been ideal. Thus, in this investigation special importance has been attached to an accurate determination of N_t^* from the lifetime measurements and to an improved data preparation in order to extend the database. Although it will only be shown in Sect. 5.6 that optimized high-temperature steps reduce the defect concentration significantly, the impact of a thermal oxidation at 1050°C on the quantitative N_t^* correlations with the different background impurities is already investigated here. Finally, we focus on the quantitative correlation with intrinsic point defects, such as vacancies, since several experimental observations point towards an indirect involvement of interstitial oxygen in the defect center.

5.3.1 Experimental procedure

A Set of Cz samples

In the present study we investigated 30 different standard Cz materials from varying manufacturers, which covered two orders of magnitude in the substitutional boron concentration ($[B_s] = 6 \times 10^{14} - 4 \times 10^{16} \text{ cm}^{-3}$) and half an order of magnitude in the interstitial oxygen concentration ($[O_i] = 5 \times 10^{17} - 1 \times 10^{18} \text{ cm}^{-3}$). To increase the accessible $[O_i]$ range, three magnetic Cz materials (MCz), exhibiting extremely low oxygen concentrations, were included.

The boron and oxygen concentrations have also been determined on the wafer subject to the lifetime investigation. While the boron concentration $[B_s]$ has been calculated from resistance measurements based on the four-point probe technique (see Sect. 4.2.3), the oxygen concentration $[O_i]$ has been determined by means of infrared spectroscopy according to DIN 50438-1, using a Bruker IFS 113 FTIR spectrometer. Since $[O_i]$ has been measured on several positions of each wafer, the given errors mainly reflect the lateral homogeneity of the oxygen distribution. Prior to the FTIR measurements all samples were shiny-etched in a CP133 etchant.

B Special conditions for the N_t^* determination

To determine the normalized defect concentration N_t^* , introduced in Sect. 5.2.3, we measured the injection dependence of carrier lifetime in the annealed state (τ_0 , open circles) and the degraded state (τ_d , open triangles) by means of the QSSPC technique, as shown in Fig. 5.3 for a standard boron-doped Cz silicon sample with $N_A = 4.0 \times 10^{15} \text{ cm}^{-3}$ and $[O_i] = 1.0 \times 10^{15} \text{ cm}^{-3}$.

While the defect was deactivated (τ_0) by an annealing step of 20 min at 425°C , it was activated (τ_d) by a 36 h illumination step under 1 sun AM1.5. The difference curve τ_{Cz} (solid circles) represents the SRH lifetime related only to the Cz-specific defect center. According to SRH statistics, the bulk lifetime in Cz silicon strongly depends on both the injection density Δn – as can be seen in Fig. 5.3 – and the doping concentration N_A . In order to guarantee the full comparability of N_t^* for wafers with different doping concentrations N_A , we determined N_t^* for each material at the same constant injection level $\eta := \Delta n/N_A = 0.1$ (big open circles) and not at a constant injection density Δn . As will be shown below, this improved N_t^* determination allows a significant extension of the database for the $[O_i]$ correlation. The N_t^* errors displayed in the following graphs are calculated by means of error propagation, assuming an accuracy of 10 % for the underlying lifetime measurements.

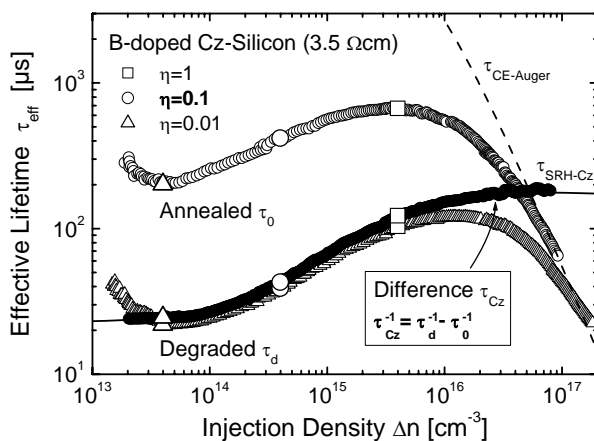


Fig. 5.3. Injection dependence of carrier lifetime in a standard boron-doped Cz silicon sample (with $N_A = 4.0 \times 10^{15} \text{ cm}^{-3}$, $[O_i] = 1.0 \times 10^{15} \text{ cm}^{-3}$), measured by means of the QSSPC technique in the annealed (τ_0 , open circles) and the degraded state (τ_d , open triangles). The difference curve τ_{Cz} (solid circles) represents the SRH lifetime related to only the Cz-specific defect center. For the determination of the normalized defect concentration N_t^* , the lifetime values are extracted at a fixed injection level $\eta = \Delta n/N_A$ (triplets of big open symbols).

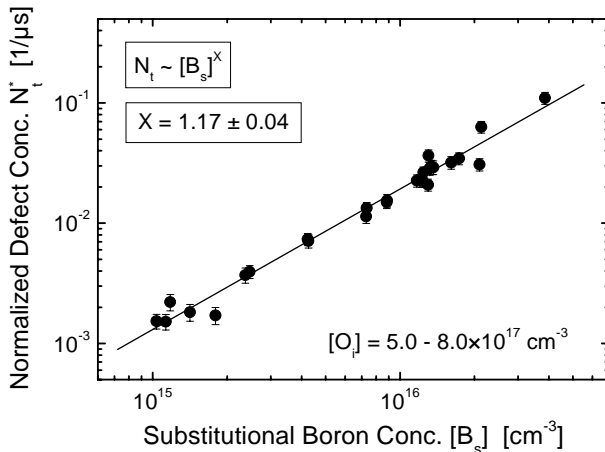


Fig. 5.4. Measured normalized defect concentration N_t^* as a function of the substitutional boron concentration $[B_s]$ for Cz-Si materials with similar oxygen concentration (symbols). The fitted line shows that N_t^* increases linearly with $[B_s]$.

5.3.2 Quantitative correlation with boron

Figure 5.4 shows the normalized defect concentration N_t^* as a function of the substitutional boron concentration $[B_s]$ for Cz-Si materials with similar oxygen concentrations $[O_i] = 5-8 \times 10^{17} \text{ cm}^{-3}$. In perfect agreement with previous studies [6, 13], we find a *linear* correlation between N_t^* and $[B_s]$. The weak scatter of the data clearly indicates direct involvement of substitutional boron in the defect center.

5.3.3 Quantitative correlation with oxygen

Up to now, the investigation of the quantitative correlation of N_t^* with the interstitial oxygen concentration $[O_i]$ has always been restricted to a selection of Cz materials within an arbitrary but narrow range for $[B_s]$. Since $[O_i]$ only varies over half an order of magnitude in standard Cz silicon ($5-10 \times 10^{17} \text{ cm}^{-3}$) and is not controlled as systematically as $[B_s]$ by the manufacturers, this restriction led to a strong reduction of the available database and thus to a larger uncertainty in the determined correlation exponent. Nevertheless, the dependence on oxygen in particular seems to be a key point when seeking a consistent model for defect reaction. In order to extend the database for the $[O_i]$ correlation, we used the linear $[B_s]$ correlation to correct N_t^* for the boron concentration $[B_s]$. If a $[B_s]$ -normalized

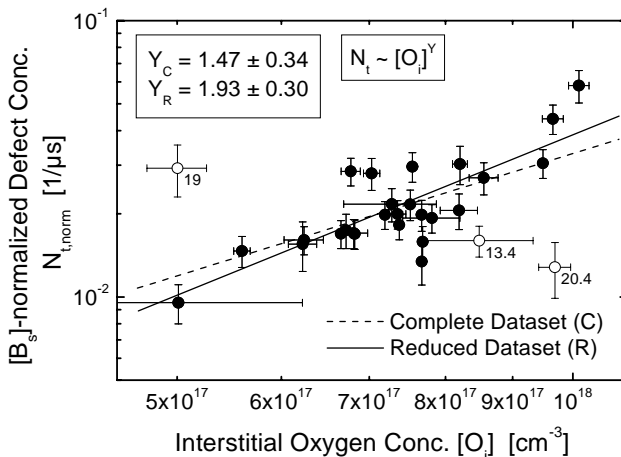


Fig. 5.5. Defect concentration $N_{t,\text{norm}}$ (after normalization to a fixed boron concentration of 10^{16} cm^{-3}) measured as a function of the interstitial oxygen concentration $[O_i]$ on standard Cz silicon (symbols). The extracted correlation exponent ranges between 1.5 (dashed line) and 1.9 (solid line), depending on whether or not the data points from the wafers with the highest resistivity (open circles) are considered.

defect concentration $N_{t,\text{norm}} \equiv N_t^* \times ([B_s]_{\text{norm}}/[B_s])^X$ with $[B_s]_{\text{norm}} = 10^{16} \text{ cm}^{-3}$ and $X=1$ is defined, the impact of $[B_s]$ can be completely eliminated from the data. In order to minimize the model uncertainty which is introduced by assuming a linear $[B_s]$ dependence, the chosen $[B_s]_{\text{norm}}$ equals approximately the average doping concentration of all samples. Figure 5.5 shows $N_{t,\text{norm}}$ as a function of $[O_i]$. Fitting the complete data set (all symbols), we find that $N_{t,\text{norm}}$ increases with increasing $[O_i]$ by a power of $Y=1.5 \pm 0.3$ (dashed line). Nevertheless, the strong scatter of the $[O_i]$ correlation is conspicuous. A closer look at the data points (open circles) which deviate most from the fitted trend line reveals their origin from the lowest doped samples with $[B_s] = 7-10 \times 10^{14} \text{ cm}^{-3}$. Due to the high carrier lifetimes which are expected and observed for these high-resistivity samples, the original N_t^* values are very low and are shifted by more than an order of magnitude by the $[B_s]$ normalization. While the calculated error bars correctly reflect the increased measurement error, they do not account for the model uncertainty introduced by the assumed $[B_s]$ -dependence with $X=1$. Since this model uncertainty increases with increasing deviation of the actual $[B_s]$ from the chosen $[B_s]_{\text{norm}}$ and is thus the highest for the three samples under discussion, we restrict the $[O_i]$ correlation graph to samples within a $[B_s]$ interval of two orders of magnitude around $[B_s]_{\text{norm}}$ and reject the wafers with the highest resistivity, keeping in mind the stronger scatter in

the complete $[O_i]$ correlation graph (see discussion in Sect. 5.3.6). Fitting the reduced data set (closed circles), we find an approximately *quadratic* increase ($Y_R = 1.9 \pm 0.3$) of $N_{t,norm}$ with increasing $[O_i]$ (solid line).

In order to scrutinize the quantitative $[O_i]$ correlation, we included three magnetic Cz silicon (MCz-Si) materials in the investigation, with extremely low oxygen concentrations ranging from 6×10^{16} to $5 \times 10^{17} \text{ cm}^{-3}$. This led to a significant extension of the accessible $[O_i]$ range. Figure 5.6 displays the $N_{t,norm}$ values for both magnetic (open circles) and standard (closed circles) Cz silicon as a function of $[O_i]$. Against the background of the strong scatter of the $[O_i]$ correlation, the extracted exponents for the $[O_i]$ correlation within the different material groups agree well with each other. With $Y = 1.6 \pm 0.03$, the exponent for the MCz samples lies in-between the exponents $Y = 1.5 \pm 0.3$ and $Y = 1.9 \pm 0.3$ which have been found for the complete and the reduced sets of Cz samples, respectively. Thus, our data allow the extraction of a unique model for the $[O_i]$ correlation of N_t^* which is valid in the whole $[O_i]$ range from 6×10^{16} to $1 \times 10^{18} \text{ cm}^{-3}$, with a correlation exponent which varies between $Y = 1.7 \pm 0.2$ and $Y = 1.8 \pm 0.1$, depending on whether the complete or the reduced set of Cz samples is combined with the MCz samples. Thus, the improved data evaluation reveals an *almost quadratic* dependence of N_t^* on $[O_i]$, the exact correlation coefficient being highly uncertain.

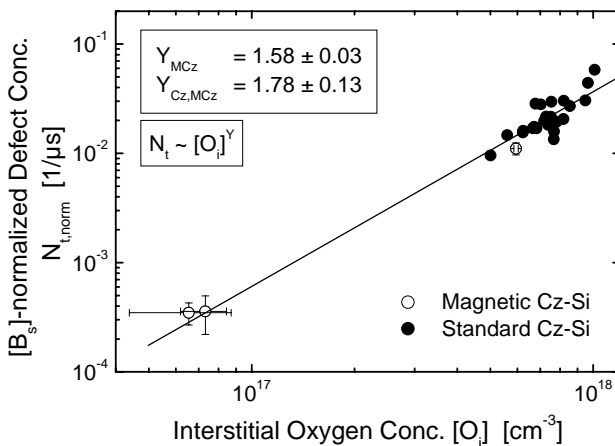


Fig. 5.6. Defect concentration $N_{t,norm}$ (after normalization to a fixed boron concentration) measured on standard (closed circles) and magnetic (open circles) Cz silicon as a function of the interstitial oxygen concentration $[O_i]$. The $[O_i]$ correlation exponent of Fig. 5.5 is well confirmed, allowing a unique model for the $[O_i]$ correlation to be extracted in the whole $[O_i]$ range.

5.3.4 Impact of thermal pretreatments

Irrespective of the exact correlation coefficient, the observed $[O_i]$ -dependence is much weaker than the one we determined in a previous work [6]. One reason for this discrepancy might be the different thermal history of the investigated samples. In contrast to the present study, the sample surfaces in [6] were passivated by SiO_2 layers grown thermally at 1050°C rather than by low-temperature SiN films. A possible impact of such a high-temperature step on bulk properties was investigated by repeating the study described above on a set of 18 Cz materials covering the whole $[O_i]$ range from $5-10 \times 10^{17} \text{ cm}^{-3}$, including a 1050°C thermal oxide growth (using process parameters which have been optimized for Cz silicon as will be shown in Sect. 5.6.2) prior to the degradation study. In order to issue a proper comparison of results from the two groups, lifetime measurements on both groups of samples [with (HT) or without (LT) the 1050°C treatment] were, however, made using the same PECVD-SiN layers as before for surface passivation. The thermally oxidized samples were etched in hydrofluoric acid to completely remove the thermally grown SiO_2 layers prior to the deposition of the passivation layer.

Analogously to Fig. 5.4, Fig. 5.7 displays the normalized defect concentration N_t^* after the mentioned HT step (closed circles) as a function of $[B_s]$ for samples with similar $[O_i]$. A comparison with the data obtained on the LT (starting material) samples (open circles) shows that the HT step only causes a parallel shift of the N_t^* - $[B_s]$ curve to lower values and thus results in an N_t^* reduction by some fixed $[B_s]$ -independent factor. Improvement by high-temperature treatments had already been observed in previous studies [6, 14, 15], although it has not been investigated quantitatively as a function of different background impurities. The fact that neither the $[B_s]$ correlation exponent nor the correlation quality (represented by the scatter of the $[B_s]$ -dependent N_t^* data) are affected by the HT step is a further indication that boron is directly involved in the defect center.

Figure 5.8 shows the impact of the HT step on the $[B_s]$ -normalized defect concentration $N_{t,\text{norm}}$ as a function of $[O_i]$. Since no high-resistivity samples were included in the HT experiment (closed circles), the experiment on the starting material is represented by a reduced data set from Fig. 5.5 (open circles). Despite the strong scatter which is equally observed for the $[O_i]$ correlation of $N_{t,\text{norm}}$ with or without the HT pretreatment, an apparent fit to both data sets reveals that the exponent for the $[O_i]$ correlation drops significantly from $Y=1.9\pm0.3$ in the starting material to $Y=1.5\pm0.3$ in the HT-pretreated material. Thus, the HT step induces a drift from an almost quadratic dependence towards a linear dependence of $N_{t,\text{norm}}$ on $[O_i]$.

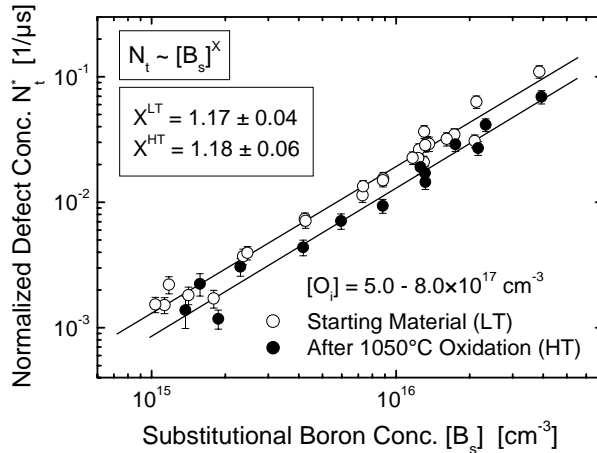


Fig. 5.7. Impact of a high-temperature step on the measured $[B_s]$ -dependence of normalized defect concentration N_t^* for Cz-Si materials with similar $[O_i]$. Due to a uniform reduction of N_t^* , the $[B_s]$ correlation exponent remains unchanged.

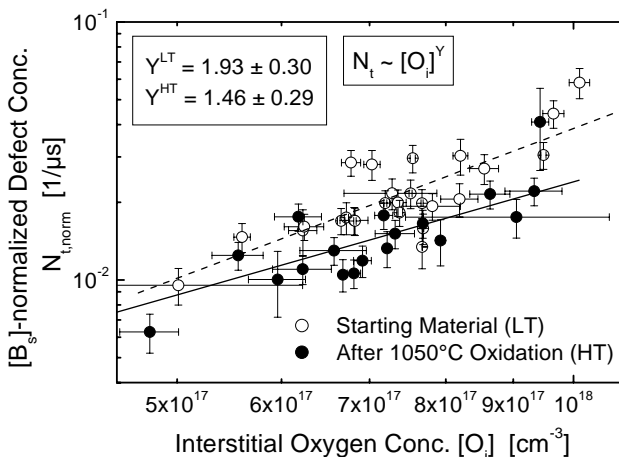


Fig. 5.8. Impact of a high-temperature (HT) step on the measured $[O_i]$ -dependence of the $[B_s]$ -normalized defect concentration $N_{t,norm}$ for standard Cz-Si materials within a $[B_s]$ range of 1×10^{15} – $5 \times 10^{16} \text{ cm}^{-3}$. Due to a non-uniform reduction of N_t^* , the $[O_i]$ correlation exponent decreases from 1.9 (dashed line) to 1.5 (solid line) when the HT pretreatment is applied.

An explanation for this change in the $[O_i]$ correlation can be found in Fig. 5.9, which displays the ratio of the values after an HT pretreatment to the values in the LT starting material for the defect and the oxygen concentration, respectively. As already observed in a previous work [14], the strong reduction of N_t^* by an average of 40 % correlates with a moderate

reduction of $[O_i]$ by an average of 4 %. Plotting both ratios as a function of $[O_i]$, as done in Fig. 5.9, it turns out that the relative N_t^* reduction increases more significantly with increasing $[O_i]$ than the relative $[O_i]$ reduction which remains almost constant. As a result, the $[O_i]$ correlation exponent decreases due to the high-temperature step. The scatter observed for both ratios in Fig. 5.9 can be partly ascribed to the fact that the underlying absolute quantities were measured on different wafers of the same material, which show natural fluctuations especially in $[O_i]$. This explains the $[O_i]$ ratios bigger than unity which have been observed for three materials (crossed open circles) and have been neglected in the fit (dashed line).

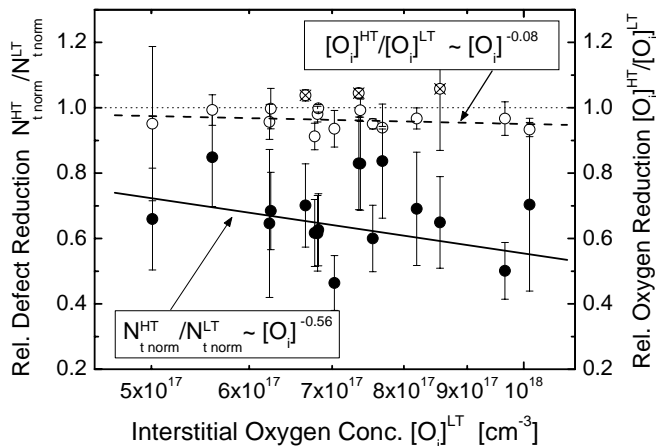


Fig. 5.9. Relative reduction of the defect concentration (closed symbols) and the oxygen concentration (open symbols) due to an applied high-temperature step as a function of $[O_i]$ in the starting material. The relative N_t^* reduction (solid line) increases more significantly with increasing $[O_i]$ than the relative $[O_i]$ reduction (dashed line) and results in the decrease in the $[O_i]$ correlation exponent observed in Fig. 5.8.

5.3.5 Quantitative correlation with carbon

Apart from boron and oxygen, carbon is a third background impurity which is often met in significant amounts in Cz silicon. In order to discover the impact of the substitutional carbon concentration $[C_s]$ on the metastable defect concentration N_t^* , we chose 4 samples with varying carbon (5×10^{15} – $5 \times 10^{16} \text{ cm}^{-3}$) and similar boron (1.1 – $1.6 \times 10^{16} \text{ cm}^{-3}$) and oxygen (6.2 – $7.8 \times 10^{16} \text{ cm}^{-3}$) concentrations. As displayed in Fig. 5.10, an exponent $Z = -0.1 \pm 0.3$ is found for the $[C_s]$ correlation. Thus, the impact of carbon on the metastable defect can be neglected at least in the covered $[C_s]$ range from 5×10^{15} (FTIR detection limit) to $5 \times 10^{16} \text{ cm}^{-3}$.

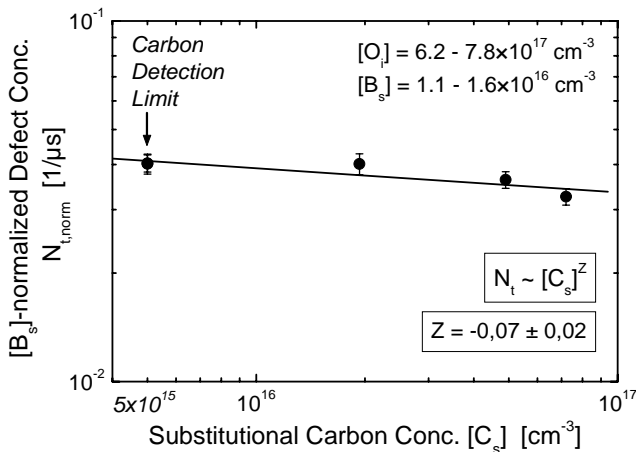


Fig. 5.10. Measured defect concentration $N_{t,\text{norm}}$ (after normalization to a fixed boron concentration) as a function of the substitutional carbon concentration $[C_s]$ for Cz-Si materials with similar O_i concentration (symbols). The fitted line shows that $N_{t,\text{norm}}$ is almost independent of $[C_s]$.

5.3.6 Discussion and preliminary defect model

Our experiments confirm previous results that boron and oxygen are involved in the metastable defect center observed in Cz silicon. Nevertheless, the study reveals a fundamental difference concerning the dependence of N_t^* on these quantities.

In perfect agreement with previous studies [6, 13], we find a linear correlation between N_t^* and $[B_s]$. The weak scatter of the data and the stability of the correlation exponent upon a HT treatment clearly indicate a direct involvement of substitutional boron in the defect center.

In contrast to the accurate determination of the $[B_s]$ correlation, the exponent determined for the correlation between N_t^* and $[O_i]$ varies between 1.5 and 1.9 depending on the selection of materials and the thermal pretreatment. Irrespective of the exact correlation coefficient, the observed $[O_i]$ -dependence is much weaker than the one we determined in a previous work [6]. Since samples with the same thermal pretreatment have been investigated in the present study, the stronger $[O_i]$ -dependence of N_t^* must have been produced by systematic errors³ which could not be avoided in

³ In the study of [6], two sources for systematic errors can be identified: on the one hand, N_t^* has been determined from lifetime measurements performed at fixed bias light intensity using the MW-PCD technique, which results in a systematic overestimate of N_t^* (for details

the experimental setup used there and has to be rejected in favor of the accurate determination presented here.

The upper limit for the $[O_i]$ correlation exponent found here ($Y=1.9$) is in good agreement with the findings in a recent study [13] in which a correlation exponent $Y=1.8$ has been determined on a small number of data points. It should be stated, though, that this upper limit was determined neglecting the N_t^* values of three high resistivity samples and thus artificially reducing the scatter of the $[O_i]$ correlation (see Fig. 5.5). To estimate the credibility of these data points, the observed high carrier lifetimes have been double-checked on parallel wafers and were reproduced within the assumed 10% error. The comparison of the average lifetime results on these samples raises further questions concerning the direct involvement of oxygen in the defect center. While the 13 and $20\Omega\text{cm}$ samples exhibit high carrier lifetimes of $490\text{--}680\mu\text{s}$ in the degraded state and $1120\text{--}2640\mu\text{s}$ in the annealed state, which is expected for high-resistivity samples, the carrier lifetime in the $19\Omega\text{cm}$ sample is limited to $250\mu\text{s}$ (τ_d) and $530\mu\text{s}$ (τ_0), respectively, despite the low boron and oxygen concentration, which leads to the significantly increased $N_{t,\text{norm}}$ value displayed in Fig. 5.5. Since the determination of N_t^* , $[B_s]$ and $[O_i]$ has been performed with maximum precision and high reproducibility, this result implies that the observed strong scatter in the $[O_i]$ correlation has a physical origin which has not yet been revealed. Thus taking the scatter completely into account, the exponent for the correlation of N_t^* and $[O_i]$ is determined as $Y=1.5$. This value is found on the starting material as well as after a thermal pretreatment at 1050°C .

Thus, the metastable defect center seems to be a complex B_sX consisting of a single boron atom and a second component X which directly or indirectly correlates with oxygen. Recently, Schmidt et al. [13] proposed a defect reaction model in which fast diffusing O_{2i} dimers are captured by substitutional boron to form a B_sO_{2i} complex which acts as a highly efficient recombination center. The finding that the process of defect formation is thermally activated could be well explained by the diffusion of these oxygen dimers. Although it is likely that the transport of oxygen and thus the kinetics of the defect formation is dominated by the transport of oxygen dimers,⁴ our results on the $[O_i]$ correlation of N_t^* raise doubts as to

see Sect. 5.4.2). On the other hand, $[O_i]$ has been determined from a comparison of the O_i -absorption peaks in a test and a calibration wafer with known $[O_i]$. Systematic errors may arise from the extreme sensitivity of this technique to variations between test sample and calibration sample concerning the optics and thickness. These $[O_i]$ errors are avoided by applying DIN 50438-1, as in the present study.

⁴ The supposition that oxygen dimers dominate the transport of oxygen (at least below 600°C) is supported by a recent study on the locking of dislocations by oxygen [16].

whether the oxygen involved in the metastable defect is in the form of these oxygen dimers. For physical reasons this is not required, since at room temperature the vast majority of the oxygen actually in the system is still in the form of interstitial oxygen. Although the quantitative results for the $[O_i]$ correlation do not contradict the B_sO_{2i} model, the strong scatter of the $[O_i]$ correlation and especially the decrease of the correlation exponent to 1.5 upon a thermal pretreatment at high temperatures points towards an indirect rather than a direct involvement of oxygen in the defect center.

Possible candidates for such a stimulated background impurity are intrinsic point defects, such as vacancies (V) and self-interstitials (I), since their concentration strongly correlates with oxygen behavior and significantly depends on the thermal treatment of the samples. Since all studies on the quantitative correlation of N_t^* on $[O_i]$ have been performed on material from different manufacturers, significant variations in the concentration of intrinsic point defects are very likely and may explain the observed strong scatter in the $[O_i]$ correlation.

5.3.7 Impact of intrinsic point defects

To pursue this new approach we investigated the impact of the vacancy concentration [V] on a set of Cz samples in which [V] has been well adjusted by a special thermal treatment [17]. In order to investigate the main effect of [V] as well as possible interactions of $[V]^*[B_s]$ and $[V]^*[O_i]$, a set of samples was investigated in which each of the three parameters was adjusted to a high and a low level. The 2^3 different parameter combinations were realized on 8 different materials. The levels chosen were 5 and $24 \times 10^{14} \text{ cm}^{-3}$ for $[B_s]$, 5.9 and $7.7 \times 10^{17} \text{ cm}^{-3}$ for $[O_i]$ and below $1 \times 10^{11} \text{ cm}^{-3}$ and $5 \times 10^{12} \text{ cm}^{-3}$ for [V]. The vacancy concentrations were installed via heat treatments in a controlled ambient and under controlled cooling conditions using rapid thermal annealing [17]. The high and low vacancy concentrations were installed using process temperatures of 1200 and 950°C, respectively. In the high concentration samples the vacancy concentration is not uniform as they contain a region of lower vacancy concentration of about 50 microns due to out-diffusion.

The special compilation of samples fulfilled the prerequisites of an experiment with 2^3 factorial design, which enabled us to evaluate of the results using the commercial statistics software Statistica 5.1 [18]. In our case the benefit of such a statistical analysis is that it allows a direct identification of all factors and factor interactions which affect the normalized defect concentration N_t^* (which is considered as the response quantity of the system), giving at the same time an estimate for the significance of the

observed effects. Thus, the analysis provides the maximum information on a minimum number of experiments.

The sample preparation and the determination of N_t^* has been performed as in the previous investigations. The excellent performance of the material and its limitation by the metastable defect is manifested by carrier lifetimes as high as 230 to 1700 μs in the degraded state and 930 to 2520 μs in the annealed state. The result of the statistical analysis is displayed in Fig. 5.11 in the form of a pareto chart of the defect concentration N_t^* . The diagram shows the estimated effects of the controlled quantities and their interactions (vertical bars). The horizontal lines represent the confidence limits for different error probabilities given on the right edge of the diagram. These confidence limits were calculated on the basis of the N_t^* measurement errors and are interpreted in such a way that a factor whose effect exceeds a special significance limit has an impact on the response parameter with the corresponding error probability. The diagram reveals the known fact that boron (1), oxygen (2) and the boron-oxygen interaction (1*2) increase N_t^* and are statistically relevant with an error probability below 0.1 %. However, no direct effect of vacancies (3) on N_t^* could be identified. Nevertheless, with an error probability of 5% an indirect effect via the boron-vacancy interaction (1*3) is observed. Although it is statistically only regarded as “possibly relevant”, this would mean that the impact of boron is increased with increasing [V], since [V] itself showed no effect on N_t^* . Thus, it is most likely that vacancies have to be ruled out as a source of the unknown background impurity responsible for the strong scatter of the $[O_i]$ correlation.

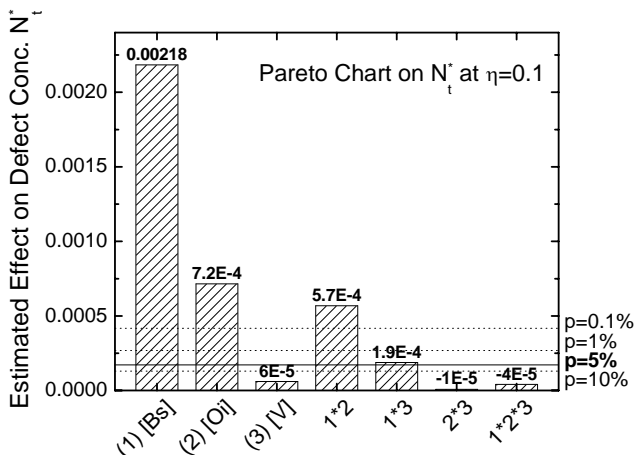


Fig. 5.11. Pareto chart on the normalized defect concentration N_t^* showing the estimated effects of the controlled quantities and their interactions. The *horizontal lines* represent the significance limits for different error probabilities.

5.3.8 Conclusion

In the present study the correlation of the metastable defect concentration N_t^* with different impurities has been investigated quantitatively on 30 different Cz-Si materials. The correlation has been found to be linear with boron ($N_t^* \propto [B_s]^{1.1}$), almost quadratic with oxygen ($N_t^* \propto [O_i]^{1.5-1.9}$) and vanishing with carbon. The study has revealed a fundamental difference in the $[B_s]$ and $[O_i]$ correlations: while the $[B_s]$ correlation shows an excellent quality with an exponent that is stable upon a high-temperature (HT) pretreatment, the $[O_i]$ correlation shows a strong scatter with an exponent which decreases upon an HT pretreatment. This points towards a direct involvement of substitutional boron in the defect center, while the involvement of oxygen seems to be indirect. Thus, we suppose a defect complex B_sX with an unknown component X which is stimulated by oxygen. Possible candidates for X are, for example, intrinsic point defects. In a first experiment, we found that vacancies most likely have to be ruled out as source for this unknown impurity.

5.4 Analysis III: mechanism of defect transformation

A major characteristic of the metastable defect in Cz silicon is the reversible defect transformation between the recombination-active (active) state A and the recombination-inactive (passive) state P. To give deeper insight into the underlying physical mechanisms, the kinetics of defect formation and annihilation are analyzed quantitatively, as this may provide further hints concerning the oxygen-stimulated component X of the defect complex B_sX (see Sect. 5.3).

To investigate the kinetics of defect transformation by means of lifetime measurements, the normalized defect concentration $N_t^*(t)$ has to be determined from the measured carrier lifetimes as defined in Eq. (5.1). As pointed out in Sect. 5.2.3, an accurate analysis of the time dependence of $N_t^*(t)$ requires the same Δn and T for all N_t^* values to ensure their full comparability, due to the strong injection and temperature dependence of SRH lifetime. This principle was considered in all dynamic experiments carried out below.

5.4.1 Kinetics of defect annihilation

First we examined the kinetics of defect annihilation. As the transformation of the defect from state A to state P occurs above a threshold temperature

[19], defect annihilation seems to be thermally activated. If the annihilation process is formulated as a decay process, a continuous annealing step at temperature T should lead to a mono-exponential decrease of the defect concentration $N_t(t)$ given by

$$N_t(T, t) = N_t(T, 0) \times \exp[-R_{ann}(T) \times t] \quad (5.2)$$

The thermal activation of this decay process is introduced into Eq. (5.2) by assuming an annihilation rate $R_{ann}(T)$ that increases exponentially with temperature:

$$R_{ann}(T) = R_{ann}(T \rightarrow \infty) \times \exp\left(-\frac{E_{ann}}{kT}\right) \quad (5.3)$$

Thus, the kinetics of defect annihilation is controlled by an activation energy E_{ann} . As the annihilation process depends on time and temperature, E_{ann} can be determined from two experiments: (i) from an *isothermal* experiment observing the time-dependent decay of $N_t(t)$ at a constant temperature T_{iso} and (ii) from an *isochronal* experiment observing the temperature-dependent decay $N_t(T)$ for a constant annealing time t_{iso} at each temperature.

In the present work, we performed an isothermal annihilation experiment on a boron-doped Cz-Si sample with a bulk resistivity of $3.1 \Omega\text{cm}$. The lifetime measurements were performed by means of the MW-PCD method using the MW-PCD system with integrated cryostat (see Sect. 2.3). Before each annealing cycle the sample was fully degraded, which was controlled by a lifetime measurement at room temperature. During ramping-up to the appropriate temperature T_{iso} , the sample was illuminated with a maximum light intensity of 300 mW/cm^2 , which allowed the annihilation process to be almost completely suppressed. Having reached the constant temperature T_{iso} , we switched off the degradation light at $t=0$ and measured the effective lifetime repeatedly at the annealing temperature T_{iso} . In order to avoid superposed formation of defects by the measurement light, the sample was measured at a minimum bias intensity that only just allowed trapping effects to be excluded and was kept in the dark in-between subsequent measurements. Thus, the presented data are not affected by the systematic errors discussed in following Sect. 5.4.2B. In order to guarantee a precise temperature control, the temperature was measured directly on the sample surface with a Pt100 temperature sensor.

As discussed in Sect. 5.2.3, the defect concentration $N_t^*(t)$ and its time dependence can be determined from lifetimes measured at T_{iso} [see Eq. (5.1)]:

$$N_t^*(T_{iso}, t) = \frac{1}{\tau(T_{iso}, t)} - \frac{1}{\tau_0(T_{iso})} \quad (5.4)$$

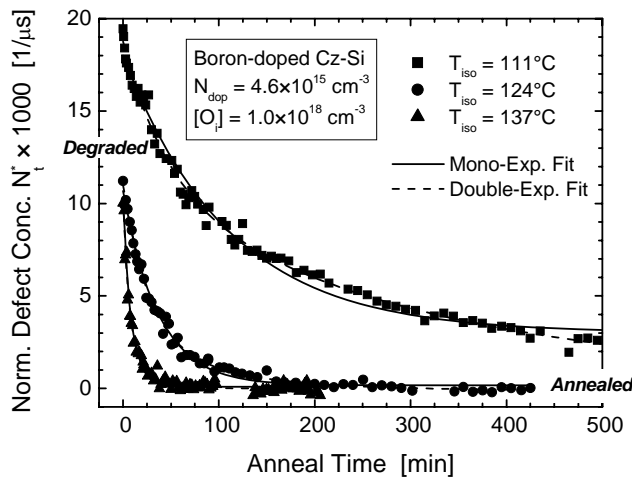


Fig. 5.12. Isothermal annealing curves for the same Cz-Si sample measured at different temperatures starting from the fully degraded state ($t=0$). The underlying carrier lifetimes are measured at the corresponding annealing temperatures.

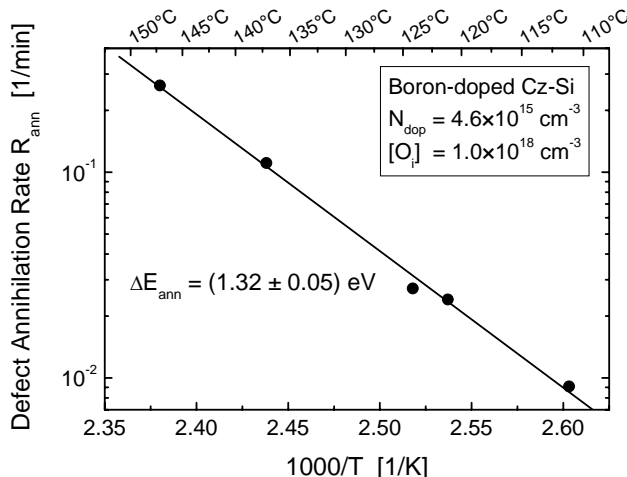


Fig. 5.13. Arrhenius plot of the defect annihilation rates (symbols) determined from a mono-exponential fit to the isothermal annealing curves in Fig. 5.12. The energy barrier E_{ann} for the thermally activated annihilation process results from a linear fit to the data.

Figure 5.12 shows the measured decay of $N_t^*(t)$ for three different annealing temperatures. As predicted by the model in Eq. (5.2), the time dependence of the decay curves can be described by a mono-exponential fit. As expected, the annihilation process occurs the faster with higher annealing temperatures. This is reflected by the time constants $\tau_{ann}(T_{iso})$ of the mono-exponential decay which range between 110 and 3.7 min for temperatures between 111°C and 147°C. It should be stressed that a significant annihilation of the defect in state A can already be reached at an annealing temperature around 110°C.

An Arrhenius plot of the annihilation rates $R_{ann}(T_{iso})$ determined from the mono-exponential fits to the $N_t^*(t, T_{iso})$ curves reveals that the annihilation process is thermally activated (see Fig. 5.13) with an energy barrier $E_{ann} = (1.32 \pm 0.05)$ eV determined for the first time. This value lies in a typical range if compared for example with the potential barrier of 1.2 eV measured for the thermal dissociation of FeB pairs [20].

5.4.2 Kinetics of defect formation

Second, the transformation of the Cz-specific defect from the passive state P to the active state A has been examined. As already mentioned, this process is not photon-induced but excess-carrier-induced since the degradation can also be achieved in the dark by injection of carriers (see Fig. 5.1a) [2, 7]. A possible explanation for this transformation could be the so-called recombination-enhanced defect reaction (REDR) [5, 21, 22].

A Theory of recombination-enhanced defect reaction (REDR)

In REDR theory [21, 22], the energy necessary for a transformation of a defect from state I to state II is obtained from the energy gained by the recombination process over defect I . In the case of the Cz-specific defect, the energy for the transformation from state P to state A should be delivered by the recombination at the metastable defect in state P . The densities of the defect in active and passive state, N_{tA} and N_{tP} , respectively, should then follow an exponential law [22]

$$N_{tA}(t) = N_{tP}(0) \times \left[1 - \exp\left(-\frac{t}{\tau_{gen}}\right) \right] \quad (5.5)$$

where τ_{gen} is the time constant describing the activation process. For the corresponding defect generation rate R_{gen} REDR theory predicts [22]:

$$R_{gen} = \frac{1}{\tau_{gen}} = \Pi R_n \quad (5.6)$$

where R_n is the recombination rate of a single defect P and Π the probability of the transformation process.

In a previous study of ours [23], two observations supported the applicability of REDR theory. First, the time dependence of the defect generation process measured on Cz samples over a wide resistivity range was in good agreement with the time-dependent behavior predicted in Eq. (5.5) [6]. And second, the observed large increase in R_{gen} with increasing doping level also fitted in REDR theory, as it is well known from SRH theory that the recombination activity R_n of shallow levels such as that of the Cz-specific defect in the passive state P is strongly doping-dependent (see Fig. 3.2b).

B Impact of the boron concentration

To check whether REDR really is the mechanism responsible for defect formation in Cz silicon, we analyzed the doping dependence of the defect generation rate quantitatively. For the recombination rate R_P via a shallow level ($n_1 \gg p_0$ or $p_1 \gg p_0$), the following expression can be derived from general SRH theory [24], assuming a p -type semiconductor ($p_0 \gg n_0$) under low-level injection (LLI) ($\Delta n \ll p_0$) [see Eq. (3.7a)]:

$$R_n := R_P / N_{nP} = g(E_{nP}, \sigma_{nP}, \sigma_{pP}) \times \Delta n \times p_0 \quad (5.7)$$

As the factor g only depends on the energy level E_{nP} and the capture cross-sections σ_{nP} and σ_{pP} of the defect in state P , the recombination rate R_n increases linearly with the doping concentration $N_A = p_0$ and the excess carrier density Δn . According to Eq. (5.6), this linear dependence on the doping concentration N_A and the excess carrier density Δn should also be expected for the defect generation rate R_{gen} .

A fit to our experimental data published in [23] led to a doping dependence of R_{gen} to the power of 1.5. But a closer look at the experimental details makes it obvious that these data are not suitable for a quantitative analysis, as two systematic errors could not be avoided by the experimental setup. On the one hand the lifetime measurements were performed at fixed bias light intensity. As the lifetime level decreases by more than one order of magnitude from the start to the end of degradation, the injection level corresponding to the fixed bias intensity decreases monotonically to the same extent. This leads to an additional decrease in the measured carrier lifetime, since the injection dependence of the carrier lifetime in Cz silicon exhibits the typical SRH increase for a deep defect. On the other

hand the lifetime measurements were performed with the microwave-detected photoconductance decay technique (MW-PCD) [25] leading to differential lifetimes $\tau_{\text{eff},\text{diff}}$ instead of absolute (physical) lifetimes τ_{eff} [26]. Due to the typical SRH increase in the injection-dependent carrier lifetime in Cz silicon, the physical recombination lifetime τ_{eff} is overestimated by the measured $\tau_{\text{eff},\text{diff}}$, which leads to a further decrease in the measured carrier lifetime.

To eliminate these systematic errors, we repeated the time-resolved degradation experiment on Cz materials in a doping range from 6.1×10^{15} to $3.9 \times 10^{16} \text{ cm}^{-3}$ with the quasi-steady-state photoconductance technique (QSSPC) using a WCT-100 system from Sinton Consulting [27]. The use of the QSSPC technique allows on the one hand a direct measurement of the physical recombination parameters and on the other hand a lifetime measurement at fixed injection level. To investigate the kinetics of defect formation, the samples were annealed at 425°C for 10 min ($t=0$) and then degraded under 50 mW/cm^2 illumination, while being measured continuously with the flash-lamp of the QSSPC system. During the QSSPC measurements the halogen lamps used as degradation light were switched off. The temperature of the stage was controlled with a Pt100 thermosensor and could be held at $(33.25 \pm 0.75)^\circ\text{C}$ due to cooling by an adjustable N_2 flow. A fixed temperature turned out to be important since the sensitivity of the high-frequency circuit of the WCT-100 system changes with temperature.

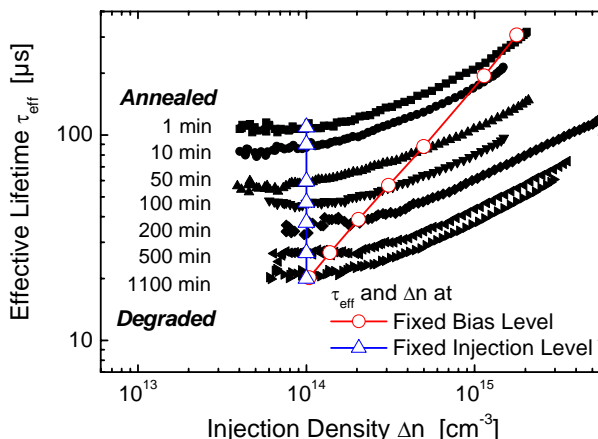


Fig. 5.14. Time-dependent decrease in QSSPC lifetime curves measured on a Cz-Si sample under 50 mW/cm^2 illumination after an anneal at 425°C for 10 min ($t=0$). The illumination times are given on the left.

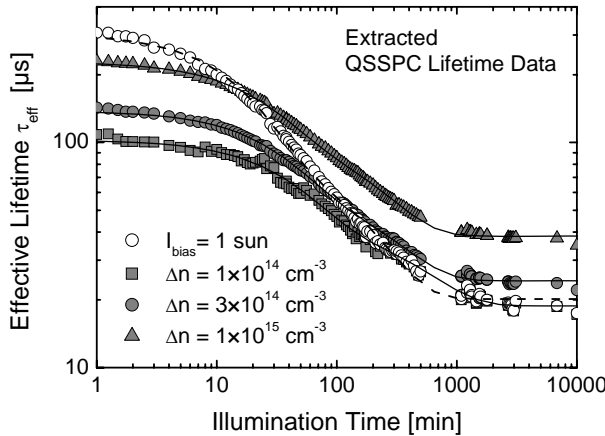


Fig. 5.15. Time-dependent lifetime decrease of a Cz silicon sample under 50 mW/cm^2 illumination after an anneal at 425°C for 20 min ($t=0$). Lifetime data are extracted at three fixed injection levels (gray symbols) and at fixed bias intensity (open circles).

Figure 5.14 shows a time-resolved series of subsequent QSSPC lifetime curves measured during degradation. The systematic error that results from a measurement at fixed bias intensity (as discussed above) is visualized by the open symbols in Fig. 5.14. If the lifetime is measured at fixed bias intensity (open circles: 1 sun), an additional lifetime decrease due to the reduction of the injection level is superposed on the lifetime decrease due to the activation of the Cz-specific defect (open triangles). Thus, an isolated measurement of the lifetime decrease due to defect formation requires a measurement at fixed injection level as realized in the present work.

Figure 5.15 shows the lifetime curves extracted at three different injection levels from the series of subsequent QSSPC curves in Fig. 5.14 and plotted versus illumination time (solid symbols). For comparison, the lifetime curve extracted at 1 sun intensity is displayed as well (open circles). The overestimate of lifetime degradation becomes obvious.

In order to determine the defect generation rate R_{gen} for the different $\tau(t)$ curves, we plotted the quantity $1/\tau_d - 1/\tau(t)$, since this quantity is determined with better accuracy than the usual $N_{ta}(t)$. For $1/\tau_d - 1/\tau(t)$, which describes that part of the concentration of the defect in state A remaining for activation, i.e. $N_{tp}(0) - N_{ta}(t)$, REDR predicts a mono-exponential decay to zero with the same time constant as in Eq. (5.5):

$$\frac{1}{\tau_d} - \frac{1}{\tau(t)} = N_{tp}(0) \times \exp\left(-\frac{t}{\tau_{gen}}\right) \quad (5.8)$$

While some samples show the expected mono-exponential decay, the modeling of the entire decay curve of other samples requires a double-exponential fit. The slight deviation of the mono-exponential decay can be explained, e.g., by REDR theory: as the lifetime changes by more than one order of magnitude between the annealed and the fully degraded state, the carrier density generated by the constant light intensity of the degradation lamps decreases to the same extent. According to Eq. (5.7), the consequence is a reduction of the recombination rate R_n via the passive defect which leads to a reduced defect generation rate R_{gen} and results in a slower decay of $1/\tau_d - 1/\tau(t)$. As it is not possible to avoid this effect in the experiment, we took it into account for the data evaluation: as the first half of decay curves was always free of such superposed effects, we fitted this part of all $1/\tau_d - 1/\tau(t)$ curves mono-exponentially. Additionally, we fitted all (non-exponential) curves double-exponentially over the whole time range and identified the shorter of the two time constants with τ_{gen} .

By plotting the defect generation rates $R_{gen} \propto N_A^\alpha$ on a double logarithmic scale versus the doping concentration N_A of the samples, the exponent α for the doping dependence of R_{gen} results from a linear fit to the data. In order to estimate the influence of the fitting model on the exponent α , we fitted the R_{gen} vs. N_A data for all three injection levels and both fitting models of $1/\tau_d - 1/\tau(t)$. The results are displayed in Table 5.2. Furthermore, we combined both fitting models by determining R_{gen} for each $1/\tau_d - 1/\tau(t)$ curve from the better of the two fits. The results are labeled as “combined” fit in Table 5.2. Finally, we averaged the R_{gen} values obtained for the three different Δn values for each sample and each fitting model. The three resulting averaged $R_{gen}(N_A)$ data sets are plotted in Fig. 5.16. As can be seen from Fig. 5.16, the slopes of all three curves are very similar leading to exponents α all close to 2. From the data based on the “combined” exponential $1/\tau_d - 1/\tau(t)$ fit, the doping dependence of the defect generation rate is determined to be given by $\alpha = 2.00 \pm 0.02$. This result contradicts the REDR theory, at least in the simple version discussed here, which predicts a linear doping dependence of R_{gen} .

Table 5.2. Influence of the model used to fit the $1/\tau_d - 1/\tau(t)$ curves on the doping dependence of R_{gen} .

Exponent α $R_{gen} \propto (N_A)^\alpha$	$1/\tau_d - 1/\tau$ fit mono-exponential	$1/\tau_d - 1/\tau$ fit double-exponential	$1/\tau_d - 1/\tau$ fit combined
$1 \times 10^{14} \text{ cm}^{-3}$	2.03 ± 0.14	2.02 ± 0.20	1.99 ± 0.12
$3 \times 10^{14} \text{ cm}^{-3}$	1.95 ± 0.07	1.94 ± 0.11	1.99 ± 0.09
$1 \times 10^{15} \text{ cm}^{-3}$	1.79 ± 0.04	1.93 ± 0.12	2.02 ± 0.09
Δn average	1.92 ± 0.12	1.97 ± 0.05	2.00 ± 0.02

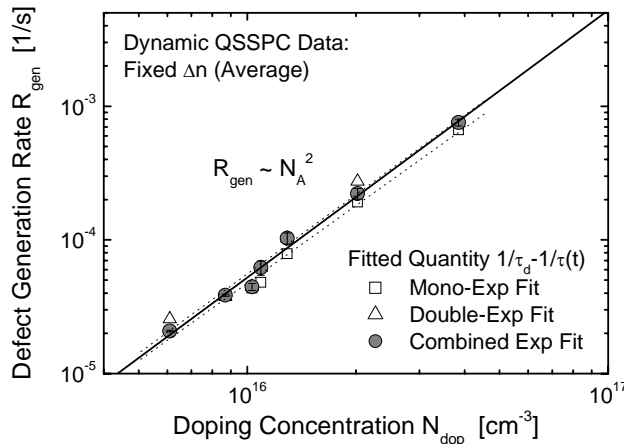


Fig. 5.16. Defect generation rates R_{gen} for different boron-doped Cz-Si materials determined from the fits to the $1/\tau_d - 1/\tau(t)$ curves measured at fixed injection level using QSSPC. The quadratic dependence contradicts the simple REDR theory as a model for the defect formation process.

C Impact of light intensity

As a second test for the applicability of REDR theory, we investigated the influence of light intensity on the defect generation rate. We measured the dynamic lifetime degradation on the same Cz sample three times choosing illumination intensities of 1, 10 and 100 mW/cm² for the degradation light. To estimate the difference in the defect generation rate that should be expected from REDR, the injection density $\Delta n(I_{deg})$ induced by the degradation light has to be estimated. Theoretically, $\Delta n(I_{deg})$ is given by $\Delta n(I_{deg}) = G \times \tau \propto I_{deg} \times \tau$, where G is the generation rate due to illumination and τ the effective carrier lifetime at the injection density $\Delta n(I_{deg})$. As the injection-dependent lifetime curves of Cz silicon increase with increasing Δn (in the annealed and the degraded state as shown for example in Fig. 5.3), the relative difference between the $\Delta n(I_{deg})$ values can only be equal to or higher than the relative difference of the corresponding intensities I_{deg} . From this, it can be concluded that a linear fit to the R_{gen} data plotted versus I_{deg} instead of $\Delta n(I_{deg})$ leads to an upper limit for the exponent β describing the Δn -dependence of R_{gen} .

The averaged R_{gen} values extracted by a mono- and a double-exponential fit from the three $1/\tau_d - 1/\tau(t)$ curves at fixed injection level (see Sect. 5.2.2B) are displayed in Fig. 5.17. While REDR predicts a linear Δn -dependence of R_{gen} ($\beta=1$) [see Eqs. (5.6) and (5.7)], the experimentally observed Δn -

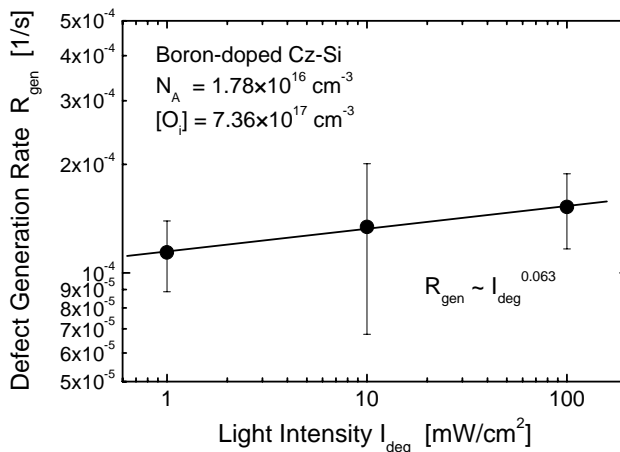


Fig. 5.17. Defect generation rate in one boron-doped Cz-Si material for different intensities of the degradation light used. The weak dependence contradicts the simple REDR theory as model for the defect formation process.

dependence of R_{gen} is much weaker, being described by an exponent $\beta < 0.063$. In contrast to the simple REDR theory, defect activation seems to occur with nearly maximum generation rate R_{gen} if the excess carrier density Δn only lies above some threshold value. From our experiments an upper limit of 10^{13} cm^{-3} was determined for this threshold carrier density. This result is in good agreement with dynamic experiments on solar cells performed by Hashigami et al. [28].

D Impact of temperature

In addition to the findings presented here, Schmidt et al. [13] found that the process of defect formation is thermally activated with a relatively low activation energy of $E_{\text{gen}} = 0.4 \text{ eV}$ which points towards a diffusion-limited defect reaction and leads to the oxygen-dimer model already mentioned in Sect. 5.3.6.

E Discussion

Although the experimental findings of the present work exclude an REDR process where the energy for defect transformation is provided by recombination via a shallow defect level, the perfectly quadratic doping dependence and vanishing injection dependence of the generation rate R_{gen} might be explained by an REDR process in which the energy for defect transformation is provided by hot carriers from Auger recombination (see Sect. 1.4.2).

Even under LLI conditions there is always a certain Auger recombination present in the sample which precisely depends on the doping and injection density as measured (see Fig. 1.13). In this case the generation rate would be expected to increase considerably above a certain threshold of the injection density, as the Auger recombination rate increases quadratically with Δn under HLI conditions. Although such an Auger-induced REDR process is pure hypothesis at this stage of the investigations, a recombination enhancement of the defect formation in whatever form is most likely, as additional results from dynamic experiments on the bias-induced degradation of solar cells, published in [29], definitely exclude the alternative mechanism of a charging process. However, a conclusive interpretation of all experimental observations on the kinetics of defect formation has not yet been achieved and requires further investigations.

In addition to the physical aspects of the results on defect formation, the finding that the defect generation rate R_{gen} already reaches its maximum value for illumination intensities as low as 1 mW/cm^2 is of practical importance, as it shows that the upper limit of the cell performance of Cz-Si solar cells can only be measured if the cells are kept completely in the dark after the last annealing step.

5.5 Analysis IV: electronic structure of the Cz defect

Up to now, the detection of the Cz-specific defect has not been possible by standard techniques such as deep-level transient spectroscopy (DLTS). Due to its high recombination activity, all known properties of the Cz defect have been determined by means of lifetime spectroscopy. However, despite extensive investigations, the exact electronic structure of the Cz defect in its active state, which is given by the energy level E_t , and the ratio $k := \sigma_n/\sigma_p$ of the capture cross-sections for electrons and holes, is still unknown. While injection-dependent lifetime spectroscopy (IDLS) only allowed an energy range between $E_V + 0.35\text{ eV}$ and $E_C - 0.45\text{ eV}$ to be determined for the energy level E_t [30], temperature-dependent lifetime spectroscopy (TDLS) was restricted to the determination of an upper limit of 0.41 eV for the energy depth ΔE_t from either band edge [31]. Thus, the identification of the exact electronic structure of the Cz defect in its active state is the final test for the practical use of advanced lifetime spectroscopy.

For a detailed and complete characterization of the Cz-specific defect we performed TDLS and IDLS measurements on different standard boron-doped Cz-Si samples. As for the lifetime spectroscopic investigations on the metal impurities (see Chap. 4), the TDLS measurements were performed

by means of the microwave-detected photoconductance decay technique (MW-PCD), while the IDLS measurements were accomplished by the quasi-steady-state photoconductance technique (QSSPC) [32]. In order to minimize surface recombination, the samples were coated on both sides with high-quality silicon nitride, characterized in Sect. 4.2.2D.

5.5.1 TDLS analysis

The TDLS analysis of the Cz-specific defect in its active state faces the problem that the E_t -dominated Arrhenius increase of carrier lifetime due to SRH statistics is superposed by an increase due to defect annihilation, as both effects occur in the same temperature range. Thus, a fundamental prerequisite for a direct determination of E_t by TDLS is an efficient suppression of defect annihilation.

A Optimized measurement procedure

For this, the sample is fully degraded by an illumination step of 36 h under a xenon lamp (intensity 100 mW/cm^2 , approx. AM1.5) prior to the TDLS measurement and then illuminated with a maximum degradation light of 300 mW/cm^2 between subsequent lifetime measurements during temperature ramp-up. In order to control a possible defect annihilation precisely, the sample is kept on each temperature step for 15 min while being illuminated with 300 mW/cm^2 . Lifetime measurements repeated once a minute allow the defect transformation kinetics to be observed. To guarantee low-injection conditions (LLI) of the TDLS curve, the lifetime measurements themselves are performed at the minimum bias light intensity excluding trapping effects, as discussed Sect. 4.2.5B. Up to 460 K (187°C), the lifetime series at each temperature exhibits no systematic increase, which indicates the complete suppression of defect annihilation by the applied bias light. As an overcompensation of defect annihilation fails above 475 K (202°C), the temperature ramp-up is performed as quickly as possible from 475 to 520 K, only allowing a single lifetime measurement at each temperature step. The experiment reveals a critical parameter: especially for higher temperatures the measured carrier lifetime strongly depends on the delay, of the order of a few seconds, between switching off the degradation light and the lifetime measurement under LLI conditions. To reduce this systematic error in the lifetime measurements, we averaged over the five smallest lifetimes selected from the 15 measurements taken within each 15-min series. The resulting TDLS curve, which represents the active state of the Cz-specific defect, is displayed in Fig. 5.18 (gray circles).

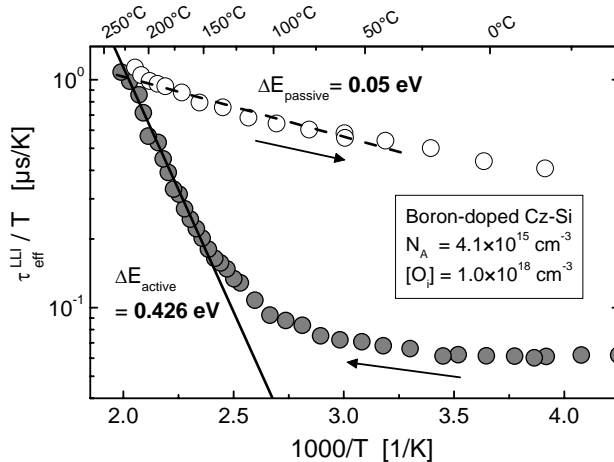


Fig. 5.18. TDLS curves measured by means of the MW-PCD method on a standard boron-doped Cz-Si sample with $N_A = 4.0 \times 10^{15} \text{ cm}^{-3}$ and $[\text{O}_i] = 1.0 \times 10^{18} \text{ cm}^{-3}$. The ramping-up TDLS curve (gray circles) reflects the active defect state, as it has been measured on the fully degraded sample, a maximum degradation light of 300 mW/cm^2 being applied in-between the lifetime measurements. The ramping-down TDLS curve (open circles) reflects the passive defect state, as it has been measured on the fully annealed sample, which has been kept in the dark in-between the lifetime measurements. A linear fit to the Arrhenius increase of the respective curves yields the energy depth of both defect states.

The observation that an overcompensation of the defect annihilation can be achieved within a broad temperature range is supported by the findings of a quantitative comparison of the kinetics of defect formation and annihilation with data published recently: as pointed out in Sect. 5.4, both processes seem to be thermally activated [13, 31]. While the defect annihilation rates $R_{ann}(T)$ were investigated from 380 to 420 K [13, 31] (see Fig. 5.13), Schmidt et al. investigated the defect generation rates $R_{gen}(T)$ from 300 to 350 K [13]. Both curves have only been determined for a $1.1 \Omega\text{cm}$ sample [13]. An extrapolation of the measured $R_{gen}(T)$ into the temperature range up to 450 K shows that $R_{gen}(T)$ exceeds $R_{ann}(T)$ up to a temperature of 425 K (152°C), which is given by the intersection point of the two curves. The higher temperature of 460 K (187°C), observed for the intersection point in this work, most likely results from the lower doping concentration of the investigated $3.5 \Omega\text{cm}$ sample.

B Hysteresis and TDLS analysis of the passive state

The effective suppression of defect annihilation by the above procedure is directly reflected in a hysteresis which is observed between TDLS curves

measured while ramping up (gray circles) and ramping down (open circles), both shown in Fig. 5.18. As the ramping-down TDLS curve has been measured on the fully annealed sample, it represents the TDLS curve related to the Cz-specific defect in its passive state (open circles). To avoid a new formation of the active defect state when ramping down, the sample was kept in the dark between the lifetime measurements, the measurement time itself being kept as short as possible. The significant gap between the ramping-up and ramping-down curves, even at temperatures around 475 K (202°C), shows that the TDLS curve measured when ramping up by the optimized procedure is dominated by the Cz-specific defect in the active state, even at such high temperatures. The fact that the carrier lifetime at room temperature is one order of magnitude higher in the ramping-down curve than for the fully degraded sample in the ramping-up curve shows that the passive defect state could be preserved when ramping down. Thus, the energy depth of the defect in the passive state can be directly determined from the linear Arrhenius increase of the ramping-down curve. A linear fit of the data (dashed line) yields an energy depth $\Delta E_{\text{passive}} = 0.05 \text{ eV}$ from either band edge. This very shallow defect level, which has been confirmed on other Cz-Si samples ($\Delta E_{\text{passive}} = 0.05\text{--}0.08 \text{ eV}$), reflects the weak recombination activity of the Cz-specific defect in the passive state.

C Advanced TDLS analysis of the active state

The advanced SRH analysis performed on the TDLS curve related to the active defect state (gray circles in Fig. 5.18) is displayed in Fig. 5.19. If just the slope of the linear Arrhenius increase is evaluated in the $\ln(\tau/T)$ plot, an energy depth $\Delta E_{\text{active}} = 0.426 \text{ eV}$ is determined, as shown by the solid line in Fig. 5.18. If the entire TDLS curve is simulated (see Fig. 5.19a), the dashed line shows that a standard SRH fit with temperature-independent capture cross-sections does not allow a correct modeling of the low-temperature part of the TDLS curve. This part of the curve is dominated by the electron capture time constant $\tau_{n0}(T) \propto 1/\sigma_n(T)$. This explains the strong dependence of the fitted defect parameters on the lower bound of the fitting region. The energy level $E_C - E_t$ ranges, e.g., from 0.40 to 0.44 eV when the lower bound is moved from 270 K (-3°C) to 310 K (37°C). Nevertheless, an adequate fit of the position and slope of the Arrhenius increase is only achieved for a defect in the band gap half close to the minority band (MinBH: upper half in *p*-type), while a reasonable simulation with a defect in the band gap half close to the majority band (MajBH: lower half in *p*-type) fails.

The observed decrease of the capture cross-section with increasing temperature follows a power law given by $\sigma(T) = \sigma_0 \times T^\alpha$ with exponent $\alpha = -2$.

Giving insight into the physical mechanism of carrier capture (for a survey see Sect. 3.5.1A), this $\sigma(T)$ -model has been found to be characteristic either of a cascade capture process [33], which is only relevant to shallow Coulomb-attractive centers, or an excitonic Auger capture process [34], which is observed for centers of arbitrary depth and charge state. Since the cascade mechanism is unlikely to be due to an energy depth of approximately 0.42 eV of the underlying Cz-specific defect, the excitonic Auger mechanism most probably is the dominant capture process, especially as it is favored by the measurement conditions used, being based on the optical injection of electron-hole pairs (see discussion in Sect. 3.5.1B). The fact that all investigated Cz-Si samples with base resistivities from 0.5 to 3.5 Ωcm showed almost the same temperature dependence in the low-temperature region, with exponents α varying from -1.5 to -2.0 , proves that the extracted $\sigma(T)$ -model represents an additional fingerprint of the Cz-specific defect in the active state, which reflects the mechanism of carrier capture.

If this $\sigma(T)$ -model with $\alpha = -2.0$ is introduced into the SRH analysis, an accurate simulation is achieved for a MinBH defect in the upper band gap half, which leads to $E_C - E_t = 0.426$ eV and $k = 15.2$ (solid line in Fig. 5.19a). As the SRH simulation for a MajBH defect with the same energy depth $E_V - E_t = 0.426$ eV completely fails for arbitrary k (dashed-dotted line in Fig. 5.19a for $k = 1$), the energy level of the Cz-specific defect in the active state can definitely be localized in the upper band gap half. Thus, the Cz-specific defect is another example of a defect which can be identified unambiguously from TDLS alone.

In order to quantify the accuracy of the determined defect parameters, two effects have to be considered: (i) the tolerance of the fitting model towards slight fluctuations of the fitting parameters and (ii) the remaining uncertainty in the slope of the Arrhenius increase, due to the superposed defect annihilation.

The investigation of the first effect is performed with maximum transparency by means of the DPSS analysis which has been introduced in Sect. 3.5.7. The defect parameter solution surface of the TDLS curve is defined by both the curves, DPSS- k and DPSS- Chi^2 , which are determined from least squares fits of the measured TDLS curve for specified but gradually varied energy levels $E_C - E_t$ of the defect center. The pair of DPSS curves displayed as dash-dotted lines in Fig. 5.19b and c is obtained when the underlying SRH modeling of the TDLS curve is performed in the T range from 230 to 520 K. If a least squares error which is increased by a factor of 2 above its optimal value of 7.1×10^{-2} is defined as “tolerable”, the following ranges of acceptable values for the defect parameters can be deduced from the DPSS diagram: $E_C - E_t = 0.39 - 0.46$ eV and $k = 6.2 - 36$.

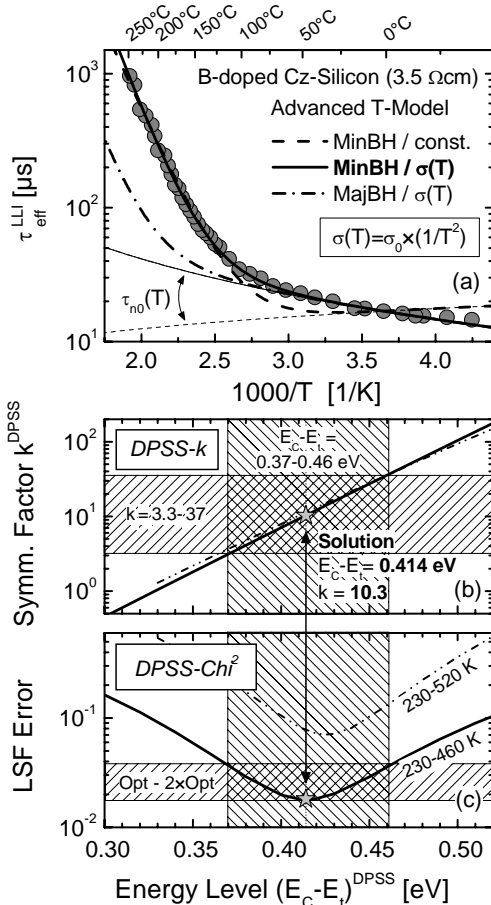


Fig. 5.19. Advanced SRH analysis of the TDLS curve from Fig. 5.18 related to the Cz-specific defect by means of the DPSS analysis introduced in Sect. 3.5.7. (a) An accurate SRH modeling of the TDLS curve (*solid line*) is only achieved for a MinBH defect in the upper band gap half and requires the insertion of a temperature-dependent capture cross-section, which is reflected in the shape of the electron capture time $\tau_{n0}(T) \propto 1/\sigma_n(T)$ (*thin dashed line* and *thin solid line*). (b,c) Two sets of DPSS curves, the underlying SRH modeling of the TDLS curve being based on two different temperature ranges. The *shaded areas* indicate the tolerance bands of the defect parameters extracted on the basis of the narrower T range.

To quantify the second effect, an additional set of DPSS curves has been determined in which the upper bound of the TDLS fit was reduced from 520 K (247°C) (dash-dotted lines in Fig. 5.19b and c) to 460 K (187°C) (solid lines in Fig. 5.19b and c). This change ensures that lifetime values are only included in the fit when they are definitely free from defect annihilation (see Sect. 5.5.1A). The best fit is achieved for a MinBH defect with slightly decreased defect parameters $E_C - E_t = 0.414$ eV and $k = 10.3$. As expected, the χ^2 curve (solid line) is shifted to lower values and becomes flatter. This is reflected in a slight broadening of the acceptable ranges for the defect parameters, $E_C - E_t = 0.37\text{--}0.46$ eV and $k = 3.3\text{--}37$. These ranges are visualized in Fig. 5.19b and c by the shaded areas.

5.5.2 IDLS analysis

Although TDLS alone already allowed a complete characterization of the Cz-specific defect in the active state, the Cz-Si sample used for the TDLS investigation in Fig. 5.19 has been subjected to an IDLS experiment to cross-check the obtained results. Figure 5.20a displays the IDLS curves measured by means of the QSSPC method after an annealing step of 25 min at 425°C in forming gas (τ_0 , open circles) and after an illumination step of 36 h under AM1.5 (intensity 100 mW/cm²) (τ_d , open triangles), respectively.

The IDLS analysis is performed on the quantity $(1/\tau_d - 1/\tau_0)^{-1}$ (closed circles). The stability of the surface recombination velocity has been controlled on an SiN-passivated high purity FZ-Si control wafer whose carrier lifetime did not notably change upon the illumination/annealing cycle. Assuming that no additional recombination centers within the Cz-Si wafer are affected by the illumination/annealing cycle, the quantity $(1/\tau_d - 1/\tau_0)^{-1}$ equals the SRH lifetime τ_{Cz} of the Cz-specific defect in the active state. Note that this evaluation scheme also eliminates the influence of all intrinsic recombination channels such as Auger and radiative recombination.

As can be seen from Fig. 5.20a, up to $\Delta n = 10^{16} \text{ cm}^{-3}$ the injection dependence of the difference curve τ_{Cz} (gray circles) can be simulated accurately with a single defect level (solid line), whereas the simulation of the complete curve requires the introduction of a second shallow defect level (dashed line). The existence of such a shallow level activated by illumination was also observed on some of the Cz samples investigated by Schmidt et al. [30]. However, as TDLS is performed under LLI conditions, only the deep center dominating the injection range up to 10^{16} cm^{-3} is relevant to the comparison of IDLS and TDLS.

Due to the strong inherent ambiguity of the SRH parameterization of a single IDLS curve, its detailed spectroscopic evaluation requires one to determine the associated defect parameter solution surface using the procedure described in Sect. 3.3.2B. The resulting DPSS- τ_{n0} and DPSS- k curves are displayed in Figs. 5.20c and d. The energy independence of the corresponding DPSS-Chi² curve, shown in Fig. 5.20b, visualizes again that the DPSS parameter triplets (E_t, k, τ_{n0}) represent equivalent solutions for the SRH parameterization of the IDLS curve. As expected for an increasing IDLS curve, the DPSS exhibits the tub-like structure with a continuous range of validity and a definition gap towards the conduction band (see Sect. 3.3.3C). The two DPSS characteristics are the energy value of the DPSS definition gap (DPSS-DG) and the plateau value of the DPSS- k curve (DPSS-PL), whose values are determined from Fig. 5.20d as $(E_C - E_t)^{\text{DPSS-DG}} = 0.29 \text{ eV}$ and $k^{\text{DPSS-PL}} = 9.5$. By definition, the DPSS-PL value represents a lower bound for the true k factor, which definitely proves a capture asymmetry for the Cz-specific

defect in the active state. However for $k \neq 1$, it has been shown in Sect. 3.3.3E that the DPSS-DG energy may be both an upper and a lower bound for the true energy depth of the underlying defect level, which makes it impossible to narrow down the possible ΔE_t values from the IDLS result alone.

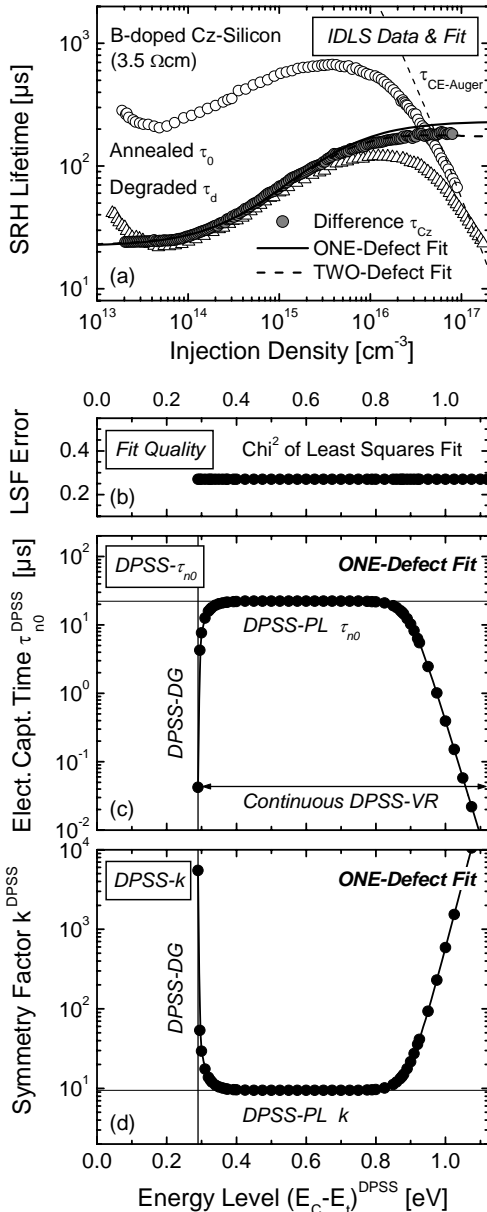


Fig. 5.20. (a) IDLS curves measured by means of the QSSPC method on the same boron-doped Cz-Si sample as investigated in Fig. 5.19 after annealing at 425°C for 25 min (τ_0 , open circles) and after degradation for 36 h under AM1.5 (intensity 100 mW/cm²) (τ_d , open triangles). The solid and dashed lines represent SRH simulations of the injection dependence of the difference curve τ_{Cz} (gray circles) assuming one and two defect levels, respectively. (b-d) Defect parameter solution surface associated with the IDLS curve τ_{Cz} . The DPSS analysis is performed on the basis of the one-defect SRH fit according to the procedure introduced in Sect. 3.3.2B.

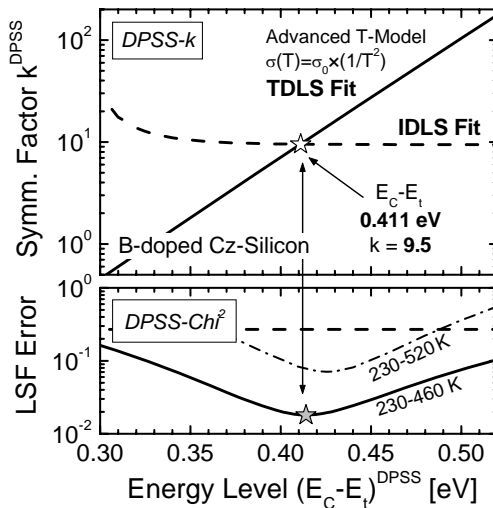


Fig. 5.21. Superposition of the DPSS diagrams associated with TDLS (solid lines) and IDLS (dashed lines) curves related to the Cz-specific defect in the active state. The original DPSS diagrams are displayed in Figs. 5.19 and 5.20, respectively. Unambiguous determination of the defect parameters of the Cz-specific defect from the intersection point of the DPSS- k curves in the MinBH (white star). The coincidence of this intersection point with the minimum of the DPSS- Chi^2 curve (gray star) manifests the accuracy of the determination. Note that a consistent determination of the Cz defect parameters is achieved by two independent LS techniques: TDLS alone and the combination of TDLS and IDLS.

5.5.3 Combined DPSS analysis of IDLS and TDLS

To verify the consistency of the spectroscopic results obtained from the IDLS and the TDLS analysis, the associated DPSS diagrams simply have to be superposed, as shown in Fig. 5.27. An accurate determination of the defect parameters of the Cz-specific defect is directly achieved from the intersection point of the DPSS- k curves (white star) associated with TDLS (solid lines) and IDLS (dashed lines). Thus, advanced lifetime spectroscopy allows for the first time the identification of the Cz-specific defect, which is localized in the upper half of the band gap at $E_c-E_t=0.411\text{ eV}$ and found to show an electron/hole capture cross-section ratio $k=9.5$.

The quality of this finding is manifested in the coincidence of the intersection point of the two DPSS- k curves with the minimum of the DPSS- Chi^2 curve obtained for the TDLS fit with reduced upper temperature limit (solid line). This demonstrates in retrospect that the defect annihilation could be absolutely suppressed at least up to 190°C . The spectroscopic results obtained from the different LS techniques are compiled in Table 5.3. The

Table 5.3. Overview of the spectroscopic results obtained for the Cz-specific defect in its active state by investigating a standard boron-doped Cz sample by means of the different LS techniques: TDLS alone (see Fig. 5.19), IDLS alone (see Fig. 5.20) and the combination of TDLS and IDLS (see Fig. 5.21). Optimum values (*bold font*) and error intervals (*standard font*) are determined from advanced DPSS analysis. The final LS result is *shaded gray*.

Technique	Boundary conditions	MinBH defect $E_C - E_t$ [eV]	k	MajBH defect $E_t - E_V$ [eV]	k
TDLS	230–520 K / $\sigma(T)$ -model	0.426 (0.39–0.46)	15.2 (6.2–36)	No solution	
TDLS	230–460 K / $\sigma(T)$ -model	0.414 (0.37–0.46)	10.3 (3.3–37)	No solution	
IDLS	One-defect fit	0.414 (E_t^{TDLS})	9.5	Arbitrary	≥ 9.3 (DPSS-PL)
IDLS & TDLS	DPSS-IP	0.411 ± 0.04	9.5	No solution	
Final result		0.411 ± 0.04	9.5	—	—

strength of the current determination is that two independent methods lead to the same result: TDLS alone and the combination of TDLS and IDLS. This demonstrates the reliability of the determined defect parameters as well as the excellent performance of both lifetime spectroscopic methods.

5.5.4 Conclusion and discussion

By applying advanced lifetime spectroscopy to standard boron-doped Cz-Si samples, the exact electronic structure of the metastable Cz defect has been decoded for the first time. The defect in its active state has been localized in the upper band gap half at $E_C - E_t = (0.41 \pm 0.04)$ eV and found to have an electron/hole capture cross-section ratio $k = \sigma_n/\sigma_p = 9.5$.

The quality and reliability of this determination manifests itself by the fact that two independent methods lead to the same result: TDLS alone and the combination of TDLS and IDLS. From the detailed SRH modeling of the entire TDLS curve, the capture cross-section has been found to be temperature-dependent with $\sigma(T) \propto T^{-2}$, which identified the excitonic Auger capture process to be the relevant physical mechanism for capture into the recombination-active defect state. For the defect in its passive state, an energy level of 0.05–0.08 eV from either band edge has been found by means of TDLS. This shallow level directly reflects the observed weak recombination activity of the defect in the passive state.

The obtained results are visualized in the band diagram shown in Fig. 5.22 in comparison with previous lifetime spectroscopic results obtained by different authors. As can be seen, the results of advanced lifetime spectroscopy are in full agreement with the upper limit for the defect energy depth

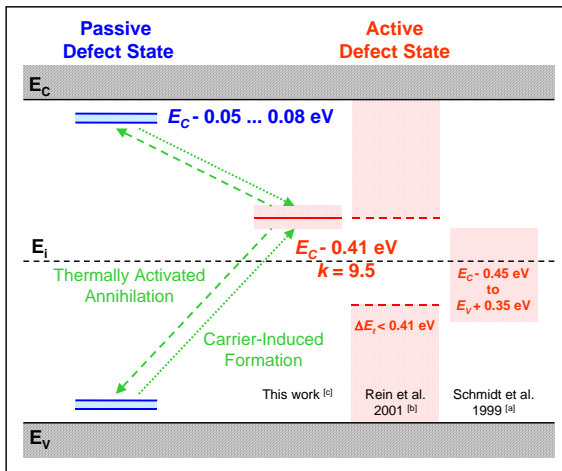


Fig. 5.22. Band diagram showing the electronic structure of the Cz-specific defect as determined in the present work. For the active state, the four bars visualize the progress made in determining the energy level. ^[a] = Ref. [30], ^[b] = Ref. [31], ^[c] = Ref. [35]. Note that all the results have been obtained by means of lifetime spectroscopy.

which Rein et al. determined from a linear TDLS analysis [31]. Nevertheless, they slightly contradict the results which Schmidt et al. obtained from the analysis of a set of IDLS curves measured on samples with different doping concentration [30]. This difference should not be over-interpreted, since the necessary simultaneous fit could not be achieved for these IDLS measurements.

The fact that the recombination-active defect center is located in the upper band gap half, explains why it could not be detected up to now by means of standard DLTS, as this technique is primarily sensitive to the lower band gap half. However, using minority-carrier injection DLTS [36], an identification seems to be possible, which at present is under research at Erlangen university [37, 38].

The unambiguous localization of the recombination-active defect state at 0.41 eV below the conduction band allows assessment of one of the models which have been proposed in the past for the metastable defect center. In a previous approach, Schmidt et al. suggested a boron-oxygen pair complex (B_iO_i) for the active defect state, which allowed both features to be explained, the quantitative correlation of the Cz defect with boron and its annealing and degradation behavior [5]. However, since the energy level associated with the boron-oxygen pair is known to lie at $E_c - E_i = 0.26 - 0.27 \text{ eV}$, as determined from DLTS measurements on electron-irradiated Cz silicon [39, 40], the present findings definitely exclude the boron-oxygen pair as a possible candidate.⁵

⁵ Even the broad energy interval Schmidt et al. had found by their lifetime spectroscopic investigations allowed this conclusion [30].

5.6 Reduction of the Cz-specific defect concentration

As lifetime degradation leads to a significant decrease of solar cell efficiency, the reduction of this effect has a high potential for the improvement of Cz-Si solar cells. From the experimental finding that there is a clear correlation of the Cz-specific defect with boron and oxygen (see Sects. 5.2 and 5.3), two different approaches for a reduction or avoidance of lifetime degradation can be derived: (1) proper material choice avoiding oxygen or boron in the starting material or (2) optimized processing using high-temperature anneals. The potential of the first approach has been shown by stable efficiencies of 22.7 % and 22.5 % achieved on oxygen-free boron-doped magnetic Cz silicon and gallium-doped Cz silicon, respectively [41]. The benefit of the second approach has been demonstrated by an investigation of the stable bulk lifetime in standard boron-doped oxygen-contaminated *p*-type Cz silicon: due to an optimized high-temperature process at 1050°C, we observed a permanent improvement in the stable bulk lifetime by a factor of 2 to 3 that was clearly reflected in a strong reduction of the metastable defect concentration [6, 12].

Starting with the main features of this high-temperature improvement, we demonstrate in Sect. 5.6.1 that an effective permanent improvement of the stable bulk lifetime is already achievable by a short oxidation process at medium temperatures. In Sect. 5.6.2 the high sensitivity of Cz silicon to the process scheme of the high-temperature oxidation will be investigated and the impact of oxygen will be shown.

5.6.1 Permanent improvement of material quality by an optimized high-temperature process

Since in normal boron-doped oxygen-contaminated Cz silicon the bulk lifetime is limited by the metastable Cz-specific defect, two quantities are suitable to investigate the improvement of the material quality due to a high-temperature process: the stable bulk lifetime τ_d after degradation (1 sun for 30 h) and the normalized defect concentration $N_t^* = 1/\tau_d - 1/\tau_0$ (see Sect. 5.2.3), where τ_0 indicates the initial bulk lifetime after an annealing step at 200°C. Most of the lifetime measurements were performed with the microwave-detected photoconductance decay method (MW-PCD), using a white bias light to control the low-injection conditions. The surfaces of all samples were passivated either by a thermal oxide or a silicon nitride, both resulting in very low surface recombination velocities. Because of the low deposition temperatures (375°C) silicon nitride was used to investigate the starting material.

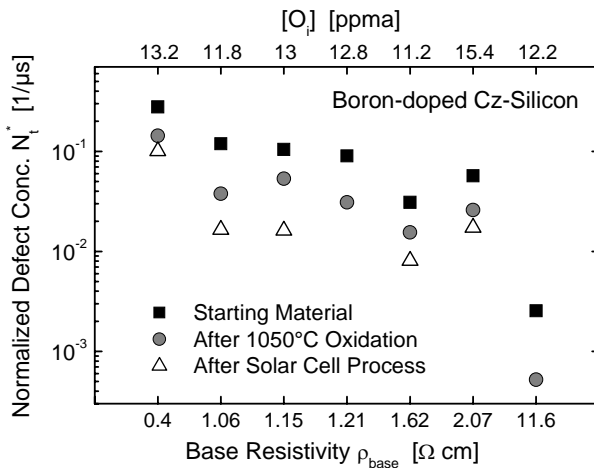


Fig. 5.23. Normalized defect concentration N_t^* for different boron-doped Cz-Si materials with similar oxygen concentrations after different process steps.

A Reduction of the defect concentration

Applying an optimized high-temperature oxidation at 1050°C , it was possible to achieve an improvement of the starting material for a broad range of different Cz silicon materials (for a detailed description of the experimental design see [6]). Figure 5.23 shows the normalized defect concentration N_t^* for different boron-doped Cz-Si materials with similar oxygen concentration. It is obvious that the normalized defect concentration is greatly reduced by the thermal oxidation and even more so by the complete RP-PERC solar cell process,⁶ including the same oxidation scheme and several additional high-temperature steps.

B Permanent improvement of the stable lifetime after degradation

This reduction of the normalized defect concentration due to a single high-temperature process or due to several subsequent ones is clearly reflected in an improvement of the stable lifetime after degradation, shown in Fig. 5.24. The average stable lifetime was increased by a factor of 2 to 3 by the high-temperature processes.

⁶ The characteristics of the RP-PERC (random pyramid passivated emitter and rear cell) are: front texturization by random pyramids, evaporated front contacts, oxide-passivated homogeneous emitter, oxide rear passivation, local ohmic aluminum point contacts and no rear diffusion. The process scheme, which includes two oxidation steps at 1050°C and one phosphorus diffusion at 820°C , is described in detail in [2].

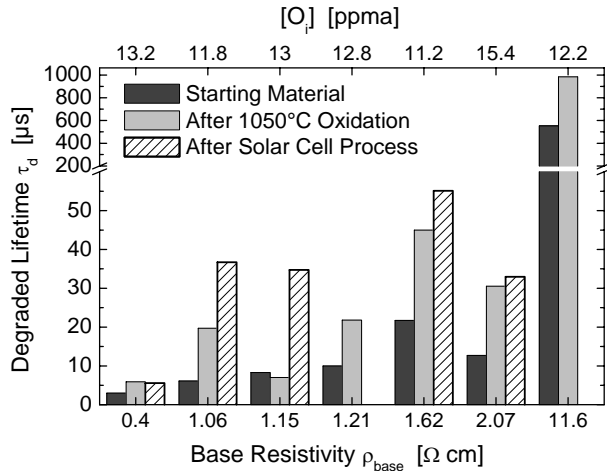


Fig. 5.24. Stable bulk lifetime (after 1 sun illumination for 48 h) measured under low-level injection for different boron-doped Cz-Si materials after different process steps.

In addition to the lifetime measurements under LLI conditions (see Figs. 5.23 and 5.24) we investigated the impact of the high-temperature process on the injection dependence of the stable lifetime after degradation. For this, two adjacent samples on the same wafer were investigated for each starting material. One of the two samples was thermally oxidized. After the removal of the thermal oxide in hydrofluoric acid, both samples were surface passivated with silicon nitride layers in order to guarantee a full comparability of the lifetime measurements in the two different process states. The injection dependence of the stable bulk lifetime⁷ with and without a high-temperature treatment is displayed in Fig. 5.25 for some of the materials of Figs. 5.23 and 5.24. It is obvious that the stable bulk lifetimes of the high-temperature-treated samples are shifted to higher values in the whole injection range and not only under low-injection conditions (see Fig. 5.24). Thus, this result proves unambiguously that a high-temperature process at 1050°C optimized for Cz silicon really leads to a reduction of the metastable defect concentration.

⁷ Using the MW-PCD with variable bias-light intensity, a bias-dependent differential effective lifetime was measured [26]. The absolute effective lifetime and the injection level were calculated with an iterative integration-routine using PC1D. From this, the injection dependent bulk lifetime was calculated using the injection-dependent S values, determined for the passivation scheme on high-lifetime FZ wafers with comparable doping concentration.

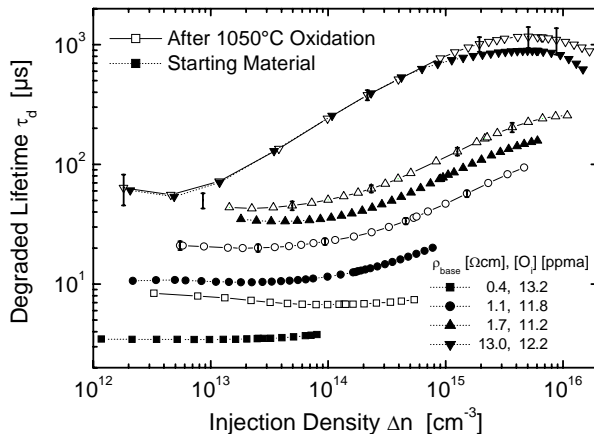


Fig. 5.25. Injection dependence of the stable bulk lifetime (after 1 sun illumination for 48 h) with (*closed symbols*) and without (*open symbols*) a high-temperature treatment for some of the materials in Figs. 5.23 and 5.24.

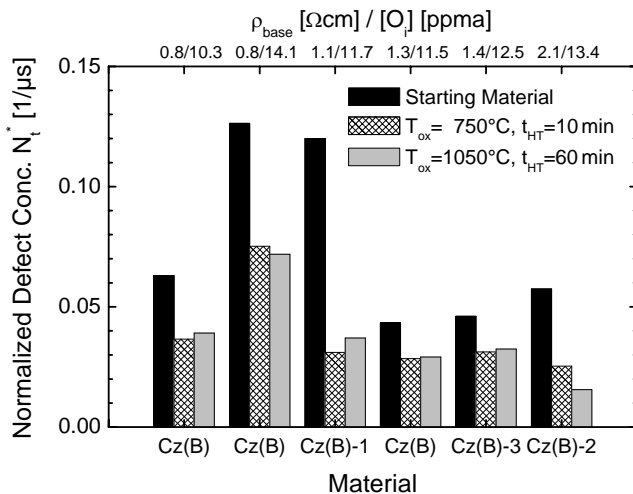


Fig. 5.26. Normalized defect concentration for different boron-doped Cz-Si materials after an optimized oxidation at 1050°C (gray) and a short oxidation at 750°C (shaded) in comparison with the defect concentration in the starting material (black).

C Short anneal at medium temperatures

In order to find processes with more relevance to industrial application, we investigated oxidation processes at medium temperatures with shorter oxidation times. We observed that an effective reduction of the defect concentration is already achievable by an oxidation at 750°C for 10 min. Figure 5.26 shows the normalized defect concentration for different boron-doped Cz silicon materials after this short oxidation at 750°C and after an optimized oxidation at 1050°C in comparison with the defect concentration in the starting material. It can be seen that both oxidation processes lead to nearly the same reduction of the defect concentration for all materials. From this it can be concluded that the 10 min oxidation at 750°C is as effective as the 60 min oxidation at 1050°C in reducing the concentration of the metastable Cz-specific defect. Thus, a permanent lifetime improvement of boron-doped Cz silicon is possible in industrial processes.

5.6.2 Impact of the process parameters

Recently, we have performed a comprehensive study of the thermal oxidation process varying ramp-up, oxidation and ramp-down parameters and studying the effect on the carrier lifetime of normal boron-doped Cz silicon [42]. Two principle effects were distinguished. If unsuitable ramping conditions were chosen, the bulk lifetime was reduced regardless of the plateau conditions. If suitable ramping conditions were chosen, a lifetime improvement as described in the previous section was observed over the whole range of oxidation parameters leading to the best results for temperatures above 1000°C.

A Ramping conditions: impact on the stable lifetime

In order to examine the sensitivity of Cz silicon to the process parameters we investigated the impact of two extreme process schemes of a 1050°C oxidation on the stable bulk lifetime: process A with unsuitable ramping conditions and process B with optimized ramping conditions. In both processes the oxidation was performed at 1050°C for 30 min under oxygen with an addition of dichlorethylene (DCE) followed by a post-oxidation anneal at the same temperature under argon for 30 min, resulting in an oxide of a comparable passivation quality. In order to analyze the role of oxygen, materials from different growth techniques resulting in different oxygen concentrations were included in the study.

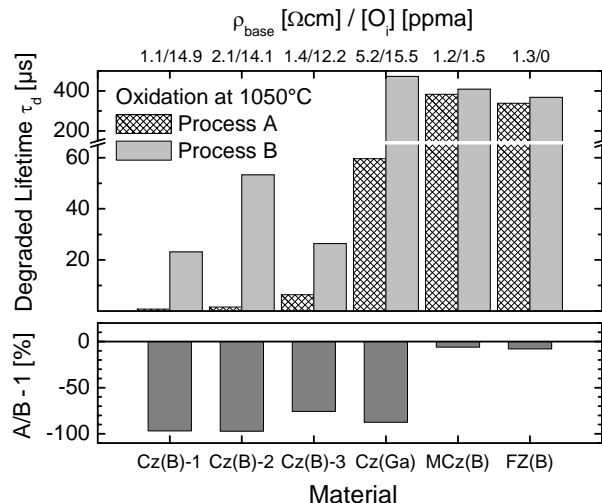


Fig. 5.27. Impact of the process scheme of a 1050°C oxidation on the stable effective lifetime (after 1 sun illumination for 48 h) for materials from different growth techniques (see bottom axis) resulting in different oxygen concentrations (see top axis). The lifetime ratio shown in the lower half can be interpreted as damage factor of the unsuitable process A (shaded) compared with the optimized process B (gray).

Figure 5.27 shows the stable effective carrier lifetimes (mean values after a 1 sun illumination for 48 h) for the different materials after the two different process schemes. The lifetime ratio displayed in the lower half of Fig. 5.27 can be interpreted as the damage factor of the unsuitable process A compared with the optimized process B. It is obvious that due to the unsuitable process A, the lifetime decreases dramatically in all oxygen-contaminated materials either boron- or gallium-doped. The lifetime reduction ranges between 75 % and 97 %, i.e., lifetime can be reduced by two orders of magnitude. In contrast, MCz silicon with a low oxygen concentration and oxygen-free FZ silicon show no sensitivity to the process scheme, as indicated by a vanishing damage factor.

In order to be able to compare the stable lifetimes after the two different oxidation schemes with the initial lifetimes in the starting material (measured on SiN-passivated samples) bulk lifetimes were calculated from all measured effective lifetimes using the S values determined for each passivation scheme on a high-lifetime FZ reference wafer with similar doping concentration. The resulting stable bulk lifetimes are displayed in Fig. 5.28. The graph in the lower half of Fig. 5.28 shows the amount of lifetime improvement and reduction by the optimized process A and the unsuitable process B, respectively.

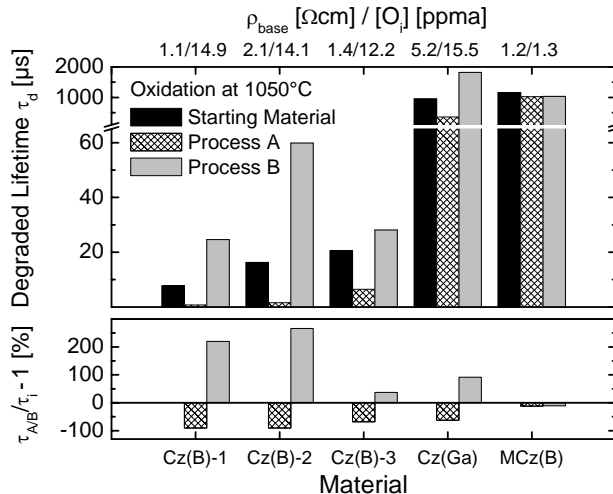


Fig. 5.28. Stable bulk lifetimes (after 1 sun illumination for 48 h) after a 1050°C oxidation with two different process schemes (see Fig. 5.27) in comparison with the stable bulk lifetime in the starting material (black) for the different materials from Fig. 5.27. The lower graph shows the amount of lifetime improvement and reduction by the non-optimized process A (shaded) and the optimized process B (gray), respectively.

The critical impact of the ramping conditions on the resulting material quality becomes obvious: while the optimized high-temperature process B leads to a strong increase in the stable lifetime on all boron-doped oxygen-contaminated Cz-Si materials, the unsuitable high-temperature process A leads to a severe reduction in the stable lifetime on all oxygen-contaminated materials, whether boron- or gallium-doped. To give an example, the optimized process B improves the stable lifetime of the boron-doped sample Cz(B)-1 by 220 % from 7.7 \(\mu\text{s}\) in the starting material to 24.6 \(\mu\text{s}\) after oxidation, while the unsuitable process A leads to a reduction of 90 % down to 0.75 \(\mu\text{s}\). In the high-purity gallium-doped sample Cz(Ga) the stable lifetime is reduced from 950 \(\mu\text{s}\) to 357 \(\mu\text{s}\) by process B, while the apparent lifetime improvement due to process A is not significant, as the uncertainty determining the bulk lifetime on a high lifetime level is large. No change in the material quality was observed for the MCz-Si sample with low oxygen concentration.

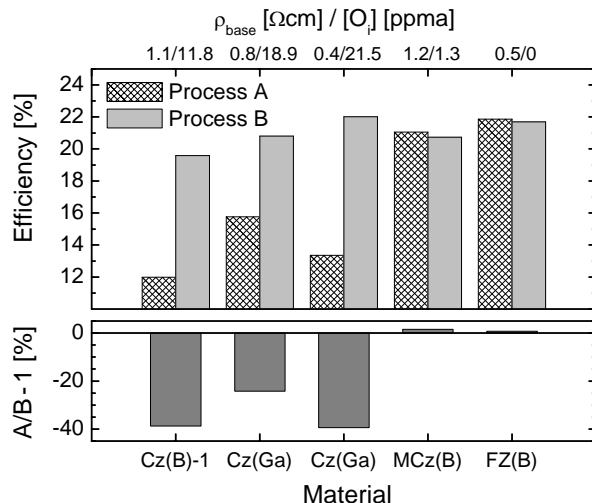


Fig. 5.29. Stable cell efficiencies (after 1 sun illumination for 48 h) achieved with the RP-PERC cell structure on some of the materials of Fig. 5.27. The process schemes of the two high-temperature oxidation steps, included in the RP-PERC process, were varied as in Figs. 5.27 and 5.28. The efficiency ratio shown in the *lower graph* can be interpreted as the damage factor of the unsuitable process A (*shaded*) compared with the optimized process B (*gray*).

B Ramping conditions: impact on solar cell performance

In order to examine the influence of these process-induced changes in the material quality on the solar cell parameters, we fabricated high-efficiency RP-PERC solar cells [2] on different low-resistivity materials,⁸ applying the two different process schemes A and B to the two high-temperature oxidation steps included in the solar cell process. The resulting stabilized cell efficiencies (mean values after 1 sun illumination for 48 h) are shown in Fig. 5.29. Analogously to Fig. 5.27 the efficiency ratio displayed in the lower half of Fig. 5.29 can be interpreted as the damage factor of the unsuitable process A relative to the optimized process B.

The fact that oxygen-free FZ silicon shows almost the same results for process A and B demonstrates that the solar cell structure itself is not changed by these process variations: for both process types the solar cell structure has the same quality and potential. Regarding MCz silicon with a very low oxygen concentration, no sensitivity to the process scheme is observed either. The situation is completely changed for the oxygen-con-

⁸ As the RP-PERC structure includes no back surface field, solar cells could only be processed on the low resistivity samples.

taminated materials [Cz(B) and Cz(Ga)]: for both dopant types, gallium and boron, the values for the optimized process B are much higher than those for the unsuitable process A. For the gallium-doped materials Cz(Ga) excellent stable efficiencies of 20.8 % and 22.0 % are achieved with process B. These values are in the same range as the values achieved with the high-quality FZ wafers. With the unsuitable process A the values are reduced to 15.8 % and 13.4 %, respectively! For the boron-doped wafer Cz(B)-1 an efficiency of 19.6 % is measured after an illumination of 48 h, using the optimized process B. With the unsuitable process A this value is reduced to 12.0 %. The strong efficiency reduction for all oxygen-contaminated materials, which results from a similar V_{OC} and J_{SC} reduction, perfectly corresponds with the findings obtained from lifetime measurements (see Figs. 5.27 and 5.28).

C Physical reason for the improvement and large reduction of the stable lifetime

In order to investigate the underlying mechanism of both the improvement and the large reduction of carrier lifetime and cell efficiency, we examined the changes in the interstitial oxygen concentration due to the two different high-temperature processes A and B. For this purpose FTIR measurements

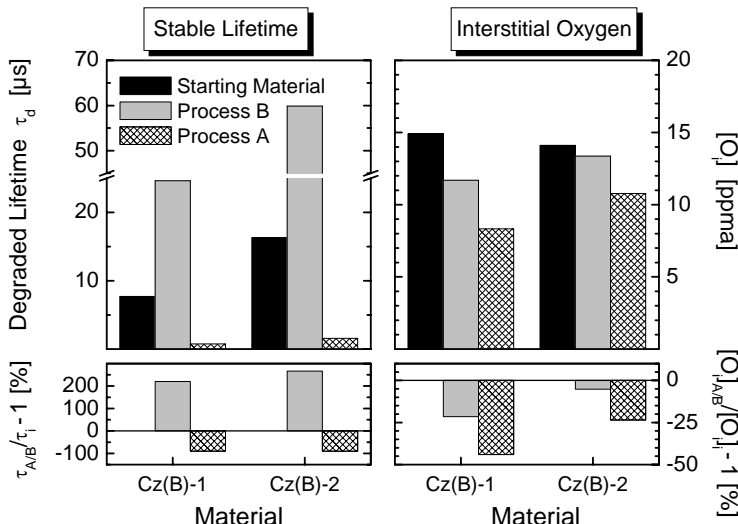


Fig. 5.30. Correlation of the process-induced lifetime changes (left) with changes of the interstitial oxygen concentration (right). The lower graphs show the changes of lifetime and interstitial oxygen concentration, respectively, in comparison with the initial value in the starting material (black).

were performed on the starting material and on the processed samples. All spectra were taken at room temperature, in a wave number range from 4000 to 400 cm^{-1} , after removing the oxide formed at the sample surfaces by a dip in an SiO etch solution. The interstitial oxygen concentration was calculated from the absorption peak at 1107 cm^{-1} .

The FTIR measurements revealed two principle effects shown in Fig. 5.30 for two boron-doped Cz-Si materials: while the strong lifetime improvement due to the optimized process B is correlated with a moderate O_i reduction, the lifetime deterioration due to the unsuitable process A is correlated with a large O_i reduction. Although the characteristic absorption bands of oxygen precipitates in the range from 1100 to 1300 cm^{-1} [43] were not observed in the FTIR spectra, the large reduction of the interstitial oxygen concentration is an indication that the unsuitable process A leads to a significant lifetime decrease due to the formation of oxygen precipitates (see discussion).

5.6.3 Discussion

The lifetime measurements and the solar cell results have clearly demonstrated that oxygen is the critical material parameter when processing solar cells on normal oxygen-contaminated Cz silicon.

The fact that the strong lifetime improvement due to an optimized high-temperature oxidation process is correlated with a moderate reduction in the interstitial oxygen concentration is in good accordance with the observation from Sect. 5.3 that the concentration of the metastable defect, limiting the lifetime in boron-doped Cz silicon, is superlinearly correlated with the oxygen concentration, the correlation exponent being determined as 1.5–1.9.

Although the characteristic absorption bands of oxygen-precipitates were not observed in the FTIR spectra of the samples treated with the unsuitable high-temperature process, the large reduction of the interstitial oxygen concentration indicates that the large lifetime decrease in these samples is caused by the formation of oxygen precipitates. This supposition is supported by the following facts: on the one hand oxygen precipitates form electrically active defect levels in the band gap [44]; on the other hand the observation of absorption bands (in room-temperature FTIR spectra) related to oxygen precipitates is only reported in the literature after typical three- or two-step annealing processes with process times which are 10 to 100 times longer than in our case [43]. Therefore we expect precipitates of small size and low concentration. Borghesi et al. reported on such oxygen micro-precipitates formed upon a short single step thermal treatment at 1100°C for only 80 min [45]. They demonstrated that a detection of such

micro-precipitates is not possible by normal FTIR measurements but only by microscopic FTIR measurements with high spatial resolution. Therefore our results can be seen as a strong indication that oxygen precipitation is the reason for the lifetime reduction observed in oxygen-contaminated Cz silicon after an unsuitable oxidation process at 1050°C.

5.6.4 Conclusion

It has been shown that a permanent improvement of the stable bulk lifetime in boron-doped Cz silicon by a factor of 2 to 3 can be achieved by an optimized high-temperature process at 1050°C. Moreover, it has been found that an effective reduction in the defect concentration is already possible by an oxidation at 750°C for 10 min.

Investigating the influence of the process parameters, it turned out that an optimization of the high-temperature process is absolutely necessary for all oxygen-contaminated materials. Otherwise lifetime and cell efficiency are severely reduced. Examining the underlying mechanism for both lifetime reduction and improvement, we were able to attribute the strong lifetime reduction due to an unsuitable high-temperature process to the formation of oxygen precipitates, as we observed a large reduction in the interstitial oxygen concentration. On the other hand it has been shown that the lifetime improvement achieved by an optimized high-temperature process is correlated with a moderate reduction in the interstitial oxygen concentration. This corresponds well with the observation that the concentration of the metastable defect depends superlinearly on the oxygen concentration.

5.7 Material quality and realistic prediction of solar cell performance

In order to investigate the material quality of Cz silicon, a comprehensive study of carrier lifetime has been performed on a set of boron- and gallium-doped Cz-Si samples with varying oxygen and doping concentration. While the investigations on the gallium-doped material are discussed in detail in [46, 47], those on the boron-doped Cz silicon are presented in the following. Based on the comprehensive lifetime study, the parameters of a widely used empirical expression which describes the bulk lifetime as a function of doping concentration are determined. On the basis of this bulk lifetime model, the cell performance which has to be expected on boron-doped Cz silicon is simulated realistically as a function of the doping concentration for a high-efficiency cell structure and for two industrial cell

structures with and without boron back surface field (BSF). For experimental verification, RP-PERC solar cells were fabricated on boron-doped Cz-Si material with different doping concentrations.

5.7.1 Carrier lifetime investigation

A Material quality in *p*-type Cz silicon

In a comprehensive study on the material quality in *p*-type Cz silicon we investigated standard boron-doped Cz-Si material from different manufacturers and a set of oxygen- or boron-free *p*-type Cz-Si materials grown by Shin-Etsu. The (low-injection) carrier lifetimes observed in the as-grown material over a broad range of different resistivities are displayed in Fig. 5.31.

For gallium-doped oxygen-contaminated Cz silicon and boron-doped oxygen-free magnetic Czochralski silicon (MCz-Si), excellent and stable lifetimes have been observed in the whole doping range. In the intermediate doping range from 10^{16} to 10^{17} cm^{-3} , both material types reach the theoretical limit determined by the Coulomb-enhanced Auger recombination [dotted line, calculated according to Eq. (1.39)], which allows cell efficiencies well above 20% for an RP-PERC cell structure. The characteristics of gallium-doped Cz silicon and the excellent cell performance are discussed in more detail in [46, 47].

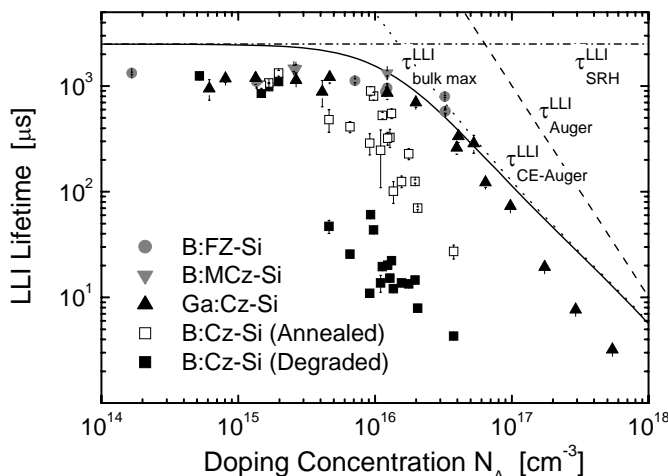


Fig. 5.31. Carrier lifetime measured under low-level injection (LLI) on gallium-doped Cz silicon and boron-doped Cz, MCz and FZ silicon as a function of base doping concentration in comparison with the theoretical limit given by Coulomb-enhanced Auger recombination (dotted line).

By contrast, the stable degraded lifetime of standard boron-doped Cz silicon is limited by Shockley-Read-Hall (SRH) recombination in the whole doping range, which is reflected in lifetime values that are two orders of magnitude lower than the lifetime values of corresponding gallium-doped Cz-Si samples (see Fig. 5.31). This significant reduction is mainly caused by the boron-related Cz-specific defect.

B Empirical bulk lifetime model for boron-doped Cz silicon

Using boron-doped Cz silicon for solar cell processing, material quality may be one of the limiting parameters of cell performance. In order to facilitate realistic cell simulations, we modeled the bulk lifetime in boron-doped Cz silicon by fitting the lifetime data with a simple empirical expression which is also used, e.g., by PC1D [48] to describe the bulk lifetime τ as a function of the doping concentration N_A :

$$\tau(N_A) = \tau_0 \quad \text{for } N_A < N_{\text{onset}}, \quad (5.9a)$$

$$\tau(N_A) = \tau_0 \times \left(\frac{N_A}{N_{\text{onset}}} \right)^\alpha \quad \text{for } N_A > N_{\text{onset}}. \quad (5.9b)$$

In the degraded state the best fit was achieved with $\tau_0 = 1047 \mu\text{s}$, $N_{\text{onset}} = 1.25 \times 10^{15} \text{ cm}^{-3}$ and $\alpha = -1.779$ (see Fig. 5.32). The scatter of the degraded

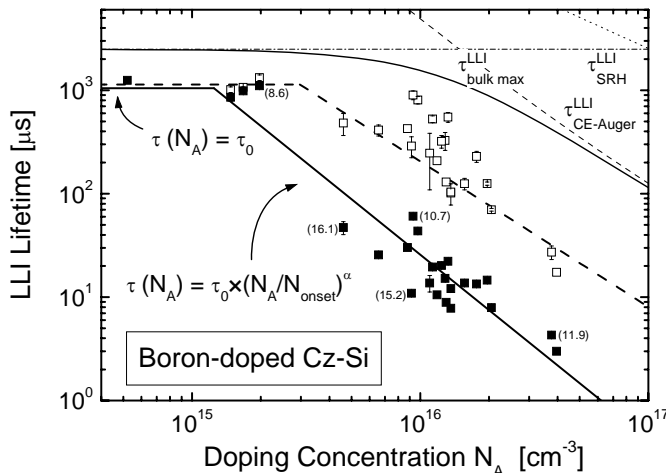


Fig. 5.32. Bulk lifetime under LLI conditions measured in standard boron-doped as-grown Cz silicon before (open symbols) and after (closed symbols) degradation and the empirical fitting curves (thick lines) adjusted to the measured doping dependence according to Eq. (5.9). The numbers in parentheses indicate the oxygen concentration (in ppma).

lifetimes can be attributed to a variation of the interstitial oxygen concentration over half an order of magnitude around an average value of 12.5 ppm (6.3×10¹⁷ cm), leading to a further variation of the defect concentration as the Cz-specific defect is also related to oxygen (see Sects. 5.2 and 5.3).

As the bulk lifetime in the annealed state is determined by residual defects, it strongly depends on the purity of the silicon used as starting material. Thus, in order not to overestimate the material quality in the annealed state, only the materials at the lower limit were included in the fit (see Fig. 5.32) leading to $\tau_0 = 1136 \mu\text{s}$, $N_{\text{onset}} = 2.97 \times 10^{15} \text{ cm}^{-3}$ and $\alpha = -1.407$ as the best parameters.

It is important to keep in mind that the bulk lifetimes in the annealed state would be the only limitation of the material quality in boron-doped Cz silicon if the injection-induced degradation could be avoided.

5.7.2 Performance of solar cells on standard boron-doped Cz silicon: specific limitations and realistic prediction

For a given solar cell structure, the empirical bulk lifetime model allows a realistic simulation of the doping dependence of the cell parameters that has to be expected on boron-doped Cz silicon. The following simulations were performed with the semiconductor device simulation software PC1D (version 5.8) [48] using for the bulk lifetime the analytical expression in Eq. (5.9) with the parameterization found in Fig. 5.32. For the three simulated cell structures, the following boundary conditions were assumed:

- cell thickness of 300 μm ,
- front surface texturization with random pyramids,
- constant contact resistances.

In cell structures without back surface field (BSF), the open-circuit voltage V_{OC} and the conversion efficiency η are overestimated for doping concentrations below 5×10¹⁵ cm⁻³, as the simplifying assumption of a constant contact resistance does not consider fill factor losses caused by an increasing series resistance at the rear contact. For the doping-induced band gap narrowing (BGN) in the *p*-base the parameterization given in [49] was used. To distinguish the parameters in the degraded and the annealed state we introduce the subscripts “d” and “0”, respectively.

A High-efficiency RP-PERC cell structure

In a first step, we simulated a high-efficiency RP-PERC (Random Pyramid Passivated Emitter and Rear Cell) cell structure [2] which is shown in Fig. 5.33. Its characteristics are a front surface texturization with random

pyramids, photolithographically-defined evaporated front contacts, an oxide-passivated homogeneous emitter, an oxide rear passivation, local ohmic aluminum point contacts at the rear side and no rear diffusion (BSF). Conversion efficiencies of 21.6 % achieved on $0.5\Omega\text{cm}$ FZ silicon [2] demonstrate the potential of both the structure and the process sequence, which are described in detail in [2]. The parameters for the analytical description of the RP-PERC cell as processed at Fraunhofer ISE, such as the doping profiles, the recombination parameters and the optical characteristics, are well known (see e.g. [50, 51]).

The simulation results obtained on the basis of the empirical bulk lifetime model are displayed in Fig. 5.34a–c (black lines). They clearly reflect the doping-dependence of bulk lifetime as will be discussed in the following. In the annealed state, the open-circuit voltage $V_{OC,0}$ increases with increasing doping concentration due to a gain in the built-in voltage (dashed line in Fig. 5.34a).⁹ In the degraded state, however, this increase is over-compensated by the larger observed lifetime decrease with increasing N_A (solid line in Fig. 5.32), which results in a lower and quasi-constant $V_{OC,d}$ level (solid line in Fig. 5.34a). While the short-circuit current J_{SC} is limited by surface recombination at the rear side for low doping concentrations, it decreases significantly towards higher doping concentrations as the ratio of diffusion length and cell thickness decreases parallel to the bulk lifetime (see Fig. 5.34b). The higher lifetime level in the annealed state is reflected in an onset of the J_{SC} decrease which is shifted to a higher doping concentration. These effects result in a broad maximum of the conversion efficiency which is shifted from $1.5 \times 10^{16} \text{ cm}^{-3}$ in the annealed state to $5 \times 10^{15} \text{ cm}^{-3}$ in the degraded state (see Fig. 5.34c).

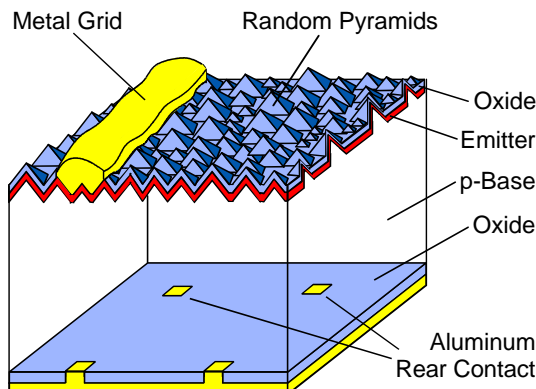


Fig. 5.33. Schematic diagram of the high-efficiency RP-PERC cell structure [2], which the experimental data and simulations in Fig. 5.34 are based on.

⁹ The somewhat abrupt transition at $N_A = 2.3 \times 10^{17} \text{ cm}^{-3}$ is due to the abrupt onset of the doping-induced band gap narrowing in the standard PC1D model [48].

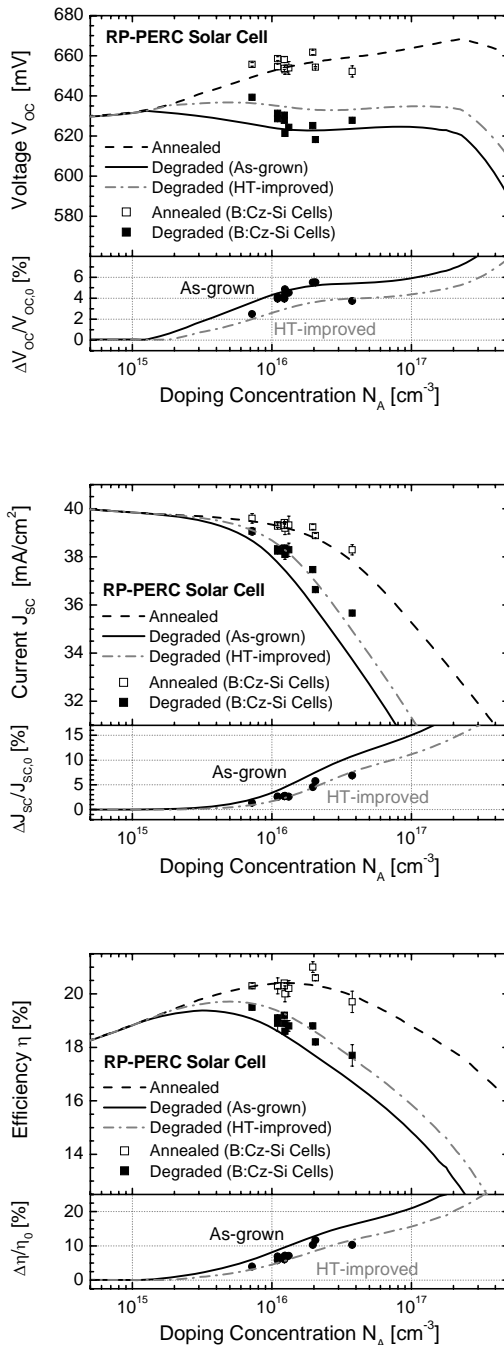


Fig. 5.34. Measured (symbols) and simulated (lines) solar cell parameters of high-efficiency RP-PERC cells, with boron-doped Cz silicon as the substrate, shown as a function of the base doping concentration: (a) open-circuit voltage; (b) short-circuit current; (c) conversion efficiency. The cells are measured before (open symbols) and after (closed symbols) degradation. The simulations are based on the empirical bulk lifetime models for the annealed and the degraded state shown in Fig. 5.32. The relative loss in cell performance due to degradation is plotted in the lower half of the graphs. In the degraded state good agreement is only achieved if the permanent lifetime improvement by a factor of two due to the optimized high-temperature steps in the PERC process is considered in the simulation (gray dash-dotted lines).

To verify the simulation results experimentally, we fabricated RP-PERC solar cells on boron-doped Cz-Si material within the doping range from 7.2×10^{15} to $3.8 \times 10^{16} \text{ cm}^{-3}$. Material with lower base doping concentration has not been included in the experiment as these cells would have suffered from the Schottky barrier which is formed at the local rear contacts without additional boron diffusion.

In the annealed state, the measured solar cell parameters correspond quite well to the calculated values. However, in the degraded state, both short-circuit current $J_{SC,d}$ and efficiency η_d are underestimated by the calculations, as shown in Fig. 5.34a–c. The likely reason for this is that the empirical fit $\tau_{d,fit}(N_A)$ used in the calculations describes the degraded lifetimes of the as-grown material. This does not take into account the permanent lifetime improvement which we observed after optimized high-temperature processes, as they are included in the RP-PERC process (see Sect. 5.6 and [6, 14]). In fact, if the empirical lifetime curve $\tau_{d,fit}(N_A)$ is shifted by a factor of two to higher values, which is realized by changing the parameters in Eq. (5.9) to $\tau_0 = 1047 \mu\text{s}$, $N_{onset} = 1.84 \times 10^{15} \text{ cm}^{-3}$ and $\alpha = -1.779$, good agreement with the measured stable cell parameters can be achieved (gray dash-dotted lines in Fig. 5.34a–c).

The relative degradation loss in cell performance displayed in the lower half of Fig. 5.34a–c increases with the doping level due to the increasing gap between the lifetime values τ_0 and τ_d in the annealed and the degraded state. While the relative loss in conversion efficiency is only 4.5 % for $N_A = 10^{16} \text{ cm}^{-3}$ (2.6 % in V_{OC} and 1.7 % in J_{SC}), it becomes higher than 10 % for $N_A > 2.7 \times 10^{16} \text{ cm}^{-3}$. This observation is also confirmed by the experimental results.

B Industrial cell structures

In a second step, we applied the analytical bulk lifetime model [see Eq. (5.9)] to simulate two industrial cell structures with and without boron back surface field (BSF), as shown in Fig. 5.35. Characteristic features are a front surface texturization with random pyramids, an oxide antireflection coating, a homogeneous highly-doped emitter, screen-printed front contacts and a full-area or mesh-structured aluminum rear contact. The industrial emitter (suitable for screen printing) was modeled by an error-function profile with a peak doping of $3 \times 10^{20} \text{ cm}^{-3}$ and a sheet resistance of $42 \Omega/\text{sq}$. Additionally, we assumed an interface surface recombination $S_{front} = 10^5 \text{ cm/s}$ and $S_{back} = 10^6 \text{ cm/s}$ for both structures. The simulated cell parameters are displayed in Fig. 5.36a–c as a function of the doping concentration. The predicted trends correspond with the trends Sterk et al. observed in 1997 on boron-doped BSF cells with different resistivities [52].

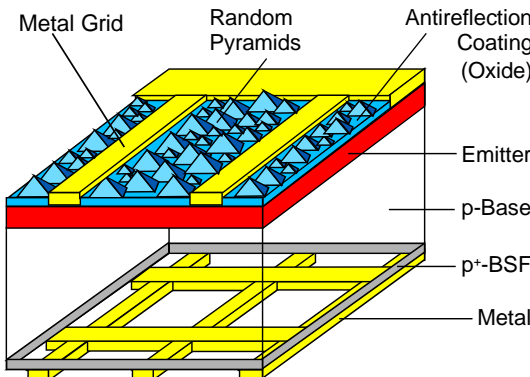


Fig. 5.35. Schematic diagram of an industrial cell structure with screen-printed contacts, as assumed in the simulations shown in Fig. 5.36.

For a cell without BSF (black lines in Fig. 5.36), the open-circuit voltage shows a broad maximum as shown in Fig. 5.36a. While the V_{OC} increase for low doping concentrations comes from an increase in the built-in voltage, the V_{OC} decrease for high doping concentrations is due to the strong decrease in the bulk lifetime. However, in the case of a cell with BSF (gray lines in Fig. 5.36), the open-circuit voltage reaches high values which are almost constant over the whole doping range as the built-in voltage no longer depends on the base resistivity but is determined by the high doping level in the BSF (see Fig. 5.36a). The interpretation of the J_{SC} curves in Fig. 5.36b is similar to the interpretation of the curves in Fig. 5.34b. The J_{SC} increase of 3 % due to the BSF observed for low doping concentrations is caused by a reduction in rear surface recombination. As this effect disappears below a certain limit for the diffusion length, the J_{SC} curves with and without BSF converge for higher doping levels. Again these effects result in a broad maximum of the conversion efficiency. While the maximum stable efficiency around 16.5 % of an industrial cell with boron BSF is predicted for an extremely low doping concentration of $1 \times 10^{15} \text{ cm}^{-3}$, the maximum of around 14.7 % for an industrial cell without BSF lies at $1 \times 10^{16} \text{ cm}^{-3}$. Regarding the relative efficiency loss due to degradation, values of 4.9 % and 1.9 % are predicted for cells with and without BSF, respectively, for $N_A = 10^{16} \text{ cm}^{-3}$ (see lower half of Fig. 5.36c).

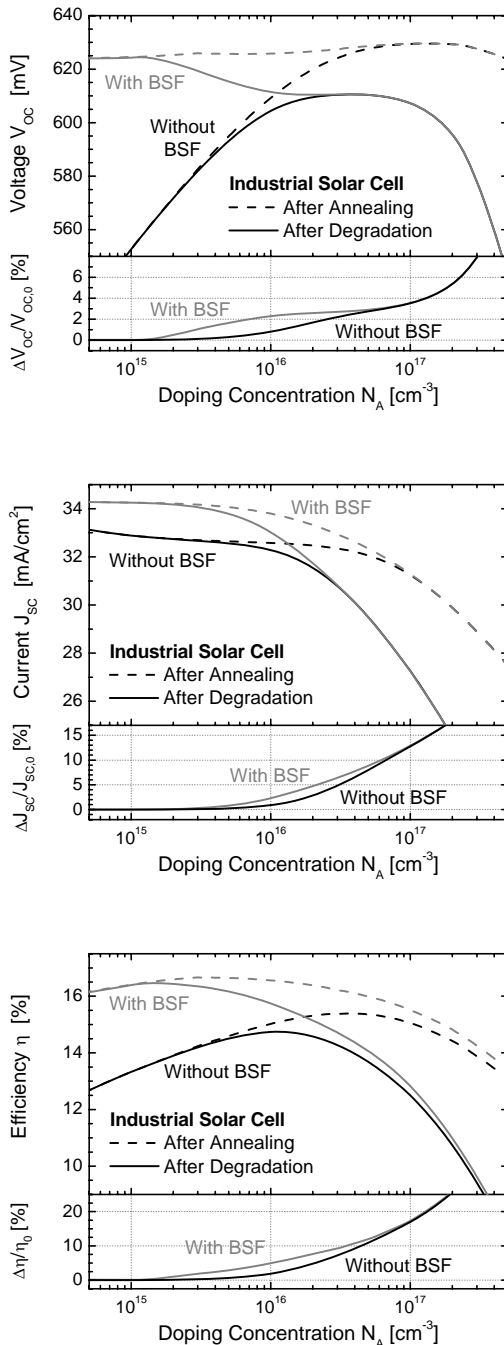


Fig. 5.36. Solar cell parameters simulated as a function of the base doping for two industrial cell structures with (gray lines) and without (black lines) boron back surface field (BSF), both with boron-doped Cz silicon as the substrate: (a) open-circuit voltage; (b) short-circuit current; (c) conversion efficiency. The simulations are performed for the stable degraded state (dashed lines) and the unstable annealed state (solid lines) on the basis of the respective empirical bulk lifetime model shown in Fig. 5.32. The expected relative loss in cell performance due to degradation is plotted in the lower half of the graphs. Note that the simulation of the cells in the degraded state does not take into account the possibility of a permanent lifetime improvement due to suitable high-temperature steps (see Sect. 5.6).

5.7.3 Conclusion

A comprehensive study on carrier lifetime in *p*-type Cz silicon revealed the excellent and stable material quality of gallium-doped Cz silicon, whereas the degraded bulk lifetime in standard boron-doped Cz silicon is greatly reduced by the Cz-specific metastable defect. In order to enable realistic predictions for cells made of boron-doped Cz silicon, the measured doping dependence of the bulk lifetime in boron-doped Cz silicon has been modeled by a simple empirical expression. It has been demonstrated that the optimal doping concentration leading to maximum efficiency shifts significantly with the solar cell structure used and the actual degradation state. While the maximum stable efficiency for a high-efficiency RP-PERC cell structure on boron-doped Cz silicon is predicted for a base doping of $5 \times 10^{15} \text{ cm}^{-3}$, the optimal value for an industrial cell varies between 10^{15} cm^{-3} for a cell with BSF and 10^{16} cm^{-3} for a cell without BSF. The theoretical predictions have been proved experimentally for RP-PERC cells. Thus, it can be concluded that cell simulations using this bulk lifetime model allow a simple, yet quite accurate, estimate of the degradation loss and of the stable performance, which have to be expected for a given cell technology if standard boron-doped Cz silicon is used as a substrate.

5.8 Chapter summary

As an example of a harmful defect center which could not be detected up to now by any of the conventional techniques, the metastable defect found in standard boron-doped Czochralski (Cz) silicon has been analyzed. The Cz-specific defect is activated under illumination or by carrier injection and deactivated by annealing at around 200°C. Its activation results in the well-known lifetime degradation by up to 90 % of its initial value. This effect is fully reversible as the initial value can be recovered by annealing.

In order to identify the major components of the Cz-specific defect, the impact of the characteristic Cz contaminants on the degradation effect has been investigated on differently doped float zone silicon wafers in the absence of other contaminants: while oxygen- and phosphorus-doped and oxygen-free boron-doped float zone silicon showed no degradation effect, boron- and oxygen-doped float zone silicon showed the same metastable defect behavior as boron-doped (oxygen-contaminated) Cz silicon, which proved a clear correlation of the Cz-specific defect with the elements boron and oxygen. This has been further confirmed by the observation that both oxygen-free, boron-doped magnetic Cz silicon (MCz) as well as oxygen-contaminated, gallium-doped *p*-type Cz silicon showed no degradation

and excellent bulk lifetimes. The quantitative correlation of the metastable defect concentration N_t^* with boron and oxygen has been examined carefully on 30 different Cz silicon materials and has been found to be linear with boron ($N_t^* \propto [B_s]^{1.1}$), almost quadratic with oxygen ($N_t^* \propto [O_i]^{1.5-1.9}$) and vanishing with carbon. The study has revealed a fundamental difference in the $[B_s]$ and $[O_i]$ correlations: while the $[B_s]$ correlation shows excellent quality which is unaffected by thermal pretreatment, the $[O_i]$ correlation shows a strong scatter with a correlation exponent that decreases slightly upon a high-temperature pretreatment. This indicates a direct involvement of substitutional boron in the defect center, while the involvement of interstitial oxygen seems to be indirect. Thus, the experiments of the present work suggest a defect complex B_sX with an unknown component X that is stimulated by oxygen. Possible candidates for X are intrinsic point defects. In a first experiment, we found that vacancies most likely have to be ruled out as the source of this unknown impurity. An alternative candidate may be the recently proposed oxygen dimer O_{i2} [13].

A quantitative analysis of the kinetics of defect formation and annihilation in Cz silicon gave insight into the physical mechanism of defect transformation. Concerning the process of defect annihilation, an isothermal annealing experiment revealed that it is thermally activated with an energy barrier $E_{ann} = (1.32 \pm 0.05)$ eV that has been determined for the first time. Concerning the process of defect formation, the findings of a quadratic doping dependence and a vanishing injection dependence for the defect generation rate R_{gen} showed that the defect formation cannot be described by the simple theory of a recombination-enhanced defect reaction (REDR), which predicts a linear R_{gen} -dependence on both quantities. However, as a simple charging model had to be excluded on the basis of additional dynamical experiments on solar cells, the results of the lifetime study point towards a more complex recombination enhancement of the defect formation than is expected from the simple REDR theory. This has to be further investigated.

The application of advanced lifetime spectroscopy allowed the exact electronic structure of the Cz-specific defect to be decoded in its active state for the first time. It has been found to be localized in the upper band gap half at $E_C - E_t = 0.41$ eV, with an electron/hole capture cross-section ratio $k = \sigma_n / \sigma_p = 9.5$. The inverse quadratic temperature dependence of the minority capture cross-section determined from the advanced TDLS analysis pointed towards the excitonic Auger capture process as the dominant capture mechanism in the recombination-active defect state. The accuracy and reliability of this determination manifested itself by the fact that two independent methods led to the same result: TDLS alone and the combination of TDLS and IDLS. In addition, a pure TDLS investigation of the annealed state revealed that the energy level of the defect in its passive state is very shallow.

As the lifetime degradation leads to a significant decrease of solar-cell efficiency by 1–2 % (absolute), the reduction or elimination of the metastable defect has a high potential for improving Cz silicon solar cells. Apart from the finding that the degradation can be completely avoided by a proper material choice, substituting or reducing one of the two major components of the metastable defect (boron or oxygen), it has been shown that even in standard boron-doped Cz silicon, the metastable defect concentration can be reduced permanently if suitable high-temperature process steps are applied. This reduction is directly reflected in an improvement of the stable bulk lifetime by a factor of 2–3 and could be attributed to a moderate reduction of the interstitial oxygen concentration. On investigating the impact of the process parameters, it turned out that an optimization of the high-temperature processes is mandatory for all oxygen-contaminated materials, including gallium-doped Cz silicon. Otherwise both bulk lifetime and cell efficiency are dramatically reduced, which could be attributed to the formation of oxygen precipitates.

In order to allow realistic predictions for cells made of boron-doped Cz silicon, the measured doping dependence of the bulk lifetime in standard boron-doped Cz silicon – obtained from a comprehensive study on more than 30 different materials – has been modeled by a simple empirical expression. It has been demonstrated that the optimal doping concentration leading to maximum solar cell efficiency shifts significantly with the solar cell structure used and the actual degradation state. While the maximum stable efficiency for a high-efficiency cell structure has been predicted for a base doping of $5 \times 10^{15} \text{ cm}^{-3}$ using boron-doped Cz silicon, the optimal value for an industrial cell structure varies between 10^{15} cm^{-3} for a cell with a back surface field and 10^{16} cm^{-3} for a cell without a back surface field. The fact that the theoretical predictions could be proved experimentally for the high-efficiency cell structure shows that cell simulations, using the bulk lifetime model determined here, allow a simple, yet quite accurate estimate of the degradation loss and the stable performance which have to be expected for a given cell technology using boron-doped Cz silicon as the substrate.

References

- [1] P.D. Maycock, PV News (2002).
- [2] J. Knobloch, S.W. Glunz, D. Biro, W. Warta, et al., *Solar cells with efficiencies above 21% processed from Czochralski-grown silicon*, Proc. 25th IEEE PVSC (Washington DC, USA, 1996), pp. 405–8.
- [3] H. Fischer and W. Pschunder, *Investigation of photon and thermal induced*

- changes in silicon solar cells*, Proc. 10th IEEE PVSC (Palo Alto, California, USA, 1973), pp. 404–11.
- [4] T. Yoshida and Y. Kitagawara, *Bulk lifetime decreasing phenomena induced by light-illumination in high-purity p-type Cz-Si crystals*, Proc. 4th International Symp. on High Purity Silicon IV (San Antonio, TX, USA, 1996), pp. 450–4.
 - [5] J. Schmidt, A.G. Aberle, and R. Hezel, *Investigation of carrier lifetime instabilities in Cz-grown silicon*, Proc. 26th IEEE PVSC (Anaheim, California, USA, 1997), pp. 13–18.
 - [6] S.W. Glunz, S. Rein, W. Warta, J. Knobloch, et al., *On the degradation of Cz-silicon solar cells*, Proc. 2nd WCPEC (Vienna, Austria, 1998), pp. 1343–6.
 - [7] V.G. Weizer, H.W. Brandhorst, J.D. Broder, R.E. Hart, et al., *Photon-degradation effects in terrestrial silicon solar cells*, J. Appl. Phys. **50** (6), 4443–9 (1979).
 - [8] J. Schmidt and R. Hezel, *Light-induced degradation in Cz silicon solar cells: Fundamental understanding and strategies for its avoidance*, Proc. 12th Workshop on crystalline silicon solar cell materials and processes (Colorado, 2002), pp. 64–71.
 - [9] M.A. Green, *Solar cells: Operating principles, technology and system applications* (UNSW, Kensington, 1986).
 - [10] T. Saitoh, X. Wang, H. Hashigami, T. Abe, et al., *Light degradation and control of low-resistivity Cz-Si solar cells – An international joint research*, Proc. 11th PVSEC (Sapporo, Japan, 1999), pp. 553–6.
 - [11] S.W. Glunz, S. Rein, W. Warta, J. Knobloch, et al., *Comparison of lifetime degradation in boron and gallium doped p-type Cz-Si*, Proc. International Workshop on light degradation of carrier lifetimes in Cz-Si solar cells (within 11th PVSEC) (Sapporo, Japan, 1999).
 - [12] S. Rein, *Untersuchung der Degradation der Ladungsträgerlebensdauer in Cz-Silizium*, Diplomarbeit, Albert-Ludwigs-Universität Freiburg (1998).
 - [13] J. Schmidt, K. Bothe, and R. Hezel, *Formation and annihilation of the metastable defect in boron-doped Czochralski silicon*, Proc. 29th IEEE PVSC (New Orleans, Louisiana, USA, 2002), pp. 178–81.
 - [14] S. Rein, J. Knobloch, and S.W. Glunz, *Analysis of the high-temperature improvement of Cz-silicon*, Proc. 16th EC PVSEC (Glasgow, UK, 2000), pp. 1201–5.
 - [15] H. Nagel, A. Merkle, A. Metz, and R. Hezel, *Permanent reduction of excess-carrier-induced recombination centers in solar-grade Cz silicon by a short yet effective anneal*, Proc. 16th EC PVSEC (Glasgow, UK, 2000), pp. 1197–200.
 - [16] R. Falster and V.V. Voronkov, *Intrinsic point defects in silicon and their control in crystal growth and wafer processing*, Proc. 11th Workshop on Crystalline Silicon Solar Cell Materials and Processes (East Park, Colorado, 2001).
 - [17] R. Falster, V.V. Voronkov, and F. Quast, *On the properties of the intrinsic point defects in silicon: A perspective from crystal growth and wafer processing*, Physica Status Solidi B **222** (1), 219–44 (2000).
 - [18] S. Inc., *STATISTICA for Windows 5.1* (Tulsa, 1998).

- [19] J. Knobloch, S.W. Glunz, V. Henninger, W. Warta, et al., *21 % efficient solar cells processed from Czochralski-grown silicon*, Proc. 13th EC PVSEC (Nice, France, 1995), pp. 9–12.
- [20] A.A. Istratov, H. Hieslmair, and E.R. Weber, *Iron and its complexes in silicon*, Appl. Phys. A **69** (1), 13–44 (1999).
- [21] L.C. Kimerling, M.T. Asom, J.L. Benton, P.J. Drevinsky, et al., *Interstitial defect reactions in silicon*, Proc. 15th International Conference on Defects in Semiconductors (Budapest, Hungary, 1988), pp. 141–50.
- [22] P.T. Landsberg, *Recombination in Semiconductors* (Cambridge University Press, 1991).
- [23] S.W. Glunz, S. Rein, and J. Knobloch, *Stable Czochralski silicon solar cells using gallium-doped base material*, Proc. 16th EC PVSEC (Glasgow, UK, 2000), pp. 1070–5.
- [24] W. Shockley and W.T.J. Read, *Statistics of the recombinations of holes and electrons*, Phys. Rev. **87** (5), 835–42 (1952).
- [25] S.W. Glunz, J. Schumacher, W. Warta, J. Knobloch, et al., *Solar cells with mesh-structured emitter*, Progr. Photovolt. **4** (6), 415–24 (1996).
- [26] R. Brendel, *Note on the interpretation of injection-level-dependent surface recombination velocities*, Appl. Phys. A **60**, 523–4 (1995).
- [27] R.A. Sinton and A. Cuevas, *Contactless determination of current-voltage characteristics and minority-carrier lifetimes in semiconductors from quasi-steady-state photoconductance data*, Appl. Phys. Lett. **69** (17), 2510–2 (1996).
- [28] H. Hashigami, Y. Itakura, A. Takaki, S. Rein, et al., *Impact of carrier injection level on light-induced degradation of Cz-Si solar cell performance*, Proc. 17th EC PVSEC (Munich, Germany, 2001), pp. 1483–6.
- [29] S.W. Glunz, E. Schäffer, S. Rein, K. Bothe, et al., *Analysis of the defect activation in Cz-Silicon by temperature-dependent bias-induced degradation of solar cells*, Proc. 3rd WCPEC (Osaka, Japan, 2003), pp. 919–22.
- [30] J. Schmidt and A. Cuevas, *Electronic properties of light-induced recombination centers in boron-doped Czochralski silicon*, J. Appl. Phys. **86** (6), 3175–80 (1999).
- [31] S. Rein, T. Rehrl, W. Warta, S.W. Glunz, et al., *Electrical and thermal properties of the metastable defect in boron-doped Czochralski silicon (Cz-Si)*, Proc. 17th EC PVSEC (Munich, Germany, 2001), pp. 1555–60.
- [32] R.A. Sinton, A. Cuevas, and M. Stuckings, *Quasi-steady-state photoconductance, a new method for solar cell material and device characterization*, Proc. 25th IEEE PVSC (Washington DC, USA, 1996), pp. 457–60.
- [33] M. Lax, *Cascade capture of electrons in solids*, Phys. Rev. **119** (5), 1502–23 (1960).
- [34] A. Hangleiter, *Nonradiative recombination via deep impurity levels in silicon: Experiment*, Phys. Rev. B **35** (17), 9149–61 (1987).
- [35] S. Rein and S.W. Glunz, *Electronic properties of the metastable defect in boron-doped Cz silicon: Unambiguous determination by advanced lifetime spectroscopy*, Appl. Phys. Lett. **82** (7), 1054–56 (2003).
- [36] D.K. Schröder, *Semiconductor Material and Device Characterization* (John

- Wiley & Sons, New York, 1990).
- [37] D. Karg, *DLTS and MCTS measurements on boron-doped Cz-Si*, private communication (2003).
 - [38] T. Frank, H. Charifi, D. Karg, G. Pensl, et al., *Recombination-active defect centers in oxygen-contaminated and boron-doped Cz-Si*, Proc. 19th EC PVSEC (Paris, France, 2004), pp. 919–22.
 - [39] I. Weinberg, S. Mehta, and C.K. Swartz, *Increased radiation resistance in lithium-counterdoped silicon solar cells*, Appl. Phys. Lett. **44** (11), 1071–3 (1984).
 - [40] P.J. Drevinsky and H.M. DeAngelis, *Interactions of interstitial silicon with B_s and O_i in electron-irradiated silicon*, Proc. 13th International Conf. on Defects in Semiconductors (Coronado, CA, USA, 1985), pp. 807–13.
 - [41] S.W. Glunz, S. Rein, J. Knobloch, W. Wetling, et al., *Comparison of boron and gallium doped p-type Czochralski silicon for photovoltaic application*, Progr. Photovolt. **7** (6), 463–9 (1999).
 - [42] S.W. Glunz, S. Rein, W. Warta, J. Knobloch, et al., *Degradation of carrier lifetime in Cz-Si solar cells*, Proc. 11th PVSEC (Sapporo, Japan, 1999), pp. 549–52.
 - [43] A. Borghesi, B. Pivac, A. Sassella, and A. Stella, *Oxygen precipitation in silicon*, J. Appl. Phys. **77** (9), 4169–244 (1995).
 - [44] G. Obermeier, J. Hage, and D. Huber, *Oxygen precipitation and denuded zone characterization with the electrolytical metal tracer technique*, J. Appl. Phys. **82** (2), 595–600 (1997).
 - [45] A. Borghesi, M. Geddo, B. Pivac, A. Sassella, et al., *Quantitative determination of high-temperature oxygen microprecipitates in Czochralski silicon by micro-Fourier transform infrared spectroscopy*, Appl. Phys. Lett. **58** (19), 2099–2101 (1991).
 - [46] S.W. Glunz, J.Y. Lee, and S. Rein, *Strategies for improving the efficiency of Cz-silicon solar cells*, Proc. 28th IEEE PVSC (Anchorage, Alaska, USA, 2000), pp. 201–4.
 - [47] S.W. Glunz, S. Rein, J.Y. Lee, and W. Warta, *Minority carrier lifetime degradation in boron-doped Cz-silicon*, J. Appl. Phys. **90** (5), 2397–404 (2001).
 - [48] D.A. Clugston and P.A. Basore, *PCID version 5: 32-bit solar cell modeling on personal computers*, Proc. 26th IEEE PVSC (Anaheim, California, USA, 1997), pp. 207–10.
 - [49] A. Cuevas, M. Stuckings, J. Lau, and M. Petracic, *The recombination velocity of boron diffused silicon surfaces*, Proc. 14th EC PVSEC (Barcelona, Spain, 1997), pp. 2416–9.
 - [50] S.W. Glunz, J. Knobloch, C. Hebling, and W. Wetling, *The range of high-efficiency silicon solar cells fabricated at Fraunhofer ISE*, Proc. 26th IEEE PVSC (Anaheim, California, USA, 1997), pp. 231–4.
 - [51] J. Dicker, *Analyse und Simulation von hocheffizienten Silizium Solarzellstrukturen für industrielle Fertigungstechniken*, Doktorarbeit, Universität Konstanz (2003).
 - [52] S. Sterk, K.A. Münzer, and S.W. Glunz, *Investigation of the degradation of crystalline silicon solar cells*, Proc. 14th EC PVSEC (Barcelona, Spain, 1997), pp. 85–7.

Summary and further work

The potential of lifetime spectroscopy (LS) as a method of defect characterization in silicon has been examined theoretically and experimentally in this monograph. The performance of many semiconductor devices, for example the energy conversion efficiency of solar cells, is directly related to the electronic material quality of the silicon used, which is generally limited by electrically active defects. Such defects may arise from impurities or crystal defects. A decisive approach to improve device performance involves the development of strategies to reduce or avoid such harmful defects, which requires their identification as a starting point.

Although deep-level transient spectroscopy (DLTS) is accepted to be one of the most sensitive techniques to detect and analyze small concentrations of electrically active defects, defect concentrations below the detection limit of DLTS can still significantly affect carrier recombination lifetime, as this quantity scales with the product of the defect concentration and the minority capture cross-section $N_i \times \sigma_n$, and not only with N_i . Due to this high sensitivity of carrier lifetime to all electrically active defects, lifetime measurements are ideally suited to characterize material quality. Apart from detecting the presence of recombination-active defects, lifetime measurements allow direct identification of impurities if the injection and temperature dependence of carrier lifetime is analyzed. The different approaches, which all rely on standard Shockley-Read-Hall theory (SRH theory), include the basic techniques of *temperature-dependent* and *injection-dependent lifetime spectroscopy* (TDLS and IDLS) as well as several related LS techniques. Their spectroscopic potential has been investigated in depth.

Apart from their high sensitivity, the principal advantage of all LS techniques over traditional defect characterization techniques is that they use the recombination process to analyze defect centers and thus provide insight precisely into those defects which are actually relevant to semiconductor devices such as solar cells and random-access memories. Moreover, lifetime spectroscopy turned out to be selective to the defect level with the highest recombination activity, involving the practical advantage that the identified impurity is definitely the one which limits material quality. The detailed analysis of SRH theory presented in this monograph identified the

energy level E_t and the capture symmetry factor $k := \sigma_n/\sigma_p$ as the two defect parameters that influence the characteristic shape of the lifetime curves and are thus accessible by means of lifetime spectroscopy. An important point is that E_t and k provide a full picture of how an impurity affects device performance and thus represent the set of defect parameters which is relevant for device simulations. The spectroscopic potential of the different LS techniques with respect to such a complete defect characterization has been investigated in depth in a detailed theoretical evaluation and demonstrated in a comprehensive experimental LS study on different metal impurities. Moreover, lifetime spectroscopy has been applied to decode the electronic structure of the metastable defect in Czochralski silicon, which has not been possible up to now by any conventional technique.

Theory of lifetime spectroscopy: physical understanding and implementation

To allow a transparent and comprehensive SRH simulation of TDLS and IDLS curves, a new modeling procedure based on the determination of the *defect parameter solution surface* (DPSS) has been introduced in the work presented here. The practical importance of the newly developed DPSS diagram is diverse. Extracted simply and directly from the original LS curves, it visualizes the strong inherent ambiguity of the SRH parameterization (E_t , k , τ_{n0}) of a single IDLS curve. Moreover, the consistency of the spectroscopic results obtained from different LS curves, which are dominated by the same defect center, can be evaluated by simple superposition of the associated DPSS diagrams. As the various DPSS diagrams also allow a direct quantitative estimate of the precision of the defect parameters obtained, the proposed DPSS analysis is a versatile tool for data evaluation in lifetime spectroscopy. Theoretical analysis of the DPSS curves gave deeper insight into the possibilities and restrictions of the different LS techniques and led to several important findings.

The spectroscopic results extracted from single IDLS curves have been found to be highly ambiguous, which proved to be unavoidable – even if the information contained in two newly found DPSS characteristics is exploited. The achievable confinement of the defect parameters turned out to depend significantly on the qualitative structure of the IDLS curve. While the continuous DPSS, associated with increasing IDLS curves, provides a lower bound for the k factor but no confinement of the defect energy depth, the split DPSS, associated with decreasing IDLS curves, provides an upper bound for the defect energy depth but no confinement of the k factor.

Contrary to the prevalent opinion in the literature, it has been shown that this ambiguity problem cannot be completely avoided if a set of IDLS curves subject to a doping variation is analyzed simultaneously. For the expanded N_{dop} -IDLS technique, the superposition of the associated DPSS curves revealed the existence of two equivalent solutions. As these solutions were found to coincide only in the k factor, this means that only the k factor but neither the band gap half nor the energy depth of the defect level can be determined unambiguously, which represents a general drawback of this technique. The ambiguity of the energy solution has been found to increase for deep levels around mid-gap.

An important finding was that the defect parameters can be identified unambiguously if the simultaneous SRH simulation is performed on a set of IDLS curves determined at different temperatures. The reason is that the superposed DPSS analysis identifies one sharp and one diffuse DPSS solution for the expanded T -IDLS technique. As the solutions have thus been found to be no longer equivalent in the case of temperature variation, T -IDLS allows unambiguous defect characterization. However, the unambiguity of the T -IDLS result has been proved to depend heavily on the investigated temperature range, as both the existence of two discrete DPSS-IPs and the identifiability of the diffuse DPSS-IP can only be ensured if the transition of the IDLS curves from an increasing to a decreasing shape is observed in the accessible temperature range. Otherwise, the ambiguity of the T -IDLS result has been found to be comparable or even higher than that of the N_{dop} -IDLS result.

The defect energy depth ΔE_t can always be determined accurately from TDLS. Although ΔE_t can be extracted from a simple linear fit of the Arrhenius increase, newly developed techniques of data linearization turned out to be necessary to achieve correct results. An important discovery was that even a complete defect characterization may be achieved from TDLS alone if the entire TDLS curve is subjected to SRH modeling. This is possible for defects located in the band gap half close to the minority band (MinBH), while for defects located in the band gap half close to the majority band (MajBH), two equivalent TDLS solutions are expected, which impedes an unambiguous identification of the k factor and the band gap half. While the k factor of the MajBH solution has been found to be completely undetermined if the TDLS curve covers a normal T range, the study revealed for the first time that consideration of the TDLS bend due to intrinsic conduction, which is generally observed above 500 K, allows at least the determination of an upper bound for k and sometimes even more. However, for an accurate modeling of the TDLS bend (high-temperature part), it turned out to be essential to base the SRH model on the advanced T -model proposed here, which takes into account not only the temperature

dependence of the equilibrium carrier concentrations but also the temperature-induced band gap narrowing. Finally, as the accurate modeling of the low-temperature part of the TDLS curve directly yields the $\sigma(T)$ -model of the defect center, TDLS provides an additional fingerprint which gives insight into the relevant capture mechanism.

To avoid the remaining ambiguity of the above LS techniques, we introduced a new LS technique, which combines TDLS and IDLS. In fact, it was demonstrated that the combined TDLS & IDLS technique always allows an unambiguous and complete defect characterization on a single sample in the whole range of defect parameters. This important discovery guarantees the general applicability of lifetime spectroscopy as a diagnostic tool. As the combined analysis may be carried out with maximum transparency by simple superposition of the associated DPSS diagrams, the combined TDLS & IDLS technique sets a new standard for advanced lifetime spectroscopy.

The comparison of the different LS techniques in terms of their spectroscopic potential reveals that a temperature variation is mandatory to achieve an unambiguous spectroscopic result. While the combined TDLS & IDLS technique and the T -IDLS technique always allow unambiguous defect characterization, the TDLS technique does so in half of the defect parameter range (MinBH defects) and provides at least the defect energy depth ΔE_t in the other half (MajBH defects). As the energy level is the only defect fingerprint tabulated up to now, knowledge of ΔE_t may in many cases suffice to identify an unknown defect center. Although it delivers two equivalent solutions, the N_{dop} -IDLS technique is interesting for industrial application as it operates at room temperature. The complete picture of the spectroscopic potential of the different LS techniques that was achieved in the presented work was obtained primarily by the use of the proposed DPSS analysis. Thus, this new evaluation technique is likely to constitute the basis for further developments in the field of lifetime spectroscopy.

Experiment: lifetime spectroscopic study of intentionally metal-contaminated samples

To confirm the theoretical predictions concerning the spectroscopic potential of the different LS techniques, LS investigations have been performed on intentionally metal-contaminated samples. For the lifetime measurements, two contactless measurement techniques have been used, which are both well-established. While the IDLS measurements have been made with the quasi-steady-state photoconductance technique (QSSPC) using com-

mercially available equipment, the TDLS measurements have been made by applying the microwave-detected photoconductance decay technique (MW-PCD). To allow temperature-dependent lifetime measurements, a liquid-nitrogen-cooled cryostat has been designed and integrated into an existing MW-PCD instrument, which made lifetime measurements in a temperature range from 100 to 600 K possible. To our knowledge, this is the broadest temperature range over which carrier lifetime has been investigated to date. For the spectroscopic analysis of the TDLS and IDLS data modular simulation software was developed using Visual Basic.

From a methodological point of view, the experimental LS results were in full agreement with the theoretical predictions. The investigation confirmed that lifetime spectroscopy always allows complete defect characterization on a single sample if TDLS and IDLS are combined. As predicted, TDLS alone proved to yield an unambiguous spectroscopic result for MinBH defects, while two equivalent solutions were obtained for most MajBH defects. Moreover, it has been demonstrated consistently that, for an accurate modeling of the entire TDLS curve in the expanded temperature range from 100 to 600 K, it is essential to base the SRH model on the proposed advanced T -model and to consider the $\sigma(T)$ -model of the respective impurity. Both aspects proved to have a significant impact on the spectroscopic result and have not been considered in previous studies. Unambiguous identification failed when the N_{dop} -IDLS technique was applied, as the superposed DPSS analysis led to the predicted two solutions which allowed only the k factor to be determined. However, the superposed DPSS analysis proposed here determined these solutions with remarkable precision, even if the boundary conditions were unfavorable, a result which has not been achieved in comparable experiments previously. As the DPSS introduced in this monograph has made it possible to evaluate the accuracy and consistency of the results from different LS curves with maximum transparency, it contributes decisively to the performance of the different LS techniques and thus sets a new standard for data evaluation in advanced lifetime spectroscopy.

From an experimental point of view, always allowing an unambiguous identification of the recombination-active defect level and an accurate determination of its energy level E_i and its symmetry factor k , the LS study completed the knowledge of the defect properties of molybdenum, titanium and nickel and provided new and deeper insight into the recombination properties of the Fe_i and FeB defects. The special correlation between the Fe_i and FeB defects even made it possible to determine the magnitude of both capture cross-sections, which, in general, is not possible with lifetime spectroscopy if the defect concentration is unknown. The results on the iron-related defects are of special practical importance, as the most sensitive

Table 6.1. List of defect parameters determined by means of lifetime spectroscopy for the recombination-active levels of the metal contaminants under investigation. *Bold font* denotes the optimum values for the defect parameters. *Standard font* denotes their error intervals determined from the advanced DPSS analysis.

Impurity	Defect type	Energy [eV]	Capture cross-sections k	σ_p [cm ²]	σ_n [cm ²]	$\sigma(T)$
Ti (*)	Double donor	$E_V + \mathbf{0.289} \pm 0.005$	12 ± 1	1.9×10^{-16} [L]	$2.3 \times 10^{-15} \pm 0.2 \times 10^{-15}$	$T^{-1.6}$
Mo	Donor	$E_V + \mathbf{0.317} \pm 0.005$	13 ± 3	6.0×10^{-16} [L]	$7.8 \times 10^{-15} \pm 1.8 \times 10^{-15}$	$T^{-1.6}$
Fe	Donor	$E_V + \mathbf{0.394} \pm 0.005$	51 ± 5	7.0×10^{-17} [L]	$3.6 \times 10^{-15} \pm 0.4 \times 10^{-15}$	$E_\infty = 24\text{ meV}$
FeB (*)	Acceptor	$E_C - \mathbf{0.260} \pm 0.030$ [L]	0.45 0.01–1	5.5×10^{-15}	2.5×10^{-15}	—
Ni (*) (<i>p</i> -Si)	Acceptor	$E_C - \mathbf{0.400} \pm 0.030$	0.7 0.3–1.3	$8.0 \times 10^{-17} \pm 5.7 \times 10^{-17}$	5.6×10^{-17} [L]	$T^{-2.4}$
Ni (*) (<i>n</i> -Si)	Donor	$E_V + \mathbf{0.189} \pm 0.050$	3500 890–12900	1.1×10^{-15} [L]	$4 \times 10^{-12} \pm 10 \times 10^{-12}$	$T^{-2.5}$

[L] Values for capture cross-sections taken from the literature (*shaded gray*).

(*) Impurities which give rise to other defect levels within the band gap, which the LS study indirectly identified to be irrelevant in terms of recombination activity.

commercial technique to detect and determine an iron contamination in silicon relies heavily on knowing the parameters of both defect states. The defect parameters of the different transition metals which have been determined in the present study are compiled in the table.

The study revealed that the capture cross-sections of most defects are temperature-dependent and identified the excitonic Auger capture process as the dominant capture mechanism under minority carrier injection, which represents the operating condition of solar cells. A comparison of the investigated impurities with respect to their recombination activity identified molybdenum as the worst and nickel as the least harmful impurity.

The excellent consistency of the spectroscopic results obtained from the different LS techniques and their good agreement with DLTS-based E_i results from the literature conclusively demonstrated the excellent performance of lifetime spectroscopy and the high reliability of the defect parameters determined. In conclusion, the experimental results of the present work demonstrate impressively that, in terms of both physical understanding and technical implementation, lifetime spectroscopy is ready to be applied as a highly sensitive diagnostic tool in the semiconductor industry.

Experiment: study of the metastable defect in Czochralski silicon

As an example of a harmful defect center which could not be detected up to now by any of the conventional techniques, the metastable defect found in standard boron-doped Czochralski (Cz) silicon has been analyzed. The Cz-specific defect is activated under illumination or by carrier injection and deactivated by annealing at around 200°C. Its activation results in the well-known lifetime degradation by up to 90 % of its initial value. This effect is fully reversible as the initial value can be recovered by annealing.

In order to identify the major components of the Cz-specific defect, the impact of the characteristic Cz contaminants on the degradation effect has been investigated on differently doped float zone silicon wafers in the absence of other contaminants: while oxygen- and phosphorus-doped and oxygen-free boron-doped float zone silicon showed no degradation effect, boron- and oxygen-doped float zone silicon showed the same metastable defect behavior as boron-doped (oxygen-contaminated) Cz silicon, which proved a clear correlation of the Cz-specific defect with the elements boron and oxygen. This has been further confirmed by the observation that both oxygen-free, boron-doped magnetic Cz silicon (MCz) as well as oxygen-contaminated, gallium-doped *p*-type Cz silicon showed no degradation and excellent bulk lifetimes. The quantitative correlation of the metastable defect concentration N_t^* with boron and oxygen has been examined carefully on 30 different Cz silicon materials and has been found to be linear with boron ($N_t^* \propto [B_s]^{1.1}$), almost quadratic with oxygen ($N_t^* \propto [O_i]^{1.5-1.9}$) and vanishing with carbon. The study has revealed a fundamental difference in the $[B_s]$ and $[O_i]$ correlations: while the $[B_s]$ correlation shows excellent quality which is unaffected by thermal pretreatment, the $[O_i]$ correlation shows a strong scatter with a correlation exponent that decreases slightly upon a high-temperature pretreatment. This indicates a direct involvement of substitutional boron in the defect center, while the involvement of interstitial oxygen seems to be indirect. Thus, the experiments of the present work suggest a defect complex B_sX with an unknown component X that is stimulated by oxygen. Possible candidates for X are intrinsic point defects. In a first experiment, we found that vacancies most likely have to be ruled out as the source of this unknown impurity. An alternative candidate may be the recently proposed oxygen dimer O_{i2} [1].

A quantitative analysis of the kinetics of defect formation and annihilation in Cz silicon gave insight into the physical mechanism of defect transformation. Concerning the process of defect annihilation, an isothermal annealing experiment revealed that it is thermally activated with

an energy barrier $E_{barr} = (1.32 \pm 0.05)$ eV that has been determined for the first time. Concerning the process of defect formation, the findings of a quadratic doping dependence and a vanishing injection dependence for the defect generation rate U_{gen} showed that the defect formation cannot be described by the simple theory of a recombination-enhanced defect reaction (REDR), which predicts a linear U_{gen} -dependence on both quantities. However, as a simple charging model had to be excluded on the basis of additional dynamical experiments on solar cells, the results of the lifetime study point towards a more complex recombination enhancement of the defect formation than is expected from the simple REDR theory. This has to be further investigated.

The application of advanced lifetime spectroscopy allowed the exact electronic structure of the Cz-specific defect to be decoded in its active state for the first time. It has been found to be localized in the upper band gap half at $E_C - E_I = 0.41$ eV, with an electron/hole capture cross-section ratio $k = \sigma_n/\sigma_p = 9.5$. The inverse quadratic temperature dependence of the minority capture cross-section determined from the advanced TDLS analysis pointed towards the excitonic Auger capture process as the dominant capture mechanism in the recombination-active defect state. The accuracy and reliability of this determination manifested itself by the fact that two independent methods led to the same result: TDLS alone and the combination of TDLS and IDLS. In addition, a pure TDLS investigation of the annealed state revealed that the energy level of the defect in its passive state is very shallow.

As the lifetime degradation leads to a significant decrease of solar cell efficiency by 1–2 % (absolute), the reduction or elimination of the metastable defect has a high potential for improving Cz silicon solar cells. Apart from the finding that the degradation can be completely avoided by a proper material choice, substituting or reducing one of the two major components of the metastable defect (boron or oxygen), it has been shown that even in standard boron-doped Cz silicon, the metastable defect concentration can be reduced permanently if suitable high-temperature process steps are applied. This reduction is directly reflected in an improvement of the stable bulk lifetime by a factor of 2–3 and could be attributed to a moderate reduction of the interstitial oxygen concentration. On investigating the impact of the process parameters, it turned out that an optimization of the high-temperature processes is mandatory for all oxygen-contaminated materials, including gallium-doped Cz silicon. Otherwise both bulk lifetime and cell efficiency are dramatically reduced, which can be attributed to the formation of oxygen precipitates.

In order to allow realistic predictions for cells made of boron-doped Cz silicon, the measured doping dependence of bulk lifetime in standard boron-doped Cz silicon – obtained from a comprehensive study on more than 30 different materials – has been modeled by a simple empirical expression. It has been demonstrated that the optimal doping concentration leading to maximum solar cell efficiency shifts significantly with the solar cell structure used and the actual degradation state. While the maximum stable efficiency for a high-efficiency cell structure has been predicted for a base doping of $5 \times 10^{15} \text{ cm}^{-3}$ using boron-doped Cz silicon, the optimal value for an industrial cell structure varies between 10^{15} cm^{-3} for a cell with a back surface field and 10^{16} cm^{-3} for a cell without a back surface field. The fact that the theoretical predictions could be proved experimentally for the high-efficiency cell structure shows that cell simulations, using the bulk lifetime model determined here, allow a simple, yet quite accurate estimate of the degradation loss and the stable performance which have to be expected for a given cell technology using boron-doped Cz silicon as the substrate.

Relevance of the results and outlook

Since the increasingly stringent requirements on electronic devices create a growing demand for increasingly sensitive techniques to track ever-diminishing amounts of impurities, it appears certain that lifetime spectroscopy will become widespread, not only in photovoltaics but also in other branches of the semiconductor industry.

As advanced lifetime spectroscopy provides a complete picture of how impurities affect device performance, information which could not be gained for most impurities by conventional techniques, it opens up a broad field for a detailed characterization of defects relevant to photovoltaic applications, as demonstrated in the present work by the LS investigation of metal impurities.

From a methodological point of view, a compelling task is the technical implementation of the *T-IDLS* technique using the QSSPC technique. Due to the decisive impact of the temperature range on the ambiguity of the spectroscopic *T-IDLS* result, it will be necessary to make a broad temperature range, as used for the TDLS investigations presented here, accessible in future measurement equipment. Further methodological developments in the field of lifetime spectroscopy will most probably be based on the newly developed DPSS evaluation technique as it allows maximum transparency of the SRH modeling.

It should be emphasized that the findings on the spectroscopic potential of the different LS techniques as well as the DPSS evaluation procedure are completely independent of the technique used to measure the injection and temperature dependence of recombination lifetime. That is why the presented methodological results are expected to initiate new developments in different fields of material characterization. Only recently, a first attempt has been made to extract TDLS data from temperature-dependent quantum efficiency measurements [2]. With the current successful development of fast lifetime mapping techniques, such as the thermography-based CDI technique [3], strong research activities are presently starting at Fraunhofer ISE and other research centers to technically realize temperature-dependent lifetime mapping aiming at spatially resolved TDLS measurements to generate “ ΔE , maps” of a sample [4]. This would allow detailed spectroscopic investigation of samples with an inhomogeneous defect distribution such as multicrystalline silicon samples, and thus provide deeper insight into unknown structures. These developments show that lifetime spectroscopy is gaining importance and its application is expanding rapidly.

References

- [1] J. Schmidt, K. Bothe, and R. Hezel, *Formation and annihilation of the metastable defect in boron-doped Czochralski silicon*, Proc. 29th IEEE PVSC (New Orleans, Louisiana, USA, 2002), pp. 178–81.
- [2] T.A. Wagner and U. Rau, *Analysis of recombination centers in epitaxial silicon thin-film solar cells by temperature-dependent quantum efficiency measurements*, Appl. Phys. Lett. **82** (16), 2637–9 (2003).
- [3] J. Isenberg, S. Riepe, S.W. Glunz, and W. Warta, *Imaging method for laterally resolved measurement of minority carrier densities and lifetimes: Measurement principle and first applications*, J. Appl. Phys. **93** (7), 4268–75 (2003).
- [4] M.C. Schubert, J. Isenberg, S. Rein, and W. Warta, *Temperature-dependent carrier lifetime images*, Proc. 19th EC PVSEC (Paris, France, 2004), pp. 500–3.

Zusammenfassung und Ausblick

In der vorliegenden Arbeit wurde das Potential der Lebensdauerspektroskopie (LS) als Methode zur Defektcharakterisierung in Silizium umfassend theoretisch und experimentell untersucht. Die Leistungsfähigkeit und Güte vieler Halbleiterbauelemente, wie zum Beispiel der Wirkungsgrad von Solarzellen, hängt direkt von der elektronischen Qualität des eingesetzten Siliziums ab, die im allgemeinen durch elektrisch aktive Defekte begrenzt ist. Ursache für derartige Defekte können Verunreinigungen oder Kristalldefekte sein, die bei der Waferherstellung oder Prozessierung eingebracht bzw. erzeugt werden. Ein wichtiger Ansatzpunkt zur Verbesserung der Bauelementeigenschaften besteht deshalb in der Entwicklung von Strategien zur Reduktion oder Vermeidung solcher Defekte, was ihre vorherige Identifikation voraussetzt.

Obwohl Deep-Level Transient Spectroscopy (DLTS) allgemein als eine der empfindlichsten Methoden angesehen wird, um auch geringe Konzentrationen elektrisch aktiver Defekte nachzuweisen und zu analysieren, können auch Defektkonzentrationen unterhalb der Nachweisgrenze von DLTS die Ladungsträgerlebensdauer stark beeinflussen, da ihr Niveau nicht nur von der Defektkonzentration sondern vom Produkt aus Defektkonzentration und Einfangquerschnitt also der Rekombinationsaktivität des Defektes abhängt. Aufgrund der hohen Empfindlichkeit der Ladungsträgerlebensdauer für alle elektrisch aktiven Defekte eignen sich Lebensdauermessungen ideal zur Charakterisierung der Materialqualität. Neben der Beurteilung der Materialqualität eröffnen Lebensdauermessungen die Möglichkeit, Defekte zu identifizieren, wenn die Temperatur- und Injektionsabhängigkeit der Ladungsträgerlebensdauer analysiert wird. Die unterschiedlichen Ansätze beruhen alle auf der Shockley-Read-Hall (SRH) Theorie und umfassen neben den grundlegenden Techniken der *injektions- und temperaturabhängigen Lebensdauerspektroskopie* (IDLS und TDLS) einige erweiterte Methoden der Lebensdauerspektroskopie, deren spektroskopisches Potential eingehend untersucht wurde.

Neben ihrer hohen Empfindlichkeit besteht ein prinzipieller Vorteil der Lebensdauerspektroskopie gegenüber traditionellen Techniken der Defektcharakterisierung darin, dass sie den Rekombinationsprozess für die Analyse von Defektzentren nutzt und somit einen Einblick genau in die

Defekte verschafft, die für Halbleiterbauelemente wie Solarzellen und RAM-Speicherbausteine relevant sind. Trotz der hohen Sensitivität der Lebensdauerspektroskopie für alle rekombinationsaktiven Defekte, ist ihr Auflösungsvermögen sehr begrenzt. So erlaubt die Lebensdauerspektroskopie nur die Identifikation des rekombinationsaktivsten Defektes, während die Detektion anderer Defekte im allgemeinen nicht möglich ist. Dennoch bringt diese Selektivität den praktischen Vorteil mit sich, dass es sich bei der nachgewiesenen Verunreinigung definitiv um den Defekt handelt, der die Materialqualität begrenzt.

Die in dieser Arbeit vorgenommene detaillierte Analyse der SRH-Theorie zeigt, dass nur das Energieniveau E_t und das Verhältnis $k := \sigma_n/\sigma_p$ der Einfangquerschnitte für Elektronen und Löcher den charakteristischen Verlauf der Lebensdauerkurven beeinflussen und somit mittels Lebensdauerspektroskopie bestimmt werden können. Entscheidend ist, dass das Energieniveau E_t und der sogenannte Symmetriefaktor k vollständig beschreiben, wie eine Verunreinigung die Bauelementeigenschaften beeinflusst, und somit den Satz von Defektparametern darstellen, der für die Simulation von Bauelementen relevant ist. Das spektroskopische Potential der unterschiedlichen Methoden der Lebensdauerspektroskopie im Hinblick auf eine solchermaßen vollständige Defektcharakterisierung wurde aus theoretischer Sicht umfassend untersucht und in einer experimentellen Studie an unterschiedlichen metallischen Verunreinigungen nachgewiesen. Zudem wurde die Methode der Lebensdauerspektroskopie angewandt, um die elektronische Struktur des metastabilen Defektes in Czochralski Silizium zu entschlüsseln, was bislang mit herkömmlichen Methoden nicht erreicht werden konnte.

Theorie der Lebensdauerspektroskopie: Physikalisches Verständnis und technische Umsetzung

Um eine transparente und umfassende SRH-Simulation von TDLS- und IDLS-Kurven zu gewährleisten, wurde in der vorliegenden Arbeit ein neues Modellierungsverfahren entwickelt, das auf einer exakten Bestimmung des Lösungsraumes für die Defektparameter (*Defect Parameter Solution Surface = DPSS*) beruht. Die praktische Bedeutung der neu entwickelten DPSS-Diagramme ist vielfältig. Zum einen lassen sie sich auf einfache Weise aus den ursprünglichen Lebensdauerkurven gewinnen. Zum anderen veranschaulichen sie die starke inherente Unbestimmtheit der SRH-Parametrisierung (E_t , k , τ_{n0}) einer einzelnen IDLS-Kurve. Ferner kann die Konsistenz der spektroskopischen Ergebnisse verschiedener LS-

Kurven, denen der gleiche Defekt zugrunde liegt, durch einfache Überlagerung der zugehörigen DPSS-Diagramme untersucht werden. Da die unterschiedlichen DPSS-Diagramme darüber hinaus eine quantitative Abschätzung der Genauigkeit der spektroskopischen Ergebnisse ermöglichen, stellt die hier vorgeschlagene DPSS-Analyse ein sehr vielseitiges Hilfsmittel für die Datenanalyse in der Lebensdauerspektroskopie dar. Die theoretische Untersuchung der DPSS-Kurven eröffnete einen tieferen Einblick in die Möglichkeiten und Grenzen der unterschiedlichen Techniken der Lebensdauerspektroskopie und führte zu einer Reihe von wichtigen Erkenntnissen.

In Bezug auf einzelne IDLS-Kurven konnte gezeigt werden, dass die erzielbaren spektroskopischen Ergebnisse in hohem Maße mehrdeutig sind. Es stellte sich heraus, dass dieses Problem unvermeidbar ist und selbst unter Hinzunahme zweier neu gefundener Charakteristika der DPSS-Kurven nicht gelöst werden kann. Es erwies sich, dass die erreichbare Einschränkung der Defektparameter entscheidend von der qualitativen Struktur der IDLS-Kurve abhängt. Während die zu ansteigenden IDLS-Kurven gehörende kontinuierliche DPSS eine Untergrenze für den k -Faktor, aber keine Einschränkung der Energietiefe des Defektes liefert, ergibt die zu abfallenden IDLS-Kurven gehörende geteilte DPSS eine Obergrenze für die Energietiefe des Defektes, aber keine Einschränkung des k -Faktors.

Im Gegensatz zur vorherrschenden Meinung in der Literatur zeigte sich, dass dieses Mehrdeutigkeitsproblem nicht vollständig gelöst werden kann, wenn ein Satz von IDLS-Kurven zu unterschiedlichen Dotierkonzentrationen einer simultanen SRH-Analyse unterzogen wird. Für diese erweiterte N_{dop} -IDLS-Methode ergab die Überlagerung der zugehörigen DPSS-Kurven die Existenz zweier gleichwertiger Lösungen. Da diese Lösungen nur im k -Faktor zusammenfallen, kann nur der k -Faktor, nicht aber die Bandhälfte und das Energieniveau des Defektes eindeutig bestimmt werden, was einen allgemeinen Nachteil dieser Methode darstellt. Es konnte nachgewiesen werden, dass die Mehrdeutigkeit der Energielösung für Energieniveaus nahe der Bandmitte weiter zunimmt.

Eine wichtige Erkenntnis war, dass ein eindeutiges spektroskopisches Ergebnis erreicht werden kann, wenn die simultane SRH-Simulation an einem Satz von IDLS-Kurven zu unterschiedlichen Temperaturen durchgeführt wird. Der Grund hierfür ist, dass die überlagerte DPSS-Analyse für die erweiterte T -IDLS-Methode einen scharfen und einen unscharfen DPSS-Schnittpunkt liefert. Da die Lösungen im Falle einer Temperaturvariation somit nicht länger gleichwertig sind, erlaubt die T -IDLS eine eindeutige Defektcharakterisierung. Allerdings stellte sich heraus, dass die Eindeutigkeit des T -IDLS-Ergebnisses stark vom untersuchten Tempera-

turbereich abhängt, da sowohl die Existenz zweier diskreter DPSS-Schnittpunkte als auch die Identifizierbarkeit des unscharfen DPSS-Schnittpunktes nur garantiert werden können, wenn der Umschlagpunkt der IDLS-Kurven von einem ansteigenden zu einem abfallenden Verlauf im zugänglichen Temperaturbereich beobachtet wird. Andernfalls ist die Mehrdeutigkeit des T -IDLS-Ergebnisses vergleichbar oder sogar höher als die des N_{dop} -IDLS-Ergebnisses.

Eine exakte Bestimmung der Energietiefe ΔE_t kann immer mit der TDLS-Methode erreicht werden. Obwohl ΔE_t aus einem einfachen linearen Fit des Arrhenius-Anstieges bestimmt werden kann, zeigte es sich, dass neu entwickelte Methoden der Datenlinearisierung notwendig sind, um ein genaues Ergebnis zu erhalten. Eine wichtige Erkenntnis war, dass TDLS allein eine vollständige Defektcharakterisierung ermöglicht, wenn die gesamte TDLS-Kurve einer SRH-Simulation unterzogen wird. Dies ist möglich für Defekte in der Minoritätsbandhälfte (MinBH), während für Defekte in der Majoritätsbandhälfte (MajBH) zwei gleichwertige TDLS-Lösungen erwartet werden, was eine eindeutige Identifikation des k -Faktors und der Bandhälfte verhindert. Während sich herausstellte, dass der k -Faktor der MajBH-Lösung für TDLS-Kurven in einem normalen Temperaturbereich vollständig unbestimmt ist, zeigte die theoretische Untersuchung erstmals, dass die Berücksichtigung des Abknickens der TDLS-Kurve infolge des Einsetzens der intrinsischen Eigenleitung – was im Allgemeinen oberhalb von 500 K beobachtet wird – zumindest die Bestimmung einer Obergrenze für den k -Faktor ermöglicht und manchmal sogar mehr. Allerdings zeigte sich, dass es für eine exakte Modellierung des TDLS-Knicks (Hochtemperaturbereich) notwendig ist, die SRH-Modellierung auf der Basis eines hier vorgeschlagenen fortgeschrittenen Temperaturmodells durchzuführen, das nicht nur die Temperaturabhängigkeit der Gleichgewichtsladungsträgerkonzentrationen berücksichtigt, sondern auch die temperaturbedingte Verringerung der Bandlücke. Da die exakte Modellierung des Tieftemperaturbereichs der TDLS-Kurve direkt das $\sigma(T)$ -Modell des Defektzentrums ergibt, liefert TDLS einen zusätzlichen Fingerabdruck, der Einblick in den physikalisch relevanten Einfangmechanismus ermöglicht.

Zur Lösung des Problems der Mehrdeutigkeit wurde eine neue Methode eingeführt, die in der Kombination von TDLS und IDLS besteht. Es konnte gezeigt werden, dass diese kombinierte TDLS&IDLS-Methode immer eine eindeutige und vollständige Defektcharakterisierung an einer einzelnen Probe für den gesamten Bereich der Defektparameter ermöglicht. Diese wichtige Entdeckung garantiert die allgemeine Anwendbarkeit der Lebensdauerspektroskopie als diagnostische Methode. Da die kombinierte Analyse durch einfache Überlagerung der zugehörigen DPSS-Diagramme mit maximaler Transparenz durchgeführt werden kann, setzt die kombinierte

TDLS&IDLS-Methode einen neuen Standard für die fortgeschrittene Lebensdauerspektroskopie.

Der Vergleich der verschiedenen Methoden der Lebensdauerspektroskopie im Hinblick auf ihr spektroskopisches Potential zeigt, dass ein eindeutiges spektroskopisches Ergebnis zwingend eine Temperaturvariation voraussetzt. Während die kombinierte TDLS&IDLS-Methode und die T-IDLS-Methode eine eindeutige Defektcharakterisierung ermöglichen, leistet dies die TDLS-Methode in einer Hälfte des Defektparamebereichs (MinBH-Defekte) und liefert in der anderen Hälfte (MajBH-Defekte) zumindest die Energietiefe ΔE_t . Da das Energieniveau bislang der einzige tabellierte Fingerabdruck von Defekten ist, wird die Kenntnis von ΔE_t in vielen Fällen für eine Identifikation eines unbekannten Defektzentrums ausreichen. Obwohl die N_{dop} -IDLS-Methode zwei gleichwertige Lösungen liefert, ist sie für den industriellen Einsatz interessant, da sie bei Raumtemperatur arbeitet. Das in dieser Arbeit erzielte vollständige Bild des spektroskopischen Potentials der unterschiedlichen Methoden der Lebensdauerspektroskopie wurde wesentlich durch die Verwendung der vorgeschlagenen DPSS-Analyse ermöglicht. Deshalb wird diese neue Auswertemethode mit hoher Wahrscheinlichkeit die Grundlage für weitere Entwicklungen im Bereich der Lebensdauerspektroskopie bilden.

Experiment:

Lebensdauerspektroskopische Untersuchungen an gezielt metallisch verunreinigten Proben

Um die theoretischen Vorhersagen im Hinblick auf das spektroskopische Potential der verschiedenen Methoden der Lebensdauerspektroskopie zu bestätigen, wurden gezielt metallisch verunreinigte Proben lebensdauerspektroskopisch untersucht. Für die Lebensdauermessungen wurden zwei weitverbreitete kontaktlose Messverfahren eingesetzt: die Methode der quasi-statischen Photoleitfähigkeitsmessung (QSSPC) für die IDLS-Messungen und die Methode des Mikrowellen-detektierten Photoleitfähigkeitsabklingens (MW-PCD) für die TDLS-Messungen. Während für die injektionsabhängigen Lebensdauermessungen ein handelsübliches QSSPC-System zum Einsatz kam, wurde für die Messung von temperaturabhängigen Lebensdauern der bestehende MW-PCD-Messaufbau durch den Anbau eines speziell angefertigten mit Flüssigkeitstickstoff gekühlten Kryostaten erweitert, was Lebensdauermessungen in einem Temperaturbereich von 100 bis 600K ermöglichte. Unseres Wissens ist dies der breiteste Temperaturbereich, in dem die Ladungsträgerlebensdauer je

untersucht wurde. Für die spektroskopische Auswertung der TDLS- und IDLS-Daten wurde eine modulare Simulationssoftware auf der Basis von Visual Basic entwickelt.

Aus methodischer Sicht stimmten die experimentellen LS-Ergebnisse voll mit den theoretischen Vorhersagen überein. Die Untersuchungsreihe bestätigte, dass die Lebensdauerspektroskopie immer eine vollständige Defektcharakterisierung an einer einzigen Probe ermöglicht, wenn TDLS und IDLS kombiniert werden. Wie vorhergesagt, lieferte die reine TDLS-Analyse ein eindeutiges spektroskopisches Ergebnis für MinBH-Defekte, während für die meisten MajBH-Defekte zwei gleichwertige Lösungen gefunden wurden. Ferner konnte durchweg gezeigt werden, dass es für die exakte Modellierung der gesamten TDLS-Kurve im erweiterten Temperaturbereich von 100 bis 600 K zwingend notwendig ist, einerseits das SRH-Modell auf das vorgeschlagene fortgeschrittene Temperaturmodell für die grundlegenden Halbleitergrößen zu stützen und andererseits das $\sigma(T)$ -Modell der jeweiligen Verunreinigung zu berücksichtigen. Beide Erweiterungen der SRH-Analyse, die in früheren Untersuchungen nicht berücksichtigt worden waren, erwiesen sich als unerlässlich aufgrund ihres wesentlichen Einflusses auf das spektroskopische Ergebnis. Bei der Anwendung der N_{dop} -IDLS-Methode schlug eine eindeutige Defektidentifikation wie erwartet fehl, da die überlagerte DPSS-Analyse zu den zwei vorhergesagten Lösungen führte, die lediglich eine Bestimmung des k -Faktors erlaubten. Die hier vorgeschlagene überlagerte DPSS-Analyse ermittelte diese Lösungen jedoch mit bemerkenswerter Genauigkeit selbst unter ungünstigen Rahmenbedingungen, was in vergleichbaren Experimenten bisher nicht erreicht werden konnte. Da die DPSS-Analyse es ermöglicht, die Genauigkeit und Konsistenz der spektroskopischen Ergebnisse unterschiedlicher LS-Kurven mit maximaler Transparenz nachzuweisen, hat sie entscheidenden Anteil an der Leistungsfähigkeit der unterschiedlichen LS-Methoden und setzt somit einen neuen Standard für die Datenauswertung in der fortgeschrittenen Lebensdauerspektroskopie.

Aus experimenteller Sicht erlaubten die lebensdauerspektroskopischen Untersuchungen immer eine eindeutige Identifikation des rekombinationsaktiven Defektniveaus sowie eine genaue Bestimmung seines Energieniveaus E_i und seines Symmetriefaktors k , was das Wissen um die Defekt-eigenschaften von Molybdän, Titan und Nickel vervollständigte und einen neuen und tieferen Einblick in die Rekombinationseigenschaften von Fe_i und FeB ergab. Die besondere Korrelation zwischen dem Fe_i und dem FeB -Defekt ermöglichte es sogar, die absolute Größe beider Einfangquerschnitte zu bestimmen, was im Allgemeinen mittels Lebensdauerspektroskopie nicht möglich ist, wenn die Defektkonzentration unbekannt ist. Die spektroskopischen Ergebnisse für die beiden eisenkorrelierten Defekte

Tab. 6.1. Liste der Defektparameter, die mittels Lebensdauerspektroskopie für die rekombinationsaktiven Niveaus der untersuchten metallischen Verunreinigungen bestimmt wurden. *Fett gedruckt* sind die Optimalwerte der Defektparameter, *nicht fett gedruckt* die Fehlerintervalle, wie sie sich aus der fortgeschrittenen DPSS Analyse ergeben.

Verunreinigung	Defektyp	Energie [eV]	Einfangquerschnitte k	σ_p [cm ²]	σ_n [cm ²]	$\sigma(T)$
Ti (*)	Doppel-donator	$E_V + \mathbf{0.289} \pm 0.005$	12 ± 1	1.9×10^{-16} [L]	$2.3 \times 10^{-15} \pm 0.2 \times 10^{-15}$	$T^{-1.6}$
Mo	Donator	$E_V + \mathbf{0.317} \pm 0.005$	13 ± 3	6.0×10^{-16} [L]	$7.8 \times 10^{-15} \pm 1.8 \times 10^{-15}$	$T^{-1.6}$
Fe	Donator	$E_V + \mathbf{0.394} \pm 0.005$	51 ± 5	7.0×10^{-17} [L]	$3.6 \times 10^{-15} \pm 0.4 \times 10^{-15}$	$E_\infty = 24$ meV
FeB (*)	Akzeptor	$E_C - \mathbf{0.260} \pm 0.030$ [L]	0.45 0.01–1	5.5×10^{-15}	2.5×10^{-15}	—
Ni (p-Si)	Akzeptor	$E_C - \mathbf{0.400} \pm 0.030$	0.7 0.3–1.3	$8.0 \times 10^{-17} \pm 5.7 \times 10^{-17}$	5.6×10^{-17} [L]	$T^{-2.4}$
Ni (n-Si)	Donator	$E_V + \mathbf{0.189} \pm 0.050$	3500 890–12900	1.1×10^{-15} [L]	$4 \times 10^{-12} \quad 1-10 \times 10^{-12}$	$T^{-2.5}$

[L] Werte für die Einfangquerschnitte, die der Literatur entnommen wurden (*grau unterlegt*).

(*) Verunreinigungen, die zusätzliche Energieniveaus in der Bandlücke ausbilden. Diese werden durch die lebensdauerspektroskopischen Untersuchungen im Hinblick auf ihre Rekombinationsaktivität indirekt als unbedeutend identifiziert.

sind von besonderer praktischer Bedeutung, da die empfindlichste kommerziell eingesetzte Methode, Eisenverunreinigungen in Silizium zu detektieren und quantitativ zu bestimmen, sehr stark von den Defektparametern beider Defektzustände abhängt. Die Defektparameter der verschiedenen Übergangsmetalle, die im Rahmen dieser Arbeit bestimmt wurden, sind in obiger Tabelle zusammengestellt.

Die Untersuchung zeigte, dass die Einfangquerschnitte der meisten Defekte temperaturabhängig sind, und identifizierte den exzitonischen Auger-Einfangprozess als den dominanten Einfangmechanismus im Falle injizierter Minoritätsladungsträger, was der Betriebsbedingung von Solarzellen entspricht. Ein Vergleich der untersuchten Verunreinigungen im Hinblick auf ihre Rekombinationsaktivität identifizierte Molybdän als die schlimmste und Nickel als die harmloseste Verunreinigung.

Die Konsistenz der spektroskopischen Ergebnisse, die mittels der unterschiedlichen Methoden der Lebensdauerspektroskopie erzielt wurden, und ihre gute Übereinstimmung mit E_V -Ergebnissen, die in der Literatur mittels DLTS bestimmt wurden, demonstrierten die hervorragende Eignung der Lebensdauerspektroskopie für die Defektcharakterisierung und die große Zuverlässigkeit der hier bestimmten Defektparameter. Alles in allem zeigen

die experimentellen Ergebnisse der vorliegenden Arbeit eindrucksvoll, dass die Lebensdauerspektroskopie sowohl im Hinblick auf das physikalische Verständnis als auch auf die technische Umsetzung reif ist, um als hoch empfindliche diagnostische Methode in der Halbleiterindustrie eingesetzt zu werden.

Experiment: Untersuchung des metastabilen Defektes in Czochralski-Silizium

Als Beispiel für einen rekombinationsaktiven Defekt, der bis heute mit konventionellen Methoden nicht nachgewiesen werden konnte, wurde der metastabile Defekt untersucht, der in bordotiertem Czochralski (Cz) Silizium auftritt. Der Cz-spezifische Defekt wird unter Beleuchtung oder durch Ladungsträgerinjektion aktiviert und durch einen Temperschritt bei 200°C deaktiviert. Seine Aktivierung löst die bekannte Lebensdauerdegradation um bis zu 90 % ihres Anfangswertes aus, die vollkommen reversibel ist, da der Ausgangswert durch die Temperung wiederhergestellt werden kann.

Um die Hauptkomponenten des Cz-spezifischen Defektes zu identifizieren, wurde der Einfluss der charakteristischen Cz-Verunreinigungen auf das Degradationsverhalten qualitativ an verschiedenen dotierten Float Zone (FZ) Siliziumwafern in Abwesenheit anderer Verunreinigungen untersucht. Während sauerstoff- und phosphordotiertes FZ-Silizium und sauerstofffreies bordotiertes FZ-Silizium keinen Degradationseffekt zeigten, zeigte bor- und sauerstoffdotiertes FZ-Silizium die gleiche Lebensdauerdegradation wie bordotiertes (sauerstoffverunreinigtes) Cz-Silizium, womit eine eindeutige Korrelation des Cz-spezifischen Defektes mit den Elementen Bor und Sauerstoff nachgewiesen werden konnte. Dies wurde weiter bestätigt durch die Beobachtung, dass sowohl sauerstofffreies bordotiertes MCz-Silizium (gezogen nach dem Cz-Verfahren unter Einwirkung eines Magnetfeldes) sowie sauerstoffverunreinigtes galliumdotiertes *p*-Typ Silizium keine Degradation zeigten und exzellente Volumenlebensdauern aufwiesen. Die quantitative Korrelation der metastabilen Defektkonzentration N_t^* mit Bor und Sauerstoff wurde an 30 unterschiedlichen Cz-Si Materialien untersucht. Dabei wurde eine lineare Abhängigkeit von Bor ($N_t^* \propto [B_s]^{1.1}$), eine fast quadratische Abhängigkeit von Sauerstoff ($N_t^* \propto [O_i]^{1.5-1.9}$) und eine verschwindend kleine Abhängigkeit von Kohlenstoff festgestellt. Die Untersuchung deckte einen fundamentalen Unterschied in der $[B_s]$ - und $[O_i]$ -Korrelation auf. Während die $[B_s]$ -Korrelation eine hohe von thermischen Vorbehandlungen unbeeinflusste Qualität auf-

weist, weist die $[O_i]$ -Korrelation eine starke Streuung auf, deren Korrelationsexponent unter einer Hochtemperaturbehandlung leicht abnimmt. Dies deutet auf eine direkte Beteiligung von substitutionellem Bor an dem Defektzentrum hin, während die Beteiligung von interstitiellem Sauerstoff indirekt zu sein scheint. Somit legen die Untersuchungen der vorliegenden Arbeit einen Defektkomplex B_sX nahe mit einer unbekannten Komponente X, die durch Sauerstoff stimuliert wird. Mögliche Kandidaten für X sind intrinsische Punktdefekte. Ein erstes Experiment ergab, dass Gitterleerstellen (vacancies) als Quelle für diese unbekannte Verunreinigung höchstwahrscheinlich ausgeschlossen werden müssen. Ein alternativer Kandidat könnte das kürzlich vorgeschlagene Sauerstoffdimer O_{12} sein [1].

Eine quantitative Analyse der Kinetik der Defektbildung und -vernichtung gab Einblick in den physikalischen Mechanismus der Defektransformation. Ein isothermes Ausheilexperiment zeigte, dass der Prozess der Defektvernichtung thermisch aktiviert ist mit einer Energiebarriere $E_{barr} = (1.32 \pm 0.05)$ eV, deren Wert erstmals bestimmt wurde. Für den Prozess der Defektbildung zeigte die Beobachtung einer quadratischen Dotierabhängigkeit und einer verschwindend kleinen Injektionsabhängigkeit der Defektgenerationsrate U_{gen} , dass die Defektbildung nicht mit der einfachen Theorie einer rekombinationsunterstützten Defektreaktion (REDR) beschrieben werden kann, da diese eine lineare U_{gen} -Abhängigkeit von beiden Größen vorhersagt. Ein einfacher Umladungsprozess muss allerdings auf Grund von zusätzlichen dynamischen Experimenten an Solarzellen ausgeschlossen werden. Somit deuten die Ergebnisse der Lebensdauerstudie auf eine komplexere Rekombinationsunterstützung der Defektbildung hin als in der einfachen REDR-Theorie angenommen. Eine Klärung erfordert weitere Untersuchungen.

Die Anwendung der fortgeschrittenen Lebensdauerspektroskopie erlaubte es erstmalig die elektronische Struktur des Cz-spezifischen Defektes in seinem aktiven Zustand zu bestimmen. Er liegt in der oberen Bandhälfte bei $E_C - E_f = 0.41$ eV und zeigt einen Symmetriefaktor von $k = \sigma_n/\sigma_p = 9.5$. Die mittels TDLS bestimmte Temperaturabhängigkeit des Elektroneneinfangquerschnitts $\sigma_n(T) \propto T^2$ identifiziert den exzitonischen Auger-Einfang als den relevanten Einfangmechanismus in den rekombinationsaktiven Defektzustand. Die Genauigkeit dieser Bestimmung äußert sich in der Tat sache, dass zwei unabhängige Methoden zum gleichen Ergebnis führten: TDLS allein und die Kombination von TDLS und IDLS. Zusätzlich wurde für den Defekt im passiven Zustand aus TDLS-Messungen ein sehr flaches Energieniveau bestimmt, was seine geringe Rekombinationsaktivität widerspiegelt.

Da die Lebensdauerdegradation einen deutlichen Abfall des Solarzellenwirkungsgrades um 1–2 % (absolut) bewirkt, besteht in der Reduktion oder Beseitigung des metastabilen Defektes ein hohes Potential für Verbesserungen von Cz-Si Solarzellen. Zusätzlich zu der Tatsache, dass die Degradation durch eine geeignete Materialwahl vollständig vermieden werden kann, indem eine der beiden Hauptkomponenten (Bor oder Sauerstoff) ersetzt wird, wurde gezeigt, dass sogar in bordotiertem Standard-Cz-Si eine dauerhafte Reduktion der Defektkonzentration erreicht werden kann, indem geeignete Hochtemperaturschritte angewendet werden. Diese Reduktion spiegelt sich direkt in einer Verbesserung der Volumenlebensdauer um einen Faktor 2–3 wider und wird durch eine moderate Abnahme der interstitiellen Sauerstoffkonzentration ausgelöst. Die Untersuchung des Einflusses der Prozessparameter zeigte, dass diese Materialverbesserung in allen sauerstoffverunreinigten Materialien eine Optimierung des Hochtemperaturprozesses voraussetzt. Ungeeignete Prozesse führen zu einem starken Einbruch der Volumenlebensdauer und des Solarzellenwirkungsgrades, was der Bildung von Sauerstoffpräzipitaten zugeordnet werden konnte.

Um realistische Vorhersagen für Solarzellen aus bordotiertem Cz-Silizium zu ermöglichen, wurde die in einer umfassenden Materialstudie gemessene Dotierabhängigkeit der Volumenlebensdauer mit einem einfachen empirischen Modell modelliert. Es zeigte sich, dass die optimale Dotierkonzentration, die zu einem maximalen Solarzellenwirkungsgrad führt, stark von der verwendeten Solarzellenstruktur und dem aktuellen Degradationszustand abhängt. Während der maximale stabile Wirkungsgrad für eine hocheffiziente Solarzellenstruktur für eine Basisdotierung $N_A = 5 \times 10^{15} \text{ cm}^{-3}$ vorhergesagt wurde, variiert der optimale Wert für eine industrielle Solarzellenstruktur zwischen $N_A = 10^{15} \text{ cm}^{-3}$ für eine Zelle mit Back-Surface-Field und $N_A = 10^{16} \text{ cm}^{-3}$ für eine Zelle ohne Back-Surface-Field. Die Tatsache, dass die theoretischen Vorhersagen für die hocheffiziente Solarzellenstruktur experimentell bewiesen werden konnten, zeigt, dass Solarzellensimulationen auf der Grundlage des hier bestimmten Lebensdauermodells eine einfache und doch recht genaue Bestimmung des Degradationsverlustes und des stabilen Wirkungsgrades ermöglichen, die für eine bestimmte Zellstruktur erwartet werden müssen, wenn bordotiertes Cz-Silizium als Substrat verwendet wird.

Relevanz der Ergebnisse und Ausblick

Da in der Halbleiterindustrie aufgrund der immer strenger werdenden Anforderungen an die elektronischen Bauelemente ein wachsender Bedarf an zunehmend sensitiven Techniken besteht, um immer geringer werdende Mengen von Verunreinigungen nachzuweisen, wird die Lebensdauerspektroskopie mit hoher Wahrscheinlichkeit in Zukunft nicht nur in der Photovoltaik, sondern auch in anderen Bereichen der Halbleiterindustrie zunehmend zum Einsatz kommen.

Die fortgeschrittene Lebensdauerspektroskopie gibt ein vollständiges Bild, wie Verunreinigungen die Bauelementeigenschaften beeinflussen und liefert somit eine Information, die mit herkömmlichen Methoden für die meisten Verunreinigungen nicht gewonnen werden konnte. Sie eröffnet damit ein breites Feld für eine detaillierte Charakterisierung von Defekten, die für die Photovoltaik relevant sind. Dies wurde in dieser Arbeit anhand der lebensdauerspektroskopischen Untersuchungen an metallischen Verunreinigungen demonstriert.

Aus methodischer Sicht ist die technische Realisierung der *T-IDLS*-Methode auf Basis der QSSPC-Technik eine drängende Aufgabe. Aufgrund des entscheidenden Einflusses des Temperaturbereichs auf die Eindeutigkeit des spektroskopischen *T-IDLS*-Ergebnisses muss in zukünftigen Messapparaturen ein breiter Temperaturbereich zugänglich gemacht werden, wie in den hier durchgeführten TDLS-Untersuchungen. Weitere methodische Entwicklungen im Feld der Lebensdauerspektroskopie werden höchstwahrscheinlich auf dem neu entwickelten DPSS-Auswerteverfahren beruhen, da dieses eine maximale Transparenz bei der SRH-Modellierung garantiert.

Es muss betont werden, dass die Erkenntnisse in Bezug auf das spektroskopische Potential der verschiedenen Techniken der Lebensdauerspektroskopie sowie das DPSS-Auswerteverfahren vollständig losgelöst sind von der Technik, die für die Messung der Injektions- und Temperaturabhängigkeit der Ladungsträgerlebensdauer eingesetzt werden. Aus diesem Grund ist zu erwarten, dass die methodischen Ergebnisse dieser Arbeit neue Entwicklungen in anderen Bereichen der Materialcharakterisierung anstoßen werden. Erst kürzlich wurde ein erster Versuch unternommen, TDLS-Daten aus temperaturabhängigen Quanteneffizienzmessungen zu bestimmen [2]. Mit der erfolgreichen Entwicklung von schnellen Messmethoden zur Bestimmung von Lebensdauertopographien, wie beispielsweise der auf Thermographie beruhenden CDI-Technik [3], beginnen gegenwärtig intensive Forschungsaktivitäten am Fraunhofer ISE und an anderen Instituten, um ein temperaturabhängiges Lebensdauermapping

technisch zu realisieren. Diese Aktivitäten zielen darauf ab, ortsaufgelöste TDLS-Messungen und somit ΔE_r -Topographien zu ermöglichen [4]. Dies würde detaillierte spektroskopische Untersuchungen an Proben mit inhomogener Defektverteilung, wie beispielsweise multikristallinen Proben, erlauben und somit tieferen Einblick in bislang unbekannte Defektstrukturen liefern. Diese Entwicklungen zeigen, dass die Lebensdauerspektroskopie an Bedeutung gewinnt und vielfältige Anwendung findet.

Literatur

- [1] J. Schmidt, K. Bothe, and R. Hezel, *Formation and annihilation of the metastable defect in boron-doped Czochralski silicon*, Proc. 29th IEEE PVSC (New Orleans, Louisiana, USA, 2002), pp. 178–81.
- [2] T.A. Wagner and U. Rau, *Analysis of recombination centers in epitaxial silicon thin-film solar cells by temperature-dependent quantum efficiency measurements*, Appl. Phys. Lett. **82** (16), 2637–9 (2003).
- [3] J. Isenberg, S. Riepe, S.W. Glunz, and W. Warta, *Imaging method for laterally resolved measurement of minority carrier densities and lifetimes: Measurement principle and first applications*, J. Appl. Phys. **93** (7), 4268–75 (2003).
- [4] M.C. Schubert, J. Isenberg, S. Rein, and W. Warta, *Temperature-dependent carrier lifetime images*, Proc. 19th EC PVSEC (Paris, France, 2004), pp. 500–3.

Index

A

Arrhenius increase 85–87
see also TDLS, linear fit

B

band gap narrowing 21–22

C

capture cross section
see defect parameters
see capture mechanisms

capture mechanisms

- Auger capture
 - classical 182
 - excitonic **182–83, 186**, 201, 312, 329, 335, 429
- cascade capture **181–82**, 335
- electron and hole capture 184–86
 - identical $\sigma(T)$ -models 184–85
- impact of experimental conditions 183–84
- multiphonon emission capture 180–81, 186, 350
- radiative capture 180
- $\sigma(T)$ -models (comparison) 179–83
 - tabular overview 179

capture time constant
see defect parameters

carrier lifetime *see* lifetime

contamination process 262–63

crossover point (IDLS) *see* iron fingerprint

cryostat 66–67

- temperature control 67

Cz defect 397, 467–69

- active state
 - IDLS, advanced analysis 431–32
 - spectroscopic results 434
- TDLS&IDLS, combined analysis 433–34

TDLS, advanced analysis 428–30

band diagram 435

defect model, preliminary 411–13

- boron-oxygen complex 412
- oxygen dimer 412

impact of thermal pretreatments 408–10

impact of vacancies 413–14

major components 399–401

normalized defect concentration

- definition 401–2
- determination 404

passive state

- TDLS, linear fit 427–28

quantitative correlation with

- boron 405
- carbon 410–11
- oxygen 405–7

spectroscopic results 434–35

Cz defect annihilation 415–18

- activation energy 417
- annihilation rate 416
- isothermal annealing 417

Cz defect formation 418–25

- activation energy 424
- generation rate
 - definition 421
 - doping dependence 421–23
 - impact of light intensity 423–24
- measurement conditions 419–21
- REDR theory 418–19

Cz defect transformation

- see* Cz defect annihilation
- see* Cz defect formation
- hysteresis (TDLS) 427–28
- optimized TDLS procedure 426–27

Cz degradation *see* degradation effect

Cz material improvement

- defect concentration, reduction 437
- physical reason 445–46

- process 439–40
 ramping conditions (HT-steps)
 impact on cell efficiency 443–44
 impact on oxygen concentration 444–45
 impact on stable lifetime 440–42
 stable lifetime, improvement 437–39
- Cz material quality
 empirical lifetime model 448–49
 lifetime study 447–48
- Cz solar cells
 see solar cell performance on Cz-Si
- Czochralski silicon (Cz) 403
- D**
- deep level transient spectroscopy (DLTS) 257
- defect center, roles 41–43
 generation center 42
 recombination center 42
 trap center 42
- defect parameter solution surface
 see also DPSS
 significance 249, 387
- defect parameters
 capture cross section 72
 capture time constant 72
 classification
 absolute parameters 73–74
 relative parameters 73–74
 defect concentration 72
 energy level 72
 symmetry factor 73
- degradation effect 397–99
 degradation, carrier-induced 398
 material dependence 401
 recovery, temperature-induced 398
 reversible cycle 398
- diffusivities (impurities) 261
- dissolved impurities 260
- doping concentration
 iterative determination 271–73
- DPSS (IDLS)
 curve, DPSS- χ^2 105
 curve, DPSS- k 105
 curve, DPSS- τ_{n0} 105
 DPSS asymmetry 107–11
 physical reason 108–9
- DPSS characteristics
 combined evaluation 133–34
 defining equations 120–23
 differences in *n*-type 123
 spectroscopic value 126–33
- DPSS diagram 104–7, 298, 357, 366, 432
- DPSS equations, analytical 111–13
 modifications in *n*-type 113–14
- DPSS structure
 division of defect parameter plane 125
 impact of band gap half 117–19
 impact of doping concentration 137
 see also DPSS (N_{dop} -IDLS)
 impact of energy level 115–17
 impact of symmetry factor 117
 impact of temperature 244
 see also DPSS (*T*-IDLS)
- DPSS-DG (definition gap) 105
 defining equation 120–21
 spectroscopic value 126–28, 299, 358, 365, 432
- DPSS-PL (plateau value) 105
 defining equation 122–23
 spectroscopic value 131–32, 299, 358, 431
- DPSS-VR (validity range)
 characteristic structure 124–25
 continuous structure 105, 298, 307, 357, 432
 split structure 116–17, 366
 zero point bound, lower 124
 zero point bound, upper 124
- DPSS-ZP (zero point) 116
 defining equation 121
 definition gap (DG/DPSS-ZP) 121–22
 spectroscopic value 129–31, 365–67
 inherent ambiguity 105, 390
- DPSS (N_{dop} -IDLS)
 DPSS intersection points 135–36, 138, 306–8
 selection method 308–9
- DPSS-VR (validity range)
 characteristic structure 142
 energy correction term 138–40, 309–10
 impact of defect depth 137, 140–41
 minimum requirements for IDLS set 141

- optimum doping range 141–43
 practical importance 143–44, 310
 superposed DPSS diagram 135–36,
 305–8, 390
- DPSS (TDLS&IDLS)
 combined DPSS diagram 228–31, 300,
 318, 319, 359, 433
 significance 231
 DPSS intersection points 229–30
 unambiguous identification 390
 MajBH defect 229–30, 299–301,
 318–21, 358–60
 MinBH defect 228, 433–34
- DPSS (TDLS)
 curve, DPSS- χ^2 210
 curve, DPSS- k 210
 DPSS diagram 210–15, 290, 312, 330,
 334, 351, 362, 430
 DPSS- χ^2 minimum
 defect identification 212–14
 error estimation 210–12
 equivalent solutions 289–92, 311–14,
 328–31
 impact of high-temperature part
 MajBH defect 212–14, 354–56
 MinBH defect 210–12
 impact of low-temperature part
 MajBH defect 289–92, 353–54
 MinBH defect 214–15
 superposed DPSS analysis 292–95
 unambiguous identification
 MajBH defect 212–14, 350–53
 MinBH defect 210–12, 333–34,
 362–65, 428–30
- DPSS (T -IDLS)
 2nd DPSS-IP
 effective energy shift 238–39
 energy correction term 236–38
 identification (necessary condition)
 240–42
 structure 241–42
 uncertainty 238
 classification of T -IDLS results 239–40
 curve, DPSS- k 234
 curve, DPSS- $\tau_{n0}(300K)$ 234
 curve, DPSS- $\tau_{n0}(T)$ 234
 DPSS intersection point
 1st DPSS-IP (sharp) 235
 2nd DPSS-IP (diffuse) 235
 DPSS-VR (validity range)
- characteristic structure 245–46
 impact of defect depth 242–43, 244
 minimum requirements for IDLS set
 245
 optimum temperature range 245–47
 superposed DPSS diagram 233–36
 $\tau_{n0}(T)$ extraction 234
- E**
- effective density of states
 basic model 8
 effective mass model 23–25
- effective lifetime 51
 approximate equations 52–53
 separation of bulk lifetime 53
 systematic error 53–55
- effective mass model
see effective densities of states
- energy band gap *see* band gap narrowing
- energy level *see* defect parameters
- F**
- Fermi energy 8, 11, 20
 doping dependence 10
 temperature dependence 20, 29
- freeze-out 14–17
 ionization degree 16, 26
 onset temperature 16
- I**
- IDLS
 advanced DPSS analysis 104–7, 297–
 99, 356–58, 365–67, 431–32
 data pre-analysis (procedure) 273–74,
 295–97, 389
 DPSS *see* DPSS(IDLS)
 fundamental restriction 102–3
 injection range, covered 273
 spectroscopic evaluation (procedure)
 275–76
 two-defect SRH simulation 99–102,
 106, 296–97, 305
 lifetime weighting factor 99, 100
- impurity depletion 12
- intrinsic conduction 17–18
see also TDLS bend
- intrinsic carrier concentration
 definition 8
 temperature dependence 18, 27

- onset temperature 18, 28
- iron
- crossover point (IDLS)
 - see* iron fingerprint
 - defect configuration
 - see* iron interstitial
 - see* iron-boron pair
 - properties and relevance 336–37
- iron defect transformation
- [Fe] determination (technique) 372–74
 - association time of FeB pairs 346
 - C factor, analytical expression 372
 - crossover point (IDLS)
 - see* iron fingerprint
 - effect on carrier lifetime
 - injection-dependent 343, 344
 - temperature-dependent 344–46
 - equilibrium fractions (FeB, Fei) 346, 347
 - pair association 341, 343
 - pair dissociation 342, 343
 - paired fraction
 - after dissociation 348–50
 - before dissociation 346–48
 - S-shape (TDLS) *see* iron fingerprint
- iron fingerprint
- crossover point (IDLS) 344, 370–72
 - analytical expression 371
 - doping dependence 377–78
 - qualitative change (TDLS) 344–46
 - S-shape (TDLS) 344–46
- iron, interstitial *see also* iron
- electronic properties 338–40
 - spectroscopic results 360–61
- iron-boron pair *see also* iron
- electronic properties 339, 340–41
 - spectroscopic results 367–69
 - capture cross sections 375–76
- L**
- lifetime 32
- Auger 35, 40
 - bulk 51
 - Coulomb-enhanced Auger 40
 - high-injection model 38
 - injection-dependent model 38
 - low-injection model 38
 - physical reason 37
 - effective *see* effective lifetime
- radiative 34, 40
- Shockley-Read-Hall *see* SRH lifetime
- lifetime degradation *see* degradation effect
- lifetime measurement techniques
 - see* MW-PCD, *see* QSSPC
- lifetime spectroscopy
- compilation of techniques 91
 - consistency of results 301–2, 324–25, 332, 334–35, 360–61, 367–69
 - consistency with DLTS results 323–24
 - injection-dependent *see* IDLS
 - injection-dependent at various doping concentrations *see* N_{dop} -IDLS
 - injection-dependent at various temperatures *see* T-IDLS
- methodological results
- comparison 386–91, 462–64
 - tabular overview 388–89
- relevance and outlook 469–70
- sensitivity 323–24, 391
- temperature-dependent *see* TDLS
- theoretical potential
- comparison 250–52
 - tabular overview 250
- M**
- magnetic Czochralski silicon (MCz) 400
- majority band half defect (MajBH) 107, 203
- majority carrier concentration 7, 8, 10, 13, 19
- impact of freeze-out 27
 - impact of intrinsic conduction 18, 27
- minority band half defect (MinBH) 107, 203
- molybdenum
- properties and relevance 285
 - spectroscopic results 301
- MW-PCD technique 63–66
- N**
- N_{dop} -IDLS 84
- DPSS *see* DPSS (N_{dop} -IDLS)
 - fundamental restriction 138–40
 - simultaneous SRH analysis 135
- nickel
- properties and relevance 326–27
 - spectroscopic results 331
 - thermal stability 327–28

O

outdiffusion 260

P

pair association

see iron defect transformation

pair dissociation

see iron defect transformation

precipitation 260

Q

QSSPC technique 61–63

R

recombination

basic concept 31–32

lifetime definition 32

superposition of recombination channels
32

recombination activity

definition 75–76

impact of defect parameters

energy level 77–78

symmetry factor 78–79

impact of doping concentration 77–78

impact of doping type 336

recombination dynamics 59–60

general case 60

quasi-steady-state case 60

quasi-transient case 60

recombination lifetime *see* lifetime

recombination mechanisms

Auger 35–39

Coulomb-enhanced Auger 36–39

extrinsic 33

intrinsic 32

comparison 39–41

radiative 33–34

Shockley-Read-Hall (bulk defects)

41–48

surface 49–50

recombination-enhanced defect reaction
(REDR) *see* Cz defect formation

S

semiconductor

extrinsic 9

intrinsic 8

Shockley-Read-Hall *see* SRH equation, ...

solar cell performance on Cz-Si

doping-dependence (industrial cell) 454

doping-dependence (RP-PERC cell) 451

solar cell structure

high-efficiency cell (RP-PERC) 450

industrial cell 453

solubilities (impurities) 261

SRH densities

definition 44, 72

temperature dependence 76

SRH equation 43–46

SRH lifetime

general expression 45, 72

high-level injection (HLI) 74

lifetime difference HLI – LLI 109–10

low-level injection (LLI) 74

simplifications 75

SRH lifetime, injection-dependent 80–84

impact of defect parameters

band gap half 108

energy level 82

symmetry factor 82

impact of doping concentration 83

impact of temperature 84

lifetime difference HLI – LLI 81

physical difference (MinBH/MajBH

levels) 111

superposed Auger recombination 97–98

superposed carrier trapping 93–96

see also trapping

SRH lifetime, temperature-dependent

84–89

Arrhenius increase 85–87

impact of band gap narrowing 193–96

impact of defect parameters

band gap half 204

energy level 87

symmetry factor 87

impact of doping concentration

88, 292–95

impact of effective mass model 193–96

impact of freeze-out 189–90

impact of intrinsic conduction

191–92, 197 *see also* TDLS bend

impact of $\sigma(T)$ -model 184–86

basic assumption 184–85

cascade capture 334

excitonic Auger capture 186, 201,

293, 312, 330, 430

- multiphonon emission capture **186**, 351
 - trapping **186–88**, 201, 293, 312
 - asymptotic lifetime 187
 - SRH model
 - critical recombination center density 47
 - prerequisites 46
 - validity **47–48**, 304–5
 - SRH recombination
 - see* recombination mechanisms
 - surface passivation
 - fundamental mechanisms 50–51
 - grinding process 265–66
 - method of thickness variation 266–68
 - silicon nitride
 - passivation quality 268–70
 - PECVD deposition 264
 - suitability 271
 - surface recombination
 - see* recombination mechanisms
 - surface recombination velocity 50
 - symmetry factor *see* defect parameters
- T**
- TDLS**
 - impact of surface recombination 280–83
 - impact of the injection level 279, 280
 - optimum measurement conditions 277–80
 - spectroscopic evaluation (procedure) 283–84
 - temperature cycles 276, 327–28
 - temperature range 200, 276, **386**
 - TDLS bend (intrinsic conduction) 191–92
 - analytical expression 205–8
 - IC onset temperature 197–200
 - actuating variables 199
 - impact of defect parameters
 - energy level 192, **207**
 - symmetry factor 207
 - impact of doping concentration 192, 293
 - impact of *T*-model **197**, 201, 287, 315
 - TDLS&IDLS (combined analysis)
 - see* DPSS (TDLS&IDLS)
 - TDLS, advanced analysis 386
 - ambiguity and unambiguity **204–5**, 387
 - applicability of TDLS 216–20
 - critical parameter constellation 219
 - visualization 218, 219–20
 - Arrhenius onset temperature 204
 - actuating variables 218
 - defining equation 216
 - doping shift 293
 - Arrhenius temperature width
 - actuating variables 218
 - defining equation 217
 - basic assumptions
 - general $\sigma(T)$ impact 220
 - T -independent energy depth 222–23
 - T -independent k factor 220–21
 - cross-check of doping concentration 208–10
 - DPSS *see* DPSS(TDLS)
 - high-temperature part **202**, 286, 314–16
 - impact of $\sigma(T)$ -model
 - see* low-temperature part
 - impact of the fitted T range 387
 - impact of *T*-model *see* TDLS bend
 - low-temperature part **200–202**, 292, 329, 333, 350, 428–29
 - optimum model configuration **200–203**, 286–89, 311–14, 328–31, 333–34, 350–53, 428–30
 - physical difference (MinBH/MajBH levels) 203–4
 - TDLS bend 205–10
 - see also* TDLS bend
 - TDLS characteristics 226
 - extractable defect parameters 225
 - influencing parameters 225
 - trapping **202**, 292, 311
 - TDLS, data linearization
 - extracted energy depth
 - systematic error 157–59
 - theoretical deviations 155–57
 - impact of $\sigma(T)$ -model 154, 155–57
 - linearization procedures
 - advanced 158, 159–61
 - comparison 159
 - optimum choice of T_L 153, 154–55
 - simple 151–54
 - TDLS, linear fit 148–49
 - Arrhenius increase 149
 - basic problem 149–51
 - temperature regions 148
 - TDLS, resolution capability
 - accuracy of energy determination 164–71

-
- defect separation 171–76
 - evaluation (application) 174–76
 - evaluation (comparison) 175
 - evaluation (procedures) 172–73
 - fundamental restriction 176
 - TDLS cascade structure 172
 - theoretical requirements 171
 - deviation term 165–66
 - ratio of recombination activities 165
 - relative energy distance 165
 - energy error, generalized 168–71
 - actuating variables 169
 - definition 168
 - unaffected TDLS accuracy 171
 - energy error, systematic 166–68
 - analytical expression 167
 - impact of energy distance 167
 - TDLS cascade structure
 - see also* defect separation
 - measured 174
 - simulated 172
 - two-level systems 162–64
 - temperature models
 - advanced 25–30
 - basic 11–12
 - comparison 30
 - standard 19–20
 - T*-IDLS 84
 - DPSS *see* DPSS (*T*-IDLS)
 - simplifications, limited potential 232–33
 - simultaneous SRH analysis 233–36
 - transition temperature 233
 - titanium
 - properties and relevance 303–4
 - spectroscopic results 322, 324–25
 - transition metals
 - crystallographic properties 260–62
 - defect parameters **380–82**, 464–66
 - tabular overview 381
 - diffusivities 261
 - impact on solar cell efficiency (comparison) 384–85
 - recombination activity (comparison) 382–84
 - solubilities 261
 - trapping
 - asymptotic lifetime 187
 - impact of trap concentration 188
 - impact of trap energy 188
 - bias light correction **94–96**, 296
 - distortion of the PCD signal 279
 - external trapping 48
 - injection-dependent **93**, 296
 - temperature-dependent 186–88
 - internal trapping 47

Springer Series in MATERIAL SCIENCE

Editors: R. Hull R. M. Osgood, Jr. J. Parisi H. Warlimont

- 20 **Microcluster Physics**
By S. Sugano and H. Koizumi
2nd Edition
- 21 **The Metal-Hydrogen System**
By Y. Fukai 2nd Edition
- 22 **Ion Implantation in Diamond,
Graphite and Related Materials**
By M. S. Dresselhaus and R. Kalish
- 23 **The Real Structure
of High-T_c Superconductors**
Editor: V. Sh. Shekhtman
- 24 **Metal Impurities
in Silicon-Device Fabrication**
By K. Graff 2nd Edition
- 25 **Optical Properties of Metal Clusters**
By U. Kreibig and M. Vollmer
- 26 **Gas Source Molecular Beam Epitaxy**
Growth and Properties of Phosphorus
Containing III-V Heterostructures
By M. B. Panish and H. Temkin
- 27 **Physics of New Materials**
Editor: F. E. Fujita 2nd Edition
- 28 **Laser Ablation**
Principles and Applications
Editor: J. C. Miller
- 29 **Elements of Rapid Solidification**
Fundamentals and Applications
Editor: M. A. Otooni
- 30 **Process Technology
for Semiconductor Lasers**
Crystal Growth
and Microprocesses
By K. Iga and S. Kinoshita
- 31 **Nanostructures
and Quantum Effects**
By H. Sakaki and H. Noge
- 32 **Nitride Semiconductors and Devices**
By H. Morkoc
- 33 **Supercarbon**
Synthesis, Properties and Applications
Editors: S. Yoshimura and R. P. H. Chang
- 34 **Computational Materials Design**
Editor: T. Saito
- 35 **Macromolecular Science
and Engineering**
New Aspects
Editor: Y. Tanabe
- 36 **Ceramics**
Mechanical Properties,
Failure Behaviour,
Materials Selection
By D. Munz and T. Fett
- 37 **Technology and Applications
of Amorphous Silicon**
Editor: R. A. Street
- 38 **Fullerene Polymers
and Fullerene Polymer Composites**
Editors: P. C. Eklund and A. M. Rao
- 39 **Semiconducting Silicides**
Editor: V. E. Borisenko
- 40 **Reference Materials
in Analytical Chemistry**
A Guide for Selection and Use
Editor: A. Zschunke
- 41 **Organic Electronic Materials**
Conjugated Polymers and Low
Molecular Weight Organic Solids
Editors: R. Farchioni and G. Grossos
- 42 **Raman Scattering
in Materials Science**
Editors: W. H. Weber and R. Merlin
- 43 **The Atomistic Nature
of Crystal Growth**
By B. Mutafitschiev
- 44 **Thermodynamic Basis
of Crystal Growth**
P-T-X Phase Equilibrium
and Non-Stoichiometry
By J. Greenberg
- 45 **Thermoelectrics**
Basic Principles
and New Materials Developments
By G. S. Nolas, J. Sharp,
and H. J. Goldsmid
- 46 **Fundamental Aspects
of Silicon Oxidation**
Editor: Y. J. Chabal
-

Springer Series in MATERIAL SCIENCE

Editors: R. Hull R. M. Osgood, Jr. J. Parisi H. Warlimont

- 49 **Alkali Halides**
A Handbook of Physical Properties
By D. B. Sirdeshmukh, L. Sirdeshmukh,
and K. G. Subhadra
- 50 **High-Resolution Imaging
and Spectrometry of Materials**
Editors: F. Ernst and M. Rühle
- 51 **Point Defects in Semiconductors
and Insulators**
Determination of Atomic
and Electronic Structure
from Paramagnetic Hyperfine
Interactions
By J.-M. Spaeth and H. Overhof
- 52 **Polymer Films
with Embedded Metal Nanoparticles**
By A. Heilmann
- 53 **Nanocrystalline Ceramics**
Synthesis and Structure
By M. Winterer
- 54 **Electronic Structure and Magnetism
of Complex Materials**
Editors: D.J. Singh and
D. A. Papaconstantopoulos
- 55 **Quasicrystals**
An Introduction to Structure,
Physical Properties and Applications
Editors: J.-B. Suck, M. Schreiber,
and P. Häussler
- 56 **SiO₂ in Si Microdevices**
By M. Itsumi
- 57 **Radiation Effects
in Advanced Semiconductor Materials
and Devices**
By C. Claeys and E. Simoen
- 58 **Functional Thin Films
and Functional Materials**
New Concepts and Technologies
Editor: D. Shi
- 59 **Dielectric Properties of Porous Media**
By S.O. Gladkov
- 60 **Organic Photovoltaics**
Concepts and Realization
Editors: C. Brabec, V. Dyakonov, J. Parisi
and N. Sariciftci
- 61 **Fatigue in Ferroelectric Ceramics
and Related Issues**
By D.C. Lupascu
- 62 **Epitaxy**
Physical Principles
and Technical Implementation
By M.A. Herman, W. Richter, and H. Sitter
- 63 **Fundamentals
of Ion-Irradiated Polymers**
By D. Fink
- 64 **Morphology Control of Materials
and Nanoparticles**
Advanced Materials Processing
and Characterization
Editors: Y. Waseda and A. Muramatsu
- 65 **Transport Processes
in Ion-Irradiated Polymers**
By D. Fink
- 66 **Multiphased Ceramic Materials**
Processing and Potential
Editors: W.-H. Tuan and J.-K. Guo
- 67 **Nondestructive
Materials Characterization**
With Applications to Aerospace Materials
Editors: N.G.H. Meyendorf, P.B. Nagy,
and S.I. Rokhlin
- 68 **Diffraction Analysis
of the Microstructure of Materials**
Editors: E.J. Mittemeijer and P. Scardi
- 69 **Chemical–Mechanical Planarization
of Semiconductor Materials**
Editor: M.R. Oliver
- 70 **Applications of the Isotopic Effect
in Solids**
By V.G. Plekhanov